

FOLDED SYNTHETIC PEPTIDES FOR BIOMEDICAL APPLICATIONS

EDITED BY: Alessandro Contini and Jutta Eichler
PUBLISHED IN: Frontiers in Chemistry





frontiers

Frontiers Copyright Statement

© Copyright 2007-2019 Frontiers Media SA. All rights reserved.

All content included on this site, such as text, graphics, logos, button icons, images, video/audio clips, downloads, data compilations and software, is the property of or is licensed to Frontiers Media SA ("Frontiers") or its licensees and/or subcontractors. The copyright in the text of individual articles is the property of their respective authors, subject to a license granted to Frontiers.

The compilation of articles constituting this e-book, wherever published, as well as the compilation of all other content on this site, is the exclusive property of Frontiers. For the conditions for downloading and copying of e-books from Frontiers' website, please see the Terms for Website Use. If purchasing Frontiers e-books from other websites or sources, the conditions of the website concerned apply.

Images and graphics not forming part of user-contributed materials may not be downloaded or copied without permission.

Individual articles may be downloaded and reproduced in accordance with the principles of the CC-BY licence subject to any copyright or other notices. They may not be re-sold as an e-book.

As author or other contributor you grant a CC-BY licence to others to reproduce your articles, including any graphics and third-party materials supplied by you, in accordance with the Conditions for Website Use and subject to any copyright notices which you include in connection with your articles and materials.

All copyright, and all rights therein, are protected by national and international copyright laws.

The above represents a summary only. For the full conditions see the Conditions for Authors and the Conditions for Website Use.

ISSN 1664-8714

ISBN 978-2-88963-045-5

DOI 10.3389/978-2-88963-045-5

About Frontiers

Frontiers is more than just an open-access publisher of scholarly articles: it is a pioneering approach to the world of academia, radically improving the way scholarly research is managed. The grand vision of Frontiers is a world where all people have an equal opportunity to seek, share and generate knowledge. Frontiers provides immediate and permanent online open access to all its publications, but this alone is not enough to realize our grand goals.

Frontiers Journal Series

The Frontiers Journal Series is a multi-tier and interdisciplinary set of open-access, online journals, promising a paradigm shift from the current review, selection and dissemination processes in academic publishing. All Frontiers journals are driven by researchers for researchers; therefore, they constitute a service to the scholarly community. At the same time, the Frontiers Journal Series operates on a revolutionary invention, the tiered publishing system, initially addressing specific communities of scholars, and gradually climbing up to broader public understanding, thus serving the interests of the lay society, too.

Dedication to Quality

Each Frontiers article is a landmark of the highest quality, thanks to genuinely collaborative interactions between authors and review editors, who include some of the world's best academicians. Research must be certified by peers before entering a stream of knowledge that may eventually reach the public - and shape society; therefore, Frontiers only applies the most rigorous and unbiased reviews.

Frontiers revolutionizes research publishing by freely delivering the most outstanding research, evaluated with no bias from both the academic and social point of view. By applying the most advanced information technologies, Frontiers is catapulting scholarly publishing into a new generation.

What are Frontiers Research Topics?

Frontiers Research Topics are very popular trademarks of the Frontiers Journals Series: they are collections of at least ten articles, all centered on a particular subject. With their unique mix of varied contributions from Original Research to Review Articles, Frontiers Research Topics unify the most influential researchers, the latest key findings and historical advances in a hot research area! Find out more on how to host your own Frontiers Research Topic or contribute to one as an author by contacting the Frontiers Editorial Office: researchtopics@frontiersin.org

FOLDED SYNTHETIC PEPTIDES FOR BIOMEDICAL APPLICATIONS

Topic Editors:

Alessandro Contini, Università degli Studi di Milano, Italy

Jutta Eichler, University of Erlangen–Nürnberg, Germany

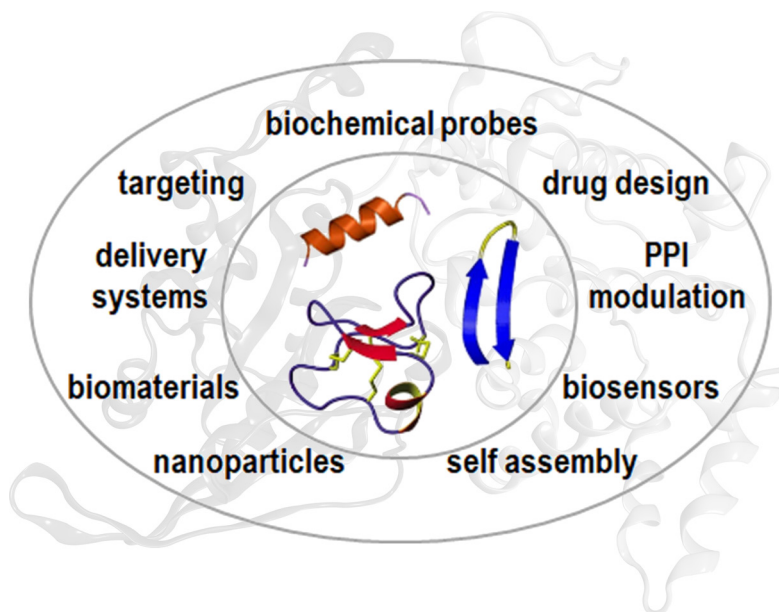


Image: Folded Synthetic Peptides in Biomedicine.

by Alessandro Contini and Jutta Eichler

Folded peptides - and peptide motifs within proteins - are abundant in living organisms, where they are essential for the biological activities of the peptides and proteins. During the past decades, much research has been dedicated to understanding the rules that govern peptide folding. Simultaneously, a range of strategies have been established for the conformational stabilization of bioactive peptides, as well as for the de novo design of peptides with defined secondary structures. These methods are either based on the chemical modification of the peptide backbone, such as cyclization and stapled peptides, or on the use of a range of non-proteinogenic amino acids that, in a defined sequential arrangement, induce secondary structures peptides. Such building blocks include D- and other non-proteinogenic amino acids, as well as beta- and gamma-amino acids.

This Research Topic comprises a collection of papers by an international group of 77 scientists with a background in synthetic, analytical, computational and medicinal chemistry, as well as in biochemistry and pharmacology. Their research is presented here in a total of 11 papers (8 original research reports and 3 reviews), covering diverse aspects of folded synthetic peptides. These studies include the preparation and characterization of new peptide monomers with interesting folding properties,

the synthesis and conformational analysis of non-natural peptides, as well as the use of folded peptidomimetics as molecular switches. Additionally, a range of biomedical applications, such as antimicrobial, anti-inflammatory, antiangiogenic and immune-stimulating activities, are also reported.

We hope this eBook will be a source of inspiration and knowledge for scientist in various disciplines related to folded peptides and their many applications, as well as for those who want to learn more about this fascinating field of research.

Citation: Contini, A., Eichler, J., eds. (2019). *Folded Synthetic Peptides for Biomedical Applications*. Lausanne: Frontiers Media. doi: 10.3389/978-2-88963-045-5

Table of Contents

- 06 Editorial: Folded Synthetic Peptides for Biomedical Applications**
Jutta Eichler and Alessandro Contini

CHAPTER 1

NON-NATURAL AMINO ACIDS AND PEPTIDOMIMETICS FOR PEPTIDE FOLDING

- 08 1,4-Disubstituted 1H-1,2,3-Triazole Containing Peptidotriazolamers: A New Class of Peptidomimetics With Interesting Foldamer Properties**
David C. Schröder, Oliver Kracker, Tanja Fröhr, Jerzy Góra, Michał Jewginski, Anke Nieß, Iris Antes, Rafał Latajka, Antoine Marion and Norbert Sewald
- 27 Bicyclic Pyrrolidine-Isoxazoline γ Amino Acid: A Constrained Scaffold for Stabilizing α -Turn Conformation in Isolated Peptides**
Francesco Oliva, Raffaella Bucci, Lucia Tamborini, Stefano Pieraccini, Andrea Pinto and Sara Pellegrino
- 37 Fluoro-Aryl Substituted $\alpha,\beta^{2,3}$ -Peptides in the Development of Foldameric Antiparallel β -Sheets: A Conformational Study**
Raffaella Bucci, Alessandro Contini, Francesca Clerici, Egle Maria Beccalli, Fernando Formaggio, Irene Maffucci, Sara Pellegrino and Maria Luisa Gelmi
- 48 A Photochromic Azobenzene Peptidomimetic of a β -Turn Model Peptide Structure as a Conformational Switch**
Francesca Nuti, Cristina Gellini, Maud Larregola, Lorenzo Squillantini, Riccardo Chelli, Pier Remigio Salvi, Olivier Lequin, Gangaetano Pietraperzia and Anna Maria Papini

CHAPTER 2

BIOPHARMACEUTICAL APPLICATIONS OF FOLDED SYNTHETIC PEPTIDES

- 57 Folded Synthetic Peptides and Other Molecules Targeting Outer Membrane Protein Complexes in Gram-Negative Bacteria**
John A. Robinson
- 68 Rational Design of Antiangiogenic Helical Oligopeptides Targeting the Vascular Endothelial Growth Factor Receptors**
Simone Zanella, Gianfranco Bocchini, Marta De Zotti, Daniela Arosio, Franca Marino, Stefano Raniolo, Luca Pignataro, Giovanni Sacco, Antonio Palleschi, Alvaro S. Siano, Umberto Piarulli, Laura Belvisi, Fernando Formaggio, Cesare Gennari and Lorenzo Stella
- 81 Multifunctional Scaffolds for Assembling Cancer-Targeting Immune Stimulators Using Chemoselective Ligations**
Anne C. Conibear, Karine Thewes, Nadja Groysbeck and Christian F. W. Becker
- 93 Probing Anti-inflammatory Properties Independent of NF- κ B Through Conformational Constraint of Peptide-Based Interleukin-1 Receptor Biased Ligands**
Azade Geranurimi, Colin W. H. Cheng, Christiane Quiniou, Tang Zhu, Xin Hou, José Carlos Rivera, Daniel J. St-Cyr, Kim Beauregard, Vadim Bernard-Gauthier, Sylvain Chemtob and William D. Lubell

CHAPTER 3

FOLDED SYNTHETIC PEPTIDES FOR THE DESIGN OF FUNCTIONAL BIOMATERIALS

113 *Self-Assembling Peptides as Extracellular Matrix Mimics to Influence Stem Cell's Fate*

Katharina S. Hellmund and Beate Kokschi

121 *Novel Materials From the Supramolecular Self-Assembly of Short Helical β^3 -Peptide Foldamers*

Ketav Kulkarni, Nathan Habila, Mark P. Del Borgo and Marie-Isabel Aguilar

133 *Enhancement of the Stability and Anti-DPPIV Activity of Hempseed Hydrolysates Through Self-Assembling Peptide-Based Hydrogels*

Carmen Lammi, Carlotta Bollati, Fabrizio Gelain, Anna Arnoldi and Raffaele Pugliese



Editorial: Folded Synthetic Peptides for Biomedical Applications

Jutta Eichler¹ and Alessandro Contini^{2*}

¹ Department of Chemistry and Pharmacy, University of Erlangen–Nürnberg, Erlangen, Germany, ² Dipartimento di Scienze Farmaceutiche, Sezione di Chimica Generale e Organica “Alessandro Marchesini”, Università Degli Studi di Milano, Milan, Italy

Keywords: foldamer, bioactive peptide, conformational analysis, molecular switches, hydrogels

Editorial on the Research Topic

Folded Synthetic Peptides for Biomedical Applications

Folded peptides—and peptide motifs within proteins—are abundant in living organisms, where they are essential for the biological activities of the peptides and proteins. During the past decades, numerous research programs have been dedicated to understanding the rules that govern peptide folding. Simultaneously, a range of strategies have been established for the conformational stabilization of bioactive peptides, as well as for the *de novo* design of peptides with defined secondary structures. These methods are either based on the chemical modification of the peptide backbone, such as cyclization and side chain stapling, or on the use of a range of non-proteinogenic amino acids that, in a defined sequential arrangement, induce secondary structures in peptides. Such building blocks include D- and other non-proteinogenic amino acids, as well as β - and γ -amino acids.

This Research Topic comprises a collection of papers by an international group of 77 scientists with a background in synthetic, analytical, computational, and medicinal chemistry, as well as in biochemistry and pharmacology. Their research is presented here in a total of 11 papers (8 original research reports and 3 reviews), covering diverse aspects of folded synthetic peptides. These studies include the preparation and characterization of new peptide monomers with interesting folding properties, the synthesis and conformational analysis of non-natural peptides, as well as the use of folded peptidomimetics as molecular switches. Additionally, a range of biomedical applications, such as antimicrobial, anti-inflammatory, antiangiogenic, and immune-stimulating activities, are also reported.

Examples for the use of non-peptidic chemical moieties or non-natural amino acids for the generation of folded synthetic peptides include the use of 1,4-disubstituted 1*H*-1,2,3-triazoles (Schröder et al.) to mimic the amide bond. This bioisosteric replacement led to peptidomimetics whose foldamer properties were confirmed by both instrumental analysis and computational simulations. Similarly, two enantiomers of a bicyclic pyrrolidine-isoxazoline γ -amino acid were used to prepare diastereoisomeric model peptides (Oliva et al.). NMR, FT-IR, circular dichroism and molecular modeling studies confirmed that the (+) enantiomer was able to stabilize an α -turn conformation. Conversely, Bucci et al. used syn- β 2,3-diarylamino acids in conjunction with S-alanine for the generation of foldameric antiparallel β -sheets. As in the study by Oliva et al., foldamer properties were confirmed here as well by combining instrumental analysis and theoretical calculations. Applications of synthetic peptides/peptidomimetics include their use as molecular switches, utilizing the light-triggered reversible shift from one conformation to another. In this context, Nuti et al. investigated the ability of a new photochromic azobenzene amino acid derivative to act as a conformational switch, when inserted into a model peptide.

OPEN ACCESS

Edited and reviewed by:

Tony D. James,
University of Bath, United Kingdom

*Correspondence:

Alessandro Contini
alessandro.contini@unimi.it

Specialty section:

This article was submitted to
Supramolecular Chemistry,
a section of the journal
Frontiers in Chemistry

Received: 14 May 2019

Accepted: 03 June 2019

Published: 20 June 2019

Citation:

Eichler J and Contini A (2019)
Editorial: Folded Synthetic Peptides
for Biomedical Applications.
Front. Chem. 7:448.
doi: 10.3389/fchem.2019.00448

A broad range of biopharmaceutical applications of synthetic peptides are also reported in this Research Topic. Recent applications of folded synthetic peptides targeting proteins of the outer membrane of gram-negative bacteria are reviewed by Robinson. In particular, synthetic β -hairpin mimetic peptides were found to interact with β -barrel and β -jellyroll domains in bacterial lipopolysaccharide transport and β -barrel folding machine complexes, thus representing a new frontier in the discovery of novel antimicrobial agents. Folded peptides are also reported to target tumor angiogenesis. Zanella et al. present oligopeptides, designed by structural analysis and computational calculations, where $C\alpha, \alpha$ -disubstituted amino acids are exploited to stabilize the helical conformation that is essential to bind to the VEGF receptor at nanomolar concentration. Synthetic peptides as cancer-targeting immune system engagers (ISERs) are reported by Conibear et al. These molecule are generated using a range of chemoselective ligations, including copper-catalyzed azide-alkyne “click,” oxime, maleimide, and native chemical ligations. Furthermore, anti-inflammatory peptides targeting the interleukin-1 receptor (IL-1R) are reported by Geranurimi et al. The authors describe the structure-activity relationships of 12 peptides, in which different configurations of the α -amino- γ -lactam and β -hydroxy- α -amino- γ -lactam moieties were used to conformationally constrain an IL-1R peptide ligand.

This Research Topic also presents articles on the use of folded synthetic peptides for the design of functional biomaterials. Hellmund and Kokscho review the recent literature on the use of self-assembling peptides as mimics of the extracellular matrix. This is illustrated by peptide- and protein-based biomaterials that are able to support proliferation and differentiation of stem cells, demonstrating great potential of these peptides as tools in regenerative medicine. Applications of *N*-acetyl- β 3-peptides

to obtain innovative bio- and nanomaterials by supramolecular self-assembly are reviewed by Kulkarni et al. Compared to other organic and inorganic self-assembled systems, these foldamers show advantages in terms of biocompatibility, toxicity and functionalization potential. Last but not least, Lammi et al. report a strategy to increase the stability and anti-diabetic properties of hempseed protein hydrolysates. This was achieved through encapsulation of hempseed hydrolysates into ionic self-complementary RADA16 peptide-based hydrogels. This study also evaluated the synergistic activity of RADA16-hemp hydrogels and sitagliptin, an orally available DPPIV inhibitor.

As a collection, the papers of this Research Topic demonstrate the broad impact of folded synthetic peptides on various fields of biological and biomedical research. It can be expected that research on folded synthetic peptides will continue to result in applications in medicinal chemistry and drug design, as well as the design of novel biomaterials.

AUTHOR CONTRIBUTIONS

AC and JE edited the articles of this research topic and wrote the editorial.

Conflict of Interest Statement: The authors declare that the research was conducted in the absence of any commercial or financial relationships that could be construed as a potential conflict of interest.

Copyright © 2019 Eichler and Contini. This is an open-access article distributed under the terms of the Creative Commons Attribution License (CC BY). The use, distribution or reproduction in other forums is permitted, provided the original author(s) and the copyright owner(s) are credited and that the original publication in this journal is cited, in accordance with accepted academic practice. No use, distribution or reproduction is permitted which does not comply with these terms.



1,4-Disubstituted 1*H*-1,2,3-Triazole Containing Peptidotriazolamers: A New Class of Peptidomimetics With Interesting Foldamer Properties

David C. Schröder¹, Oliver Kracker¹, Tanja Fröhr¹, Jerzy Góra^{1,2}, Michał Jewginski², Anke Nieß¹, Iris Antes³, Rafał Latajka², Antoine Marion^{3,4*} and Norbert Sewald^{1*}

¹ Organic and Bioorganic Chemistry, Department of Chemistry, Bielefeld University, Bielefeld, Germany, ² Department of Bioorganic Chemistry, Wrocław University of Science and Technology, Wrocław, Poland, ³ Center for Integrated Protein Science, TUM School of Life Sciences, TU Munich, Freising, Germany, ⁴ Department of Chemistry, Middle East Technical University, Ankara, Turkey

OPEN ACCESS

Edited by:

Jutta Eichler,
University of Erlangen Nuremberg,
Germany

Reviewed by:

Nicolas Inguibert,
Université de Perpignan Via Domitia,
France
Yuji Nishiuchi,
GlyTech, Inc., Japan
Norbert Schaschke,
Hochschule Aalen, Germany

*Correspondence:

Norbert Sewald
norbert.sewald@uni-bielefeld.de
Antoine Marion
amarion@metu.edu.tr

Specialty section:

This article was submitted to
Chemical Biology,
a section of the journal
Frontiers in Chemistry

Received: 30 November 2018

Accepted: 01 March 2019

Published: 26 March 2019

Citation:

Schröder DC, Kracker O, Fröhr T, Góra J, Jewginski M, Nieß A, Antes I, Latajka R, Marion A and Sewald N (2019) 1,4-Disubstituted 1*H*-1,2,3-Triazole Containing Peptidotriazolamers: A New Class of Peptidomimetics With Interesting Foldamer Properties. *Front. Chem.* 7:155. doi: 10.3389/fchem.2019.00155

Peptidotriazolamers are hybrid foldamers with features of peptides and triazolamers, containing alternation of amide bonds and 1,4-disubstituted 1*H*-1,2,3-triazoles with conservation of the amino acid side chains. We report on the synthesis of a new class of peptidomimetics, containing 1,4-disubstituted 1*H*-1,2,3-triazoles in alternation with amide bonds and the elucidation of their conformational properties in solution. Based on enantiomerically pure propargylamines bearing the stereogenic center in the propargylic position and α -azido esters, building blocks were obtained by copper-catalyzed azide-alkyne cycloaddition. With these building blocks the peptidotriazolamers were readily available by solution phase synthesis. A panel of homo- and heterochiral tetramers, hexamers, and heptamers was synthesized and the heptamer Boc-Ala-Val- Ψ [4Tz]Phe-Leu Ψ [4Tz]Phe-Leu Ψ [4Tz]Val-OAll as well as an heterochiral and a Gly-containing equivalent were structurally characterized by NMR-based molecular dynamics simulations using a specifically tailored force field to determine their conformational and solvation properties. All three variants adopt a compact folded conformation in DMSO as well as in water. In addition to the heptamers we predicted the conformational behavior of similar longer oligomers i.e., Boc-Ala-(Ala Ψ [4Tz]Ala)₆-OAll as well as Boc-Ala-(D-Ala Ψ [4Tz]Ala)₆-OAll and Boc-Ala-(Gly Ψ [4Tz]Ala)₆-OAll. Our calculations predict a clear secondary structure of the first two molecules in DMSO that collapses in water due to the hydrophobic character of the side chains. The homochiral compound folds into a regular helical structure and the heterochiral one shows a twisted “S”-shape, while the Gly variant exhibits no clear secondary structure.

Keywords: peptidotriazolamers, 1, 4-disubstituted 1*H*-1, 2, 3-triazole, peptide bond isoster, foldamer, molecular dynamic simulations

INTRODUCTION

Since the discovery of the Cu^I catalyzed azide-alkyne cycloaddition (CuAAC) by the groups of Meldal (Tornøe et al., 2002) and Sharpless (Rostovtsev et al., 2002), this so-called “click”-reaction proved to be suitable for a broad number of applications in bioorganic and pharmaceutical chemistry (Kolb and Sharpless, 2003; Bock et al., 2006a;

Angell and Burgess, 2007; Gil et al., 2007; Moses and Moorhouse, 2007; Hein et al., 2008; Tron et al., 2008; Nwe and Brechbiel, 2009) The CuAAC is compatible with most functional groups present in biomolecules and the 1,4-disubstituted 1*H*-1,2,3-triazole obtained as reaction product is metabolically inert (Kolb and Sharpless, 2003). Size and dipole moment of the 1,4-disubstituted triazole ring are larger compared to a *trans*-amide bond (Kolb and Sharpless, 2003), but overall physicochemical properties are similar enough to enable these triazoles to act as *trans*-amide mimetics (**Figure 1**; Brik et al., 2003, 2005; Horne et al., 2004, 2009; Angell and Burgess, 2005, 2007; van Maarseveen et al., 2005; Bock et al., 2006b, 2007; Wang et al., 2006; Appendino et al., 2007; Kim et al., 2007; Lee et al., 2007; Beierle et al., 2009).

In 2005 the counterpart of the CuAAC, the ruthenium(II)-catalyzed azide-alkyne-cycloaddition (RuAAC), yielding selectively 1,5-disubstituted 1*H*-1,2,3-triazoles, was presented by Zhang et al. (2005). The latter can act as *cis*-amide mimetic (**Figure 1**; Zhang et al., 2005; Pedersen and Abell, 2011).

Several amide bonds within biologically active substances have already been replaced by triazoles. The bio-isosterism has been exemplified by triazole analogs of a matrix metalloprotease inhibitor (Wang et al., 2006), of the immune-stimulating natural compound α -galactosylceramide (Kim et al., 2007; Lee et al., 2007), and of capsaicin in its role as agonist of the vanilloid-receptor TRPV1 (Appendino et al., 2007). Small bivalent peptidomimetics based on triazole formation from amino acid-derived propargylamines and amino acid-derived α -azido acids were shown to adopt turn-like conformations and serve as ligands for the receptor TrkC (Chen et al., 2009).

Further examples are triazole analogs of the peptidic tyrosinase inhibitor *cyclo*-[Pro-Tyr-Pro-Val] (Bock et al., 2006b, 2007), of the histone deacetylase inhibitor apicidin (Horne et al., 2009), the antimitotic cyclodepsipeptide cryptophycin (Nahrwold et al., 2010) and of peptides containing the pharmacophoric residues of somatostatin (Beierle et al., 2009). Moreover, X-ray crystal structure analysis revealed that the triazole ring within an analog of the HIV-1-protease inhibitor amprenavir interacts with the enzyme in the same way as an amide bond in the parent compound (Brik et al., 2003, 2005). Recently Ben Haj Salah et al. gave a good overview on the topic of substituting single or isolated amide moieties by 1*H*-1,2,3-triazoles and showed the influence of isolated triazole-amide-bond substitution as well as two cases with multiple substitutions containing a motif of two triazole replacements separated by one amide bond in two antimicrobial peptides with helical conformations (Ben Haj Salah et al., 2018).

Triazolamers, oligomers of 1,4-disubstituted triazoles connect a series of triazole rings by single C₁ unit that, at the same time, is a stereogenic center (Angelo and Arora, 2005, 2007; Jochim et al., 2009). The CuAAC can be performed either in solution or on solid phase to provide the 1,4-disubstituted triazoles. Best results are obtained in a sequential protocol when using triflic azide and Cu(II) for the diazo transfer, where the copper was subsequently reduced by ascorbate to bring about the CuAAC (**Figure 2**; Angelo and Arora, 2005; Beckmann and Wittmann, 2007).

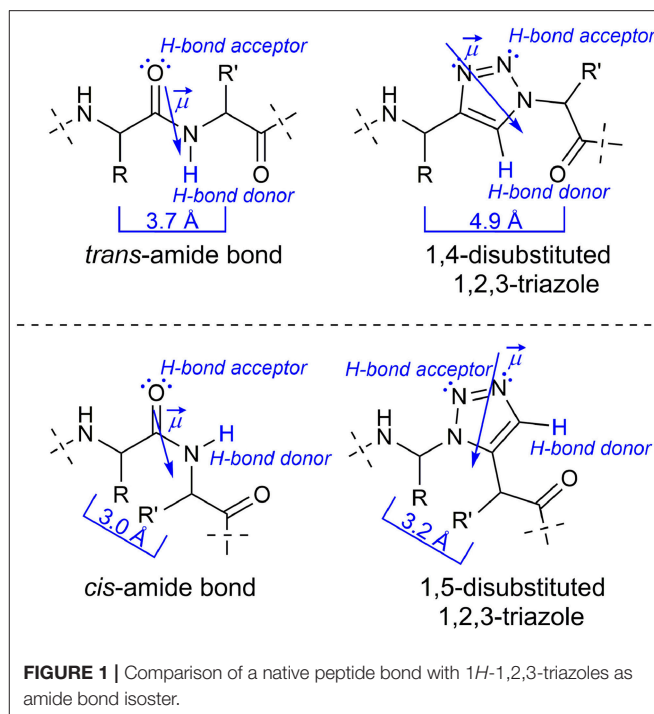


FIGURE 1 | Comparison of a native peptide bond with 1*H*-1,2,3-triazoles as amide bond isosteres.

Since the triazole ring is characterized by a large dipole moment it might stabilize discrete conformations by dipole-dipole interactions. The Arora group investigated relatively short oligomers and found out that they are likely to adopt a zigzag conformation reminiscent of β -strands found in peptides. Indeed, the dipole-dipole-interaction of neighboring triazole moieties seems to crucially influence the overall conformation in polar solvents (Angelo and Arora, 2005).

The zigzag triazolamer structure also resembles the oligopyrrolinones described by Smith and Hirschmann (Smith et al., 1992). The axial C ^{β} to C ^{β} distance between the *i* and *i*+2 side chain residues in peptide β -strands is 7.2 Å; this distance is roughly 7.9 Å in the zigzag triazolamer. The C ^{β} to C ^{β} distances in adjacent residues are 5.5 Å in peptide β -strands and a little longer (6.8 Å) in the triazolamer (Angelo and Arora, 2005).

In addition, the group of L. Mindt investigated besides the substitution of isolated peptide bonds by 1,4-disubstituted triazoles also the replacement of multiple adjacent peptide bonds attempting to improve the tumor targeting qualities of bombesin, an amphibious analog of the gastrin releasing peptide (Valverde et al., 2015).

Peptidotriazole foldamers represent repetitive hybrid structures of peptides, where e.g., every second amide bond is being replaced by a triazole. Such short triazole-based peptide analogs have been obtained from achiral propargylamines and α -amino acid derived α -azido carboxylic acids (**Figure 3**, left). They were found to self-dimerize and act as organogelators (Ke et al., 2012).

In a similar fashion, the Hecht group synthesized bifunctional monomers from amino acid-derived α -azido acids and propargylamine for “click”-polyaddition (**Figure 3**, right; Hartwig and Hecht, 2010).

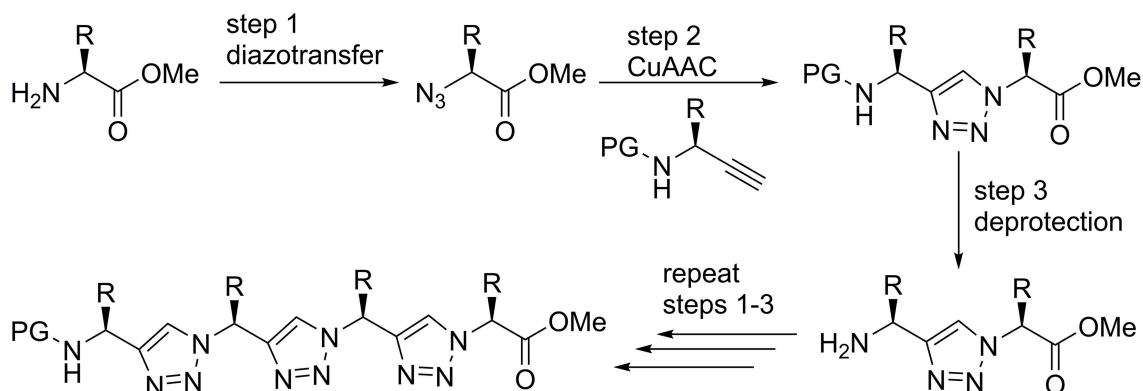


FIGURE 2 | Solution phase synthesis of triazolamers according to Angelo and Arora (2005).

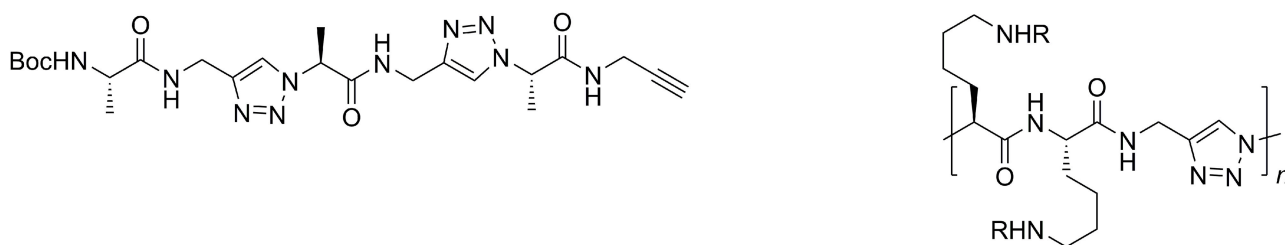


FIGURE 3 | Triazole-based peptidomimetic with unsubstituted propargylamines (left) and "Click"-polyaddition oligomer; bifunctional monomers from amino acid-derived α -azido acids and unsubstituted propargylamine (right).

In accordance with recommendations for nomenclature of amide bond replacements we will use Ψ [4Tz] in this publication as a placeholder of a 1,4-disubstituted 1*H*-1,2,3-triazole—i.e., a dipeptide H-Xaa-Yaa-OH is replaced by H-Xaa Ψ [4Tz]Yaa-OH. In a similar fashion Ψ [5Tz] stands for a 1,5-disubstituted 1*H*-1,2,3-triazole replacement in the same orientation.

Recently we published on 1,5-disubstituted 1,2,3-triazole containing peptidotriazolamers (Kracker et al., 2018). Beside the robust synthetic route it was shown that the homochiral and heterochiral oligomers adopt versatile foldamer conformations. Furthermore, the solid state conformation of the homochiral tetramer Boc-Val Ψ [5Tz]Ala-Leu Ψ [5Tz]Val-OBzl was in an excellent agreement with an *in silico* conformational analysis, which was performed using a specifically truncated TZLff molecular mechanics force-field parametrization for 1,4- and 1,5-disubstituted peptidotriazolamers that we recently established (Marion et al., 2018).

For the synthesis of the chiral propargylamines, we used the methodology previously described by Ellman et al. using (*R*)- or (*S*)-*tert*-butylsulfinamide as a chiral auxiliary (Patterson and Ellman, 2006). According to the protocol of Ellman et al. the chiral *tert*-butylsulfinamide is prepared by enantioselective oxidation of di-*tert*-butyl disulfide with a chiral catalyst, followed by reaction with lithiumamide (Weix and Ellman, 2005). After formation of the imine using the auxiliary and an aldehyde as starting material, the diastereoselective synthesis of propargylamines is possible by reaction of the *N*-sulfinyl

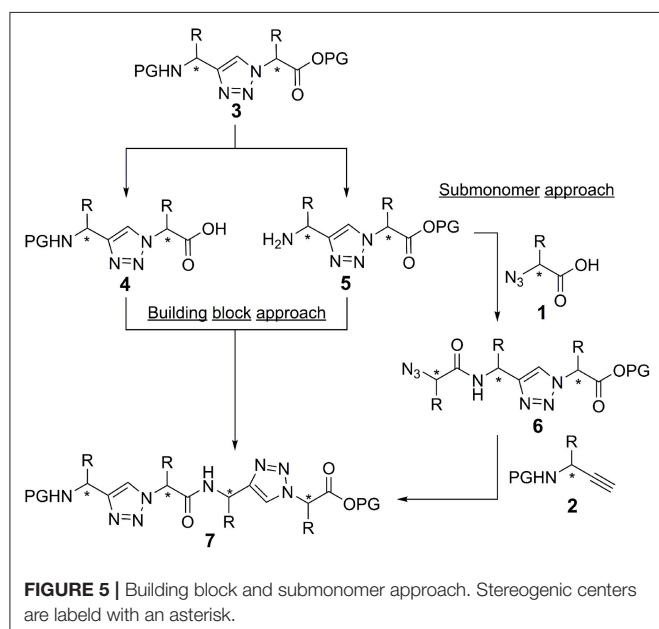
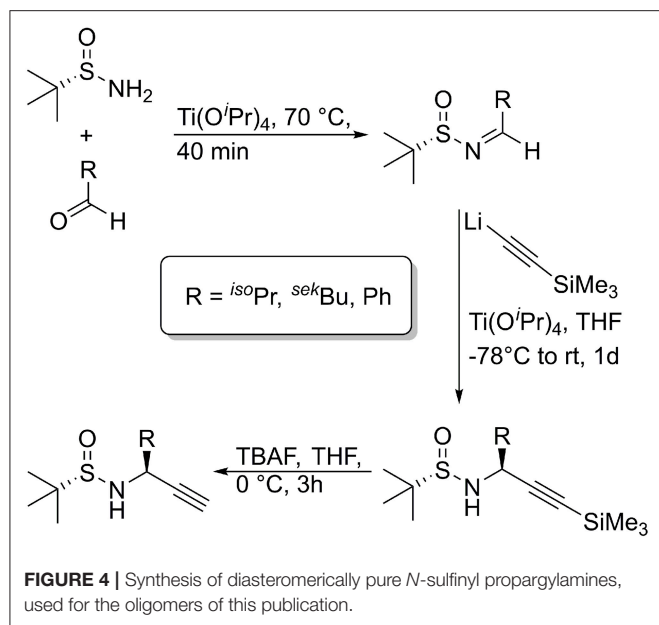
imine with lithium trimethylsilylacetylide (Wünsch et al., 2017). Cleavage of the trimethylsilyl protecting group is achieved with TBAF or AgNO₃ to provide the *N*-sulfinylpropargylamines with a terminal alkyne moiety. Numerous *tert*-butylsulfinyl protected propargylamines [(*S*)- or (*R*)-Bus-Xaa \equiv CH] have been prepared in our group, bearing natural amino acid side chains as well as non-amino acid like side chains (Figure 4; Wünsch et al., 2017).

RESULTS AND DISCUSSION

Synthesis

Inspired by the Arora triazolamers, we embarked on a project directed toward the synthesis and characterization of peptidotriazole foldamers, where both components, the propargylamine and the α -azido carboxylic acids are chiral. The chiral propargylamines were synthesized via the Ellman strategy and the α -azidocarboxylic acids from commercially available α -amino acids by diazotransfer (Yan et al., 2005). Several α -azidocarboxylic acids as well as the corresponding amino acid allyl esters can be synthesized under mild reaction conditions with good to very good yields.

In principle, there are two strategies for the synthesis of peptidotriazole foldamers: the building block approach (Figure 5), where the triazole is formed from the propargylamine and the azide by CuAAC and then coupled by amide bond formation, and the submonomer approach (Figure 5), where first



the α -azido carboxylic acid is coupled and then the *N*-protected propargylamine is reacted by CuAAC.

In the case of activation of the free acid of the triazole-building block **4** (Val side chain), epimerization was observed even upon using TBTU/HOBt/DIPEA or HATU/HOAt/DIPEA as the coupling reagents. Therefore, the submonomer approach was initially chosen for the synthesis of the peptidotriazole foldamers. In this case the α -azido carboxylic acid can be activated with e.g., HATU/HOAt without any epimerization. Eventually it has been shown, that a carbodiimide-mediated preactivation in DCM, without the use of a base, and subsequent coupling with the use of 2,4,6-collidine, effectively prevents epimerization during the coupling of the free acid of the

triazole-building block **4** (Kracker et al., 2018). K Ben Haj Salah et al. also used the building block approach for their synthesis of peptaibols analogs containing Aib Ψ [4Tz]-Xaa dipeptides (Ben Haj Salah et al., 2015).

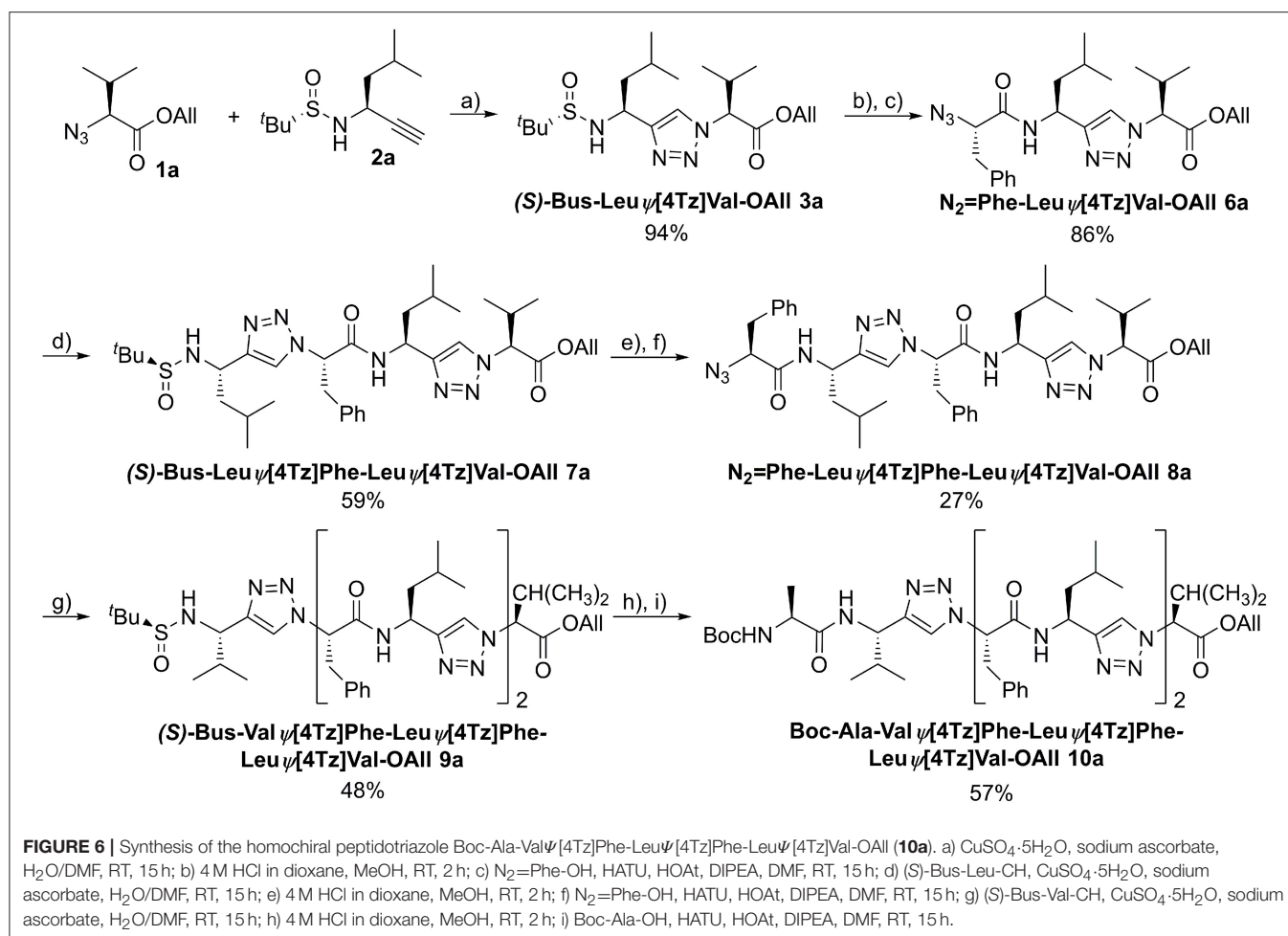
The C-terminal component was protected as allyl ester and the propargylamines were employed as sulfinamide as well as Boc protected derivatives. The *tert*-butylsulfinyl group (Bus) is acid-labile and can be cleaved e.g., by treatment with 4 M HCl in dioxane at room temperature. In addition, it was reported to be cleavable with 50% trifluoroacetic acid in CH₂Cl₂ (Lee and Silverman, 2000).

An example of the peptidotriazole foldamer synthesis is given in **Figure 6**. Triazole formation was achieved by CuAAC in the presence of 0.5 eq. of CuSO₄·5 H₂O and 1 eq. sodium ascorbate in DMF/water mixtures. Lower amounts of copper salt and reductant led to incomplete conversion, as had been previously observed by others (Angelo and Arora, 2005).

Several homo- (**7a**, **9a**, **10a**) and heterochiral (**7b**, **9b**, **10b**) peptidotriazole foldamers as well as one where every second amino acid side chain is exchanged by a hydrogen atom (**7c**, **9c**, **10c**), have been obtained (**Figure 7**). Some peptidotriazole foldamers with *N*-terminal Bus group that had been purified by HPLC with an acetonitrile/water/TFA gradient slowly decomposed in DMSO solution upon standing. Notably, this instability also depends on the sequence. After cleavage of the Bus group and acylation e.g., with Boc-Ala the resulting heptamers were completely stable. The *tert*-butylsulfinyl group had been suggested as a substitute for the Boc group. However, its stability, in particular at elevated temperatures, is not sufficient to qualify Bus as a versatile protecting group. According to the rearrangement suggested for the Ellman auxiliary by Arava et al. (2011) we found out that a fragment (S) or (R)-BusXaa Ψ [4Tz]Yaa-OAll rearranges with a second equivalent to form (S) or (R)-H-Xaa Ψ [4Tz]Yaa-OAll and (tert-Bu-SO₂)(tert-Bu-S)Xaa Ψ [4Tz]Yaa-OAll.

Conformational Analysis

We analyzed the conformational preferences of 1,4-disubstituted peptidotriazolamers in solution by means of CD spectroscopy and molecular dynamics (MD) simulations based on the specific molecular mechanics force-field parameterization TZLff (Marion et al., 2018). As representative molecules, we selected compounds **10a**, **10b**, and **10c** (further referred to as homochiral, heterochiral, and homochiral*, respectively) to investigate the effect of chirality and of the introduction of glycine-like moieties on the conformational preferences of the peptide mimetics. Schematic representations of the three molecules are given in **Figure 8**. Therein, we additionally indicate our definition for the backbone conformational degrees of freedom for peptidotriazolamers as the ϕ and ψ torsion angles. In the following, ϕ and ψ notations are used indifferently whether it refers to a standard amino acid or to a triazole-based derivative (Marion et al., 2018).



CD Spectroscopy

CD spectra were recorded to get a first experimental insight into the conformational properties of the three oligomer types. It should be emphasized that the solvent used for the measurements is acetonitrile since DMSO is not applicable due to its strong absorbance below 270 nm. It becomes clear (**Figure 9**) that the different types of peptidotriazole heptamers have characteristic CD signatures. The heterochiral compound **10b** has a positive CD below 210 nm, while the CD remains negative for the homochiral all-(S)-configured **10a**. The CD spectrum of **10c** is somewhat intermediate, with a sign inversion at about 202 nm.

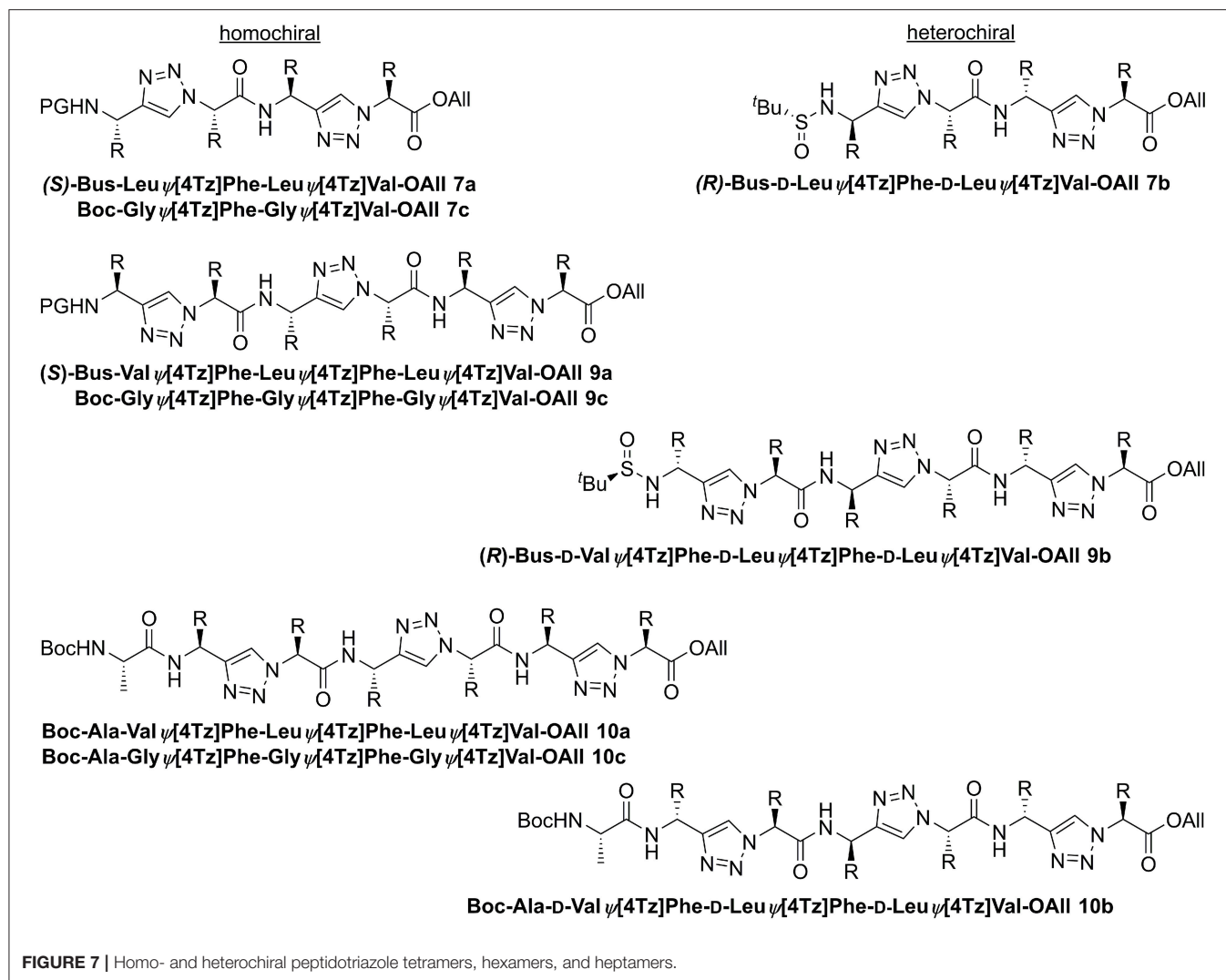
Molecular Dynamics

For each of the three representative molecules (**10a-c**), we performed one simulation in DMSO (i.e., the solvent used for NMR measurements) and one simulation in water, as representative of a more biologically relevant environment. The simulations in solution were started using an initial structure derived from an extensive, simulated annealing-based sampling in gas phase during which NMR-derived interproton distance restraints were applied (see section Methodology for details).

Monitoring of the backbone root mean square deviations (RMSD) along the trajectories of each molecule showed that

most compounds adopt one main stable conformation in both solvents, with standard deviations ranging from 0.18 to 0.79 Å over the whole trajectory for all six MD trajectories (**Supplementary Figure 10**). Repetitive bumps in the RMSD time series of **10c** in water show that the molecules adopt at least two stable conformations in water and that our MD simulations sampled them appropriately. Radius of gyration (ROG) time series indicate similar results for all compounds with mean values ranging from 3.5 to 4.0 Å with minor amplitudes of fluctuations after 100 ns (**Supplementary Figure 11**). Such small values for the ROG of the 1,4-disubstituted peptidotriazolamers are indicative for a compact folded conformation for all three variants. All the time series indicate that the simulations reached convergence after 100 ns at most. We therefore considered the last 100 ns as converged and used this part in each simulation for the following analysis.

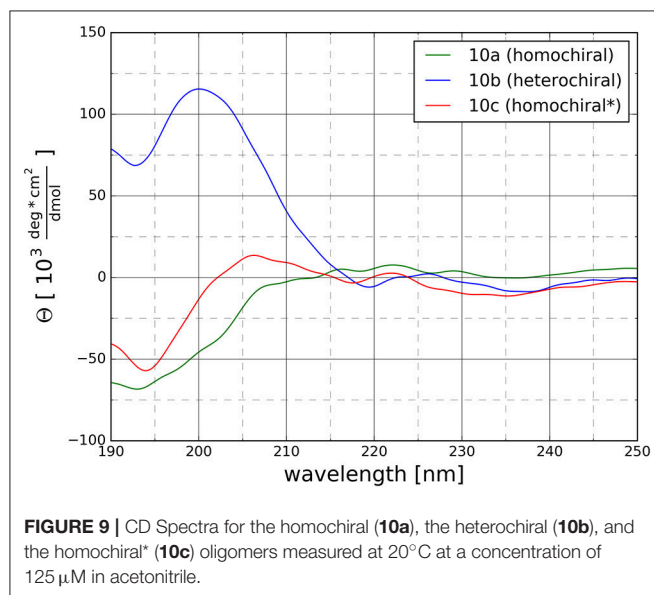
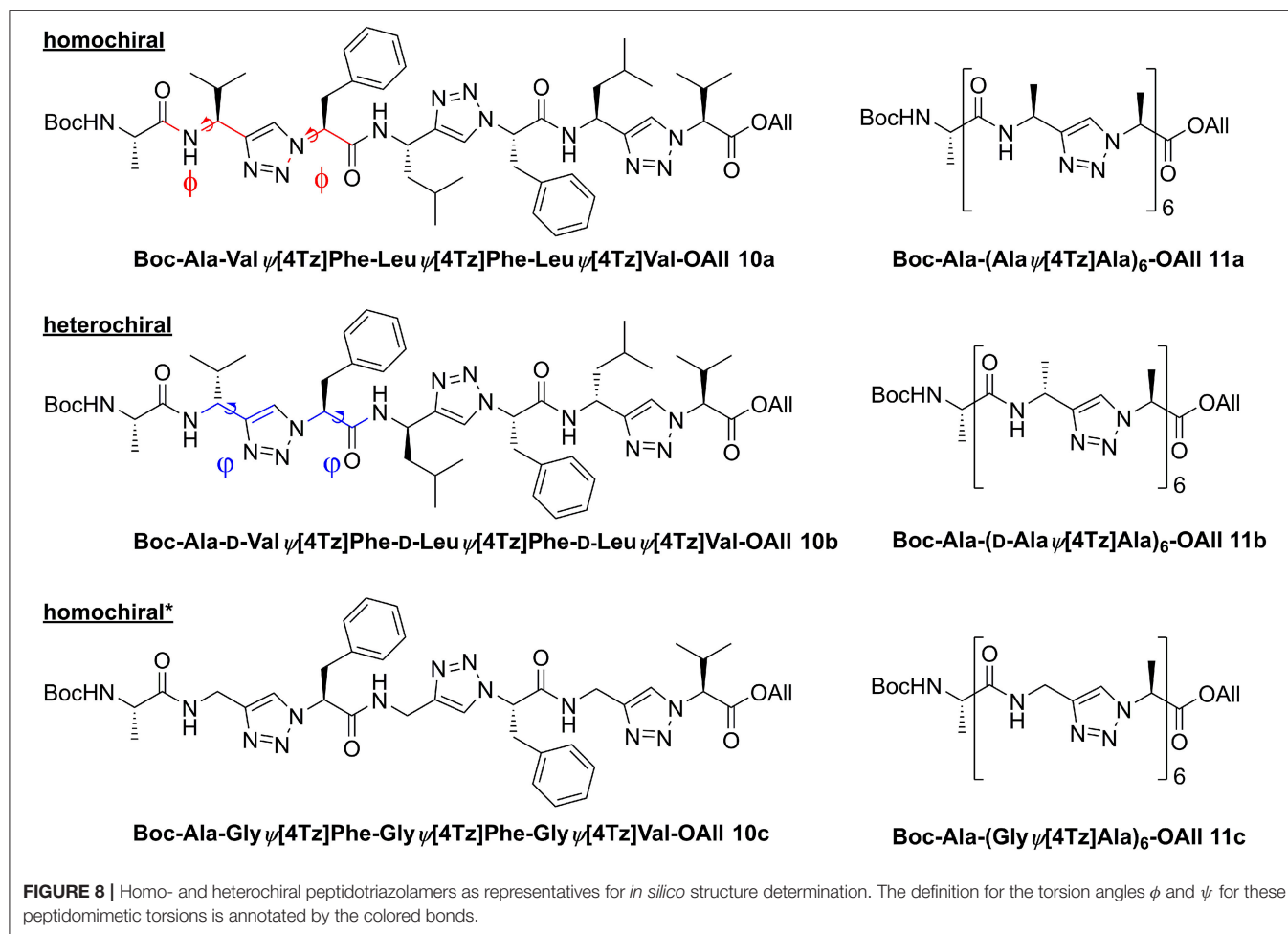
The distribution of ϕ/ψ backbone torsional degrees of freedom is depicted in **Figure 10** for each molecule in both solvents. Although the plots resemble Ramachandran distributions, a direct comparison with known patterns for standard peptides is not straightforward due to the introduction of the triazole moieties in the sequence. Nevertheless, the plots give a qualitative picture of the differences and similarities



between the three variants considered in this analysis and of the effect of the solvent polarity on their conformational preferences. Overall, all three molecules appear to have their own unique signature in terms of distribution of backbone torsion angles. While distribution maxima depict distinct patterns for homo- and heterochiral, the glycine-containing derivative (homo-chiral*) shows features of both parent oligomers. The polarity of the solvent appears to have little to no effect on the ϕ/ψ distribution for all three molecules.

Clustering based on the backbone RMSD of the oligomers for the second half of the simulations in DMSO and in water resulted in the following populations for the main structural clusters: 94 and 52% for the homo-chiral molecule in DMSO and in water, respectively, 71 and 59% for the heterochiral, and 60 and 76% for the homo-chiral* compound. For the heterochiral compound in water, a second structural cluster was found with a population of 40% that differed from the main representative structure with a backbone RMSD value of 0.54 Å. The differences were localized on the flexible

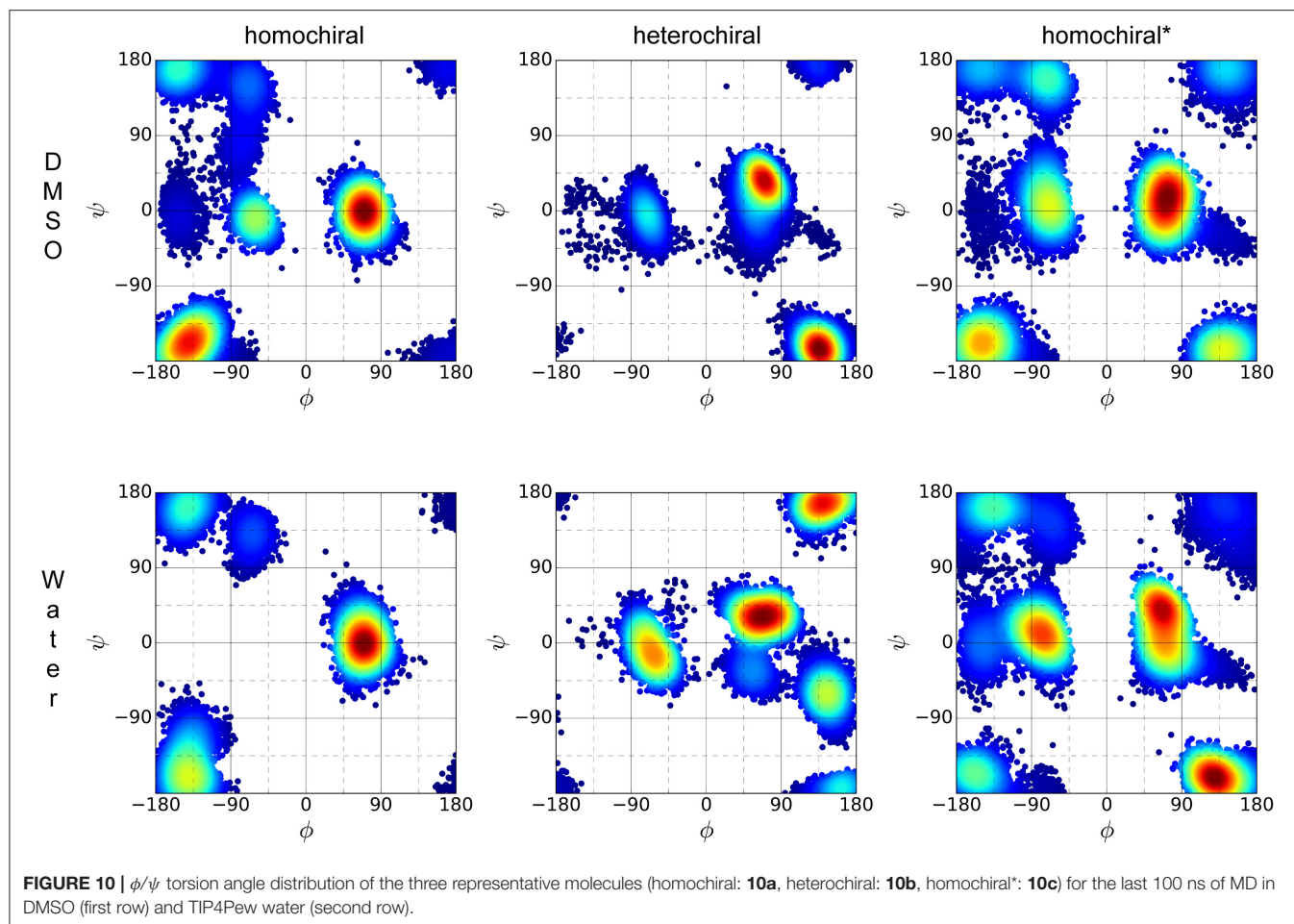
terminal residues and both structures can, therefore, be formally assigned to the same conformation with a total population of 99%, as confirmed by the rather flat RMSD and radius of gyration time-series (**Supplementary Figures 10, 11**). Similarly, the homo-chiral* variant in DMSO results in a second main cluster with a trajectory fraction of 21% and a backbone RMSD value of 0.81 Å, primarily caused by both flexible ends pointing in orthogonal direction. Thus, the two main clusters can be joined with a combined trajectory fraction of 81%. Such large populations are consistent with the rigid character of the peptidomimetics already observed from the RMSD time series. To a given extent, the homo-chiral* molecule appears to be slightly more flexible than the others when plunged in water. The representative structure for the main cluster of each simulation is depicted in the upper panel of **Figure 11**. In general, all oligomers considered in this analysis fold with a helically twisted conformation. Consistently with our observations thus far, the solvent has little to no effect on the conformation of the oligomers. The values of backbone torsional angles for the



representative structure in DMSO and in water are listed in **Table 1**. The lower panel of **Figure 11** shows a direct comparison of the backbone of the homochiral and homochiral* variants,

the heterochiral and homochiral* ones, as well as a comparison between homo- and heterochiral ones. The figure illustrates that the homochiral and homochiral* compounds fold into a nearly identical conformation in DMSO and in water, while the heterochiral molecule adopts a slightly different orientation of the triazole rings in DMSO and a significantly yet still compact conformation in water. Taking the homochiral molecule as reference, the homochiral* and heterochiral compounds have a backbone RMSD value of 0.45 and 1.97 in DMSO, respectively, and of 1.27 and 3.61 Å in water.

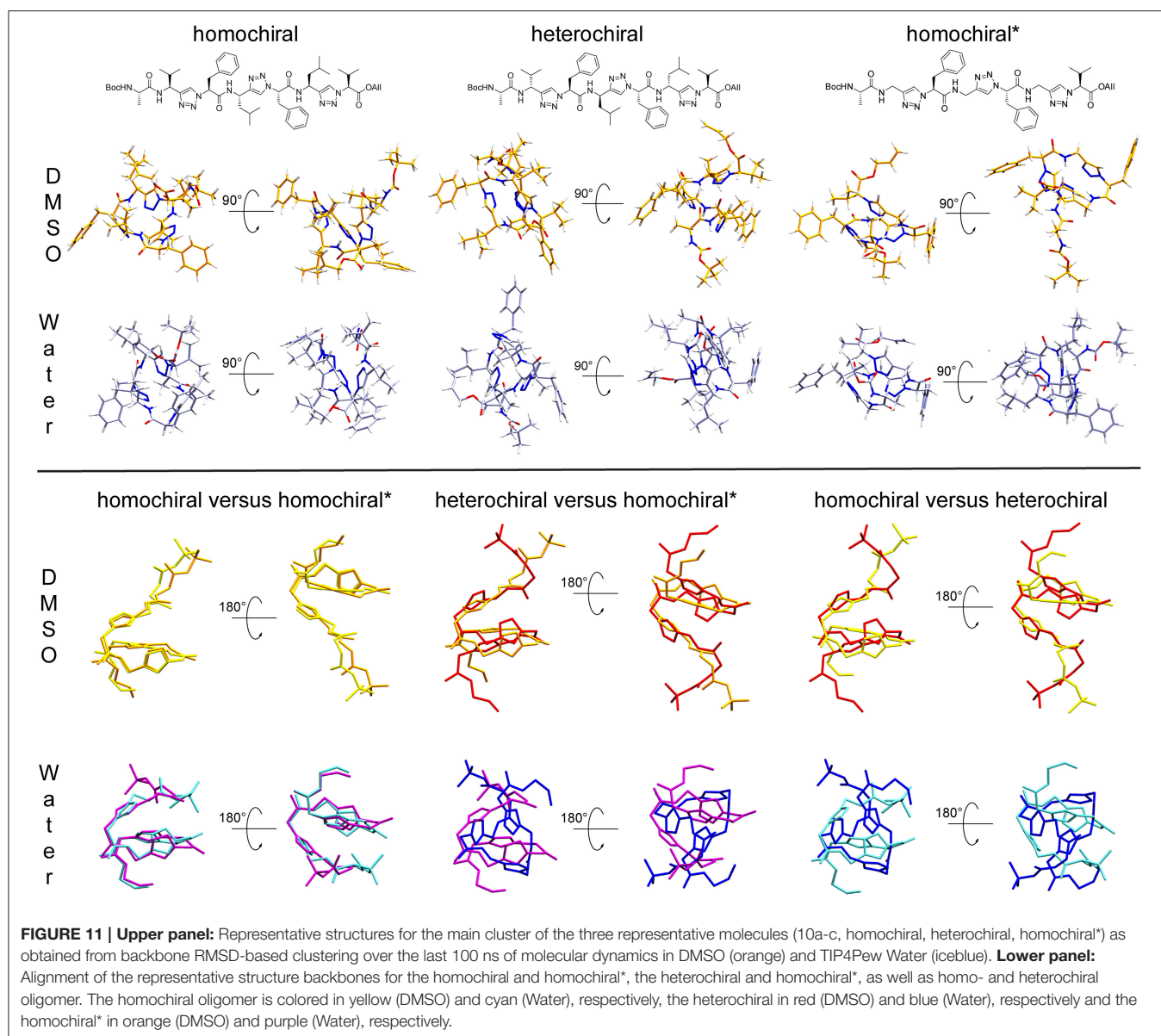
We further analyzed the potential solvation properties of the three oligomers in water by calculating the radial distribution functions (RDF) around key chemical groups. The complete results are available as supporting information (**Supplementary Figures 12–14**). In general, the RDFs show that the molecules are poorly solvated in water, which is expected regarding the highly hydrophobic character of the side chains. Only specific groups such as the backbone carbonyl moiety show stable interactions with one water molecule over the whole simulation with distances characteristic of hydrogen bonds. Such interactions are conserved over all three molecules, as illustrated by the RDF for the carbonyl group of the first alanine amino acid in **Figure 12**. Therein, we observe a sharp peak at about 1.8 Å, but no further structure formation at larger distances



due to the hydrophobic character of the rest of the molecule. Among all the potential hydrogen bond donor/acceptor groups in the peptidomimetic considered in this work, we noted only few significant differences. (i) A shallow peak is present at short distances in the RDF of the nitrogen atom (N3) of the first triazole ring for both the homochiral and the homochiral* molecules. The integration of this peak returns a value corresponding to a sporadic interaction with a water molecule occurring for about a third of the simulation time only. This weak interaction, however, is totally absent in the case of the heterochiral compound. (ii) Similar observations can be made regarding the hydrogen of that same triazole ring, which is involved in a weak interaction with water in two of the three molecules. As opposed to (i), however, this interaction is absent for the homochiral molecule and present for the two others. We also notice that, considering the sharpness of the peak, this interaction is tighter in the case of the heterochiral molecules than it is for the homochiral* one. (iii) Comparison of the RDF around the amide nitrogen of the 8th residue (i.e., Leu or Gly) indicates that this site is slightly more solvent accessible in the case of the heterochiral compound than it is for the two other molecules. These differences are due to a slightly better orientation of the corresponding chemical groups favoring interactions with the solvent and potentially

with other polar compounds in different environments. Although these interactions with water are somewhat weak for these oligomers, the differences that we observed are indicative of potential interaction sites that could discriminate one molecule from another in a hypothetical protein environment.

Overall our conformational analysis revealed only little differences between the three variants of the oligomers under investigation. All three adopt a compact folded conformation in DMSO. The homochiral compound (**10a**) and the glycine containing analog (**10c**) adopt nearly identical conformations in DMSO, which tends to correlate with the observation of a similar pattern on the CD spectra for these two molecules. Considering the high hydrophobic character of the side chains, it is not surprising that the molecules remain folded in water in order to minimize the interaction surface area with the polar environment. This observation that the chirality of the different stereocenters has no significant impact on the conformation of the 1,4-disubstituted peptidotriazolamers is in contrast with our results for the 1,5-disubstituted counterpart (Kracker et al., 2018). There we identified that changes in the chirality of the α -carbons can induce drastic changes in the conformation of the molecules, i.e., while the homochiral hexapeptidotriazolamer Boc-Ala Ψ [5Tz]Phe-Val Ψ [5Tz]Ala-Leu- Ψ [5Tz]Val-OBzl formed



a compact β -turn-like structure, the heterochiral equivalent was observed and predicted in an extended polyproline I-like conformation (Ke et al., 2012).

To further characterize the conformational properties of 1,4-disubstituted peptidotriazolamers, we analyzed a longer, hypothetical oligomer bearing only methyl side chains to mimic a poly-alanine peptide (Figure 8). Similarly, to the case of shorter molecules, we considered three variants labeled as homochiral, heterochiral, and homochiral*. Due to the significantly larger conformational space of these oligomers, we performed four parallel 200 ns simulations for each molecule in each of the two solvents (i.e., in DMSO and in water, for a total of 24 simulations) in order to reach a statistically significant sampling.

The RMSD time series for the whole trajectory of each replicate simulation are shown in Figure 13. As expected,

the simulations took longer to reach their local equilibrium compared to the case of the smaller molecules. After 150 ns, all trajectories reach a stable value of RMSD or oscillate between two conformational basins in a balanced manner. Compared to the case of shorter oligomers in which we had NMR information to produce relevant initial structures, the lack of experimental data in the present case translates into higher RMSD values since our initial geometries are likely to be far from a minimum conformation. Nevertheless, all simulations reached equilibrium and yield a distribution of stable conformers.

In contrast to the case of short oligomers, the homo- and heterochiral polyalanine derivatives suffer from a significant decrease of flexibility when moving from DMSO to water. This is illustrated in Figure 13 by the fact that all four simulations systematically converge toward the same value of

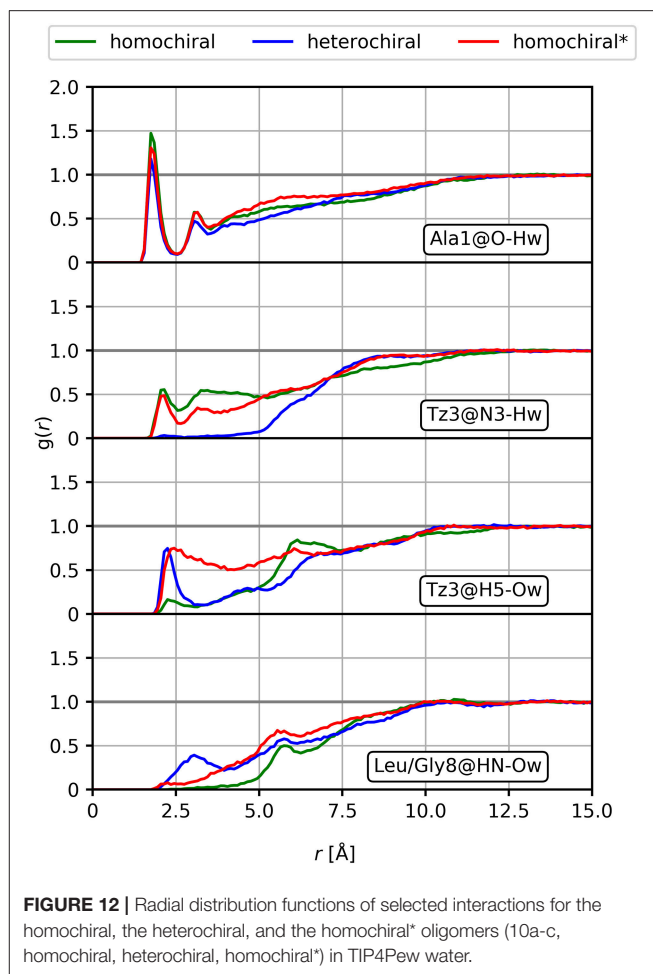
TABLE 1 | Dihedral angles of the representative structures for the main cluster of the three representative molecules (10a-c, homochiral, heterochiral, homochiral*) as obtained from molecular dynamics in DMSO and TIP4Pew Water.

	Homochiral		Heterochiral		Homochiral*	
	Φ	Ψ	Φ	Ψ	Φ	Ψ
DMSO						
Ala1	-61.9	132.4	-64.3	1.1	-78.8	158.2
V/G4n2	-148.7	-176.8	143.2	-169.5	-146.2	-170.3
F4c4	-58.6	-13.8	72.2	39.2	-58.2	2.8
L/G4n5	-117.6	-148.0	132.9	-163.6	-156.9	-142.0
F4c7	62.3	3.1	75.8	24.8	72.9	24.1
L/G4n8	-168.7	-171.1	142.8	-175.4	154.2	-166.1
V4c10	57.0	3.4	65.0	-13.3	62.1	0.0
WATER						
Ala1	-67.0	131.8	-97.4	19.5	-133.1	15.5
V/G4n2	-136.4	-112.8	167.0	-168.5	-130.4	165.5
F4c4	75.7	1.5	64.6	39.4	-67.1	22.5
L/G4n5	-155.0	175.3	131.4	-48.1	172.3	-153.7
F4c7	68.2	-3.8	71.6	37.5	65.0	37.4
L/G4n8	-152.0	-168.6	125.1	168.7	131.5	-153.5
V4c10	51.5	3.9	-51.1	-34.1	83.9	-15.2

RMSD in water only. Once this stable plateau is reached, the amplitude of fluctuations also decreases, showing the tight conformational restraints exerted by the solvent on the solute. Such a drastic effect of the solvent was, however, not observed in the case of the glycine-containing variant (homochiral*), which is most likely due to the significantly reduced hydrophobic character of that molecule. ROG time series are available as supporting information (**Supplementary Figure 15**) for the whole trajectories and show that even significant fluctuations in RMSD do not result in large changes in the compactness of the conformations. The ϕ/ψ torsion angle distributions (**Supplementary Figure 16**) are in a good agreement with the RMSD fluctuations, showing that all three molecules have a unique conformational signature.

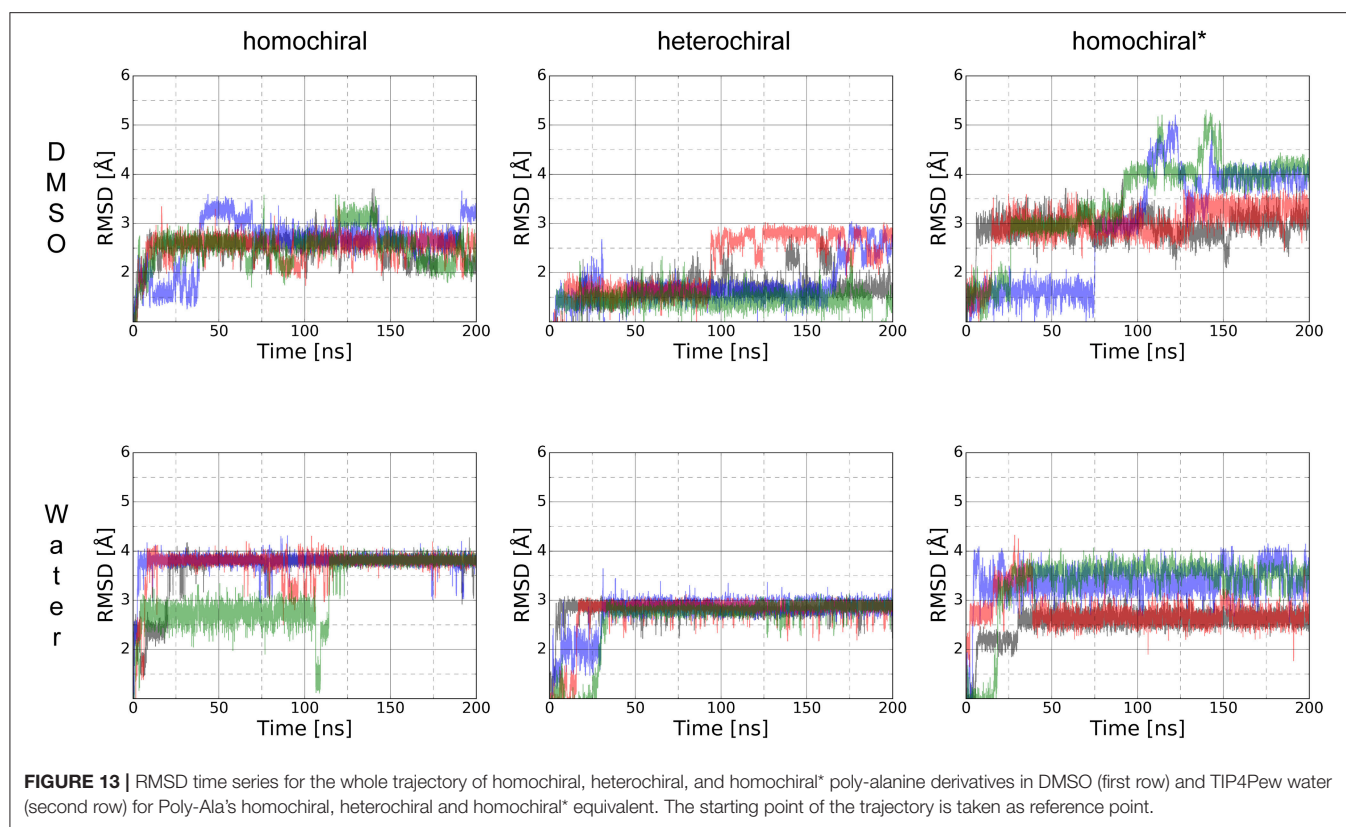
We performed the clustering analysis over the last 50 ns of the trajectories of all four replica. The main structural clusters in DMSO and water showed a population of 55 and 95%, respectively for the homochiral, 72 and 91% for the heterochiral, and 52 and 40% for the homochiral* oligomer. For the homochiral* molecule in water three other clusters with significant population (i.e., 32 and 27%) were identified, but showing a high similarity with the main cluster as indicated by backbone RMSD values as low as 1.4 and 0.8 Å.

The representative structures are shown in **Figure 14**. The homochiral molecule shows a clear helical conformation in DMSO, which collapses in water. The heterochiral molecule shows a compactness in DMSO similar to that of the homochiral one. However, the conformation of the former describes a twisted “S”-shape, which also collapses in water. The Gly-substituted oligomer shows no clear secondary structure in either of the solvents, which is in agreement with the more flexible character of this molecule as interpreted from the RMSD time series.

**FIGURE 12** | Radial distribution functions of selected interactions for the homochiral, the heterochiral, and the homochiral* oligomers (10a-c, homochiral, heterochiral, homochiral*) in TIP4Pew water.

CONCLUSION

Herein we present a new class of peptidomimetics containing 1,4-disubstituted 1*H*-1,2,3-triazoles and amide bonds in an alternating fashion. The synthesis is based on chiral propargylamines and chiral α -azido acids. Beside the introduction of a versatile and robust synthetic strategy we elucidated their foldamer properties by means of molecular dynamics simulations in explicit solvent. Homo- and heterochiral tetra-, hexa-, and heptamers based on two different sequences as well as a homochiral oligomer, in which every second sidechain is replaced by a proton, have been synthesized based on a submonomer approach. Molecular modeling of the Boc-Ala-Val Ψ [4Tz]Phe-Leu Ψ [4Tz]Phe-Leu Ψ [4Tz]Val-OAll sequence (homo- and heterochiral) as well as a Gly-substituted derivative revealed a compact folded conformation in DMSO, similar for all three variants. The conformation of these molecules remains compactly folded in water as well, due to the hydrophobic character of the non-polar side chains. In addition, we predicted the conformations of homo-, heterochiral, and glycine-containing poly-alanine peptidotriazole oligomers. In contrast to the shorter oligomers, our calculations suggest a well-defined and significantly different secondary structure



for the homo- (helix) and heterochiral (twisted S) variants in DMSO, which collapses in water. The glycine-substituted oligomers, however, shows no clear secondary structure and a significantly higher flexibility compared to the two other variants, with a conformational space that is little-affected by the solvent's polarity.

EXPERIMENTAL SECTION

Synthesis

All chemicals were purchased from *Sigma Aldrich* (Taufkirchen, Germany), *Acros* (Geel, Belgium), *Alfa Aesar* (Ward Hill, USA), *VWR* (Darmstadt, Germany), *Chempur* (Karlsruhe, Germany), *Iris Biotech* (Marktredwitz, Germany), *Bachem* (Bubendorf, Switzerland), and were employed without additional purification. Moisture- and air-sensitive reaction steps were conducted in flame-dried glassware and under argon atmosphere. Dichloromethane and toluene were freshly distilled from CaH_2 and Na, respectively. THF was pre-dried over KOH followed by drying over sodium/benzophenone under reflux conditions and was distilled freshly prior usage.

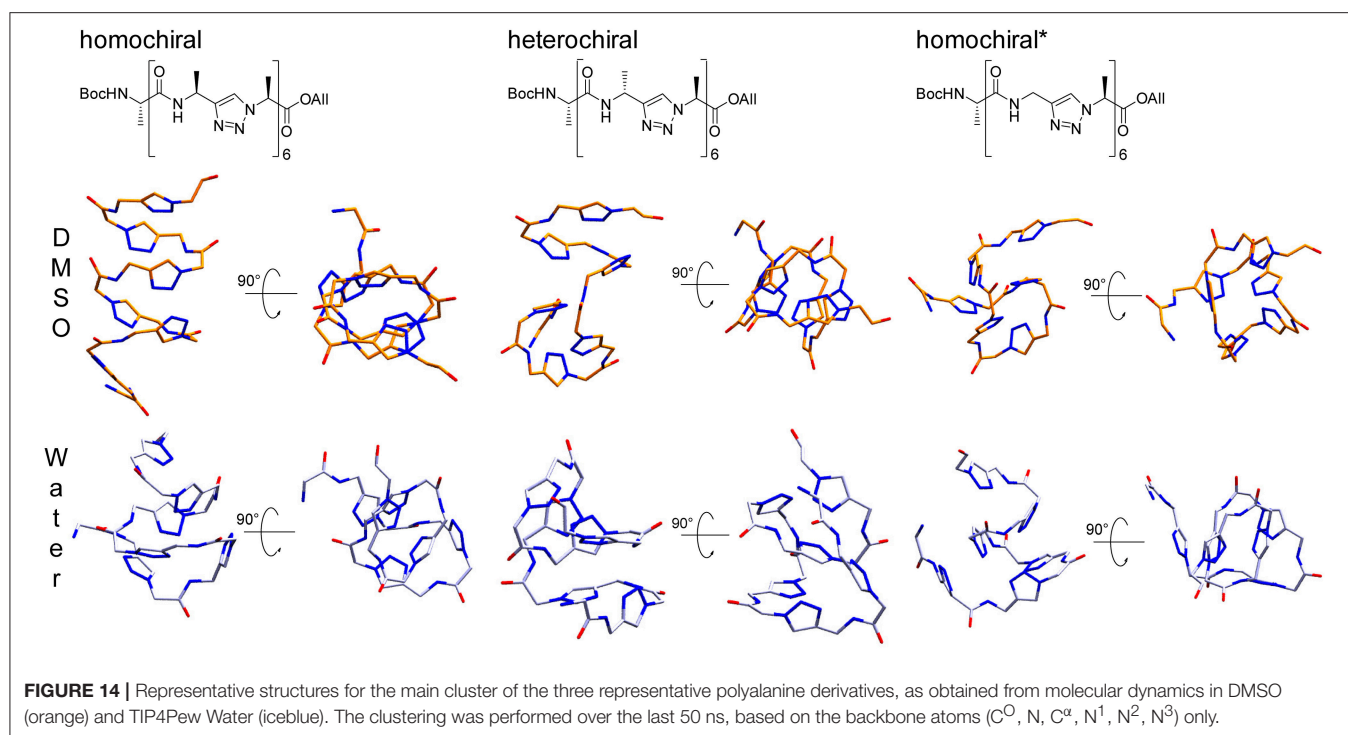
Analytical RP-HPLC was performed on a *Thermo Separation Products* system equipped with a UV-6000 LP detector, a P-4000 pump, a Hypersil Gold 3 μm (C18; 150 \times 2.1 mm) column. A flow rate of 0.7 mL min^{-1} using Eluent A: $\text{H}_2\text{O}/\text{CH}_3\text{CN}/\text{TFA}$ (95/5/0.1) and Eluent B: $\text{CH}_3\text{CN}/\text{H}_2\text{O}/\text{TFA}$ (95/5/0.1) was employed. Method A1: 0–3 min (100% \rightarrow A 0% A), 3–4 min (0% A), 4–5 min (0% A \rightarrow 100% A). Method A2: 0–0.5 min (100% A),

0.5–7.5 min (100% A \rightarrow 0% A), 7.5–8.5 min (0% A), 8.5–9.5 min (0% A 100% \rightarrow A), 9.5–10 min (100% A).

Preparative RP-HPLC was performed on a *Hitachi MERCK LaChrom* system equipped with a UV-Vis L-7420 detector, a L-7150 pump and a *Phenomenex* Jupiter 10 μm column (C18; 300 Å, 250 \times 21.1 mm). A flow rate of 10.0 mL min^{-1} using Eluent A: $\text{H}_2\text{O}/\text{CH}_3\text{CN}/\text{TFA}$ (95/5/0.1) and Eluent B: $\text{CH}_3\text{CN}/\text{H}_2\text{O}/\text{TFA}$ (95/5/0.1) was employed. Method P1: 0–3 min (100% A \rightarrow 75% A), 3–20 min (75% A \rightarrow 0% A), 20–100 min (0% A), 100–110 min (0% A \rightarrow 100% A). Method P2: 0–3 min (100% A), 3–35 min (100% A \rightarrow 15% A), 35–100 min (15% A), 100–110 min (15% A \rightarrow 100% A). Method P3: 0–5 min (100% A), 5–35 min (100% A \rightarrow 0% A), 35–40 min (0% A), 40–45 min (0% A \rightarrow 100% A).

In addition, a *Thermo Separation Products* system equipped with a UV-1000 detector, a P-4000 pump, was used utilizing the same methods.

NMR spectra were recorded at 298 K on a DRX 500 (^1H : 500 MHz, ^{13}C : 126 MHz), an Avance III 500 (^1H : 500 MHz, ^{13}C : 126 MHz), and an Avance 600 spectrometer (^1H : 600 MHz, ^{13}C : 151 MHz) (*Bruker Biospin*, Rheinstetten, Germany). Chemical shifts are reported relative to residual solvent peaks (DMSO- d_6 : ^1H : 2.50 ppm, ^{13}C : 39.52 ppm; CDCl_3 : ^1H : 7.26 ppm, ^{13}C : 77.16 ppm) (Gottlieb et al., 1997). ^1H - and ^{13}C -NMR spectra (**Supplementary Figures 1–9**) as well as ^1H - ^1H -COSY-, ^1H - ^1H -TOCSY, ^1H - ^{13}C -HMBC, and ^1H - ^{13}C -HMQC-NMR spectra were used for the signal assignments. ^1H - ^1H -ROESY-NMR spectra were only taken for the restraints list.



ESI/APCI mass spectra were recorded using an Esquire 3000 ion trap mass spectrometer (Bruker Daltonik GmbH, Bremen, Germany) equipped with a standard ESI/APCI source. Samples were introduced directly with a syringe pump. Nitrogen served both as the nebulizer gas and the dry gas. Nitrogen was generated using a Bruker nitrogen generator NGM 11. Helium served as cooling gas for the ion trap and collision gas for MS experiments.

MALDI TOF mass spectra were recorded with a Ultraflex MALDI-TOF/TOF mass spectrometer (Bruker Daltonik GmbH, Bremen, Germany) operated in reflectron mode. 2,5-Dihydroxybenzoic acid was used as the matrix. Ionization was achieved using a LTB nitrogen laser MNL 200 (337 nm beam wavelength, 50 Hz repetition rate).

High-resolution masses were recorded using a MicroToF mass spectrometer (Bruker Daltonik GmbH, Bremen, Germany) with sample-loop injection. Mass calibration was performed immediately prior measurement with sodium formate cluster and quasi-internal calibration.

CD-spectra were recorded on a JASCO J-810 spectrometer in acetonitrile (HPLC grade) at 20°C.

General Procedures

Bus-protected propargylamines were synthesized according to Wünsch et al. (2017) as well as the α -azido acids in the style of Kracker et al. (2018).

GP-1: The azide (1.1 equivalent) and the alkyne (1.0 equivalent) were dissolved in DMF/H₂O (10:1, 0.1 M solution). Afterwards, CuSO₄·5H₂O (0.5 equivalents) and sodium ascorbate (1.0 equivalent) are added. The mixture was stirred 15 h at room temperature. After completion of the reaction the solvent was evaporated. The residue was dissolved with saturated NaCl-solution. After extraction with DCM (3×),

drying over Na₂SO₄, and evaporation of the solvent, the pure triazole was delivered after purification via preparative HPLC or column chromatography.

GP-2: The free amine was dissolved in DMF (0.1 M solution). After addition of HATU (1.5 equivalents), HOAt (1.5 equivalents), DIPEA (9.0 equivalents) and an azidocarboxylic acid (1.1 equivalents) the reaction mixture is stirred 15 h at rt. After evaporation of the solvent purification via preparative HPLC or column chromatography yields the pure amide.

Explicit Experimental Procedures

(S)-Bus-Leu Ψ [4Tz]Val-OAll (3a): N₂=Val-OAll (1a, 132 mg, 0.720 mmol), (S)-Bus-Leu-CH (2a, 104 mg, 0.483 mmol), CuSO₄·5H₂O (60 mg, 0.24 mmol) and sodium ascorbate (96 mg, 0.48 mmol) were stirred according to **GP-1**. Purification via column chromatography (DCM/MeOH 80:1, *R_f* = 0.13) yielded the product as yellow oil. Yield: 180 mg (0.452 mmol, 94%); ¹H-NMR (500 MHz, CDCl₃): δ [ppm] = 7.88 (s, 1H); 5.88 (m, 1H); 5.31 (dddd, ⁴*J* = 1.3 Hz, 1.3 Hz, ³*J* = 17.1 Hz, ²*J* = 1.1 Hz, 1H); 5.25 (dddd, ⁴*J* = 1.3 Hz, 1.3 Hz, ³*J* = 10.5 Hz, ²*J* = 1.1 Hz, 1H); 5.10 (d, ³*J* = 8.8 Hz, 1H); 4.68–4.60 (m, 2H); 4.53 (m, 1H); 3.69 (d, ³*J* = 8.1 Hz, 1H); 2.47 (m, 1H); 1.90–1.77 (m, 2H); 1.68 (m, 1H); 1.19 (s, 9H); 1.00 (d, ³*J* = 6.7 Hz, 3H); 0.91 (d, ³*J* = 6.7 Hz, 3H); 0.89 (d, ³*J* = 6.6 Hz, 3H); 0.83 (d, ³*J* = 6.8 Hz, 3H); ¹³C-NMR (126 MHz, CDCl₃): δ [ppm] = 168.5; 150.2; 131.0; 121.3; 119.8; 68.9; 66.6; 56.4; 51.4; 45.5; 32.5; 24.6; 22.9; 22.8; 21.9; 19.3; 18.8; MS (ESI): *m/z* = 421.3 ([M+Na]⁺); HRMS (ESI): *m/z* calcd. for C₁₉H₃₄N₄O₃Sn⁺ ([M+Na]⁺): 421.2244, found: 421.2253.

N₂=Phe-Leu Ψ [4Tz]Val-OAll (6a): (S)-Bus-Leu Ψ [4Tz]Val-OAll (3a, 171 mg, 0.429 mmol) was dissolved in MeOH (4 mL). After addition of 4 M HCl in dioxane (2.15 mL, 8.6 mmol) the mixture was stirred for 2 h at rt. After evaporation of the

solvent the product was used for the next step without further purification. $^1\text{H-NMR}$ (500 MHz, CDCl_3): δ [ppm] = 8.53 (s, 3H); 8.09 (s, 1H); 5.89 (m, 1H); 5.33 (dddd, $^4J = 1.4$ Hz, $^3J = 17.2$ Hz, $^2J = 1.2$ Hz, 1H); 5.27 (dddd, $^4J = 1.2$ Hz, $^3J = 10.3$ Hz, $^2J = 1.0$ Hz, 1H); 5.14 (d, $^3J = 8.5$ Hz, 1H); 4.71–4.60 (m, 3H); 2.49 (m, 1H); 2.00 (m, 1H); 1.90 (m, 1H); 1.48 (m, 1H); 0.99 (d, $^3J = 6.7$ Hz, 3H); 0.90 (d, $^3J = 6.5$ Hz, 3H); 0.87 (d, $^3J = 6.6$ Hz, 3H); 0.81 (d, $^3J = 6.7$ Hz, 3H).

$\text{H-Leu}\Psi[4\text{Tz}]\text{Val-OAll-HCl}$ was stirred with the azido carboxylic acid $\text{N}_2=\text{Phe-OH}$ (1b, 90 mg, 0.47 mmol), HATU (247 mg, 0.650 mmol), HOAt (88 mg, 0.65 mmol) and DIPEA (0.65 mL, 3.87 mmol) according to **GP-2**. Purification via column chromatography (DCM/MeOH 50:1, $R_f = 0.27$) yielded the product as colorless solid. Yield: 181 mg (0.387 mmol, 86%); $^1\text{H-NMR}$ (500 MHz, CDCl_3): δ [ppm] = 7.75 (s, 1H); 7.32–7.25 (m, 5H); 6.80 (d, $^3J = 8.7$ Hz, 1H); 5.89 (m, 1H); 5.33 (dddd, $^4J = 1.5$ Hz, $^3J = 17.1$ Hz, $^2J = 1.1$ Hz, 1H); 5.28 (dddd, $^4J = 1.5$ Hz, $^3J = 10.2$ Hz, $^2J = 1.0$ Hz, 1H); 5.21 (m, 1H); 5.13 (d, $^3J = 8.7$ Hz, 1H); 4.71–4.62 (m, 2H); 4.18 (dd, $^3J = 7.8$ Hz, $^2J = 14.2$ Hz, 1H); 3.32 (dd, $^3J = 4.3$ Hz, $^2J = 14.0$ Hz, 1H); 3.06 (dd, $^3J = 8.1$ Hz, $^2J = 14.2$ Hz, 1H); 2.47 (m, 1H); 1.70–1.67 (m, 2H); 1.34 (m, 1H); 1.02 (d, $^3J = 6.7$ Hz, 3H); 0.89 (d, $^3J = 6.6$ Hz, 3H); 0.88 (d, $^3J = 6.5$ Hz, 3H); 0.82 (d, $^3J = 6.7$ Hz, 3H); $^{13}\text{C-NMR}$ (126 MHz, CDCl_3): δ [ppm] = 168.5; 167.7; 148.2; 136.1; 131.0; 129.7; 128.7; 127.3; 120.8; 119.9; 68.9; 66.6; 65.5; 44.1; 44.0; 38.5; 32.5; 24.7; 22.7; 22.3; 19.3; 18.8; MS (ESI): $m/z = 490.2$ ($[\text{M}+\text{Na}]^+$); HRMS (ESI): m/z calcd. for $\text{C}_{24}\text{H}_{33}\text{N}_7\text{O}_3\text{Na}^+$ ($[\text{M}+\text{Na}]^+$): 490.2537, found: 490.2542.

(S)-Bus-Leu Ψ [4Tz]Phe-Leu Ψ [4Tz]Val-OAll (7a): $\text{N}_2=\text{Phe-Leu}\Psi[4\text{Tz}]\text{Val-OAll}$ (6a, 181 mg, 0.387 mmol) was stirred with the alkyne (S)-Bus-Leu-CH (2a, 92 mg, 0.43 mmol), $\text{CuSO}_4 \cdot 5\text{H}_2\text{O}$ (50 mg, 0.20 mmol) and sodium ascorbate (77 mg, 0.39 mmol) according to **GP-1**. Purification via preparative RP-HPLC yielded the product as colorless solid. Yield: 155 mg (0.227 mmol, 59%); Analytical RP-HPLC (Method A1): $t_R = 3.49$ min; Preparative RP-HPLC (Method P2, 220 nm): $t_R = 42.0$ min; $^1\text{H-NMR}$ (500 MHz, CDCl_3): δ [ppm] = 7.67 (s, 1H); 7.59 (s, 1H); 7.15–7.14 (m, 3H); 7.06 (d, $^3J = 8.4$ Hz, 1H); 6.99–6.97 (m, 2H); 5.90 (m, 1H); 5.32 (dddd, $^4J = 1.2$ Hz, $^3J = 17.1$ Hz, $^2J = 1.6$ Hz, 1H); 5.28 (dddd, $^4J = 1.2$ Hz, $^3J = 10.3$ Hz, $^2J = 1.2$ Hz, 1H); 5.26–5.19 (m, 2H); 5.10 (d, $^3J = 8.8$ Hz, 1H); 4.71–4.61 (m, 2H); 4.46 (m, 1H); 3.88 (m, 1H); 3.56 (dd, $^3J = 6.5$ Hz, $^2J = 14.1$ Hz, 1H); 3.38 (dd, $^3J = 9.2$ Hz, $^2J = 14.1$ Hz, 1H); 2.47 (m, 1H); 1.86–1.77 (m, 2H); 1.74–1.70 (m, 2H); 1.58 (m, 1H); 1.45 (m, 1H); 1.19 (s, 9H); 1.01 (d, $^3J = 6.7$ Hz, 3H); 0.91 (m, 12H); 0.81 (d, $^3J = 6.7$ Hz, 3H); $^{13}\text{C-NMR}$ (126 MHz, CDCl_3): δ [ppm] = 168.4; 166.8; 149.7; 148.2; 135.7; 131.0; 129.1; 128.8; 127.3; 122.7; 121.1; 119.9; 69.0; 66.7; 66.1; 56.5; 51.4; 45.1; 44.6; 43.8; 39.1; 32.5; 24.9; 24.6; 22.8; 22.7; 22.7; 22.2; 21.2; 19.3; 18.8; MS (ESI): $m/z = 705.4$ ($[\text{M}+\text{Na}]^+$); HRMS (ESI): m/z calcd. for $\text{C}_{35}\text{H}_{54}\text{N}_8\text{O}_4\text{SNa}^+$ ($[\text{M}+\text{Na}]^+$): 705.3881, found: 705.3871.

$\text{N}_2=\text{Phe-Leu}\Psi[4\text{Tz}]\text{Phe-Leu}\Psi[4\text{Tz}]\text{Val-OAll}$ (8a): (S)-Bus-Leu $\Psi[4\text{Tz}]\text{Phe-Leu}\Psi[4\text{Tz}]\text{Val-OAll}$ (7a, 33 mg, 0.048 mmol) was dissolved in MeOH (2 mL) and stirred at rt with 4 M HCl in dioxane (24 μL solution). After 2 h the solvent was evaporated. The free amine was dissolved in DMF and stirred with the azido carboxylic $\text{N}_2=\text{Phe-OH}$ (1b, 10 mg, 0.052 mmol), HATU (28 mg,

0.073 mmol), HOAt (10 mg, 0.073 mmol) and DIPEA (74 μL , 0.44 mmol) according to **GP-2**. Purification via preparative RP-HPLC yielded the product as colorless solid. Yield: 10 mg (13 μmol , 27%); Preparative RP-HPLC: $t_R = 27.2$ min (Method P1, 220 nm); $^1\text{H-NMR}$ (500 MHz, $\text{DMSO}-d_6$): δ [ppm] = 8.94 (d, $^3J = 8.4$ Hz, 1H); 8.56 (d, $^3J = 8.6$ Hz, 1H); 7.98 (s, 1H); 7.93 (s, 1H); 7.29–7.26 (m, 2H); 7.22–7.21 (m, 3H); 7.17–7.11 (m, 5H); 5.90 (m, 1H); 5.61 (dd, $^3J = 9.5$ Hz, $^2J = 14.2$ Hz, 1H); 5.29–5.20 (m, 3H); 5.06–5.01 (m, 2H); 4.70–4.63 (m, 2H); 4.00 (dd, $^3J = 9.0$ Hz, $^2J = 14.0$ Hz, 1H); 3.35 (dd, $^3J = 6.4$ Hz, $^2J = 14.2$ Hz, 1H); 3.30 (dd, $^3J = 9.4$ Hz, $^2J = 14.0$ Hz, 1H); 3.02 (dd, $^3J = 5.4$ Hz, $^2J = 13.9$ Hz, 1H); 2.90 (dd, $^3J = 9.0$ Hz, $^2J = 13.9$ Hz, 1H); 2.57 (m, 1H); 1.73–1.60 (m, 4H); 1.47–1.37 (m, 2H); 0.96 (d, $^3J = 6.7$ Hz, 3H); 0.88 (m, 6H); 0.83 (d, $^3J = 6.6$ Hz, 3H); 0.72 (m, 6H); $^{13}\text{C-NMR}$ (126 MHz, $\text{DMSO}-d_6$): δ [ppm] = 168.2; 167.9; 166.7; 148.1; 147.9; 136.8; 136.1; 133.8; 129.0; 128.9; 128.4; 128.2; 126.7; 126.7; 122.1; 121.3; 118.4; 67.6; 65.7; 63.7; 62.1; 43.7; 43.6; 43.4; 43.4; 37.4; 36.9; 30.6; 24.3; 24.2; 22.6; 22.6; 21.9; 21.8; 18.8; 18.2; MS (ESI): $m/z = 774.4$ ($[\text{M}+\text{Na}]^+$).

(S)-Bus-Val Ψ [4Tz]Phe-Leu Ψ [4Tz]Phe-Leu Ψ [4Tz]Val-OAll (9a): $\text{N}_2=\text{Phe-Leu}\Psi[4\text{Tz}]\text{Phe-Leu}\Psi[4\text{Tz}]\text{Val-OAll}$ (8a, 10 mg, 13 μmol) was stirred with the (S)-Bus-Val-CH (2b, 4.0 mg, 20 μmol), $\text{CuSO}_4 \cdot 5\text{H}_2\text{O}$ (2.5 mg, 10 μmol) and sodium ascorbate (2.6 mg, 13 μmol) according to **GP-1**. Purification via preparative RP-HPLC yielded the product as colorless solid. Yield: 6.0 mg (6.3 μmol , 48%); Analytical RP-HPLC: $t_R = 3.60$ min (Method A1); Preparative RP-HPLC: $t_R = 43.4$ min (Method P2, 220 nm); $^1\text{H-NMR}$ (600 MHz, $\text{DMSO}-d_6$): δ [ppm] = 8.94 (d, $^3J = 8.5$ Hz, 1H); 8.83 (d, $^3J = 8.5$ Hz, 1H); 8.15 (s, 1H); 8.00 (s, 1H); 7.93 (s, 1H); 7.18–7.09 (m, 10H); 5.90 (m, 1H); 5.59 (dd, $^3J = 9.5$ Hz, $^2J = 14.2$ Hz, 1H); 5.55 (dd, $^3J = 9.5$ Hz, $^2J = 14.2$ Hz, 1H); 5.28 (d, $^3J = 8.5$ Hz, 1H); 5.27 (dddd, $^4J = 1.5$ Hz, $^3J = 17.2$ Hz, $^2J = 1.5$ Hz, 1H); 5.23 (s (*br*), 1H); 5.21 (dddd, $^4J = 1.3$ Hz, $^3J = 10.5$ Hz, $^2J = 1.4$ Hz, 1H); 5.06–4.99 (m, 2H); 4.70–4.64 (m, 2H); 4.12 (dd, $^3J = 7.0$ Hz, $^2J = 14.2$ Hz, 1H); 3.37–3.24 (m, 4H); 2.57 (m, 1H); 2.07 (m, 1H); 1.70 (m, 1H); 1.67–1.62 (m, 2H); 1.59 (m, 1H); 1.43 (m, 1H); 1.33 (m, 1H); 1.11 (s, 9H); 0.96 (d, $^3J = 6.7$ Hz, 3H); 0.84 (d, $^3J = 6.7$ Hz, 3H); 0.83–0.78 (m, 15H); 0.74 (d, $^3J = 6.7$ Hz, 3H); $^{13}\text{C-NMR}$ (151 MHz, $\text{DMSO}-d_6$): δ [ppm] = 167.8; 166.7; 166.6; 148.3; 148.1; 147.8; 136.1; 136.1; 131.8; 128.9; 128.9; 128.2; 128.2; 126.7; 126.7; 122.0; 122.0; 121.2; 118.4; 67.5; 65.7; 63.7; 63.7; 57.9; 55.7; 43.7; 43.7; 43.1; 43.4; 37.8; 37.4; 33.4; 30.6; 24.3; 24.1; 22.7; 22.5; 22.4; 21.9; 21.8; 18.8; 18.8; 18.6; 18.3; MS (ESI): $m/z = 975.5$ ($[\text{M}+\text{Na}]^+$).

Boc-Ala-Val Ψ [4Tz]Phe-Leu Ψ [4Tz]Phe-Leu Ψ [4Tz]Val-OAll (10a): (S)-Bus-Val $\Psi[4\text{Tz}]\text{Phe-Leu}\Psi[4\text{Tz}]\text{Phe-Leu}\Psi[4\text{Tz}]\text{Val-OAll}$ (9a, 5.0 mg, 5.2 μmol) was dissolved in MeOH (0.5 mL) and 4 M HCl in dioxane (26 μL solution) was added. After 2 h stirring at rt the solvent was evaporated and the free amine was dissolved in DMF. It was stirred with Boc-Ala-OH (1.5 mg, 7.9 μmol), HATU (3.0 mg, 7.9 μmol), HOAt (1.0 mg, 7.3 μmol) and DIPEA (8.0 μL , 47 μmol) according to **GP-2**. Purification via preparative RP-HPLC yielded the product as colorless solid. Yield: 3.0 mg (2.9 μmol , 57%); Preparative RP-HPLC: $t_R = 42.5$ min (Method P2, 220 nm); $^1\text{H-NMR}$ (600 MHz, $\text{DMSO}-d_6$): δ [ppm] = 8.93 (d, $^3J = 8.4$ Hz, 1H); 8.87 (d, $^3J = 8.5$ Hz, 1H); 8.05 (s, 1H); 8.01 (s, 1H); 7.93 (s, 1H); 7.93 (d,

$^3J = 9.1$ Hz, 1H); 7.18–7.08 (m, 10H); 6.93 (d, $^3J = 7.7$ Hz, 1H); 5.90 (m, 1H); 5.59 (dd, $^3J = 9.5$ Hz, 6.2 Hz, 1H); 5.56 (dd, $^3J = 9.9$ Hz, 5.8 Hz, 1H); 5.28 (d, $^3J = 8.4$ Hz, 1H); 5.27 (dddd, $^4J = 1.5$ Hz, 1.5 Hz, $^3J = 17.2$ Hz, $^2J = 1.5$ Hz, 1H); 5.22 (dddd, $^4J = 1.2$ Hz, 1.2 Hz, $^3J = 10.4$ Hz, $^2J = 1.6$ Hz, 1H); 5.04 (m, 1H); 5.00 (m, 1H); 4.81 (dd, $^3J = 9.1$ Hz, 7.0 Hz, 1H); 4.70–4.64 (m, 2H); 4.02 (m, 1H); 3.37–3.22 (m, 4H); 2.57 (m, 1H); 2.00 (m, 1H); 1.71 (m, 1H); 1.67–1.62 (m, 2H); 1.57 (m, 1H); 1.42 (m, 1H); 1.37 (s, 9H); 1.32 (m, 1H); 1.14 (d, $^3J = 7.1$ Hz, 3H); 0.96 (d, $^3J = 6.7$ Hz, 3H); 0.84 (d, $^3J = 6.7$ Hz, 3H); 0.81–0.76 (m, 15H); 0.73 (d, $^3J = 6.7$ Hz, 3H); ^{13}C -NMR (151 MHz, DMSO- d_6): δ [ppm] = 172.5; 168.2; 167.2; 167.1; 154.4; 148.5; 148.2; 147.5; 136.5; 136.2; 132.4; 130.1; 129.3; 129.0; 128.6; 127.6; 127.3; 122.4; 121.8; 121.7; 118.9; 78.4; 68.1; 66.1; 64.2; 64.2; 51.2; 50.2; 44.1; 44.1; 43.9; 43.8; 38.5; 37.9; 33.1; 31.1; 29.0; 25.0; 24.4; 23.0; 23.0; 22.2; 22.2; 19.2; 18.7; 18.5; 18.4; 18.0; MS(ESI): $m/z = 1042.6$ ($[\text{M}+\text{Na}]^+$); HRMS(ESI): m/z calcd. for $\text{C}_{54}\text{H}_{77}\text{N}_{13}\text{O}_7\text{Na}^+$ ($[\text{M}+\text{Na}]^+$): 1042.5967, found: 1042.5967.

(R)-Bus-D-Leu Ψ [4Tz]Val-OAll (3b): The azide $\text{N}_2=\text{Val-OAll}$ (1a, 70 mg, 0.38 mmol) was stirred with the alkyne (R)-Bus-D-Leu-CH (2c, 41 mg, 0.19 mmol), $\text{CuSO}_4 \cdot 5\text{H}_2\text{O}$ (24 mg, 96 μmol) and sodium ascorbate (38 mg, 0.19 mmol) according to **GP-1**. Purification via column chromatography (DCM/MeOH 80:1, $R_f = 0.18$) yielded the product as yellow oil. Yield: 74 mg (0.19 mmol, 98%); ^1H -NMR (500 MHz, CDCl_3): δ [ppm] = 7.90 (s, 1H); 5.84 (m, 1H); 5.26 (dddd, $^4J = 1.4$ Hz, 1.4 Hz, $^3J = 17.3$ Hz, $^2J = 1.3$ Hz, 1H); 5.20 (dddd, $^4J = 1.2$ Hz, 1.2 Hz, $^3J = 10.4$ Hz, $^2J = 1.1$ Hz, 1H); 5.06 (d, $^3J = 8.6$ Hz, 1H); 4.74–4.64 (m, 2H); 4.55 (m, 1H); 3.61 (d, $^3J = 6.8$ Hz, 1H); 2.43 (m, 1H); 1.85 (m, 1H); 1.77 (m, 1H); 1.70 (m, 1H); 1.19 (s, 9H); 0.94 (d, $^3J = 6.7$ Hz, 3H); 0.91 (d, $^3J = 6.5$ Hz, 3H); 0.90 (d, $^3J = 6.5$ Hz, 3H); 0.78 (d, $^3J = 6.7$ Hz, 3H); ^{13}C -NMR (126 MHz, CDCl_3): δ [ppm] = 168.4; 150.7; 131.0; 121.6; 119.7; 68.8; 66.5; 56.4; 51.7; 45.7; 32.4; 24.5; 23.0; 22.7; 21.7; 19.2; 18.6; MS (ESI): $m/z = 421.2$ ($[\text{M}+\text{Na}]^+$); HRMS(ESI): m/z calcd. for $\text{C}_{19}\text{H}_{34}\text{N}_4\text{O}_3\text{SNa}^+$ ($[\text{M}+\text{Na}]^+$): 421.2244, found: 421.2239.

$\text{N}_2=\text{Phe-D-Leu}\Psi$ [4Tz]Val-OAll (6b): (R)-Bus-D-Leu Ψ [4Tz]Val-OAll (3b, 74 mg, 0.19 mol) was dissolved in MeOH (2 mL). After addition of 4 M HCl in dioxane (0.14 mL) the mixture was stirred 2 h at rt. After evaporation of the solvent the product was used for the next step without further purification. ^1H -NMR (500 MHz, CDCl_3): δ [ppm] = 8.45 (s, 3H); 8.13 (s, 1H); 5.89 (m, 1H); 5.33 (dddd, $^4J = 1.3$ Hz, 1.3 Hz, $^3J = 17.2$ Hz, $^2J = 1.2$ Hz, 1H); 5.28 (dddd, $^4J = 1.2$ Hz, 1.2 Hz, $^3J = 10.3$ Hz, $^2J = 1.0$ Hz, 1H); 5.14 (d, $^3J = 8.4$ Hz, 1H); 4.72–4.61 (m, 3H); 2.50 (m, 1H); 2.00 (m, 1H); 1.92 (m, 1H); 1.50 (m, 1H); 0.99 (d, $^3J = 6.7$ Hz, 3H); 0.90 (d, $^3J = 6.5$ Hz, 3H); 0.89 (d, $^3J = 6.5$ Hz, 3H); 0.81 (d, $^3J = 6.7$ Hz, 3H). H-D-Leu[4Tz]Val-OAll-HCl (81 mg, 0.19 mmol) was stirred with the $\text{N}_2=\text{Phe-OH}$ (1b, 39 mg, 0.21 mmol), HATU (106 mg, 0.279 mmol), HOAt (38 mg, 0.28 mmol), and DIPEA (282 μL , 1.66 mmol) according to **GP-2**. Purification via column chromatography (DCM/MeOH 50:1, $R_f = 0.35$) yielded the product as colorless solid. Yield: 34 mg (73 μmol , 39%); ^1H -NMR (500 MHz, CDCl_3): δ [ppm] = 7.68 (s, 1H); 7.24–7.18 (m, 5H); 6.67 (d, $^3J = 8.7$ Hz, 1H); 5.90 (m, 1H); 5.34 (dddd, $^4J = 1.4$ Hz, 1.4 Hz, $^3J = 17.2$ Hz, $^2J = 1.1$ Hz, 1H); 5.29 (dddd, $^4J = 1.1$ Hz, 1.1 Hz, $^3J = 10.4$ Hz, $^2J = 1.0$ Hz,

1H); 5.21 (m, 1H); 5.12 (d, $^3J = 8.8$ Hz, 1H); 4.72–4.62 (m, 2H); 4.15 (dd, $^3J = 8.1$ Hz, 4.2 Hz, 1H); 3.29 (dd, $^3J = 4.7$ Hz, $^2J = 14.0$ Hz, 1H); 2.96 (dd, $^3J = 8.1$ Hz, $^2J = 14.0$ Hz, 1H); 2.46 (m, 1H); 1.83–1.73 (m, 2H); 1.45 (m, 1H); 1.03 (d, $^3J = 6.7$ Hz, 3H), 0.93 (d, $^3J = 6.6$ Hz, 3H); 0.92 (d, $^3J = 6.4$ Hz, 3H); 0.82 (d, $^3J = 6.7$ Hz, 3H); ^{13}C -NMR (126 MHz, CDCl_3): δ [ppm] = 168.4; 168.0; 148.1; 136.2; 131.0; 129.5; 128.8; 127.3; 120.8; 120.0; 69.0; 66.7; 65.5; 44.1; 44.0; 38.7; 32.6; 25.0; 22.7; 22.4; 19.3; 18.7; MS(ESI): $m/z = 490.2$ ($[\text{M}+\text{Na}]^+$); HRMS(ESI): m/z calcd. for $(\text{C}_{24}\text{H}_{33}\text{N}_7\text{O}_3)_2\text{Na}^+$ ($[2\text{M}+\text{Na}]^+$): 957.5182, found: 957.5158.

(R)-Bus-D-Leu Ψ [4Tz]Phe-D-Leu Ψ [4Tz]Val-OAll (7b): $\text{N}_2=\text{Phe-D-Leu}\Psi$ [4Tz]Val-OAll (6b, 34 mg, 73 μmol), the alkyne (R)-Bus-D-Leu-CH (2c, 17 mg, 79 μmol), $\text{CuSO}_4 \cdot 5\text{H}_2\text{O}$ (9.0 mg, 36 μmol) and sodium ascorbate (14 mg, 71 μmol) were stirred according to **GP-1**. Purification via preparative RP-HPLC yielded the product as colorless solid. Yield: 39 mg (56 μmol , 77%); Analytical RP-HPLC: $t_R = 3.60$ min (Method A1); Preparative RP-HPLC: $t_R = 42.6$ min (Method P2, 220 nm); ^1H -NMR (500 MHz, CDCl_3): δ [ppm] = 7.72 (s, 1H); 7.69 (s, 1H); 7.22–7.20 (m, 3H); 7.09–7.08 (m, 2H); 6.84 (d, $^3J = 8.1$ Hz, 1H); 5.90 (m, 1H); 5.34 (dd, $^3J = 8.4$ Hz, 6.9 Hz, 1H); 5.33 (dddd, $^4J = 1.4$ Hz, 1.4 Hz, $^3J = 17.1$ Hz, $^2J = 1.3$ Hz, 1H); 5.28 (dddd, $^4J = 1.2$ Hz, 1.2 Hz, $^3J = 10.5$ Hz, $^2J = 1.2$ Hz, 1H); 5.19 (m, 1H); 5.10 (d, $^3J = 8.8$ Hz, 1H); 4.71–4.61 (m, 2H); 4.79 (m, 1H); 3.62 (s (br), 1H); 3.58 (dd, $^3J = 6.9$ Hz, $^2J = 14.0$ Hz, 1H); 2.96 (dd, $^3J = 8.7$ Hz, $^2J = 13.9$ Hz, 1H); 2.47 (m, 1H); 1.84 (m, 1H); 1.75 (m, 1H); 1.69–1.58 (m, 2H); 1.32–1.24 (m, 2H); 1.19 (s, 9H); 1.01 (d, $^3J = 6.7$ Hz, 3H), 0.91 (d, $^3J = 7.0$ Hz, 3H); 0.90 (d, $^3J = 6.7$ Hz, 3H); 0.85 (d, $^3J = 6.5$ Hz, 3H); 0.84 (d, $^3J = 6.6$ Hz, 3H); 0.80 (d, $^3J = 6.7$ Hz, 3H); ^{13}C -NMR (126 MHz, CDCl_3): δ [ppm] = 168.5; 166.8; 150.4; 148.3; 135.6; 131.1; 129.2; 128.9; 127.4; 122.3; 120.9; 119.9; 68.9; 66.7; 66.0; 56.4; 51.8; 45.2; 44.8; 43.6; 39.2; 32.6; 24.8; 24.6; 22.9; 22.8; 22.7; 22.3; 21.9; 19.3; 18.7; MS (ESI): $m/z = 705.4$ ($[\text{M}+\text{Na}]^+$); HRMS (ESI): m/z calcd. for $\text{C}_{35}\text{H}_{54}\text{N}_8\text{O}_4\text{SNa}^+$ ($[\text{M}+\text{Na}]^+$): 705.38809, found: 705.38774.

$\text{N}_2=\text{Phe-D-Leu}\Psi$ [4Tz]Phe-D-Leu Ψ [4Tz]Val-OAll (8b): (R)-Bus-D-Leu Ψ [4Tz]Phe-D-Leu Ψ [4Tz]Val-OAll (15 mg, 22 μmol) was dissolved in MeOH (2 mL). After addition of 4 M HCl in dioxane (11 μL solution) the mixture was stirred 2 h at rt. After evaporation of the solvent the free amine was dissolved in DMF and stirred with the azido $\text{N}_2=\text{Phe-OH}$ (1b, 5.0 mg, 26 μmol), HATU (13 mg, 34 μmol), HOAt (4.0 mg, 29 μmol), and DIPEA (34 μL , 0.20 mmol) according to **GP-2**. Purification via preparative RP-HPLC yielded the product as colorless solid. Yield: 9.0 mg (12 μmol , 54%); Preparative RP-HPLC: $t_R = 28.2$ min (Method P1, 220 nm); ^1H -NMR (500 MHz, DMSO- d_6): δ [ppm] = 8.96 (d, $^3J = 8.6$ Hz, 1H); 8.53 (d, $^3J = 8.7$ Hz, 1H); 8.16 (s, 1H); 8.01 (s, 1H); 7.32–7.18 (m, 10H); 5.87 (m, 1H); 5.61 (dd, $^3J = 8.6$ Hz, 6.7 Hz, 1H); 5.27 (d, $^3J = 8.4$ Hz, 1H); 5.23 (dddd, $^4J = 1.4$ Hz, 1.4 Hz, $^3J = 17.3$ Hz, $^2J = 1.5$ Hz, 1H); 5.19 (dddd, $^4J = 1.3$ Hz, 1.3 Hz, $^3J = 10.6$ Hz, $^2J = 1.5$ Hz, 1H); 5.03–4.96 (m, 2H); 4.67–4.60 (m, 2H); 3.95 (dd, $^3J = 7.9$ Hz, 6.7 Hz, 1H); 3.39 (dd, $^3J = 6.7$ Hz, $^2J = 13.5$ Hz, 1H); 3.34 (dd, $^3J = 8.2$ Hz, $^2J = 13.5$ Hz, 1H); 3.07 (dd, $^3J = 6.8$ Hz, $^2J = 13.5$ Hz, 1H); 2.98 (dd, $^3J = 8.2$ Hz, $^2J = 13.5$ Hz, 1H); 2.54 (m, 1H); 1.57 (m, 2H); 1.48–1.45 (m, 2H); 1.25 (m, 1H); 1.10 (m, 1H); 0.92 (d, $^3J = 6.7$ Hz, 3H), 0.82–0.78 (m, 9H); 0.75 (d, 3J

= 6.5 Hz, 3H); 0.72 (d, 3J = 6.7 Hz, 3H); ^{13}C -NMR (126 MHz, DMSO- d_6): δ [ppm] = 168.1; 167.9; 165.5; 148.1; 147.8; 136.6; 135.8; 133.7; 129.1; 129.1; 128.3; 128.2; 126.; 126.7; 122.0; 121.3; 118.5; 67.5; 65.7; 63.7; 62.1; 43.7; 43.6; 43.5; 43.3; 39.5; 37.0; 30.6; 24.1; 23.9; 22.7; 22.5; 21.9; 21.8; 18.8; 18.2; MS(ESI): m/z = 774.4 ($[\text{M}+\text{Na}]^+$).

(R)-Bus-D-Val Ψ [4Tz]Phe-D-Leu Ψ [4Tz]Phe-D-Leu Ψ [4Tz]Val-OAll (9b): $\text{N}_2=\text{Phe-D-Leu}\Psi[4\text{Tz}]\text{Phe-D-Leu}\Psi[4\text{Tz}]\text{Val-OAll}$ (8b, 24 mg, 32 μmol), the alkyne (R)-Bus-D-Val-CH (9.0 mg, 45 μmol) $\text{CuSO}_4\cdot 5\text{H}_2\text{O}$ (4.0 mg, 16 μmol) and sodium ascorbate (6.0 mg, 30 μmol) were stirred according to **GP-1**. Purification via preparative RP-HPLC yielded the product as colorless solid. Yield: 17 mg (18 μmol , 56%); Analytical RP-HPLC: t_R = 3.74 min (Method A1); Preparative RP-HPLC: t_R = 46.2 min (Method P2, 220 nm); ^1H -NMR (600 MHz, DMSO- d_6): δ [ppm] = 8.90 (d, 3J = 8.6 Hz, 1H); 8.85 (d, 3J = 8.6 Hz, 1H); 8.21 (s, 1H); 8.11 (s, 1H); 7.98 (s, 1H); 7.23–7.15 (m, 10H); 5.87 (m, 1H); 5.62–5.56 (m, 2H); 5.26 (d, 3J = 8.4 Hz, 1H); 5.23 (dddd, 4J = 1.5 Hz, 1.5 Hz, 3J = 17.2 Hz, 2J = 1.6 Hz, 1H); 5.20 (s (br), 1H); 5.18 (dddd, 4J = 1.5 Hz, 1.5 Hz, 3J = 10.6 Hz, 2J = 1.2 Hz, 1H); 5.01–4.96 (m, 2H); 4.67–4.60 (m, 2H); 4.11 (dd, 3J = 6.5 Hz, 1H); 3.39–3.27 (m, 4H); 2.52 (m, 1H); 2.05 (m, 1H); 1.57–1.54 (m, 2H); 1.54–1.47 (m, 2H); 1.24 (m, 1H); 1.17 (m, 1H); 1.12 (s, 9H); 0.91 (d, 3J = 6.7 Hz, 3H); 0.82–0.78 (m, 15H); 0.75 (d, 3J = 6.7 Hz, 3H); 0.72 (d, 3J = 6.7 Hz, 3H); ^{13}C -NMR (151 MHz, DMSO- d_6): δ [ppm] = 167.9; 166.5; 166.5; 148.3; 148.1; 147.6; 135.8; 135.8; 131.7; 129.1; 129.0; 128.2; 128.2; 126.7; 126.7; 122.2; 122.0; 121.3; 118.; 67.5; 65.7; 63.7; 63.7; 58.3; 55.7; 43.8; 43.6; 43.5; 43.4; 38.4; 37.9; 33.3; 30.6; 24.1; 24.0; 22.7; 22.6; 22.5; 21.9; 21.8; 19.0; 18.8; 18.3; 18.2; MS(ESI): m/z = 975.5 ($[\text{M}+\text{Na}]^+$); HRMS(ESI): m/z calcd. for $\text{C}_{35}\text{H}_{54}\text{N}_8\text{O}_4\text{SNa}^+$ ($[\text{M}+\text{Na}]^+$): 975.5362, found: 975.5332.

Boc-Ala-D-Val Ψ [4Tz]Phe-D-Leu Ψ [4Tz]Phe-D-Leu Ψ [4Tz]Val-OAll (10b): (R)-Bus-D-Val Ψ [4Tz]Phe-D-Leu Ψ [4Tz]Phe-D-Leu Ψ [4Tz]Val-OAll (9b, 23.3 mg, 25.0 μmol) is dissolved in 1 mL of a 1:1 mixture of DCM and HCl (4 M in dioxane) and stirred for 2 h at rt. After complete cleavage of the Boc-group, the free amine is evaporated to dryness. In a second flask, Boc-Ala-OH (9.5 mg, 50 μmol) and HOAt (7.5 mg, 55 μmol) are dissolved in DCM (2 mL, dry). After addition of DIC (8.5 μL , 55 μmol), the mixture is stirred 5 min at RT for preactivation and is then added to the free amine, followed by TMP (16.5 μL ; 125 μmol). This solution is left stirring over night at rt. After evaporation of the solvent, the crude product is purified by preparative HPLC. Yield: 15.4 mg (15.1 μmol , 60%); Analytical RP-HPLC: t_R = 6.60 min (Method A2); ^1H -NMR (600 MHz, DMSO- d_6): δ [ppm] = 8.92 (d, J = 8.6 Hz, 1H), 8.89 (d, J = 8.7 Hz) 8.19 (s, 1H), 8.14 (s, 1H), 8.00 (s, 1H), 7.88 (d, J = 9.2 Hz), 7.23–7.14 (m, 10H) 6.89 (d, J = 7.6 Hz, 1H), 5.86 (ddt, J = 17.2, 10.6, 5.5 Hz, 1H), 5.63–5.58 (m, 2H), 5.26 (d, J = 8.4 Hz, 1H), 5.23 (dd, J = 17.2, 1.7 Hz, 1H), 5.18 (dd, J = 10.6, 1.5 Hz, 1H), 5.01–4.96 (m, 2H), 4.81 (dd, J = 9.2, 6.4 Hz, 1H), 4.64 (m, 2H), 4.03 (dq, J = 7.6, 7.2 Hz, 1H), 3.40–3.26 (m, 4H), 2.50 (m, 1H), 2.05–1.96 (m, 1H), 1.58–1.50 (m, 4H), 1.36 (s, 9H), 1.28–1.14 (m, 2H), 1.18 (d, J = 7.2 Hz), 0.91 (d, J = 6.7 Hz, 3H), 0.82–0.78 (m, 12H), 0.75 (d, J = 6.7 Hz, 3H), 0.72 (d, J = 6.8 Hz, 3H), 0.70 (d, J = 6.8 Hz, 3H); ^{13}C -NMR (151 MHz, DMSO- d_6):

δ [ppm] = 172.77, 168.32, 166.96, 166.94, 155.42, 148.53, 148.04, 147.33, 136.27, 136.22, 132.16, 129.50, 129.48, 128.62, 127.20, 122.46, 122.28, 121.82, 118.91, 78.49, 67.96, 66.14, 64.17, 50.82, 50.38, 44.21, 44.05, 43.90, 38.81, 38.41, 32.80, 31.08, 28.63, 24.56, 24.46, 23.09, 22.97, 22.37, 22.26, 19.34, 19.24, 18.84, 18.68, 18.41; HRMS (ESI): m/z calcd. for $\text{C}_{54}\text{H}_{78}\text{N}_{13}\text{O}_7^+$ ($[\text{M}+\text{H}]^+$): 1020.6142, found: 1020.6126.

Boc-Gly Ψ [4Tz]Val-OAll (3c): $\text{N}_2=\text{Val-OAll}$ (104 mg, 0.568 mmol), the alkyne Boc-Gly-CH (2e, 100 mg, 0.644 mmol), $\text{CuSO}_4\cdot 5\text{H}_2\text{O}$ (71 mg, 0.29 mmol) and sodium ascorbate (112 mg, 0.565 mmol) were stirred according to **GP-1**. Purification via column chromatography (PE/EE 2:1, R_f = 0.54) yielded the product as colorless solid. Yield: 138 mg (0.408 mmol, 72%); $[\alpha]_D^{20}$ = 40.8 (c = 0.7, CHCl_3); ^1H -NMR (500 MHz, CDCl_3): δ [ppm] = 7.86 (s, 1H); 5.90 (m, 1H); 5.34 (dddd, 4J = 1.5 Hz, 1.5 Hz, 3J = 17.2 Hz, 2J = 1.2 Hz, 1H); 5.29 (dddd, 4J = 1.5 Hz, 1.5 Hz, 3J = 10.4 Hz, 2J = 1.0 Hz, 1H); 5.23 (s (br), 1H); 5.12 (d, 3J = 8.6 Hz, 1H); 4.71–4.64 (m, 2H); 4.42 (d, 3J = 5.3 Hz, 2H); 2.49 (m, 1H); 1.43 (s, 9H); 1.02 (d, 3J = 6.7 Hz, 3H); 0.83 (d, 3J = 6.7 Hz, 3H); ^{13}C -NMR (126 MHz, CDCl_3): δ [ppm] = 168.3; 156.0; 145.5; 131.0; 122.0; 120.0; 80.0; 69.2; 66.8; 36.0; 32.5; 28.5; 19.3; 18.6; MS (ESI): m/z = 361.2 ($[\text{M}+\text{Na}]^+$).

$\text{N}_2=\text{Phe-Gly}\Psi[4\text{Tz}]\text{Val-OAll}$ (6c): Boc-Gly Ψ [4Tz]Val-OAll (3c, 63 mg, 0.19 mmol) was dissolved in TFA (2 mL) and stirred for 12 h. After evaporation of TFA in vacuo the crude product was used for the next step without further purification. ^1H -NMR (500 MHz, CDCl_3): δ [ppm] = 8.62 (s, 3H); 8.16 (s, 1H); 5.89 (m, 1H); 5.33 (dddd, 4J = 1.4 Hz, 1.4 Hz, 3J = 17.2 Hz, 2J = 1.3 Hz, 1H); 5.27 (dddd, 4J = 1.3 Hz, 1.3 Hz, 3J = 10.4 Hz, 2J = 1.0 Hz, 1H); 5.14 (d, 3J = 8.5 Hz, 1H); 4.71–4.60 (m, 2H); 4.37 (s (br), 2H); 2.50 (m, 1H); 0.99 (d, 3J = 6.7 Hz, 3H); 0.81 (d, 3J = 6.7 Hz, 3H); ^{13}C -NMR (126 MHz, CDCl_3): δ [ppm] = 168.2; 161.9 (q); 140.3; 131.0; 124.2; 120.0; 116.3 (q); 69.2; 66.9; 34.8; 32.3; 19.1; 18.3. H-Gly Ψ [4Tz]Val-OAll·TFA (55 mg, 0.16 mmol) and the azido acid $\text{N}_2=\text{Phe-OH}$ (1b, 34 mg, 0.18 mmol) were stirred with HATU (93 mg, 0.24 mmol), HOAt (33 mg, 0.24 mmol) and DIPEA (0.25 mL, 1.5 mmol) according to **GP-2**. Purification via preparative RP-HPLC yielded the product as colorless solid. Yield: 34 mg (83 μmol , 52% over two steps); Preparative RP-HPLC: t_R = 23.8 min (Method P1, 220 nm); ^1H -NMR (500 MHz, CDCl_3): δ [ppm] = 7.82 (s, 1H); 7.29–7.21 (m, 5H); 7.01 (dd, 3J = 5.2 Hz, 5.2 Hz, 1H); 5.91 (m, 1H); 5.35 (dddd, 4J = 1.3 Hz, 1.3 Hz, 3J = 17.2 Hz, 2J = 1.2 Hz, 1H); 5.30 (dddd, 4J = 1.2 Hz, 1.2 Hz, 3J = 10.4 Hz, 2J = 1.1 Hz, 1H); 5.13 (d, 3J = 8.6 Hz, 1H); 4.72–4.64 (m, 2H); 4.56–4.48 (m, 2H); 4.19 (dd, 3J = 8.3 Hz, 4.4 Hz, 1H); 3.32 (dd, 3J = 4.4 Hz, 2J = 14.0 Hz, 1H); 3.00 (dd, 3J = 8.3 Hz, 2J = 14.0 Hz, 1H); 2.49 (m, 1H); 1.03 (d, 3J = 6.7 Hz, 3H); 0.85 (d, 3J = 6.7 Hz, 3H); ^{13}C -NMR (126 MHz, CDCl_3): δ [ppm] = 169.0; 168.2; 144.0; 136.1; 130.9; 129.6; 128.8; 127.4; 122.3; 120.1; 69.2; 66.8; 65.5; 38.7; 34.8; 32.5; 19.3; 18.7; MS (ESI): m/z = 434.2 ($[\text{M}+\text{Na}]^+$).

Boc-Gly Ψ [4Tz]Phe-Gly Ψ [4Tz]Val-OAll (7c): $\text{N}_2=\text{Phe-Gly}\Psi[4\text{Tz}]\text{Val-OAll}$ (6c, 34 mg, 83 μmol) was stirred with Boc-Gly-CH (2e, 19 mg, 0.12 mmol), $\text{CuSO}_4\cdot 5\text{H}_2\text{O}$ (10 mg, 0.040 mmol) and sodium ascorbate (16 mg, 81 μmmol) according to **GP-1**. Purification via preparative RP-HPLC yielded the product as colorless solid. Yield: 19 mg (34 μmol , 41%); Analytical

RP-HPLC: t_R = 3.04 min (Method A1); Preparative RP-HPLC: t_R = 32.9 min (Method P2, 220 nm); $^1\text{H-NMR}$ (600 MHz, CDCl_3): δ [ppm] = 7.74 (s, 1H); 7.59 (s, 1H); 7.22–7.19 (m, 3H); 7.03–7.02 (m, 2H); 6.99 (dd, 3J = 5.8 Hz, 5.8 Hz, 1H); 5.89 (m, 1H); 5.34 (dddd, 4J = 1.5 Hz, 1.5 Hz, 3J = 17.2 Hz, 2J = 1.4 Hz, 1H); 5.29 (dddd, 4J = 1.3 Hz, 1.3 Hz, 3J = 10.4 Hz, 2J = 1.3 Hz, 1H); 5.27 (dd, 3J = 8.6 Hz, 6.9 Hz, 1H); 5.11 (d, 3J = 8.6 Hz, 1H); 5.11 (s (*br*), 1H); 4.70 (dddd, 4J = 1.3 Hz, 1.3 Hz, 3J = 6.0 Hz, 2J = 13.0 Hz, 1H); 4.65 (dddd, 4J = 1.3 Hz, 1.3 Hz, 3J = 6.0 Hz, 2J = 13.0 Hz, 1H); 4.74–4.64 (m, 2H); 4.35 (m, 2H); 3.56 (dd, 3J = 6.5 Hz, 2J = 13.9 Hz, 1H); 3.38 (dd, 3J = 8.9 Hz, 2J = 13.9 Hz, 1H); 2.47 (m, 1H); 1.43 (s, 9H); 1.03 (d, 3J = 6.7 Hz, 3H); 0.83 (d, 3J = 6.7 Hz, 3H); $^{13}\text{C-NMR}$ (151 MHz, CDCl_3): δ [ppm] = 168.4; 167.4; 155.9; 145.7; 143.9; 135.4; 131.0; 129.0; 128.9; 127.6; 122.4; 122.0; 120.1; 79.9; 69.1; 66.8; 66.3; 39.5; 36.2; 35.5; 32.6; 28.5; 19.3; 18.8; MS (ESI): m/z = 589.3 ($[\text{M}+\text{Na}]^+$); HRMS (ESI): m/z calcd. for $\text{C}_{19}\text{H}_{34}\text{N}_4\text{O}_3\text{SNa}^+$ ($[\text{M}+\text{Na}]^+$): 589.2857, found: 589.2852.

$\text{N}_2=\text{Phe-Gly}\Psi[4\text{Tz}]\text{Phe-Gly}\Psi[4\text{Tz}]\text{Val-OAll}$ (8c): Boc-Gly $\Psi[4\text{Tz}]\text{Phe-Gly}\Psi[4\text{Tz}]\text{Val-OAll}$ (7c, 78 mg, 0.138 mmol) was dissolved in TFA (2 mL) and stirred for 18 h. After evaporation of TFA in vacuo the free amine, the azido carboxylic acid $\text{N}_2=\text{Phe-OH}$ (1b, 39 mg, 0.21 mmol), HATU (79 mg, 0.20 mmol), HOAt (28 mg, 0.21 mmol) and DIPEA (0.21 mL, 1.2 mmol) were stirred according to **GP-2**. Purification via preparative RP-HPLC yielded the product as colorless solid. Yield: 38 mg (59 μmol , 43%); Preparative RP-HPLC: t_R = 34.2 min (Method P3, 254 nm); $^1\text{H-NMR}$ (500 MHz, CDCl_3): δ [ppm] = 7.75 (s, 1H); 7.58 (s, 1H); 7.48 (dd, 3J = 5.6 Hz, 5.6 Hz, 1H); 7.28–7.16 (m, 8H); 7.08 (dd, 3J = 5.1 Hz, 5.1 Hz, 1H); 7.03–7.01 (m, 2H); 5.88 (m, 1H); 5.38 (dd, 3J = 8.4 Hz, 7.1 Hz, 1H); 5.32 (dddd, 4J = 1.5 Hz, 1.5 Hz, 3J = 17.1 Hz, 2J = 1.5 Hz, 1H); 5.28 (dddd, 4J = 1.3 Hz, 1.3 Hz, 3J = 10.4 Hz, 2J = 1.3 Hz, 1H); 5.09 (d, 3J = 8.6 Hz, 1H); 4.70–4.60 (m, 2H); 4.74–4.46 (m, 2H); 4.43–4.38 (m, 2H); 4.16 (dd, 3J = 8.4 Hz, 4.4 Hz, 1H); 3.55 (dd, 3J = 6.8 Hz, 2J = 13.9 Hz, 1H); 3.35 (dd, 3J = 8.7 Hz, 2J = 13.9 Hz, 1H); 3.29 (dd, 3J = 4.4 Hz, 2J = 14.0 Hz, 1H); 2.97 (dd, 3J = 8.4 Hz, 2J = 14.0 Hz, 1H); 2.47 (m, 1H); 1.01 (d, 3J = 6.7 Hz, 3H); 0.81 (d, 3J = 6.7 Hz, 3H); $^{13}\text{C-NMR}$ (126 MHz, CDCl_3): δ [ppm] = 169.0; 168.3; 167.4; 144.2; 143.9; 136.3; 135.3; 131.0; 129.6; 129.0; 128.9; 128.8; 127.5; 127.3; 122.8; 122.2; 120.0; 69.1; 66.8; 65.9; 65.3; 39.4; 38.6; 35.3; 34.9; 32.5; 19.3; 18.7; MS(MALDI): m/z = 640.3 ($[\text{M}+\text{H}]^+$); 662.3 ($[\text{M}+\text{Na}]^+$); 678.3 ($[\text{M}+\text{K}]^+$).

Boc-Gly $\Psi[4\text{Tz}]\text{Phe-Gly}\Psi[4\text{Tz}]\text{Phe-Gly}\Psi[4\text{Tz}]\text{Val-OAll}$ (9c): $\text{N}_2=\text{Phe-Gly}\Psi[4\text{Tz}]\text{Phe-Gly}\Psi[4\text{Tz}]\text{Val-OAll}$ (8c, 38 mg, 59 μmol) was stirred with the alkyne Boc-Gly-CH (2e, 14 mg, 88 μmol), $\text{CuSO}_4\cdot 5\text{H}_2\text{O}$ (7.4 mg, 30 μmol) and sodium ascorbate (11.7 mg, 59.0 μmol) according to **GP-1**. Purification via preparative RP-HPLC yielded the product as colorless solid. Yield: 7.0 mg (9 μmol , 15%); Analytical RP-HPLC: t_R = 3.12 min (Method A1); Preparative RP-HPLC: t_R = 34.0 min (Method P3, 220 nm); $^1\text{H-NMR}$ (500 MHz, $\text{DMSO}-d_6$): δ [ppm] = 9.05 (dd, 3J = 5.5 Hz, 5.5 Hz, 1H); 8.99 (dd, 3J = 5.6 Hz, 5.6 Hz, 1H); 8.07 (s, 1H); 8.05 (s, 1H); 7.94 (s, 1H); 7.28 (dd, 3J = 6.0 Hz, 6.0 Hz, 1H); 7.22–7.14 (m, 10H); 5.90 (m, 1H); 5.67–5.57 (m, 2H); 5.31 (d, 3J = 8.2 Hz, 1H); 5.28 (dddd, 4J = 1.5 Hz, 1.5 Hz, 3J = 17.2 Hz, 2J = 1.5 Hz, 1H); 5.23 (dddd, 4J = 1.4 Hz, 1.4 Hz,

3J = 10.5 Hz, 2J = 1.4 Hz, 1H); 4.70–4.62 (m, 2H); 4.41–4.34 (m, 2H); 4.33–4.26 (m, 2H); 4.14 (m, 2H); 3.41–3.30 (m, 4H); 2.55 (m, 1H); 1.30 (s, 9H); 0.95 (d, 3J = 6.7 Hz, 3H); 0.77 (d, 3J = 6.7 Hz, 3H); $^{13}\text{C-NMR}$ (126 MHz, $\text{DMSO}-d_6$): δ [ppm] = 167.9; 167.4; 167.3; 155.6; 145.3; 143.8; 143.6; 136.2; 136.0; 131.8; 128.9; 128.9; 128.3; 128.3; 126.8; 126.8; 123.1; 122.2; 121.9; 118.6; 77.9; 67.5; 65.8; 63.7; 63.7; 37.8; 37.6; 35.6; 34.4; 34.4; 30.7; 28.2; 18.8; 18.3; MS(ESI): m/z = 817.5 ($[\text{M}+\text{Na}]^+$); HRMS(ESI): m/z calcd. for $\text{C}_{40}\text{H}_{50}\text{N}_{12}\text{O}_6\text{Na}^+$ ($[\text{M}+\text{Na}]^+$): 817.3868, found: 817.3874.

Boc-Ala-Gly $\Psi[4\text{Tz}]\text{Phe-Gly}\Psi[4\text{Tz}]\text{Phe-Gly}\Psi[4\text{Tz}]\text{Val-OAll}$ (10c): Boc-Gly $\Psi[4\text{Tz}]\text{Phe-Gly}\Psi[4\text{Tz}]\text{Phe-Gly}\Psi[4\text{Tz}]\text{Val-OAll}$ (9c, 50 mg, 63 μmol) is dissolved in 2 mL of a 1:1 mixture of DCM and HCl (4 M in dioxane) and stirred for 2 h at rt. After complete cleavage of the Boc-group, the free amine is evaporated to dryness. In a second flask, Boc-Ala-OH (24 mg, 0.13 mmol) and HOAt (19 mg, 0.14 mmol) are dissolved in DCM (5 mL, dry). After addition of DIC (22 μL , 0.14 mmol), the mixture is stirred 5 min at RT for preactivation and is then added to the free amine, followed by TMP (42 μL , 0.32 mmol). This solution is left stirring over night at rt. After evaporation of the solvent, the crude product is purified by preparative HPLC. Yield: 41 mg (47 μmol , 75%); Analytical RP-HPLC: t_R = 5.3 min (Method A2); $^1\text{H-NMR}$ (600 MHz, $\text{DMSO}-d_6$): δ [ppm] = 9.04 (dd, J = 5.61, 5.57 Hz, 1H), 9.00 (dd, J = 5.56, 5.43 Hz, 1H), 8.26 (dd, J = 5.99, 5.93 Hz, 1H), 8.08 (s, 1H), 8.04 (s, 1H), 7.94 (s, 1H), 7.25–7.08 (m, 10H), 6.91 (d, J = 7.4 Hz, 1H), 5.94–5.85 (m, 1H), 5.62–5.57 (m, 2H), 5.30 (d, J = 8.4 Hz, 1H), 5.28 (dd, J = 17.2, 1.7 Hz, 1H), 5.23 (dd, J = 10.5, 1.6 Hz, 1H), 4.70–4.62 (m, 2H), 4.41–4.24 (m, 6H), 3.97 (dq, 1H, J = 7.4, 7.2 Hz), 3.42–3.27 (m, 4H) 2.54 (dq, J = 8.4, 6.7, 6.5 Hz, 1H), 1.38 (s, 9H), 1.17 (d, J = 7.2 Hz, 3H), 0.94 (d, J = 6.5 Hz, 3H), 0.77 (d, J = 6.7 Hz, 3H); $^{13}\text{C-NMR}$ (151 MHz, $\text{DMSO}-d_6$): δ [ppm] = 173.15, 168.33, 167.73, 155.51, 145.26, 144.25, 144.03, 136.52, 136.49, 132.21, 129.25, 128.24, 127.24, 123.49, 122.66, 122.40, 119.06, 78.44, 67.98, 66.23, 64.16, 50.13, 38.29, 38.08, 34.84, 34.83, 34.80, 31.12, 28.68, 19.26, 18.71; HRMS (ESI): m/z calcd. for $\text{C}_{43}\text{H}_{56}\text{N}_{13}\text{O}_7^+$ ($[\text{M}+\text{H}]^+$): 866.4420, found: 866.4413.

Conformational Analysis

Molecular dynamics (MD) simulations were performed on a compute cluster located at the Center for Biotechnology (CeBiTec), Bielefeld University, using the CUDA accelerated version of the pmemd program as implemented in AMBER (Amber 16, AmberTools 17) (Case et al., 2017). All simulations were based on the additional force-field TZLff (Marion et al., 2018) parametrized for 1,4- and 1,5-disubstituted peptidotriazolamers.

Identical simulation strategies were applied for the conformational analysis of all molecules. First, 100 parallel simulated annealing (SA) runs were performed in the gas phase by applying NMR-derived inter-proton restraints (**Supplementary Tables 1–3**). No cutoff was applied on non-bonded interactions and the temperature ramp was set to gradually heat up the molecule from 0 to 600 K and finally cool it down to 0 K over a 1 ns-long MD run (10 K, 5 ps; 100 K, 5 ps; 200 K, 90 ps; 600 K, 400 ps; 400 K, 100 ps; 200 K, 200 ps; 100 K, 75 ps; 10 K, 20 ps; 0 K, 5 ps). Interproton distances were calculated

from ROESY-NMR spectra using equation 3 by Ämmälähti et al. (1996). The harmonic restraints were applied only to the upper bound, with a force constant of 32 kcal·mol⁻¹·Å⁻² (as set in the input of AMBER). After an initial series of 100 runs, NMR restraint restraints causing penalties <5 kcal·mol⁻¹, were regarded as potential artifacts from the spectrum interpretation and removed from the set of restraints. The procedure was then repeated until no restraint passed the penalty ceiling.

The representative structure of the main cluster (based on backbone atoms only) among the SA replica was further selected as a starting structure for MD simulations in solvent. Each molecule was solvated in a truncated octahedron box of (i) TIP4Pew water (Horn et al., 2004) molecules and (ii) DMSO (Fox and Kollman, 1998) molecules, the solvent used for NMR, with a 15 Å buffer region. After minimization, the systems were gradually heated up, first in the NVT ensemble from 0 to 100 K, and then in the NPT ensemble from 100 to 300 K over a total of 890 ps (10 K, 10 ps; 50 K, 10 ps; 100 K, 20 ps; 100 K, 50 ps; 200 K, 100 ps; 300 K, 200 ps; 300 K, 500 ps). Production runs were then performed in the NPT ensemble for 200 ns. All simulations of solvated systems used a time step of 2 fs, periodic boundary conditions with particle mesh Ewald and a non-bonded cutoff of 12 Å, and the SHAKE algorithm to constrain the length of all bonds involving a hydrogen atom. Temperature and pressure were controlled with Langevin dynamics (collision frequency of 2.0 ps⁻¹) and isotropic position scaling, respectively. For each system, one simulation in water and one simulation in DMSO were performed without applying any NMR restraint.

The simulations for the longer poly-alanine mimics (poly-Ala) followed the same protocol and were performed without restraints in water and in DMSO. For each poly-Ala system, four parallel simulations were ran starting from the same coordinates after heatup but with different initial velocities in order to increase the sampling of the conformational space and ensure convergence of our analysis.

Analysis of the trajectories were performed using cpptraj module of AmberTools17 (Roe and Cheatham, 2013). The output data was post processed using python 2 including NumPy and matplotlib modules (Hunter, 2007; Oliphant, 2007). Cluster analysis was performed using cpptraj's hierarchical agglomerative approach with a total of 10 clusters based on backbone RMSD (N, C^O, C^α, ψ[4Tz]). Root mean square deviation (RMSD) and radius of gyration (RoG) analysis were performed based on backbone atoms only (N, C^O, C^α, ψ[4Tz]) using the heatup structure as reference point in the case of RMSD. Dihedral analysis was done using the ϕ- and ψ- torsion angles defined in Figure 4. The torsion angle distribution was plotted in a Ramachandran like style using matplotlib. Radial distribution functions (RDFs) were calculated using a bin spacing of 0.1 Å and normalized using the default density of water as implemented in cpptraj. The representative structures of

the main clusters were prepared using the VMD software (Humphrey et al., 1996).

DATA AVAILABILITY

This manuscript contains previously unpublished data. The name of the repository and accession number are not available.

AUTHOR CONTRIBUTIONS

The project was designed, coordinated and supervised by NS. Synthesis of the peptidotriazolamers was performed by TF, OK and AN as well as the measurement of spectroscopic data by TF, OK, AN, and DS. Analysis of the NMR data for the use as distance restraints was done by DS, MJ, JG, under supervision of RL. The molecular modeling study was designed by AM and IA, supervised by AM, and executed mainly by DS, with assistance of MJ and JG. DS analyzed and compiled the data and prepared the manuscript with support of AM, NS, RL, and IA. The final manuscript was read and approved by all authors.

FUNDING

The authors gratefully acknowledge financial support from Deutsche Forschungsgemeinschaft (DFG, Project SE 609/10-1, SFB 749, project C8, CIPSM), Deutscher Akademischer Austauschdienst (DAAD, Project ID 57333947) and the Leading National Research Centre (KNOW, Poland), the BioNam: Bionanomaterials project. This work was supported by the BMBF-funded de.NBI Cloud within the German Network for Bioinformatics Infrastructure (de.NBI) (031A537B, 031A533A, 031A538A, 031A533B, 031A535A, 031A537C, 031A534A, 031A532B). We acknowledge support for the Article Processing Charge by the Deutsche Forschungsgemeinschaft and the Open Access Publication Fund of Bielefeld University.

ACKNOWLEDGMENTS

The authors gratefully thank the de.NBI Cloud Team for the access to the de.NBI Cloud as major computational resource for this project. The authors thank the NMR spectroscopy as well as the Mass spectrometry department of Bielefeld University.

SUPPLEMENTARY MATERIAL

The Supplementary Material for this article can be found online at: <https://www.frontiersin.org/articles/10.3389/fchem.2019.00155/full#supplementary-material>

Supplementary Material as mentioned above as well as NMR data and PDB files of the representative structures are available online.

REFERENCES

Ämmälähti, E., Bardet, M., and Molko, D., Cadet, J. (1996). Evaluation of distances from ROESY experiments with the intensity-ratiomethod. *J. Magn. Reson. Ser. A*. 122, 230–232.

Angell, Y., and Burgess, K. (2005). Ring closure to β-turn mimics via copper-catalyzed azide/alkynecycloadditions. *J. Org. Chem.* 70, 9595–9598. doi: 10.1021/jo0516180

Angell, Y. L., and Burgess, K. (2007). Peptidomimetics via copper-catalyzed azide-alkynecycloadditions. *Chem. Soc. Rev.* 36, 1674–1689. doi: 10.1039/b701444a

- Angelo, N. G., and Arora, P. S. (2005). Nonpeptidic foldamers from amino acids: synthesis and characterization of 1,3-substituted triazole oligomers. *J. Am. Chem. Soc.* 127, 17134–17135. doi: 10.1021/ja056406z
- Angelo, N. G., and Arora, P. S. (2007). Solution- and solid-phase synthesis of triazole oligomers that display protein-like functionality. *J. Org. Chem.* 72, 7963–7967. doi: 10.1021/jo701292h
- Appendino, G., Bacchiaga, S., Minassi, A., Cascio, M. G., De Petrocellis, L., and Di Marzo, V. (2007). The 1,2,3-triazole ring as a peptido- and olefinomimetic element: discovery of click vanilloids and cannabinoids. *Angew. Chem. Int. Ed.* 46, 9312–9315. doi: 10.1002/anie.200703590
- Arava, V. R., Gorentla, L., and Dubey, P. K. (2011). Thermal rearrangement of tert-butylsulfonamide. *Beilstein J. Org. Chem.* 7, 9–12. doi: 10.3762/bjoc.7.2
- Beckmann, H. S. G., and Wittmann, V. (2007). One-pot procedure for diazo transfer and azide-alkyne cycloaddition: triazole linkages from amines. *Org. Lett.* 9, 1–4. doi: 10.1021/ol0621506
- Beierle, J. M., Horne, W. S., van Maarseveen, J. H., Waser, B., Reubi, J. C., and Ghadiri, M. R. (2009). Conformationally homogeneous heterocyclic pseudotetrapeptides as three-dimensional scaffolds for rational drug design: receptor-selective somatostatin analogues. *Angew. Chem. Int. Ed.* 48, 4725–4729. doi: 10.1002/anie.200805901
- Ben Haj Salah, K., Legrand, B., Das, S., Martinez, J., and Inguibert, N. (2015). Straightforward strategy to substitute amide bonds by 1,2,3-triazoles in peptaibols analogs using Aibψ/[Tz]-Xaadipeptide. *Biopolymers* 104, 611–621. doi: 10.1002/bip.22641
- Ben Haj Salah, K., Das, S., Ruiz, N., Andreu, V., Martinez, J., Wenger, E., et al. (2018). How are 1,2,3-triazoles accommodated in helical secondary structures? *Org. Biomol. Chem.* 16, 3576–3583. doi: 10.1039/C8OB00686E
- Bock, V. D., Hiemstra, H., and van Maarseveen, J. H. (2006a). CuI-catalyzed alkyne-azide “Click” Cycloadditions from a mechanistic and synthetic perspective. *Eur. J. Org. Chem.* 1, 51–68. doi: 10.1002/ejoc.200500483
- Bock, V. D., Perciaccante, R., Jansen, T. P., Hiemstra, H., and van Maarseveen, J. H. (2006b). Click chemistry as a route to cyclic tetrapeptide analogues: synthesis of cyclo-[Pro-Val-ψ(triazole)-Pro-Tyr]. *Org. Lett.* 8, 919–922. doi: 10.1021/ol053095o
- Bock, V. D., Speijer, D., Hiemstra, H., and van Maarseveen, J. H. (2007). 1,2,3-Triazoles as peptide bond isosteres: synthesis and biological evaluation of cyclotetrapeptidomimics. *Org. Biomol. Chem.* 5, 971. doi: 10.1039/b616751a
- Brik, A., Alexandratos, J., Y.-Lin, C., Elder, J. H., Olson, A. J., Wlodawer, A., Goodsell, D. S., et al. (2005). 1,2,3-triazole as a peptide surrogate in the rapid synthesis of HIV-1 protease inhibitors. *Chem. Bio. Chem.* 6, 1167–1169. doi: 10.1002/cbic.200500101
- Brik, M. J., Lin, Y.-C., Elder, J. H., Goodsell, D. S., Olson, A. J., Fokin, V. V., et al. (2003). Rapid diversity-oriented synthesis in microtiter plates for *in situ* screening of HIV protease inhibitors. *Chem. Bio. Chem.* 4, 1246. doi: 10.1002/cbic.200300724
- Case, C. D. S., Cheatham, T. E., Darden, T. A., Duke, R. E., Giese, T. J., Gohlke, H., et al. (2017). *AMBER*. San Francisco, CA: University of California.
- Chen, D., Brahimi, F., Angell, Y., Y.-Li, C., Moskowicz, J., Saragovi, H. U., et al. (2009). Bivalent peptidomimetic ligands of TrkC are biased agonists and selectively induce neuritegenesis or potentiate neurotrophin-3 trophic signals. *ACS Chem. Biol.* 4, 769–781. doi: 10.1021/cb9001415
- Fox, T., and Kollman, P. A. (1998). Application of the RESP methodology in the parametrization of organicsolvents. *J. Phys. Chem. B.* 102, 8070–8079. doi: 10.1021/jp9717655
- Gil, B. V., Arévalo, M. J., and López, O. (2007). Click chemistry - what's in a name? triazole synthesis and beyond. *Synthesis* 11, 1589–1620. doi: 10.1002/chin.200735250
- Gottlieb, H. E., Kotlyar, V., and Nudelman, A. (1997). NMR chemical shifts of common laboratory solvents as trace impurities. *J. Org. Chem.* 62, 7512–7515. doi: 10.1021/jo971176v
- Hartwig, S., and Hecht, S. (2010). Polypseudopeptides with variable stereochemistry: synthesis via click-chemistry, postfunctionalization and conformational behavior in solution. *Macromolecules* 43, 242–248. doi: 10.1021/ma902018w
- Hein, C. D., X.-, and Liu, M., Wang, D. (2008). Click chemistry, a powerful tool for pharmaceutical sciences. *Pharm. Res.* 25, 2216–2230. doi: 10.1007/s11095-008-9616-1
- Horn, H. W., Swope, W. C., Pitera, J. W., Madura, J. D., Dick, T. J., Hura, G. L., et al. (2004). Development of an improved four-site water model for biomolecular simulations: TIP4P-Ew. *J. Chem. Phys.* 120, 9665–9678. doi: 10.1063/1.1683075
- Horne, W. S., Olsen, C. A., Beierle, J. M., Montero, A., and Ghadiri, M. R. (2009). Probing the bioactive conformation of an archetypal natural product HDAC inhibitor with conformationally homogeneous triazole-modified cyclotetrapeptides. *Angew. Chem. Int. Ed.* 48, 4718–4724. doi: 10.1002/anie.200805900
- Horne, W. S., Yadav, M. K., Stout, C. D., and Ghadiri, M. R. (2004). Heterocyclic peptide backbone modifications in an alpha-helical coiled coil. *J. Am. Chem. Soc.* 126, 15366–15367. doi: 10.1021/ja0450408
- Humphrey, W., Dalke, A., and Schulten, K. (1996). VMD: visual molecular dynamics. *J. Molec. Graph.* 14, 33–38. doi: 10.1016/0263-7855(96)00018-5
- Hunter, J. D. (2007). Matplotlib: A 2D Graphics Environment. *Comput. Sci. Eng.* 9, 90–95. doi: 10.1109/MCSE.2007.55
- Jochim, L., Miller, S. E., Angelo, N. G., and Arora, P. S. (2009). Evaluation of triazolamers as active site inhibitors of HIV-1 protease. *Bioorg. Med. Chem. Lett.* 19, 6023–6026. doi: 10.1016/j.bmcl.2009.09.049
- Ke, Z., Chow, H. F., Chan, M. C., Liu, Z., and Sze, K. H. (2012). Head-to-tail dimerization and organogelating properties of click peptidomimetics. *Org. Lett.* 14, 394–397. doi: 10.1021/ol2031685
- Kim, S., Cho, M., Lee, T., Lee, S., H.-, Min, Y., and Kook, S. (2007). Design, synthesis, and preliminary biological evaluation of a novel triazole analogue of ceramide. *Bioorg. Med. Chem. Lett.* 17, 4584–4587. doi: 10.1016/j.bmcl.2007.05.086
- Kolb, H. C., and Sharpless, K. B. (2003). The growing impact of click chemistry on drug discovery. *Drug Disc. Today* 8, 1128–1137. doi: 10.1016/S1359-6446(03)02933-7
- Kracker, O., Gora, J., Krzciuk-Gula, J., Marion, A., Neumann, B., H.-, Stammer, G., et al. (2018). 1,5-Disubstituted 1,2,3-Triazole-Containing Peptidotriazolamers: Design Principles For A Class Of Versatile Peptidomimetics. *Chem. Eur. J.* 24, 953–961. doi: 10.1002/chem.201704583
- Lee, T., Cho, M., Ko, S. Y., Youn, H.-J., Baek, D. J., Cho, W.-J., et al. (2007). Synthesis and evaluation of 1,2,3-triazole containing analogues of the immunostimulant alpha-GalCer. *J. Med. Chem.* 50, 585–589. doi: 10.1021/jm061243q
- Lee, Y., and Silverman, R. B. (2000). Traceless solid-phase synthesis of chiral 3-aryl β-amino acid containing peptides using a side-chain-tethered β-amino acid building block. *Org. Lett.* 2, 303–306. doi: 10.1021/ol9912480
- Marion, A., Gora, J., Kracker, O., Froehr, T., Latajka, R., Sewald, N., et al. (2018). Amber-compatible parametrization procedure for peptide-like compounds: application to 1,4- and 1,5-substituted triazole-based peptidomimetics. *J. Chem. Inf. Model.* 58, 90–110. doi: 10.1021/acs.jcim.7b00305
- Moses, J. E., and Moorhouse, A. D. (2007). The growing applications of click chemistry. *Chem. Soc. Rev.* 36, 1249–1262. doi: 10.1039/B613014N
- Nahrwold, B. T., Eissler, S., Verma, S., and Sewald, N. (2010). “Clicktophycin-52”: a bioactive cryptophycin-52 triazole analogue. *Org. Lett.* 12, 1064–1067. doi: 10.1021/ol1000473
- Nwe, K., and Brechbiel, M. W. (2009). Growing applications of “click chemistry” for bioconjugation in contemporary biomedical research. *Cancer Biother. Radiopharm.* 24, 289–302. doi: 10.1089/cbr.2008.0626
- Oliphant, T. E. (2007). A guide to NumPy. USA: Trelgol Publishing 2006. Available online at: <https://www.scipy.org/> (accessed November 29, 2018).
- Patterson, W., and Ellman, J. A. (2006). Asymmetric synthesis of α,α-dibranched propargylamines by acetylide additions to N-tert-butanesulfinylketimines. *J. Org. Chem.* 71, 7110–7112. doi: 10.1021/jo061160h
- Pedersen, D. S., and Abell, A. (2011). 1,2,3-triazoles in peptidomimetic chemistry. *Eur. J. Org. Chem.* 2011, 2399–2411. doi: 10.1002/ejoc.201100157
- Roe, D. R., and Cheatham, T. E. III. (2013). PTRAJ and CPPTRAJ: software for processing and analysis of molecular dynamics trajectory data. *J. Chem. Theory Comput.* 9, 3084–3095. doi: 10.1021/ct400341p
- Rostovtsev, V. V., Green, L. G., Fokin, V. V., and Sharpless, K. B. (2002). A stepwise Huisgen cycloaddition process: copper(I)-catalyzed regioselective “ligation” of azides and terminal alkynes. *Angew. Chem. Int. Ed.* 41, 2596–2599. doi: 10.1002/1521-3773(20020715)41:14<2596::AID-ANIE2596>3.0.CO;2-4
- Smith, B. III., Keenan, T. P., Holcomb, R. C., Sprengeler, P. A., Guzman, M. C., et al. (1992). Design, synthesis, and crystal structure of a pyrrolinone-based peptidomimetic possessing the conformation of a β-strand: potential

- application to the design of novel inhibitors of proteolytic enzymes. *J. Am. Chem. Soc.* 114, 10672–10674. doi: 10.1021/ja00052a093
- Tornøe, C. W., Christensen, C., and Meldal, M. (2002). Peptidotriazoles on solid phase: [1,2,3]-triazoles by regioselective copper(I)-catalyzed 1,3-dipolar cycloadditions of terminal alkynes to azides. *J. Org. Chem.* 67, 3057–3064. doi: 10.1021/jo011148j
- Tron, G. C., Pirali, T., Billington, R. A., Canonico, P. L., Sorba, G., and Genazzani, A. A. (2008). Click chemistry reactions in medicinal chemistry: Applications of the 1,3-dipolar cycloaddition between azides and alkynes. *Med. Res. Rev.* 28, 278–308. doi: 10.1002/med.20107
- Valverde, E., Vomstein, S., Fischer, C. A., Mascarin, A., and Mindt, T. L. (2015). Probing the backbone function of tumor targeting peptides by an amide-to-triazole substitution strategy. *J. Med. Chem.* 58, 7475–7484. doi: 10.1021/acs.jmedchem.5b00994
- van Maarseveen, J. H., Horne, W. S., and Ghadiri, M. R. (2005). Efficient Route to C₂ Symmetric Heterocyclic Backbone Modified Cyclic Peptides. *Org. Lett.* 7, 4503–4506. doi: 10.1021/ol0518028
- Wang, J., Uttamchandani, M., Li, J., Hu, M., and Yao, S. Q. (2006). Rapid assembly of matrix metalloprotease inhibitors using click chemistry. *Org. Lett.* 8, 3821–3824. doi: 10.1021/ol061431a
- Weix, D. J., and Ellman, J. A. (2005). (R,S)-(+)-2-Methyl-2-propanesulfonamide. *Org. Synth.* 82, 157–165. doi: 10.15227/orgsyn.082.0157
- Wünsch, M., Fröhr, T., Schröder, D., Teichmann, L., Rudloff, J., Holtkamp, P., et al. (2017). Asymmetric synthesis of propargylamines as amino acid surrogates in peptidomimetics. *Beilstein J. Org. Chem.* 13, 2428–2441. doi: 10.3762/bjoc.13.240
- Yan, R. B., Yang, F., Wu, Y., Zhang, L. H., and Ye, X. S. (2005). An efficient and improved procedure for preparation of triflyl azide and application in catalytic diazotransfer reaction. *Tetrahedron Lett.* 46, 8993–8995. doi: 10.1016/j.tetlet.2005.10.103
- Zhang, L., Chen, X., Xue, P., Sun, H. H. Y., Williams, I. D., Sharpless, K. B., et al. (2005). Ruthenium-catalyzed cycloaddition of alkynes and organic azides. *J. Am. Chem. Soc.* 127, 15998–15999. doi: 10.1021/ja054114s

Conflict of Interest Statement: The authors declare that the research was conducted in the absence of any commercial or financial relationships that could be construed as a potential conflict of interest.

Copyright © 2019 Schröder, Kracker, Fröhr, Góra, Jewginski, Nieß, Antes, Latajka, Marion and Sewald. This is an open-access article distributed under the terms of the Creative Commons Attribution License (CC BY). The use, distribution or reproduction in other forums is permitted, provided the original author(s) and the copyright owner(s) are credited and that the original publication in this journal is cited, in accordance with accepted academic practice. No use, distribution or reproduction is permitted which does not comply with these terms.



Bicyclic Pyrrolidine-Isoxazoline γ Amino Acid: A Constrained Scaffold for Stabilizing α -Turn Conformation in Isolated Peptides

Francesco Oliva¹, Raffaella Bucci², Lucia Tamborini², Stefano Pieraccini^{1*}, Andrea Pinto^{3*} and Sara Pellegrino^{2*}

OPEN ACCESS

Edited by:

Jutta Eichler,
Friedrich-Alexander-Universität
Erlangen-Nürnberg, Germany

Reviewed by:

Lihua Yuan,
Sichuan University, China
Cheng Yang,
Sichuan University, China

*Correspondence:

Stefano Pieraccini
stefano.pieraccini@unimi.it
Andrea Pinto
andrea.pinto@unimi.it
Sara Pellegrino
sara.pellegrino@unimi.it

Specialty section:

This article was submitted to
Supramolecular Chemistry,
a section of the journal
Frontiers in Chemistry

Received: 29 November 2018

Accepted: 20 February 2019

Published: 18 March 2019

Citation:

Oliva F, Bucci R, Tamborini L,
Pieraccini S, Pinto A and Pellegrino S
(2019) Bicyclic Pyrrolidine-Isoxazoline
 γ Amino Acid: A Constrained Scaffold
for Stabilizing α -Turn Conformation in
Isolated Peptides.
Front. Chem. 7:133.
doi: 10.3389/fchem.2019.00133

Unnatural amino acids have tremendously expanded the folding possibilities of peptides and peptide mimics. While α,α -disubstituted and β -amino acids are widely studied, γ -derivatives have been less exploited. Here we report the conformational study on the bicyclic unnatural γ amino acid, 4,5,6,6a-tetrahydro-3aH-pyrrolo[3,4-d]isoxazole-3-carboxylic acid **1**. In model peptides, the (+)-(3aR6aS)-enantiomer is able to stabilize α -turn conformation when associated to glycine, as showed by ¹H-NMR, FT-IR, and circular dichroism experiments, and molecular modeling studies. α -turn is a structural motif occurring in many biologically active protein sites, although its stabilization on isolated peptides is quite uncommon. Our results make the unnatural γ -amino acid **1** of particular interest for the development of bioactive peptidomimetics.

Keywords: unnatural γ -amino acids, peptidomimetic, isoxazoline, α -turn, metadynamic studies, conformational analysis

INTRODUCTION

Amino acids are the key building blocks of proteins and biomolecules and are widely exploited in different applications, from pharmaceutical chemistry and biomedicine to material science, optoelectronics and catalysis (Zhang et al., 2012; Mikhalevich et al., 2017; Solomon et al., 2017; López-Andarias et al., 2018; Raymond and Nilsson, 2018). The insertion of unnatural amino acids (UAAs) in peptides and peptide mimics could add specific features to these molecules, such as proteolytic stability, active functional groups and new reactivity (Clerici et al., 2016; Pellegrino et al., 2016, 2017; Bucci et al., 2017). α,α disubstituted and β - homologs of natural amino acids have been particularly studied during the years for their ability to introduce conformational constraints in peptides and to stabilize specific secondary structures (Bonetti et al., 2015; Pellegrino et al., 2015; Fanelli et al., 2017; Kobayashi et al., 2017). On the other hand, γ UAAs provide a further opportunity to engineer the available backbone through the incorporation of an additional methylene group

(Vasudev et al., 2011; Sohora et al., 2018). Recent studies report that γ -peptides are able to form helices, sheets and turns, whose conformational stability is increased by introducing substituents on the backbone chain (Bouillère et al., 2011). Moreover, cyclic γ UAAs, as gabapentin (Gpn) (Chatterjee et al., 2009; Konda et al., 2018) and γ -cyclohexyl amino acid (Guo et al., 2012) are able to stabilize both turn and helix conformation in oligomers and in mixed α - γ and β - γ sequences. On the other hand, the use of bicyclic γ amino acids for the stabilization of the peptide structure is much less investigated (Machetti et al., 2000).

In this work, we investigated the conformational behavior of both the enantiomers of the bicyclic unnatural γ amino acid 4,5,6,6a-tetrahydro-3aH-pyrrolo[3,4-*d*]isoxazole-3-carboxylic acid **1**, obtained starting from the corresponding ethyl esters recently described by us (Tamborini et al., 2015). Compound **1** is a conformationally constrained dipeptide analog and, in principle, it could substitute two amino acids in a peptide chain. The presence of the constrained bicyclic system could induce specific secondary structure allowing a proper orientation of the peptide arms at C- and N- termini. Furthermore, the presence of the isoxazoline ring, a core often found in biologically active compounds, could be particularly useful for future applications in the pharmaceutical field. In fact, isoxazoline derivatives are important scaffolds found in many naturally occurring and biologically active compounds possessing a wide range of bioactivities, such as antibacterial, antifungal, antiparasitic (Conti et al., 2011; Bruno et al., 2014; Pinto et al., 2016a), anticancer (Castellano et al., 2011; Kaur et al., 2014), anti-inflammatory and anticonvulsant activity (Sperry and Wright, 2005; Pinto et al., 2011, 2016b). Isoxazolines are also considered to be important precursors for the synthesis of β -hydroxyketones (Kozikowski and Park, 1990; Tsantali et al., 2007), β -aminoalcohols (Fuller et al., 2005), isoxazolidines (Itoh et al., 2002), and many other valuable compounds. Recently, peptidomimetics containing the isoxazoline ring have been reported as β -turn mimics (Bucci et al., 2018; Memeo et al., 2018).

Starting from the (-)-(3aS,6aR)-**1** and (+)-(3aR,6aS)-**1** enantiomers, model peptides containing Leu-Val dipeptide at C-terminus and variable sequences at N-terminus were prepared. Their conformational behavior was investigated by NMR spectroscopy, FT-IR, circular dichroism, and molecular modeling. Our results indicated that (+)-(3aR,6aS)-**1** enantiomer, in combination with glycine, is effective in stabilizing the α -turn conformation in peptides (Figure 1). This structural motif occurs quite often in many key sites of proteins, such as enzyme active site, and metal binding domains (Wintjens et al., 1996), although few molecules are known to mimic or stabilize it on isolated peptides (Kelso et al., 2004; Hoang et al., 2011; Krishna et al., 2014; Wang et al., 2018). Our results make thus the unnatural γ -amino acid **1** of particular interest for future development of bioactive peptidomimetics.

MATERIALS AND METHODS

Materials

Chemicals were obtained from Zentek (Italy) and used without further purification. Melting points were determined in a Stuart Scientific melting point apparatus in open capillary tubes and are certified. ESI mass spectra were recorded on an LCQESI. MS was recorded on a LCQ Advantage spectrometer from Thermo Finnigan and a LCQ Fleet spectrometer from Thermo Scientific. CD experiments were carried out on a Jasco J-810 instrument. Spectra were obtained from 195 to 250 nm with a 0.1 nm step and 1 s collection time per step, taking three averages. The CD spectra were plotted as mean residue ellipticity θ (degree \times cm² \times dmol⁻¹) vs. wave length λ (nm). Noise-reduction was obtained using a Fourier-transform filter program from Jasco. The NMR spectroscopic experiments were carried out on a Varian OXFORD 300 MHz (300 and 75 MHz for ¹H and ¹³C, respectively). Chemical shifts, δ , are given in ppm relative to the CHCl₃ internal standard, and the coupling constants, *J*, are reported in hertz (Hz).

Methods

Synthesis of (-)-(3aS,6aR)-**1** and (+)-(3aR,6aS)-**1**

Compound (-)-**2** or (+)-**2** (200 mg, 0.70 mmol) was dissolved in MeOH (3.0 mL) and treated with 1N NaOH aqueous solution (1.4 mL). The mixture was stirred at room temperature for 1 h and the disappearance of the starting material was monitored by TLC (Cyclohexane/EtOAc 7:3). The mixture was diluted in water (20 mL), made acidic with 2N aqueous HCl and extracted with EtOAc. The organic phase was dried over anhydrous Na₂SO₄ and after evaporation of the solvent, the acid derivate (-)-(3aS,6aR)-**1** or (+)-(3aR,6aS)-**1** (170 mg, 95%) was obtained as a white solid.

(-)-(3aS,6aR)-1****: *R_f* (CH₂Cl₂/MeOH 9:1 + 1% AcOH): 0.40; [α]_D²⁰: (-) 192.2 (c: 0.55 in MeOH); mp = dec. *T* > 137°C; ¹H NMR (300 MHz, CD₃OD): δ 5.35 (dd, *J* = 4.8, 9.2, 1H); 4.10 (ddd, *J* = 2.2, 9.2, 9.2, 1H); 3.86–3.96 (m, 2H); 3.38–3.50 (m, 2H); 1.44 (s, 9H) ppm; ¹³C NMR (75 MHz, CD₃OD): δ 161.28, 154.77, 152.95, 87.62, 80.33, 53.06, 50.93, 49.10, 27.12 (3C) ppm.

HRMS (ESI) [*M* + Na]⁺ calculated for C₁₁H₁₆N₂O₅Na: 279.0957, found: 279.0950.

(+)-(3aR,6aS)-1****: [α]_D²⁰: (+) 192.5 (c: 0.57 in MeOH).

General Procedure for Coupling Reaction

Free carboxylic acid (1 equiv.) was dissolved in CH₂Cl₂ (0.01M solution) and the mixture was cooled to 0°C. HOBt (1.1 equiv.) and EDC (1.1 equiv.) were added. After 1 h, free amino compound (1 equiv.) was added, followed by the addition of DIEA (2 equiv.). The reaction mixture was stirred at room temperature for 24 overnight (TLC analysis). The organic layer was washed with a 5% solution of KHSO₄ (3 times), with a saturated solution of NaHCO₃ (3 times) and with brine (1 time). The organic phase was dried over Na₂SO₄ and the solvent was removed under vacuum. The products were purified by column flash chromatography on silica gel (hexane/ethyl acetate gradient) followed by a crystallization from a mixture of ethyl acetate/hexane.

Abbreviations: ACN, Acetonitrile; Boc, tert-butyloxycarbonyl; DIEA, N,N-Diisopropylethylamine; DMF, Dimethylformamide; EDC, 1-Ethyl-3-(3-dimethylaminopropyl)carbodiimide; Gly, Glycine; HOBt, Hydroxybenzotriazole; Leu, Leucine; Phe, Phenylalanine; TFA, Trifluoroacetic acid; Val, Valine.

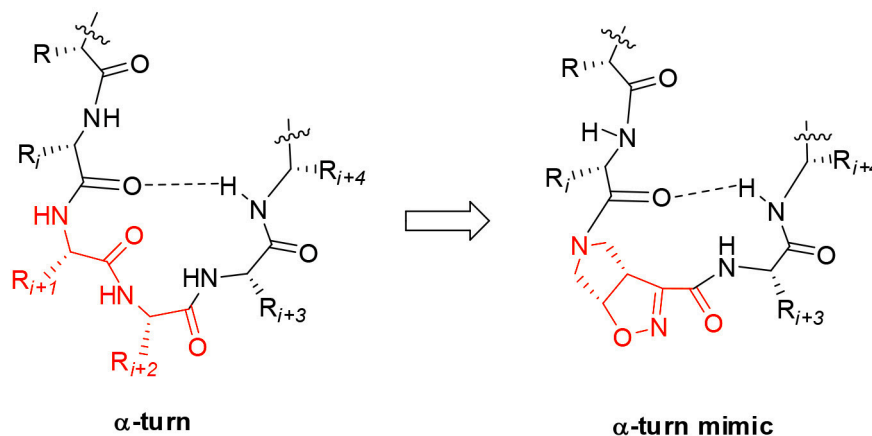


FIGURE 1 | Natural α -turn and the proposed α -turn mimic containing the bicyclic pyrrolidine-isoxazoline γ amino acid.

Product	Yield (%)	Product	Yield (%)
<i>N</i> -Boc-Leu-Val-CONH ₂ ^a	96	8	77
4	65	9	80
5	63	10	65

^asee Steinke and Kula (1990).

N-Boc-(-)- Δ^2 -isox-Leu-Val-CONH₂ (**4**)

¹H NMR (300 MHz, CDCl₃): δ 7.11 (bs, 1H), 6.88 (d, J = 8.8 Hz, 1H), 6.19 (bs, 1H), 5.72 (bs, 1H), 5.34–5.29 (m, 1H), 4.56–4.48 (m, 1H), 4.31 (dd, J = 8.2; 6.9 Hz, 1H), 4.17–3.83 (m, 3H), 3.56–3.42 (m, 2H), 2.23–2.07 (m, 1H), 1.85–1.61 (m, 3H), 1.43 (s, 9H), 0.99–0.92 (m, 12H) ppm.

¹³C NMR (75 MHz, CDCl₃): δ 173.04, 171.32, 159.44, 154.28, 153.93, 87.40, 80.43, 58.24, 53.26, 52.30, 50.53, 49.32, 40.87, 30.53, 28.31, 24.82, 22.91, 21.92, 19.27, 17.93 ppm.

HRMS (ESI) [M + Na]⁺ calculated for C₂₂H₃₇N₅O₆Na: 490.2642, found: 490.2635.

N-Boc-(+)- Δ^2 -isox-Leu-Val-CONH₂ (**5**)

¹H NMR (300 MHz, CDCl₃): δ 7.05 (bs, 1H), 6.73 (d, J = 7.9 Hz, 1H), 6.13 (bs, 1H), 5.69 (bs, 1H), 5.37–5.28 (m, 1H), 4.56–4.47 (m, 1H), 4.36–4.27 (m, 1H), 4.18–4.07 (m, 1H), 3.99–3.77 (m, 2H), 3.61–3.41 (m, 2H), 2.28–2.10 (m, 1H), 1.78–1.57 (m, 3H), 1.49 (s, 9H), 1.01–0.90 (m, 12H) ppm.

¹³C NMR (75 MHz, CDCl₃): δ 173.16, 171.54, 159.33, 154.16, 153.96, 80.34, 60.38, 58.16, 53.27, 52.25, 49.41, 41.02, 30.67, 28.32, 24.83, 22.87, 21.99, 19.20, 18.02 ppm.

HRMS (ESI) [M + Na]⁺ calculated for C₂₂H₃₇N₅O₆Na: 490.2642, found: 490.2635.

NH-Boc-Phe-(-)- Δ^2 -isox-Leu-Val-CONH₂ (**8**) –Mixture of two conformers–

¹H NMR (300 MHz, CDCl₃): δ 7.36–7.16 (m, 5H), 7.15–7.08 (m, 1H), 7.05–6.97 (m, 1H), 6.88–6.77 (m, 1H), 6.05 (bs, 1H), 5.71 (bs, 1H), 5.43 (d, J = 8.4 Hz, 1H), 5.33–5.22 (m, 3H), 5.09–4.9 (m, 1H), 4.64–4.44 (m, 3H), 4.33–4.23 (m, 2H), 4.17–4.03 (m, 2H),

3.99–3.91 (m, 1H), 3.87–3.75 (m, 2H), 3.70–3.50 (m, 2H), 3.42–3.30 (m, 1H), 3.13–3.03 (m, 1H), 2.97–2.74 (m, 3H), 2.51 (dd, J = 12.2; 4.8 Hz, 1H), 2.21–2.05 (m, 1H), 1.51–1.33 (m, 9H), 1.06–0.84 (m, 12H) ppm.

¹³C NMR (75 MHz, CDCl₃): δ 172.91, 171.38, 170.09, 159.11, 157.88, 157.30, 153.83, 152.33, 136.34, 129.46, 129.30, 128.56, 128.44, 127.12, 126.85, 96.33, 87.21, 85.98, 58.09, 53.31, 52.77, 52.36, 50.95, 49.64, 49.00, 48.59, 41.05, 40.91, 30.83, 30.62, 29.69, 28.35, 24.84, 22.81, 22.71, 19.18, 17.94 ppm.

HRMS (ESI) [M + Na]⁺ calculated for C₃₁H₄₆N₆O₇Na: 637.3326, found: 637.3332.

NH-Boc-Phe-(+)- Δ^2 -isox-Leu-Val-CONH₂ (**9**) –Mixture of two conformers–

¹H NMR (300 MHz, CDCl₃): δ 7.33–7.05 (m, 6H), 7.04–6.91 (m, 1H), 6.70 (d, J = 8.5 Hz, 1H), 6.13–5.91 (m, 2H), 5.46 (d, J = 8.5 Hz, 1H), 5.36–5.10 (m, 2H), 4.87–4.71 (m, 1H), 4.67–4.43 (m, 1H), 4.38–4.23 (m, 2H), 4.23–3.69 (m, 4H), 3.69–3.41 (m, 1H), 3.21 (dd, J = 14.3, J = 5.0 Hz, 1H), 3.10–2.79 (m, 2H), 2.54 (dd, J = 14.3, J = 5.0 Hz, 1H), 2.30–1.99 (m, 1H), 1.89–1.55 (m, 3H), 1.49 (m, 9H), 1.31 (m, 12H) ppm.

¹³C NMR (75 MHz, CDCl₃): δ 173.14, 172.90, 171.92, 171.23, 170.66, 170.49, 159.68, 158.86, 155.92, 155.18, 153.77, 153.59, 136.00, 129.63, 129.43, 129.15, 128.60, 128.41, 127.14, 127.05, 86.96, 85.53, 79.99, 79.88, 58.23, 57.68, 54.13, 53.47, 52.97, 52.19, 51.05, 48.82, 41.04, 40.85, 39.32, 30.88, 30.66, 28.45, 28.30, 25.05, 24.81, 22.91, 22.01, 21.51, 19.28, 17.98, 17.84 ppm.

HRMS (ESI) [M + Na]⁺ calculated for C₃₁H₄₆N₆O₇Na: 637.3326, found: 637.3332.

NH-Boc-Phe-Gly-(+)- Δ^2 -isox-Leu-Val-CONH₂ (**10**)

¹H NMR (300 MHz, CD₃CN): δ 7.47 (d, J = 6.9 Hz, 1H), 7.30–7.26 (m, 6H), 6.95 (d, J = 8.5 Hz, 1H), 6.72 (bs, 1H), 6.42 (bs, 1H), 5.63 (bs, 1H), 5.47–5.31 (m, 1H), 4.52–4.47 (m, 1H), 4.40–3.39 (m, 8H), 3.23–3.07 (m, 1H), 2.70–2.93 (m, 1H), 2.14–2.08 (m, 1H), 1.78–1.55 (m, 3H), 1.35 (s, 9H), 1.02–0.77 (m, 12H) ppm.

¹³C NMR (75 MHz, CD₃CN): δ 173.43, 171.63, 167.09, 159.52, 154.34, 137.64, 129.27, 128.31, 126.53, 109.99, 87.41, 86.02, 79.09,

58.06, 56.82, 55.76, 53.67, 52.65, 51.39, 49.79, 48.71, 41.62, 40.43, 40.10, 37.60, 31.51, 30.55, 29.34, 27.49, 24.77, 22.27, 20.81, 18.86, 17.21, 16.63 ppm.

HRMS (ESI) $[M + Na]^+$ calculated for $C_{33}H_{49}N_7O_8Na$: 694.3540, found: 694.3539.

General Procedure for *N*-Boc-Deprotection

N-Boc protected compound (1 equiv.) was dissolved in CH_2Cl_2 (0.01M) and the solution cooled at 0°C. TFA (50% v/v) was added dropwise, the solution was warmed up at room temperature and was stirred for 2 h. The solvent was removed under vacuum with the obtainment of the trifluoroacetate salt that was directly used in the next coupling step.

Product	Yield (%)
3^a	95
6	95
7	95

^a see Smith and Spackman (1955).

NH-(-)- Δ^2 -isox-Leu-Val-CONH₂ (**6**)

¹H NMR (300 MHz, CD₃OD): δ 7.90 (d, J = 8.7 Hz, 1H), 5.53 (dd, J = 9.5, 4.9 Hz, 1H), 4.54 (dd, J = 9.8, 4.9 Hz, 1H), 4.42 (t, J = 8.8 Hz, 1H), 4.26 – 4.17 (m, 1H), 3.90 – 3.84 (m, 1H), 3.89 – 3.75 (m, 2H), 3.58 – 3.49 (m, 2H), 3.22 (dd, J = 5.9, 4.1 Hz, 1H), 2.05 (dq, J = 13.6, 6.8 Hz, 1H), 1.80 – 1.59 (m, 3H), 1.05 – 0.82 (m, 12H) ppm.

¹³C NMR (75 MHz, CD₃OD): δ 147.47, 172.82, 159.52, 152.51, 85.48, 58.22, 52.96, 52.21, 50.55, 49.27, 40.31, 30.68, 24.54, 21.98, 20.47, 18.32, 17.08 ppm.

HRMS (ESI) $[M + Na]^+$ calculated for $C_{17}H_{29}N_5O_4Na$: 390.2117, found: 390.2111.

NH-(+)- Δ^2 -isox-Leu-Val-CONH₂ (**7**)

¹H NMR (300 MHz, CD₃OD): δ 7.97 (d, J = 8.6 Hz, 1H), 5.53 (dd, J = 9.5, 4.9 Hz, 1H), 4.55 (m, 1H), 4.39 (m, 1H), 4.26 – 4.16 (m, 1H), 3.90 – 3.72 (m, 2H), 3.58 – 3.43 (m, 2H), 3.24 – 3.16 (m, 1H), 2.05 (m, 1H), 1.75 – 1.58 (m, 3H), 1.02 – 0.81 (m, 12H) ppm.

¹³C NMR (75 MHz, CD₃OD): δ 147.47, 172.99, 159.40, 152.40, 128.72, 85.21, 58.05, 53.12, 52.17, 50.66, 49.14, 40.21, 30.91, 29.36, 24.84, 21.99, 20.25, 18.26, 16.90 ppm.

HRMS (ESI) $[M + Na]^+$ calculated for $C_{17}H_{29}N_5O_4Na$: 390.2117, found: 390.2111.

Molecular Modeling

Compound **9** and **10** were modeled in explicit solvent with periodic boundary conditions using metadynamics and restrained molecular dynamics simulations. For each of the compounds two isomers (*cis* and *trans* with respect to the amide bond) were considered, resulting in a set of four peptides. Such molecules were solvated in a cubic box of 4 nm with chloroform (compound **8**) and acetonitrile (compound **10**) to reproduce the NMR experiment conditions. Every system has been submitted to geometry optimization with the steepest descent algorithm with a convergence of 100 kJ mol⁻¹ nm⁻¹. Then we performed a 1 ns equilibration in NVT conditions at 300 K, followed by a 1

ns NPT equilibration at the 1 bar and at the same temperature. After the equilibration phase, we ran a 50 ns Well Tempered Metadynamics (WTMD) with a 8.0 kJ mol⁻¹ bias-factor, at a reference temperature of 300 K. To study the open and closed state of both peptides, we selected as collective variable (CV) the distance between C β VAL and the *N*-tert-butoxy carbonyl (*N*-Boc) quaternary carbon. A Gaussian hill with σ = 0.1 Å and an initial height of 1 kJ mol⁻¹ was added once every 100 steps. The simulation was sped up by saving the Gaussian hills on a grid that ranged from 0 to 16 Å and spaced 0.02 Å. Compound **10** was also simulated using a 50 ns restrained molecular dynamics. Special potentials are used for imposing restraints on the motion of the system, to include knowledge from experimental data such as the NMR derived interatomic distances. Distance restraints add a penalty to the potential when the distance between specified pairs of atoms exceeds a threshold value (Abraham et al., 2014). The threshold values used in our simulation are reported in the **Supplementary Materials**.

The restraints are applied in a progressive way to give time to the peptide to relax, using a τ equal to 500 ps. Since we are using multiple distance restraints, they are not necessary satisfied at each simulation step but as a time average. The atoms restrained and the relative distances are shown in **Table S1**. Compound **9** and **10** have been described using the Amber99SB-ILDN Force Field (Hornak et al., 2006). 4,5,6,6a-Tetrahydro-3aH-pyrrolo[3,4-*d*]isoxazole-3-carboxylic acid residues were parameterized according to standard procedures as explained in reference (Gandini et al., 2018). During molecular dynamics (MD) and metadynamics simulations, temperature was held constant with the v-rescale algorithm (Bussi et al., 2007), while pressure was kept constant through the Berendsen barostat (Berendsen et al., 1984). MD simulations were performed using the leap-frog algorithm with 2 fs time-step, with holonomic constraints on every bond enforced using the LINCS algorithm. Simulations and subsequent analysis were performed with the GROMACS 5.0.4 (Van Der Spoel et al., 2005) program suite, while metadynamics was run along with PLUMED version 2.2.2 (Tribello et al., 2014).

RESULTS AND DISCUSSION

The two enantiomers of compound **1** were obtained starting from the corresponding ethyl esters recently described by us (Tamborini et al., 2015). Racemate (\pm)-**2** (Conti et al., 2006) was synthesized in a flow chemistry reactor exploiting the 1,3-dipolar cycloaddition reaction of *N*-Boc-3-pyrroline with ethoxycarbonyl formonitrile oxide. An excellent enantiomeric separation (e.e. >99%) of the racemate was achieved by semi-preparative chiral HPLC. Alkaline hydrolysis of (-)-(3aS6aR)-**2** and (+)-(3aR6aS)-**2** gave the desired (-)-(3aS6aR)-**1** and (+)-(3aR6aS)-**1**, respectively (**Scheme 1**).

The ability of compound **1** to stabilize secondary structures was evaluated in model peptides containing (L)-Phe at *N*-terminus and (L)-Leu-(L)-Val sequence at *C*-terminus and (**Schemes 2, 3**). This last dipeptide was chosen as it normally adopts extended conformation in solution. Compound **1** was used in both the 3aS6aR and 3aR6aS

stereochemistries $[(-)-1$ and $(+)-1$, respectively], as a different effect on peptide conformations could be expected depending on the stereochemistry of the unnatural amino acids (Pellegrino et al., 2012).

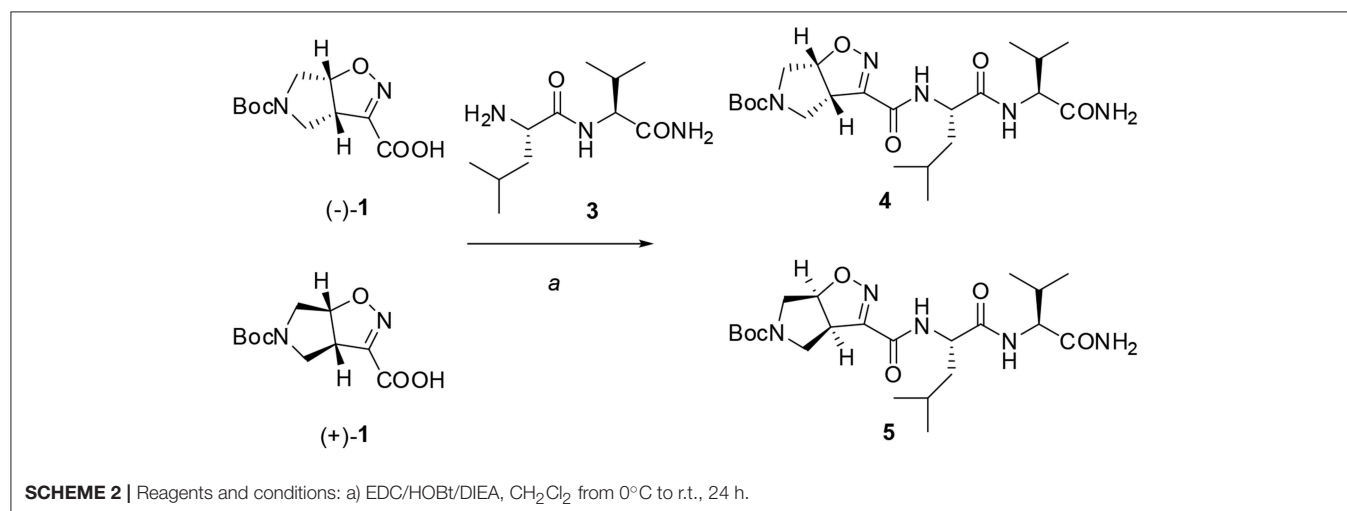
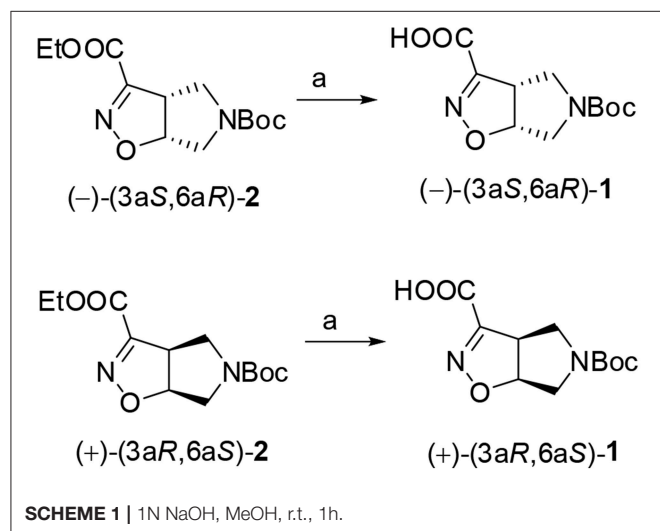
Firstly, Leu-Val dipeptide **3** was prepared starting from (L)-Valinamide and *NH*-Boc-(L)-Leu, according to the general coupling procedure, followed by *N*-terminus deprotection in TFA (91% overall yield). Diastereoisomeric dipeptides **4** and **5** were then achieved in good yields (65% and 63%, respectively) by a coupling reaction of $(-)-1$ or $(+)-1$ with dipeptide **3** (Scheme 2).

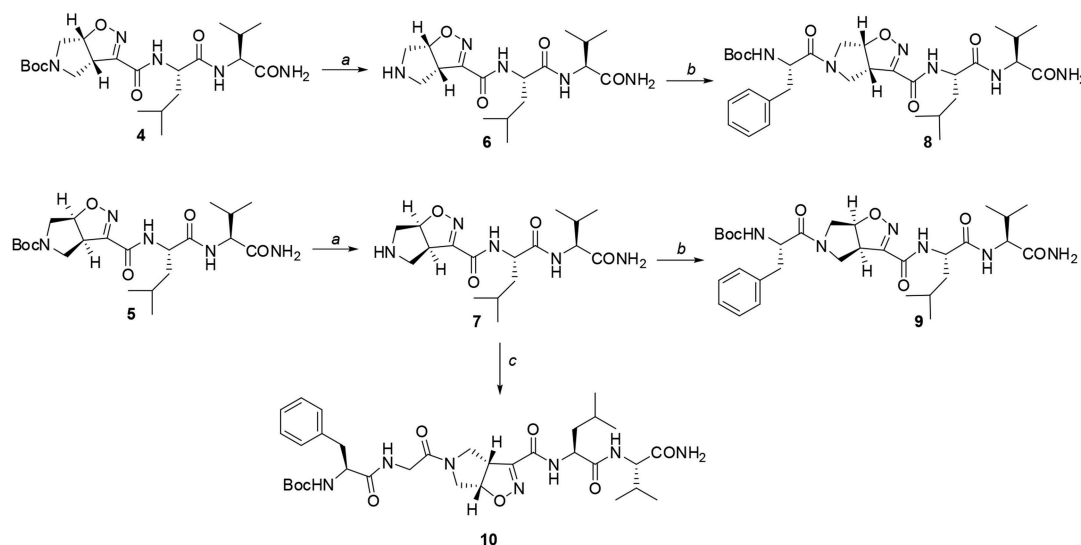
Both **4** and **5** compounds were completely characterized by NMR spectroscopy (CDCl_3 , see SI for complete proton assignment). In both tripeptides, no significant Noesy effects between Leu-Val dipeptide and the scaffold were detected. Furthermore, in variable temperature experiments, the obtained $\Delta\delta/\Delta T$ is higher than 5 ppb/K for all the amide protons, indicating the absence of H-bonds stabilizing a particular

conformation. The $J_{\text{NH}-\text{CH}\alpha}$ value for NH-Val is of 8.8 Hz and 7.9 Hz, for **4** and **5**, respectively (NH-Leu appears as a broad signal for each compound). From these findings, we hypothesized that both **4** and **5** adopt an extended conformation and that the isoxazoline scaffold is not interacting with Leu-Val dipeptide.

The peptide chain was then elongated at *N*-terminus, through Boc-deprotection and coupling with (L)-Phe. Diastereoisomeric dipeptides **8** and **9** were achieved in good overall yields (73% and 76%, respectively) (Scheme 3). From NMR studies, it was found that both model peptides **8** and **9** are present as a mixture of conformers in 2:1 ratio in CDCl_3 solution. The presence of these two conformers is probably due to the low-energy barrier *cis/trans* isomerization of the tertiary amide on the pyrrolidine as it is frequently observed on the acylated proline and in the case of tertiary cyclic amides (Laursen et al., 2013; Pellegrino et al., 2014). Regarding compound **8**, this rotation led to a splitting of the (L)-Phe proton signals only. Furthermore, no significative Noesy effects were detected, and, in variable temperature experiments, the obtained $\Delta\delta/\Delta T$ coefficient is high for all the amide protons. Taking all these data together, we can assume that Phe and Leu-Val dipeptide are oriented in opposite directions and that the 3aS6aR stereochemistry of the scaffold is not effective in inducing specific secondary structures when used in combination with (L)- α -amino acids.

A different scenario was observed for compound **9**. Its two rotamers are indeed characterized by different chemical shifts, suggesting that the isomerization of the tertiary amide leads to two different structures conformations influencing the entire molecule. Unfortunately, due to several overlapping signals, it was not possible to assess significant Noesy proximities. Variable temperature experiments were thus done, in order to investigate if the NH were involved in hydrogen bonds and, as a consequence, if the two isomers of **9** were characterized by a stable conformation in solution. In the case of the major isomer, the obtained $\Delta\delta/\Delta T$ is around 4 ppb/K for NH-Phe, indicating that this proton could be involved in a weak/medium hydrogen bond. All the other amide protons had higher $\Delta\delta/\Delta T$. On the





SCHEME 3 | Reagents and conditions: a) TFA, CH_2Cl_2 from 0°C to r.t., 2 h; b) EDC/HOBt/DIEA, *N*-Boc-(L)-Phe, CH_2Cl_2 from 0°C to r.t., 24 h; c) EDC/HOBt/DIEA, *N*-Boc-(L)-Phe-Gly-OH, CH_2Cl_2 from 0°C to r.t., 24 h.

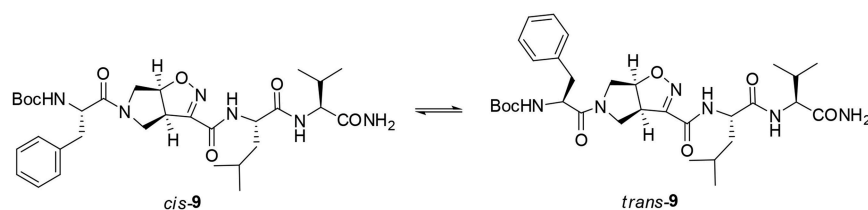


FIGURE 2 | *Cis* and *trans* isomers of compound **9**.

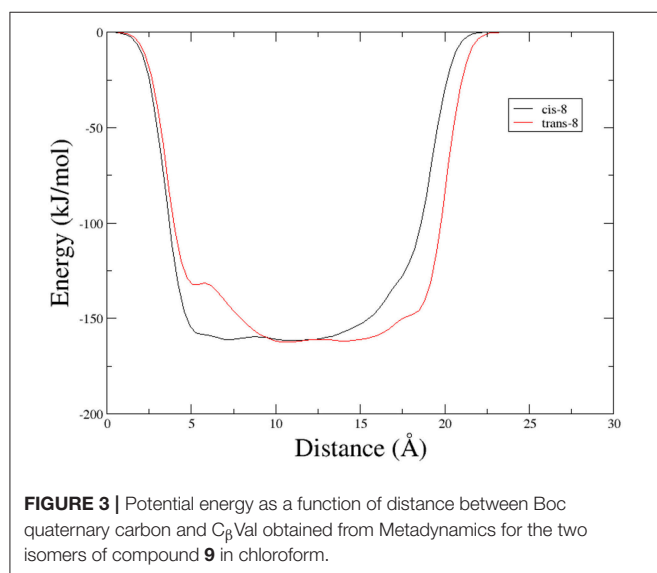


FIGURE 3 | Potential energy as a function of distance between Boc quaternary carbon and C_β Val obtained from Metadynamics for the two isomers of compound **9** in chloroform.

other hand, in the minor conformer the obtained $\Delta\delta/\Delta T$ is of around 2 ppb/K for NH-Val, indicating that this proton is involved in a strong hydrogen bond. Metadynamic studies were

then performed on the *cis*/*trans* tertiary amide conformers of compound **9** (Figure 2).

In particular, we performed two 50 ns long metadynamics simulations, using the distance between Boc quaternary carbon and C_β Val as collective variable (CV). This geometric parameter was selected as a suitable CV because it discriminates well between closed and extended states of the peptide. In this way, it could be possible to evaluate if the two conformers had an intrinsic tendency toward turn conformation. The *cis* isomer showed a broad free energy minimum corresponding to CV values between 5 and 8 Å, while the *trans* isomer showed much higher free energy values in this region, exhibiting a shallow minimum around 10–15 Å (Figure 3).

This different behavior could be indicative of a preference of *cis*-**9** toward a more closed conformation, although from these data it was not possible to make any further assumptions. For this reason, we envisaged that the introduction of a Gly residue between Phe and isoxazoline scaffold could increase the conformational flexibility of the *N*-terminus peptide arm favoring its interaction with the C-terminus part of the molecule. Compound **7** was thus elongated at *N*-terminus, through coupling with *N*-Boc-(L)-Phe-Gly-OH dipeptide using general coupling reaction conditions to obtain peptide **10**

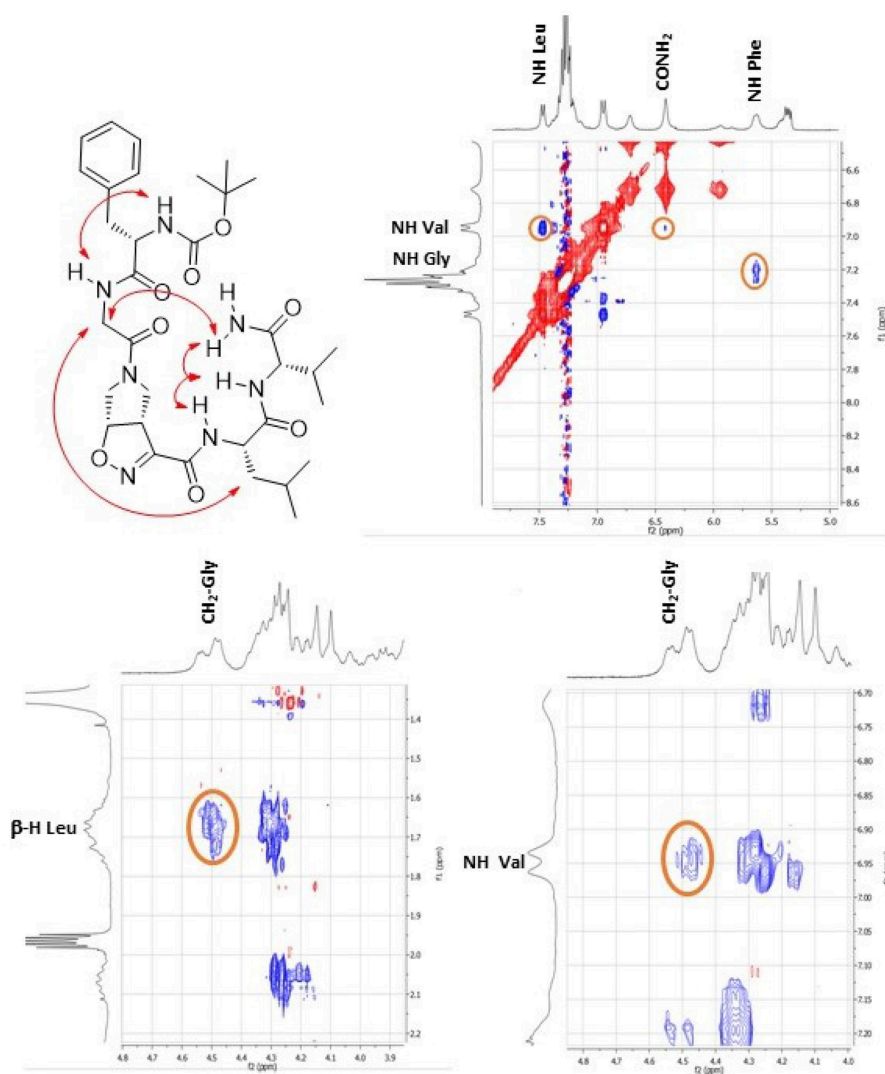


FIGURE 4 | Noesy proximity (red) observed for compound **10** (CD_3CN). On the top right: zoom of the amide region. On the bottom left: Zoom of the aliphatic region. On the bottom right: zoom of the NH-aliphatic region.

(65%, **Scheme 3**). The NMR study on **10** (CD_3CN , see SI for complete assignment), showed that it is present in solution as a single stable conformer (only trace amounts of a second isomer were detected). A complete set of $\text{NH}_i\text{-NH}_{i+1}$ Noesy proximities, whose calculated distances ranged from 2.68 to 2.96 Å, were observed (**Figure 4** on the top right). Furthermore, long range Noesy effects involving $\text{H}\alpha\text{Gly}$ and NHVal (3.03 Å) and $\text{H}\beta\text{Leu}$ (2.73 Å) were found (**Figure 4** on the bottom).

In variable temperature experiments (**Figure 5**), the obtained $\Delta\delta/\Delta T$ is of around 2 ppb/K for NH-Val, while NH-Leu and one of the C-terminus amide protons possess $\Delta\delta/\Delta T$ of around 3 and 4 ppb/K, respectively. The presence of hydrogen bonds was also confirmed by FT-IR analysis. N-H stretching bands A and B ($3,500\text{--}3,000\text{ cm}^{-1}$ region, **Figure S20**) are indeed downshifted as frequently observed in intramolecular hydrogen

bonded conformations (Tonan and Ikawa, 1996; Barth, 2007). Furthermore, the deconvolution of the amide I band ($1,700\text{--}1,600\text{ cm}^{-1}$) showed the presence of a band at $1,655\text{ cm}^{-1}$ (**Figure S20**), typical of α structures (Kong and Yu, 2007).

In order to gain more information on the conformation of compound **10**, far-UV circular dichroism (CD) analysis in CH_3CN (0.1 mM solution) was then performed. In **Figure 6** the obtained CD spectrum is reported.

It showed a maximum at around 250 nm due to the strong absorption of the isoxazoline ring, as observed by Memeo et al. (2018) on similar compounds (see also the UV spectrum in the SI). In the amide bond region, two negative minima at 225 and 208 nm, with the same intensity, and a slightly positive band at 200 nm were also observed. The presence of the exciton splitting of the $\pi \rightarrow \pi^*$ transition band suggested that a α -turn conformation was present (Wang et al., 2018), although in short

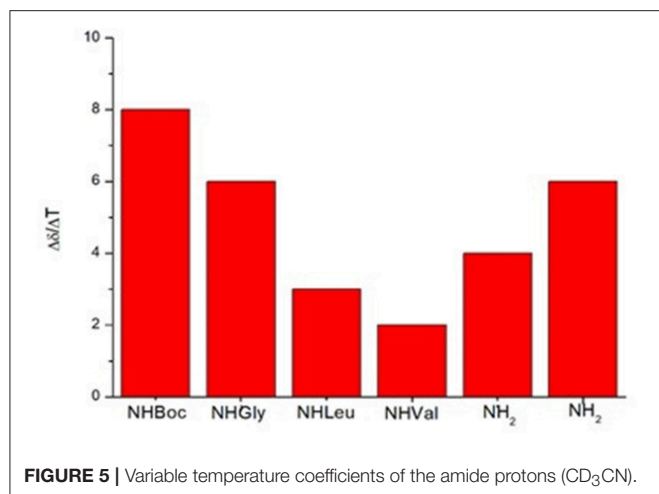


FIGURE 5 | Variable temperature coefficients of the amide protons (CD₃CN).

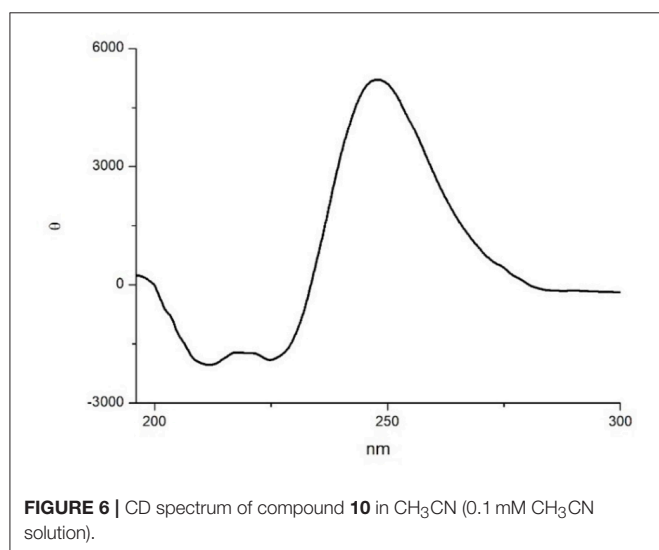


FIGURE 6 | CD spectrum of compound **10** in CH₃CN (0.1 mM CH₃CN solution).

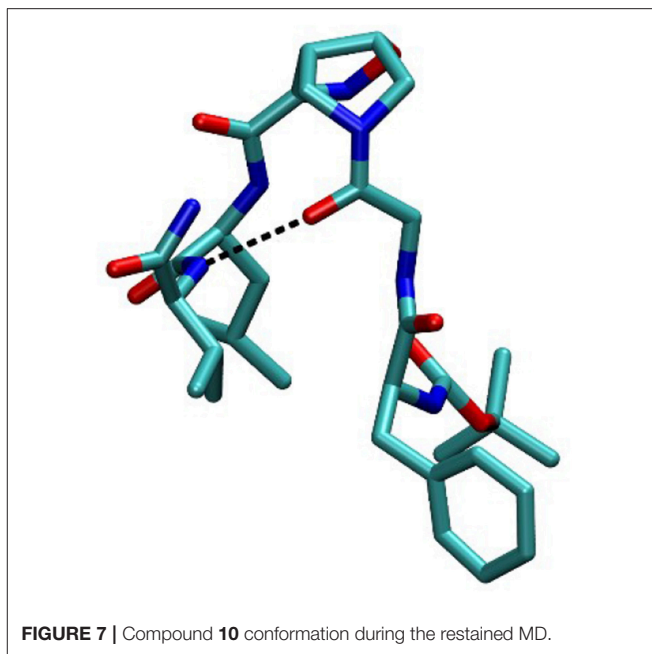


FIGURE 7 | Compound **10** conformation during the restrained MD.

peptides it is difficult to correctly evaluate the intensity of Cotton effects with respect to secondary structure motifs (Chin et al., 2002; Wang et al., 2018).

In order to completely elucidate the conformation of peptide **10**, a restrained molecular dynamic was finally performed. The restraints were based on the obtained NOESY values. When the hydrogen was not uniquely defined, like in H $_{\alpha}$ Gly and H $_{\beta}$ Leu, we used the closest carbon, e.g., C $_{\alpha}$ Gly and C $_{\beta}$ Leu to implement distance restraints (Figure S3). The analysis showed that C $_{\alpha}$ Gly-C $_{\beta}$ Leu (A) and C $_{\alpha}$ Gly-H $_{NH}$ Val (B) are mutually exclusive in the *trans* isomer but not in the *cis* one as shown in Figure S1. Furthermore, H-bond analysis resulted in the observation that a H-bond is between CO-Gly and NH-Val. In Figure 7 the most representative structure is reported.

Taking together both experimental and molecular modeling data, we can assume that, in solution, compound **10** effectively adopts a α -turn conformation. This motif is normally formed

by 5 α -amino acids and is characterized by a H-bond between *i* and *i*+4 residues. In our case, the isoxazoline scaffold replaces two of the three core amino acids (Figure 1) and the H-bond is formed by the CO-Gly and NH-Val, leading to the formation of a 12 member pseudo-cycle. Furthermore, the overall structure of the peptidomimetic is reinforced by medium-weak H-bonds involving NH-Leu and one C-terminus-NH₂, as evicted from NMR data. The presence of a α -turn conformation is also confirmed by the computational analysis of the dihedral angles of the residue *i*+3 and of the distances between residues *i* and *i*+4 (Table S9), as their values rely within the α -turn parameters (Pavone et al., 1996).

In conclusion, as α -turns are often found on biologically active sites and few molecules have been reported to mimic or stabilize them, the ability of compound (+)-**1** to stabilize α -turn conformation on isolated peptide is particularly important in view of future biological applications.

DATA AVAILABILITY

All datasets generated for this study are included in the manuscript and/or the supplementary files.

AUTHOR CONTRIBUTIONS

FO and RB equally contributed to this work. The project was conceived by SaP, LT, and AP. SaP designed and coordinated the research. LT and RB chemically synthesized and analyzed the materials, RB performed NMR, FT-IR and CD experiments, FO and StP performed molecular modeling. SaP, StP, LT, and AP analyzed and compiled the data and co-wrote the manuscript. The final manuscript was read and approved by all the authors.

ACKNOWLEDGMENTS

We thank Donatella Nava for the NMR analysis and Michele Consonni and Sabrina Giofrè for practical help in the synthesis.

REFERENCES

- Abraham, M., Van Der Spoel, D., Lindahl, E., and Hess, B. (2014). *GROMACS User Manual Version 5.0.4*. Available online at: <https://ftp.gromacs.org/pub/manual/manual-5.0.4.pdf>
- Barth, A. (2007). Infrared spectroscopy of proteins. *BBA Bioenerg.* 1767, 1073–1101. doi: 10.1016/j.bbabo.2007.06.004
- Berendsen, H. J. C., Postma, J. P. M., van Gasteren, W. F., and DiNola, A. (1984). Molecular dynamics with coupling to an external bath. *J. Chem. Phys.* 81, 3684–3690. doi: 10.1063/1.448118
- Bonetti, A., Pellegrino, S., Das, P., Yuran, S., Bucci, R., Ferri, N., et al. (2015). Dipeptide Nanotubes Containing Unnatural Fluorine-Substituted β 2,3-Diarylamino Acid and L-Alanine as candidates for biomedical applications. *Org. Lett.* 17, 4468–4471. doi: 10.1021/acs.orglett.5b02132
- Bouillère, F., Thétiot-Laurent, S., Kouklovsky, C., and Alezra, V. (2011). Foldamers containing γ -amino acid residues or their analogues: structural features and applications. *Amino Acids* 41, 687–707. doi: 10.1007/s00726-011-0893-3
- Bruno, S., Pinto, A., Paredi, G., Tamborini, L., De Micheli, C., La Pietra, V., et al. (2014). Discovery of covalent inhibitors of glyceraldehyde-3-phosphate dehydrogenase, a target for the treatment of malaria. *J. Med. Chem.* 57, 7465–7471. doi: 10.1021/jm500747h
- Bucci, R., Das, P., Iannuzzi, F., Feligioni, M., Gandolfi, R., Gelmi, M. L., et al. (2017). Self-assembly of an amphipathic $\alpha\beta$ -tripeptide into cationic spherical particles for intracellular delivery. *Org. Biomol. Chem.* 15, 6773–6779. doi: 10.1039/C7OB01693J
- Bucci, R., Giofrè, S., Clerici, F., Contini, A., Pinto, A., Erba, E., et al. (2018). Tetrahydro-4H-(pyrrolo[3,4-d]isoxazol-3-yl)methanamine: a bicyclic diamino scaffold stabilizing parallel turn conformations. *J. Org. Chem.* 83, 11493–11501. doi: 10.1021/acs.joc.8b01299
- Bussi, G., Donadio, D., and Parrinello, M. (2007). Canonical sampling through velocity rescaling. *J. Phys. Chem.* 126:014101. doi: 10.1063/1.2408420
- Castellano, S., Kuck, D., Viviano, M., Yoo, J., López-Vallejo, F., Conti, P., et al. (2011). Synthesis and biochemical evaluation of δ 2-isoxazoline derivatives as DNA methyltransferase 1 inhibitors. *J. Med. Chem.* 54, 7663–7677. doi: 10.1021/jm2010404
- Chatterjee, S., Vasudev, P. G., Raghothama, S., Ramakrishnan, C., Shamala, N., and Balaram, P. (2009). Expanding the peptide β -turn in $\alpha\gamma$ hybrid sequences: 12 atom hydrogen bonded helical and hairpin turns. *J. Am. Chem. Soc.* 131, 5956–5965. doi: 10.1021/ja900618h
- Chin, D.-H., Woody, R. W., Rohl, C. A., and Baldwin, R. L. (2002). Circular dichroism spectra of short, fixed-nucleus alanine helices. *Proc. Natl. Acad. Sci. U.S.A.* 99, 15416–15421. doi: 10.1073/pnas.232591399
- Clerici, F., Erba, E., Gelmi, M. L., and Pellegrino, S. (2016). Non-standard amino acids and peptides: from self-assembly to nanomaterials *Tetrahedron Lett.* 57, 5540–5550. doi: 10.1016/j.tetlet.2016.11.022
- Conti, P., De Amici, M., Pinto, A., Tamborini, L., Grazioso, G., Frolund, B., et al. (2006). Synthesis of 3-hydroxy- and 3-carboxy- Δ 2-isoxazoline amino acids and evaluation of their interaction with GABA receptors and transporters. *Eur. J. Org. Chem.* 24, 5533–5542. doi: 10.1002/ejoc.200600628
- Conti, P., Pinto, A., Wong, P. E., Major, L. L., Tamborini, L., Iannuzzi, M. C., et al. (2011). Synthesis and *in vitro/in vivo* evaluation of the antitrypanosomal activity of 3-bromoacetic acid, a potent CTP synthetase inhibitor. *ChemMedChem* 6, 329–333. doi: 10.1002/cmdc.201000417
- Fanelli, R., Berthomieu, D., Didierjean, C., Doudouh, A., Lebrun, A., Martinez, J., et al. (2017). Hydrophobic α,α -disubstituted disilylated TESDpg induces incipient 310-Helix in short tripeptide sequence. *Org. Lett.* 19, 2937–2940. doi: 10.1021/acs.orglett.7b01172
- Fuller, A., Chen, B., Minter, A. R., and Mapp, A. K. (2005). Succinct synthesis of β -amino acids via chiral isoxazolines. *J. Am. Chem. Soc.* 127, 5376–5383. doi: 10.1021/ja0431713
- Gandini, E., Dapiaggi, F., Oliva, F., Pieraccini, S., and Sironi, M. (2018). Well-Tempered MetaDynamics based method to evaluate universal peptidomimetics. *Chem. Phys. Lett.* 706, 729–735. doi: 10.1016/j.cplett.2018.07.029
- Guo, L., Zhang, W., Guzei, I. A., Spencer, L. C., and Gellman, S. H. (2012). New preorganized γ -amino acids as foldamer building blocks. *Org. Lett.* 14, 2582–2585. doi: 10.1021/ol3008815
- Hoang, H. N., Driver, R. W., Beyer, R. L., Malde, A. K., Le, G. T., Abbenante G., et al. (2011). Protein α -turns recreated in structurally stable small molecules. *Angew. Chem. Int. Ed.* 50, 11107–11111. doi: 10.1002/anie.201105119
- Hornak, V., Abel, R., Okur, A., Strockbine, B., Roitberg, A., and Simmerling, C. (2006). Comparison of multiple Amber force fields and development of improved protein backbone parameters. *Proteins* 65, 712–725. doi: 10.1002/prot.21123
- Itoh, T., Watanabe, M., and Fukuyama, T. (2002). Synthetic approach to tetrodotoxin. *Synlett* 8, 1323–1325. doi: 10.1055/s-2002-32984
- Kaur, K., Kumar, V., Sharma, A. K., and Gupta, G. K. (2014). Isoxazoline containing natural products as anticancer agents: a review. *Eur. J. Med. Chem.* 77, 121–133. doi: 10.1016/j.ejmech.2014.02.063
- Kelso, M. J., Beyer, R. L., Hoang, H. N., Lakdawala, A. S., Snyder, J. P., Oliver, W. V., et al. (2004). Alpha-turn mimetics: short peptide alpha-helices composed of cyclic metallopeptide modules. *J. Am. Chem. Soc.* 126, 4828–4842. doi: 10.1021/ja037980i
- Kobayashi, H., Misawa, T., Matsuno, K., and Demizu, Y. (2017). Preorganized cyclic α,α -disubstituted α -amino acids bearing functionalized side chains that act as peptide-helix inducers. *J. Org. Chem.* 82, 10722–10726. doi: 10.1021/acs.joc.7b01946
- Konda, M., Jadhav, R. G., Maiti, S., Mobin, S. M., Kauffmann, B., and Das, A. K. (2018). Understanding the conformational analysis of gababutin based hybrid peptides. *Org. Biomol. Chem.* 16, 1728–1735. doi: 10.1039/C8OB00035B
- Kong, J., and Yu, S. (2007). Fourier transform infrared spectroscopic analysis of protein secondary structures. *Acta Biochim. Biophys. Sinica.* 39, 549–559. doi: 10.1111/j.1745-7270.2007.00320.x
- Kozikowski, A. P., and Park, P. U. (1990). Synthesis of streptazolin: use of the aza-Ferrier reaction in conjunction with the INOC process to deliver a unique but sensitive natural product. *J. Org. Chem.* 55, 4668–4682. doi: 10.1021/jo00302a036
- Krishna, Y., Sharma, S., Ampapathi, R. S., and Koley, D. (2014). Furan-based locked Z-vinyllogous γ -amino acid stabilizing protein α -turn in water-soluble cyclic $\alpha\beta\gamma$ tetrapeptides. *Org. Lett.* 16, 2084–2087. doi: 10.1021/ol5002126
- Laursen, J. S., Engel-Andreasen, J., Fristrup, P., Harris, P., Olsen, C. A. (2013). Cis-trans amide bond rotamers in β -peptides and peptoids: evaluation of stereoelectronic effects in backbone and side chains. *J. Am. Chem. Soc.* 135, 2835–2844. doi: 10.1021/ja312532x
- López-Andarias, A., López-Andarias, J., Atienza, C., Chichón, F. J., Carrascosa, J. L., and Martín, N. (2018). Tuning optoelectronic and chiroptic properties of peptide-based materials by controlling the pathway complexity. *Chem. Eur. J.* 24, 7755–7760. doi: 10.1002/chem.201801238
- Machetti, F., Ferrali, A., Menchi, G., Occhiato, E. G., and Guarna, A. (2000). Oligomers of enantiopure bicyclic γ/δ -amino acids (BTAA). 1. Synthesis and conformational analysis of 3-aza-6,8-dioxabicyclo[3.2.1]octane-7-carboxylic acid oligomers (PolyBTG). *Org. Lett.* 2, 3987–3990. doi: 10.1021/ol006548s
- Memeo, M. G., Bruschi, M., Bergonzi, L., Desimoni, G., Fatta, G., and Quadrelli, P. (2018). Cyclopenta[d]isoxazoline β -turn mimics: synthetic approach, turn driving force, scope, and limitations. *ACS Omega* 3, 13551–13558. doi: 10.1021/acsomega.8b01670

SUPPLEMENTARY MATERIAL

The Supplementary Material for this article can be found online at: <https://www.frontiersin.org/articles/10.3389/fchem.2019.00133/full#supplementary-material>

- Mikhalevich, V., Craciun, I., Kyropoulou, M., Palivan, C. G., and Meier, W. (2017). Amphiphilic peptide self-assembly: expansion to hybrid materials. *Biomacromolecules* 18, 3471–3480. doi: 10.1021/acs.biomac.7b00764
- Pavone, V., Gaeta, G., Lombardi, A., Nastri, F., Maglio, O., Isernia, C., et al. (1996). Discovering protein secondary structures: classification and description of isolated α -turns. *Biopolymers* 38, 705–721. doi: 10.1002/(SICI)1097-0282(199606)38:6<705::AID-BIP3>3.0.CO;2-V
- Pellegrino, S., Bonetti, A., Clerici, F., Contini, A., Moretto, A., Soave, R., et al. (2015). 1H-azepine-2-oxo-5-amino-5-carboxylic acid: a 310 helix inducer and an effective tool for functionalized gold-nanoparticles. *J. Org. Chem.* 80, 5507–5516. doi: 10.1021/acs.joc.5b00396
- Pellegrino, S., Contini, A., Clerici, F., Gori, A., Nava, D., and Gelmi, M. L. (2012). 1H-Azepine-4-amino-4-carboxylic acid: a new α,α disubstituted ornithine analogue capable of inducing helix conformations in short Ala-Aib pentapeptides. *Chem. Eur. J.* 18, 8705–8715. doi: 10.1002/chem.201104023
- Pellegrino, S., Contini, A., Gelmi, M. L., Lo Presti, L., Soave, R., and Erba, E. (2014). Asymmetric modular synthesis of a semirigid dipeptide mimetic by cascade cycloaddition/ring rearrangement and borohydride reduction. *J. Org. Chem.* 79, 3094–3102. doi: 10.1021/jo500237j
- Pellegrino, S., Facchetti, G., Contini, A., Gelmi, M. L., Erba, E., Gandolfi, R., et al. (2016). Ctr-1 Mets7 motif inspiring new peptide ligands for Cu(I)-catalyzed asymmetric Henry reaction under green conditions. *RSC Adv.* 6, 71529–71533. doi: 10.1039/C6RA16255J
- Pellegrino, S., Tonali, N., Erba, E., Kaffy, J., Taverna, M., Contini, A., et al. (2017). β -Hairpin mimics containing a piperidine-pyrrolidine scaffold modulate the β -amyloid aggregation process preserving the monomer species. *Chem. Sci.* 8, 1295–1302. doi: 10.1039/C6SC03176E
- Pinto, A., Conti, P., Grazioso, G., Tamborini, L., Madsen, U., Nielsen, B., et al. (2011). Synthesis of new isoxazoline-based acidic amino acids and investigation of their affinity and selectivity profile at ionotropic glutamate receptors. *Eur. J. Med. Chem.* 46, 787–793. doi: 10.1016/j.ejmech.2010.12.020
- Pinto, A., Tamborini, L., Cullia, G., Conti, P., and De Micheli, C. (2016a). Inspired by nature: the 3-halo-4,5-dihydroisoxazole moiety as a novel molecular warhead for the design of covalent inhibitors. *ChemMedChem* 1, 10–14. doi: 10.1002/cmdc.201500496
- Pinto, A., Tamborini, L., Pennacchietti, E., Coluccia, A., Silvestri, R., Cullia, G., et al. (2016b). Bicyclic γ -amino acids as inhibitors of γ -aminobutyrate aminotransferase. *J. Enzyme Inhib. Med. Chem.* 2, 295–301. doi: 10.3109/14756366.2015.1021251
- Raymond, D. M., and Nilsson, B. L. (2018). Multicomponent peptide assemblies. *Chem. Soc. Rev.* 47, 3659–3720. doi: 10.1039/C8CS00115D
- Smith, E. L., and Spackman, D. H. (1955). Leucine aminopeptidase. V. activation, specificity, and mechanism of action. *J. Biol. Chem.* 122, 271–299.
- Sohora, M., Vazdar, M., Savić, I., Mlinarić-Majerski, K., and Basarić, N. (2018). Photocyclization of tetra- and pentapeptides containing adamantylphthalimide and phenylalanines: reaction efficiency and diastereoselectivity. *J. Org. Chem.* 83, 14905–14922. doi: 10.1021/acs.joc.8b01785
- Solomon, L. A., Kronenberg, J. B., and Fry, H. C. (2017). Control of heme coordination and catalytic activity by conformational changes in peptide-amphiphile assemblies. *J. Am. Chem. Soc.* 139, 8497–8507. doi: 10.1021/jacs.7b01588
- Sperry, J. B., and Wright, D. L. (2005). Furans, thiophenes and related heterocycles in drug discovery. *Curr. Opin. Drug Discov. Dev.* 8, 723–740. doi: 10.1002/chin.200615242
- Steinke, D., and Kula, M. R. (1990). Selektive desamidierung von peptidamiden. *Angew. Chemie* 102, 1204–1206. doi: 10.1002/ange.19901021035
- Tamborini, L., Mastronardi, F., Dall'Oglio, F., De Micheli, C., Nielsen, B., Lo Presti, L., et al. (2015). Synthesis of unusual isoxazoline containing β and γ -dipeptides as potential glutamate receptor ligands. *MedChemComm* 6, 1260–1266. doi: 10.1039/C5MD00159E
- Tonan, K., and Ikawa, S. (1996). Intramolecular hydrogen bonding and conformation of small peptides: variable-temperature FTIR study on N-Acetyl-L-Pro-L-Leu-Gly-NH₂ and related compounds. *J. Am. Chem. Soc.* 118, 6960–6965. doi: 10.1021/ja953380a
- Tribello, G. A., Bonomi, M., Branduardi, D., Camilloni, C., and Bussi, G. (2014). PLUMED 2: new feathers for an old bird. *Comp. Phys. Comm.* 185, 604–613. doi: 10.1016/j.cpc.2013.09.018
- Tsantali, G. G., Dimtsas, J., Tsoleridis, C. A., and Takakis, I. M. (2007). Preparation of sixteen 3-hydroxy-4- and 7-hydroxy-1-hydrindanones and 3-hydroxy-4- and 8-hydroxy-1-hydroazulenones. *Eur. J. Org. Chem.* 2007, 258–265. doi: 10.1002/ejoc.200600639
- Van Der Spoel, D., Lindahl, E., Hess, B., Groenhof, G., Mark, A. E., and Berendsen, H. J. (2005). GROMACS: fast, flexible, and free. *J. Comput. Chem.* 26, 1701–1718. doi: 10.1002/jcc.20291
- Vasudev, P. G., Chatterjee, S., Shamala, N., and Balaram, P. (2011). Structural chemistry of peptides containing backbone expanded amino acid residues: conformational features of β , γ , and hybrid peptides. *Chem. Rev.* 111, 657–687. doi: 10.1021/cr100100x
- Wang, L., Coric, P., Zhu, K., Liu, W.-Q., Vidal, M., Bouaziz, S., et al. (2018). Synthesis and characterization of water-soluble macrocyclic peptides stabilizing protein α -turn. *Org. Biomol. Chem.* 16, 459–471. doi: 10.1039/C7OB02852K
- Wintjens, R. T., Rooman, M. J., and Wodak, S. J. (1996). Automatic classification and analysis of alpha alpha-turn motifs in proteins. *J. Mol. Biol.* 255, 235–253. doi: 10.1006/jmbi.1996.0020
- Zhang, X. X., Eden, H. S., and Chen, X. (2012). Peptides in cancer nanomedicine: drug carriers, targeting ligands and protease substrates. *J. Control Release* 159, 2–13. doi: 10.1016/j.jconrel.2011.10.023

Conflict of Interest Statement: The authors declare that the research was conducted in the absence of any commercial or financial relationships that could be construed as a potential conflict of interest.

Copyright © 2019 Oliva, Bucci, Tamborini, Pieraccini, Pinto and Pellegrino. This is an open-access article distributed under the terms of the Creative Commons Attribution License (CC BY). The use, distribution or reproduction in other forums is permitted, provided the original author(s) and the copyright owner(s) are credited and that the original publication in this journal is cited, in accordance with accepted academic practice. No use, distribution or reproduction is permitted which does not comply with these terms.



Fluoro-Aryl Substituted $\alpha,\beta^{2,3}$ -Peptides in the Development of Foldameric Antiparallel β -Sheets: A Conformational Study

Raffaella Bucci¹, Alessandro Contini¹, Francesca Clerici¹, Egle Maria Beccalli¹, Fernando Formaggio², Irene Maffucci^{3,4}, Sara Pellegrino¹ and Maria Luisa Gelmi^{1*}

¹ Department of Pharmaceutical Sciences (DISFARM), University of Milan, Milan, Italy, ² Department of Chemistry, University of Padova, Padova, Italy, ³ CNRS UMR 7025, Génie Enzymatique et Cellulaire, Centre de Recherche de Royallieu, Compiègne, France, ⁴ Génie Enzymatique et Cellulaire, Centre de Recherche de Royallieu, Sorbonne Universités, Université de Technologie de Compiègne, Compiègne, France

OPEN ACCESS

Edited by:

Assaf Friedler,
Hebrew University of Jerusalem, Israel

Reviewed by:

Vladimir Torbeev,
Université de Strasbourg, France
James Gardiner,
Commonwealth Scientific and
Industrial Research Organisation
(CSIRO), Australia

*Correspondence:

Maria Luisa Gelmi
marialuisa.gelmi@unimi.it

Specialty section:

This article was submitted to
Chemical Biology,
a section of the journal
Frontiers in Chemistry

Received: 31 January 2019

Accepted: 13 March 2019

Published: 02 April 2019

Citation:

Bucci R, Contini A, Clerici F,
Beccalli EM, Formaggio F, Maffucci I,
Pellegrino S and Gelmi ML (2019)
Fluoro-Aryl Substituted
 $\alpha,\beta^{2,3}$ -Peptides in the Development
of Foldameric Antiparallel β -Sheets: A
Conformational Study.
Front. Chem. 7:192.
doi: 10.3389/fchem.2019.00192

$\alpha,\beta^{2,3}$ -Distereoisomeric foldamers of general formula Boc(S-Ala- β -2R,3R-Fpg)_nOMe or Boc(S-Ala- β -2S,3S-Fpg)_nOMe were prepared from both enantiomers of syn H-2-(2-F-Phe)-h-PheGly-OH (named β -Fpg) and S-alanine. Our peptides show two appealing features for biomedical applications: the presence of fluorine, attractive for non-covalent interactions, and aryl groups, crucial for π -stacking. A conformational study was performed, using IR, NMR and computational studies of diastereoisomeric tetra- and hexapeptides containing the $\beta^{2,3}$ -amino acid in the R,R- and S,S-stereochemistry, respectively. We found that the stability of peptide conformation is dependent on the stereochemistry of the β -amino acid. Combining S-Ala with β -2R,3R-Fpg, a stable extended β -strand conformation was obtained. Furthermore, β -2R,3R-Fpg containing hexapeptide self-assembles to form antiparallel β -sheet structure stabilized by intermolecular H-bonds and π,π -interactions. These features make peptides containing the $\beta^{2,3}$ -fluoro amino acid very appealing for the development of bioactive proteolytically stable foldameric β -sheets as modulators of protein-protein interaction (PPI).

Keywords: $\beta^{2,3}$ -diaryl-amino acid, $\alpha,\beta^{2,3}$ -peptide, extended peptide, antiparallel β -sheet, conformational analyses, foldamers

INTRODUCTION

Amino acids are small molecules able to induce high molecular complexity, promoting discrete three-dimensional folded structures in peptides. α -Amino acid-based peptides show some drawbacks such as the low stability to proteases, and, in the case of short peptides, the lack of a stable secondary structure. The use of oligomers with unnatural backbones is a powerful strategy to overcome those issues, while maintaining the desired fragment structure.

In particular, β -peptide foldamers (Seebach et al., 1996, 2004; Gellman, 1998) have been extensively studied in the last two decades. These molecules can adopt specific compact conformations despite the increased conformational space due to the additional methylene group of the β -amino acid. Furthermore, their substitution pattern can influence the conformation of

β -peptides, as reported in several experimental (Cheng et al., 2001; Seebach et al., 2006; Seebach and Gardiner, 2008; Pilsl and Reiser, 2011; Vasudev et al., 2011; Berlicki et al., 2012; Johnson and Gellman, 2013; Basuroy et al., 2014; Lee et al., 2014; Wang and Schepartz, 2016; Bucci et al., 2017a) and molecular modeling studies (Wu et al., 2008; Zhu et al., 2010; Baldauf and Hofmann, 2012). An even larger pool of secondary structure motifs could be obtained, by the combination of α - and both acyclic and cyclic β -amino acids ($\alpha\beta$; $\alpha\alpha\beta$; $\alpha\beta\beta$; etc). Inspired by the diversity of folded structures and functions manifested by peptides and proteins, β -peptide mimics and foldamers have been thus exploited for different applications ranging from biomedicine (Horne, 2011; Cabrele et al., 2014; Checchio and Gellman, 2016) to material science (Gopalan et al., 2015; Clerici et al., 2016; Del Borgo et al., 2017).

Only few examples are reported related to α,β -repeating sequences containing acyclic amino acids (Sharma et al., 2005; Srinivasulu et al., 2006; Angelici et al., 2007; Balamurugan and Muralaeddharan, 2012; Basuroy et al., 2014), the majority of them giving helix constructs.

Our interest toward the preparation of non-natural amino acids (Pellegrino et al., 2008; Penso et al., 2012; Ruffoni et al., 2015) and their use for peptidomimetic synthesis for different applications (Pellegrino et al., 2015, 2016; Ruffoni et al., 2016; Bucci et al., 2018, 2019; Tonali et al., 2018) is well-documented. Recently, our research group reported on a diastereoselective synthesis of a new class of β -amino acids, *syn*- S^* , $S^{*-}\beta^{2,3}$ -diarylamino acids, differently substituted on the aromatic ring (Bonetti et al., 2014).

Due to the lack of information related to $\alpha,\beta^{2,3}$ -amino acids repeating sequences, here we report on the preparation and conformational studies of $\alpha,\beta^{2,3}$ -peptides, containing *syn* H-2-(2-F-Phe)-h-PheGly-OH, named β -Fpg, and helicogenic *S*-alanine (Figure 1). This scaffold shows two features that can be appealing for biomedical applications: the presence of a fluorine, useful for non-covalent interactions, and two aryl groups, crucial for π -stacking and hydrophobic interactions. Taking advantage of the use of fluorine-substituted β -2S,3S-Fpg (Figure 1), in combination with *S*-Ala or *S*-Arg-*S*-Ala, we recently prepared short peptides able to generate proteolytically stable nanotubes (Bonetti et al., 2015) and spherical aggregates (Bucci et al., 2017b) as drug delivery systems.

Here we report on a conformational study on diastereoisomeric tetra- and hexapeptides $\alpha,\beta^{2,3}$ -foldamers

of general formula $\text{Boc}(\text{S-Ala-}\beta\text{-2R,3R-Fpg})_n\text{OMe}$ and $\text{Boc}(\text{S-Ala-}\beta\text{-2S,3S-Fpg})_n\text{OMe}$ (Figure 1).

Our results showed that the stability of peptide conformation is dependent on the stereochemistry of the β -amino acid. Combining *S*-Ala with β -2R,3R-Fpg, a stable extended β -strand conformation was obtained. Moreover, it was found that hexapeptide **11** (Figure 1) self-assembles to form antiparallel β -sheet structure stabilized by intermolecular H-bonds and π,π -interactions. This result is important since, to the best of our knowledge, no examples of extended $\alpha,\beta^{2,3}$ -foldamers are reported. Furthermore, there is a need of the development of bioactive proteolytically stable foldameric β -sheets that might be useful as modulators of protein-protein interactions (PPI) (Hegedüs et al., 2016). The design of this secondary structure is indeed not trivial, although β -sheet interfaces frequently occurred in PPI.

MATERIALS AND METHODS

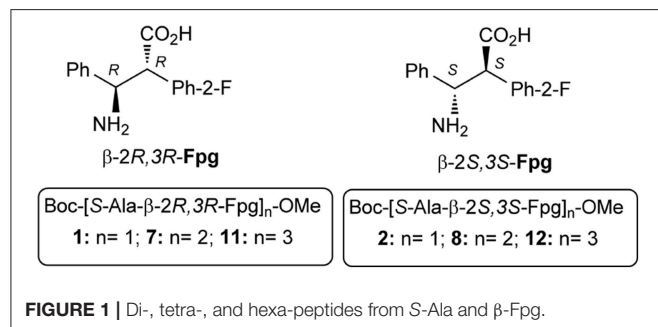
Chemistry

Experimental procedures, compound characterization data for newly synthesized peptides (3-5 and 7-12; for ^1H , ^{13}C , and ^{19}F NMR spectra see Figures S10-S39) are reported in the **Supplementary Material**. Dipeptide **1**, **2** (Bonetti et al., 2015) and **6** (Bucci et al., 2017b) are known compounds.

Melting points were determined with a Stuart Scientific melting point apparatus in open capillary tubes and are uncorrected. Chemicals were purchased from Sigma Aldrich and were used without further purification. ESI MS were recorded on a LCQ Advantage spectrometer from Thermo Finnigan and a LCQ Fleet spectrometer from Thermo Scientific. The FT-IR absorption spectra were recorded with a Perkin-Elmer 1720X spectrophotometer, nitrogen flushed, equipped with a sample-shuttle device, at 2 cm^{-1} nominal resolution, averaging 100 scans. Solvent (base-line) spectra were recorded under the same conditions. Cells with path lengths of 1.0 and 10 mm (with CaF_2 windows) were used. Spectrograde CDCl_3 (99.8% D) was purchased from Fluka. The NMR spectroscopic experiments were carried out either on a Varian MERCURY 200 MHz (200 and 50 MHz for ^1H and ^{13}C , respectively), Varian MERCURY 300 MHz (300, 75, 282 MHz for ^1H , ^{13}C , and ^{19}F , respectively), or Bruker Avance I 500 MHz spectrometers (500 and 125 MHz for ^1H and ^{13}C , respectively). Chemical shifts (δ) are given in ppm relative to the CHCl_3 internal standard, and the coupling constants J are reported in Hertz (Hz). Optical rotations were measured on a Perkin-Elmer 343 polarimeter at 20°C (concentration in g/100 mL).

Computational Methods

The non-natural β -amino acids, capped respectively with an acetyl (Ac) and an OMe group at the *N*- and *C*-termini, were designed using MOE (Molecular Operating Environment, 2013) and submitted to a “low mode” conformational search (MMFF94x force field, Born solvation, iteration limit = 40 000, MM iteration limit = 2,500, rejection limit = 500). The two lowest energy conformations having ϕ , θ , and ψ dihedrals corresponding to two different secondary structures, namely



the extended one and a β -turn, were selected to derive partial charges with the R.E.D.III.52 software (Dupradeau et al., 2010). Each geometry was optimized at the HF/6-31G(d) level, and two different spatial orientations were used to derive orientation- and conformation-independent RESP-A1 charges.

The tetra- (**m7** and **m8**) and hexapeptides (**m11** and **m12**) of general formula 8 were built with the *tleap* module of Amber14 (Case et al., 2014) by imposing an extended conformation ($\phi = \psi = \omega = \theta = 180^\circ$), and solvated with an octahedral box of CHCl_3 . All the systems were consequently submitted to a preliminary equilibration with the *pmemd* module of Amber14 package, using the ff14SB (Maier et al., 2015) force field. In detail, the systems were relaxed by minimizing hydrogens and solvent (2,000 cycles of steepest descent and 5,000 cycles of conjugated gradient). The solvent box was equilibrated at 300 K by 100 ps of NVT and 100 ps of NPT simulation using a Langevin thermostat with a collision frequency of 2.0 ps^{-1} . Successively, a minimization of side chains and CHCl_3 with restraints on backbone atoms of 25 kcal/mol and a total minimization (2,500 cycles of steepest descent and 5,000 cycles of conjugated gradient) were performed. The systems were then heated up to 300 K in 6 steps of 5 ps each ($\Delta T = 50 \text{ K}$), where backbone restraints were reduced from 10.0 to 5 kcal/mol. Full equilibration was performed in the NVT ensemble (100 ps, backbone restraints = 5.0 kcal/mol) and in the NPT ensemble (1 step of 200 ps, backbone restraints = 5 kcal/mol; 3 steps of 100 ps each, reducing the backbone restraints from 5.0 to 1.0 kcal/mol, and 1 step 1 ns with 1.0 kcal/mol of nd backbone restraints). Finally, unrestrained production runs were run at 300 K for 15 ns. An electrostatic cutoff of 8.0 Å was applied to all the calculations. The equilibrated geometries and the average dihedral energies and potential obtained through the accurate systems equilibrations were used as starting point for accelerated MD (aMD) simulations, where the α value was set to 0.2 and 0.16, for the dihedral and potential factors, respectively.

The aMD simulations of each peptide were run until convergence, for a total of 500 ns for the tetrapeptides **m7** and **m8**, and 800 ns for hexapeptides **m11** and **m12**, respectively. The root mean square displacement of backbone heavy atoms from the extended conformation was used as a metric of convergence (Figure S1). All the analyses were conducted on the last 200 ns of trajectory. Cluster analyses were performed with the *cpptraj* module of Amber14 by sampling one of every 8 frames, using the average-linkage algorithm and requesting ten clusters; the pairwise mass-weighted RMSD on backbone C_α atoms was used as a metric. H-bonds were computed with *cpptraj* by setting a donor-acceptor distance threshold of 4.0 Å and an angle cutoff of 110° . Only H-bonds with an occupancy $>20\%$ were considered. *Cpptraj* was used also for computing the radius of gyration of investigated peptides.

RESULTS AND DISCUSSION

Synthesis

Dipeptides **1** and **2** were efficiently synthesized in gram scale starting from a racemic mixture of amino acid β -Fpg, according to a known procedure (Bonetti et al., 2015). Pure dipeptides

were used for the preparation of $\alpha,\beta,2,3$ -tetra- and hexa-peptide sequences (Scheme 1).

The deprotection of the carboxyl group of dipeptides **1** and **2** with LiOH or KOH gave a partial epimerization of the benzylic- C_α position of the β -amino acid, even at low temperature. To avoid this problem, we moved to the deprotection of both C- and N-termini operating in 1 M HCl (80 °C, 12 h, 99%), followed by Boc-protection of N-terminus (Boc_2O , DCM, TEA, 25 °C, 12 h, 96%). Dipeptide **3** and **4** were obtained in excellent overall yields. The deprotection of nitrogen atom was performed in standard conditions (TFA in CH_2Cl_2 , 0 °C, 1 h) affording dipeptides **5** and **6** from **1** and **2** (99%), respectively. Good yields in the

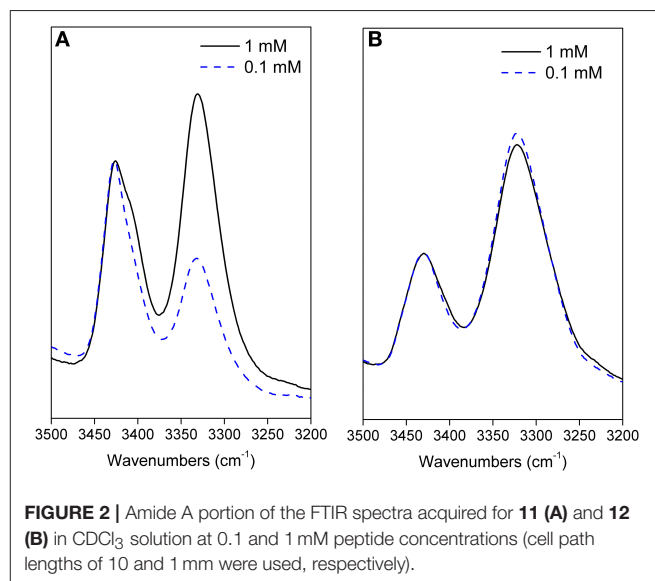
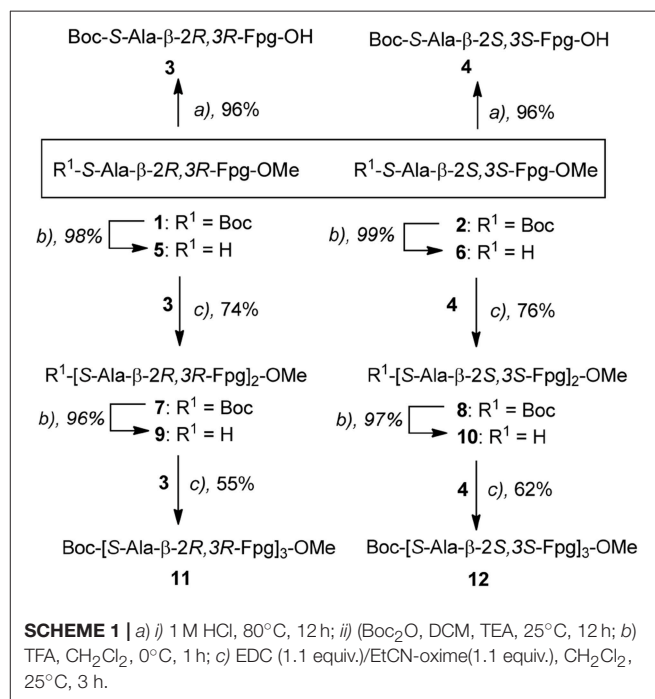
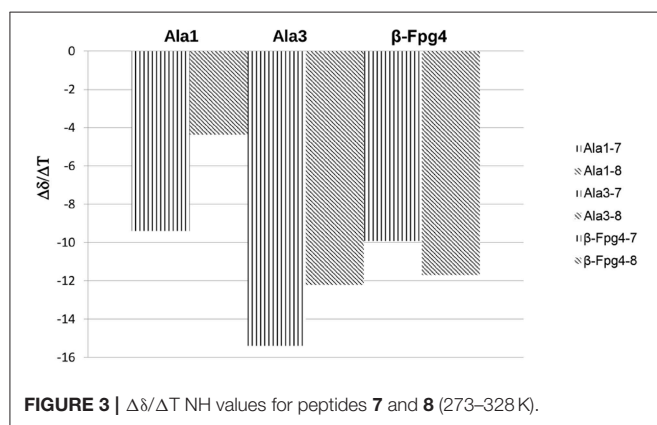
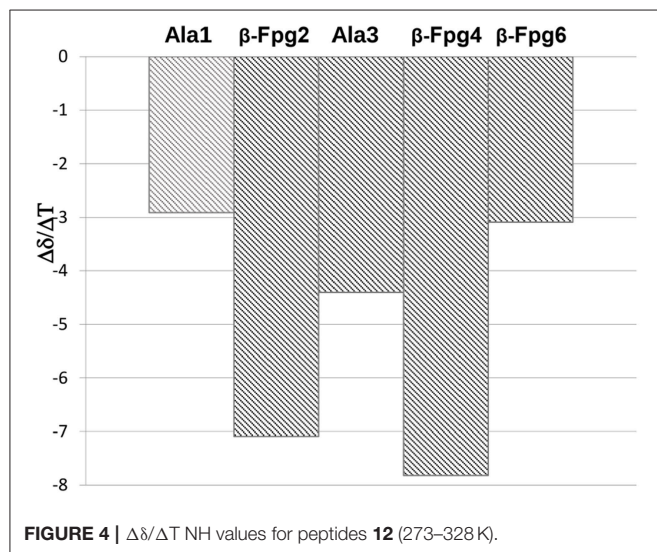


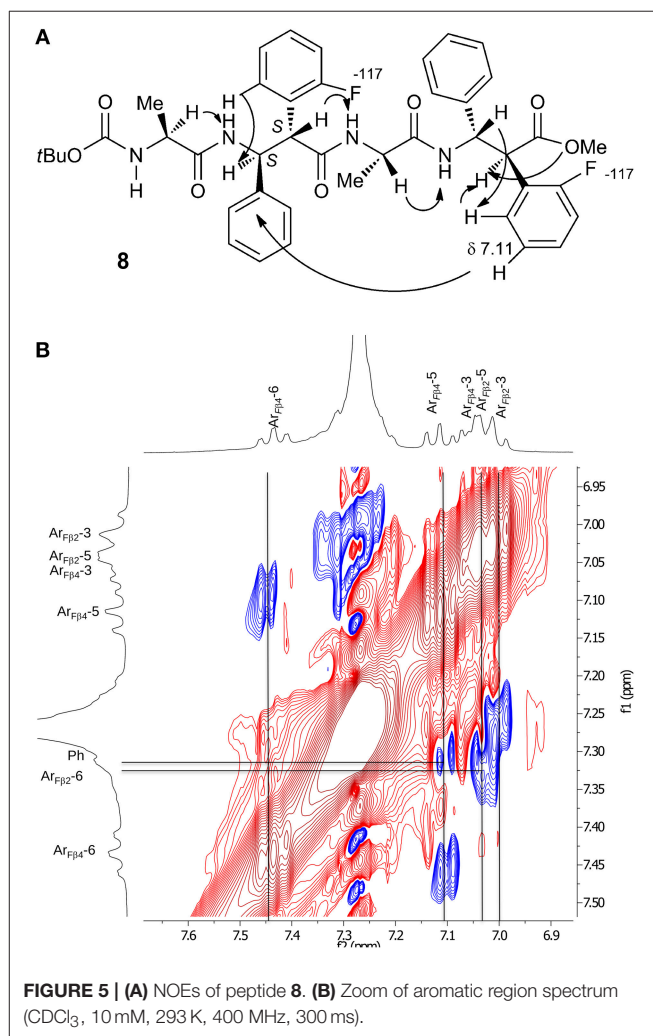
TABLE 1 | ^1H NMR parameters for di- (**1,2**) tetra- (**7,8**) and hexapeptides (**11,12**).

Compd.	Amino acid	β -2 <i>R</i> ,3 <i>R</i> -Fpg series				β -2 <i>S</i> ,3 <i>S</i> -Fpg series			
		NH_δ	$J_{\text{NH-CH}\alpha}$	$J_{\text{NH-CH}\beta}$	$J_{2,3}$	NH_δ	$J_{\text{NH-CH}\alpha}$	$J_{\text{NH-CH}\beta}$	$J_{2,3}$
1 and 2	Ala-1	5.38	brs	—	—	5.38	brs	—	—
	Beta-2	7.07	—	10.8	10.9	7.07	—	9.9	10.5
7 and 8	Ala-1	5.08	brs	—	—	4.83	brs	—	—
	Beta-2	6.99	—	^a	11	7.37	—	9.0	8.3
	Ala-3	6.39	brs	—	—	6.36	brs	—	—
	Beta-4	6.52	—	10.3	10.7	6.69	—	8.4	10.3
11 and 12	Ala-1	5.49	6.8	—	—	5.12	brs	—	—
	Beta-2	7.49	—	9.4	11.1	8.09	—	8.2	6.4
	Ala-3	7.43	^a	—	—	7.56	brs	—	—
	Beta-4	6.88	—	10.7	11.4	8.18	—	9.7	6.0
	Ala-5	6.91	^a	—	—	7.24	^a	—	—
	Beta-6	6.76	—	11.2	10.6	6.58	—	8.6	9.4

^aOverlapped signals.**FIGURE 3** | $\Delta\delta/\Delta T$ NH values for peptides **7** and **8** (273–328 K).**FIGURE 4** | $\Delta\delta/\Delta T$ NH values for peptides **12** (273–328 K).

coupling reactions between **3** with **5** and **4** with **6** affording **7** (74%) and **8** (76%), respectively, were achieved using EDC (1.1 equiv.)/EtCN-oxime/(1.1 equiv.) in CH_2Cl_2 (25°C, 3h).

Using similar *N*-deprotection/condensation protocols, hexapeptides **11** and **12** were prepared, *via* esters **9** and **10**.

**FIGURE 5** | (A) NOEs of peptide **8**. (B) Zoom of aromatic region spectrum (CDCl_3 , 10 mM, 293 K, 400 MHz, 300 ms).

IR Analysis

In our FTIR absorption investigation we focused on the N-H stretching (amide A) region (3,470–3,240 cm^{-1}). Absorptions

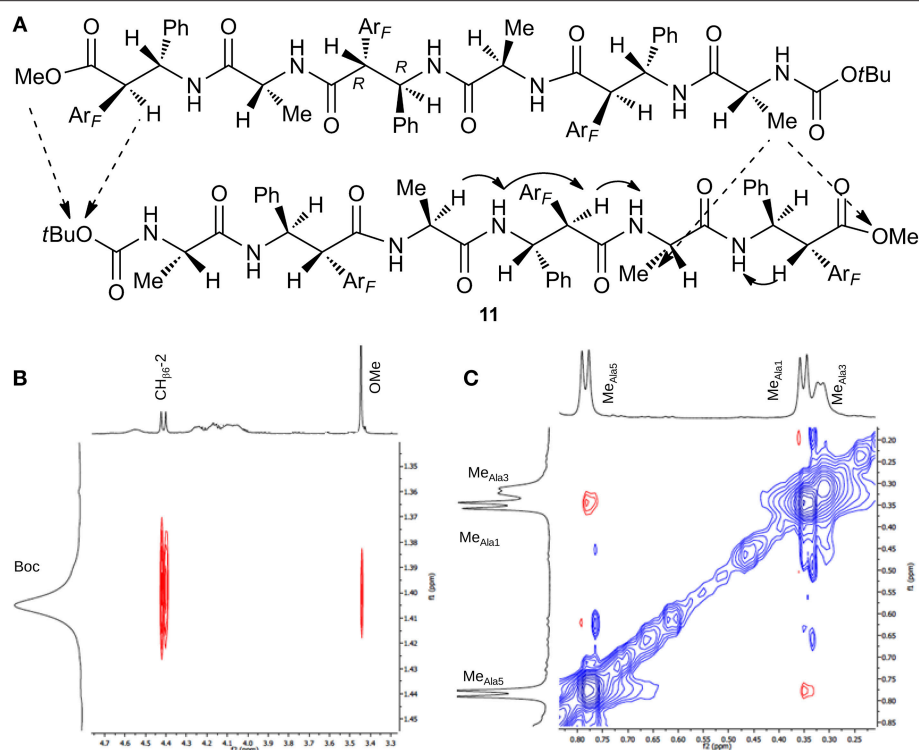


FIGURE 6 | (A) Intra- (continuous arrow) and inter- (dotted arrow) strand NOEs for peptide **11**. **(B)** ROESY zoom of Boc region. **(C)** ROESY zoom of Me region spectrum (CDCl_3 , 10 mM, 293 K, 400 MHz, 200 ms).

in this region are highly dependent on H-bond formation and, consequently, they are conformationally informative. To get insights into the modes of folding and self-association we chose as solvent CDCl_3 . It has a relatively low polarity and it is known to support ordered secondary structures in peptides.

As the peptide chain is elongated, the relative intensity of the N-H stretching band at about $3,330\text{ cm}^{-1}$ markedly increases as compared to that of the band at about $3,430\text{ cm}^{-1}$ (**Figure S9**). The first band is assigned to H-bonded NH groups, while the second is due to free (solvated) NH groups (Palumbo et al., 1976; Toniolo et al., 1985).

In the absence of aggregation, this behavior can be ascribed to the formation of ordered secondary structures, stabilized by intramolecular H-bonds. From our analysis we conclude that the chirality of the two stereogenic centers of the fluoro amino acid remarkably affects the peptide 3D-structure. In particular, the maximum of the bonded N-H band is located at $3,320\text{ cm}^{-1}$ for peptide **12**, but at higher energy, $3,330\text{ cm}^{-1}$, for peptide **11** (**Figure 2**). This latter observation implies that the H-bonds in the **11** hexapeptide are weaker. Indeed, an inspection to the behavior of the two hexapeptides at two concentrations (0.1 and 1 mM) is highly informative (**Figure 2**). For peptide **12** the relative intensities of the bands centered at $3,430\text{ cm}^{-1}$ (free NHs) and at $3,320\text{ cm}^{-1}$ (H-bonded NHs) do not significantly change upon diluting 10 times (**Figure 2B**). Therefore, we assume that the H-bonded NHs originate mainly from intramolecular interactions in **12**. Conversely, a clear

TABLE 2 | H-bonds analysis for tetrapeptides **m7** and **m8** performed on the last 200 ns of the aMD trajectories.

Acceptor	Donor	Fraction%	Avg Dist (\AA) ^a	Avg Ang ($^\circ$) ^b
m7				
Ac(O)	β -2(NH)	51.6	3.0	138.4
β -2(O)	β -4(NH)	35.4	3.1	135.9
m8				
Ac(O)	β -2(N)	74.1	3.0	139.8
β -2(O)	β -4(N)	50.8	3.1	135.6

^aA donor-acceptor distance cutoff of 4.0 \AA was requested.

^bA donor-H...acceptor angle cutoff of 110° was requested.

dilution effect is observed for **11** (**Figure 2A**) highlighting an important contribution from intermolecular H-bonds. The onset of a β -sheet conformation can thus be hypothesized for **11** based on this FTIR absorption analysis.

In conclusion, this IR absorption analysis indicates that the longer oligomers adopt secondary structures strongly dependent on the chirality of the fluoro- $\beta^{2,3}$ -diarylamino acid.

NMR Characterization

All synthesized peptides were fully characterized by NMR (^1H , ^{13}C , COSY, TOCSY, HMBC, HMQC, NOESY, ROESY) in CDCl_3 . In many cases broad CH and NH signals were detected, thus

preventing a clear information on spatial proximities. Detailed data are reported in the **Supporting Material** (7: **Table TS1**; 8: **Table TS2**; 11: **Tables TS3, TS4**; 12: **Table TS5**). Finally, fluorine NMR was performed for all peptides. In all cases, fluorine atoms resonate in δ -118 - -117 region, except for fluorine of Ar β_2 and Ar β_4 of **11** that resonate at lower fields (δ -116.1, -114.8, broad signals; not assigned).

As reported in the literature (Cheng et al., 2001; Balamurugan and Muraleedharan, 2012; March et al., 2012), $J_{2,3}$ and $J_{\text{NH}-\text{CH}\beta}$ values help to predict the secondary structure of peptides containing β -amino acids. Large values (10–12 Hz) indicate the antiperiplanar arrangement of $\text{C}_\alpha/\text{C}_\beta$ substituents and of $\text{NH}-\text{CH}_\beta$ and are consistent with an extended conformation. Smaller values (3–4 Hz) indicate a gauche conformation corresponding to turn/helix constructs. Since we started from a *syn*-amino acid, an extended conformation could be expected. On the other hand, the presence of helicogenic alanine could influence the secondary conformation of the peptide. As shown in **Table 1**, large $J_{2,3}$ and $J_{\text{NH}-\text{CH}\beta}$ values were detected for peptides containing β -2R,3R-Fpg amino acid indicating their extended conformation. Lower J values were detected for peptides containing β -2S,3S-Fpg amino acid, mostly for $J_{2,3}$ of amino acids at position 2 and 4 of peptide **12**. On the other hand, these J values are higher with respect to those reported for helix constructs containing β -amino acids (J 3–4 Hz), suggesting that for **12** more than one preferred conformation is present (Seebach et al., 1999).

A further main difference between the two series is the Me_{Ala} resonances. According to an extended conformation, $\text{Me}_{\text{Ala}3}$ of **7** (see **Figure 7A**) is located between Ph β_2 and Ar $\text{F}\beta_4$ possessing the same orientation. This induces a strong shielding effect on the methyl group that resonates at higher field (δ 0.48). Similarly, **11** is characterized by two shielded methyl groups [$\text{Me}_{\text{Ala}3}$ (δ 0.32); $\text{Me}_{\text{Ala}5}$ (δ 0.35)], in agreement with an extended conformation (**Figure 8A**). $\text{Me}_{\text{Ala}3}$ (δ 0.97) in **8**, as well as all three Me_{Ala} [$\text{Me}_{\text{Ala}1}$ (δ 1.36); $\text{Me}_{\text{Ala}3}$ (δ 1.20); $\text{Me}_{\text{Ala}5}$ (δ 1.01)] of **12**, not affected by this electronic effect, resonate at lower field. Furthermore, differences of NH chemical shift are mostly found for hexapeptides **11** and **12**, being the NH resonances of this last at lower field.

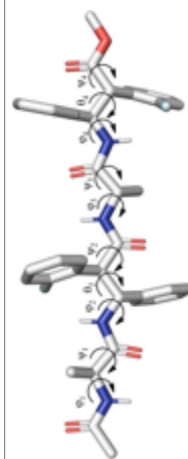
The temperature dependence experiments of the NH proton chemical shifts variation, giving insights on NH inaccessibility or on NH-bond network (Augspurger et al., 1995) were performed for peptides **7**, **8**, and **12** (NHs proximity to aromatic protons prevented a clear overview of their behavior in peptide **11**).

Very high $\Delta\delta/\Delta T$ values (> -9.4 ppb K^{-1} ; this value is not detectable for NH β_2 , overlapped signal) were found for **7** and **8**, indicating absence of H-bonds. As exception, a medium value (-4.3 ppb K^{-1}) was detected for NH $\text{Ala}1$ of **8**, indicating an equilibrium between a H-bonded and non-bonded status or a shielded environmental (**Figure 3**).

These results agree with IR data indicating, for both peptides, a low intensity of the bond at about $3,320\text{ cm}^{-1}$ and a lower area for **7** with respect to **8** (**Figure 2**).

Smaller $\Delta\delta/\Delta T$ values were found for NHs of **12** with respect to **8**, mostly for NH $\text{Ala}1$, NH β_6 , and NH $\text{Ala}3$ (-2.9 , -3.01 , -4.4 ppb K^{-1} , respectively; **Figure 4**). These data are consistent with

TABLE 3 | Structural analysis^a of the top clusters for the **m7** and **m8** tetrapeptides obtained from the analysis of the last 200 ns of the aMD simulations.



c#	pop%	ϕ_1	ψ_1	ϕ_2	θ_2	ψ_2	ϕ_3	ψ_3	ϕ_4	θ_4	ψ_4
m7											
0	45.6	57.7 ± 128.8	-32.5 ± 118.9	-100.8 ± 131.5	175.9 ± 8.4	120.1 ± 16.0	-160.6 ± 22.2	164.5 ± 17.5	-113.0 ± 20.5	-174.6 ± 12.2	131.2 ± 23.0
1	35.0	-79.0 ± 44.4	96.8 ± 57.7	-106.3 ± 27.9	163.4 ± 13.9	77.6 ± 47.0	-58.4 ± 27.8	81.6 ± 38.7	-93.0 ± 38.7	-163.6 ± 23.4	104.6 ± 30.8
m8											
0	87.7	-112.3 ± 41.2	-1.5 ± 73.4	112.2 ± 23.1	-175.7 ± 9.5	-121.4 ± 28.3	-57.6 ± 52.3	102.5 ± 71.9	128.1 ± 26.0	-179.9 ± 11.3	-119.8 ± 58.7
1	9.1	-71.3 ± 34.0	150.7 ± 84.6	107.1 ± 21.5	-177.8 ± 10.1	-153.2 ± 15.5	-166.9 ± 20.0	174.6 ± 20.1	115.9 ± 38.0	170.5 ± 17.9	-98.7 ± 41.0

^a Dihedrals are measured on the non-minimized most representative conformation of each cluster. Intervals are the mean deviations of the whole cluster population from the centroid.

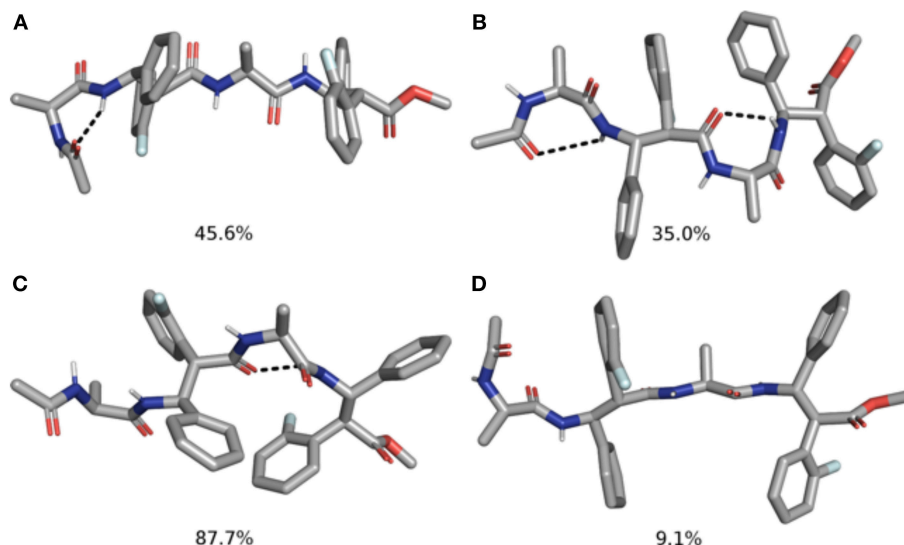


FIGURE 7 | Top 2 clusters representative structures of **m7** (A,B) and **m8** (C,D) tetrapeptides. The populations of each cluster are indicated as a percentage. Hydrogen bonds are indicated as dashed black lines.

IR analyses (**Figure 2B**) indicating the tendency of **12** to give strong/medium intramolecular C=O...H-N H-bonds.

A complete set of $\text{CH}_\alpha/\text{NH}_\beta$ ($i, i+1$) and $\text{H}_\beta\text{-2}/\text{NH}_\alpha$ ($i, i+1$) NOEs characterizes peptides **7** (**Figure S2**), **8** (**Figure S3**), and **12** (**Figure S8**). A peculiar NOE for **8** is between H-5 of $\text{Ar}_{\beta 4}$ (δ 7.11) with $\text{Ph}_{\beta 2}$ (δ 7.31, **Figure 5**). The resonances of Ph protons in both $\text{Ph-}\beta_{\beta 2}$ and $\text{Ph-}\beta_{\beta 4}$ range in δ 7.31–7.22 region. On the other hand, the antiperiplanar position of Ph with Ar_F of β -4 amino acid ($J_{2,3}$ 10.3 Hz) excludes that the detected spatial proximity between Ar_F and Ph derives from the aromatic moieties of the same amino acid. The formation of a turn in β -2/Ala3/ β -4 region is suggested, as confirmed by computational data (**Figure 7C**), that is consistent with the deviation of $J_{\text{NH-CH}_\alpha}$ values characterizing the extended peptides (**Table 1**).

Considering peptide **12**, apart the above-mentioned NOEs, only a weak spatial proximity was detected between NH-2 and NH-3 (**Figure S8**). Detection of possible NOEs between non-sequential Ph/Ar protons, as shown for **8**, were prevented because of the presence of several overlapped aryl protons.

Focusing on **11**, only some $\text{CH}_\alpha/\text{NH}_\beta$ ($i, i+1$) and $\text{H}_\beta\text{-2}/\text{NH}_\alpha$ ($i, i+1$) NOEs were detected, because several signals are overlapped preventing certain NOEs. Interestingly, the formation of an antiparallel pleated sheet arrangement in which the C-terminus of one strand is faced on the N-terminus of a second strand is supported by Noesy/Roesy experiments. Different inter-strand spatial proximities are present that are Me_{Ala1} with both $\text{Me}_{\text{Ala5}}(\text{m})$ and OMe (vw) and Boc with both $\text{CH}_{\beta 6\text{-2}}(\text{m})$ and OMe(w) (**Figure 6**). ^1H NMR studies at variable concentration (1.15–9.10 mM; **Figure S32**) showed concentration dependence chemical shift changes indicating aggregation. Noesy/Roesy experiments confirmed this tendency also at very low concentration (1.5 mM in CDCl_3 , **Figure S5**). DMSO-solvent titration of **11** was performed that was matched with Tocsy experiments (0%, 8% and 20% v/v of DMSO in

CDCl_3) to ensure the correct correlation between NH with the corresponding amino acid. A strong NH downshift was detected for $\text{NH}_{\beta 6}$, $\text{NH}_{\beta 4}$, and $\text{NH}_{\text{Ala-3}}$ ($\Delta\delta > 1$, 0.89, and 0.54, respectively) indicating their solvent exposure. A medium-weak H-bond ($\Delta\delta$ 0.35) was detected for NH-2. Instead, NH-1 and NH-5 are strongly involved in a H-bond ($\Delta\delta < 0.05$) (**Figure S7**). As a result, our hypothesis is that this antiparallel sheet is stabilized by intermolecular H-bond.

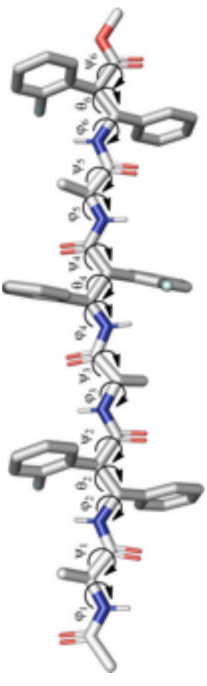
The NMR analysis of **11** is also performed in DMSO-d_6 (10 mM), that is known to be a dissociating solvent. A similar ^1H NMR spectrum was detected concerning protons multiplicity, indicating an extended architecture, except for the NH resonances that are at lower field (**Table TS4**). This allowed to detect a complete set of $\text{CH}_\alpha/\text{NH}_\beta$ and $\text{H}_\beta\text{-2}/\text{NH}_\alpha$ ($i, i+1$) spatial proximities. As expected, inter-strand spatial proximities were absent in the ROESY experiment (**Figure S6**).

Computational Studies

To gain additional insight on the conformational behavior of both tetra (**m7** and **m8**) and hexapeptides (**m11** and **m12**), we performed accelerated molecular dynamics (aMD) simulations in explicit CHCl_3 solvent (Pierce et al., 2012).

Concerning the tetrapeptides, both clustering and hydrogen bond (H-bond) analyses suggested a significantly different conformational behavior for **m7** and **m8**. The analyses of the aMD trajectories of both peptides only evidenced two potential H-bonds, one between the acetyl carbonyl and $\text{NH}_{\beta 2}$, the other between $\text{C=O}_{\beta 2}$ and $\text{NH}_{\beta 4}$. However, the occupancy is about 20% higher in the case of **m8** (**Table 2**), suggesting that **m8** can adopt a more compact conformation. This behavior is also confirmed by the analysis of the ϕ , ψ , and θ dihedrals of the representative structures of the most populated clusters (**Table 3**).

Indeed, **m7** prefers an almost completely extended conformation (**Figure 7A**), except for a γ -turn involving

TABLE 4 | Structural analysis of the top 3 clusters for the **m11** and **m12** hexapeptides obtained from the analysis of the last 200 ns of the aMD simulations.


c#	pop%	ϕ_1	ψ_1	ϕ_2	θ_2	ψ_2	ϕ_3	ψ_3	ϕ_4	θ_4	ψ_4	ϕ_5	ψ_5	ϕ_6	θ_6	ψ_6
m11																
0	43.3	-59.2 \pm 51.6	75.0 \pm 59.5	-110.1 \pm 25.8	179.8 \pm 9.2	133.5 \pm 18.4	-150.9 \pm 20.1	140.6 \pm 20.2	-117.7 \pm 20.5	173.8 \pm 8.5	122.4 \pm 19.9	-104.5 \pm 35.1	115.0 \pm 47.6	-101.6 \pm 27.9	155.6 \pm 23.8	110.5 \pm 26.2
1	29.5	-155.7 \pm 58.5	164.9 \pm 64.6	-147.4 \pm 27.5	170.9 \pm 9.3	126.0 \pm 23.6	-123.6 \pm 48.5	51.1 \pm 40.7	-165.6 \pm 31.2	172.5 \pm 10.8	152.9 \pm 32.3	-151.2 \pm 23.1	128.7 \pm 34.7	-89.0 \pm 35.1	-161.2 \pm 24.2	152.2 \pm 30.2
2	19.8	-78.0 \pm 35.2	77.3 \pm 52.9	-162.7 \pm 36.8	-179.1 \pm 10.0	148.2 \pm 29.2	-62.0 \pm 24.8	57.5 \pm 32.4	-106.5 \pm 31.1	175.2 \pm 9.0	90.6 \pm 38.6	-89.3 \pm 15.8	36.1 \pm 37.7	-124.8 \pm 24.1	-169.5 \pm 19.3	143.5 \pm 26.2
m12																
0	27.4	-74.1 \pm 19.9	-20.8 \pm 76.2	106.5 \pm 24.8	-175.6 \pm 9.3	-140.6 \pm 25.5	65.3 \pm 102.2	-34.7 \pm 66.5	117.2 \pm 21.5	-171.8 \pm 10.2	-161.9 \pm 40.3	80.3 \pm 99.5	-45.2 \pm 81.5	102.0 \pm 32.9	173.1 \pm 14.7	-150.1 \pm 26.6
1	27.0	-72.5 \pm 21.8	0.5 \pm 71.3	101.6 \pm 29.2	177.5 \pm 11.8	-141.3 \pm 21.6	-110.1 \pm 54.6	-8.8 \pm 50.3	174.0 \pm 54.5	-165.8 \pm 14.8	-148.2 \pm 26.3	-150.5 \pm 35.5	157.1 \pm 60.6	88.3 \pm 46.4	175.5 \pm 14.3	-106.0 \pm 29.5
2	16.4	-176.2 \pm 85.5	114.2 \pm 61.7	103.3 \pm 26.1	178.9 \pm 12.4	-144.4 \pm 22.7	-129.3 \pm 27.6	-168.7 \pm 37.1	89.2 \pm 53.6	-175.7 \pm 9.2	-106.0 \pm 37.5	-136.0 \pm 36.8	147.4 \pm 51.4	179.9 \pm 44.0	175.1 \pm 16.8	-134.3 \pm 21.5

the acetyl cap at the *N*-terminus. This conformation is consistent with the high chemical shift observed for Me_{Ala}3 (see above). At a minor extent, a geometry characterized by two γ -turns, the first involving the acetyl cap and the NH β_2 , the second between the C=O β_2 carbonyl and NH β_4 , is also observed as the secondary cluster (**Figure 7B**). This conformation is possibly stabilized by a π - π interaction between the Ph β_2 and the Ar β_4 . However, the low H-bond population, the relatively long donor-acceptor distances and narrow donor-H...angles (**Table 2**) suggest that these γ -turns are not stable. Overall, these data suggest that **m7** can switch from a completely extended conformation to a partially folded conformation. However, this last is only marginally stabilized by π - π interactions between the two β -amino acids and by γ -turn H-bonds. The equilibrium is consequently shifted toward the extended conformation, coherently with NMR observations.

Conversely, **m8** tetrapeptide showed an opposite behavior. A highly populated primary cluster (pop = 87.7%; **Figure 7C**) is indeed characterized by a relatively compact geometry, showing a γ -turn between β -2 and β -4 and a π - π interaction between the Ph β_2 and Ar β_4 . This interaction is consistent with Noesy experiments (see above). A poorly sampled fully extended conformation (pop = 9.1%) was also found as a secondary cluster (**Figure 7D**).

The analysis of the aMD simulations performed on **m11** and **m12** hexapeptides led to similar conclusions, compared to the tetrapeptide series. Indeed, **m11** most populated cluster (pop = 43.3%) corresponds to an extended conformation, as showed by the ϕ , ψ , and θ dihedrals of the corresponding representative structure (**Table 4** and **Figure 8A**). The second most populated cluster (pop = 29.5%) represents conformations showing π - π interactions involving the Ar β of both β -2 and β -4, while the C-terminus remains extended (**Table 4** and **Figure 8B**). Only the third cluster (pop = 19.8%) presented the Ar β /Ph π - π interactions between the aryl groups of β -2/ β -4 and of β -4/ β -6, similarly to what observed in **m7**. We could also observe γ -turns between the backbone C=O of Ac capping group with NH β_2 , and carbonyls of β -2 and β -4 with NH β_4 and NH β_6 (**Table 5**).

The top two clusters of the **m12** hexapeptide are relatively low populated (pop = 27.4 and 27.0%, respectively). However, they both show a folded conformation, with π - π interactions between the aromatic rings of the β -amino acids, and the above described γ -turns (**Figures 8C,D**; **Table 4**). This behavior resembles what previously observed for the tetrapeptides series, where **m8** principal geometry was more compact, compared to **m7**. A similar behavior between the hexa- and tetrapeptide series was also observed in terms of H-bonds. Indeed, the occupancies of the H-bonds defining the γ -turns are about 15% higher in **m12**, compared to **m11** (**Table 5**). In the hexapeptide series, also a relatively populated third cluster (pop = 16.4%) showed a partially folded representative structure. Indeed, computed ϕ , ψ , and θ dihedrals (ψ_3 , ϕ_4 , and θ_4 , in particular), assume values that are compatible with interactions between the Ph β_2 and the Ar β_4 , as well as between the Ph β_4 and Ar β_6 .

Overall, the computational analysis shows a coherent influence of the stereochemical configuration of α and β carbons on the investigated β -amino acids inserted in model

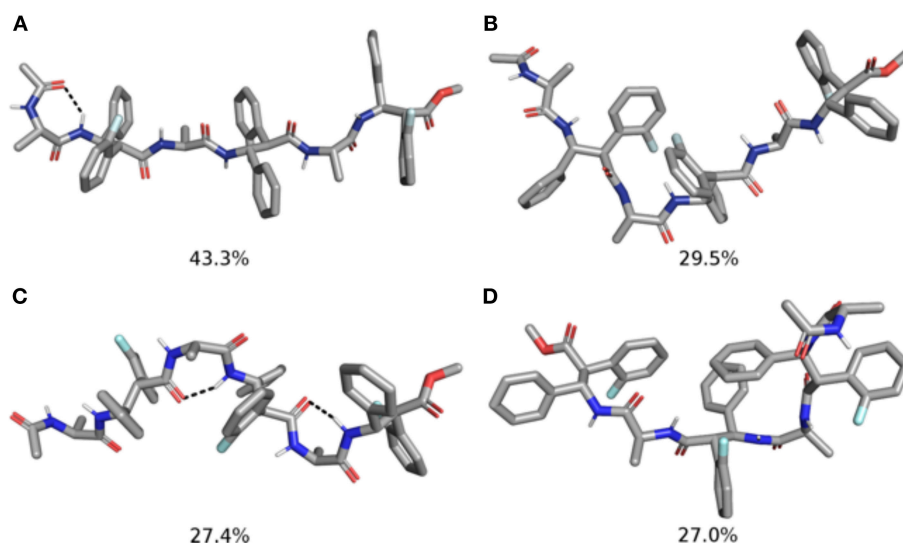


FIGURE 8 | Representative structures of the two most populated clusters of **m11** (A,B) and **m12** (C,D) hexapeptides. The population of each cluster is indicated as a percentage. Hydrogen bonds are depicted as dashed black lines.

TABLE 5 | H-bonds Analysis for Hexapeptides **m11** and **m12** Performed on the Last 200 ns of the aMD Trajectory.

Acceptor	Donor	Fraction%	Avg Dist (Å) ^a	Avg Ang (°) ^b
m11				
Ac(O)	β -2(N)	43.8	3.0	137.7
β -2(O)	β -4(N)	39.0	3.1	136.4
β -4(O)	β -6(N)	31.7	3.1	136.2
m12				
Ac(O)	β -2(N)	60.4	3.1	139.6
β -2(O)	β -4(N)	47.5	3.0	137.2
β -4(O)	β -6(N)	46.9	3.0	137.0

^aA donor-acceptor distance cutoff of 4.0 Å was requested.

^bA donor-H...acceptor angle cutoff of 110° was requested.

Ac(S-Ala- β -Fpg)_nOMe peptides. Indeed, our observation suggest that β -2R,3R-Fpg helps to stabilize an extended conformation. Conversely, β -2S,3S-Fpg seems to induce more compact conformations, possibly stabilized by inter-residue π - π interactions and/or by γ -turns. This behavior is also supported by $J_{NH-CH\beta}$ and $J_{2,3}$ coupling constants obtained by 1H NMR experiments. Indeed, larger J values were obtained for both **7** and **11**, compared to **8** and **12**, suggesting a more folded conformation for these latter peptides (Li et al., 2015). To provide additional evidences of this behavior, we compared the frequency of the radius of gyrations (RoG) sampled in the last 200 ns of simulation (Figure 9). For both tetra- and hexapeptides, it can be observed that a larger RoG is sampled more frequently for peptides containing β -2R,3R-Fpg, compared to peptides containing β -2S,3S-Fpg. Figure 9 also shows that two peaks are found for **m11**, centered at 6.5 and 8.0 Å. This is coherent with the results of the clustering analysis, which evidence the possibility of a “bending” of the extended geometry

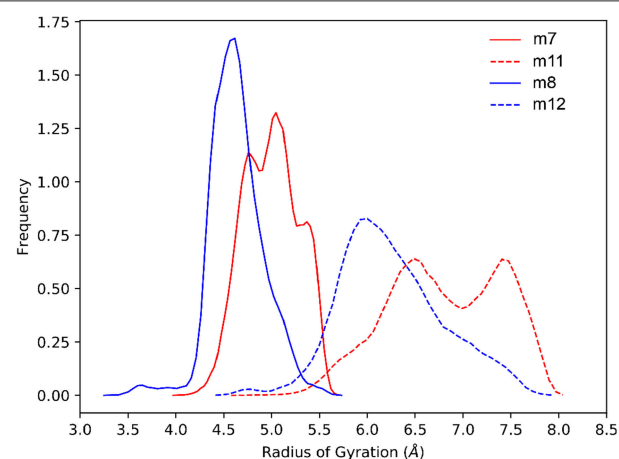


FIGURE 9 | Comparison of the normalized sampling frequencies of RoG calculated from the last 200 ns of the aMD trajectories of **m7**, **m8**, **m11**, and **m12**.

at the Ala3/ β 4 level (Figure 8). **m7** instead shows a “spiked” peak centered at 5.0 Å, corresponding to the representative geometry shown in Figure 7A. The two “spikes” at 4.8 and 5.4 Å correspond to the breaking of the N -terminal γ -turn (involving the acetyl cap) and to the forming of the additional γ -turn (involving β -2 and β -4), respectively. Conversely, both **m8** and **m12** show a main peak (sharper, for **m8**) that is centered onto a RoG value that is significantly lower to that computed for the corresponding peptides containing β -2R,3R-Fpg.

CONCLUSIONS

Taken together these data, we can conclude that the architecture of the above peptides depends on the balance between the

features of the selected amino acids, i.e., the *syn* β -amino acid, favoring an extended conformation, and alanine, inducing turns. The chirality of the two stereogenic centers of β -amino acid remarkably affects the peptide 3D-structures. A preferred extended conformation was found matching the β -*R,R*-amino acid with *S*-alanine. This is confirmed by *J* values of both tetra- and hexapeptides containing β -2*R*,3*R*-Fpg as well as by computational analysis. The extended conformation of this peptide induces the formation of an antiparallel β -sheet, also at low concentration, as documented by NMR data of **11**. Our hypothesis is that the formation of this pleated sheet is favored by π , π -interactions of aromatic moieties and is stabilized by H-bonds. IR analysis of this peptide indicates the involvement of NHs in H-bonds, confirmed by the titration experiment (NH-1 and NH-6 involvement). The NH-network proposed by computational experiments does not fit with NMR data. On the other hand, computational data are consistent with a **11** single strand and not with pleated sheet architecture. In this case the formation of H-bonds is driven by γ -turn formation.

β -*S,S*-amino acid with *S*-alanine gives more compact folded structures that are probably driven by alanine moieties. In fact, peptides containing β -2*S*,3*S*-Fpg display a higher stability and a larger content of an ordered secondary structure as compared to the peptides containing β -2*R*,3*R*-Fpg. Both NMR and computational data support the formation of a turn for **8** stabilized by π - π interactions between Ph β_2 and

Ar β_4 . IR absorption analysis and experiments at variable temperature confirm that the longer oligomer **12** is stabilized by intramolecular C=O \cdots H-N bonds. On the other hand, *J* values indicate that an equilibrium occurred between multiple compact conformations.

AUTHOR CONTRIBUTIONS

MG conceived the research. RB and SP carried out change with RB, EB, and SP carried out the synthesis. MG, FC, and FF carried out the spectroscopic analyses. AC and IM carried out the computational studies. MG and AC supervised the work. MG, AC, and RB wrote the paper. All the authors revised the manuscript.

FUNDING

We are grateful to MIUR for funding (2015 PRIN project Prot. 20157WW5EH) and to European Union's Horizon 2020 research and innovation programme (Marie Skłodowska-Curie grant agreement No. 675527).

SUPPLEMENTARY MATERIAL

The Supplementary Material for this article can be found online at: <https://www.frontiersin.org/articles/10.3389/fchem.2019.00192/full#supplementary-material>

REFERENCES

- Angelici, G., Luppi, G., Kaptein, B., Broxterman, Q. B., Hofmann, H. J., and Tomasini, C. (2007). Synthesis and secondary structure of alternate α , β -hybrid peptides containing oxazolidin-2-one moieties. *Eur. J. Org. Chem.* 2007, 2713–2721. doi: 10.1002/ejoc.200700134
- Augsburger, J. D., Bindra, V. A., Scheraga, H. A., and Kuki, A. (1995). Helical stability of de Novo designed α -aminoisobutyric acid-rich peptides at high temperatures. *Biochemistry* 34, 2566–2576. doi: 10.1021/bi00008a022
- Balamurugan, D., and Muraleedharan, K. M. (2012). Unprecedented torsional preferences in trans- β 2,3-amino acid residues and formation of 11-helices in α , β 2,3-hybrid peptides. *Chem. A Eur. J.* 18, 9516–9520. doi: 10.1002/chem.201201415
- Baldauf, C., and Hofmann, H. J. (2012). Ab initio MO theory—An important tool in foldamer research: prediction of helices in oligomers of ω -amino acids. *Helv. Chim. Acta* 95, 2348–2383. doi: 10.1002/hlca.201200436
- Basuroy, K., Karuppiiah, V., and Balaram, P. (2014). C11/C9 Helices in crystals of α β hybrid peptides and switching structures between helix types by variation in the α -residue. *Org. Lett.* 16, 4614–4617. doi: 10.1021/ol5021866
- Berlicki, L., Pilsl, L., Wéber, E., Mándity, I. M., Cabrele, C., Martinek, T. A., et al. (2012). Unique α , β - and α , α , β , β -peptide foldamers based on cis- β -aminocyclopentanecarboxylic acid. *Angew. Chemie Int. Ed.* 51, 2208–2212. doi: 10.1002/anie.201107702
- Bonetti, A., Clerici, F., Foschi, F., Nava, D., Pellegrino, S., Penso, M., et al. (2014). *syn/anti* Switching by specific heteroatom–titanium coordination in the mannich-like synthesis of 2,3-Diaryl- β -amino acid derivatives. *Eur. J. Org. Chem.* 15, 3203–3209. doi: 10.1002/ejoc.201400142
- Bonetti, A., Pellegrino, S., Das, P., Yuran, S., Bucci, R., Ferri, N., et al. (2015). Dipeptide nanotubes containing unnatural fluorine-substituted β 2,3-diarylamino acid and L-alanine as candidates for biomedical applications. *Org. Lett.* 17, 4468–4471. doi: 10.1021/acs.orglett.5b02132
- Bucci, R., Bonetti, A., Clerici, F., Contini, A., Nava, D., Pellegrino, S., et al. (2017a). Tandem tetrahydroisoquinoline-4-carboxylic acid/ β -alanine as a new construct able to induce a flexible turn. *Chem. A Eur. J.* 23, 10822–10831. doi: 10.1002/chem.201701045
- Bucci, R., Contini, A., Clerici, F., Pellegrino, S., and Gelmi, M. L. (2019). From glucose to enantiopure morpholino β -amino acid: a new tool for stabilizing γ -turns in peptides. *Org. Chem. Front.* doi: 10.1039/C8QO01116H
- Bucci, R., Das, P., Iannuzzi, F., Feligioni, M., Gandolfi, R., Gelmi, M. L., et al. (2017b). Self-assembly of an amphipathic α α β -tripeptide into cationic spherical particles for intracellular delivery. *Org. Biomol. Chem.* 15, 6773–6779. doi: 10.1039/c7ob01693j
- Bucci, R., Giofré, S., Clerici, F., Contini, A., Pinto, A., Erba, E., et al. (2018). Tetrahydro-4H-(pyrrolo[3,4-d]isoxazol-3-yl)methanamine: a bicyclic diamino scaffold stabilizing parallel turn conformations. *J. Org. Chem.* 83, 11493–11501. doi: 10.1021/acs.joc.8b01299
- Cabrele, C., Martinek, T. A., Reiser, O., and Berlicki, L. (2014). Peptides containing β -amino acid patterns: challenges and successes in medicinal chemistry. *J. Med. Chem.* 57, 9718–9739. doi: 10.1021/jm5010896
- Case, D. A., Babin, V., Berryman, J. T., Betz, R. M., Cai, Q., Cerutti, D. S., et al. (2014). *AMBER 14*. San Francisco: University of California.
- Checchio, J. W., and Gellman, S. H. (2016). Targeting recognition surfaces on natural proteins with peptidic foldamers. *Curr. Opin. Struct. Biol.* 39, 96–105. doi: 10.1016/j.sbi.2016.06.014
- Cheng, R. P., Gellman, S. H., and DeGrado, W. F. (2001). β -Peptides: from structure to function. *Chem. Rev.* 101:3219–3232. doi: 10.1021/cr000045i
- Clerici, F., Erba, E., Gelmi, M. L., and Pellegrino, S. (2016). Non-standard amino acids and peptides: from self-assembly to nanomaterials. *Tetrahedron Lett.* 57, 5540–5550. doi: 10.1016/j.tetlet.2016.11.022
- Del Borgo, M. P., Kulkarni, K., and Aguilar, M.-I. (2017). Using β -amino acids and β -peptide templates to create bioactive ligands and biomaterials. *Curr. Pharm. Des.* 23, 3772–3785. doi: 10.2174/1381612823666170616083031
- Dupradeau, F.-Y., Pigache, A., Zaffran, T., Savineau, C., Lelong, R., Grivel, N., et al. (2010). The R.E.D. tools: advances in RESP and ESP charge derivation and force field library building. *Phys. Chem. Chem. Phys.* 12:7821. doi: 10.1039/c0cp00111b

- Gellman, S. H. (1998). Foldamers: a manifesto. *ACC. Chem. Res.* 31, 173–180. doi: 10.1021/ar960298r
- Gopalan, R. D., Borgo, M. P., Del Mechler, A. I., Perlmutter, P., and Aguilar, M.-I. (2015). Geometrically precise building blocks: the self-assembly of β -peptides. *Chem. Biol.* 22, 1417–1423. doi: 10.1016/j.chembiol.2015.10.005
- Hegedüs, Z., Makra, I., Imre, N., Hetényi, A., Mándity, I. M., Monostori, É., et al. (2016). Foldameric probes for membrane interactions by induced β -sheet folding. *Chem. Commun.* 52, 1891–1894. doi: 10.1039/c5cc09257d
- Horne, W. S. (2011). Peptide and peptoid foldamers in medicinal chemistry. *Expert Opin. Drug Discov.* 6:1247. doi: 10.1517/17460441.2011.632002
- Johnson, L. M., and Gellman, S. H. (2013). “Chapter nineteen— α -helix mimicry with α/β -peptides,” in *Methods in Protein Design Methods in Enzymology*, ed A. E. Keating (Amsterdam: Academic Press), 407–429.
- Lee, W., Kwon, S., Kang, P., Guzei, I. A., and Choi, S. H. (2014). Helical folding of α/β -peptides containing β -amino acids with an eight-membered ring constraint. *Org. Biomol. Chem.* 12, 2641–2644. doi: 10.1039/c4ob00266k
- Li, F., Lee, J. H., Grishaev, A., Ying, J., and Bax, A. (2015). High accuracy of karplus equations for relating three-bond j couplings to protein backbone torsion angles. *Chem. Phys. Chem.* 16, 572–578. doi: 10.1002/cphc.201402704
- Maier, J. A., Martinez, C., Kasavajhala, K., Wickstrom, L., Hauser, K. E., and Simmerling, C. (2015). ff14SB: improving the accuracy of protein side chain and backbone parameters for ff99SB. *J. Chem. Theory Comput.* 11, 3696–3713. doi: 10.1021/acs.jctc.5b00255
- March, T. L., Johnston, M. R., Duggan, P. J., and Gardiner, J. (2012). Synthesis, structure, and biological applications of α -fluorinated β -amino acids and derivatives. *Chem. Biodivers.* 9, 2410–2441. doi: 10.1002/cbdv.201200307
- Molecular Operating Environment (2013). *Chemical Computing Group Releases MOE Version 2013.08*. Montreal, QC: Chemical Computing Group Inc.
- Palumbo, M., da Rin, S., Bonora, G. M., and Toniolo, C. (1976). Linear oligopeptides, 29. Infrared conformational analysis of homo-oligopeptides in the solid state and in solution. *Die Makromol. Chem.* 177, 1477–1492. doi: 10.1002/macp.1976.021770519
- Pellegrino, S., Bonetti, A., Clerici, F., Contini, A., Moretto, A., Soave, R., et al. (2015). 1H -Azepine-2-oxo-5-amino-5-carboxylic acid: a 3.10 helix inducer and an effective tool for functionalized gold nanoparticles. *J. Org. Chem.* 80, 5507–5516. doi: 10.1021/acs.joc.5b00396
- Pellegrino, S., Clerici, F., and Gelmi, M. L. (2008). β -Hydroxynorbornane amino acid derivatives: valuable synthons for the diastereoselective preparation of substituted cyclopentylglycine derivatives. *Tetrahedron* 64, 5657–5665. doi: 10.1016/j.tet.2008.04.038
- Pellegrino, S., Facchetti, G., Contini, A., Gelmi, M. L., Erba, E., Gandolfi, R., et al. (2016). Ctr-1 Mets7 motif inspiring new peptide ligands for Cu(I)-catalyzed asymmetric Henry reactions under green conditions. *RSC Adv.* 6, 71529–71533. doi: 10.1039/c6ra16255j
- Penso, M., Foschi, F., Pellegrino, S., Testa, A., and Gelmi, M. L. (2012). Diastereoselective protocols for the synthesis of 2,3-trans- and 2,3-cis-6-methoxy-morpholine-2-carboxylic acid derivatives. *J. Org. Chem.* 77, 3454–3461. doi: 10.1021/jo300221y
- Pierce, L. C. T., Salomon-Ferrer, R., Augusto, F., de Oliveira, C., McCammon, J. A., and Walker, R. C. (2012). Routine access to millisecond time scale events with accelerated molecular dynamics. *J. Chem. Theory Comput.* 8, 2997–3002. doi: 10.1021/ct300284c
- Pilsl, L. K. A., and Reiser, O. (2011). α/β -Peptide foldamers: state of the art. *Amino Acids* 41, 709–718. doi: 10.1007/s00726-011-0894-2
- Ruffoni, A., Cavanna, M. V., Argenti, S., Locarno, S., Pellegrino, S., Gelmi, M. L., et al. (2016). Aqueous self-assembly of short hydrophobic peptides containing norbornene amino acid into supramolecular structures with spherical shape. *RSC Adv.* 6, 90754–90759. doi: 10.1039/c6ra17116h
- Ruffoni, A., Contini, A., Soave, R., Lo Presti, L., Esposto, I., Maffucci, I., et al. (2015). Model peptides containing the 3-sulfanyl-norbornene amino acid, a conformationally constrained cysteine analogue effective inducer of 3.10-helix secondary structures. *RSC Adv.* 5, 32643–32656. doi: 10.1039/c5ra03805g
- Seebach, D., Abele, S., Gademann, K., and Jaun, B. (1999). Pleated sheets and turns of β -peptides with proteinogenic side chains. *Angew. Chem. Int. Ed.* 38:1595.
- Seebach, D., Beck, A. K., and Bierbaum, D. J. (2004). The World of β - and γ -peptides comprised of homologated proteinogenic amino acids and other components. *Chem. Biodivers.* 1, 1111–1239. doi: 10.1002/cbdv.200490087
- Seebach, D., and Gardiner, J. (2008). β -peptidic peptidomimetics. *ACC. Chem. Res.* 41, 1366–1375. doi: 10.1021/ar700263g
- Seebach, D., Hook, D. F., and Glättli, A. (2006). Helices and other secondary structures of β - and γ -peptides. *Pept. Sci.* 84, 23–37. doi: 10.1002/bip.20391
- Seebach, D., Overhand, M., Kühnle, F. N. M., Martinoni, B., Oberer, L., Hommel, U., et al. (1996). β -Peptides: synthesis by Arndt-Eistert homologation with concomitant peptide coupling. *Structure determination by NMR and CD spectroscopy and by X-ray crystallography. Helical secondary structure of a β -hexapeptide in solution and its stability towards pepsin.* *Helv. Chim. Acta* 79, 913–941. doi: 10.1002/hlca.19960790402
- Sharma, G. V. M., Nagendar, P., Jayaprakash, P., Radha Krishna, P., Ramakrishna, K. V. S., and Kunwar, A. C. (2005). 9/11 Mixed helices in α/β peptides derived from C-linked carbo- β -amino acid and L-Ala repeats. *Angew. Chem. Int. Ed.* 44, 5878–5882. doi: 10.1002/anie.200501247
- Srinivasulu, G., Kiran Kumar, S., Sharma, G. V. M., and Kunwar, A. C. (2006). 11/9-Mixed helices in the ϵ α/β -peptides derived from alternating α - and β -amino acids with proteinogenic side chains. *J. Org. Chem.* 71, 8395–8400. doi: 10.1021/jo0612980
- Tonali, N., Kaffy, J., Soulier, J. L., Gelmi, M. L., Erba, E., Taverna, M., et al. (2018). Structure-activity relationships of β -hairpin mimics as modulators of amyloid β -peptide aggregation. *Eur. J. Med. Chem.* 154, 280–293. doi: 10.1016/j.ejmech.2018.05.018
- Toniolo, C., Bonora, G. M., Barone, V., Bavoso, A., Benedetti, E., Di Blasio, B., et al. (1985). Conformation of pleiomers of α -aminoisobutyric acid. *Macromolecules* 18, 895–902. doi: 10.1021/ma00147a013
- Vasudev, P. G., Chatterjee, S., Shamala, N., and Balaram, P. (2011). Structural chemistry of peptides containing backbone expanded amino acid residues: conformational features of β , γ , and hybrid peptides. *Chem. Rev.* 111, 657–687. doi: 10.1021/cr100100x
- Wang, P. S. P., and Schepartz, A. (2016). β -peptide bundles: design. build. analyze. biosynthesize. *Chem. Commun.* 52, 7420–7432. doi: 10.1039/C6CC01546H
- Wu, Y., Han, W. E. I., Wang, D., Gao, Y. I., and Zhao, Y. (2008). Theoretical analysis of secondary structures of β -peptides. *ACC. Chem. Res.* 41, 1418–1427. doi: 10.1021/ar800070b
- Zhu, X., Koenig, P., Hoffmann, M., Yethiraj, A., and Cui, Q. (2010). Establishing effective simulation protocols for β - and α/β -peptides. III. Molecular mechanical model for acyclic β -amino acids. *J. Comput. Chem.* 31, 2063–2077. doi: 10.1002/jcc.21493

Conflict of Interest Statement: The authors declare that the research was conducted in the absence of any commercial or financial relationships that could be construed as a potential conflict of interest.

Copyright © 2019 Bucci, Contini, Clerici, Beccalli, Formaggio, Maffucci, Pellegrino and Gelmi. This is an open-access article distributed under the terms of the Creative Commons Attribution License (CC BY). The use, distribution or reproduction in other forums is permitted, provided the original author(s) and the copyright owner(s) are credited and that the original publication in this journal is cited, in accordance with accepted academic practice. No use, distribution or reproduction is permitted which does not comply with these terms.



A Photochromic Azobenzene Peptidomimetic of a β -Turn Model Peptide Structure as a Conformational Switch

Francesca Nuti^{1,2†}, Cristina Gellini^{2†}, Maud Larregola³, Lorenzo Squillantini^{1,2}, Riccardo Chelli^{2,4}, Pier Remigio Salvi², Olivier Lequin⁵, Giangaetano Pietraperzia^{2,4} and Anna Maria Papini^{1,2,3*}

¹ Laboratory of Peptide and Protein Chemistry and Biology (PeptLab), Sesto Fiorentino, Italy, ² Department of Chemistry "Ugo Schiff", University of Florence, Sesto Fiorentino, Italy, ³ PeptLab@UCP Platform and Laboratory of Chemical Biology EA4505, Université Paris-Seine, Cergy-Pontoise, France, ⁴ European Laboratory for Non-Linear Spectroscopy (LENs), Sesto Fiorentino, Italy, ⁵ Laboratory of Biomolecules, CNRS, Sorbonne University, Ecole Normale Supérieure, PSL University, Paris, France

OPEN ACCESS

Edited by:

Alessandro Contini,
University of Milan, Italy

Reviewed by:

Junji Zhang,
East China University of Science and
Technology, China
Tangxin Xiao,
Changzhou University, China

*Correspondence:

Anna Maria Papini
annamaria.papini@unifi.it

[†]These authors have contributed
equally to this work

Specialty section:

This article was submitted to
Supramolecular Chemistry,
a section of the journal
Frontiers in Chemistry

Received: 10 January 2019

Accepted: 07 March 2019

Published: 29 March 2019

Citation:

Nuti F, Gellini C, Larregola M,
Squillantini L, Chelli R, Salvi PR,
Lequin O, Pietraperzia G and
Papini AM (2019) A Photochromic
Azobenzene Peptidomimetic of a
 β -Turn Model Peptide Structure as a
Conformational Switch.
Front. Chem. 7:180.
doi: 10.3389/fchem.2019.00180

The insertion of azobenzene moiety in complex molecular protein or peptide systems can lead to molecular switches to be used to determine kinetics of folding/unfolding properties of secondary structures, such as α -helix, β -turn, or β -hairpin. In fact, in azobenzene, absorption of light induces a reversible trans \leftrightarrow cis isomerization, which in turns generates a strain or a structure relaxation in the chain that causes peptide folding/unfolding. In particular azobenzene may permit reversible conformational control of hairpin formation. In the present work a synthetic photochromic azobenzene amino acid derivative was incorporated as a turn element to modify the synthetic peptide [Pro⁷,Asn⁸,Thr¹⁰]CSF114 previously designed to fold as a type I β -turn structure in biomimetic HFA/water solution. In particular, the P-N-H fragment at positions 7–9, involved in a β -hairpin, was replaced by an azobenzene amino acid derivative (synthesized *ad hoc*) to investigate if the electronic properties of the novel peptidomimetic analog could induce variations in the isomerization process. The absorption spectra of the azopeptidomimetic analog of the type I β -turn structure and of the azobenzene amino acid as control were measured as a function of the irradiation time exciting into the respective first $\pi\pi^*$ and $n\pi^*$ transition bands. Isomerization of the azopeptidomimetic results strongly favored by exciting into the $\pi\pi^*$ transition. Moreover, conformational changes induced by the cis \leftrightarrow trans azopeptidomimetic switch were investigated by NMR in different solvents.

Keywords: azobenzene, cis/trans photoisomerization, photoswitchable peptide, optical control, NMR spectroscopy, UV/Vis spectroscopy

INTRODUCTION

Azobenzene has been recognized as a potential molecular photoswitch in various fields, such as polymer science, material science, chemistry, and life sciences (Marchi et al., 2012; Goulet-Hanssens and Barrett, 2013; Dong et al., 2015; Bushuyev et al., 2018; Miniewicz et al., 2018). Azobenzene amino acids protected for solid phase synthesis proposed by Sewald et al. opened possibility the for

incorporation into photoswitchable peptides (Juodaityte and Sewald, 2004; Renner and Moroder, 2006; Aemissegger and Hilvert, 2007). In particular, compounds containing a methyl spacer between the phenyl ring and the amino group, as [3-(3-aminomethyl)-phenylazo]phenylacetic acid (AMPP) acid or (4-aminomethyl)phenylazobenzoic acid (AMPB), give more flexibility to the chemical structure of a Xaa-AMPB-Yaa fragment than the rigid chromophore, 4-[(4-amino)phenylazo]benzoic acid (APB).

When inserted into larger molecular systems, like protein chains or peptides, azobenzene can be used as a molecular switch and/or as a probe to determine kinetics of folding/unfolding of the corresponding secondary structure, like α -helix, β -turn, or β -hairpin (Behrendt et al., 1999; Kumita et al., 2000; Renner et al., 2000; Spörlein et al., 2002; Komarov et al., 2018). In fact, absorption of light by azobenzene induces a reversible *trans* \leftrightarrow *cis* isomerization, which in turns generates a strain or a structure relaxation in the chain that causes peptide unfolding/folding. The process can be easily monitored looking at the absorption spectrum of azobenzene itself, that is strongly different in the two forms, *trans* and *cis* (Schultz et al., 2003; Satzger et al., 2004; Quick et al., 2014). In particular, the AMPP chromophore incorporation in a peptide sequence led to a β -hairpin structure after irradiation (Dong et al., 2006, 2017; Rampp et al., 2018), and the AMPB was described as a trigger molecule in cyclic peptide structures (Ulysse et al., 1995; Renner et al., 2005).

When a chromophore unit is integrated into a linear or cyclic peptide, the *trans* \leftrightarrow *cis* isomerization of an azobenzene derivative induced by UV/VIS photo-irradiation, has been demonstrated to induce a reversible change in the peptide structure modulating its biological activity (Ali et al., 2015). For example azobenzene amino acid has been reported for antigen-antibody photocontrol (Beharry et al., 2008; Parisot et al., 2009). In a cyclic polypeptide ligand, azobenzene *trans* \leftrightarrow *cis* isomerization induced drastic changes in recognition by neural NO synthase leading to reversible photocontrol of muscle fibers (Hoppmann et al., 2011). Finally, in an amyloid azobenzene containing peptide, isomerization plays an active role in self-assembly into β -amyloid fibrils (Deeg et al., 2011).

β -Hairpins are very interesting structures as they are involved in many biological processes i.e., often constitute binding epitopes and are implied in protein-protein or protein-DNA interactions (Hillier et al., 1999; Gajiwala et al., 2000; Wong et al., 2000; Schumacher et al., 2001; Zavala-Ruiz et al., 2004). Thus, the development of highly stable β -hairpins based on introduction of molecules as azobenzene allowed to control the hairpin structure and initiate a folding or unfolding transition with high isomerization yield, remarkable photostability, and ultra-fast kinetics.

In previous studies, the family of structure-based designed β -hairpin peptides termed CSF114(Glc) has been developed to expose aberrant post-translational modifications (PTMs) to characterize antibodies as biomarkers of autoimmune diseases in patient sera (Lolli et al., 2005a,b; Papini, 2009; Pandey et al., 2012). In fact, we demonstrated that the β -turn structure is

crucial for the correct exposure of the PTM and allows a specific and high affinity antibody interaction in the context of solid-phase immunoenzymatic assays (Carotenuto et al., 2006, 2008). In this work, a modified sequence of [Pro⁷,Asn⁸,Thr¹⁰]CSF114 was selected as an optimized type I β -turn structure. Aim of the present work is the design and synthesis of a photocontrolled probe, based on AMPB azobenzene as a turn element in the central part of the amino acid sequence, to investigate if the electronic properties of the new molecule could induce variations in the isomerization process of the azobenzene unit and to study the effect of the photoswitch on its conformation.

MATERIALS AND METHODS

Reagents

All Fmoc-protected amino acids, Fmoc-Wang resins, DIC (*N,N'*-Diisopropylcarbodiimide), and Oxyma were purchased from Iris Biotech GmbH (Marktredwitz, Germany). The following amino acid side-chain-protecting groups were used: OtBu (Asp, Glu), tBu (Ser, Thr), Pbf (Arg), Trt (Gln, His), and Boc (Lys). Peptide-synthesis grade *N,N*-dimethylformamide (DMF) was purchased from Scharlau (Barcelona, Spain); acetonitrile (ACN) from Carlo Erba (Milan, Italy); dichloromethane (DCM), trifluoroacetic acid (TFA), piperidine were purchased from Sigma-Aldrich (Milan, Italy).

MW-Assisted Solid-Phase Peptide Synthesis

The azopeptide **1** was synthesized by microwave-assisted solid-phase peptide synthesis (MW-SPPS) following the Fmoc/tBu strategy, using the Liberty BlueTM automated microwave peptide synthesizer (CEM Corporation, Matthews, NC, USA) following the protocol described elsewhere (Rizzolo et al., 2011). The resin used was a Fmoc-Lys(Boc)-Wang (loading 0.24 mmol/g). Modified amino acids were introduced using the synthesized protected building-blocks suitable for Fmoc/tBu SPPS (Paolini et al., 2007; Rentier et al., 2015). Coupling was performed with the azobenzene amino acid AMPB (2.5 eq), HATU as activator (2.5 eq), and DIPEA (3.5 eq) for 30 min at room temperature. Uncertain peptide coupling steps were checked by the ninhydrin test as described by Kaiser (Kaiser et al., 1970), or micro-cleavages performed with a microwave apparatus CEM DiscoverTM single-mode MW reactor (CEM Corporation, Matthews, NC, USA). Final cleavage was performed using a mixture of TFA/TIS/H₂O (95:2.5:2.5 v:v:v) for 3 h at room temperature.

The crude azopeptide was pre-purified by Reverse Phase Liquid Chromatography (RP-HPLC) using a Li-Chroprep C-18 column on an Armen Instrument (Armen Instrument, Saint-Avé, France) working at 20 ml/min with H₂O (MilliQ) and CH₃CN as solvent systems. The second step of purification was performed by semipreparative RP-HPLC on a Waters instrument (Separation Module 2,695, detector diode array 2,996) using a Phenomenex (Torrance, CA, USA) Jupiter column C18 (10 μ m, 250 \times 10 mm), at 4 mL/min with solvent systems A (0.1% TFA in H₂O) and B (0.1% TFA in CH₃CN).

The azopeptide **1** was characterized by RP-HPLC-ESI-MS, obtaining a final purity \geq 98% (**Figure S1**). HPLC: t_r =

3.17 min (*cis* isomer) and 3.78 min (*trans* isomer), gradient 35–55% of B in 5 min; Mr = calcd. for C₁₁₆ H₁₇₀ N₂₉ O₂₅ S₁: 2402,88 ESI-MS: m/z: 1202,47 [M+2H]²⁺; 802,02 [M+3H]³⁺ RP-HPLC system is an Alliance Chromatography (Waters, Milford Massachusetts, USA) with a Bioshell A160 C18 (Sigma Aldrich, Milano Italy; 1.7 μm 2.1 × 50 mm) column at 35°C, at 0.6 mL/min coupled to a single quadrupole ESI-MS Micromass ZQ (Waters, Milford Massachusetts, USA). The solvent systems used were A (0.1% TFA in H₂O) and B (0.1% TFA in CH₃CN). Peptides were lyophilized using an Edward Modulyo lyophilizer (Richmond scientific Ltd., Lancashire, Great Britain).

UV/Vis Spectra Experiments

The experimental set up used for the irradiation procedure consists of a Xe “Ozone free” Orion lamp emitting 450 W in the spectral range 200–2,000 nm. The light is focalized through a lens (*f* = 200 mm) onto the entrance slit of a monochromator. The exit beam, having 1 nm bandwidth, is shaped by means of a pin-hole and collimated with a 50 mm lens on the sample cuvette (quartz, 1 cm optical path length). A magnetic stirrer placed inside the cuvette ensures that the irradiating beam always interacts with fresh solution. Incident beam cross section has been estimated 0.8 × 0.8 cm². Incident power has been measured with a Coherent Field Max II power meter. The power we used for the irradiation was around 500 μW for all the three excitation wavelengths used 313, 440, and 330 nm. Absorption spectra have been obtained with a Varian Cary 5 spectrophotometer, with 2 nm bandwidth resolution.

Azobenzene was purchased by Sigma-Aldrich (purity 98%). [(4-aminomethylphenyl)diazonyl] phenylacetic acid was synthesized as described by Juodaityte and Sewald (2004) and azopeptide **1** was synthesized as described. Solution concentrations were all around 10^{−4} M, using ethanol (Merck, purity grade: Uvasol) as a solvent. Unknown molar extinctions were determined for the new synthetic azopeptide **1** in the *trans* form (amino derivative ε_{t(326)} = 9,000 cm^{−1}M^{−1}; aminopeptide ε_{t(330)} = 5,090 cm^{−1}M^{−1}). The extinctions of the corresponding *cis* form was calculated considering still valid the ratio ε_{cis}/ε_{trans} in azobenzene **3**.

NMR Experiments

NMR experiments were recorded on a 500 MHz Bruker Avance III spectrometer (Wissembourg, France) equipped with a TCI ¹H/¹³C/¹⁵N cryoprobe. The lyophilized azopeptide **1** was dissolved in 550 μL of 50% TFE-d₃/50% H₂O, 50% TFE-d₃/50% D₂O, or 50% ACN-d₃/50% H₂O at ~0.5 mM concentration for experiments before irradiation. For induction of azobenzene *trans* ↔ *cis* isomerization, the sample was irradiated in 100% TFE-d₃ or 50% ACN-d₃/50% H₂O with a VL-6.L UV-lamp (Vilber, Germany) emitting 6 W at 365 nm for 1–5 h. Suitable volumes of solvents were added after irradiation to recover the same solvent conditions as for experiments before irradiation. ¹H and ¹³C resonance assignments were obtained from the analysis of 2D ¹H-¹H TOCSY (DIPS12 isotropic scheme of 66 ms duration), ¹H-¹H NOESY (200 or

400 ms mixing time), ¹H-¹H ROESY (250, 300, or 400 ms mixing time), ¹H-¹³C HSQC, and ¹H-¹³C HSQC-TOCSY. NMR experiments were processed with TOPSPIN 3.5 (Bruker) and analyzed with NMRFAM-Sparky program (Lee et al., 2015). NMR chemical shifts were calibrated with respect to the residual protiated solvent signal on 1D ¹H or 2D ¹H-¹³C HSQC experiments.

RESULTS AND DISCUSSION

In this work we designed, synthesized and studied the reversible *cis* ↔ *trans* photoisomerization of the [Pro⁷,Asn⁸,Thr¹⁰]CSF114 analog peptide **1**, where from the original sequence the P-N-H tripeptide was replaced by the photoswitch (4-aminomethyl)phenylazobenzoic acid (AMPB). The photoisomerization of the synthetic azopeptide **1** was explored and its reversibility was compared with more simple systems, the azobenzene amino acid **2** and the azobenzene **3**.

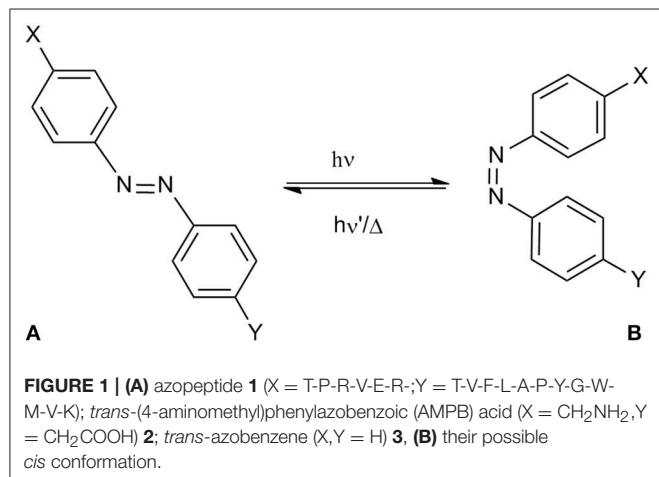
Design of the azopeptide 1. In the literature photochromic compounds, i.e., azobenzene, have been reported as molecules able to isomerize reversibly, when exposed to light of appropriate wavelength.

The 21-mer peptide [Pro⁷,Asn⁸,Thr¹⁰]CSF114, derived from the family of structure-based designed β-turn peptides termed CSF114(Glc), is characterized by a type I β-turn motif (Carotenuto et al., 2006, 2008). In this sequence the β-turn structure was shown around the proline and asparagine residues in positions 7–8. The role of conformation in the recognition and binding of this synthetic antigenic probe to autoantibodies in the context of an immunoenzymatic assay (ELISA) was previously determined to be fundamental.

Because of the importance of the conformation and of the correct exposure of epitopes involved in autoantibody recognition, the light-induced conformational change of the synthetic peptide [Pro⁷,Asn⁸,Thr¹⁰]CSF114, after the introduction of the azobenzene moiety into the sequence is the object of the present study (Figure 1). Starting from the [Pro⁷,Asn⁸,Thr¹⁰]CSF114 sequence, the P-N-H segment was targeted for replacement by an AMPB azobenzene amino acid, as a turn element.

The photoswitch (4-aminomethyl)phenylazobenzoic acid (AMPB) was obtained by the condensation of a 4-nitrophenylacetic acid with 4-aminobenzylamine as described previously (Ulysse and Chmielewski, 1994; Juodaityte and Sewald, 2004; Aemissegger et al., 2005). The amino function of 4-aminobenzylamine was protected as Fmoc to obtain 4-[2-[4-[[[(9H-fluorenyl-9-methoxy)carbonyl]amino]methyl]phenyl]diazonyl]benzenacetic acid to be used in Fmoc solid-phase peptide synthesis. Its incorporation into the peptide sequence proceeded into a straightforward manner applying the standard Fmoc-solid phase methodology, using HATU as coupling reagent. The synthesis of the azobenzene-containing peptide **1** was carried out on a 0.1 mmol scale following the standard Fmoc/tBu solid phase peptide synthesis (SPPS) starting from Fmoc-Lys(Boc)-Wang resin. After coupling the amino acids of the sequence protected

for SPPS, the peptide was cleaved from the resin and purified and characterized by RP-HPLC coupled to Mass Spectrometry. The ability of AMPB to induce variations in the isomerization process was elucidated by UV-Vis and NMR.

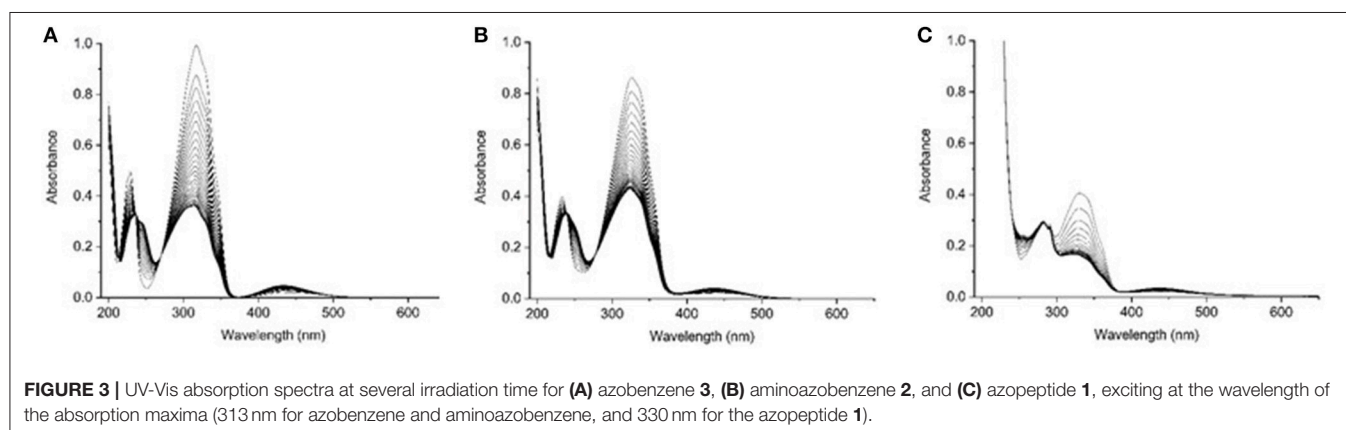
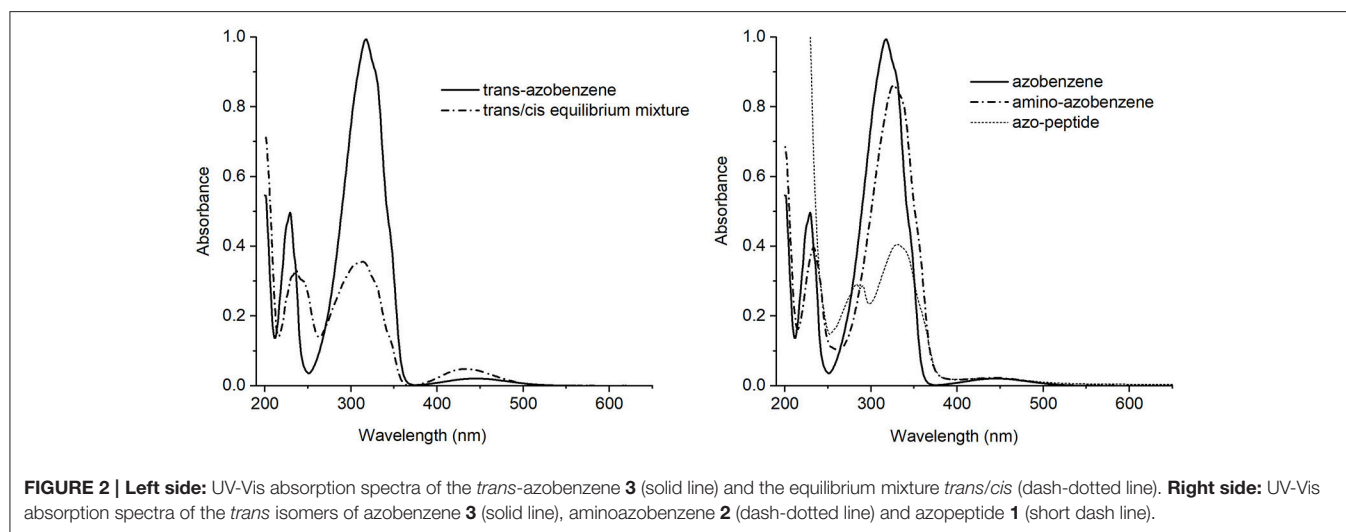


The Azobenzene Peptide as Molecular Switch

In order to propose the synthetic azobenzene as a molecular switch, a deep characterization of its response to light excitation is mandatory to fully understand the effect of substituents on isomerization (**Figure 2**).

The *trans*-azobenzene **3** spectrum showed in **Figure 2** (left), is characterized by a strong absorption centered around 317 nm and a medium one at 230 nm, both assigned as $\pi\pi^*$ electronic transitions. At longer wavelength, about 440 nm, a weak band is observed due to the $n\pi^*$ state. Appearance of the *cis* form is revealed by the intensity decrease of the main band and a simultaneous growing of a medium intensity absorption at 238 nm.

The absorption spectra of the *trans* isomers of amino-azobenzene **2** and azopeptide **1** are shown in **Figure 2** (right). While the correspondence of the electronic transitions is maintained, a small red shift of the bands is observed in the amino-derivative probably due to a moderate conjugation and/or electron-donor effect induced by the substituents on the aromatic rings. In the azopeptide **1**, on the blue side of



the aromatic $\pi\pi^*$ transition whose maximum is red-shifted at 330 nm, the characteristic absorption of tryptophan is also observed at 290 nm.

Addition of substituents to azobenzene affects the electronic distribution and can also modify the *trans-cis* isomerization process and its photochemical yields (Crecca and Roitberg, 2006; Bandara and Burdette, 2012). Therefore, the absorption spectra of the three compounds have been measured as a function of the irradiation time, exciting into the respective first $\pi\pi^*$ and $n\pi^*$ transition bands. For all the three examined compounds, the *trans*→*cis* conversion is more effective when excitation is performed into the maximum of the $\pi\pi^*$ band rather than into the $n\pi^*$. For this reason we focused our attention only on the *trans*→*cis* conversion obtained exciting into the $\pi\pi^*$ absorption band (Figure S2). The resulting absorption spectra of azobenzene, aminoazobenzene and azopeptide are shown in Figures 3A–C, respectively.

In the absorption spectra, isosbestic points are observed, indicating the presence of the *trans-cis* equilibrium in solution. Azobenzene absorption spectrum shows up to four isosbestic points, at 373, 270, 236, and 213 nm. On the opposite the azopeptide **1** shows only one isosbestic point at longer wavelength, due to the overlap in the blue side of the spectrum, with the large tryptophan absorption. In all three cases, after some time, a photostationary state is obtained, where the *trans*→*cis* and *cis*→*trans* isomerization rates equalize and no further variation is observed in the absorption intensity.

In Figure 4, the absorption maxima are plotted as a function of the irradiation time at those wavelengths. From this graph, quantitative information can be gained about the isomerization kinetics and the relative photochemical yields, following known

kinetic procedure (Zimmermann et al., 1958; Bortolus and Monti, 1979).

In Figure 4, the absorption maxima are plotted as a function of the irradiation time at those wavelengths. From this graph, quantitative information can be gained about the isomerization kinetics and the relative photochemical yields, following known kinetic procedure (Zimmermann et al., 1958; Bortolus and Monti, 1979). In this respect, we have considered the kinetic equation:

$$\frac{d[cis]}{dt} = \Phi_t I_{\lambda,t} - \Phi_c I_{\lambda,c} - k[cis] \quad (1)$$

where $[cis] = C_0 \cdot Y$, being C_0 the initial molar concentration of the *trans* isomer and Y the *cis* molar fraction appearing in time. Φ_t is the photochemical yield of the *trans*→*cis* reaction, while Φ_c of the *cis*→*trans* one. k is the constant relative to the thermic isomerization. Since this last mechanism is much slower than the photochemistry, it can be neglected in our experiment (Zimmermann et al., 1958). I_{λ} is the power density absorbed by the *trans/cis* isomer. After some manipulations, the kinetic equation assumes the following aspect:

$$\frac{d[Y]}{dt} = \Phi_t I_{0,\lambda} \frac{[\epsilon_t (Y_{\infty} - Y)]}{FY_{\infty}} \quad (2)$$

where ϵ_t is the extinction coefficient of the *trans* form, $F = A/(1-10^{-A})$, being A the absorbance plotted in Figure 4. This last equation may be integrated giving a function whose time dependence is linear. The slope m of this line is related to the photochemical yield of the *trans* isomer (Zimmermann et al., 1958):

$$\Phi_t = \frac{-mY_{\infty}}{I_{0,\lambda}\epsilon_t} \quad (3)$$

By using this kinetic analysis, the photochemical yield Φ_t shown in the inset of Figure 4 is obtained.

In agreement with previous data (Bortolus and Monti, 1979; Siampiringue et al., 1987; Satzger et al., 2004), azobenzene photochemical yield in ethanol was found to be 0.15. In the amino derivative **2**, the ring substitution has the effect to increase the yield to 0.22. The major change is observed in the case of azopeptide **1**, where the isomerization results strongly favored giving a yield of 0.70.

Adding electron-donor or electron-acceptor groups to the aromatic rings alters the isomerization process due to the modification of the electron density on the molecule (Crecca and Roitberg, 2006; Bandara and Burdette, 2012). In the amino derivative AMBP, the presence of CH_2 spacers reduces the electron-donor effect of the amino groups. Nevertheless, a small change in the isomerization yield is observed. Also in the azopeptide **1**, the ring substituents are bonded through CH_2 spacers. However a strong increase in the *trans-cis* quantum yield value is observed according to a faster isomerization kinetics (Yamamura et al., 2014). Such a different behavior can then be ascribed to some effective interactions involving the amino acid residues of the side chains, which stabilize the *cis* form

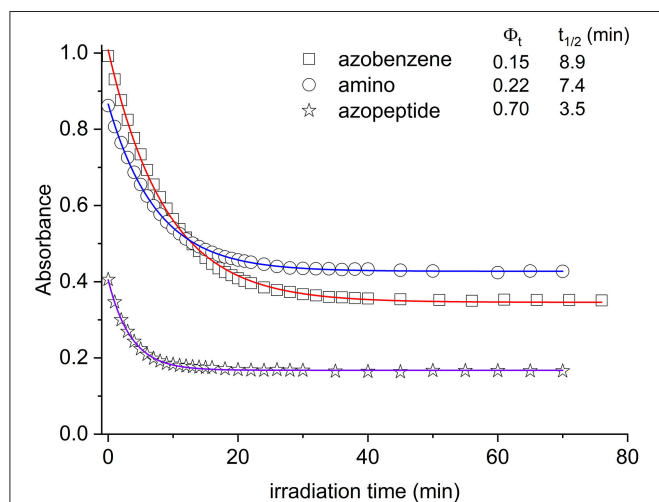


FIGURE 4 | Absorbance decrease of the $\pi\pi^*$ transition as a function of the irradiation time (azobenzene, squares; aminoazobenzene, circles; azopeptide **1**, stars). The time evolution is due to the conversion between the *trans* and *cis* forms. In the inset the photoconversion quantum yields are reported, along with the respective decay times obtained by fitting the absorbance data (solid lines in the graph).

of the azobenzene moiety. However, from the absorption data, the nature of this interaction cannot be known. The NMR data suggest the presence of interactions between the azobenzene aromatic protons and the side chains of amino acid residues, influencing the isomerization kinetic and the thermodynamic parameters (Renner et al., 2000).

Further investigations on thermal *cis*→*trans* reversion kinetics confirm the stability of the final compound, accordingly to the NMR results. In fact, keeping irradiated solutions of the azopeptide **1** 48 h in the dark at 50°C, only half *trans* form is thermally recovered, while for azobenzene and α -helix short peptide chain derivatives the recovery is complete, on this time scale, also at room temperature (Kumita et al., 2000).

Conformational Analysis

The effects of azobenzene *trans* ↔ *cis* isomerization on azopeptide **1** (Figure 5) conformation were investigated by NMR under different solvent conditions. Azopeptide **1** was found to be poorly soluble in water and organic solvents such as methanol and acetonitrile. Azopeptide was soluble in DMSO but exhibited poor spectrum quality with large H^N signals. A previous NMR study of CSF114 analogs exhibiting β -hairpin propensity was carried out in HFA:water mixture (1:1) to stabilize folded conformations (Carotenuto et al., 2008). However, in the case of azopeptide **1**, this solvent condition led to broad NMR signals that precluded conformational studies. We then turned to trifluoroethanol (TFE) as a different fluorinated cosolvent, which is commonly used to stabilize

peptide structures. TFE/water 1:1 mixture yielded satisfactory quality of NMR spectra (Figures S3, S4). The stabilization of secondary structures by TFE is well-known for α -helices (Roccatano et al., 2002) but far less documented for β -hairpin structures (Blanco et al., 1994). Therefore, we also decided to investigate the use of ACN/water 1:1 mixture to analyze the effect of organic cosolvent on azopeptide folding.

Complete 1H assignments of the *trans* form were obtained both in TFE/water 1:1 and ACN/water 1:1 mixtures, using 2D TOCSY and 2D NOESY (or ROESY) experiments (Tables S1, S3, supporting information). Upon irradiation, the resonances of the *cis* form was observed on NMR spectra, with a population reaching 75–80% after 5 h irradiation. The *cis*→*trans* conversion was slow enough (>2 weeks) to record NMR spectra over several days, enabling to fully assign the *cis* form (Tables S2, S4). The *cis* form was characterized by a large (~1 ppm) upfield shift of aromatic *meta* resonances (with respect to methylene group) of azobenzene moiety, confirming the *trans*→*cis* isomerization of the N = N azo-bond (Figure S4).

A comparison of backbone H^α and H^N chemical shift differences between *cis* and *trans* forms is shown in Figure 6, for both solvents. Large chemical shift variation is observed for the azobenzene group and neighboring residues Arg⁶ and Thr⁹. Interestingly, more distant residues in the two peptide arms are also affected, mostly in segment 9–13 and 4–5. Similar trends are observed under both solvent conditions, albeit to a lesser extent in ACN/water. The chemical shift changes can be ascribed to

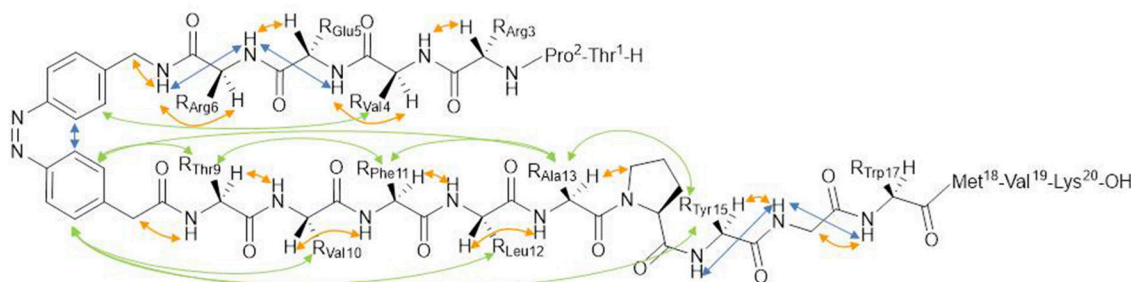


FIGURE 5 | Structure of the *cis*-azopeptide **1** with observed NOEs indicated by arrows.

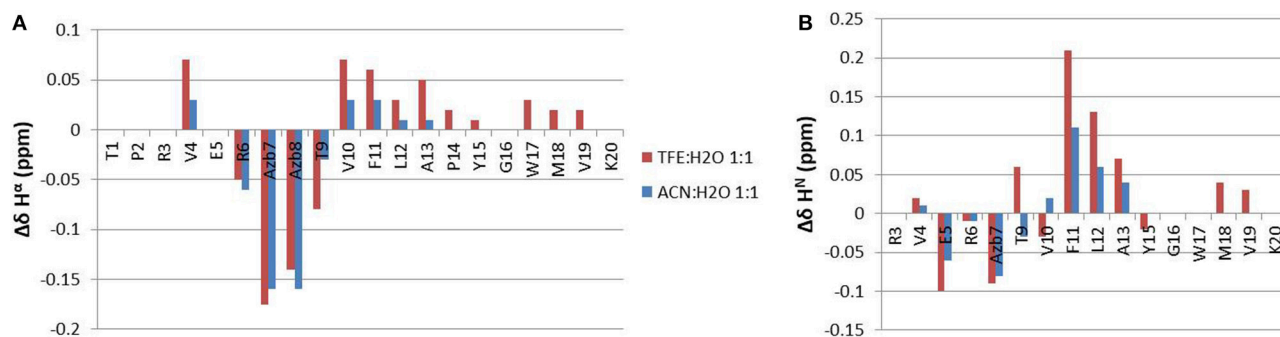


FIGURE 6 | $\Delta\delta$ chemical shift differences between the *cis* and the *trans* forms of azopeptide **1**, calculated for H^α (A) and H^N protons (B).

magnetic susceptibility anisotropy effects as the two aromatic groups get closer in space and/or to conformational effects.

The analysis of backbone and sequential NOEs reveals the presence of complex equilibria between extended and turn/helical folded conformations, in both *cis* and *trans* forms. H^N - H^α sequential NOEs are stronger than intraresidual ones, indicating that extended backbone conformations are largely populated. However, the observation of sequential H^N - H^N NOEs (V4/E5, E5/R6, Y15/G16, G16/W17 in particular) can be ascribed to turn or helical conformations. These folded conformations are further supported by weak NOEs of azobenzene aromatic protons with methyl protons of Val⁴ and Leu¹². Importantly, no NOEs could be detected between the two peptide arms in both forms. This result is in agreement with the observation that the *trans*→*cis* isomerization does not stabilize a β -hairpin structure.

CONCLUSION

In this work photoisomerization of the azopeptide **1** was explored and its reversibility was compared with more simple systems, such as azobenzene amino acid **2** and azobenzene **3**. To this aim azopeptide **1** was modified introducing the photoswitch (4-aminomethyl)phenylazobenzoic acid (AMPB) to replace in [Pro7,Asn8,Thr10]CSF114 the P-N-H tripeptide on the tip of the β -hairpin.

The absorption spectra of azobenzene **3**, AMPB amino acid **2**, and azopeptide **1** were measured as a function of irradiation time, exciting into the $\pi\pi^*$ band. The major differences are observed in the case of **1**, where the isomerization results favored by exciting into the $\pi\pi^*$ transition and the corresponding *cis* isomer results strongly stabilized.

Detailed NMR structural studies of azopeptide **1** confirmed that the AMPB chromophore insertion into the sequence allowed

reversible control of peptide conformation in solution, but the *trans*→*cis* isomerization does not stabilize a β -hairpin structure, characteristic of the original sequence. Thus, incorporation of different photocontrolled switches, such as AMPP, will require further investigations to verify their possible role in controlling β -hairpin conformations.

DATA AVAILABILITY

No datasets were generated or analyzed for this study.

AUTHOR CONTRIBUTIONS

FN designed the experiments, performed the synthesis, interpreted the data, and wrote the manuscript. CG, RC, PRS, and GP designed, performed and interpreted the data of the UV/Vis experiments, wrote the manuscript. ML and OL designed, performed and interpreted the data of the NMR experiments, wrote the manuscript. LS provided technical support to the experiments. AMP developed the project, designed the experiments, interpreted the data, and wrote the manuscript.

FUNDING

This work was supported by the Fondazione Ente Cassa di Risparmio Firenze (grant n. 2014.0306).

SUPPLEMENTARY MATERIAL

The Supplementary Material for this article can be found online at: <https://www.frontiersin.org/articles/10.3389/fchem.2019.00180/full#supplementary-material>

REFERENCES

- Aemissegger, A., and Hilvert, D. (2007). Synthesis and application of an azobenzene amino acid as a light-switchable turn element in polypeptides. *Nat. Protoc.* 2, 161–167. doi: 10.1038/nprot.2006.488
- Aemissegger, A., Kräutler, V., van Gunsteren, W. F., and Hilvert, D. (2005). A photoinducible beta-hairpin. *J. Am. Chem. Soc.* 127, 2929–2936. doi: 10.1021/ja0442567
- Ali, A. M., Forbes, M. W., and Woolley, G. A. (2015). Optimizing the photocontrol of bZIP coiled coils with azobenzene crosslinkers: role of the crosslinking site. *ChemBiochem* 16, 1757–1763. doi: 10.1002/cbic.201500191
- Bandara, H. M., and Burdette, S. C. (2012). Photoisomerization in different classes of azobenzene. *Chem. Soc. Rev.* 41, 1809–1825. doi: 10.1039/c1cs15179g
- Beharry, A. A., Sadovskii, O., and Woolley, G. A. (2008). Photo-control of peptide conformation on a timescale of seconds with a conformationally constrained, blue-absorbing, photo-switchable linker. *Org. Biomol. Chem.* 6, 4323–4332. doi: 10.1039/b810533b
- Behrendt, R., Renner, C., Schenk, M., Wang, F., Wachtveitl, J., Oesterheld, D., and Moroder, L. (1999). Photomodulation of the conformation of cyclic peptides with azobenzene moieties in the peptide backbone. *Angew. Chem. Int. Ed Engl.* 38, 2771–2774.
- Blanco, F. J., Jiménez, M. A., Pineda, A., Rico, M., Santoro, J., and Nieto, J. L. (1994) NMR solution structure of the isolated N-terminal fragment of protein-G B1 domain. Evidence of trifluoroethanol induced native-like beta-hairpin formation. *Biochemistry* 33, 6004–6014
- Bortolus, P., and Monti, S. (1979). Cis-trans photoisomerization of azobenzene. Solvent and triplet donors effects. *J. Phys. Chem.* 83, 648–652. doi: 10.1021/j100469a002
- Bushuyev, O. S., Aizawa, M., Shishido, A., and Barrett, C. J. (2018). Shape-shifting azo dye polymers: towards sunlight-driven molecular devices. *Macromol. Rapid Commun.* 39:1700253. doi: 10.1002/marc.201700253
- Carotenuto, A., Alcaro, M. C., Saviello, M. R., Peroni, E., Nuti, F., Papini, A. M., Novellino, E., and Rovero, P. (2008). Designed glycopeptides with different beta-turn types as synthetic probes for the detection of autoantibodies as biomarkers of multiple sclerosis. *J. Med. Chem.* 51, 5304–5309. doi: 10.1021/jm800391y
- Carotenuto, A., D'Ursi, A. M., Mulinacci, B., Paolini, I., Lolli, F., Papini, A. M., Novellino, E., and Rovero, P. (2006). Conformation-activity relationship of designed glycopeptides as synthetic probes for the detection of autoantibodies, biomarkers of multiple sclerosis. *J. Med. Chem.* 49, 5072–5079. doi: 10.1021/jm060117j
- Crecca, C. R., and Roitberg, A. E. (2006). Theoretical study of the isomerization mechanism of azobenzene and disubstituted azobenzene derivatives. *J. Phys. Chem. A* 110, 8188–8203. doi: 10.1021/jp057413c
- Deeg, A. A., Schrader, T. E., Kempter, S., Pfizer, J., Moroder, L., and Zinth, W. (2011). Light-triggered aggregation and disassembly of amyloid-like structures. *Chemphyschem* 12, 559–562. doi: 10.1002/cphc.201001012
- Dong, M., Babalhavaej, A., Collins, C. V., Jarrar, K., Sadovskii, O., Dai, Q., and Woolley, G. A. (2017). Near-infrared photoswitching of azobenzenes

- under physiological conditions. *J. Am. Chem. Soc.* 139, 13483–13486. doi: 10.1021/jacs.7b06471
- Dong, M., Babalhavaej, A., Samanta, S., Beharry, A. A., and Woolley, G. A. (2015). Red-shifting azobenzene photoswitches for *in vivo* use. *Acc. Chem. Res.* 48, 2662–2670. doi: 10.1021/acs.accounts.5b00270
- Dong, S. L., Löweneck, M., Schrader, T. E., Schreier, W. J., Zinth, W., Moroder, L., and Renner, C. (2006). A photocontrolled β -hairpin peptide. *Chem. Eur. J.* 12, 1114–1120. doi: 10.1002/chem.200500986
- Gajiwala, K. S., Chen, H., Cornille, F., Roques, B. P., Reith, W., Mach, B., and Burley, S. K. (2000). Structure of the winged-helix protein hRFX1 reveals a new mode of DNA binding. *Nature* 403, 916–921. doi: 10.1038/3502634
- Goulet-Hanssens, A., and Barrett, C. J. (2013). Photo-control of biological systems with azobenzene polymers. *J. Polym. Sci. Part A Polym. Chem.* 51, 3058–3070. doi: 10.1002/pola.26735
- Hillier, B. J., Christopherson, K. S., Prehoda, K. E., Bredt, D. S., and Lim, W. A. (1999). Unexpected modes of PDZ domain scaffolding revealed by structure of nNOS-syntrophin complex. *Science* 284, 812–815. doi: 10.1126/science.284.5415.812
- Hoppmann, C., Schmieder, P., Domaing, P., Vogelreiter, G., Eichhorst, J., Wiesner, B., Morano, I., Rück-Braun, K., and Beyermann, M. (2011). Photocontrol of contracting muscle fibers. *Angew. Chem. Int. Ed Engl.* 50, 7699–7702. doi: 10.1002/anie.201101398
- Juodaityte, J., and Sewald, N. (2004). Synthesis of photoswitchable amino acids based on azobenzene chromophores: building blocks with potential for photoresponsive biomaterials. *J. Biotechnol.* 112, 127–138. doi: 10.1016/j.jbiotec.2004.03.017
- Kaiser, E., Colescott, R. L., Bossinger, C. D., and Cook, P. I. (1970). Color test for detection of free terminal amino groups in the solid-phase synthesis of peptides. *Anal. Biochem.* 34, 595–598. doi: 10.1016/0003-2697(70)90146-6
- Komarov, I. V., Afonin, S., Babii, O., Schober, T., and Ulrich, A. S. (2018). Efficiently Photocontrollable or Not? Biological activity of photoisomerizable diarylethenes. *Chemistry* 24, 11245–11254. doi: 10.1002/chem.201801205
- Kumita, J. R., Smart, O. S., and Woolley, G. A. (2000). Photo-control of helix content in a short peptide. *Proc. Natl. Acad. Sci. U.S.A.* 97, 3803–3808. doi: 10.1073/pnas.97.8.3803
- Lee, W., Tonelli, M., and Markley, J. L. (2015). NMRFAM-SPARKY: enhanced software for biomolecular NMR spectroscopy. *Bioinformatics* 31, 1325–1327. doi: 10.1093/bioinformatics/btu830
- Lolli, F., Mazzanti, B., Pazzagli, M., Peroni, E., Alcaro, M. C., Sabatino, G., et al. (2005a). The glycopeptide CSF114(Glc) detects serum antibodies in multiple sclerosis. *J. Neuroimmunol.* 167, 131–137. doi: 10.1016/j.jneuroim.2005.05.016
- Lolli, F., Mulinacci, B., Carotenuto, A., Bonetti, B., Sabatino, G., Mazzanti, B., et al. (2005b). An N-glucosylated peptide detecting disease-specific autoantibodies, biomarkers of multiple sclerosis. *Proc. Natl. Acad. Sci. U.S.A.* 102, 10273–10278. doi: 10.1073/pnas.0503178102
- Marchi, E., Baroncini, M., Bergamini, G., Van Heyst, J., Vögtle, F., and Ceroni, P. (2012). Photoswitchable metal coordinating tweezers operated by light-harvesting dendrimers. *J. Am. Chem. Soc.* 134, 15277–15280. doi: 10.1021/ja307522f
- Miniewicz, A., Orlikowska, H., Sobolewska, A., and Bartkiewicz, S. (2018). Kinetics of thermal cis-trans isomerization in a phototropic azobenzene-based single-component liquid crystal in its nematic and isotropic phases. *Phys. Chem. Chem. Phys.* 20, 2904–2913. doi: 10.1039/c7cp06820d
- Pandey, S., Alcaro, M. C., Scrima, M., Peroni, E., Paolini, I., Di Marino, S., et al. (2012). Designed glucopeptides mimetics of myelin protein epitopes as synthetic probes for the detection of autoantibodies, biomarkers of multiple sclerosis. *J. Med. Chem.* 55, 10437–10447. doi: 10.1021/jm301031r
- Paolini, I., Nuti, F., de la Cruz Pozo-Carrero, M., Barbetti, F., Kolesinska, B., Kaminski, Z. J., Chelli, M., and Papini, A. M. (2007). A convenient microwave-assisted synthesis of N-glycosyl amino acids. *Tetrahedron Lett.* 48, 2901–2904. doi: 10.1016/j.tetlet.2007.02.087
- Papini, A. M. (2009). The use of post-translationally modified peptides for detection of biomarkers of immune-mediated diseases. *J. Pept. Sci.* 15, 621–628. doi: 10.1002/psc.1166
- Pariset, J., Kurz, K., Hilbrig, F., and Freitag, R. (2009). Use of azobenzene amino acids as photo-responsive conformational switches to regulate antibody-antigen interaction. *J. Sep. Sci.* 32, 1613–1624. doi: 10.1002/jssc.200800698
- Quick, M., Dobryakov, A. L., Gerecke, M., Richter, C., Berndt, F., Ioffe, I. N., Granovsky, A. A., Mahrwald, R., Ernsting, N. P., and Kovalenko, S. A. (2014). Photoisomerization dynamics and pathways of trans- and cis-azobenzene in solution from broadband femtosecond spectroscopies and calculations. *J. Phys. Chem. B* 118, 8756–8771. doi: 10.1021/jp504999f
- Rampp, M. S., Hofmann, S. M., Podewin, T., Hoffmann-Röder, A., Moroder, L., and Zinth, W. (2018). Time-resolved infrared studies of the unfolding of a light triggered β -hairpin peptide. *Chem. Phys.* 512, 116–121. doi: 10.1016/j.chemphys.2018.02.003
- Renner, C., Behrendt, R., Spörlein, S., Wachtveitl, J., and Moroder, L. (2000). Photomodulation of conformational states. I. Mono- and bicyclic peptides with (4-amino)phenylazobenzoic acid as backbone constituent. *Biopolymers* 54, 489–500. doi: 10.1002/1097-0282(200012)54:7<489::AID-BIP20>3.0.CO;2-F
- Renner, C., Kusebauch, U., Löweneck, M., Milbradt, A. G., and Moroder, L. (2005). Azobenzene as photoresponsive conformational switch in cyclic peptides. *J. Pept. Res.* 65, 4–14. doi: 10.1111/j.1399-3011.2004.00203.x
- Renner, C., and Moroder, L. (2006). Azobenzene as conformational switch in model peptides. *Chembiochem* 7, 868–878. doi: 10.1002/cbic.200500531
- Rentier, C., Pacini, G., Nuti, F., Peroni, E., Rovero, P., and Papini, A. M. (2015). Synthesis of diastereomerically pure Lys(Ne-lipoyl) building blocks and their use in Fmoc/tBu solid phase synthesis of lipoyl-containing peptides for diagnosis of primary biliary cirrhosis. *J. Pept. Sci.* 21, 408–414. doi: 10.1002/psc.2761
- Rizzolo, F., Testa, C., Lambardi, D., Chorev, M., Chelli, M., Rovero, P., and Papini, A. M. (2011). Conventional and microwave-assisted SPPS approach: a comparative synthesis of PTHrP(1-34)NH(2). *J. Pept. Sci.* 17, 708–714. doi: 10.1002/psc.1395
- Roccatano, D., Colombo, G., Fioroni, M., and Mark, A. E. (2002). Mechanism by which 2,2,2-trifluoroethanol/water mixtures stabilize secondary-structure formation in peptides: a molecular dynamics study. *Proc Natl Acad Sci U.S.A.* 99, 12179–12184. doi: 10.1073/pnas.182199699
- Satzger, H., Root, C., and Braun, M. (2004). Excited-State dynamics of trans- and cis-azobenzene after UV excitation in the $\pi\pi^*$ band. *J. Phys. Chem. A* 108, 6265–6271. doi: 10.1021/jp049509x
- Schultz, T., Quenneville, J., Levine, B., Toniolo, A., Martínez, T. J., Lochbrunner, S., Schmitt, M., Shaffer, J. P., Zgierski, M. Z., and Stölow, A. (2003). Mechanism and dynamics of azobenzene photoisomerization. *J. Am. Chem. Soc.* 125, 8098–8099. doi: 10.1021/ja021363x
- Schumacher, M. A., Hurlburt, B. K., Brennan, R. G. (2001). Crystal structures of SarA, a pleiotropic regulator of virulence genes in *S. aureus*. *Nature* 409, 215–219. doi: 10.1038/35051623
- Siampiringue, N., Guyot, G., Monti, S., and Bortolus, P. (1987). The Cis-Trans photoisomerization of azobenzene: an experimental reexamination. *J. Photochem.* 37, 185–188. doi: 10.1016/0047-2670(87)85039-6
- Spörlein, S., Carstens, H., Satzger, H., Renner, C., Behrendt, R., Moroder, L., Tavan, P., Zinth, W., and Wachtveitl, J. (2002). Ultrafast spectroscopy reveals subnanosecond peptide conformational dynamics and validates molecular dynamics simulation. *Proc. Natl. Acad. Sci. U.S.A.* 99, 7998–8002. doi: 10.1073/pnas.122238799
- Ulysse, L., and Chmielewski, J. (1994). The synthesis of a light-switchable amino acid for inclusion into conformationally mobile peptides bioorg. *Med. Chem. Lett.* 4, 2145–2146. doi: 10.1016/S0960-894X(01)80118-9
- Ulysse, L., Cubillos, J., and Chmielewski, J. (1995). Photoregulation of cyclic peptide conformation. *J. Am. Chem. Soc.* 117, 8466–8467. doi: 10.1021/ja00137a023
- Wong, H. C., Mao, J., Nguyen, J. T., Srinivas, S., Zhang, W., Liu, B., Li, L., Wu, D., and Zheng, J. (2000). Structural basis of the recognition of the dishevelled DEP domain in the Wnt signaling pathway. *Nat. Struct. Biol.* 7, 1178–11784. doi: 10.1038/820477, 1178–1184

- Yamamura, M., Yamakawa, K., Okazaki, Y., and Nabeshima, T. (2014). Coordination-driven macrocyclization for locking of photo- and thermal cis→ trans isomerization of azobenzene. *Chemistry* 20, 16258–16265. doi: 10.1002/chem.201404620
- Zavala-Ruiz, Z., Strug, L., Walker, B. D., Norris, P. J., and Stern, L. J. (2004). A hairpin turn in a class II MHC-bound peptide orients residues outside the binding groove for T cell recognition. *Proc. Natl. Acad. Sci. U.S.A.* 101, 13279–13284. doi: 10.1073/pnas.0403371101
- Zimmermann, G., Chow, L.-Y., and Paik, U.-J. (1958) The photochemical isomerization of azobenzene. *J. Am. Chem. Soc.* 80, 352–3531. doi: 10.1021/ja01547a010

Conflict of Interest Statement: The authors declare that the research was conducted in the absence of any commercial or financial relationships that could be construed as a potential conflict of interest.

Copyright © 2019 Nuti, Gellini, Larregola, Squillantini, Chelli, Salvi, Lequin, Pietraperzia and Papini. This is an open-access article distributed under the terms of the Creative Commons Attribution License (CC BY). The use, distribution or reproduction in other forums is permitted, provided the original author(s) and the copyright owner(s) are credited and that the original publication in this journal is cited, in accordance with accepted academic practice. No use, distribution or reproduction is permitted which does not comply with these terms.



Folded Synthetic Peptides and Other Molecules Targeting Outer Membrane Protein Complexes in Gram-Negative Bacteria

John A. Robinson*

Department of Chemistry, University of Zurich, Zurich, Switzerland

OPEN ACCESS

Edited by:

Alessandro Contini,
University of Milan, Italy

Reviewed by:

Lorenzo Stella,
University of Rome Tor Vergata, Italy
David Andreu,
Universidad Pompeu Fabra, Spain

*Correspondence:

John A. Robinson
john.robinson@chem.uzh.ch

Specialty section:

This article was submitted to
Chemical Biology,
a section of the journal
Frontiers in Chemistry

Received: 27 November 2018

Accepted: 17 January 2019

Published: 06 February 2019

Citation:

Robinson JA (2019) Folded Synthetic Peptides and Other Molecules Targeting Outer Membrane Protein Complexes in Gram-Negative Bacteria. *Front. Chem.* 7:45. doi: 10.3389/fchem.2019.00045

Conformationally constrained peptidomimetics have been developed to mimic interfacial epitopes and target a wide selection of protein-protein interactions. β -Hairpin mimetics based on constrained macrocyclic peptides have provided access to excellent structural mimics of β -hairpin epitopes and found applications as interaction inhibitors in many areas of biology and medicinal chemistry. Recently, β -hairpin peptidomimetics and naturally occurring β -hairpin-shaped peptides have also been discovered with potent antimicrobial activity and novel mechanisms of action, targeting essential outer membrane protein (OMP) complexes in Gram-negative bacteria. This includes the Lpt complex, required for transporting LPS to the cell surface during OM biogenesis and the BAM complex that folds OMPs and inserts them into the OM bilayer. The Lpt complex is a macromolecular superstructure comprising seven different proteins (LptA-LptG) that spans the entire bacterial cell envelope, whereas the BAM complex is a folding machine comprising a β -barrel OMP (BamA) and four different lipoproteins (BamB-BamE). Folded synthetic and natural β -hairpin-shaped peptides appear well-suited for interacting with proteins within the Lpt and BAM complexes that are rich in β -structure. Recent progress in identifying antibiotics targeting these complexes are reviewed here. Already a clinical candidate has been developed (murepavadin) that targets LptD, with potent antimicrobial activity specifically against pseudomonads. The ability of folded synthetic β -hairpin epitope mimetics to interact with β -barrel and β -jellyroll domains in the Lpt and Bam complexes represent new avenues for antibiotic discovery, which may lead to the development of much needed new antimicrobials to combat the rise of drug-resistant pathogenic Gram-negative bacteria.

Keywords: antibiotic, gram-negative bacteria, lipopolysaccharides (LPS), Lpt complex, Bam complex, β -hairpin mimetics, β -barrel, β -jellyroll

INTRODUCTION

Mimics of protein epitopes mediating macromolecular interactions have attracted great interest in chemical biology and drug design. One of the early drivers of protein epitope mimetic design was in targeting protein-protein interactions (PPIs) (Arkin et al., 2014). It has become clear, however, that epitope mimetics may have many other uses, such as targeting protein-nucleic acid interactions, the active sites of enzymes, and membrane bound receptors, to name but a few

(Robinson, 2008; Zerbe et al., 2017). The structure-based design of protein epitope mimetics is often focused on the secondary and tertiary structures involved in biomolecular interactions, including α -helical, β -turn, β -strand, and β -hairpin conformations (Bullock et al., 2011; Watkins and Arora, 2014). A diverse variety of molecular scaffolds for mimetic design has been explored, including conformationally constrained peptides that maintain some or all of the backbone and amino acid side-chain groups of the epitope. Naturally occurring, highly stable mini-protein scaffolds may also be engineered to display target epitope(s) (Wuo and Arora, 2018). The approach is not limited to peptides, however, as illustrated by rigid or constrained organic scaffolds that can display side chain groups important for protein recognition (Gopalakrishnan et al., 2016). With synthetic epitope mimetics, the possibility exists to harness the robust tools of synthetic chemistry to optimize properties, such as target affinity and selectivity, as well as pharmacological and related drug-like (ADMET) properties (Morrison, 2018).

In this focused review, the application of β -hairpin-shaped peptides and peptidomimetics in the field of antibiotic research is highlighted, in particular, molecules with new antimicrobial mechanisms of action targeting outer membrane (OM) biogenesis in Gram-negative bacteria. This research is set against the backdrop of the growing global health threat caused by the rapid evolution and spread of antibiotic resistance, particularly in Gram-negative bacteria such as *Klebsiella pneumoniae*, *Acinetobacter baumannii*, *Pseudomonas aeruginosa*, and *Enterobacter sp.* (Rice, 2008; Boucher et al., 2009; WHO, 2017) as well as the great difficulties encountered in discovering new antibiotics with novel mechanisms of action.

OUTER MEMBRANE BIOGENESIS

Gram-negative bacteria possess two membranes around the cytoplasm. The inner membrane (IM) is a typical symmetric glycerophospholipid bilayer, whereas the OM is an asymmetric bilayer containing an inner leaflet of glycerophospholipid and an outer leaflet containing lipopolysaccharide (LPS) (Henderson et al., 2016; May and Silhavy, 2017). The periplasm is an aqueous compartment between the IM and OM, containing the peptidoglycan cell wall (Figure 1). Both the IM and the OM harbor many anchored lipoproteins (Narita and Tokuda, 2017), as well as numerous integral membrane proteins. In the IM, these integral membrane proteins contain multiple transmembrane helical domains, whereas those in the OM, with one known exception, fold into transmembrane β -barrel domains (Ranava et al., 2018). LPS is a complex glycolipid with many known structural variants, but with a common lipidated and phosphorylated bis-glucosamine core called lipid-A (Figure 1; Raetz et al., 2007). The phosphate groups in lipid A and inner core regions of neighboring LPS molecules coordinate to Mg^{2+} or Ca^{2+} ions, thereby strengthening the OM, which is important for OM function and stability. It was shown recently that not only the peptidoglycan layer but also the OM contributes as a load-bearing structure with mechanical strength to help resist osmotic forces occurring across the cell envelope

(Rojas et al., 2018). The outer oligosaccharide segment of LPS may contain over a hundred sugar residues, including the so-called O-antigen responsible for characteristic immunological serotypes. The combined IM and OM represent a formidable permeability barrier, with hydrophobic molecules unable to penetrate the OM unless they can gain access through OM porins, and most hydrophilic molecules unable to cross the IM, again unless specific transporters are available (Nikaido, 2003). For those antibiotics that are able to gain entry to the cytoplasm, a formidable array of drug export pumps has evolved in Gram-negative bacteria to pump antibiotics across both membranes and back out of the cell (Poole, 2005; Masi et al., 2017).

The unusual architecture of the OM does not arise spontaneously. Important progress has been made recently in understanding how LPS is transported from its site of biosynthesis at the IM to the cell surface during growth (Konovalova et al., 2017). LPS transport to the cell surface is mediated by seven lipopolysaccharide transport (Lpt) proteins (LptA-LptG) that assemble into a macromolecular complex spanning the cell envelope (Figure 1) (Freinkman et al., 2012; May et al., 2015; Simpson et al., 2015; Okuda et al., 2016; Sherman et al., 2018). The entire protein complex must form before LPS transport can begin. The 3D structures of all seven Lpt proteins, from various Gram-negative bacteria, have now been solved (Suits et al., 2008; Tran et al., 2010; Dong et al., 2014, 2017; Qiao et al., 2014; Bollati et al., 2015; Botos et al., 2016). A computer model representing the entire Lpt complex is shown in Figure 1. The IM adenosine 5'-triphosphate (ATP)-binding cassette transporter LptFGB₂ associates with the membrane anchored LptC and uses ATP hydrolysis in the cytoplasm to power the extraction of LPS from the outer leaflet of the IM and transfer to LptC. Subsequently, LPS molecules are pushed over the periplasm across a bridge formed by LptA (Okuda et al., 2012; Luo et al., 2017). The LptA bridge, possibly as a monomer or as an oligomer (LptA_n), interacts with LptC in the IM and with the LptD/E complex anchored in the OM (Freinkman et al., 2012). The essential function of the LptD/E complex is to receive LPS molecules coming across the LptA bridge and translocate them into the outer leaflet of the OM. Much experimental evidence has now accrued in support of the so-called PEZ-model (in analogy to the candy dispenser) of LPS transport, in which ATP hydrolysis within the LptB₂ dimer powers LPS extraction from the IM (Okuda et al., 2016; Sherman et al., 2018). With each power stroke, LPS molecules are pushed across the LptA bridge toward LptD/E in the OM, and eventually onto the cell surface. During exponential growth, the flux of LPS through the Lpt pathway is estimated to be $\approx 1,200$ molecules s^{-1} (Lima et al., 2013).

Almost all bacterial outer membrane proteins (OMPs) fold into transmembrane β -barrel domains, with their N and C termini facing the periplasm. The C-terminal region of LptD contains one of the largest β -barrels so far characterized, with 26 β -strands integrated into the OM bilayer (Figure 1; Dong et al., 2014; Qiao et al., 2014; Botos et al., 2016). Importantly, the N-terminal segment of LptD is located in the periplasm and contains a β -jellyroll domain. The same highly conserved β -jellyroll fold is also present in the soluble periplasmic protein LptA, and in membrane-anchored LptC

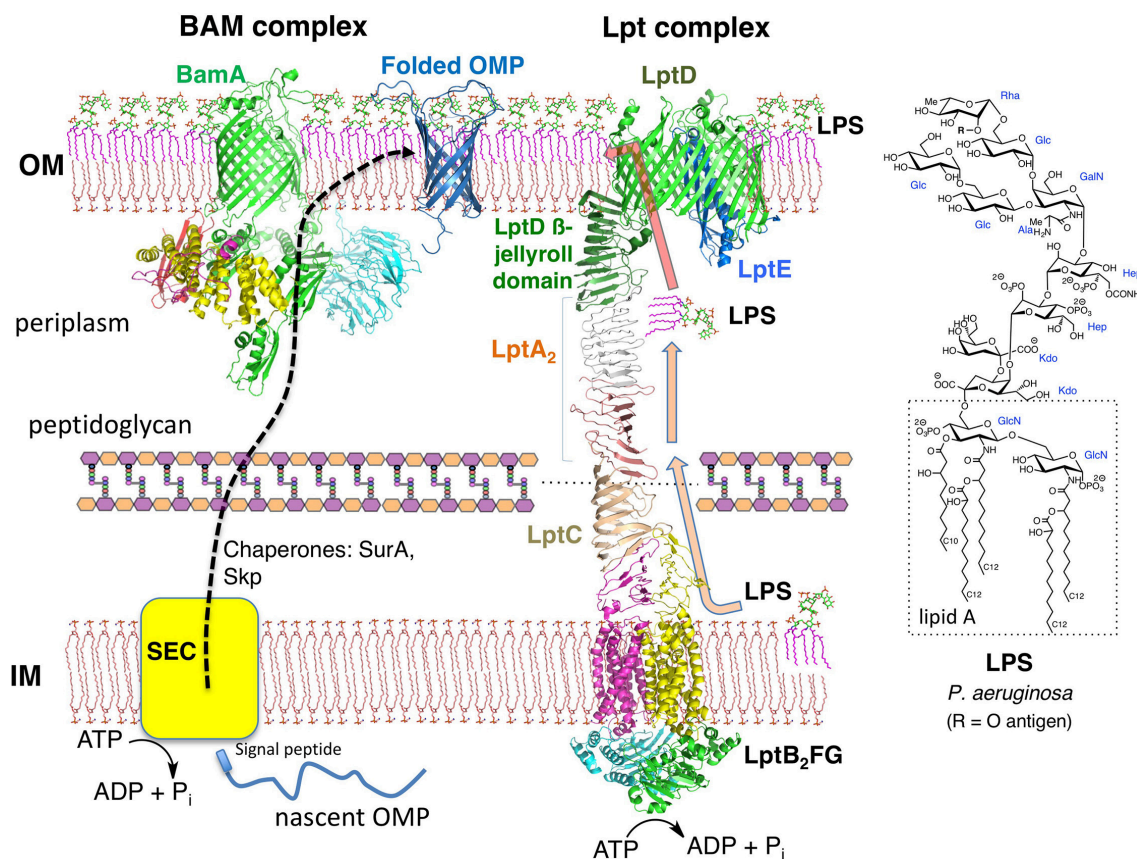


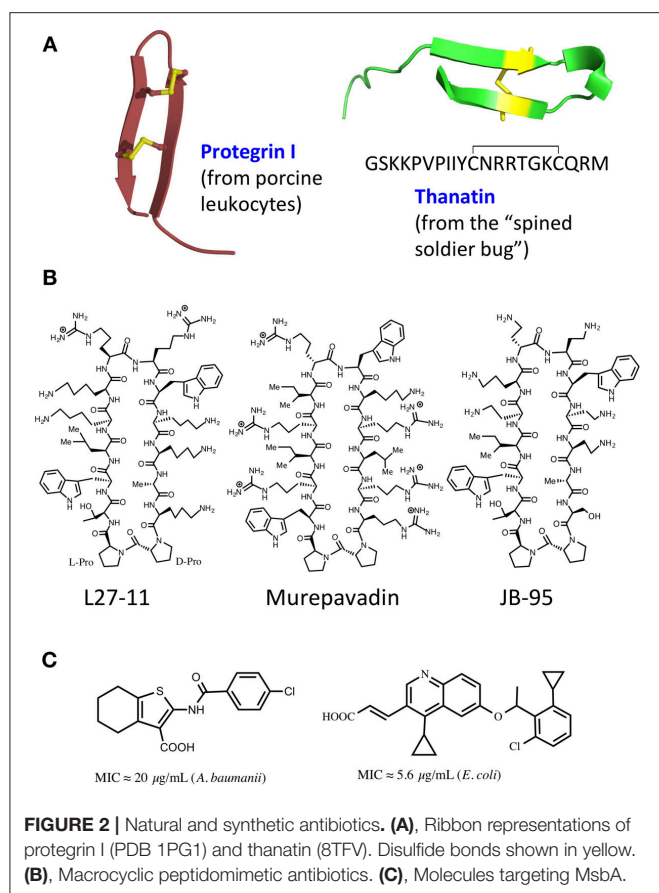
FIGURE 1 | The Gram-negative envelope. The OM is an asymmetric bilayer, while the IM is a symmetric bilayer composed mainly of glycerophospholipids. The BAM complex (BamABCDE) functions as a β -barrel folding catalyst, whereas the Lpt complex (LptAB₂CDEFG, LptA dimer shown) is essential for LPS transport to the OM. Crystal structures from the PDB of the BAM complex and individual components of the Lpt complex were used to make the figure. The structure of a typical LPS from *P. aeruginosa* is shown.

(Suits et al., 2008; Tran et al., 2010; Laguri et al., 2017). The V-shaped sides of the β -jellyroll comprise 16 antiparallel β -strands that possess a twisted hydrophobic internal channel suitable for interacting with the fatty acyl chains of LPS, whilst leaving the polar sugar residues of LPS exposed to solvent (Villa et al., 2013). The β -jellyrolls in LptC-LptA-LptD associate through PPIs. *In-vitro* binding studies have shown that individual LptA-LptA and LptA-LptC β -jellyrolls interact with binding constants in the low to sub-micromolar range (Merten et al., 2012; Schultz et al., 2017). Alignment of the V-shaped grooves formed by association of the β -jellyrolls in LptC, LptA, and LptD, therefore, provide a path for LPS to be shuttled across the periplasm to the LptD/E complex in the OM (Okuda et al., 2016; Laguri et al., 2017).

Given its essential role for OM biogenesis in Gram-negative bacteria and its in-part exposed position on the cell surface, it is perhaps remarkable that during the golden age of antibiotic discovery in the latter half of the twentieth century, no antibiotics were reported that target the Lpt complex.

MOLECULES TARGETING THE LPT COMPLEX

The β -hairpin secondary structure is found in many naturally occurring cationic antimicrobial peptides (CAMPs) produced by the innate immune systems in a wide variety of organisms (Panteleev et al., 2017). Some disulfide cross-linked CAMPs have amphipathic hairpin structures, which result in an ability to disrupt biological membranes by pore formation (class-I). For example, protegrin I (PG-I) (**Figure 2**) isolated from porcine leukocytes, shows potent broad-spectrum antimicrobial activity in the micromolar range, and disrupts membranes in both Gram-positive and Gram-negative bacteria, as well as in eukaryotes (Zhao et al., 1994). Both enantiomers of PG-I are equally active as antibiotics, due to the target being the lipid bilayer of the cell membrane (Wang et al., 2016). However, other naturally occurring hairpin CAMPs do not disrupt bacterial membranes and their antimicrobial activity shows a high enantioselectivity (class-II), which points to a quite different mechanism of action (MoA).



Interestingly, the first reported example of a hairpin-shaped cationic antimicrobial peptide targeting the Lpt complex arose from efforts to produce structural mimics of the class-I CAMP protegrin I (Shankaramma et al., 2002; Robinson et al., 2005). The macrocyclic peptide called L27-11 (**Figure 2**) was derived by iterative optimization of β -hairpin mimetics, that led from an initial hit with broad-spectrum antimicrobial activity and micromolar minimal inhibitory concentrations (MICs), to nanomolar activity against Gram-negative pseudomonads, in particular *P. aeruginosa* (Srinivas et al., 2010). L27-11 does not lyse bacterial membranes and the enantiomer is inactive. Structure-activity studies showed that the folded β -hairpin conformation of the peptide is critical for its antimicrobial activity (Schmidt et al., 2013; Vetterli et al., 2016). Further, optimization of drug-like properties led to a clinical candidate called murepavadin (also called POL7080) (**Figure 2**). Murepavadin is currently undergoing phase III clinical studies to treat lung infections caused by *Pseudomonas aeruginosa* (Martin-Loeches et al., 2018; Wach et al., 2018), which is recognized as a critical priority 1 pathogen by the WHO (2017).

The identification of the target for L27-11 and murepavadin in *Pseudomonas* spp. as LptD came from photoaffinity labeling studies and the analysis of spontaneously drug-resistant *P. aeruginosa* strains, which could be isolated at low frequency (Srinivas et al., 2010). The resistant isolates typically contained mutations in the periplasmic β -jellyroll domain of LptD, and

the mutant allele was able to confer resistance to the antibiotic when introduced into the sensitive wild-type strain. Further mechanistic studies provided evidence that L27-11 indeed causes inhibition of LPS transport to the cell surface in *P. aeruginosa*, as implied from its interaction with LptD (Werneburg et al., 2012).

The unique specificity of these antibiotics for *Pseudomonas* spp. arises from structural differences between LptD within Gram-negative bacteria. The crystal structure of a truncated LptD from *P. aeruginosa* revealed the C-terminal ca. 600 residue β -barrel domain, which is highly conserved in LptD from all Gram-negative bacteria (Botos et al., 2016). So far, no 3D structure is available for the periplasmic segment of LptD from pseudomonads. However, the β -jellyroll domain is present and highly conserved, consistent with its key interaction with LptA and function as a landing stage for LPS molecules crossing the periplasmic bridge. However, the periplasmic domain of LptD in pseudomonads is longer than in most other γ -proteobacteria, due to an extra domain of ca 100 residues at the N-terminus. The structure and function of this insert domain is currently unknown. Photolabeling studies showed recently that the antibiotics L27-11 and murepavadin interact at a site in LptD close to both the β -jellyroll and the insert domain (Andolina et al., 2018). Moreover, mutations in LptD that give rise to spontaneous resistance to the antibiotics (Srinivas et al., 2010), discussed above, lie within the β -jellyroll domain. These observations narrow down the binding site for the antibiotic in LptD to the periplasmic domains, provide an explanation for the unique selectivity of the antibiotic, and for its ability to interfere with LPS transport to the cell surface.

There is now considerable interest in discovering new inhibitors of the LPS transport pathway, as potential antibiotics against Gram-negative bacteria. Many inhibitors of the LPS biosynthetic enzyme LpxC, which catalyzes the first committed step in LPS biosynthesis, have been reported over the past 20 years (Erwin, 2016). However, LpxC is a soluble enzyme for which a convenient activity assay is available. In the case of LPS transport, a convenient assay for inhibitor discovery has been less straightforward to develop, given that the seven-protein trans-envelope Lpt complex connects two membranes and contains multiple integral membrane proteins as well as the soluble periplasmic protein LptA. However, an ingenious solution to this problem was reported recently, by reconstituting membrane-to-membrane transport of LPS *in-vitro* using two different proteoliposomes, one containing the purified LptB₂FGC complex (IM proteoliposomes) and the other containing the LptD/E complex (Sherman et al., 2018). Addition of soluble LptA to create a bridge between the IM and OM proteoliposomes enabled LPS transport, driven by ATP hydrolysis, as monitored by cross-linking of LPS to photoactive sites in Lpt components. More recent mechanistic studies have revealed in this fully reconstituted *in-vitro* system a mechanism for coupling between the OM LptD/E translocon and ATP hydrolysis at the IM (Xie et al., 2018). This coupling appears to allow the LptD/E translocon to call a halt to ATP hydrolysis and LPS transport once a critical concentration of LPS is achieved in the OM.

A different cell-based screen for LPS biosynthesis and transport has also been described recently and used to identify

inhibitors of an earlier step of LPS transport, namely that mediated by MsbA, an integral IM protein (Zhang et al., 2018). MsbA is a member of the ABC ATP-dependent transporter superfamily that mediates an earlier step of LPS transport, by flipping core LPS from its site of synthesis on the inner leaflet to the periplasmic side of the IM (Ward et al., 2007; Mi et al., 2017). The screen made use of engineered *Acinetobacter baumannii* strains lacking efflux pumps and LPS-modifying enzymes and comparing effects on growth compared to the WT strain. The best identified inhibitors showed MICs in the low micromolar range and contained a tetrahydrobenzothiophene scaffold (**Figure 2C**). Mechanistic studies revealed that these molecules bind to MsbA, stimulating the ATPase activity while decoupling it from LPS translocation. This leads to elevated levels of LPS at the IM, which has a deleterious effect on the membrane. In a different study, a high throughput *in-vitro* assay with purified MsbA led to the identification of a family of quinoline derivatives that specifically inhibit the activity of MsbA on cells (**Figure 2C**; Alexander et al., 2018; Ho et al., 2018). These molecules typically inhibit the growth of *E. coli* and *Klebsiella pneumoniae* with MICs in the low micromolar range. Crystal structures were also obtained of *E. coli* MsbA with bound quinoline inhibitors, which show the protein trapped in an inward-facing LPS-bound conformation. Unfortunately, the hydrophobic nature of these active quinolines correlated with high levels of plasma protein binding and a significant loss of antimicrobial activity in the presence of serum, indicating non-optimal drug-like properties (Alexander et al., 2018). Nevertheless, these studies validate MsbA as an antibacterial target and establish screening methods that can be used to discover new LPS transport inhibitors.

A stimulator of the ATPase LptB, the IM component of the Lpt complex that powers the seven protein Lpt complex and LPS transport (**Figure 1**), has also been identified recently (May et al., 2017; Mandler et al., 2018). Novobiocin belongs to a family of antibiotics largely directed against aerobic Gram-positive organisms, which function by blocking the ATPase activity of the B subunit of DNA gyrase. Novobiocin has lower activity against Gram-negative bacteria due to the permeability barrier posed by the OM. However, using an *E. coli* strain with a leaky OM, it was shown that novobiocin also binds and stimulates LptB, leading to improved LPS transport (May et al., 2017). A crystal structure revealed that novobiocin binds at a critical position at the LptB-LptFG interface. This binding may facilitate one or more steps in the catalytic cycle of the ATPase, coordinating nucleotide binding with LPS release. Novobiocin contains a substituted coumarin nucleus. An analog that retains LptB-stimulatory activity but is unable to inhibit DNA gyrase, although not toxic on its own, acts synergistically with polymyxin against Gram-negative bacteria (Mandler et al., 2018). With the new insights gained from these studies, it may become possible to discover new derivatives of novobiocin that inhibit rather than activate the LPS transporter.

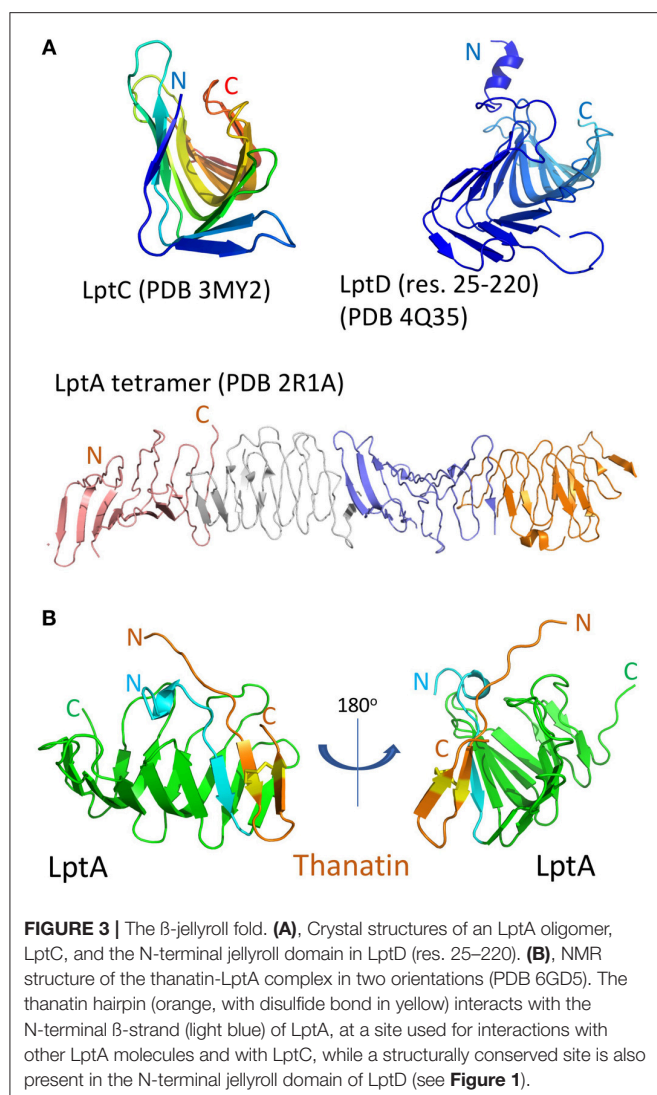
The synthetic peptidomimetic antibiotics described earlier were until recently the only compounds known to target the Lpt complex and inhibit LPS transport in pseudomonads. Their discovery not only validated the Lpt complex as a valuable target in antibiotic discovery but raised the intriguing question whether antimicrobial natural products might exist with a similar

mechanism of action. The first example of a natural product targeting the Lpt complex in *E. coli* was reported recently, namely the cationic antimicrobial peptide thanatin (**Figure 2**; Vetterli et al., 2018). Thanatin was first isolated from the hemipteran insect *Podisus maculiventris* (spined soldier bug) (Fehlbaum et al., 1996), and shows antimicrobial activity against several Gram-negative bacteria with MICs $<1.5 \mu\text{M}$. Although no activity is seen against *Staphylococcus aureus*, thanatin is also active against some other Gram-positive bacteria with MICs $\approx 1\text{--}5 \mu\text{M}$. Of special interest is the observation that the enantiomeric form (D-thanatin) loses much of its activity against all the Gram-negative strains tested, indicating a likely chiral target.

Evidence that thanatin interacts with the Lpt complex came again from *in-vivo* photoaffinity interaction mapping with *E. coli*. Potential interaction partners were identified following photolabeling, using a powerful mass spectrometry (MS)-based proteomic analysis. Three photolabeled OMPs revealed by this study were LptD, LptA, and BamB, of which LptD and LptA were the most significantly labeled (Vetterli et al., 2018). A second line of evidence implicating LptA as a target for thanatin came from analysis of spontaneous thanatin-resistant *E. coli* (Than^R) mutants. Of several Than^R mutants isolated, all contained mutations in LptA, and the mutated *lptA* gene when introduced into wild-type *E. coli* could confer resistance to the antibiotic. Indirect evidence that thanatin inhibits LPS transport was provided by transmission electron microscopy (EM) of thanatin-treated *E. coli* cells, which revealed a major perturbation to the membrane architecture, and the accumulation of membrane-like material inside the cell, which is typical of effects seen when individual components of the Lpt complex are down-regulated. However, direct evidence for an effect on LPS transport might be forthcoming with the emergence of the powerful *in-vitro* assays discussed above.

LptD is a large β -barrel membrane protein, whereas LptA is a small soluble periplasmic protein, so why should thanatin interact with both? Despite this major difference in size and location, both LptD and LptA, as well as LptC, all contain structurally homologous β -jellyroll domains, which mediate formation of the Lpt trans-periplasmic bridge (**Figure 3**). The crystal structure of an *E. coli* LptA oligomer revealed how LptA subunits interact in a head-to-tail fashion through their N- and C-terminal β -strands, by β -strand complementation (Suits et al., 2008). In analogy, the C-terminal strands of the jellyroll in LptC should interact with the N-terminal strands in LptA, and the C-terminal region of LptA interacts with the N-terminal β -strands in the jellyroll in LptD (Tran et al., 2010).

In-vitro assays revealed that thanatin binds to both recombinant LptA and the LptD/E complex, each in the low nanomolar range. An NMR solution structure of the thanatin-LptA complex showed how the N-terminal β -strand of the thanatin hairpin docks in a parallel orientation onto the first N-terminal β -strand in the LptA jellyroll (**Figure 3B**; Vetterli et al., 2018). The second β -strand of thanatin is mostly solvent exposed, although key side chains make contact with hydrophobic pockets on LptA. An array of hydrophobic, π - π -stacking, polar hydrogen-bonding and charge-charge electrostatic interactions appear to be involved



in stabilizing the complex. Moreover, the thanatin binding site in the N-terminal strand of LptA overlaps the site used for LptA-oligomer formation, for the interaction of LptA with LptC, and for the interaction of LptA with LptD. Modeling studies suggest that the thanatin binding site in LptA should be highly conserved in the jellyroll at the N-terminus of LptD (**Figure 3**). These results suggest that thanatin should inhibit multiple PPIs, including those between LptC-LptA, LptA-LptA, and LptA-LptD, required for assembly of the trans-periplasmic Lpt bridge. To conclude, these results highlight a new paradigm for an antibiotic action, targeting a network of PPIs required for the assembly of the Lpt complex in *E. coli*.

The LptA-thanatin complex reveals how the β -hairpin fold in thanatin is well-suited for binding to a protein through an exposed β -strand, a mechanism called β -augmentation (Remaut and Waksman, 2006). Interestingly, β -strand augmentation is believed to occur in other complexes that bind unfolded OMPs. Of special interest are components of the β -barrel

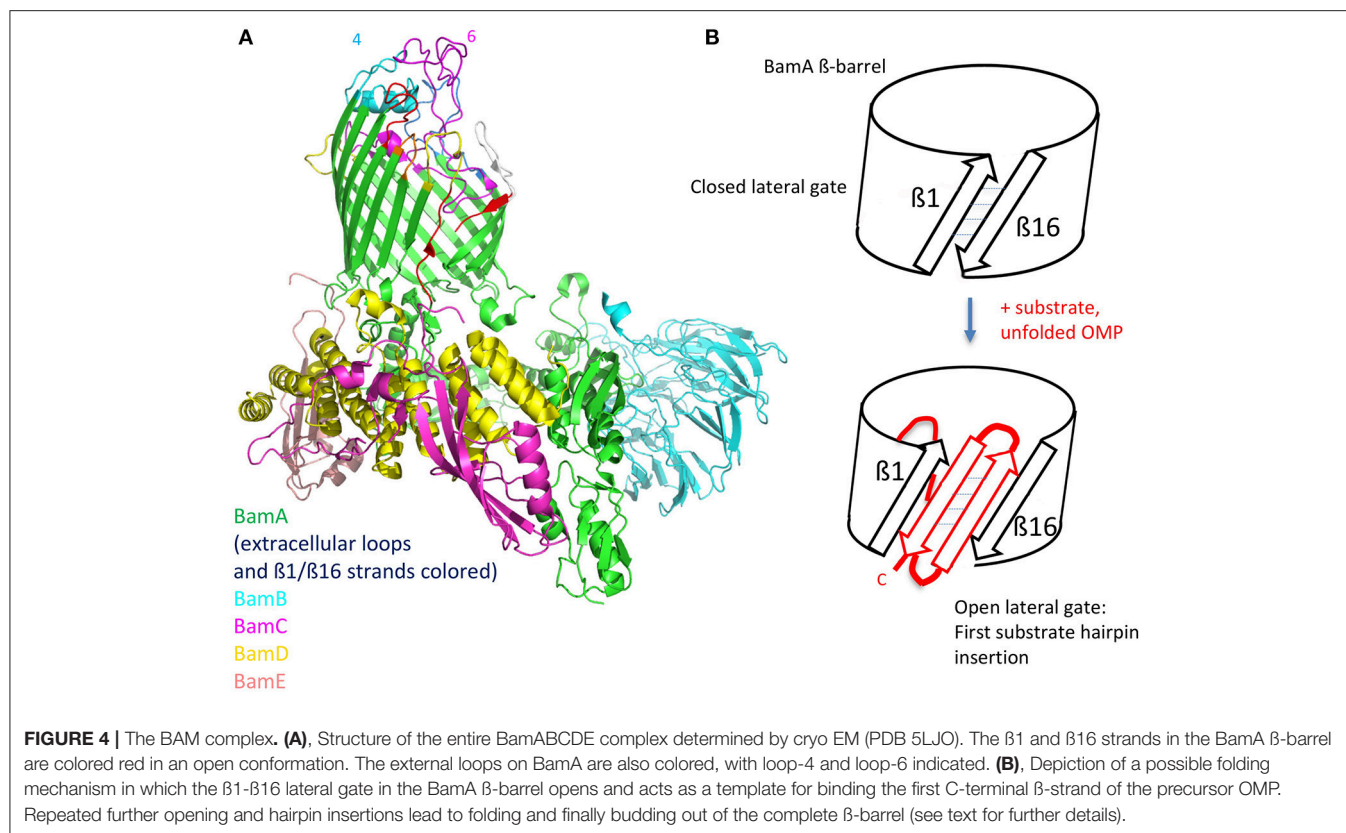
folding machine (BAM), which catalyzes the folding and insertion of unfolded β -barrel proteins into the OM during OM biogenesis. Exposed β -sheet edges in both BamA and BamB have been implicated in peptide binding by β -strand augmentation (Kim et al., 2007; Heuck et al., 2011). As mentioned above, it is interesting to note that a third OMP identified by photoaffinity interaction mapping with thanatin was BamB. However, so far it is not known whether thanatin can bind *in-vitro* to BamB or other members of the BAM complex.

MOLECULES TARGETING THE BAM COMPLEX

The β -barrel OMP LptD is essential for the biogenesis of the OM. β -Barrel OMPs, however, are also dependent on specialized machinery in the OM to catalyze their folding and insertion into the OM. After biosynthesis in the cytoplasm, newly expressed unfolded OMPs are exported across the IM using the Sec translocon and escorted across the periplasm bound to dedicated chaperones, before delivery to the BAM complex in the OM (**Figure 1**; Hagan et al., 2011). The BAM complex, comprising the β -barrel OMP BamA and four lipoproteins BamB-BamE, catalyzes the folding and insertion of β -barrel OMPs into the OM. Indeed, LptD is an important substrate of the BAM complex. It has been estimated that folding, OM insertion and disulfide oxidation of an LptD molecule into the OM requires about 20 min, a remarkably long time given that *E. coli* doubles during exponential growth every ≈ 20 –40 min (Lee et al., 2016).

The structures of individual BAM subunits, sub-complexes as well as the entire BAM complex have been solved by both X-ray crystallography and by cryo-EM (Bakelar et al., 2016; Gu et al., 2016; Han et al., 2016; Iadanza et al., 2016). BamA contains a 16-stranded β -barrel and five N-terminal periplasmic polypeptide transport-associated (POTRA) domains that interact with the four lipoproteins (BamB-E) forming a ring-like structure underneath the β -barrel (**Figure 4**). BamA and BamD are the only essential components of the complex, with conserved homologs found in all Gram-negative bacteria. Crystal and EM structures have caught the BamA barrel and its components within the complex in multiple conformations. Importantly, one structure shows the BamA barrel closed on its extracellular face and open to the periplasm, whereas a second has the barrel distorted, with displacement of several extracellular loops and a separation of the $\beta 1$ and $\beta 16$ strands. This lateral open state leaves the barrel open to the outer leaflet of the OM. These lateral open and closed structures are thought to represent at least two functional states in the BAM folding pathway.

The mechanism of Bam-mediated β -barrel folding and insertion into the OM is still under intensive investigation (Hagan et al., 2011; Noinaj et al., 2015, 2017). Briefly, it is thought that after delivery of unfolded OMPs to the periplasmic complex, a rotation of the ring-like structure leads to opening of the unstable junction between the first (1st) and last (16th) β -strands of the β -barrel, through which the folding OMP passes en route



to its final location in the OM bilayer. Supporting this conclusion, an engineered disulfide bond linking the β -1 and β -16 strands, thereby preventing the opening of the lateral gate, is lethal in *E. coli* (Noinaj et al., 2014).

One hypothesis is that the physical properties of the BAM complex and its interaction with the membrane bilayer may create a thinner less densely packed bilayer near to the $\beta 1$ - $\beta 16$ strand-junction, thereby destabilizing the membrane to assist folding and insertion of the new β -barrel OMP (Noinaj et al., 2013; Fleming, 2015). In this way, the BAM complex would act like a membrane disruptase to promote β -barrel folding and insertion. The POTRA domains, likely aided by other components of the BAM complex, appear to provide a recognition site for initial binding of their unfolded OMP targets (Kim et al., 2007).

The conserved machinery for the biogenesis of β -barrel membrane proteins is also found in mitochondria and chloroplasts. The sorting and assembly machinery (SAM) of mitochondria is required for folding and insertion of β -barrel precursors into the mitochondrial OM. The mitochondrial homolog of BamA is called Sam50, which appears to function with a similar folding mechanism. Recent investigations of β -barrel folding by the mitochondrial SAM complex suggest that folding precursors adopt transient β -hairpin-like elements (Höhr et al., 2018). It is proposed that after translocating into the lumen of the barrel they may insert as β -hairpin structures into the lateral opening between the $\beta 1$ and $\beta 16$ strands of Sam50

(Figure 4) (Höhr et al., 2018). Further, strands of the precursor, also in β -hairpin-like structures, are then inserted sequentially into the widening lateral gate, until the entire new folded barrel can bud out from the barrel into the OM. The BamA-induced membrane thinning mentioned above may contribute to β -barrel folding in bacteria by facilitating insertion of the new barrel into the membrane bilayer. β -Hairpin structures and β -strand augmentation clearly play a key role in each step of this folding mechanism.

In other work, it was shown that the BAM complex together with other β -barrel proteins are not uniformly distributed in the bacterial OM, but rather are located in clusters or “islands” (Rassam et al., 2015). This implies that many (or most) β -barrel proteins exist in a unique clustered environment in the bacterial OM, close to the site of folding and insertion mediated by the BAM complex. Given its essential role in β -barrel assembly and location in the OM, it is not surprising that the BAM complex has attracted interest as a target in the search for inhibitors with antimicrobial activity.

The first inhibitor of OMP folding by the BAM complex was reported recently (Hagan et al., 2015). The inhibitor comprised a 15-mer peptide with a sequence derived from a region close to the C-terminus of BamA. The background to this study was that BamD was shown to bind to unfolded BamA. More detailed *in-vitro* assays with the BAM complex reconstituted into proteoliposomes revealed that the sequence 765–779 in BamA, as a linear peptide, binds to BamD and inhibits folding

of full-length β -barrel OMPs by the BAM complex. Moreover, a peptide containing this conserved sequence, when expressed with a signal sequence and a FLAG tag in *E. coli*, was shown by photolabeling to interact *in-vivo* with BamD, and produces growth, OM permeability and OMP biogenesis defects. At this stage, the minimal peptide sequence identified is not expected to show antimicrobial activity on whole cells, due to its inability to traverse the OM. However, this study opens the possibility of finding peptidomimetic antibiotics that exploit this mechanism to interfere with OMP assembly.

Unfolded β -barrel proteins en route to the BAM complex contain a signal sequence (β -signal), typically in a region corresponding to the C-terminal β -strand, which targets them for initial interaction with the BAM complex (Robert et al., 2006; Noinaj et al., 2017). Although not a strictly conserved sequence, the β -signal typically contains a characteristic array of hydrophobic (h) and intervening non-conserved polar (p) residues, such as Ghphph (Robert et al., 2006). In the context of a β -sheet or β -hairpin backbone conformation, this motif places the hydrophobic residues on one face, and polar residues on the other of the β -sheet/ β -hairpin. A cyclic peptide was reported recently that functions as a mimetic of the β -signal involved in targeting unfolded β -barrel OMPs to the mitochondrial SAM complex (Jores et al., 2016). Using *in-vitro* assays, a 25-residue cyclic peptide containing the β -signal was shown to inhibit the import of β -barrel proteins into mitochondria. NMR analysis of the cyclic peptide suggested that it was more structured than a corresponding linear sequence. Photoaffinity cross-linking studies with isolated mitochondria, confirmed interactions of the peptide with several components of the folding complex. This work further indicates the potential of targeting β -barrel assembly machines using peptides and suitably designed folded peptidomimetics.

Another cyclic β -hairpin-shaped peptide called JB-95 (Figure 2) was reported recently that shows low micromolar MICs against *E. coli*, and an ability to interact with the BAM complex (Urfer et al., 2016). This β -hairpin-shaped cyclic peptide arose from studies of macrocyclic β -hairpin peptidomimetics containing a hairpin-inducing D-Pro-L-Pro template. The sequence attached to the template (WRIRrWKRLRR) resembles in its distribution of polar and hydrophobic residues the β -signal recognized by the BAM complex (Robert et al., 2006; Noinaj et al., 2017). The cyclic peptide exhibits no significant lytic activity on red blood cell membranes, but a variety of whole cell assays revealed an ability to selectively disrupt the OM but not the IM of *E. coli*. The lack of permeabilizing activity on the IM is consistent with the lack of general lytic activity on glycerophospholipid bilayers but leaves unanswered how the OM is selectively targeted. Whole cell staining with a fluorescently labeled derivative of JB-95 revealed a punctated staining pattern, consistent with selective labeling of discrete islands or patches of OMPs across the cell surface. Photochemical labeling experiments performed *in-vivo* with *E. coli* revealed cross-linking to several β -barrel OMPs, including BamA, LptD, BtuB, and others. The binding of JB-95 to BamA/LptD in OM clusters or “islands” might therefore explain both the punctated fluorescence staining pattern and the photochemical labeling

results. Finally, a proteomic analysis revealed that the peptide causes significant depletion of many OMPs (but not BamA) from treated cells. The lack of an effect on the levels of BamA in treated cells might be explained by up-regulation of *bamA* expression by an envelope stress response (σ^E). While the results reported are consistent with inhibition of the BAM complex by JB-95, direct proof for this is still outstanding.

The exposed surface loops of BamA are potentially of interest in vaccine design as well as for antibody-based anti-Gram-negative therapeutic agents. However, bacteria use the complex carbohydrate structures in LPS as well as capsular polysaccharides to shield potential protein epitopes that might be targeted by the immune system. Nevertheless, a monoclonal antibody (mAb) called MAB1 was described recently, directed against BamA in *E. coli* (Storek et al., 2018). MAB1 was isolated from a large library of anti-BamA IgG mAbs by screening for growth inhibitory effects on an *E. coli* mutant ($\Delta waaD$) displaying a truncated LPS. MAB1 showed a bactericidal activity against this strain, in the low nanomolar range over the course of several hours. Indirect evidence that MAB1 inhibits BamA folding activity was indicated by the significantly lowered levels of several OMPs in *E. coli* in the presence of MAB1. The mAb also caused activation of the σ^E stress response. Evidence for a permeabilizing effect of MAB1 on the cell envelope was shown by enhanced uptake of ethidium bromide, a rapid loss of periplasmic mCherry and a slower release of cytoplasmic Green Fluorescent Protein (GFP) from cells exposed to MAB1. Epitope mapping studies revealed that MAB1 interacts with residues in BamA extracellular loop 4 (light blue in Figure 4) that are distally located from the lateral gate in the β -barrel, the POTRA domains, the BamBCDE lipoproteins and periplasmic chaperones. Further studies suggested that the ability of MAB1 to antagonize BamA function seems to correlate with structural changes to LPS that influence membrane fluidity. A direct effect of MAB1 on BamA folding activity, which is expected to be toxic for the bacteria, might be caused by an allosteric mechanism, perhaps by affecting key conformational changes required for BamA to fulfill its function as a folding catalyst.

A natural antimicrobial peptide has also been discovered that targets BamA. The lectin-like bacteriocin called LlpA, a protein of ca. 28 kDa, mediates killing of selective Gram-negative bacteria, by a mechanism that is not yet fully defined. However, BamA was recently identified as a receptor for LlpA-mediated killing in *Pseudomonas* spp. (Ghequire et al., 2018). LlpA-resistant mutants were shown to carry mutations mainly in BamA surface loop L6 (Figure 4) or genes involved in capsular polysaccharide (LPS) biosynthesis. Genetic analyses also showed that *bamA* mediates the killing effects of LlpA on sensitive strains. The results suggest that LlpA interacts with BamA loop 6, and this is facilitated and/or stabilized by interaction of the lectin-like domains of LlpA with specific carbohydrate moieties in LPS. The crystal structure of LlpA from *Pseudomonas* sp. shows the protein to be rich in β -structure, with two mannose-binding lectin domains and a C-terminal β -hairpin extension (Ghequire et al., 2013). A mechanism for killing by LlpA was suggested, which involves interference of the gating dynamics of BamA by the β -hairpin loop extension, leading to the accumulation of unfolded OMPs

in the periplasm and to associated downstream responses. Interestingly, BamA was also identified earlier as a receptor for ligands mediating contact-dependent growth inhibition in *E. coli* (Aoki et al., 2008), a phenomenon whereby bacterial cell growth is regulated by direct cell-to-cell contact. Again residues in loop L6, as well as L7, were implicated in BamA targeting (Ruhe et al., 2013).

These examples demonstrate that molecules interacting with the exposed external loops of BamA may have antimicrobial activity. Conceivably, molecules smaller than mAbs might be developed with similar mechanisms of action, including not only engineered antibody fragments but also smaller folded

peptidomimetics better suited to circumventing the bacterial carbohydrate shield around the OM. Although one swallow does not make a summer, the intriguing discoveries highlighted in this review provide encouragement and starting points for the development of a new generation of antimicrobial agents specifically targeting Gram-negative pathogens. The need and scope for innovation in this area certainly seems to be large.

AUTHOR CONTRIBUTIONS

The author confirms being the sole contributor of this work and has approved it for publication.

REFERENCES

- Alexander, M. K., Miu, A., Oh, A., Reichelt, M., Ho, H. D., Chalouni, C., et al. (2018). Disrupting gram-negative bacterial outer membrane biosynthesis through inhibition of the lipopolysaccharide transporter MsbA. *Antimicrob. Agents Chemother.* 62, e01142–e01118. doi: 10.1128/aac.01142-18
- Andolina, G., Bencze, L. C., Zerbe, K., Muller, M., Steinmann, J., Kocherla, H., et al. (2018). A peptidomimetic antibiotic interacts with the periplasmic domain of LptD from *Pseudomonas aeruginosa*. *ACS Chem. Biol.* 13, 666–675. doi: 10.1021/acscchembio.7b00822
- Aoki, S. K., Malinverni, J. C., Jacoby, K., Thomas, B., Pamma, R., Trinh, B. N., et al. (2008). Contact-dependent growth inhibition requires the essential outer membrane protein BamA (YaeT) as the receptor and the inner membrane transport protein AcrB. *Mol. Microbiol.* 70, 323–340. doi: 10.1111/j.1365-2958.2008.06404.x
- Arkin, M. R., Tang, Y., and Wells, J. A. (2014). Small-molecule inhibitors of protein-protein interactions: progressing toward the reality. *Chem. Biol.* 21, 1102–1114. doi: 10.1016/j.chembiol.2014.09.001
- Bakelar, J., Buchanan, S. K., and Noinaj, N. (2016). The structure of the beta-barrel assembly machinery complex. *Science* 351, 180–186. doi: 10.1126/science.aad3460
- Bollati, M., Villa, R., Gourlay, L. J., Benedet, M., Dehò, G., Polissi, A., et al. (2015). Crystal structure of LptH, the periplasmic component of the lipopolysaccharide transport machinery from *Pseudomonas aeruginosa*. *FEBS J.* 282, 1980–1997. doi: 10.1111/febs.13254
- Botos, I., Majdalani, N., Mayclin, S. J., McCarthy, J. G., Lundquist, K., Wojtowicz, D., et al. (2016). Structural and functional characterization of the LPS transporter LptDE from gram-negative pathogens. *Structure* 24, 965–976. doi: 10.1016/j.str.2016.03.026
- Boucher, H. W., Talbot, G. H., Bradley, J. S., Edwards, J. E., Gilbert, D., Rice, L. B., et al. (2009). Bad bugs, no drugs: no ESCAPE! An update from the Infectious Diseases Society of America. *Clin. Infect. Dis.* 48, 1–12. doi: 10.1086/595011
- Bullock, B. N., Jochim, A. L., and Arora, P. S. (2011). Assessing helical protein interfaces for inhibitor design. *J. Am. Chem. Soc.* 133, 14220–14223. doi: 10.1021/ja206074j
- Dong, H. H., Xiang, Q. J., Gu, Y. H., Wang, Z. S., Paterson, N. G., Stansfeld, P. J., et al. (2014). Structural basis for outer membrane lipopolysaccharide insertion. *Nature* 511, 52–56. doi: 10.1038/nature13464
- Dong, H. H., Zhang, Z. Y., Tang, X. D., Paterson, N. G., and Dong, C. J. (2017). Structural and functional insights into the lipopolysaccharide ABC transporter LptB(2)FG. *Nat. Comm.* 8:222. doi: 10.1038/s41467-017-00273-5
- Erwin, A. L. (2016). Antibacterial drug discovery targeting the lipopolysaccharide biosynthetic enzyme LpxC. *Cold Spring Harb. Perspect. Med.* 6:a025304. doi: 10.1101/cshperspect.a025304
- Fehlbaum, P., Bulet, P., Chernysh, S., Briand, J. P., Roussel, J. P., Letellier, L., et al. (1996). Structure-activity analysis of thanatin, a 21-residue inducible insect defense peptide with sequence homology to frog skin antimicrobial peptides. *Proc. Natl. Acad. Sci. U.S.A.* 93, 1221–1225. doi: 10.1073/pnas.93.3.1221
- Fleming, K. G. (2015). A combined kinetic push and thermodynamic pull as driving forces for outer membrane protein sorting and folding in bacteria. *Phil. Trans. Roy. Soc. B* 370:20150026. doi: 10.1098/rstb.2015.0026
- Freinkman, E., Okuda, S., Ruiz, N., and Kahne, D. (2012). Regulated assembly of the transenvelope protein complex required for lipopolysaccharide export. *Biochemistry* 51, 4800–4806. doi: 10.1021/bi300592c
- Ghequire, M. G. K., Garcia-Pino, A., Lebbe, E. K. M., Spaepen, S., Loris, R., and De Mot, R. (2013). Structural determinants for activity and specificity of the bacterial toxin LlpA. *PLOS Path.* 9:e1003199. doi: 10.1371/journal.ppat.1003199
- Ghequire, M. G. K., Swings, T., Michiels, J., Buchanan, S. K., and De Mot, R. (2018). Hitting with a BAM: selective killing by lectin-like bacteriocins. *Mbio* 9:e02138–e02117. doi: 10.1128/mBio.02138-17
- Gopalakrishnan, R., Frolov, A. I., Knerr, L., Drury, W. J., and Valeur, E. (2016). Therapeutic potential of foldamers: from chemical biology tools to drug candidates? *J. Med. Chem.* 59, 9599–9621. doi: 10.1021/acs.jmedchem.6b00376
- Gu, Y. H., Li, H. Y., Dong, H. H., Zeng, Y., Zhang, Z. Y., Paterson, N. G., et al. (2016). Structural basis of outer membrane protein insertion by the BAM complex. *Nature* 531, 64–69. doi: 10.1038/nature17199
- Hagan, C. L., Silhavy, T. J., and Kahne, D. (2011). β -Barrel membrane protein assembly by the Bam complex. *Annu. Rev. Biochem.* 80, 189–210. doi: 10.1146/annurev-biochem-061408-144611
- Hagan, C. L., Wzorek, J. S., and Kahne, D. (2015). Inhibition of the β -barrel assembly machine by a peptide that binds BamD. *Proc. Natl. Acad. Sci. U.S.A.* 112, 2011–2016. doi: 10.1073/pnas.1415955112
- Han, L., Zheng, J. G., Wang, Y., Yang, X., Liu, Y. Q., Sun, C. Q., et al. (2016). Structure of the BAM complex and its implications for biogenesis of outer-membrane proteins. *Nat. Struct. Mol. Biol.* 23, 192–196. doi: 10.1038/nsmb.3181
- Henderson, J. C., Zimmerman, S. M., Crofts, A. A., Boll, J. M., Kuhns, L. G., Herrera, C. M., et al. (2016). The power of asymmetry: architecture and assembly of the gram-negative outer membrane lipid bilayer. *Annu. Rev. Microbiol.* 70, 255–278. doi: 10.1146/annurev-micro-102215-095308
- Heuck, A., Schleiffer, A., and Clausen, T. (2011). Augmenting β -augmentation: structural basis of how BamB binds BamA and may support folding of outer membrane proteins. *J. Mol. Biol.* 406, 659–666. doi: 10.1016/j.jmb.2011.01.002
- Ho, H., Miu, A., Alexander, M. K., Garcia, N. K., Oh, A., Zilberley, I., et al. (2018). Structural basis for dual-mode inhibition of the ABC transporter MsbA. *Nature* 557, 196–201. doi: 10.1038/s41586-018-0083-5
- Höhr, A. I. C., Lindau, C., Wirth, C., Qiu, J., Stroud, D. A., Kutik, S., et al. (2018). Membrane protein insertion through a mitochondrial β -barrel gate. *Science* 359:eaah6834. doi: 10.1126/science.aah6834
- Iadanza, M. G., Higgins, A. J., Schiffrin, B., Calabrese, A. N., Brockwell, D. J., Ashcroft, A. E., et al. (2016). Lateral opening in the intact β -barrel assembly machinery captured by cryo-EM. *Nat. Commun.* 7:12865. doi: 10.1038/ncomms12865
- Jores, T., Klinger, A., Gross, L. E., Kawano, S., Flinner, N., Duchardt-Ferner, E., et al. (2016). Characterization of the targeting signal in mitochondrial β -barrel proteins. *Nat. Commun.* 7:16. doi: 10.1038/ncomms12036
- Kim, S., Malinverni, J. C., Sliz, P., Silhavy, T. J., Harrison, S. C., and Kahne, D. (2007). Structure and function of an essential component of

- the outer membrane protein assembly machine. *Science* 317, 961–964. doi: 10.1126/science.1143993
- Konovalova, A., Kahne, D. E., and Silhavy, T. J. (2017). Outer membrane biogenesis. *Annu. Rev. Microbiol.* 71, 539–556. doi: 10.1146/annurev-micro-090816093754
- Laguri, C., Sperandio, P., Pounot, K., Ayala, I., Silipo, A., Bougault, C. M., et al. (2017). Interaction of lipopolysaccharides at intermolecular sites of the periplasmic Lpt transport assembly. *Sci. Rep.* 7:srep9715. doi: 10.1038/s41598-017-10136-0
- Lee, J., Xue, M. Y., Wzorek, J. S., Wu, T., Grabowicz, M., Gronenberg, L. S., et al. (2016). Characterization of a stalled complex on the beta-barrel assembly machine. *Proc. Nat. Acad. Sci. U.S.A.* 113, 8717–8722. doi: 10.1073/pnas.1604100113
- Lima, S., Guo, M. S., Chaba, R., Gross, C. A., and Sauer, R. T. (2013). Dual molecular signals mediate the bacterial response to outer-membrane stress. *Science* 340, 837–841. doi: 10.1126/science.1235358
- Luo, Q. S., Yang, X., Yu, S., Shi, H. G., Wang, K., Xiao, L., et al. (2017). Structural basis for lipopolysaccharide extraction by ABC transporter LptB(2)FG. *Nat. Struct. Mol. Biol.* 24, 469–474. doi: 10.1038/nsmb.3399
- Mandler, M. D., Baidin, V., Lee, J., Pahil, K. S., Owens, T. W., and Kahne, D. (2018). Novobiocin enhances polymyxin activity by stimulating lipopolysaccharide transport. *J. Am. Chem. Soc.* 140, 6749–6753. doi: 10.1021/jacs.8b02283
- Martin-Loeches, I., Dale, G. E., and Torres, A. (2018). Murepavadin: a new antibiotic class in the pipeline. *Exp. Rev. Anti-Infect. Ther.* 16, 259–268. doi: 10.1080/14787210.2018.1441024
- Masi, M., Matthieu, R., Pos, K. M., and Pages, J. M. (2017). Mechanisms of envelope permeability and antibiotic influx and efflux in Gram-negative bacteria. *Nat. Microbiol.* 2:17001. doi: 10.1038/nmicrobiol.2017.1
- May, J. M., Owens, T. W., Mandler, M. D., Simpson, B. W., Lazarus, M. B., Sherman, D. J., et al. (2017). The antibiotic novobiocin binds and activates the ATPase that powers lipopolysaccharide transport. *J. Am. Chem. Soc.* 139, 17221–17224. doi: 10.1021/jacs.7b07736
- May, J. M., Sherman, D. J., Simpson, B. W., Ruiz, N., and Kahne, D. (2015). Lipopolysaccharide transport to the cell surface: periplasmic transport and assembly into the outer membrane. *Phil. Trans. Roy. Soc. B.* 370:7. doi: 10.1098/rstb.2015.0027
- May, K. L., and Silhavy, T. J. (2017). Making a membrane on the other side of the wall. *Biochim. Biophys. Acta.* 1862, 1386–1393. doi: 10.1016/j.bbalip.2016.10.004
- Merten, J. A., Schultz, K. M., and Klug, C. S. (2012). Concentration-dependent oligomerization and oligomeric arrangement of LptA. *Protein Sci.* 21, 211–218. doi: 10.1002/pro.2004
- Mi, W., Li, Y., Yoon, S. H., Ernst, R. K., Walz, T., and Liao, M. (2017). Structural basis of MsbA-mediated lipopolysaccharide transport. *Nature* 549, 233–237. doi: 10.1038/nature23649
- Morrison, C. (2018). Constrained peptides' time to shine? *Nat. Revs. Drug Disc.* 17, 531–533. doi: 10.1038/nrd.2018.125
- Narita, S.-i., and Tokuda, H. (2017). Bacterial lipoproteins; biogenesis, sorting and quality control. *Biochim. Biophys. Acta.* 1862, 1414–1423. doi: 10.1016/j.bbalip.2016.11.009
- Nikaido, H. (2003). Molecular basis of bacterial outer membrane permeability revisited. *Microbiol. Mol. Biol. Rev.* 67, 593–656. doi: 10.1128/MMBR.67.4.593-656.2003
- Noinaj, N., Gumbart, J. C., and Buchanan, S. K. (2017). The beta-barrel assembly machinery in motion. *Nat. Revs. Microbiol.* 15, 197–204. doi: 10.1038/nrmicro.2016.191
- Noinaj, N., Kuszak, A. J., Balusek, C., Gumbart, J. C., and Buchanan, S. K. (2014). Lateral opening and exit pore formation are required for BamA function. *Structure* 22, 1055–1062. doi: 10.1016/j.str.2014.05.008
- Noinaj, N., Kuszak, A. J., Gumbart, J. C., Lukacik, P., Chang, H. S., Easley, N. C., et al. (2013). Structural insight into the biogenesis of beta-barrel membrane proteins. *Nature* 501, 385–390. doi: 10.1038/nature12521
- Noinaj, N., Rollauer, S. E., and Buchanan, S. K. (2015). The β -barrel membrane protein insertase machinery from Gram-negative bacteria. *Curr. Opin. Struct. Biol.* 31, 35–42. doi: 10.1016/j.sbi.2015.02.012
- Okuda, S., Freinkman, E., and Kahne, D. (2012). Cytoplasmic ATP hydrolysis powers transport of lipopolysaccharide across the periplasm in *E. coli*. *Science* 338, 1214–1217. doi: 10.1126/science.1228984
- Okuda, S., Sherman, D. J., Silhavy, T. J., Ruiz, N., and Kahne, D. (2016). Lipopolysaccharide transport and assembly at the outer membrane: the PEZ model. *Nat. Rev. Microbiol.* 14, 337–345. doi: 10.1038/nrmicro.2016.25
- Panteleev, P. V., Balandin, S. V., Ivanov, V. T., and Ovchinnikova, T. V. (2017). A therapeutic potential of animal beta-hairpin antimicrobial peptides. *Curr. Med. Chem.* 24, 1724–1746. doi: 10.2174/0929867324666170424124416
- Poole, K. (2005). Efflux-mediated antimicrobial resistance. *J. Antimicrob. Chemother.* 56, 20–51. doi: 10.1093/jac/dki171
- Qiao, S., Luo, Q. S., Zhao, Y., Zhang, X. J. C., and Huang, Y. H. (2014). Structural basis for lipopolysaccharide insertion in the bacterial outer membrane. *Nature* 511, 108–111. doi: 10.1038/nature13484
- Raetz, C. R. H., Reynolds, C. M., Trent, M. S., and Bishop, R. E. (2007). Lipid A modification systems in Gram-negative bacteria. *Annu. Rev. Biochem.* 76, 295–329. doi: 10.1146/annurev.biochem.76.010307.145803
- Ranava, D., Caumont-Sarcos, A., Albenne, C., and Ieva, R. (2018). Bacterial machineries for the assembly of membrane-embedded beta-barrel proteins. *FEMS Microbiol. Lett.* 365, 12. doi: 10.1093/femsle/fny087
- Rassam, P., Copeland, N. A., Birkholz, O., Toth, C., Chavent, M., Duncan, A. L., et al. (2015). Supramolecular assemblies underpin turnover of outer membrane proteins in bacteria. *Nature* 523, 333–336. doi: 10.1038/nature14461
- Remaut, H., and Waksman, G. (2006). Protein-protein interaction through β -strand addition. *Trends Biochem. Sci.* 31, 436–444. doi: 10.1016/j.tibs.2006.06.007
- Rice, L. B. (2008). Federal funding for the study of antimicrobial resistance in nosocomial pathogens: no ESKAPE. *J. Infect. Dis.* 197, 1079–1081. doi: 10.1086/533452
- Robert, V., Volokhina, E. B., Senf, F., Bos, M. P., Gelder, P. V., and Tommassen, J. (2006). Assembly factor Omp85 recognizes its outer membrane protein substrates by a species-specific C-terminal motif. *PLOS Biol.* 4:e377. doi: 10.1371/journal.pbio.0040377
- Robinson, J. A. (2008). β -Hairpin peptidomimetics: design, structures and biological activities. *Acc. Chem. Res.* 41, 1278–1288. doi: 10.1021/ar700259k
- Robinson, J. A., Shankaramma, S. C., Jetter, P., Kienzl, U., Schwendener, R. A., Vrijbloed, J. W., et al. (2005). Properties and structure-activity studies of cyclic beta-hairpin peptidomimetics based on the cationic antimicrobial peptide protegrin I. *Bioorg. Med. Chem.* 13, 2055–2064. doi: 10.1016/j.bmc.2005.01.009
- Rojas, E. R., Billings, G., Odermatt, P. D., Auer, G. K., Zhu, L., Miguel, A., et al. (2018). The outer membrane is an essential load-bearing element in Gram-negative bacteria. *Nature* 559, 617–621. doi: 10.1038/s41586-018-0344-3
- Ruhe, Z. C., Wallace, A. B., Low, D. A., and Hayes, C. S. (2013). Receptor polymorphism restricts contact-dependent growth inhibition to members of the same species. *mBio* 4:e00480–e00413. doi: 10.1128/mBio.00480-13
- Schmidt, J., Patora-Komisarska, K., Moehle, K., Obrecht, D., and Robinson, J. A. (2013). Structural studies of β -hairpin peptidomimetic antibiotics that target LptD in *Pseudomonas* sp. *Bioorg. Med. Chem.* 21, 5806–5810. doi: 10.1016/j.bmc.2013.07.013
- Schultz, K. M., Lundquist, T. J., and Klug, C. S. (2017). Lipopolysaccharide binding to the periplasmic protein LptA. *Prot. Sci.* 26, 1517–1523. doi: 10.1002/pro.3177
- Shankaramma, S. C., Athanassiou, Z., Zerbe, O., Moehle, K., Mouton, C., Bernardini, F., et al. (2002). Macrocyclic hairpin mimetics of the cationic antimicrobial peptide protegrin I: A new family of broad-spectrum antibiotics. *ChemBioChem.* 3, 1126–1133. doi: 10.1002/1439-7633(20021104)3:11<1126::AID-CBIC1126>3.0.CO;2-I
- Sherman, D. J., Xie, R., Taylor, R. J., George, A. H., Okuda, S., Foster, P. J., et al. (2018). Lipopolysaccharide is transported to the cell surface by a membrane-to-membrane protein bridge. *Science* 359, 798–801. doi: 10.1126/science.aar1886
- Simpson, B. W., May, J. M., Sherman, D. J., Kahne, D., and Ruiz, N. (2015). Lipopolysaccharide transport to the cell surface: biosynthesis and extraction from the inner membrane. *Phil. Trans. Roy. Soc. B.* 370:8. doi: 10.1098/rstb.2015.0029
- Srinivas, N., Jetter, P., Ueberbacher, B. J., Werneburg, M., Zerbe, K., Steinmann, J., et al. (2010). Peptidomimetic antibiotics target outer-membrane biogenesis in *Pseudomonas aeruginosa*. *Science* 327, 1010–1013. doi: 10.1126/science.1182749
- Storek, K. M., Auerbach, M. R., Shi, H. D., Garcia, N. K., Sun, D. W., Nickerson, N. N., et al. (2018). Monoclonal antibody targeting the ss-barrel assembly machine of *Escherichia coli* is bactericidal. *Proc. Natl. Acad. Sci. U.S.A.* 115, 3692–3697. doi: 10.1073/pnas.1800043115

- Suits, M. D. L., Sperandeo, P., Deho, G., Polissi, A., and Jia, Z. (2008). Novel structure of the conserved Gram-negative lipopolysaccharide transport protein A and mutagenesis analysis. *J. Mol. Biol.* 380, 476–488. doi: 10.1016/j.jmb.2008.04.045
- Tran, A. X., Dong, C., and Whitfield, C. (2010). Structure and functional analysis of LptC, a conserved membrane protein involved in the lipopolysaccharide export pathway in *Escherichia coli*. *J. Biol. Chem.* 285, 33529–33539. doi: 10.1074/jbc.M110.144709
- Urfer, M., Bogdanovic, J., Lo Monte, F., Moehle, K., Zerbe, K., Omasits, U., et al. (2016). A peptidomimetic antibiotic targets outer membrane proteins and disrupts selectively the outer membrane in *Escherichia coli*. *J. Biol. Chem.* 291, 1921–1938. doi: 10.1074/jbc.M115.691725
- Vetterli, S. U., Moehle, K., and Robinson, J. A. (2016). Synthesis and antimicrobial activity against *Pseudomonas aeruginosa* of macrocyclic β -hairpin peptidomimetic antibiotics containing N-methylated amino acids. *Bioorg. Med. Chem.* 24, 6332–6339. doi: 10.1016/j.bmc.2016.05.027
- Vetterli, S. U., Zerbe, K., Müller, M., Urfer, M., Mondal, M., Wang, S.-Y., et al. (2018). Thanatin targets the intermembrane protein complex required for lipopolysaccharide transport in *Escherichia coli*. *Sci. Adv.* 4:eaa2634. doi: 10.1126/sciadv.aau2634
- Villa, R., Martorana, A. M., Okuda, S., Gourlay, L. J., Nardini, M., Sperandeo, P., et al. (2013). The *Escherichia coli* Lpt transenvelope protein complex for lipopolysaccharide export is assembled via conserved structurally homologous domains. *J. Bacteriol.* 195, 1100–1108. doi: 10.1128/JB.02057-12
- Wach, A., Dembowski, K., and Dale, G. E. (2018). Pharmacokinetics and safety of intravenous murepavadin infusion in healthy adult subjects administered single and multiple ascending doses. *Antimicrob. Agents Chemother.* 62:10. doi: 10.1128/aac.02355-17
- Wang, C. K., King, G. J., Conibear, A. C., Ramos, M. C., Chaousis, S., Henriques, S. T., et al. (2016). Mirror images of antimicrobial peptides provide reflections on their functions and amyloidogenic properties. *J. Am. Chem. Soc.* 138, 5706–5713. doi: 10.1021/jacs.6b02575
- Ward, A., Reyes, C. L., Yu, J., Roth, C. B., and Chang, G. (2007). Flexibility in the ABC transporter MsbA: alternating access with a twist. *Proc. Nat. Acad. Sci. U.S.A.* 104, 19005–19010. doi: 10.1073/pnas.0709388104
- Watkins, A. M., and Arora, P. S. (2014). Anatomy of β -strands at protein–protein interfaces. *ACS Chem. Biol.* 9, 1747–1754. doi: 10.1021/cb500241y
- Werneburg, M., Zerbe, K., Juhas, M., Bigler, L., Stalder, U., Kaeck, A., et al. (2012). Inhibition of lipopolysaccharide transport to the outer membrane in *Pseudomonas aeruginosa* by peptidomimetic antibiotics. *Chembiochem* 13, 1767–1775. doi: 10.1002/cbic.201200276
- WHO, A. r. b. t. (2017). *Global Priority List of Antibiotic-resistant Bacteria to Guide Research, Discovery, and Development of New Antibiotics*. Geneva: World Health Organization.
- Wuo, M. G., and Arora, P. S. (2018). Engineered protein scaffolds as leads for synthetic inhibitors of protein-protein interactions. *Cur. Opin. Chem. Biol.* 44, 16–22. doi: 10.1016/j.cbpa.2018.05.013
- Xie, R., Taylor, R. J., and Kahne, D. (2018). Outer membrane translocon communicates with inner membrane ATPase to stop lipopolysaccharide transport. *J. Am. Chem. Soc.* 140, 12691–12694. doi: 10.1021/jacs.8b07656
- Zerbe, K., Moehle, K., and Robinson, J. A. (2017). Protein epitope mimetics: from new antibiotics to supramolecular synthetic vaccines. *Acc. Chem. Res.* 50, 1323–1331. doi: 10.1021/acs.accounts.7b00129
- Zhang, G., Baidin, V., Pahil, K. S., Moison, E., Tomasek, D., Ramadoss, N. S., et al. (2018). Cell-based screen for discovering lipopolysaccharide biogenesis inhibitors. *Proc. Nat. Acad. Sci. U.S.A.* 115, 6834–6839. doi: 10.1073/pnas.1804670115
- Zhao, C., Liu, L., and Lehrer, R. I. (1994). Identification of a new member of the protegrin family by cDNA cloning. *FEBS Lett.* 346, 285–288. doi: 10.1016/0014-5793(94)00493-5

Conflict of Interest Statement: The author declares that the research was conducted in the absence of any commercial or financial relationships that could be construed as a potential conflict of interest.

Copyright © 2019 Robinson. This is an open-access article distributed under the terms of the Creative Commons Attribution License (CC BY). The use, distribution or reproduction in other forums is permitted, provided the original author(s) and the copyright owner(s) are credited and that the original publication in this journal is cited, in accordance with accepted academic practice. No use, distribution or reproduction is permitted which does not comply with these terms.



Rational Design of Antiangiogenic Helical Oligopeptides Targeting the Vascular Endothelial Growth Factor Receptors

Simone Zanella^{1†}, Gianfranco Bocchinfuso^{2†}, Marta De Zotti^{3†}, Daniela Arosio⁴, Franca Marino⁵, Stefano Raniolo², Luca Pignataro¹, Giovanni Sacco¹, Antonio Palleschi², Alvaro S. Siano⁶, Umberto Piarulli⁵, Laura Belvisi^{1,4}, Fernando Formaggio^{3*}, Cesare Gennari^{1,4*} and Lorenzo Stella^{2*}

OPEN ACCESS

Edited by:

Alessandro Contini,
University of Milan, Italy

Reviewed by:

Maria Jesús Pérez De Vega,
Instituto de Química Médica (IQM),
Spain
Nicolas Inguimbert,
Université de Perpignan Via Domitia,
France

*Correspondence:

Fernando Formaggio
fernando.formaggio@unipd.it
Cesare Gennari
cesare.gennari@unimi.it
Lorenzo Stella
stella@stc.uniroma2.it

[†]These authors have contributed
equally to this work

Specialty section:

This article was submitted to
Chemical Biology,
a section of the journal
Frontiers in Chemistry

Received: 11 January 2019

Accepted: 05 March 2019

Published: 29 March 2019

Citation:

Zanella S, Bocchinfuso G, De Zotti M,
Arosio D, Marino F, Raniolo S,
Pignataro L, Sacco G, Palleschi A,
Siano AS, Piarulli U, Belvisi L,
Formaggio F, Gennari C and Stella L
(2019) Rational Design of
Antiangiogenic Helical Oligopeptides
Targeting the Vascular Endothelial
Growth Factor Receptors.
Front. Chem. 7:170.
doi: 10.3389/fchem.2019.00170

¹ Department of Chemistry, University of Milan, Milan, Italy, ² Department of Chemical Science and Technologies, University of Rome Tor Vergata, Rome, Italy, ³ Padova Unit, Department of Chemistry, Institute of Biomolecular Chemistry, CNR, University of Padova, Padova, Italy, ⁴ National Research Council, Institute of Molecular Science and Technologies, Milan, Italy, ⁵ Center for Research in Medical Pharmacology, University of Insubria, Varese, Italy, ⁶ Departamento de Química Orgánica, Facultad de Bioquímica y Ciencias Biológicas, Universidad Nacional del Litoral, Santa Fe, Argentina

Tumor angiogenesis, essential for cancer development, is regulated mainly by vascular endothelial growth factors (VEGFs) and their receptors (VEGFRs), which are overexpressed in cancer cells. Therefore, the VEGF/VEGFR interaction represents a promising pharmaceutical target to fight cancer progression. The VEGF surface interacting with VEGFRs comprises a short α -helix. In this work, helical oligopeptides mimicking the VEGF-C helix were rationally designed based on structural analyses and computational studies. The helical conformation was stabilized by optimizing intramolecular interactions and by introducing helix-inducing $C^{\alpha,\alpha}$ -disubstituted amino acids. The conformational features of the synthetic peptides were characterized by circular dichroism and nuclear magnetic resonance, and their receptor binding properties and antiangiogenic activity were determined. The best hits exhibited antiangiogenic activity *in vitro* at nanomolar concentrations and were resistant to proteolytic degradation.

Keywords: helical folded peptides, protein-protein interactions, $C^{\alpha,\alpha}$ -disubstituted amino acids, VEGF-C, angiogenesis

INTRODUCTION

Angiogenesis—i.e., the formation of new blood vasculature from the established blood vessel network—can be associated to both physiological and pathological processes (e.g., inflammation, tumor growth, and metastasis). Among the latter, tumor angiogenesis is essential for cancer development, since neovascularization provides a steady supply of oxygen and nutrients, supporting the proliferation of cancer cells (Mizejewski, 1999; Danhier et al., 2012; Johannessen et al., 2013). For this reason, antiangiogenic agents are used to impede or retard cancer progression and metastasis (Ferrara and Adamis, 2016).

Different receptors are involved in angiogenesis regulation, and their expression depends on the conditions of the cell environment (e.g., pH, oxygen or supply of nutrients) (Mizejewski, 1999). Angiogenic processes are also mediated by cross-talk mechanisms that trigger direct association and cluster formation between specific receptors.

For example, the cooperation between integrins and vascular endothelial growth factor receptors (VEGFRs) was found to be crucial in pathological processes such as tumor growth and development (Somanath et al., 2009; Desgrosellier and Cheresh, 2010).

VEGFRs are receptor tyrosine kinases (RTKs) that have a central role in tumor angiogenesis and progression. Indeed, the hypoxic conditions characteristic of the tumor environment induce both up-regulation of VEGFRs and gene expression of vascular endothelial growth factors (VEGFs) (Ferrara et al., 2003; Hoeben et al., 2004; Olsson et al., 2006; Carmeliet and Jain, 2011; Shibuya, 2013). In addition to the tumor promoting effects of neovascularization, autocrine VEGF/VEGFR signaling favors growth, proliferation and migration of cancer cells (Su et al., 2007; Simon et al., 2017).

Dimerization and activation of VEGFRs are triggered by binding of VEGFs to the extracellular domain of the receptors (Ferrara and Adamis, 2016). The VEGF family consists of five members [VEGF-A, VEGF-B, VEGF-C, VEGF-D, and PlGF (placental growth factor)], and there are three distinct receptors (VEGFR-1, VEGFR-2, VEGFR-3). The various growth factors have differential selectivity: for instance, VEGF-A binds to VEGFR-1 and VEGFR-2, while VEGF-C binds to VEGFR-2 and VEGFR-3. In addition, the three receptors have different functions, with VEGFR-2 being mainly involved in angiogenesis and VEGFR-3 regulating lymphangiogenesis (Ferrara and Adamis, 2016; Nasir, 2019).

Three main approaches targeting VEGF-A/VEGFR-2 signaling in human cancer have been approved for clinical practice (Nasir, 2019). One strategy involves inhibition of the tyrosine kinase activity of VEGFR-2 by small molecules interacting with the intracellular segment of the receptor, such as sorafenib and sunitinib (Musumeci et al., 2012). Alternatively, VEGF-mediated angiogenesis can be impaired by blocking the VEGF-A/VEGFR-2 interaction. This has been accomplished by binding and neutralizing circulating VEGF-A with monoclonal antibodies (bevacizumab) or recombinant proteins mimicking the receptor (aflibercept) (Ferrara et al., 2004; Ferrara and Adamis, 2016). Alternatively, VEGFR-2 has been targeted with therapeutic monoclonal antibodies, such as ramucirumab. These molecules are now a standard of care for the treatment of several metastatic cancers (Ferrara and Adamis, 2016), even though clinical results have not met in all cancer types the initial high hopes for this therapeutic strategy, underlining the need for more effective antiangiogenic drugs (Vasudev and Reynolds, 2014; Ronca et al., 2017). Anti-VEGF-A/VEGFR-2 therapy has proven more effective in ophthalmology, in the treatment of intraocular neo vascular disorders, such as age-related macular degeneration (Ferrara and Adamis, 2016). However, each of the above mentioned approved drugs has its own limitations: kinase inhibitors have limited selectivity, while antibodies suffer from poor pharmacokinetics, limited tissue penetration and high costs (Chames et al., 2009; Howard et al., 2015). Their use in the therapy of eye diseases requires repeated intravitreal injections, and new drugs that can be administered by simpler and safer routes are highly desirable (Sidman et al., 2015).

Peptides and peptidomimetics with a well-defined conformation (foldamers) represent a promising alternative to biological therapeutics for the inhibition of protein-protein interactions, and are currently experiencing a revival of interest from the pharmaceutical industry (Henninot et al., 2018). Among those able to interact with the extracellular domain of VEGFRs, it is worth mentioning the peptoid ligands described by Kodadek and colleagues (Udugamasooriya et al., 2008), the helical peptides developed starting from VEGF-A and Vammin hotspots (García-Aranda et al., 2013), and cyclopeptides isolated by phage display technique (Zilberberg et al., 2003), or rationally designed (Gautier et al., 2010). In 2011, D'Andrea and coworkers developed a α -helical decapeptide based on the natural sequence of VEGF-A, with potent inhibitory activity against VEGF-stimulated angiogenesis *in vivo* (Basile et al., 2011; Diana et al., 2013). Because of its synthetic accessibility and antiangiogenic properties, recently some of us selected that peptide to prepare a dual-action compound able to interfere with the integrin $\alpha_v\beta_3$ -VEGFR-1 cross-talk (Zanella et al., 2015). This conjugate was able to bind *in vitro* both integrin $\alpha_v\beta_3$ and VEGFR-1, and exerted a strong antiangiogenic effect in VEGF-stimulated morphogenesis assays on human umbilical vein endothelial cells (HUVECs).

Herein, we report the results of our efforts to develop new VEGFR antagonists based on a helical fragment of VEGF-C, with promising activity against VEGF-mediated angiogenesis.

RESULTS

Design

A Short Helix Is an Important Element of the VEGF/VEGFR Interface

The extracellular domain of VEGFRs consists of seven Ig homology domains. VEGF binding takes place mostly on domain D2. **Figure 1** shows the structure of the VEGF-A/VEGFR-1 (D2 domain) interface, whose main features are conserved in all VEGF/VEGFR complexes (Leppänen et al., 2013). We started our analysis from this complex, because all currently approved antiangiogenic drugs are targeted to VEGF-A or to VEGFR-1. VEGF residues are colored from green to red in order of increasing penalty in the standard binding free energy caused by their substitution to Ala, as predicted by *in silico* alanine scanning. This analysis indicates that a short helix, located at the N-terminal region of the growth factor, represents a significant portion of the interaction interface. Previous experimental studies have shown that this helix is involved in receptor specificity and protein dimerization of VEGFs (Siemeister et al., 1998; Robinson and Stringer, 2001; Leppänen et al., 2010). In the case of VEGF-A, the helix comprises residues 17–25 (a nonapeptide). **Table 1** reports the numerical results of the *in silico* Ala scan for those residues, showing that the interaction with the receptor is mediated principally by amino acid residues at positions 1, 2, 5, 6, and 9 of the helical nonapeptide. This finding is consistent with experimental Ala scan data (Muller et al., 1997; Li et al., 2000). A similar analysis performed on the structure of the VEGF-A/VEGFR-2 complex confirmed the N-terminal helix as an important interacting element (**Figure S1**).

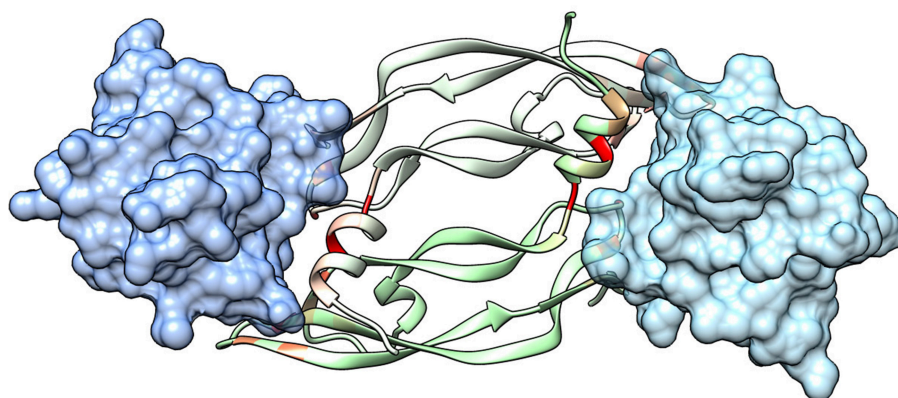


FIGURE 1 | Structure of a VEGF/VEGFR complex (PDB code 1FLT). Ig-homology domain 2 of the receptor (VEGFR-1) is shown in surface representation (light blue and blue for the two subunits), while the two subunits of VEGF-A are shown as ribbons of two different shades of green. VEGF residues are colored depending on the standard binding free energy penalty associated with their mutation to Ala, as predicted by DrugScorePPI (values from 0 to 1.5 kcal/mol are reported in shades of color going from green to red; values 1.5 kcal/mol and above, up to the maximum of 2.4 kcal/mol, are all reported in red).

TABLE 1 | *In silico* Ala scan of the VEGF-A helix interacting with VEGFR-1 (PDB code 1FLT)^a.

Position in the helix	Residue	FoldX	DrugScorePPI	KFC2	PCRPI
		$\Delta\Delta G_{\text{binding}}^{\circ}$ (kcal/mol)	$\Delta\Delta G_{\text{binding}}^{\circ}$ (kcal/mol)	Hot spots	Probability (%)
1	Phe 17	1.6	0.4	X	48
2	Met 18	2.0	0.4	X	8
3	Asp 19	0.1	–	–	0
4	Val 20	0.1	–	–	0
5	Tyr 21	2.4	2.4	X	14
6	Gln 22	0.7	0.3	–	2
7	Arg 23	0.2	0.1	–	0
8	Ser 24	0.2	–	–	0
9	Tyr 25	0.5	1.4	X	4

^aFoldX and DrugScorePPI predict the penalty in standard binding free energy for substitution of each residue to Ala, the KFC2 server simply predicts hotspots and PCRPI reports the probability that a given residue is a hotspot. Substitutions that are predicted to have a strong effect on the binding are colored in red (i.e., those with a $\Delta\Delta G_{\text{binding}}^{\circ}$ higher than 1.0 kcal/mol or indicated by KFC2 as hot spots or with a PCRPI probability greater than 10). Substitutions that are predicted to have a mild effect on the binding are colored in light red (i.e., those with $\Delta\Delta G_{\text{binding}}^{\circ}$ comprised between 0.3 and 1.0 kcal/mol or with a PCRPI probability comprised between 1 and 10).

The Helix of VEGF-C Presents the Most Promising Inter- and Intra-molecular Interactions

Figure 2 shows the corresponding helical sequences in various growth factors, together with the available crystallographic structures of their complexes with receptors. In most cases, the interaction is largely based on hydrophobic effects. The only significant exception is provided by VEGF-C, which forms an intermolecular salt bridge with Arg164 of VEGFR-2 through the Asp residue at position 2 of the helix. This specific interaction is predicted to improve the selective recognition of the VEGF-C helix by VEGFR-2. **Figure S1** shows the results of an *in silico* Ala

scan performed on the VEGFR-2/VEGF-C complex, confirming the centrality of the N-terminal helix in the recognition process.

The VEGF-C helix presents also another interesting property. Short helical segments are usually largely disordered when separated from the protein that contained them. Without the stabilization provided by the rest of the protein structure, competition by water molecules breaks the intramolecular H-bond network that holds the helical conformation together. On the other hand, binding to the receptor requires a helical conformation. Therefore, a disordered peptide pays a significant entropic cost for association to the receptor. Thus, stabilization of the helical conformation in such short peptides is advisable. Interestingly, the helix of VEGF-C presents three pairs of side chains that potentially form interactions stabilizing a helical conformation, being located at an $i - i+3$ or $i - i+4$ distance. In particular, Ile1 and Trp5 can form a hydrophobic cluster, while both Asp2 and Arg6 and Glu4 and Lys7 can form salt bridges (numbers correspond to positions in the helix).

Replica exchange molecular dynamics (REMD) simulations were used to verify the stability of the VEGF-C helix, when free in solution. **Figure 3** reports the secondary structure of the peptide, a representative conformation and the histograms of the distances between the side-chains mentioned above during the simulation trajectory. The data confirm that the ion pairs and hydrophobic cluster are significantly populated and stabilize the helical conformation of the peptide in solution.

For all these reasons, we decided to focus on the VEGF-C helix sequence (peptide 1) (**Figure 4**) to develop VEGF/VEGFR interaction inhibitors.

Substitution of Two Residues in the VEGF-C Sequence Is Predicted to Increase Binding Affinity

In order to optimize peptide affinity for VEGFRs, *in silico* mutagenesis was performed, concentrating on the VEGF-C/VEGFR-2 complex (PDB code 2X1X). All residues of the helix previously identified as hot spots were mutated to all possible

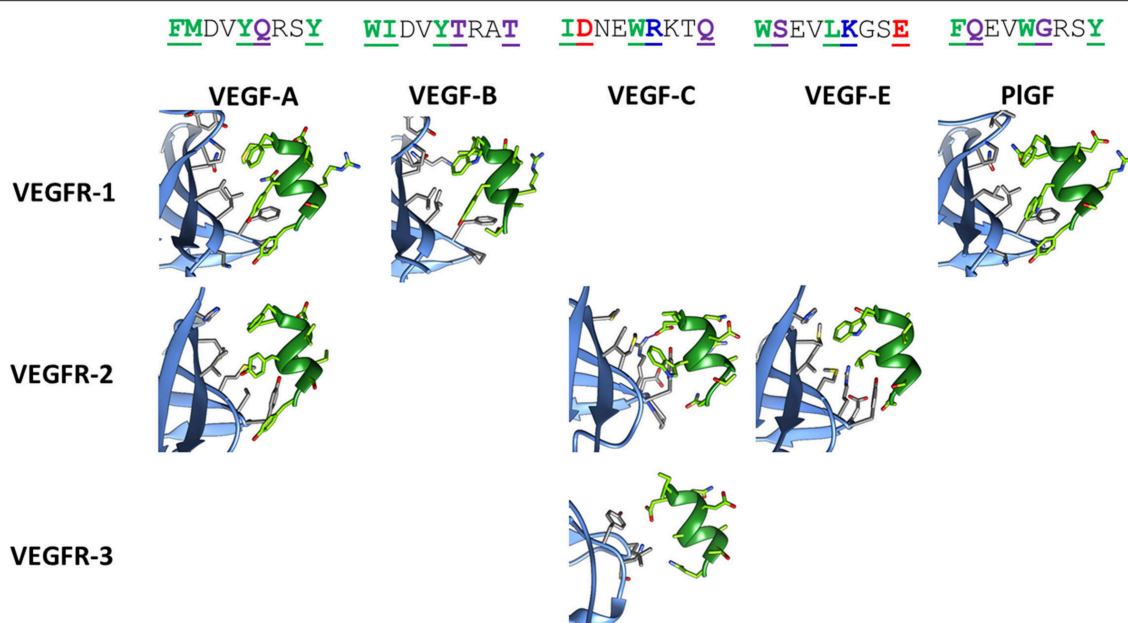


FIGURE 2 | Structures of the helix-interacting interface in VEGF/VEGFR receptor complexes. The receptor is shown in light blue and the growth factor helix in green. The following crystallographic structures were used: 1FLT for VEGF-A/VEGFR-1, 3V2A for VEGF-A/VEGFR-2, 2XAC for VEGF-B/VEGFR-1, 2X1X for VEGF-C/VEGFR-2, 4BSK for VEGF-C/VEGFR-3, 3VSB for VEGF-E/VEGFR-2, 1RV6 for PlGF/VEGFR-1. Sequences of the helix correspond to residues 17–25 for VEGF-A, -B and -E, residues 122–130 for VEGF-C, and residues 25–33 for PlGF. In the sequences, reported on top in the single letter code, interacting residues are underlined, bolded, and colored, according to the following code: green, purple, red, and blue for hydrophobic, polar, anionic, and cationic residues, respectively. The ion bridge formed in the VEGF-C/VEGFR-2 complex is indicated by a purple line.

coded amino acids, evaluating the effect of the substitution on the standard binding free energy. This analysis identified substitution of the first residue from Ile to Trp, and of the last one from Gln to Trp or Val as the only mutations that would lead to a significant predicted improvement in standard binding free energy (>1 kcal/mol). Either hydrophobic substitution at position 1 would maintain the helix-stabilizing cluster identified above, but Trp has a higher intrinsic helix propensity than Ile (Chakrabarty et al., 1994; Pace and Scholtz, 1998). Based on these findings, sequence 2 was designed (Figure 4). Figure 5 shows how the N- and C-terminal Trp residues increase the interactions between helix and receptor.

A more comprehensive computational analysis on the proposed substitutions, carried out by molecular mechanics—Poisson Boltzmann surface area calculations (MM-PBSA) (Hou et al., 2010), confirmed the prediction, showing that the presence of Trp residues at each peptide terminus should indeed lead to an increased binding affinity (Table 2).

C^{α,α}-Disubstituted Amino Acids Can Be Inserted to Increase Peptide Helicity and Stability

C^{α,α}-disubstituted α amino acids strongly stabilize helical structures: due to steric interactions between the gem alkyl and methyl groups linked to the α -carbon, the accessible conformational space of such residues is extremely limited and is located in the region of the Ramachandran plot corresponding to helical structures. For this reason, such C^{α,α}-disubstituted amino acids constitute suitable building blocks to synthesize

oligopeptide with a stable helical folding (Toniolo et al., 2001). In addition, insertion of non-proteinogenic amino acids strongly reduces peptide susceptibility to proteolysis (De Zotti et al., 2009). The simplest and most studied C^{α,α}-disubstituted amino acid residue is α -amino isobutyric acid or Aib. Aib is a natural amino acid featuring two methyl groups on its α -carbon. It is non-ribosomally included in peptide sequences by fungal synthases. This achiral residue is a well-known helix inducer. One peptide sequence modified to include Aib is the well-known commercial drug semaglutide (Al Musaimi et al., 2018). Positions not involved in the interaction (i.e., 3, 4, 7, and 8 in the helix, see above) were considered for possible modifications. Position 2 was analyzed as well, as the C^{α,α}-disubstituted amino acids analogue of Asp, α -methyl-aspartic acid (α -Me)Asp, is commercially available. Although literature reports on the conformational properties of this specific residue are lacking, the preference for helical conformations is a common feature of methyl-containing disubstituted residues, and its homologue (α -Me)Asn was reported to promote type III β turn (i.e., a portion of a 3_{10} helix) in short peptides (Hopkins et al., 2000). Analysis of the structure of the VEGF-C/VEGFR-2 complex showed that addition of a methyl group on the alpha carbon at these positions, or addition of a residue at the N-terminus, would not cause any intermolecular clashes.

Based on these considerations, four analogues were designed, based on sequence 2 (Figure 4). In analogues 5 and 6, Glu4 was substituted by (α -Me)Asp, and Lys7 by the cationic amino acid Api (4-aminopiperidine-4-carboxylic acid). Such cyclic residue can promote a helical conformation to some extent when

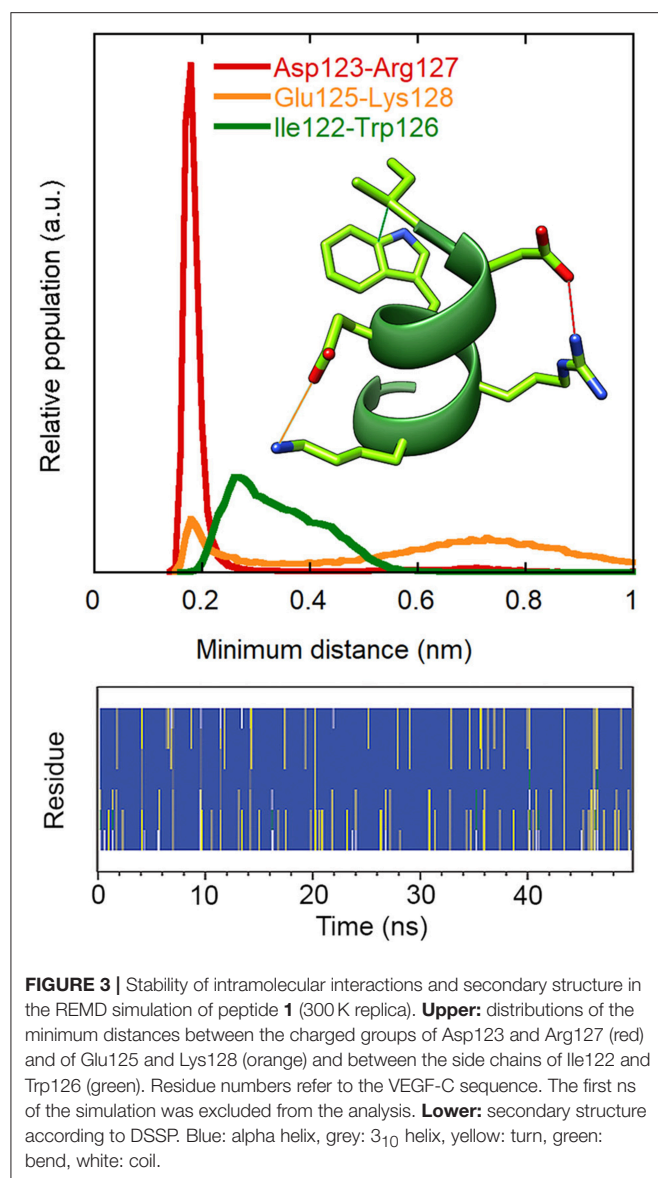


FIGURE 3 | Stability of intramolecular interactions and secondary structure in the REMD simulation of peptide **1** (300 K replica). **Upper:** distributions of the minimum distances between the charged groups of Asp123 and Arg127 (red) and of Glu125 and Lys128 (orange) and between the side chains of Ile122 and Trp126 (green). Residue numbers refer to the VEGF-C sequence. The first ns of the simulation was excluded from the analysis. **Lower:** secondary structure according to DSSP. Blue: alpha helix, grey: 3_{10} helix, yellow: turn, green: bend, white: coil.

incorporated into peptides (Cho et al., 2010; Dalzini et al., 2016). In addition, in peptide **5** Asp2 was substituted by (α -Me)Asp, too, while in **6** an Api residue was added at the N-terminus. In analogue **4**, Aib was inserted at positions 4 and 8, and also added at the N-terminus. For comparison, analogue **3** has been synthesized, with the same sequence of **4**, but without the Trp substitutions.

Synthesis of VEGF-C Derived Peptides 1–6

Peptide sequences **1–6** (Figure 4) were conveniently prepared by solid-phase peptide synthesis (SPPS) on Rink Amide 4-methylbenzhydrylamine (MHBA) resin using the 9-fluorenylmethoxycarbonyl/*t*-butyl ether (Fmoc/*t*Bu) strategy. Each step of the SPPS was performed with a semi-automatic synthesizer, assisting coupling reactions with microwaves. First, the resin was swelled in dimethylformamide (DMF) and

treated with a 25% solution of piperidine in DMF to remove the Fmoc-protecting group, releasing the reactive amino moiety on the beads (step a). The Fmoc-amino acid to be attached to the solid support was activated with *N,N'*-diisopropylcarbodiimide (DIC) and 1-hydroxy-7-azabenzotriazole (HOAt) coupling reagents in the presence of *N,N*-diisopropylethylamine (*i*Pr₂NEt) in DMF: after stirring for 25 min at 0°C, the mixture was added to the resin and a cycle of coupling, capping and deprotection was performed (step b). This procedure was repeated until the sequence was completed, then the N-terminal residue was acetylated and the beads were treated with TFA in the presence of thioanisole, 1,2-ethanedithiol (EDT) and anisole as scavengers. Subsequent purification of the crude peptide with reversed phase high-performance liquid chromatography (RP-HPLC) and freeze-drying from glacial acetic acid gave the pure compound as a fluffy solid.

Due to the high steric congestion, α,α -disubstituted residues are poorly reactive even after activation. For this reason, the coupling reaction was performed twice whenever a quaternary amino acid had to be attached to the resin: according to this synthetic protocol, after the first coupling step, a second aliquot of the activated quaternary amino acid was added to the resin and another condensation reaction was carried out. This procedure allowed to minimize the number of unreacted amino moieties on the beads.

Further details are provided in the Supplementary Information (Figures S2–S14, Tables S1–S6, Scheme S1).

Structural Investigation

Circular dichroism (CD) experiments in water demonstrated that all analogues populate helical conformations in solution to some extent, as predicted by REMD simulations for the natural sequence **1**. As shown in Figure 6, the positive peak at approximately 190 nm, and the negative bands at about 205 and 220 nm, typical of helical structures, are present in the spectra of all analogues (Kelly and Price, 1997). Quantitative determinations of the degree of helicity is complicated by the presence of multiple aromatic residues, whose side-chains can contribute significantly to the CD in the far UV region. However, several features indicate that analogues **5** and **6** are more helical than the other peptides: compared to the spectra of analogues **1–4**, the positive peak is higher, the negative band at short wavelengths is red-shifted and the ratio of the two negative bands at approximately 220 and 205 nm is closer to one (Kelly and Price, 1997). Actually, for **5** this ratio is even higher than one, possibly indicating that some peptide aggregation is taking place (Dai et al., 2004). A stabilizing effect of the introduced $C^{\alpha,\alpha}$ -disubstituted amino acids was less obvious in the spectra of analogues **3** and **4**.

In near UV CD spectra, the induced dichroism band of Trp was more intense for analogues **3–6** than for peptides **1** and **2**, which comprise coded amino acids only. This finding indicates that the $C^{\alpha,\alpha}$ -disubstituted amino acids rigidified the helical conformation. To confirm this conclusion also in the case where far UV CD spectra were less informative, analogues **1** and **3** were directly compared in 2D nuclear magnetic

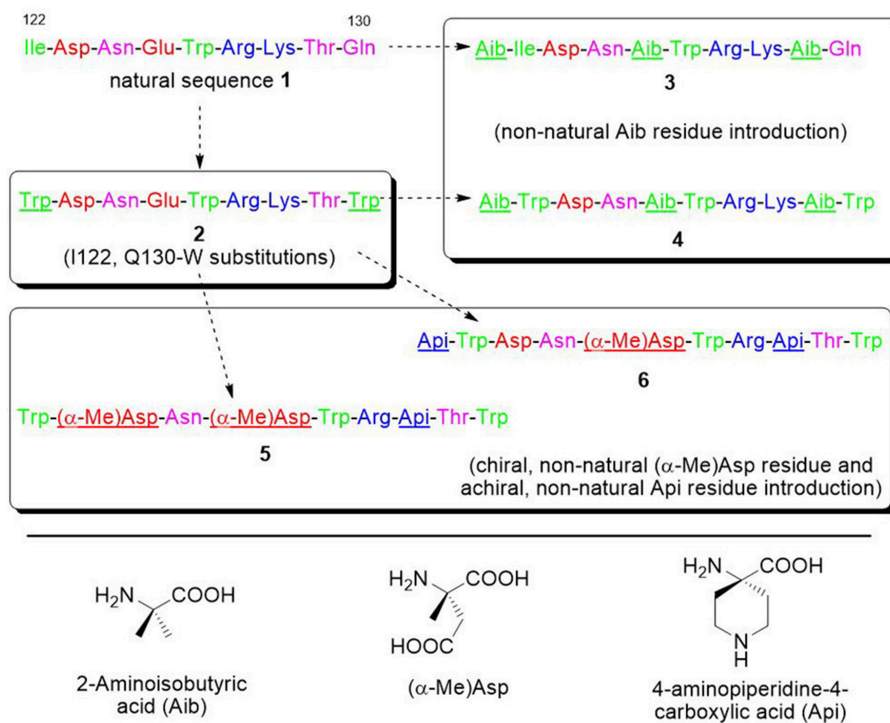


FIGURE 4 | Sequences of the VEGF-C natural portion **1** and of the derived peptides **2–6**. Sequences are colored in green, purple, red, and blue for hydrophobic, polar, anionic, and cationic residues. The introduced modifications are underlined.

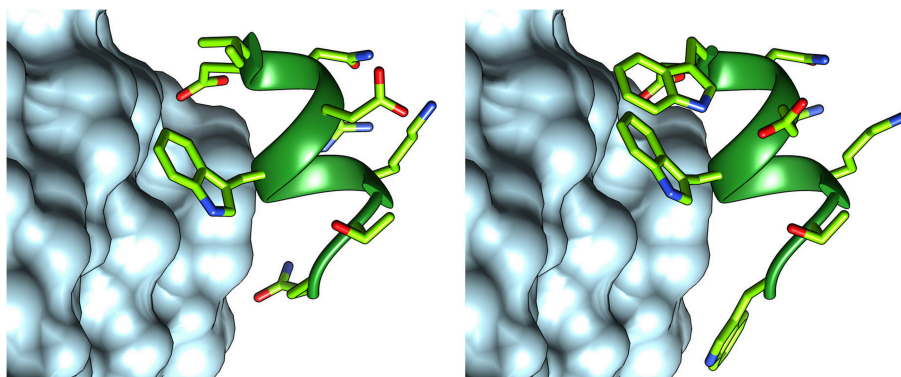


FIGURE 5 | Structures of peptides **1** (left) and **2** (right), interacting with VEGFR-2. The structure of peptide **1** was taken from the VEGF-C structure (PDB code 2X1X), while that of peptide **2** was modeled with FoldX.

TABLE 2 | Results of the MM-PBSA calculations of the interaction of peptides **1** and **2** with VEGFR-2^a.

Peptide	ΔE_{pot} (kcal/mol)	$\Delta G^{\circ}_{\text{PB}}$ (kcal/mol)	ΔSAS (nm ²)	$\Delta G^{\circ}_{\text{binding}}$ (kcal/mol)
1	-32 ± 1	26 ± 1	-3.59 ± 0.02	-8 ± 2
2	-39 ± 1	27 ± 1	-4.42 ± 0.02	-14 ± 2

^aThe various terms are described in the Methods section.

resonance (NMR) measurements in water (Figure 7). For both peptides, all sequential NH-NH cross peaks were present in the

ROESY (Rotating-frame nuclear Overhauser Effect correlation Spectroscopy) spectrum, indicating the onset of a helical structure. However, the spectra did not show any long range connectivity for **1**, while the presence of two long-range cross-peaks (Asp3HA-Aib5HN and Trp6HA-Aib9HN) for peptide **3**, including an $\alpha\text{H}_i \rightarrow \text{NH}_{i+2}$ interaction, is a clear indication that this analogue adopts a well-developed 3_{10} -helical conformation in water.

Overall, these data indicate that the introduction of $\text{C}^{\alpha,\alpha}$ -disubstituted amino acids stabilized the helical conformations, particularly in analogs **5** and **6**, where chiral (α -Me)Asp residues were inserted in the sequence.

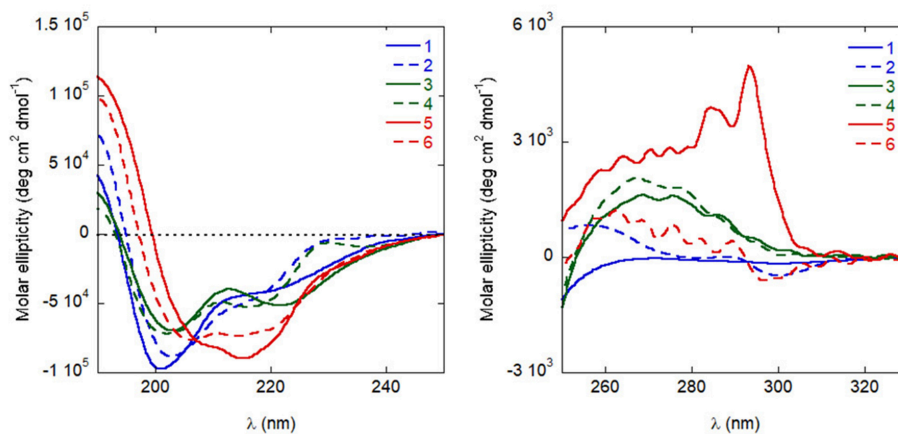


FIGURE 6 | CD spectra of the peptides in distilled H₂O (10⁻⁴ M), in the far UV (**left**) and near UV (**right**).

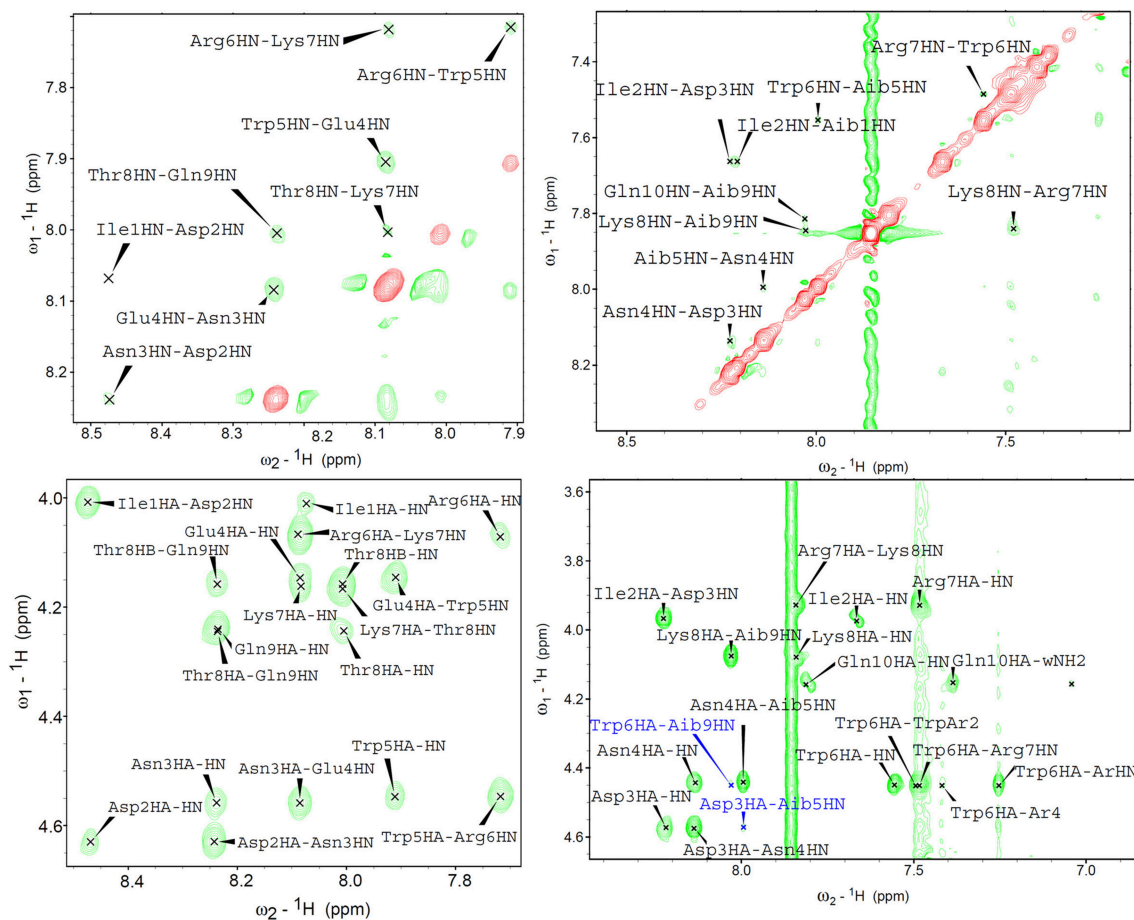


FIGURE 7 | 2D proton NMR ROESY spectra in H₂O:D₂O 9:1 (600 MHz, 298K) for compounds **1** (**left**) and **3** (**right**) (concentrations 1.1 and 1.4 mM, respectively). Top panels report NH-NH sequential correlations, while the bottom panels correspond to the fingerprint region showing long-range αH-NH correlations. In the case of compound **3**, long range cross-peaks, including the αH_{*i*} → NH_{*i*+2} diagnostic of 3₁₀-helical structures, are highlighted in blue.

Biological Studies

Inhibition of VEGF-A/VEGFR-1 Complex Formation *in vitro*

A chemiluminescent assay to determine the inhibition of complex formation between VEGF-A (isoform VEGF₁₆₅) and the extracellular domain of VEGFR-1 (Goncalves et al., 2007; García-Aranda et al., 2013) had been previously employed in our group (Zanella et al., 2015). VEGF-C (from which analogue 1 was derived) is not selective for VEGFR-1 (Su et al., 2007), but unfortunately the same assay protocol turned out to be ineffective with VEGFR-2, at least in our hands. The assay based on VEGFR-1 was therefore applied here as a very stringent test of the affinity of our peptides for VEGFRs, and to assess the different peptides comparatively. All peptides were able to inhibit complex formation (Table 3), although in the high micromolar range. The introduction of quaternary amino acids resulted in a beneficial effect in terms of affinity toward VEGFR-1, with analogs 3, 5 and 6 being the most effective. Further studies were focused on analogues 5 and 6, considering also the higher stability of their secondary structure, which affects resistance to proteolytic degradation.

Resistance to Proteolytic Degradation

Peptides 5 and 6 were very stable against proteases, presumably thanks to the presence of non-natural amino acids in their sequences and to their stable secondary structure. HPLC analysis (Figures S15–S24) demonstrated that peptide 5 was fully stable to trypsin, chymotrypsin and pronase for 90 minutes and it persisted even after many days, although some degradation was slowly occurring. Peptide 6 was fully stable even after 6 days. By contrast, the natural sequence 1 was degraded within 15 min by all three enzymes.

Inhibition of HUVEC Morphogenesis

The ability of peptides 5 and 6 to affect neovessel formation *in vitro* was investigated on HUVECs according to the previously reported procedure (Fanelli et al., 2014). Experiments were performed in the presence of peptide 5 or 6 under resting (absence of stimuli) or stimulated (VEGF₁₆₅) conditions. As expected, under resting conditions, HUVECs did not show any significant network formation, while the presence of VEGF₁₆₅ induced a strong increase in loop and branches formation (Figure 8). Pre-incubation with either 5 or 6 significantly reduced VEGF₁₆₅-induced loop and branches formation and

this effect was concentration-dependent, reaching statistical significance at 10 nM for loop and 1 μ M for branches formation (Figure 8). Interestingly, these values are much lower than the concentrations needed to inhibit VEGF-A/VEGFR-1 association, possibly indicating a significant selectivity toward VEGFR-2. It is worth noting that inhibition of loop formation was more marked for analogue 5 than for 6, at all concentrations tested.

DISCUSSION

Several peptides able to bind to VEGFRs have been reported in the literature. Some of them were identified by library screening or phage display approaches, while others were developed by rational design, reproducing different epitopes of the VEGFR interacting surface of VEGFs. However, most of these studies were focused on mimicking VEGF-A, which is traditionally considered the master regulator of angiogenesis through VEGFR-2 binding (Ferrara and Adamis, 2016). In particular, all helical foldamers mimicking the N-terminal helix were developed based exclusively on the interacting elements of VEGF-A, i.e., hydrophobic residues only. Examples include the MA peptide (Diana et al., 2013) and peptides developed by Pérez De Vega and coworkers (García-Aranda et al., 2013; Balsera et al., 2017). Due to their hydrophobic driving force for association, these peptides are prone to selectivity issues, since binding sites for amphipathic helical peptides are extremely common at protein-protein interfaces (Bonache et al., 2014). It is also worth mentioning that some of the peptides modeled on the VEGF-A helix exhibited pro-angiogenic, rather than anti-angiogenic, activity (De Rosa et al., 2018).

In the present study, from an analysis of the available crystallographic structures of VEGFs/VEGFRs complexes, we noted that the same helix in VEGF-C exhibits several interesting features, including an intermolecular salt bridge with VEGFR-2, and multiple intramolecular helix-stabilizing interactions. For these reasons, we focused our study on the VEGF-C sequence.

VEGF-C binds to both VEGFR-2 and VEGFR-3 (Su et al., 2007; Leppänen et al., 2010; Chen et al., 2013; Wang and Tsai, 2015). Traditionally, regulation of lymphangiogenesis through association with VEGFR-3 has been considered its prevalent activity. Indeed, VEGF-C expression is closely related to lymphangiogenesis and lymphatic metastasis in a variety of human tumors (Chen et al., 2013). However, more recently, VEGF-C has been demonstrated to play an important role also in the regulation of physiological and pathological angiogenesis (Chen et al., 2013). In addition, it has fundamental functions in the autocrine signaling of cancer cells. VEGF-C is expressed in a number of human malignancies, and high levels of expression correlate with poor prognosis (Chen et al., 2013). Autocrine VEGF-C signaling regulates cell invasion, proliferation, and resistance to chemotherapy (Su et al., 2007). VEGF-C can also modulate the immune system so that tumor cells more easily escape immune surveillance (Wang and Tsai, 2015). A very recent, groundbreaking article (Michaelsen et al., 2018; Niclou, 2018), identified VEGF-C, rather than VEGF-A, as the main responsible for autocrine VEGFR-2 activation and cell

TABLE 3 | Inhibition of biotinylated VEGF₁₆₅ binding to isolated VEGFR-1.

Peptide	% Inhibition ^a
1	27 ± 1
2	29 ± 7
3	86 ± 1
4	40 ± 10
5	82 ± 1
6	83 ± 3

^a % of inhibition of biotinylated VEGF₁₆₅ binding to VEGFR-1 at 500 μ M.

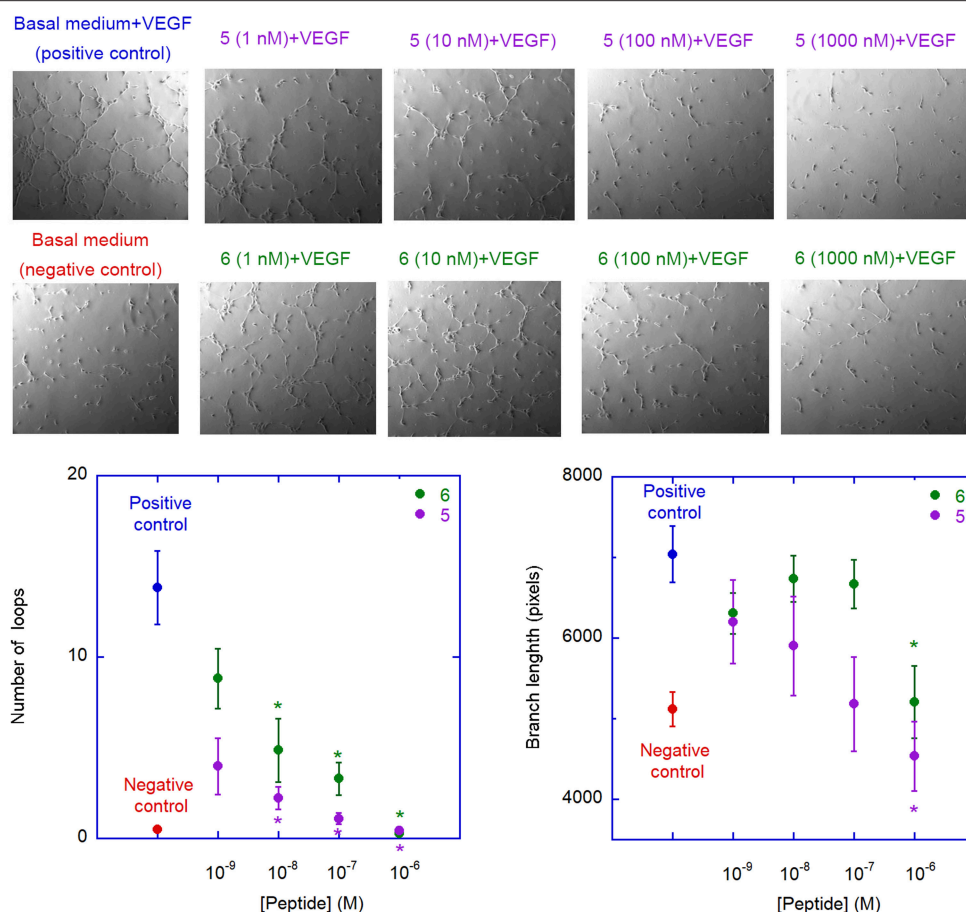


FIGURE 8 | Antiangiogenic activity of analogues **5** and **6**. The images are representative phase contrast photomicrographs of HUVECs plated on Matrigel under resting conditions (lower left) or after stimulation with VEGF₁₆₅, 10 ng/mL (upper left); the effect of VEGF on loop formation, in comparison to medium alone, is clearly evident in the upper panel. **5** (upper panels) and **6** (lower panels) were added at different concentration on VEGF-stimulated cells; both **5** and **6** are able to reduce, in a concentration-dependent manner, the ability of VEGF to induce loops formation. The graphs describe the effect of addition of **5** (purple) and **6** (green) on VEGF-induced neovessel formation measured as total number of loops (left graph) or total branch length (right graph). Data are expressed as mean \pm SEM of 5 separate experiments. Asterisks indicate significant differences with respect to the positive control (basal medium + VEGF), with $p < 0.05$, according to a two-tailed paired t -test. Negative controls (basal medium only) are also shown.

proliferation in glioblastoma. In this study, VEGF-C silencing was superior to bevacizumab therapy in improving tumor control. Interestingly, bevacizumab treatment increased VEGF-C expression (Michaelsen et al., 2018), and up-regulation of VEGF-C has been observed in tumor cells that have acquired resistance to anti-VEGF-A therapy (Wang and Tsai, 2015), suggesting that VEGF-C may compensate for VEGF-A depletion. For all these reasons, molecules inhibiting VEGF-C signaling, rather than, or in addition to VEGF-A interactions, might find important therapeutic applications. In principle, our peptides, based on the VEGF-C helix, can compete with both growth factors for binding to the receptors.

The VEGF-C nonapeptide helix sequence has some intrinsic helix propensity, but CD and NMR studies demonstrated that insertion of $C^{\alpha,\alpha}$ -disubstituted amino acids led to a significant stabilization of the secondary structure. In

particular, analogues **5** and **6**, containing the chiral (α -Me)Asp amino acids, had a more stable helical conformation than peptides **3** and **4**, where achiral Aib residues were introduced. Peptides comprising these modifications were highly resistant to proteolytic degradation, and stabilization of the helical conformation probably contributed to favor receptor binding, by reducing the entropic cost of the association process. Indeed, these molecules were able to bind even receptor VEGFR-1, where specific ion-pair interactions are not possible, although in the high micromolar range. More importantly, they inhibited VEGF-induced morphogenesis in the low nM range, possibly through their interaction with the VEGFR-2 receptor.

One point worth mentioning is that the N-terminal VEGF helix, mimicked by our peptides, is involved also in the interface of the growth factor dimer (see **Figure 1**). Therefore, inhibition

of VEGF dimerization could contribute to the antiangiogenic activity of the compounds developed here.

Further studies are warranted to characterize the interaction of the designed peptides with different VEGFRs and the molecular mechanisms of their antiangiogenic activity. However, our data clearly indicate that the development of antiangiogenic folded synthetic peptides inspired by the VEGF-C N-terminal helix might open the way to a novel class of anticancer agents.

METHODS

In silico Mutagenesis

in silico alanine scanning was performed with FoldX 4.0 (Schymkowitz et al., 2005) and the DrugScorePPI (Krüger and Gohlke, 2010), KFC2 (Zhu and Mitchell, 2011), and PCRPI (Segura Mora et al., 2010) servers. *In silico* mutagenesis was performed with FoldX, by first repairing the PDB file (PDB code 2X1X), then introducing the mutations and finally calculating the complex standard binding free energy, and subtracting the value of the WT complex. Structural images were obtained using the Chimera software (Pettersen et al., 2004).

Molecular Dynamics Simulations

Molecular dynamics (MD) simulations were carried out by using the GROMACS 4.6.3 software package (Hess et al., 2008). The ff53a6 parameters (Oostenbrink et al., 2004) were adopted for the complexes and the SPC model (Berendsen et al., 1981) was used for the water molecules. Short-range electrostatic interactions were cut-off at 1.2 nm and long range electrostatic interactions were calculated using the particle mesh Ewald (PME) algorithm (Essmann et al., 1995). Simulations were run with a 2 fs time step. The Berendsen algorithm was used to keep temperature and pressure constant (Berendsen et al., 1984). Bond lengths were constrained with the LINCS algorithm (Hess et al., 1997). The structure with PDB code 2X1X from the Protein Data Bank was used as a starting point for the simulations. After solvating the proteins with roughly 6500 water molecules and an opportune number of Na⁺ and Cl⁻ ion to ensure electroneutrality in a box of about 180 nm³, the potential energy of the systems was minimized. A multi-step procedure was adopted for equilibration, first constraining both the protein and the peptide, then releasing the constraints on the peptide conformation, and finally removing all constraints. In each step, the temperature was gradually raised from 50 K to 300 K in 8 ns, and the conformation with the most favorable peptide-protein interaction energy was selected as the starting structure for the successive step. Finally, 50 ns production runs were performed.

MM-PBSA Calculations

The protein-peptide binding energies were obtained from MD simulations by using the MM-PBSA protocol. The binding free energies were calculated according to the following equation

$$\Delta G_{\text{binding}}^{\circ} = G_{\text{complex}}^{\circ} - G_{\text{receptor}}^{\circ} - G_{\text{ligand}}^{\circ}$$

In these free energy values, the potential energy terms were obtained by using the GROMACS *g_energy* tool. The

electrostatic solvation terms were calculated with the APBS software (Baker et al., 2001). The dielectric constant was set equal to 78.54 for water and 2 for the solute. The input files for APBS were generated with the PDB2PQR server (Dolinsky et al., 2004).

The non-polar solvation energies were computed as

$$G_{\text{surf}}^{\circ} = \gamma \text{ SAS}$$

in which γ was set equal to 0.543 kcal mol⁻¹ nm⁻² (Fogolari et al., 2003), solvent accessible surface (SAS) values were obtained by using the *g_sas* tool of GROMACS.

REMD Simulations

REMD simulations were performed using the GROMACS software package. An extended conformation was used as the starting structure. After minimization and equilibration, 16 replicas were simulated with temperatures ranging from 260 to 650 K, chosen to ensure an exchange probability between replicas equal to 55% (Patriksson and van der Spoel, 2008); exchanges were attempted every 2 ps and the simulation time of each replica was 50 ns. The Amber FF99-SB parameters were used to describe the peptide (Hornak et al., 2006) and the OBC (Onufriev, Bashford, and Case) GBSA implicit solvent model (Onufriev et al., 2004) was used to mime the solvent. Bond lengths were constrained with the SHAKE algorithm (Ryckaert et al., 1977) and simulations were run with a 2-fs time step. Temperatures were kept constant by using the velocity-rescale algorithm (Bussi et al., 2007). Secondary structure was assigned by means of Dictionary of Protein Secondary Structures (DSSP) (Kabsch and Sander, 1983). The *g_mindist* tool in GROMACS was used to calculate the minimum distances between groups of atoms.

SPPS

Semi-automatic SPPS was accomplished through the Biotage[®] Initiator[™] synthesizer, assisted by microwave (MW) irradiation; Fmoc/*t*Bu strategy and Rink Amide MHBA Resin (100–200 mesh; loading: 0.5 mmol/g) were used. Peptides were obtained with yields up to 30% and purities between 97% and >99%. Refer to the Supporting Information for a detailed description of materials, procedures, and methods.

CD

Jasco J-715 (Tokyo, Japan) spectropolarimeter—equipped with a Haake thermostat (Thermo Fisher Scientific, Waltham, MA)—was used to collect circular dichroism spectra. Bidistilled water was used as solvent. Fused quartz cells of either 1 or 10 mm pathlength (Hellma, Mühlheim, Germany) were used. Spectra were baseline subtracted as expressed in terms of $[\theta]_T$, total molar ellipticity (deg × cm² × dmol⁻¹).

NMR

2D-NMR experiments for conformational studies were carried out on a Bruker Avance DMX-600 instrument, using TOPSPIN 1.3 software package. For peptide **3**, COSY (COReLation SpectroscopY), CLEAN-TOCSY (TOtal COReLation SpectroscopY), and ROESY spectra (all with watergate for water suppression) were acquired.

COSY was phase sensitive. TOCSY spectrum (spin-lock pulse, 70 ms) was acquired by collecting 400 recordings of 76 scans each. For the ROESY spectrum (200 ms mixing time), 512 experiments, each one consisting of 80 scans, were acquired. The full assignment was achieved exploiting the procedure proposed by K. Wüthrich (Wüthrich, 1986).

Inhibition of VEGF/VEGFR Complex Formation *in vitro*

The chemiluminescent screening assay for the detection of VEGFR-1 ligands was accomplished according to the procedure described in the Supporting Information. Unlabeled VEGF₁₆₅, employed as reference compound, showed an IC₅₀ value of 146 pM (Zanella et al., 2015), comparable with the previously reported value (Goncalves et al., 2007).

Inhibition of HUVEC Morphogenesis

To assess angiogenic activity, HUVECs (2.5×10^4 cells) were seeded in a 24-well plate coated with 100 μ L/well of Matrigel previously polymerized for 1 h at 37°C. Cells were then incubated for 5 h at 37°C in a moist atmosphere of 5% CO₂. The experiments were performed without or in the presence of **5** and **6** under either resting (absence of stimuli, cell cultured in EndoGRO medium alone, without FBS and all the growth factors) or stimulated conditions (addition of VEGF₁₆₅, 10 ng/mL). Network formation was evaluated by phase-contrast microscopy using a fluorescence microscope (AxioVert 40CFL, Carl Zeiss S.p.A. Milan, Italy). Five photos of each well were recorded with 10X magnification. Network formation was finally quantified in terms of mean number of loops per field as topological parameters and the total length of the branches. For the purpose of the analysis, loops were defined as any complete ring formed by HUVECs, while open ramifications were considered as branches. The analysis of the images was performed using the free software ImageJ (<https://imagej.nih.gov/ij/>).

Resistance to Proteolytic Degradation

The proteolytic stability of peptides **1**, **5**, and **6** was assessed against three enzymes: pronase, trypsin and chymotrypsin (Sigma-Aldrich). Each peptide was dissolved in the appropriate buffer [i.e., (2-amino-2-hydroxymethyl-propane-1,3-diol (Tris)·HCl 20 mM, containing 20 mM CaCl₂ pH 7.6 for pronase; Tris·HCl 50 mM, pH 7.8 for trypsin and chymotrypsin). Then,

it was incubated with and without the enzyme solution (1.25 μ g of enzyme in 150 mL buffer) at 37°C for 12 h. The mixture was analyzed by RP-HPLC (column: Phenomenex Jupiter 5 μ C18 300 Å) every ten minutes for the first hour, then every half hour. Gradients: 5–25%B in 10 min for peptide **1**; 15–35%B in 10 min for peptide **5**; 15–25%B in 10 min for peptide **6**. Eluants: A, H₂O:CH₃CN 9/1 + 0.05% trifluoroacetic acid (TFA); B: CH₃CN:H₂O 9/1 + 0.05% TFA.

DATA AVAILABILITY

All datasets generated for this study are included in the manuscript and/or the **Supplementary Files**.

AUTHOR CONTRIBUTIONS

SZ, LP, and GS synthesized the peptides. GB, together with SR, AP, and LS, performed the *in silico* studies. MD carried out the conformational studies. DA designed and performed the binding experiments and FM determined the biological activity of the synthesized compounds. AS performed proteolytic stability assays. LB and UP supervised the binding and activity studies, FF the structural characterization, CG the peptide synthesis, LS conceived the original idea and supervised peptide design. SZ, LB, and LS wrote the manuscript. All authors discussed the results and commented on the manuscript.

FUNDING

This project was supported by the Italian Ministry of Education, Universities and Research, grant PRIN 20157WW5EH. LS, GB, and AP acknowledge support from AIRC, IG2016 19171 and from PRACE (grant 2017174118), which awarded computational resources at CINECA, Italy.

ACKNOWLEDGMENTS

We thank Dr. Monica Pinoli for technical assistance in the processing of the optical microscopy images of morphogenesis.

SUPPLEMENTARY MATERIAL

The Supplementary Material for this article can be found online at: <https://www.frontiersin.org/articles/10.3389/fchem.2019.00170/full#supplementary-material>

REFERENCES

- Al Musaimi, O., Al Shaer, D., de la Torre, B. G., and Albericio, F. (2018). 2017 FDA peptide harvest. *Pharmaceuticals* 11:42. doi: 10.3390/ph11020042
- Baker, N. A., Sept, D., Joseph, S., Holst, M. J., and McCammon, J. A. (2001). Electrostatics of nanosystems: application to microtubules and the ribosome. *Proc. Natl. Acad. Sci. U.S.A.* 98, 10037–10041. doi: 10.1073/pnas.181342398
- Balsara, B., Bonache M^Á, M., Reille-Seroussi, M., Gagey-Eilstein, N., Vidal, M., González-Muñiz, R., et al. (2017). Disrupting VEGF-VEGFR1 interaction: de novo designed linear helical peptides to mimic the VEGF13-25 fragment. *Molecules* 22:1846. doi: 10.3390/molecules22111846
- Basile, A., Del Gatto, A., Diana, D., Di Stasi, R., Falco, A., Festa, M., et al. (2011). Characterization of a designed vascular endothelial growth factor receptor antagonist helical peptide with antiangiogenic activity *in vivo*. *J. Med. Chem.* 54, 1391–1400. doi: 10.1021/jm101435r
- Berendsen, H. J., Postma, J. P., van Gunsteren, W. F., and Hermans, J. (1981). "Interaction models for water in relation to protein hydration," in *Intermolecular Forces* ed B. Pullman (Dordrecht: Springer), 331–342.
- Berendsen, H. J., Postma, J. V., van Gunsteren, W. F., DiNola, A., and Haak, J. R. (1984). Molecular dynamics with coupling to an external bath. *J. Chem. Phys.* 81, 3684–3690. doi: 10.1063/1.448118

- Bonache, M. A., Balsera, B., López-Méndez, B., Millet, O., Brancaccio, D., Gómez-Monterrey, I., et al. (2014). De novo designed library of linear helical peptides: an exploratory tool in the discovery of protein–protein interaction modulators. *ACS Comb. Sci.* 16, 250–258. doi: 10.1021/co500005x
- Bussi, G., Donadio, D., and Parrinello, M. (2007). Canonical sampling through velocity rescaling. *J. Chem. Phys.* 126:014101. doi: 10.1063/1.2408420
- Carmeliet, P., and Jain, R. K. (2011). Principles and mechanisms of vessel normalization for cancer and other angiogenic diseases. *Nat. Rev. Drug Discov.* 10, 417–427. doi: 10.1038/nrd3455
- Chakraborty, A., Kortemme, T., and Baldwin, R. L. (1994). Helix propensities of the amino acids measured in alanine-based peptides without helix-stabilizing side-chain interactions. *Protein Sci.* 3, 843–852. doi: 10.1002/pro.5560030514
- Chames, P., Van Regenmortel, M., Weiss, E., and Baty, D. (2009). Therapeutic antibodies: successes, limitations and hopes for the future. *Br. J. Pharmacol.* 157, 220–233. doi: 10.1111/j.1476-5381.2009.00190.x
- Chen, J. C., Chang, Y. W., Hong, C. C., Yu, Y. H., and Su, J. L. (2013). The role of the VEGF-C/VEGFRs axis in tumor progression and therapy. *Int. J. Mol. Sci.* 14, 88–107. doi: 10.3390/ijms14010088
- Cho, J. I., Tanaka, M., Sato, S., Kinbara, K., and Aida, T. (2010). Oligo (4-aminopiperidine-4-carboxylic acid): an unusual basic oligopeptide with an acid-induced helical conformation. *J. Am. Chem. Soc.* 132, 13176–13178. doi: 10.1021/ja106118w
- Dai, Q., Castellino, F. J., and Prorok, M. (2004). A single amino acid replacement results in the Ca²⁺-induced self-assembly of a helical conantokin-based peptide. *Biochemistry* 43, 13225–13232. doi: 10.1021/bi048796s
- Dalchini, A., Bergamini, C., Biondi, B., De Zotti, M., Panighel, G., Fato, R., et al. (2016). The rational search for selective anticancer derivatives of the peptide Trichogin GA IV: a multi-technique biophysical approach. *Sci. Rep.* 6:24000. doi: 10.1038/srep24000
- Danhier, F., Le Breton, A., and Pr  at, V. (2012). RGD-based strategies to target α (v) β (3) integrin in cancer therapy and diagnosis. *Mol. Pharm.* 9, 2961–2973. doi: 10.1021/mp3002733
- De Rosa, L., Di Stasi, R., and D'Andrea, L. D. (2018). Pro-angiogenic peptides in biomedicine. *Arch. Biochem. Biophys.* 660, 72–86. doi: 10.1016/j.abb.2018.10.010
- De Zotti, M., Biondi, B., Formaggio, F., Toniolo, C., Stella, L., Park, Y., et al. (2009). Trichogin GA IV: an antibacterial and protease-resistant peptide. *J. Pept. Sci.* 15, 615–619. doi: 10.1002/psc.1135
- Desgrosellier, J. S., and Cheresch, D. A. (2010). Integrins in cancer: biological implications and therapeutic opportunities. *Nat. Rev. Cancer* 10, 9–22. doi: 10.1038/nrc2748
- Diana, D., Di Stasi, R., De Rosa, L., Isernia, C., D'Andrea, L., and Fattorusso, R. (2013). Structural investigation of the VEGF receptor interaction with a helical antagonist peptide. *J. Pept. Sci.* 19, 214–219. doi: 10.1002/psc.2480
- Dolinsky, T. J., Nielsen, J. E., McCammon, J. A., and Baker, N. A. (2004). PDB2PQR: an automated pipeline for the setup of Poisson–Boltzmann electrostatics calculations. *Nucleic Acids Res.* 32, W665–W667. doi: 10.1093/nar/gkh381
- Essmann, U., Perera, L., Berkowitz, M. L., Darden, T., Lee, H., and Pedersen, L. G. (1995). A smooth particle mesh Ewald method. *J. Chem. Phys.* 103, 8577–8593. doi: 10.1063/1.470117
- Fanelli, R., Schembri, L., Piarulli, U., Pinoli, M., Rasini, E., Paolillo, M., et al. (2014). Effects of a novel cyclic RGD peptidomimetic on cell proliferation, migration and angiogenic activity in human endothelial cells. *Vascular Cell* 6:11. doi: 10.1186/2045-824X-6-11
- Ferrara, N., and Adams, A. P. (2016). Ten years of anti-vascular endothelial growth factor therapy. *Nat. Rev. Drug Discov.* 15, 385–403. doi: 10.1038/nrd.2015.17
- Ferrara, N., Gerber, H. P., and LeCouter, J. (2003). The biology of VEGF and its receptors. *Nat. Med.* 9, 669–676. doi: 10.1038/nm0603-669
- Ferrara, N., Hillan, K. J., Gerber, H. P., and Novotny, W. (2004). Discovery and development of bevacizumab, an anti-VEGF antibody for treating cancer. *Nat. Rev. Drug Discov.* 3, 391–400. doi: 10.1038/nrd1381
- Fogolari, F., Brigo, A., and Molinari, H. (2003). Protocol for MM/PBSA molecular dynamics simulations of proteins. *Biophys. J.* 85, 159–166. doi: 10.1016/S0006-3495(03)74462-2
- Garc  a-Aranda, M. I., Gonz  lez-L  pez, S., Santiveri, C. M., Gagey-Eilstein, N., Reille-Seroussi, M., Mart  n-Mart  nez, M., et al. (2013). Helical peptides from VEGF and Vammin hotspots for modulating the VEGF–VEGFR interaction. *Org. Biomol. Chem.* 11, 1896–1905. doi: 10.1039/c3ob27312a
- Gautier, B., Goncalves, V., Diana, D., Di Stasi, R., Teillet, F., Lenoir, C., et al. (2010). Biochemical and structural analysis of the binding determinants of a vascular endothelial growth factor receptor peptidic antagonist. *J. Med. Chem.* 53, 4428–4440. doi: 10.1021/jm1002167
- Goncalves, V., Gautier, B., Garbay, C., Vidal, M., and Inguibert, N. (2007). Development of a chemiluminescent screening assay for detection of vascular endothelial growth factor receptor 1 ligands. *Anal. Biochem.* 366, 108–110. doi: 10.1016/j.ab.2007.03.027
- Henninot, A., Collins, J. C., and Nuss, J. M. (2018). The current state of peptide drug discovery: back to the future?. *J. Med. Chem.* 61, 1382–1414. doi: 10.1021/acs.jmedchem.7b00318
- Hess, B., Bekker, H., Berendsen, H. J., and Fraaije, J. G. (1997). LINCS: a linear constraint solver for molecular simulations. *J. Comp. Chem.* 18, 1463–1472. doi: 10.1002/(SICI)1096-987X(199709)18:12<1463::AID-JCC4>3.0.CO;2-H
- Hess, B., Kutzner, C., Van Der Spoel, D., and Lindahl, E. (2008). GROMACS 4: algorithms for highly efficient, load-balanced, and scalable molecular simulation. *J. Chem. Theory Comput.* 4, 435–447. doi: 10.1021/ct700301q
- Hoeben, A., Landuyt, B., Highley, M. S., Wildiers, H., van Oosterom, A. T., and De Bruijn, E. A. (2004). Vascular endothelial growth factor and angiogenesis. *Pharmacol. Rev.* 56, 549–580. doi: 10.1124/pr.56.4.3
- Hopkins, S. A., Konopelski, J. P., Olmstead, M. M., and Banks, H. D. (2000). Conformational analysis of peptides containing enantiomerically pure α -methylasparagine: correspondence between computed and solid state structures. *Tetrahedron* 56, 9733–9737. doi: 10.1016/S0040-4020(00)00880-2
- Hornak, V., Abel, R., Okur, A., Strockbine, B., Roitberg, A., and Simmerling, C. (2006). Comparison of multiple Amber force fields and development of improved protein backbone parameters. *Proteins Struct. Funct. Gen.* 65, 712–725. doi: 10.1002/prot.21123
- Hou, T., Wang, J., Li, Y., and Wang, W. (2010). Assessing the performance of the MM/PBSA and MM/GBSA methods. 1. The accuracy of binding free energy calculations based on molecular dynamics simulations. *J. Chem. Inf. Model.* 51, 69–82. doi: 10.1021/ci100275a
- Howard, D. H., Bach, P. B., Berndt, E. R., and Conti, R. M. (2015). Pricing in the market for anticancer drugs. *J. Econ. Perspect.* 29, 139–162. doi: 10.1257/jep.29.1.139
- Johannessen, T. C., Wagner, M., Straume, O., Bjerkvig, R., and Eikesdal, H. P. (2013). Tumor vasculature: the Achilles' heel of cancer? *Expert Opin. Ther. Targets* 17, 7–20. doi: 10.1517/14728222.2013.730522
- Kabsch, W., and Sander, C. (1983). Dictionary of protein secondary structure: pattern recognition of hydrogen-bonded and geometrical features. *Biopolymers* 22, 2577–2637. doi: 10.1002/bip.360221211
- Kelly, S. M., and Price, N. C. (1997). The application of circular dichroism to studies of protein folding and unfolding. *Biochim. Biophys. Acta Protein Struct. Mol. Enzymol.* 1338, 161–185. doi: 10.1016/S0167-4838(96)00190-2
- Kr  ger, D. M., and Gohlke, H. (2010). DrugScore^{PP1} webserver: fast and accurate *in silico* alanine scanning for scoring protein–protein interactions. *Nucleic Acids Res.* 38, W480–W486. doi: 10.1093/nar/gkq471
- Lepp  nen, V. M., Prota, A. E., Jeltsch, M., Anisimov, A., Kalkkinen, N., Strandin, T., et al. (2010). Structural determinants of growth factor binding and specificity by VEGF receptor 2. *Proc. Natl. Acad. Sci. U.S.A.* 107, 2425–2430. doi: 10.1073/pnas.0914318107
- Lepp  nen, V. M., Tvorogov, D., Kisko, K., Prota, A. E., Jeltsch, M., Anisimov, A., et al. (2013). Structural and mechanistic insights into VEGF receptor 3 ligand binding and activation. *Proc. Natl. Acad. Sci. U.S.A.* 110, 12960–12965. doi: 10.1073/pnas.1301415110
- Li, B., Fuh, G., Meng, G., Xin, X., Gerritsen, M. E., Cunningham, B., et al. (2000). Receptor-selective variants of human vascular endothelial growth factor. *J. Biol. Chem.* 275, 29823–29828. doi: 10.1074/jbc.M002015200
- Mich  elsen, S. R., Staberg, M., Pedersen, H., Jensen, K. E., Majewski, W., Broholm, H., et al. (2018). VEGF-C sustains VEGFR2 activation under bevacizumab therapy and promotes glioblastoma maintenance. *Neuro Oncol.* 20, 1462–1474. doi: 10.1093/neuonc/noy103

- Mizejewski, G. J. (1999). Role of integrins in cancer: survey of expression patterns. *Proc. Soc. Exp. Biol. Med.* 222, 124–138. doi: 10.1046/j.1525-1373.1999.d01-122.x
- Segura Mora, J., Assi, S. A., and Fernandez-Fuentes, N. (2010). Presaging critical residues in protein interfaces-web server (PCRPI-W): a web server to chart hot spots in protein interfaces. *PLoS ONE* 5:e12352. doi: 10.1371/journal.pone.0012352
- Muller, Y., Li, B., Christinger, H., Wells, J., Cunningham, B., and de Vos, A. (1997). Vascular endothelial growth factor: crystal structure and functional mapping of the kinase domain receptor binding site. *Proc. Natl. Acad. Sci. U.S.A.* 94, 7192–7197. doi: 10.1073/pnas.94.14.7192
- Musumeci, F., Radi, M., Brullo, C., and Schenone, S. (2012). Vascular endothelial growth factor (VEGF) receptors: drugs and new inhibitors. *J. Med. Chem.* 55, 10797–10822. doi: 10.1021/jm301085w
- Nasir, A. (2019). “Angiogenic signaling pathways and anti-angiogenic therapies in human cancer,” in *Predictive Biomarkers in Oncology* eds S. Badve, G. Kumar (Cham: Springer), 243–262
- Niclou, S. P. (2018). Revival of the VEGF ligand family? *Neuro Oncol.* 20, 1421–1422. doi: 10.1093/neuonc/noy127
- Olsson, A. K., Dimberg, A., Kreuger, J., and Claesson-Welsh, L. (2006). VEGF receptor signalling — in control of vascular function. *Nat. Rev. Mol. Cell Biol.* 7, 359–371. doi: 10.1038/nrm1911
- Onufriev, A., Bashford, D., and Case, D. A. (2004). Exploring protein native states and large-scale conformational changes with a modified generalized born model. *Proteins Struct. Funct. Genet.* 55, 383–394. doi: 10.1002/prot.20033
- Oostenbrink, C., Villa, A., Mark, A. E., and Van Gunsteren, W. F. (2004). A biomolecular force field based on the free enthalpy of hydration and solvation: the GROMOS force-field parameter sets 53A5 and 53A6. *J. Comput. Chem.* 25, 1656–1676. doi: 10.1002/jcc.20090
- Pace, C. N., and Scholtz, J. M. (1998). A helix propensity scale based on experimental studies of peptides and proteins. *Biophys. J.* 75, 422–427. doi: 10.1016/S0006-3495(98)77529-0
- Patriksson, A., and van der Spoel, D. (2008). A temperature predictor for parallel tempering simulations. *Chem. Chem. Phys.* 10, 2073–2077. doi: 10.1039/b716554d
- Pettersen, E. F., Goddard, T. D., Huang, C. C., Couch, G. S., Greenblatt, D. M., Meng, E. C., et al. (2004). UCSF chimera—a visualization system for exploratory research and analysis. *J. Comput. Chem.* 25, 1605–1612. doi: 10.1002/jcc.20084
- Robinson, C. J., and Stringer, S. E. (2001). The splice variants of vascular endothelial growth factor (VEGF) and their receptors. *J. Cell Sci.* 114, 853–865.
- Ronca, R., Benkheil, M., Mitola, S., Struyf, S., and Liekens, S. (2017). Tumor angiogenesis revisited: regulators and clinical implications. *Med. Res. Rev.* 37, 1231–1274. doi: 10.1002/med.21452
- Ryckaert, J. P., Ciccotti, G., and Berendsen, H. J. (1977). Numerical integration of the cartesian equations of motion of a system with constraints: molecular dynamics of n-alkanes. *J. Comp. Phys.* 23, 327–341. doi: 10.1016/0021-9991(77)90098-5
- Schymkowitz, J., Borg, J., Stricher, F., Nys, R., Rousseau, F., and Serrano, L. (2005). The FoldX web server: an online force field. *Nucleic Acids Res.* 33, W382–W388. doi: 10.1093/nar/gki387
- Shibuya, M. (2013). Vascular endothelial growth factor and its receptor system: physiological functions in angiogenesis and pathological roles in various diseases. *J. Biochem.* 153, 13–19. doi: 10.1093/jb/mvs136
- Sidman, R. L., Li, J., Lawrence, M., Hu, W., Musso, G. F., Giordano, R. J., et al. (2015). The peptidomimetic Vasotide targets two retinal VEGF receptors and reduces pathological angiogenesis in murine and nonhuman primate models of retinal disease. *Sci. Trans. Med.* 7:309ra165. doi: 10.1126/scitranslmed.aac4882
- Siemeister, G., Marmé, D., and Martiny-Baron, G. (1998). The alpha-helical domain near the amino terminus is essential for dimerization of vascular endothelial growth factor. *J. Biol. Chem.* 273, 11115–11120. doi: 10.1074/jbc.273.18.11115
- Simon, T., Gagliano, T., and Giamas, G. (2017). Direct effects of anti-angiogenic therapies on tumor cells: VEGF signaling. *Trends Mol. Med.* 23, 282–292. doi: 10.1016/j.molmed.2017.01.002
- Somanath, P. R., Malinin, N. L., and Byzova, T. V. (2009). Cooperation between integrin alphavbeta3 and VEGFR2 in angiogenesis. *Angiogenesis* 12, 177–185. doi: 10.1007/s10456-009-9141-9
- Su, J. L., Yen, C. J., Chen, P. S., Chuang, S. E., Hong, C. C., Kuo, I. H., et al. (2007). The role of the VEGF-C/VEGFR-3 axis in cancer progression. *Br. J. Cancer* 96, 541–545. doi: 10.1038/sj.bjc.6603487
- Toniolo, C., Crisma, M., Formaggio, F., and Peggion, C. (2001). Control of peptide conformation by the Thorpe-Ingold effect (Ca-tetrasubstitution). *Pept. Sci.* 60, 396–419. doi: 10.1002/1097-0282(2001)60:6<396::AID-BIP10184>3.0.CO;2-7
- Udugamasooriya, D. G., Dineen, S. P., Brekken, R. A., and Kodadek, T. (2008). A peptoid “Antibody Surrogate” that antagonizes VEGF receptor 2 activity. *J. Am. Chem. Soc.* 130, 5744–5752. doi: 10.1021/ja711193x
- Vasudev, N. S., and Reynolds, A. R. (2014). Anti-angiogenic therapy for cancer: current progress, unresolved questions and future directions. *Angiogenesis* 17, 471–494. doi: 10.1007/s10456-014-9420-y
- Wang, C. A., and Tsai, S. J. (2015). The non-canonical role of vascular endothelial growth factor-C axis in cancer progression. *Exp. Biol. Med.* 240, 718–724. doi: 10.1177/1535370215583802
- Wüthrich, K. (1986). *NMR of Proteins and Nucleic Acids*. New York, NY: Wiley.
- Zanella, S., Mingozzi, M., Dal Corso, A., Fanelli, R., Arosio, D., Cosentino, M., et al. (2015). Synthesis, characterization, and biological evaluation of a dual-action ligand targeting $\alpha_v\beta_3$ integrin and VEGF receptors. *ChemistryOpen* 4, 633–641. doi: 10.1017/1535370215000062
- Zhu, X., and Mitchell, J. C. (2011). KFC2: a knowledge-based hot spot prediction method based on interface solvation, atomic density, and plasticity features. *Proteins Struct. Funct. Bioinf.* 79, 2671–2683. doi: 10.1002/prot.23094
- Zilberberg, L., Shinkaruk, S., Lequin, O., Rousseau, B., Hagedorn, M., Costa, F., et al. (2003). Structure and inhibitory effects on angiogenesis and tumor development of a new vascular endothelial growth inhibitor. *J. Biol. Chem.* 278, 35564–35573. doi: 10.1074/jbc.M304435200

Conflict of Interest Statement: The authors declare that the research was conducted in the absence of any commercial or financial relationships that could be construed as a potential conflict of interest.

The reviewer NI declared a past co-authorship and collaboration with one of the authors (LS).

Copyright © 2019 Zanella, Bocchinfuso, De Zotti, Arosio, Marino, Raniolo, Pignataro, Sacco, Palleschi, Siano, Piarulli, Belvisi, Formaggio, Gennari and Stella. This is an open-access article distributed under the terms of the Creative Commons Attribution License (CC BY). The use, distribution or reproduction in other forums is permitted, provided the original author(s) and the copyright owner(s) are credited and that the original publication in this journal is cited, in accordance with accepted academic practice. No use, distribution or reproduction is permitted which does not comply with these terms.



Multifunctional Scaffolds for Assembling Cancer-Targeting Immune Stimulators Using Chemoselective Ligations

Anne C. Conibear^{*†}, Karine Thewes, Nadja Groysbeck and Christian F. W. Becker

Faculty of Chemistry, Institute of Biological Chemistry, University of Vienna, Vienna, Austria

OPEN ACCESS

Edited by:

Jutta Eichler,
Friedrich-Alexander-Universität
Erlangen-Nürnberg, Germany

Reviewed by:

Sébastien Vidal,
Centre National de la Recherche
Scientifique (CNRS), France
Oleg Melnyk,
Centre National de la Recherche
Scientifique (CNRS), France

*Correspondence:

Anne C. Conibear
anne.conibear@univie.ac.at

†Present Address:

Anne C. Conibear,
School of Biomedical Sciences,
University of Queensland, St Lucia,
Brisbane, QLD, Australia

Specialty section:

This article was submitted to
Supramolecular Chemistry,
a section of the journal
Frontiers in Chemistry

Received: 26 November 2018

Accepted: 12 February 2019

Published: 06 March 2019

Citation:

Conibear AC, Thewes K, Groysbeck N
and Becker CFW (2019)
Multifunctional Scaffolds for
Assembling Cancer-Targeting Immune
Stimulators Using Chemoselective
Ligations. *Front. Chem.* 7:113.
doi: 10.3389/fchem.2019.00113

Chemoselective ligations allow chemical biologists to functionalise proteins and peptides for biomedical applications and to probe biological processes. Coupled with solid phase peptide synthesis, chemoselective ligations enable not only the design of homogeneous proteins and peptides with desired natural and unnatural modifications in site-specific locations but also the design of new peptide and protein topologies. Although several well-established ligations are available, each method has its own advantages and disadvantages and they are seldom used in combination. Here we have applied copper-catalyzed azide-alkyne “click,” oxime, maleimide, and native chemical ligations to develop a modular synthesis of branched peptide and polymer constructs that act as cancer-targeting immune system engagers (ISERs) and functionalised them for detection in biological systems. We also note some potential advantages and pitfalls of these chemoselective ligations to consider when designing orthogonal ligation strategies. The modular synthesis and functionalization of ISERs facilitates optimisation of their activity and mechanism of action as potential cancer immunotherapies.

Keywords: ligation, click chemistry, orthogonal ligations, protein conjugation, peptide functionalization, peptide-polymer conjugates

INTRODUCTION

The use of antibodies for cancer therapy takes advantage of the specific binding of antibodies to their targets and has led to the introduction of several antibody-based cancer therapeutics into the clinic (Scott et al., 2012; Sliwkowski and Mellman, 2013). Although antibodies have high specificity, limited tissue penetration and difficulties in generating large amounts of homogeneous antibody products cost-effectively initially restricted their use, and a wide range of antibody fragments, antibody-drug conjugates and antibody-like molecules have been developed to address these challenges (Casi and Neri, 2015; Weiner, 2015; Haußner et al., 2017). In particular, peptides and peptide-polymer conjugates can mimic the functions of large folded proteins such as antibodies and have the advantage that they are synthetically accessible and readily modified and optimized for specific biological functions (Ahrens et al., 2012; Fosgerau and Hoffmann, 2015; Gross et al., 2015; Conibear et al., 2017a). Furthermore, peptides, polymers, proteins and small molecules can be ligated together to generate highly specific multifunctional compounds for biomedical applications (Jewett and Bertozzi, 2010; Schumacher and Hackenberger, 2014; Agarwal and Bertozzi, 2015; Merten et al., 2015; Bondalapati et al., 2016).

Chemoselective ligation reactions have enabled the generation of numerous molecular tools and probes. The diverse applications of chemoselective ligations are possible due to the ready availability of molecules bearing the respective functional groups, their compatibility with biological systems, and aqueous buffers in particular, and their generally stable and non-toxic products (Patterson et al., 2014; Patterson and Prescher, 2015). Amongst the most commonly used ligation reactions for biomedical applications are copper-catalyzed azide-alkyne “click” (CuAAC), oxime, maleimide and native chemical (NCL) ligations, illustrated in **Figure 1**. The functional groups involved in these reactions can be installed in peptides using commercially available building blocks that are stable to solid phase peptide synthesis conditions. Choosing a ligation strategy when designing a particular conjugate, however, is not always straightforward, and extensive optimisation often needs to be carried out for each application (Patterson and Prescher, 2015). Nevertheless, combining chemoselective ligations can provide access to sophisticated highly-functionalized biomolecules with precisely designed properties. For example, Galibert et al. have demonstrated the use of oxime, CuAAC and maleimide ligations in various combinations to functionalize a cyclic peptide scaffold with Arg-Gly-Asp (RGD)-moieties, as well as carbohydrate, nucleic acid and a fluorophore (Galibert et al., 2009, 2011). In this work, we have applied the chemoselective reactions above for the functionalization of peptide-polymer scaffolds that mimic the functions of natural antibodies, enabling modular syntheses and rapid optimisation and modification.

We have previously reported the development of a prototype innate immune system engager (ISER), a peptide-polymer conjugate that mimics the functions of antibodies in targeting cancer cells and eliciting an immune response (Brehs et al., 2017). ISERs are synthesized entirely by solid phase peptide synthesis (SPPS) and comprise two or more “binder” peptides that specifically target receptors overexpressed on cancer cells and are conjugated *via* polyethylene glycol (PEG) linkers to an “effector” peptide that stimulates an immune response (**Figure 1**) (Brehs et al., 2017). To explore the cancer cell specificity and immune stimulatory activity of ISERs, we have generated variants bearing two or more “binders” targeting the same or different receptors and have also used them for targeting cytotoxic drug molecules to cancer cells (Conibear et al., 2017b, 2018a). Further development and optimisation of the ISER concept and its application to other types of cancer cells requires investigation of additional binder and effector peptides, combinations of binder and effector peptides and labeling of the ISERs to detect them in cells and tissues.

Here we describe how we have used chemoselective ligation strategies and combinations thereof to functionalise ISERs for biomedical applications. The ability to attach various binder peptides and labels to ISERs chemoselectively increases the modularity of the synthesis, the affinity and selectivity of ISERs for cancer cells and their ease of detection in biological contexts. We also highlight some of the advantages and disadvantages of the chemoselective ligation strategies and discuss points to consider in selecting a ligation reaction, as well as how to

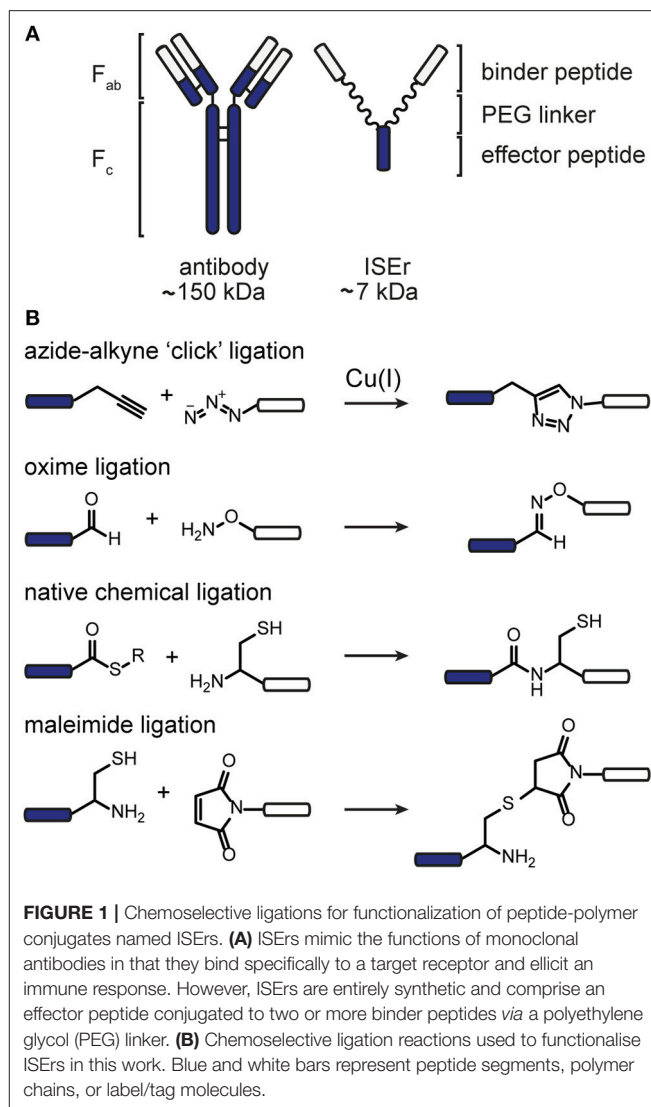


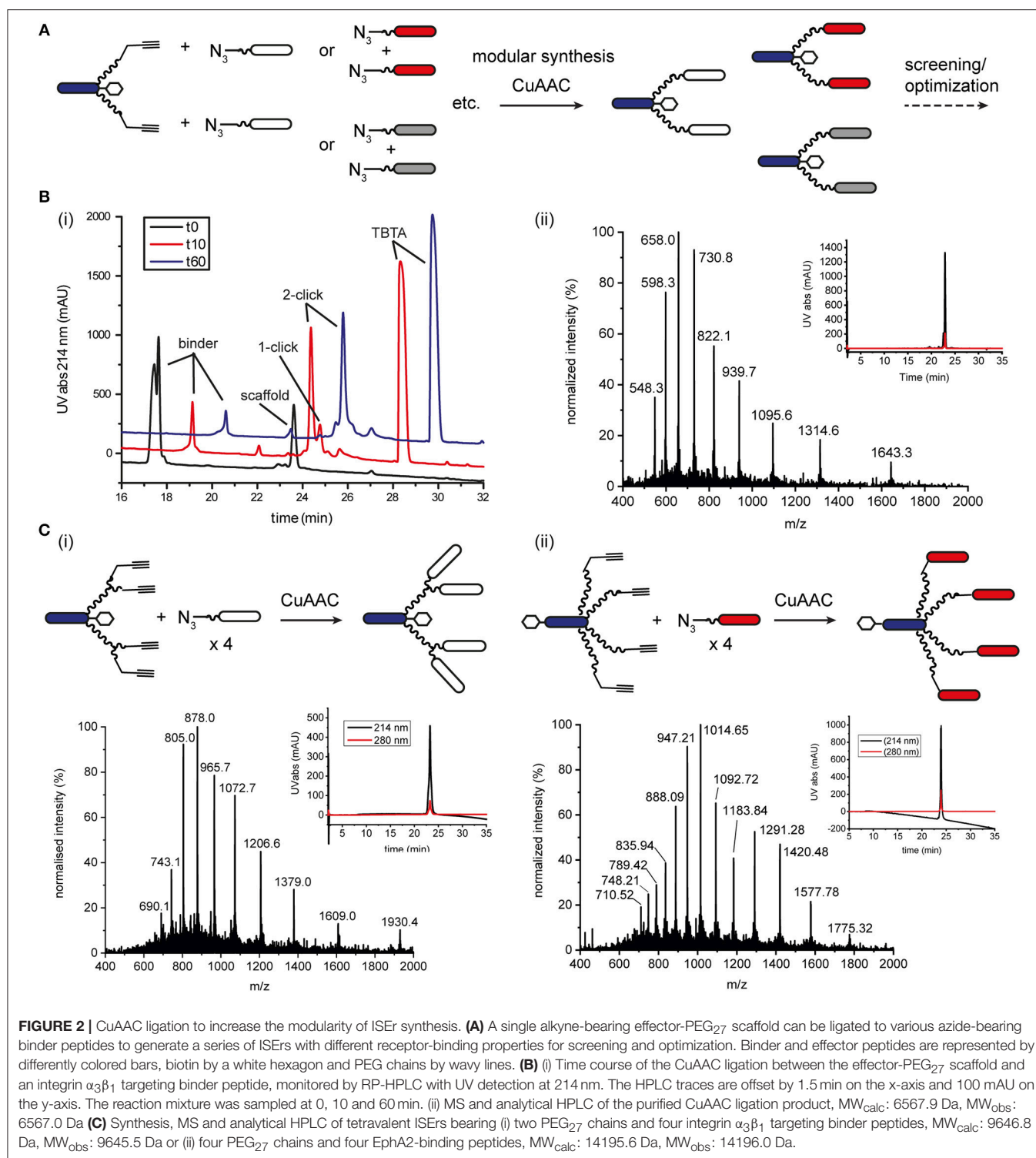
FIGURE 1 | Chemoselective ligations for functionalization of peptide-polymer conjugates named ISERs. **(A)** ISERs mimic the functions of monoclonal antibodies in that they bind specifically to a target receptor and elicit an immune response. However, ISERs are entirely synthetic and comprise an effector peptide conjugated to two or more binder peptides *via* a polyethylene glycol (PEG) linker. **(B)** Chemoselective ligation reactions used to functionalise ISERs in this work. Blue and white bars represent peptide segments, polymer chains, or label/tag molecules.

optimize these reactions and pairs of orthogonal reactions for peptide functionalization.

RESULTS AND DISCUSSION

Increasing the Modularity of the Synthesis Using Chemoselective Ligations

We sought to develop a modular synthesis of ISERs that would enable the attachment of several different binder peptides to the same peptide-polymer scaffold using chemoselective ligations, so that multiple binders could be tested rapidly. We therefore used the CuAAC ligation to attach the binder peptides to the ends of the PEG₂₇ linkers (**Figure 2A**; Rostovtsev et al., 2002; Tornøe et al., 2002). The widely-used CuAAC ligation is generally fast, selective, compatible with aqueous environments and many azide- and alkyne-functionalised building blocks are commercially available (Kolb and Sharpless, 2003; Meldal and Tornøe, 2008). The Cu(I)-catalyzed cycloaddition between an



azide and a terminal alkyne (Figure 1) yields a 1,4-disubstituted 1,2,3-triazole that is stable in biological systems and is similar in length to a peptide bond. Although Cu(I) can be used directly in the form of CuBr or CuI, it is less stable than Cu(II) and therefore the Cu(I) catalyst is often generated *in situ* from CuSO₄

and a reducing agent such as sodium ascorbate. Several ligands are available to stabilize the Cu(I) species and to reduce oxidative damage of proteins (Meldal and Tornøe, 2008).

The ISEr peptide-polymer scaffold was synthesized by SPPS as described previously with a L-propargyl glycine (alkyne

TABLE 1 | Optimisation of solution-phase CuAAC ligation conditions.

Binder	Cu source	Additives	Solvent(s)	Comments
B2	CuI (0.5 equivalents)	DIPEA (20 equivalents)	ACN/H ₂ O (80:20)	Product observed, reaction incomplete, M+125, M+250 (iodination of Tyr?)
B2	CuI (2 equivalents)	DIPEA (20 equivalents)	THF/ACN (27:73)	Product observed after overnight reaction, reaction incomplete
B2	CuSO ₄ (4 equivalents)	TBTA (4 equivalents), ascorbic acid (20 equivalents)	H ₂ O/DMSO (50:50)	Product observed, oxidation of Met
B3	CuSO ₄ (4 equivalents)	TBTA (4 equivalents), ascorbic acid (20 equivalents)	DMF/H ₂ O (84:16)	Product observed, reaction incomplete after 21 h. Some oxidation of Met
B3	CuSO ₄ (4 equivalents)	TBTA (4 equivalents), sodium ascorbate (40 equivalents)	DMF/H ₂ O (83:17)	Reaction complete in < 5 min. Good solvent mixture and large excess of sodium ascorbate keeps Cu reduced.
B9	CuSO ₄ (2 × 3 equivalents)	TBTA (2 × 3.5 equivalents), sodium ascorbate (30 equivalents)	DMF/H ₂ O (84:16)	Product observed but reaction incomplete after 80 min. Binder peptide with cysteine residues reacts slowly.
B9	CuSO ₄ (6 equivalents)	THPTA (30 equivalents), sodium ascorbate (55 equivalents)	H ₂ O	No product observed, decomposition of starting materials after extended reaction time (17 h).
B9	CuSO ₄ (36 equivalents)	TentaGel-TBTA (10 equivalents), sodium ascorbate (260 equivalents)	DMF/H ₂ O (85:15)	Product observed but reaction incomplete after 72 h. Separation of product easier but CuAAC would require further optimization with on-resin TBTA.
B9	CuSO ₄ (6 equivalents)	TBTA (6.5 equivalents), sodium ascorbate (50 equivalents)	DMF/H ₂ O (81:19)	Reaction almost complete after 1 h. Large excess of Cu(I) required for peptides containing cysteine.

B2: H-YLFSVHWPLKA-OH.

B3: H-PQNSKIPGPTFLDPH-OH.

B9: H-cdGY(3-NO₂)GHypNc-NH₂.

functionality) on the end of each PEG₂₇ chain (Conibear et al., 2018a). The short N-formylated “effector” peptide fMIFL (Rot et al., 1987) bore a glycine spacer and two lysine residues to which the PEG₂₇ chains were coupled *via* the side chains (**Figure S1**). As α -carbonyl alkynes have been reported to be more reactive than alkyl-substituted alkynes (Meldal and Tornøe, 2008), we initially coupled propiolic acid to the N-termini of the PEG₂₇ chains as the alkyne functionality. Although coupling of the propiolic acid appeared to be successful and several coupling conditions were tested, many side products were observed, possibly involving addition of benzotriazole or azabenzotriazole anions to the activated alkyne (Massif et al., 2012). We therefore proceeded with Fmoc-L-2-propargylglycine, which coupled efficiently to the PEG₂₇ chains and, as it is an amino acid, also allows for incorporation of the alkyne moiety at any position in the binder peptide. Several binder peptides were synthesized by SPPS bearing an azidolysine residue (azide functionality), separated from the main peptide chain by a short PEG₃ linker (**Figure 2A** and **Figures S2–S5**). Analytical data, yields and approximate times for synthesis and purification are given in the **Supplementary Information**.

We tested several conditions to optimize the CuAAC ligation, with different copper sources, ligands and solvents. Initially, the CuAAC ligation was attempted with the alkyne-bearing effector-PEG scaffold on resin, employing CuI as the catalyst, a nitrogen base (2,6-lutidine or diisopropylamine) and the purified azide-bearing binder peptide in solution. In principle, CuI can be used without a reducing agent, but might require a nitrogen base to form the copper-acetylide complex (Rostovtsev et al., 2002). Although the desired triazole-linked ISEr product was observed in some cases, the reaction depended on the length of the PEG

chain, with the shorter PEG₄ reacting more successfully than the longer PEG₂₇. Furthermore, the solubility of CuI and stability of the Cu(I) species proved problematic and therefore the solution-phase CuAAC ligation was chosen and optimized for the modular synthesis of ISErs. Nevertheless, on-resin CuAAC ligations have been widely used, especially for intramolecular cyclisation and stapling reactions (Ingale and Dawson, 2011; Lau et al., 2015).

Optimisation of the CuAAC ligation in solution involved screening several copper sources, ligands, reducing agents, temperatures, solvents and reagent concentrations, as summarized in **Table 1**, which shows a selection of the conditions tested. All reactions were carried out between a purified effector-PEG₂₇ alkyne-bearing scaffold and various purified binder peptides targeting different cell surface receptors overrepresented on cancer cells. Use of CuI was partially successful with diisopropylethylamine (DIPEA) as a nitrogen base but, as CuI is not soluble in water or THF, it was difficult to find a suitable solvent mixture for this reaction. Moreover, several side products were observed, probably involving iodination over the prolonged reaction times (12–20 h), as has previously been reported (Goyard et al., 2012, 2014) so we proceeded with *in situ* generation of the Cu(I) species. In this strategy, Cu(II) is reduced to Cu(I) with a reducing agent such as ascorbate in the presence of a stabilizing ligand (Meldal and Tornøe, 2008). We found that the presence of a ligand was necessary for the reaction to proceed and that it was essential to mix the copper and ligand tris[(1-benzyl-1H-1,2,3-triazol-4-yl)methyl]amine (TBTA) before addition of the reducing agent. Using sodium ascorbate as the reducing agent in large excess greatly increased the rate of the reaction. Although Cu(I) is theoretically a catalyst, we found that several

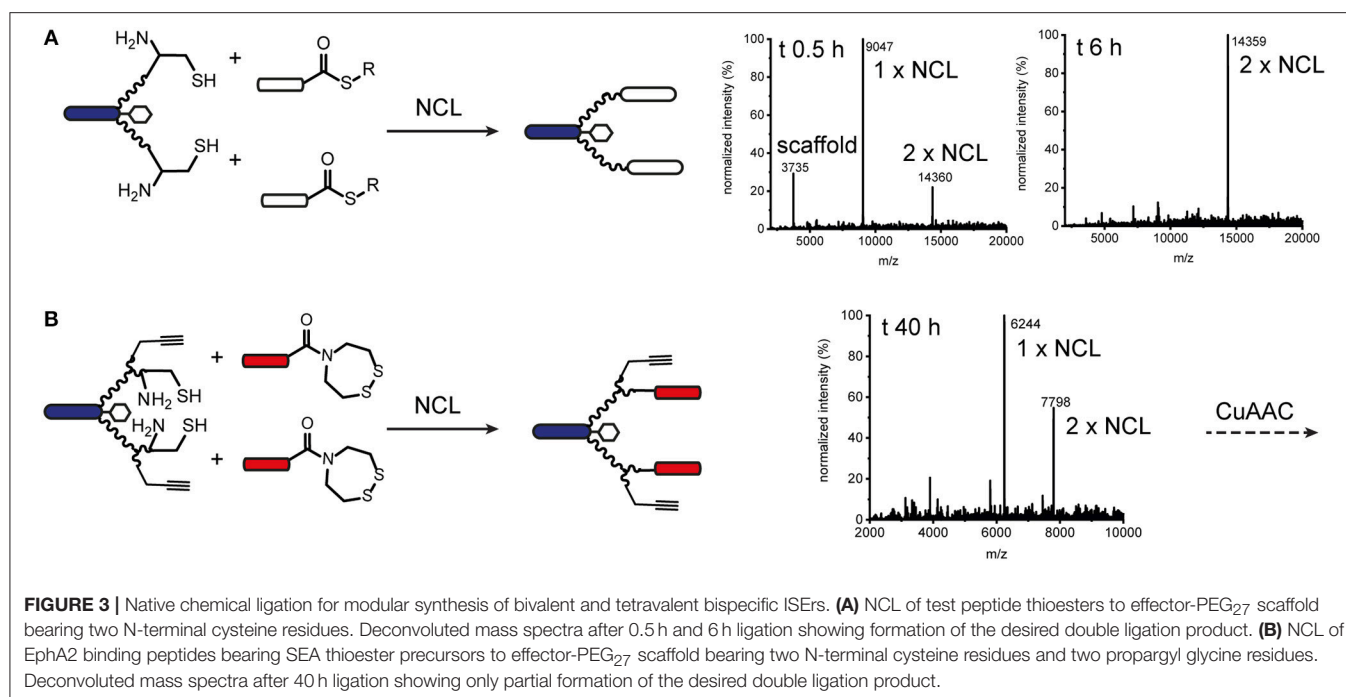
equivalents were required for efficient and complete reaction, especially in the case of the cysteine-containing $\alpha_3\beta_1$ integrin-targeting binder peptide ("B9"), where we added additional batches of the copper-ligand mixture during the reaction. As ligand, we further explored tris[(1-hydroxypropyl-1H-1,2,3-triazol-4-yl)methyl]amine (THPTA), a water-soluble analog of TBTA, and TentaGel-supported TBTA, which should facilitate separation of the ligand after the reaction. No product was observed with THPTA and, although some product was observed with the polymer-supported TBTA, the reaction was slow and incomplete, so we proceeded with TBTA in a water/DMF mixture. We obtained the best results with TBTA (tris[(1-benzyl-1H-1,2,3-triazol-4-yl)methyl]amine) (Chan et al., 2004) as a ligand to stabilize Cu(I), which was formed *in situ* from Cu(II) using sodium ascorbate. As shown in **Figure 2B**, the reaction was monitored by LC-MS and showed formation of first the "one-click" and then the "two-click" ligation product (**Figure 2B**).

The rate of CuAAC ligation varied widely with different binder peptides, ranging from 5 min to over an hour to reach completion. We found that the reaction rate depended on the amino acid composition of the binder peptides; peptides containing cysteine residues reacted much slower than those without and peptides containing arginine residues were modified by excess ascorbate in the reaction mixture. In the former case, free cysteine thiols likely complexed with the copper catalyst and we found that the reaction rate and purity was improved if disulfide bonds in the peptide were formed prior to the CuAAC ligation. The modification of arginine by dehydroascorbate was explored in more detail and could be minimized by using a smaller excess of ascorbate and monitoring the reaction carefully to avoid prolonged exposure of the peptides to the dehydroascorbate (Conibear et al., 2016). Overall however, we found the CuAAC ligation to be a fast and reliable means of increasing the modularity of peptide-polymer scaffold synthesis and the products were purified from excess starting materials and TBTA by RP-HPLC to give the desired bivalent triazole-linked ISERs (**Figure 2B**). Although the rates of the CuAAC ligations varied for the different binders, overall preparation times were approximately the same as most time is required for HPLC purification and analysis. We were able to generate ISERs with binder peptides targeting integrin $\alpha_3\beta_1$ (CD49c/VLA-3), (Yao et al., 2009a,b) integrin $\alpha_v\beta_6$, (Zhou et al., 2004) c-Met/HGFR, and EphA2 (Koolpe et al., 2002) receptors, as well as their scrambled counterparts as controls, all using the same effector-PEG₂₇ scaffold.

In addition to increasing the modularity of ISER synthesis, we further used CuAAC ligations to generate multivalent ISERs to explore avidity and affinity effects of cancer cell binding (Conibear et al., 2018a). Using a similar strategy to that described for the bivalent ISERs above, we synthesized an effector-PEG₂₇ scaffold with either two L-propargyl glycine residues on the ends of each of two PEG₂₇ chains, or four PEG₂₇ chains each with one L-propargyl glycine residue (**Figures S6, S7**). Tetravalent ISERs were then generated by carrying out four CuAAC ligations simultaneously to attach four binder peptides. As shown in **Figure 2C**, this yielded the desired tetravalent products after

HPLC purification. Similarly to the bivalent examples, we found that prolonged exposure to the CuAAC reaction reagents was detrimental and that the reaction was most efficient for peptides that did not contain cysteine residues. Furthermore, the tetravalent product sometimes co-eluted with the excess TBTA, complicating the purification process and resulting in decreased yields. TBTA is poorly water-soluble and so could be partially removed from the reaction mixture by precipitation after dilution with water. Although there are several water-soluble ligands that we could have explored (Besanceney-Webler et al., 2011; Ekholm et al., 2016) carrying out the CuAAC ligation in DMF (in which TBTA is highly soluble) also allows the peptide reagents to be dissolved at high concentrations, increasing the reaction rate and yield. In general, although the reactions appeared to reach completion by LC-MS analysis, we achieved isolated yields of 30–40% for the CuAAC ligations. An alternative strategy, which would avoid the need for copper and TBTA, is the strain-promoted azide-alkyne click (SPAAC) ligation developed in the Bertozzi group (Agard et al., 2004). This method has found wide application in biological systems where the use of copper could cause toxicity. However, the large and hydrophobic alkyne moiety is not easily compatible with the conditions employed in SPSS so we did not pursue this strategy for synthetic ISERs.

We also explored native chemical ligation (NCL) for attaching thioester-functionalised binder peptides to an effector-PEG₂₇ scaffold bearing cysteine residues on the ends of the PEG₂₇ chains (**Figure 3** and **Figure S8**). NCL is widely used for the synthesis and semi-synthesis of proteins as it can be carried out under mild aqueous conditions and yields a native peptide bond at the ligation site (Dawson et al., 1994; Conibear et al., 2018b). Similarly to the CuAAC ligations, the efficiencies of the native chemical ligations varied with the binder peptide thioesters. Whereas a test peptide ligated cleanly and efficiently to the ISER scaffold (**Figure 3A**), synthetic epidermal growth factor (EGF) segments ligated slowly and incompletely and were prone to aggregation in the ligation buffer, especially as the peptide chain grew longer with successive ligations (Gell et al., 2017). The efficiency of NCL is dependent on the nature of the C-terminal residue of the thioester fragment and the solubility and length of the peptides. Recent developments in and extensions to NCL, including new methods for generating peptide thioesters, new thiol additives and selenocysteine-mediated ligations, have greatly expanded the scope of NCL (Conibear et al., 2018b), but were not explored extensively for ISERs. For bispecific ISERs generated using two orthogonal ligation strategies, we explored the *bis*(2-sulfanylethyl)amino (SEA) thioester precursor strategy that enables synthesis of the binder peptides by Fmoc-SPSS followed by *in-situ* formation of the C-terminal thioester by N-S-acyl rearrangement under reducing conditions (Ollivier et al., 2010). Synthesis of the effector scaffold bearing handles for both NCL and CuAAC (**Figure S9**) and binder peptide precursors (**Figure S10**) proceeded smoothly but ligation at both PEG₂₇ termini did not reach completion (**Figure 3B**). A possible explanation for this could be the lack of an electron-withdrawing group alpha to the carbonyl of the thioester surrogate, which increases reactivity. Although alternative strategies for optimizing the ligation or generating the C-terminal



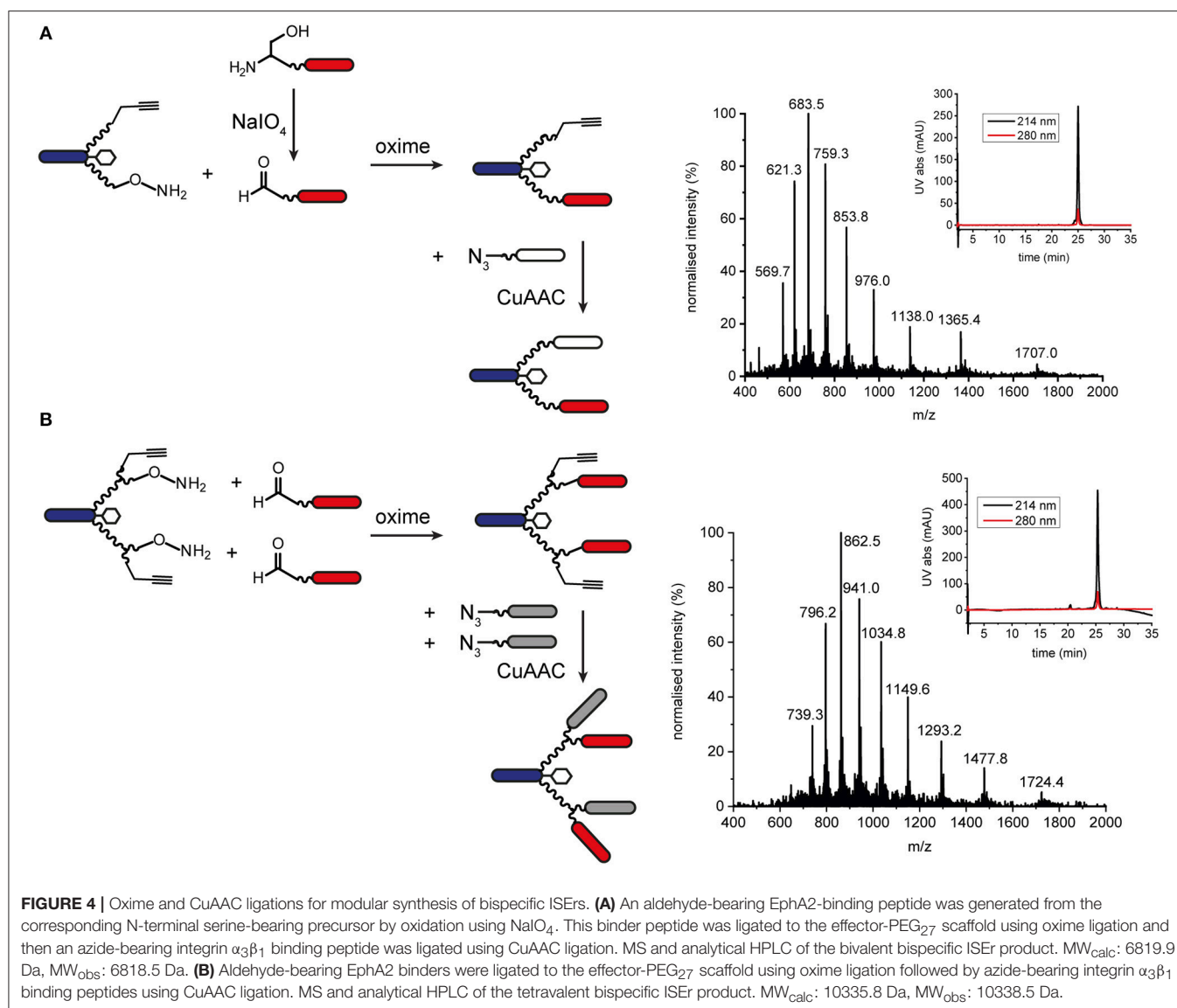
thioesters on the binder peptides are available (Conibear et al., 2018b; Kulkarni et al., 2018) the strategy would have required additional selective protection of the $\alpha_3\beta_1$ integrin binder, which contains an N-terminal D-cysteine that is important for biological activity (Yao et al., 2009a) so we turned to oxime ligation as an orthogonal alternative to use in combination with CuAAC.

Generating Multispecific Peptide-Polymer Conjugates Using Orthogonal Chemoselective Ligations

Orthogonal chemoselective ligations were used to synthesize peptide-polymer conjugates bearing two different binder peptides targeting different cell surface receptors to increase specificity and affinity. For this strategy, we employed the CuAAC ligation described above for one binder and oxime ligation for the second. The reaction between a hydroxylamine and an aldehyde or ketone under aqueous conditions at slightly acidic pH gives rise to an oxime linkage between the two components (Figure 1; Rose, 1994; El-Mahdi and Melnyk, 2013). As previous experiments had shown that the N-terminal cysteine residue of the $\alpha_3\beta_1$ integrin binder ("B9") was important for activity (Yao et al., 2009a) we chose to ligate this binder to the scaffold using CuAAC ligation and the second binder, an EphA2-binding peptide ("B59"), (Koolpe et al., 2002) using oxime ligation. For this strategy, we synthesized scaffolds bearing either an aminooxy acetic acid (Aoa) functionality on one PEG₂₇ chain and a propargyl glycine on the other (Figure S11, to give a bivalent bispecific ISER, Figure 4A) or an aminooxy acetic acid and a propargyl glycine on each PEG₂₇ chain (Figure S12, to give a tetravalent bispecific ISER, Figure 4B). In both cases, we

observed side-products with two or no Aoa functionalities that were challenging to purify. Nevertheless, the desired bispecific ISERs were obtained in acceptable purity for bioactivity assays, which showed that the bispecific bivalent ISER had higher affinity for PC-3 cancer cells ($K_d = 13.0 \pm 2.3$ nM) than either of the two monospecific bivalent ISERs ($K_d = 30.4 \pm 10.0$ nM and 68.9 ± 19.0 nM) (Conibear et al., 2018a).

We explored several strategies for installing the aldehyde or ketone moiety on the binder peptides. Whereas, a keto-functionality can be installed at either the N- or C-terminus, the aldehyde was generated by periodate oxidation of an N-terminal serine (Geoghegan and Stroh, 1992), separated from the binder peptide by a short PEG₃ linker. Several methods for increasing the rate and yield of oxime ligations have been published, including catalysis by aniline and by freezing (Dirksen et al., 2006; El-Mahdi and Melnyk, 2013; Agten et al., 2016), however, in our hands, we were able to obtain the best results by reacting an aldehyde with the aminooxy peptide in acetonitrile/water at pH 4.5 in acetate buffer. Several bispecific ISERs were obtained using oxime ligation followed by CuAAC ligation in both bivalent and tetravalent forms (Figure 4). Although the two reactions are theoretically orthogonal, it was necessary to do the oxime ligations first, as the aminooxy functionalities on the scaffold underwent several side-reactions on incubation in DMF with the CuAAC reagents, even in the absence of an azide component. This problem could potentially have been overcome by using a protected aminooxy functionality, such as 1-ethoxyethylidene (Eei) (Foillard et al., 2008; Galibert et al., 2009). The design of the synthesis strategy and choice of ligations was also influenced by the sequences of the binder peptides; as the EphA2 binder already contains an N-terminal serine in the binding sequence, which might affect binding affinity if oxidized to an aldehyde, it



was necessary to insert a PEG₃ linker between this residue and the N-terminal serine that was oxidized to form the aldehyde moiety for oxime ligation (Geoghegan and Stroh, 1992).

Functionalizing Peptide-Polymer Scaffolds With Tags and Labels for Detection

In addition to functionalising our peptide-polymer conjugates with varying numbers and arrangements of binder peptides, we have also used chemoselective ligations to functionalise ISERs with biotin tags and fluorescent dyes to enable measurement of their binding affinities and biodistribution. Initially, we synthesized the effector-PEG₂₇ scaffold using SPPS and coupled either Fmoc-biotinyl-PEG₂-OH or a fluorescent dye N-hydroxy succinimide (NHS) ester in place of the N-formyl moiety on the N-terminus of the effector peptide. These biotinylated or fluorescently labeled effector-PEG₂₇ scaffolds could then be used in CuAAC ligations as described above. For example, DY680

activated NHS ester (Dyomics GmbH) was coupled to the effector-PEG₂₇ scaffold on resin (**Figure S13**). The resulting DY680-labeled effector-PEG₂₇ scaffold was then ligated to two integrin $\alpha_3\beta_1$ binding peptides *via* CuAAC ligation (**Figure 5**). Similarly, an N-terminally biotin-labeled effector-PEG₂₇ scaffold was ligated to two cMET binding peptides (**Figure 5** and **Figure S14**). Although these N-terminally labeled scaffolds were used to detect binding of the respective ISERs to cancer cells after ligation of the binder peptides, using either indirect detection with streptavidin-FITC (biotin-tagged) or direct fluorescence detection (dye-labeled), the disadvantage was that they lacked effector activity due to the replacement of the N-terminal formyl group with the biotin or dye.

Two strategies were developed to enable labeling of the peptide-polymer scaffolds at the C-terminal end of the effector peptide, which is not involved in either the immune-stimulating or cancer-targeting activity (**Figure 1** and **Figure S1**): In the first

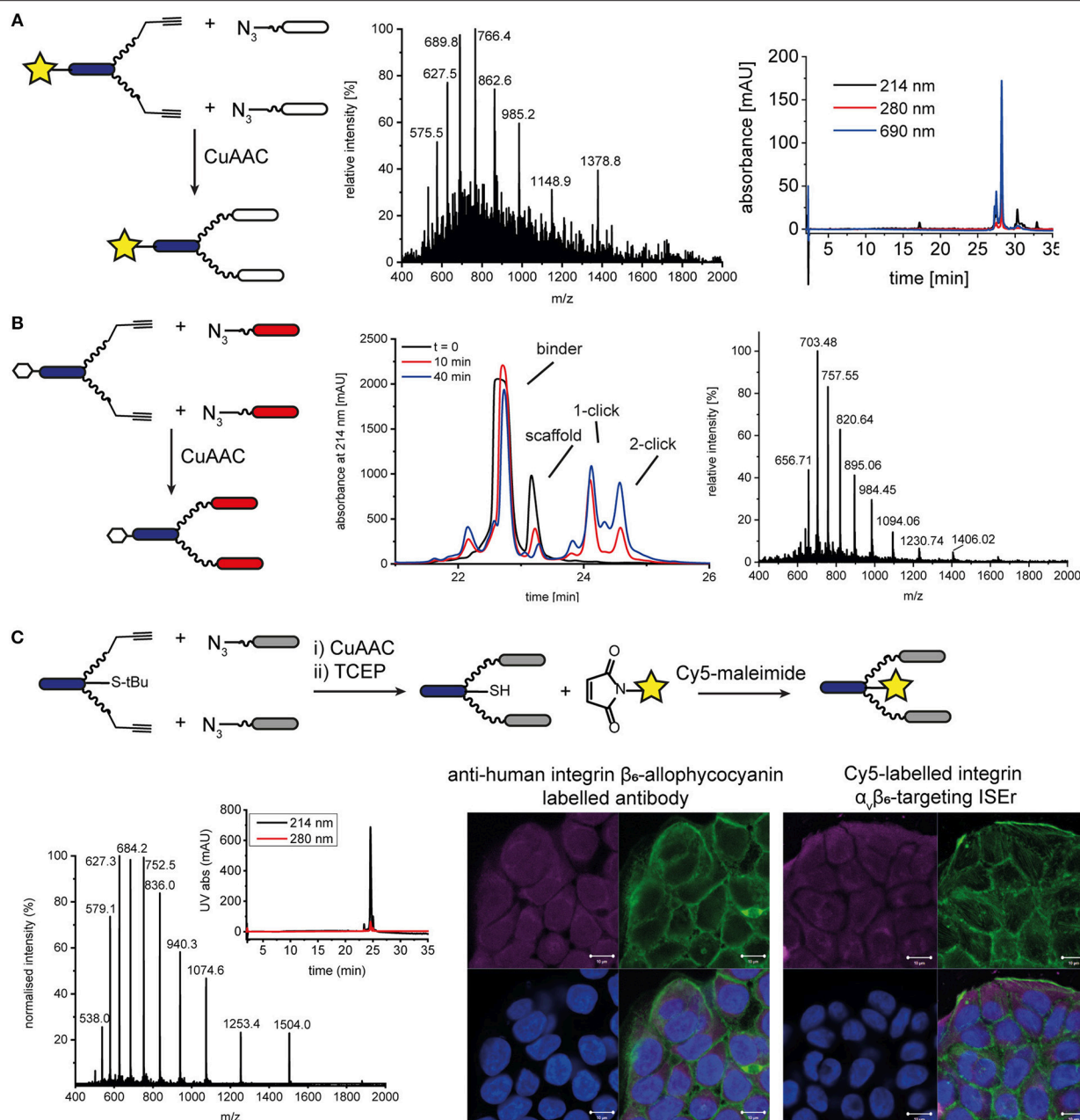


FIGURE 5 | N- and C-terminal labeling of ISEr scaffold for detection. **(A)** A fluorescent dye DY680 (yellow star) was coupled via NHS-ester to the N-terminus of the effector-PEG₂₇ scaffold and two integrin $\alpha_3\beta_1$ binding peptides were ligated using CuAAC ligation. MS and analytical HPLC (with fluorescence detection at 690 nm) traces are shown for the purified product: MW_{calc}: 6889.0 Da, MW_{obs}: 6890.5 Da. **(B)** CuAAC ligation of cMET binders to N-terminal biotinylated effector-PEG₂₇ scaffold. Biotin is represented by a white hexagon. The reaction was monitored by RP-HPLC and the purified product was analyzed by MS: MW_{calc}: 9836.4 Da, MW_{obs}: 9837.0 Da. **(C)** C-terminal labeling of ISErs using orthogonal chemoselective ligations. Integrin $\alpha_v\beta_6$ -targeting binder peptides were ligated to the effector-PEG₂₇ scaffold by CuAAC ligation. After removal of the S-tBu cysteine protecting group with TCEP, the fluorescent dye maleimide was coupled to the free thiol. MS and analytical HPLC trace of purified Cy5-labeled ISEr (MW_{calc}: 7513.5 Da, MW_{obs}: 7514.0 Da). Fluorescence microscopy image showing binding of a commercial anti-human integrin β_6 -allophycocyanin-labeled antibody (left) and Cy5-labeled integrin $\alpha_v\beta_6$ -targeting ISEr (right) to HT-29 cells, detected at 647 nm (top left, magenta), cell cytoskeleton stained with phalloidin (top right, green), nuclei stained with 4',6-diamidino-2-phenylindole (DAPI, bottom left, blue) and overlay (bottom right). Scale bar = 10 μ m.

strategy, the effector peptide was synthesized on a biotin-linked resin (Novabiochem) to yield the C-terminal biotinylated effector-PEG₂₇ scaffold after cleavage; In the second strategy,

a maleimide ligation was used as an orthogonal reaction to attach a maleimide-functionalised fluorescent dye to a thiol group (Cy5, sulfo-Cy5, or Alexa-750). Both strategies maintain

the cancer cell-binding and immune activating activities of the binder and effector peptides, respectively. Whereas, the first strategy is straightforward and does not require any additional steps, it relies on the compatibility of the chosen dye or tag to SPPS conditions. The C-terminal biotin was used to determine the immune-activating and cancer cell-binding activities of a series of multivalent and multispecific ISERs generated using the CuAAC and oxime ligations described above (Conibear et al., 2018a).

Attachment of a fluorescent dye to the C-terminus by maleimide ligation required synthesis of the effector-PEG₂₇ scaffold with a cysteine residue at the C-terminus of the effector peptide (**Figure 5** and **Figure S15**). This was easily achieved by loading the SPPS resin using a sulfonyl *tert*-butyl (S-tBu)-protected cysteine. The CuAAC ligation to attach the binder peptides was carried out prior to the maleimide ligation to attach the dye in order to minimize use of the expensive dyes. However, for binder peptides that contain cysteine residues, the maleimide ligation would need to be carried out first to prevent labeling of cysteine residues in the binder peptide, or would require orthogonal protection of the cysteine residues. After removing the S-tBu protecting group from the cysteine with *tris*(2-carboxyethyl)phosphine (TCEP), the peptide was purified by HPLC and kept at acidic pH under argon to maintain the reduced thiol. The additional HPLC step decreased the overall yield but was necessary to remove TCEP from the solution, as the phosphine can compete with the thiol for reaction with the maleimide, resulting in undesired phosphine-dye adducts (Henkel et al., 2016). If the TCEP was not removed, no maleimide product was formed and we observed formation of a side-product corresponding to an adduct of TCEP and Cy5 maleimide (MW 855 Da). After removing the TCEP, the maleimide-functionalised dye (Cy5, sulfo-Cy5, or Alexa750) was added in degassed water or DMF and the ligation was complete within minutes. For the coupling of Cy5, which is poorly soluble in water, the maleimide coupling was carried out in a mixture of DMF/water 1:3 and satisfactory ligation was observed. After HPLC purification to remove excess dye, the peptide-polymer conjugates were characterized by MS and HPLC with fluorescence detection (**Figure 5** and **Figure S16**) and used for fluorescence microscopy (**Figure 5**). Although the CuAAC ligation, StBu removal and Cy5 maleimide coupling reactions all reached completion, based on LC-MS analysis, isolated yields ranged from 41 to 88% and resulted in an overall final yield of 2% based on the synthesis scale of the scaffold. This illustrates the benefits of one-pot approaches that avoid the need for some of the purification steps, which are costly in terms of both material and time.

As a more versatile labeling strategy, we synthesized an integrin $\alpha_3\beta_1$ binding peptide-polymer conjugate and its scrambled counterpart by SPPS, bearing an azidolysine residue at the C-terminus of the effector peptide (**Figures S17, S18**). This allows for ligation of an alkyne-functionalised fluorescent label to this cysteine-containing ISER, without orthogonal protection of the cysteine residues. Using CuAAC, we ligated alkyne-functionalised Cy7 to both the integrin $\alpha_3\beta_1$ binding ISER and its scrambled counterpart (**Figures S19, S20**) for *in vivo* biodistribution studies. While this strategy involved attachment

of the binder peptides to the scaffold on resin using standard coupling methods, we could also have combined it with the modular synthesis described above by making use of orthogonal CuAAC ligations. An example of such a strategy was recently reported for antibody protein mimics of infliximab (Longin et al., 2018). In this study, a water-soluble derivative of CycloTriVeratrilene bearing three alkyne moieties was semi-orthogonally protected with triethylsilyl or triisopropylsilyl groups. Three cyclic peptide epitopes were then sequentially ligated to the scaffold using CuAAC ligations in a one-pot strategy (Longin et al., 2018).

CONCLUSION

We have used combinations of solid phase peptide synthesis and chemoselective ligations to generate a wide variety of functionalised peptide-polymer conjugates with different arrangements of immune-stimulating peptides, PEG linkers and cancer cell-binding peptides, as well as fluorescent labels and tags. The established CuAAC, NCL, oxime, and maleimide ligations were used alone and as orthogonal pairs to develop modular synthetic strategies to access a library of ISERs. Careful consideration, however, was necessary in selecting and combining ligation reactions based on the nature of the binder peptides and the functional groups present. Although the reactions used here have the advantage that they can be used on unprotected peptides, we found that functionalization of the protected constructs on the solid phase was often higher yielding due to the better control over selectivity. Nevertheless, chemoselective reactions allow coverage of a larger chemical space in a shorter time as we were able to develop a wide range of functionalised ISERs for biological activity testing. Overall, this illustrates the versatility and potential of functionalising synthetic peptide-polymer scaffolds using chemoselective ligations.

EXPERIMENTAL

General Methods for Peptide Synthesis and Purification

SPPS Methods

Effector and binder peptides were synthesized by manual or automated fluorenylmethoxycarbonyl (Fmoc) chemistry. Peptides with a C-terminal amide were synthesized on Rink amide resin, peptides with a C-terminal acid were synthesized on Wang resin and peptides with C-terminal biotin were synthesized on Biotin NovaTag resin (Merck). For initial residue loading of Wang resin, the amino acid (10 equivalents) was stirred with N,N'-diisopropylcarbodiimide (DIC, 5 equivalents) in dry dichloromethane (DCM) on ice for 30 min. After evaporation of the DCM and dissolution in DMF, 4-(dimethylamino)-pyridine (0.1 equivalents) was added and the solution was transferred to the Wang resin and stirred for 30 min. Residue couplings for manual SPPS were achieved by stirring the resin at room temperature with the Fmoc

protected amino acid (2.5 equivalents), 2-(1H-benzotriazol-1-yl)-1,1,3,3-tetramethyluronium hexafluorophosphate (HBTU, 2.4 equivalents, 0.5 M in DMF) and diisopropylethylamine (DIPEA, 5 equivalents). Deprotection was carried out with piperidine (20% v/v in DMF, 3 × 5 min). Automated syntheses were carried out on a Liberty Blue Microwave Peptide Synthesizer (CEM) using DIC (0.25 M in DMF) and Oxyrna (0.5 M in DMF) for coupling of amino acids (5 equivalents) under microwave irradiation for 4 min at 90°C. N-terminal formylation of the effector peptide was achieved with p-nitrophenylformate (3 equivalents) in DMF for 3 h. ISEr effector-PEG₂₇ scaffolds were synthesized as described previously (Conibear et al., 2018a) by coupling Fmoc-PEG₂₇-OH on the side chains of the two lysine residues: After removal of the 4-methyltrityl (Mtt) side-chain protecting groups with DCM/triisopropyl silane(TIPS)/trifluoroacetic acid(TFA) 98:1:1 (6 × 5 min), Fmoc-PEG₂₇-OH (2.75 equivalents) was coupled in DMF/ACN (6:4 v/v) with HATU (2.4 equivalents) and DIPEA (5 equivalents) overnight. Peptides were cleaved from the resin with TFA/TIPS/H₂O/dimethylsulfide 92.5:2.5:2.5:5 for 3 h and then precipitated with cold diethyl ether, isolated by centrifugation and lyophilised. Effector-PEG₂₇ scaffolds bearing Aoa residues were cleaved from the resin in the presence of excess Boc₂-Aoa as a carbonyl scavenger (Mező et al., 2011).

HPLC Methods

Peptides were purified by RP-HPLC on C4 or C18 preparative or semi-preparative HPLC columns using a linear gradient of (ACN + 0.05% TFA) in (ddH₂O + 0.05% TFA). Purity was monitored by electrospray ionization mass spectrometry (ESI-MS) in positive ion mode and analytical RP-HPLC using a linear gradient from 5 to 65% (ACN + 0.08% TFA) in (ddH₂O + 0.1% TFA) over 30 min at 1 mL/min with UV detection at 214 and 280 nm.

CuAAC Ligations

For CuAAC ligations, all solvents were degassed and reactions were carried out under inert gas. The alkyne-bearing effector-PEG₂₇ scaffold (1 equivalent) and the azide-bearing binder peptide (2.5 equivalents) were dissolved in DMF. Fresh stock solutions (CuSO₄: 200 mM in ddH₂O, TBTA: 100 mM in DMF, and sodium ascorbate: 500 mM in ddH₂O) were prepared and the CuSO₄ (6 equivalents) and TBTA (6.5 equivalents) were mixed before addition of the sodium ascorbate solution (10 equivalents). This solution was then added to the peptide solution, giving a final reaction mixture in 1:4 H₂O/DMF (v/v). The CuAAC ligation was stirred at room temperature under inert gas and monitored by LC-MS. After completion, the reaction mixture was diluted with water and purified by RP-HPLC. CuAAC ligations between C-terminal azide-bearing ISErs (1 equivalent) and alkyne-functionalised Cy7 (Lumiprobe, 1 equivalent) were carried out as for the CuAAC ligations described above.

Maleimide Ligations

During removal of the S-tButyl cysteine protecting group and maleimide ligations, the peptides were maintained in degassed

solutions and flushed with argon to prevent oxidation of the free thiols. For removal of the S-tButyl group, the purified peptide product after CuAAC ligation was dissolved in a TCEP solution (80 mM in water, pH 6.5), flushed with argon and stirred for 30 min. The TCEP was then removed by purification using RP-HPLC. For the maleimide ligation, the peptide bearing a free cysteine thiol was dissolved in ddH₂O and the maleimide-functionalised dye (1–2 equivalents) was added in DMF to give a final reaction mixture 1:3 DMF/H₂O. The mixture was stirred in the dark for 1 h, diluted with water and purified by HPLC.

Oxime Ligations

The aldehyde functionality on the binder peptides was generated by incubating the N-terminal serine-containing peptide with sodium periodate. The N-terminal serine-containing peptide (final concentration 6 mM) was dissolved in imidazole buffer (50 mM, pH 7) and 4 equivalents of NaIO₄ in water (stock solution 120 mM) was added. The solution was stirred at room temperature for 1–2 h and the reaction monitored by LC-MS. The aldehyde product was purified by RP-HPLC. For the oxime ligation, the aminoxy-bearing ISEr scaffold (final concentration 2 mM) and the aldehyde-bearing peptide (final concentration 2 mM) were dissolved in 1:1 (v/v) ACN/sodium acetate buffer (0.1 M, pH 4.6) and stirred at room temperature for 24 h. The ligation was monitored by LC-MS and the product purified by HPLC.

Native Chemical Ligations

NCL reactions with thioester-bearing binder peptides were carried out in 6 M guanidine HCl, 200 mM Na₂HPO₄, 40 mM TCEP, and 20 mM MPAA, pH 7.0 at room temperature. NCL reactions with SEA-bearing binder peptides were carried out in 6 M guanidine HCl, 200 mM Na₂HPO₄, 200 mM TCEP, and 200 mM MPAA, pH 7.2 at 37°C. The cysteine-bearing effector-PEG₂₇ scaffold and the thioester-bearing binder peptide (2.5 equivalents) were dissolved in the ligation buffer and then mixed to give final reaction concentrations of ~ 1 and 2 mM, respectively. The reaction was stirred under inert gas and monitored by LC-MS until it reached completion, or no further change was observed.

Fluorescence Microscopy

Human colorectal adenocarcinoma HT-29 cells were seeded into 8-well microslides. Cells were incubated with MnCl₂ (4 mM) in culture medium for 1 h and then fixed with paraformaldehyde (4%). Surface receptors were blocked with bovine serum albumin and then stained in turn with Oregon Green 488 phalloidin (Invitrogen), DAPI and either the fluorescently labeled ISEr (Cy5-labeled integrin α_vβ₆-targeting ISEr, 374 pM, 647 nm) or an anti-human integrin β₆-allophycocyanin labeled antibody (~ 267 pM, R&D Systems). After washing with PBS and fixing with paraformaldehyde (4%), cells were imaged using a Zeiss LSM710 confocal laser scanning microscope.

DATA AVAILABILITY

The datasets generated for this study are available on request to the corresponding author.

AUTHOR CONTRIBUTIONS

AC, KT, and CB designed experiments. AC, KT, and NG carried out experiments. AC, KT, and NG analyzed data. AC wrote the paper. AC, KT, NG, and CB edited the paper and approved the submitted manuscript.

FUNDING

The research leading to these results has received funding from the Mahlke-Obermann Stiftung and the European Union's

Seventh Framework Programme for research, technological development and demonstration under grant agreement no 609431 to Anne Conibear.

ACKNOWLEDGMENTS

We are grateful to Manuel Felkl and Margaret Vogt for assistance with peptide synthesis and Dr. Georgia del Favero for assistance with fluorescence microscopy.

SUPPLEMENTARY MATERIAL

The Supplementary Material for this article can be found online at: <https://www.frontiersin.org/articles/10.3389/fchem.2019.00113/full#supplementary-material>

REFERENCES

- Agard, N. J., Prescher, J. A., and Bertozzi, C. R. (2004). A strain-promoted [3 + 2] azide-alkyne cycloaddition for covalent modification of biomolecules in living systems. *J. Am. Chem. Soc.* 126, 15046–15047. doi: 10.1021/ja044996f
- Agarwal, P., and Bertozzi, C. R. (2015). Site-specific antibody–drug conjugates: the nexus of bioorthogonal chemistry, protein engineering, and drug development. *Bioconjug. Chem.* 26, 176–192. doi: 10.1021/bc5004982
- Agten, S. M., Suylen, D. P., and Hackeng, T. M. (2016). Oxime catalysis by freezing. *Bioconjug. Chem.* 27, 42–46. doi: 10.1021/acs.bioconjchem.5b00611
- Ahrens, V. M., Bellmann-Sickert, K., and Beck-Sickinger, A. G. (2012). Peptides and peptide conjugates: therapeutics on the upward path. *Fut. Med. Chem.* 4, 1567–1586. doi: 10.4155/fmc.12.76
- Besanceney-Webler, C., Jiang, H., Zheng, T., Feng, L., Soriano del Amo, D., Wang, W., et al. (2011). Increasing the efficacy of bioorthogonal click reactions for bioconjugation: a comparative study. *Angew. Chem. Int. Ed. Engl.* 50, 8051–8056. doi: 10.1002/anie.201101817
- Bondalapati, S., Jbara, M., and Brik, A. (2016). Expanding the chemical toolbox for the synthesis of large and uniquely modified proteins. *Nat. Chem.* 8, 407–418. doi: 10.1038/nchem.2476
- Brehs, M., Pötgens, A. J. G., Steitz, J., Thewes, K., Schwarz, J., Conibear, A. C., et al. (2017). Synthetic integrin-binding immune stimulators target cancer cells and prevent tumor formation. *Sci. Rep.* 7:17592. doi: 10.1038/s41598-017-17627-0
- Casi, G., and Neri, D. (2015). Antibody–drug conjugates and small molecule–drug conjugates: opportunities and challenges for the development of selective anticancer cytotoxic agents. *J. Med. Chem.* 58, 8751–8761. doi: 10.1021/acs.jmedchem.5b00457
- Chan, T. R., Hilgraf, R., Sharpless, K. B., and Fokin, V. V. (2004). Polytriazoles as copper(I)-stabilizing ligands in catalysis. *Org. Lett.* 6, 2853–2855. doi: 10.1021/ol0493094
- Conibear, A. C., Farbiarz, K., Mayer, R. L., Matveenko, M., Kählig, H., and Becker, C. F. (2016). Arginine side-chain modification that occurs during copper-catalysed azide-alkyne click reactions resembles an advanced glycation end product. *Org. Biomol. Chem.* 14, 6205–6211. doi: 10.1039/C6OB00932H
- Conibear, A. C., Hager, S., Mayr, J., Klose, M. H. M., Keppler, B. K., Kowol, C. R., et al. (2017b). Multifunctional alphavbeta6 Integrin-specific peptide–Pt(IV) conjugates for cancer cell targeting. *Bioconjug. Chem.* 28, 2429–2439. doi: 10.1021/acs.bioconjchem.7b00421
- Conibear, A. C., Pötgens, A. J. G., Thewes, K., Altdorf, C., Hilzendeger, C., and Becker, C. F. W. (2018a). Synthetic cancer-targeting innate immune stimulators give insights into avidity effects. *ChemBioChem* 19, 459–469. doi: 10.1002/cbic.201700522
- Conibear, A. C., Schmid, A., Kamalov, M., Becker, C. F. W., and Bello, C. (2017a). Recent Advances in peptide-based approaches for cancer treatment. *Curr. Med. Chem.* doi: 10.2174/0929867325666171123204851. [Epub ahead of print].
- Conibear, A. C., Watson, E. E., Payne, R. J., and Becker, C. F. W. (2018b). Native chemical ligation in protein synthesis and semi-synthesis. *Chem. Soc. Rev.* 47, 9046–9068. doi: 10.1039/C8CS00573G
- Dawson, P. E., Muir, T. W., Clark-Lewis, I., and Kent, S. B. (1994). Synthesis of proteins by native chemical ligation. *Science* 266, 776–779. doi: 10.1126/science.7973629
- Dirksen, A., Hackeng, T. M., and Dawson, P. E. (2006). Nucleophilic Catalysis of Oxime Ligation. *Angew. Chem. Int. Ed. Engl.* 45, 7581–7584. doi: 10.1002/anie.200602877
- Ekhholm, F. S., Pynnönen, H., Vilkman, A., Koponen, J., Helin, J., and Satomaa, T. (2016). Synthesis of the copper chelator TGTA and evaluation of its ability to protect biomolecules from copper induced degradation during copper catalyzed azide-alkyne bioconjugation reactions. *Org. Biomol. Chem.* 14, 849–852. doi: 10.1039/C5OB02133B
- El-Mahdi, O., and Melnyk, O. (2013). alpha-Oxo aldehyde or glyoxylyl group chemistry in peptide bioconjugation. *Bioconjug. Chem.* 24, 735–765. doi: 10.1021/bc300516f
- Foillard, S., Rasmussen, M. O., Razkin, J., Boturyn, D., and Dumy, P. (2008). 1-Ethoxyethylidene, a new group for the stepwise SPPS of aminooxyacetic acid containing peptides. *J. Org. Chem.* 73, 983–991. doi: 10.1021/jo701628k
- Fosgerau, K., and Hoffmann, T. (2015). Peptide therapeutics: current status and future directions. *Drug Discov. Today* 20, 122–128. doi: 10.1016/j.drudis.2014.10.003
- Galibert, M., Dumy, P., and Boturyn, D. (2009). One-pot approach to well-defined biomolecular assemblies by orthogonal chemoselective ligations. *Angew. Chem. Int. Ed. Engl.* 48, 2576–2579. doi: 10.1002/anie.200806223
- Galibert, M., Renaudet, O., Dumy, P., and Boturyn, D. (2011). Access to biomolecular assemblies through one-pot triple orthogonal chemoselective ligations. *Angew. Chem. Int. Ed. Engl.* 50, 1901–1904. doi: 10.1002/anie.201006867
- Gell, A. L., Groysbeck, N., Becker, C. F. W., and Conibear, A. C. (2017). A comparative study of synthetic and semisynthetic approaches for ligating the epidermal growth factor to a bivalent scaffold. *J. Pept. Sci.* 23, 871–879. doi: 10.1002/psc.3051
- Geoghegan, K. F., and Stroh, J. G. (1992). Site-directed conjugation of nonpeptide groups to peptides and proteins via periodate oxidation of a 2-amino alcohol. Application to modification at N-terminal serine. *Bioconjug. Chem.* 3, 138–146. doi: 10.1021/bc00014a008
- Goyard, D., Chajistamatiou, A. S., Sotiropoulou, A. I., Chrysina, E. D., Praly, J. P., and Vidal, S. (2014). Efficient atropodistereoselective access to 5,5'-bis-1,2,3-triazoles: studies on 1-glucosylated 5-halogeno 1,2,3-triazoles and their 5-substituted derivatives as glycogen phosphorylase inhibitors. *Chemistry* 20, 5423–5432. doi: 10.1002/chem.201304989
- Goyard, D., Praly, J. P., and Vidal, S. (2012). Synthesis of 5-halogenated 1,2,3-triazoles under stoichiometric Cu(I)-mediated azide-alkyne

- cycloaddition (CuAAC or 'Click Chemistry'). *Carbohydr. Res.* 362, 79–83. doi: 10.1016/j.carres.2012.08.014
- Groß, A., Hashimoto, C., Sticht, H., and Eichler, J. (2015). Synthetic Peptides as Protein Mimics. *Front. Bioeng. Biotechnol.* 3:211. doi: 10.3389/fbioe.2015.00211
- Haufner, C., Lach, J., and Eichler, J. (2017). Synthetic antibody mimics for the inhibition of protein-ligand interactions. *Curr. Opin. Chem. Biol.* 40, 72–77. doi: 10.1016/j.cbpa.2017.07.001
- Henkel, M., Röckendorf, N., and Frey, A. (2016). Selective and efficient cysteine conjugation by maleimides in the presence of phosphine reductants. *Bioconjug. Chem.* 27, 2260–2265. doi: 10.1021/acs.bioconjchem.6b00371
- Ingale, S., and Dawson, P. E. (2011). On resin side-chain cyclization of complex peptides using CuAAC. *Org. Lett.* 13, 2822–2825. doi: 10.1021/ol200775h
- Jewett, J. C., and Bertozzi, C. R. (2010). Cu-free click cycloaddition reactions in chemical biology. *Chem. Soc. Rev.* 39, 1272–1279. doi: 10.1039/b901970g
- Kolb, H. C., and Sharpless, K. B. (2003). The growing impact of click chemistry on drug discovery. *Drug Discov. Today* 8, 1128–1137. doi: 10.1016/S1359-6446(03)02933-7
- Koolpe, M., Dail, M., and Pasquale, E. B. (2002). An ephrin mimetic peptide that selectively targets the EphA2 receptor. *J. Biol. Chem.* 277, 46974–46979. doi: 10.1074/jbc.M208495200
- Kulkarni, S. S., Sayers, J., Premjee, B., and Payne, R. J. (2018). Rapid and efficient protein synthesis through expansion of the native chemical ligation concept. *Nat. Rev. Chem.* 2:0122. doi: 10.1038/s41570-018-0122
- Lau, Y. H., de Andrade, P., Wu, Y., and Spring, D. R. (2015). Peptide stapling techniques based on different macrocyclisation chemistries. *Chem. Soc. Rev.* 44, 91–102. doi: 10.1039/C4CS00246F
- Longin, O., Hezwani, M., van de Langemheen, H., and Liskamp, R. M. J. (2018). Synthetic antibody protein mimics of infliximab by molecular scaffolding on novel CycloTriVeratrilene (CTV) derivatives. *Org. Biomol. Chem.* 16, 5254–5274. doi: 10.1039/C8OB01104D
- Massif, C., Dautrey, S., Haelele, A., Ziessel, R., Renard, P. Y., and Romieu, A. (2012). New insights into the water-solubilisation of fluorophores by post-synthetic "click" and Sonogashira reactions. *Org. Biomol. Chem.* 10, 4330–4336. doi: 10.1039/c2ob25428j
- Meldal, M., and Tornøe, C. W. (2008). Cu-catalyzed azide-alkyne cycloaddition. *Chem. Rev.* 108, 2952–3015. doi: 10.1021/cr0783479
- Merten, H., Brandl, F., Plückthun, A., and Zangemeister-Wittke, U. (2015). Antibody-drug conjugates for tumor targeting-novel conjugation chemistries and the promise of non-IgG binding proteins. *Bioconjug. Chem.* 26, 2176–2185. doi: 10.1021/acs.bioconjchem.5b00260
- Mező, G., Szabó, I., Kertész, I., Hegedűs, R., Orbán, E., Leurs, U., et al. (2011). Efficient synthesis of an (aminoxy) acetylated-somatostatin derivative using (aminoxy)acetic acid as a 'carbonyl capture' reagent. *J. Pept. Sci.* 17, 39–46. doi: 10.1002/psc.1294
- Ollivier, N., Dheur, J., Mhida, R., Blanpain, A., and Melnyk, O. (2010). Bis(2-sulfanylethyl)amino native peptide ligation. *Org. Lett.* 12, 5238–5241. doi: 10.1021/ol102273u
- Patterson, D. M., Nazarova, L. A., and Prescher, J. A. (2014). Finding the right (bioorthogonal) chemistry. *ACS Chem. Biol.* 9, 592–605. doi: 10.1021/cb400828a
- Patterson, D. M., and Prescher, J. A. (2015). Orthogonal bioorthogonal chemistries. *Curr. Opin. Chem. Biol.* 28, 141–149. doi: 10.1016/j.cbpa.2015.07.006
- Rose, K. (1994). Facile synthesis of homogeneous artificial proteins. *J. Am. Chem. Soc.* 116, 30–33. doi: 10.1021/ja00080a004
- Rostovtsev, V. V., Green, L. G., Fokin, V. V., and Sharpless, K. B. (2002). A stepwise Huisgen cycloaddition process: copper(I)-catalyzed regioselective ligation" of azides and terminal alkynes. *Angew. Chem. Int. Ed. Engl.* 41, 2596–2599. doi: 10.1002/1521-3773(20020715)41:14<2596::AID-ANIE2596>3.0.CO;2-4
- Rot, A., Henderson, L. E., Copeland, T. D., and Leonard, E. J. (1987). A series of six ligands for the human formyl peptide receptor: tetrapeptides with high chemotactic potency and efficacy. *Proc. Natl. Acad. Sci. U.S.A.* 84, 7967–7971. doi: 10.1073/pnas.84.22.7967
- Schumacher, D., and Hackenberger, C. P. (2014). More than add-on: chemoselective reactions for the synthesis of functional peptides and proteins. *Curr. Opin. Chem. Biol.* 22, 62–69. doi: 10.1016/j.cbpa.2014.09.018
- Scott, A. M., Wolchok, J. D., and Old, L. J. (2012). Antibody therapy of cancer. *Nat. Rev. Cancer* 12, 278–287. doi: 10.1038/nrc3236
- Sliwkowski, M. X., and Mellman, I. (2013). Antibody therapeutics in cancer. *Science* 341, 1192–1198. doi: 10.1126/science.1241145
- Tornøe, C. W., Christensen, C., and Meldal, M. (2002). Peptidotriazoles on solid phase: [1,2,3]-triazoles by regioselective copper(I)-catalyzed 1,3-dipolar cycloadditions of terminal alkynes to azides. *J. Org. Chem.* 67, 3057–3064. doi: 10.1021/jo011148j
- Weiner, G. J. (2015). Building better monoclonal antibody-based therapeutics. *Nat. Rev. Cancer* 15, 361–370. doi: 10.1038/nrc3930
- Yao, N., Xiao, W., Meza, L., Tseng, H., Chuck, M., and Lam, K. S. (2009b). Structure-activity relationship studies of targeting ligands against breast cancer cells. *J. Med. Chem.* 52, 6744–6751. doi: 10.1021/jm9012032
- Yao, N., Xiao, W., Wang, X., Marik, J., Park, S. H., Takada, Y., et al. (2009a). Discovery of targeting ligands for breast cancer cells using the one-bead one-compound combinatorial method. *J. Med. Chem.* 52, 126–133. doi: 10.1021/jm801062d
- Zhou, X., Chang, Y. C., Oyama, T., McGuire, M. J., and Brown, K. C. (2004). Cell-specific delivery of a chemotherapeutic to lung cancer cells. *J. Am. Chem. Soc.* 126, 15656–15657. doi: 10.1021/ja0446496

Conflict of Interest Statement: The authors declare that the research was conducted in the absence of any commercial or financial relationships that could be construed as a potential conflict of interest.

Copyright © 2019 Conibear, Thewes, Groysbeck and Becker. This is an open-access article distributed under the terms of the Creative Commons Attribution License (CC BY). The use, distribution or reproduction in other forums is permitted, provided the original author(s) and the copyright owner(s) are credited and that the original publication in this journal is cited, in accordance with accepted academic practice. No use, distribution or reproduction is permitted which does not comply with these terms.



Probing Anti-inflammatory Properties Independent of NF- κ B Through Conformational Constraint of Peptide-Based Interleukin-1 Receptor Biased Ligands

Azade Geranurimi^{1†}, Colin W. H. Cheng^{2,3,4†}, Christiane Quiniou³, Tang Zhu³, Xin Hou³, José Carlos Rivera^{3,4}, Daniel J. St-Cyr¹, Kim Beauregard¹, Vadim Bernard-Gauthier¹, Sylvain Chemtob^{2,3,4,5} and William D. Lubell^{1*}

¹ Département de Chimie, Université de Montréal, Montréal, QC, Canada, ² Department of Pharmacology and Therapeutics, McGill University, Montréal, QC, Canada, ³ CHU Sainte-Justine Research Centre, Montréal, QC, Canada, ⁴ Hôpital Maisonneuve-Rosemont Research Centre, Montréal, QC, Canada, ⁵ Departments of Pediatrics, Pharmacology and Physiology, and Ophthalmology, Université de Montréal, Montréal, QC, Canada

OPEN ACCESS

Edited by:

Alessandro Contini,
University of Milan, Italy

Reviewed by:

Christian W. Gruber,
Medical University of Vienna, Austria
Giovanni Signore,
Scuola Normale Superiore di Pisa, Italy

*Correspondence:

William D. Lubell
william.lubell@umontreal.ca

[†]These authors have contributed
equally to this work

Specialty section:

This article was submitted to
Chemical Biology,
a section of the journal
Frontiers in Chemistry

Received: 30 November 2018

Accepted: 10 January 2019

Published: 13 February 2019

Citation:

Geranurimi A, Cheng CWH, Quiniou C, Zhu T, Hou X, Rivera JC, St-Cyr DJ, Beauregard K, Bernard-Gauthier V, Chemtob S and Lubell WD (2019) Probing Anti-inflammatory Properties Independent of NF- κ B Through Conformational Constraint of Peptide-Based Interleukin-1 Receptor Biased Ligands. *Front. Chem.* 7:23. doi: 10.3389/fchem.2019.00023

Interleukin-1 β (IL-1 β) binds to the IL-1 receptor (IL-1R) and is a key cytokine mediator of inflammasome activation. IL-1 β signaling leads to parturition in preterm birth (PTB) and contributes to the retinal vaso-obliteration characteristic of oxygen-induced retinopathy (OIR) of premature infants. Therapeutics targeting IL-1 β and IL-1R are approved to treat rheumatoid arthritis; however, all are large proteins with clinical limitations including immunosuppression, due in part to inhibition of NF- κ B signaling, which is required for immuno-vigilance and cytoprotection. The all-D-amino acid peptide **1** (101.10, H-D-Arg-D-Tyr-D-Thr-D-Val-D-Glu-D-Leu-D-Ala-NH₂) is an allosteric IL-1R modulator, which exhibits functional selectivity and conserves NF- κ B signaling while inhibiting other IL-1-activated pathways. Peptide **1** has proven effective in experimental models of PTB and OIR. Seeking understanding of the structural requirements for the activity and biased signaling of **1**, a panel of twelve derivatives was synthesized employing the various stereochemical isomers of α -amino- γ -lactam (Agl) and α -amino- β -hydroxy- γ -lactam (Hgl) residues to constrain the D-Thr-D-Val dipeptide residue. Using circular dichroism spectroscopy, the peptide conformation in solution was observed to be contingent on Agl, Hgl, and Val stereochemistry. Moreover, the lactam mimic structure and configuration influenced biased IL-1 signaling in an *in vitro* panel of cellular assays as well as *in vivo* activity in murine models of PTB and OIR. Remarkably, all Agl and Hgl analogs of peptide **1** did not inhibit NF- κ B signaling but blocked other pathways, such as JNK and ROCK2 phosphorylation contingent on structure and configuration. Efficacy in preventing preterm labor correlated with a capacity to block IL-1 β -induced IL-1 β synthesis. Furthermore, the importance of inhibition of JNK and ROCK2 phosphorylation for enhanced activity was highlighted for prevention of vaso-obliteration in the OIR model. Taken together, lactam mimic structure and stereochemistry strongly influenced conformation and biased signaling. Selective modulation of IL-1 signaling was proven to be particularly beneficial

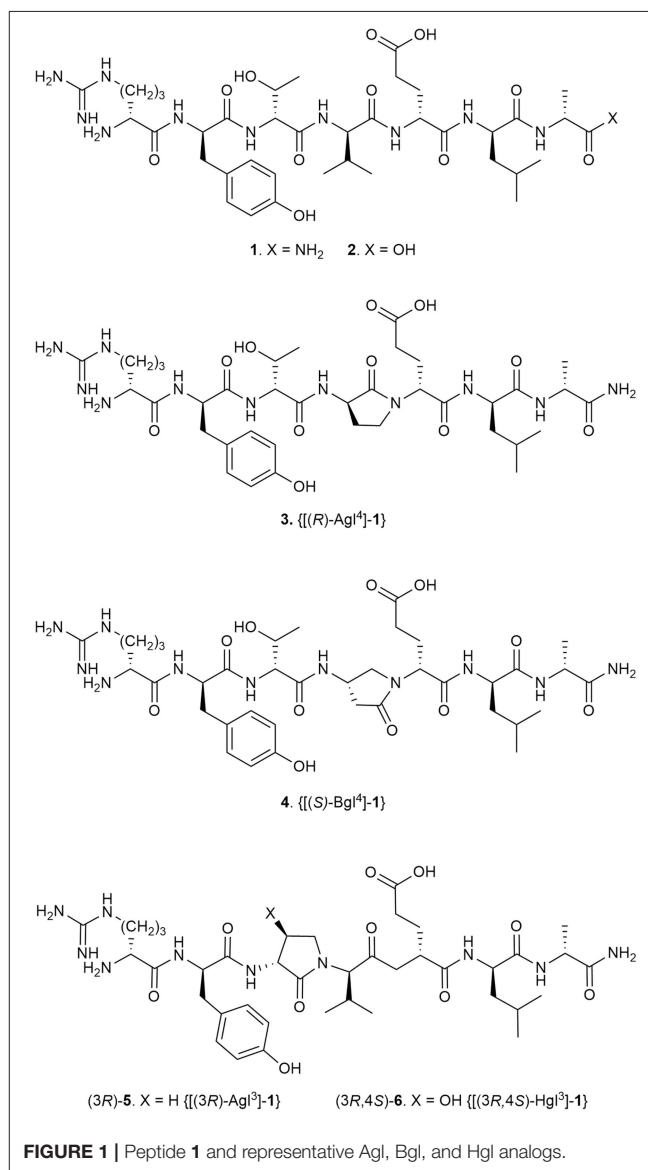
for curbing inflammation in models of preterm labor and retinopathy of prematurity (ROP). A class of biased ligands has been created with potential to serve as selective probes for studying IL-1 signaling in disease. Moreover, the small peptide mimic prototypes are promising leads for developing immunomodulatory therapies with easier administration and maintenance of beneficial effects of NF- κ B signaling.

Keywords: β -hydroxy- α -amino- γ -lactam (Hgl), interleukin-1 receptor antagonist, 101.10 (rytvela), β -turn, Freidinger lactams, solid-phase peptide synthesis, retinopathy, prematurity

INTRODUCTION

Among examples of synthetic methods to create folded peptides, the application of α -amino- γ -lactam (Agl) residues to control folding is a mainstay for biomedical research to improve biological activity (Freidinger et al., 1980; St-Cyr et al., 2017). Previously (Jamieson et al., 2009), an Agl residue scan of the all D-amino acid linear peptide 101.10 (**1**, H-D-Arg-D-Tyr-D-Thr-D-Val-D-Glu-D-Leu-D-Ala-NH₂, **Figure 1**) was used to study conformation-activity relationships of this allosteric modulator of the interleukin (IL)-1 receptor (IL-1R), which is of great interest in the treatment of many inflammatory diseases given the shortcomings of currently-approved anti-IL-1 therapeutics. The resulting lactam analogs exhibited properties that were either similar or improved relative to the parent peptide **1** (Jamieson et al., 2009; Boutard et al., 2011). Inspired by the activity of the Agl analogs but wary that the absence of side chain function may diminish potency despite a favorable geometry, the corresponding β -hydroxy- α -amino- γ -lactam (Hgl) residue was conceived to examine constraint of both backbone and side chain conformation of the D-Thr residue (St-Cyr et al., 2010). A detailed study of **1** is now reported in which all configurations of Agl, Hgl, and Val residues (e.g., **5** and **6**, **Figure 1**) are used to study the central D-Thr-D-Val dipeptide moiety.

IL-1 is a pro-inflammatory cytokine extensively involved in many diseases (Dinarello et al., 2012) and has been described to play a major role in inflammatory episodes leading to preterm birth (PTB) (Romero et al., 1989; Yoshimura and Hirsch, 2005; Puchner et al., 2011; Nadeau-Vallée et al., 2015) and its associated sequela of retinopathy of prematurity (ROP) (Rivera et al., 2013). IL-1 exerts its biological effects through complexation to the ubiquitously expressed IL-1R (Dinarello, 2002) and dimerization with the IL-1R accessory protein (IL-1RacP). IL-1 activates various downstream signaling mediators, notably PGE₂ and NF- κ B, which trigger hyperthermic and pro-inflammatory effects (Dinarello et al., 1999). Agents that block the effects of IL-1 offer the potential to treat diseases included in chronic inflammatory disorders such as rheumatoid arthritis and Crohn's disease (Hallegua and Weisman, 2002). Currently-approved IL-1R antagonists, such as the endogenous IL-1R antagonist (IL-1Ra), compete with the agonist (i.e., IL-1 β) by binding at the orthosteric, native-ligand binding site (Braddock and Quinn, 2004). Moreover, all are large proteins (17.5–251 kDa): Kineret® (recombinant IL-1ra; Biovitrium), Canakinumab (Novartis) Gevokizumab (IL-1 monoclonal antibodies; XOMA corporation), and Rilonacept



[Regeneron; soluble IL-1R (Fc-bound)]. The use of relatively large immunomodulators in clinical settings presents secondary effects such as immunosuppression, which increases the risk for opportunistic infections and pain at the site of injection. Such drawbacks may account for failures in clinical trials (Opal et al., 1997; Roerink et al., 2017; Mantero et al., 2018)

and may be related to non-selective interference of all signals triggered by IL-1 β because of the orthosteric competitive nature of these biologics. Preservation of the nuclear factor κ -light-chain-enhancer of activated B cells (NF- κ B) has been suggested to be beneficial, due to retained anti-apoptotic activity (Castro-Alcaraz et al., 2002) and promotion of the differentiation and proliferation of B and T cells, which are critical for the immune response against pathogenic insults (Gerondakis and Siebenlist, 2010).

Heptapeptide **1** (850 Da) binds at spatially distinct sites from endogenous IL-1 β , and selectively and allosterically regulates downstream signaling of inflammatory pathways (Quiniou et al., 2008; Nadeau-Vallée et al., 2015). Derived from a loop region of the IL-1RacP using a strategy for conceiving peptide modulators based on sequences from protein receptors (Hebert et al., 1996; Tan et al., 2001; Rihakova et al., 2009; Bourguet et al., 2014), peptide **1** significantly attenuated hyperoxia (oxidant stress)-induced increases in IL-1 β , tumor necrosis factor- α (TNF- α), intercellular adhesion molecule (ICAM)-1, and semaphorin (Sema)-3A (Rivera et al., 2013). These molecular changes caused by peptide **1** were associated with prevention of retinal vaso-obliteration, acceleration of normal revascularization, and normalization of vascular density. In addition, fluorescein-conjugated **1** was shown to localize principally in microglial and endothelial cells in the inflamed retina subjected to oxygen-induced retinopathy (OIR) conditions. In contrast to currently approved IL-1 inhibitors, peptide **1** exhibited pharmacological selectivity by inhibiting some IL-1-triggered pathways such as p38 mitogen-activated protein kinases (p38 MAPK) and Rho-associated coiled-coil-containing protein kinase 2 (ROCK2), while preserving NF- κ B (Nadeau-Vallée et al., 2015). In models of hyperthermia, inflammatory bowel disease and contact dermatitis, peptide **1** also proved superior to corticosteroids and FDA-approved IL-1Ra (Quiniou et al., 2008). In models of PTB, peptide **1** has been shown to be an effective early intervention for suppressing the downstream inflammatory cascade induced by bacterial lipopolysaccharide (LPS, to mimic chorioamnionitis), and for preventing the premature initiation of uterine activation proteins and subsequent onset of labor in mice (Nadeau-Vallée et al., 2015).

Conformational restriction of natural peptides has been used to identify active geometry and to enhance therapeutic potential by mitigating issues such as low oral availability and poor metabolic stability (Carney et al., 2014; Rubin and Qvit, 2016; Lubell, 2017). Since pioneering studies by Freidinger and Veber, the application of Agl residues has proven effective for constraining the backbone sequence to favor β -turn geometry in various peptides (Freidinger et al., 1980, 1982; Yu et al., 1988; Zhang et al., 1996; Aube, 1999; Perdih and Kikelj, 2006; Valle et al., 2009). In the interest of understanding the biologically active conformation responsible for the mechanism of action, Agl residues as well as their β -amino- γ -lactam (Bgl) counterparts have been used in structure-activity relationship studies of peptide **1** (Jamieson et al., 2009; Ronga et al., 2010; Boutard et al., 2011). Although systematic replacement of each residue of peptide **1** with D-Ala indicated that removal of certain side chains may lead to activity loss, analogs possessing one (R)-Agl residue,

respectively at either the D-Tyr, D-Val, D-Glu, or D-Leu positions demonstrated similar efficacy, and [(S)-Bgl⁴]-**1** increased activity compared to peptide **1** in inhibiting IL-1 β -induced DNA primase-1-dependent thymocyte TF-1 proliferation (Jamieson et al., 2009; Boutard et al., 2011). An active turn conformation situated about the D-Tyr-D-Thr-D-Val triad appeared key for potent inhibition of IL-1 β -induced thymocyte TF-1 proliferation; however, [(R)-Agl³]-**1** exhibited significantly diminished activity, likely due to loss of side chain (Jamieson et al., 2009).

Employing all configurations of Agl, Hgl, and Val residues to study the D-Thr-D-Val dipeptide of **1**, the influences of backbone and side chain conformation on modulation of IL-1R signaling has now been examined *in vitro* by assessing phosphorylation of downstream IL-1 modulators and transcription of inflammatory genes. Moreover, the effects of their lactam structures and configurations have been assessed *in vivo* on murine models of preterm birth (PTB) and oxygen-induced retinopathy (OIR). These investigations have illustrated the influences of the orientation of the hydroxyl group and backbone for activity and biased signaling, particularly with respect to inhibition of NF- κ B.

MATERIALS AND METHODS

General Chemistry Methods

Unless otherwise specified, all non-aqueous reactions were performed under an inert argon atmosphere. All glassware was dried with a flame under flushing argon gas or stored in the oven, and let cool under an inert atmosphere prior to use. Anhydrous solvents (THF, DCM, MeCN, MeOH, toluene, and DMF) were obtained by passage through solvent filtration systems (Glass Contour, Irvine, CA) and solvents were transferred by syringe. Reaction mixture solutions (after aqueous workup) were dried over anhydrous MgSO₄ or Na₂SO₄, filtered, and rotary-evaporated under reduced pressure. The syntheses under microwave conditions were performed on a 0–400 W Biotage® Robot Eight and Robot Sixty microwave synthesizer. Column chromatography was performed on 230–400 mesh silica gel, and thin-layer chromatography was performed on alumina plates coated with silica gel (Merck 60 F₂₅₄ plates). Visualization of the developed chromatogram was performed by UV absorbance or staining with iodine or potassium permanganate solutions. Melting points were obtained on a Buchi melting point B-540 apparatus and are uncorrected. Specific rotations, $[\alpha]^D$ values, were calculated from optical rotations measured at 20 and 25°C in CHCl₃ or MeOH at the specified concentrations (c in g/100 mL) using a 0.5 dm cell length (l) on an Anton Paar Polarimeter, MCP 200 at 589 nm, using the following general formula: $[\alpha]_{25}^D = (100 \times \alpha)/(l \times c)$. Accurate mass measurements were performed on an LC-MSD instrument in electrospray ionization (ESI-TOF) mode at the Université de Montréal Mass Spectrometry facility. Sodium adducts $[M + Na]^+$ were used for empirical formula confirmation. Nuclear magnetic resonance spectra (¹H NMR, ¹³C NMR) were recorded on Bruker 300, 400, 500, and 700 MHz spectrometers. ¹H NMR spectra were referenced to CDCl₃ (7.26 ppm), CD₃OD (3.31 ppm), C₆D₆ (7.16 ppm) or DMSO-d₆ (2.50 ppm), and ¹³C NMR spectra were measured in CDCl₃ (77.16 ppm), CD₃OD (49.0 ppm),

C₆D₆ (128.39 ppm) or DMSO-d₆ (39.52 ppm) as specified below. Coupling constant *J* values were measured in Hertz (Hz) and chemical shift values in parts per million (ppm). Infrared spectra were recorded in the neat on a Perkin Elmer Spectrometer FT-IR instrument, and are reported in reciprocal centimeters (cm⁻¹). Analytical LCMS and HPLC analyses were performed on a 5 μM, 50 mm × 4.6 mm C18 Phenomenex Gemini columnTM with a flow rate of 0.5 mL/min using appropriate gradients from pure water containing 0.1% formic acid (FA), to mixtures with either CH₃CN containing 0.1% FA, or MeOH containing 0.1% FA. Peptides were purified on a preparative column (C18 Gemini columnTM) using appropriate gradients from pure water containing 0.1% FA to mixtures with MeOH containing 0.1% FA at a flow rate of 10 mL/min.

Chemical Reagents

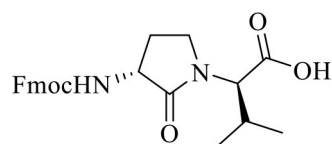
Unless specified otherwise, commercially available reagents were purchased from Aldrich, A & C American Chemicals Ltd., Fluka and Advanced ChemtechTM and used without further purification, including PPh₃, DIAD, *p*-nitrobenzoic acid, NaN₃, piperidine, DIEA, TFA, TES, TEA, CH₃I, NaH, Fmoc-OSu, Boc₂O, NaIO₄, *m*-CPBA, TFE, and HFIP. Polystyrene Rink amide resin (0.5 mmol/g) was purchased from Advanced ChemtechTM, and the manufacturer's reported resin loading was used in the calculation of yields of final product. All commercially available amino acids [e.g., Fmoc-D-Ala-OH, Fmoc-D-Leu-OH, Fmoc-D-Glu(*t*-Bu)-OH, Fmoc-D-Tyr(*t*-Bu)-OH, Fmoc-D-Arg(Pmc)-OH, Boc-D-Arg(Pmc)-OH, H-L-Met-OH, H-D-Met-OH, L-Val-O-*t*-Bu•HCl, D-Val-O-*t*-Bu•HCl, Boc-L-Met-OH and Boc-D-Met-OH] and coupling reagents (e.g., HOBt, HBTU and DCC) were purchased from GL BiochemTM and used as received. Solvents were obtained from VWR international.

H-D-Arg-D-Tyr-(R)-Agl-D-Val-D-Glu-D-Leu-D-Ala-NH₂ [(3R)-Agl³]-1, [(3R)-5]

A 10 mL plastic filtration tube equipped with a polyethylene filter was charged with polystyrene Rink amide resin, 75–100 mesh, 1%, DVB with a 0.5 mmol/g loading, (200 mg) and DCM (about 7 mL). The tube was sealed, shaken for 30 min to induce swelling and the liquid phase was removed. The Fmoc group was cleaved from the resin-bound peptide by treatment with a freshly-prepared 20% piperidine in DMF solution (about 7 mL), shaking for 30 min, and removal of the liquid phase. The resin was repeatedly (3x per solvent) washed (10 mL per wash) over a total of 6 min with DMF and DCM, and the liquid phase was removed. Generation of the free amine resin was confirmed by a positive Kaiser test. Peptide elongation was conducted by treating the DMF-swollen free amine resin with a freshly prepared acylation solution containing Fmoc-D-Ala-OH (3 eq), HBTU (3 eq), and DIEA (6 eq) in DMF (4–7 mL). After agitating for 3–5 h at room temperature, Fmoc cleavage and peptide elongation were reiterated using Fmoc-D-Leu-OH, Fmoc-D-Glu(*t*-Bu)-OH, *N*-Fmoc-(3R)-Agl³-R-Val-OH dipeptide, Fmoc-D-Tyr(*t*-Bu)-OH, and Fmoc-D-Arg(Pmc)-OH. For the coupling of *N*-Fmoc-(3R)-Agl³-R-Val-OH, only a stoichiometric quantity of dipeptide was used; for Fmoc-D-Tyr(*t*-Bu)-OH, coupling was repeated twice using a higher reaction concentration. Synthetic progress was monitored using

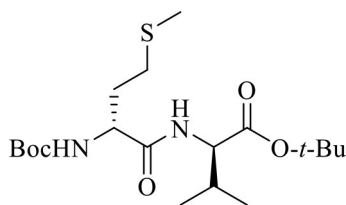
a combination of the Kaiser test and LC-MS analyses on TFA cleaved resin aliquots, which were concentrated and dissolved in mixtures of water and MeCN. The completed peptide sequence was cleaved from the resin by treatment with TFA/H₂O/TES (3 mL, 95/2.5/2.5, v/v/v), with shaking for 3 h, and the liquid phase was collected. The resin was repeatedly (2x) washed with TFA and the combined liquid phases were concentrated *in vacuo*. The residue was dissolved in a minimal volume of acetonitrile, precipitated with ice-cold diethyl ether, and centrifuged. The supernatant was removed by decantation and the precipitate was collected. The precipitation and collection process was repeated on the supernatant. The combined white solid precipitate was dissolved in water (5 mL), freeze-dried to give a white powder (44% crude purity), and purified using preparative HPLC on a WatersTM Prep LC instrument equipped with a reverse-phase GeminiTM C18 column (250 × 21.2 mm, 5 μm), using a gradient of MeOH (0.1% FA) in H₂O (0.1% FA) at a flow rate of 10.0 mL/min and UV detection at 280 nm. Fractions containing pure peptide were combined and lyophilized to afford peptide (3R)-5 (10 mg, 12% yield of >95% purity): LCMS [10–90% MeOH (0.1% FA) in water (0.1% FA) over 14 min; RT 8 min] and [10–90% MeCN (0.1% FA) water (0.1% FA) over 14 min; RT 5.6 min]; HRMS (ESI⁺) calcd *m/z* for C₃₈H₆₂N₁₁O₁₀ [M+H]⁺, 832.4676 found 832.4682.

(3R, 2'R)-2-[3-N-(Fmoc)amino-2-oxopyrrolidin-1-yl]-3-methylbutanoic acid [(3R, 2'R)-7]



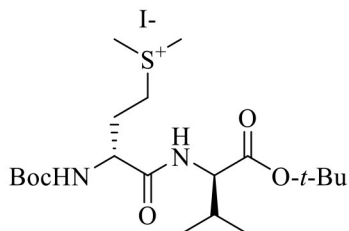
(3R, 2'R)-Acid (3R, 2'R)-14 (1 eq., 67 mg, 0.27 mmol) was dissolved in 1:1 acetone (1 mL) and H₂O (1 mL), treated with Na₂CO₃ (2 eq., 58 mg, 0.55 mmol) followed by Fmoc-OSu (1.1 eq., 100 mg, 0.3 mmol), stirred at rt for 18 h, and concentrated to a residue that was dissolved in H₂O and acidified to pH 3–4 with citric acid (0.5 N solution). The aqueous solution was extracted multiple times with EtOAc until the aqueous layer no longer exhibited the carbamate by TLC. The organic layer was extracted with saturated NaHCO₃ (2 × 3 mL). The aqueous extractions were combined, acidified to pH 3–4 with 0.5 N citric acid solution, and extracted with EtOAc. The organic layer was washed with brine, dried over MgSO₄, filtered, and concentrated to afford (3R, 2'R)-carbamate (3R, 2'R)-7 (87 mg, 0.21 mmol, 75% yield): *R*_f = 0.26 (10% MeOH:DCM); [α]_D²⁵ 13.2° (*c* 0.41, MeOH); ¹H NMR (300 MHz, MeOD) δ 7.80 (d, *J* = 7.6, 2H), 7.68 (d, *J* = 7.4, 2H), 7.40 (t, *J* = 7.1, 2H), 7.31 (t, *J* = 6.9, 2H), 5.60 (d, *J* = 5, 1H), 4.53–4.18 (m, 5H), 3.74 (t, *J* = 9.2, 1H), 3.49–3.35 (m, 1H), 2.56–2.37 (m, 1H), 2.32–2.16 (m, 1H), 2.10–1.85 (m, 1H), 1.44–1.21 (m, 1H), 1.03 (d, *J* = 6.7, 3H), 0.93 (d, *J* = 6.7, 3H); ¹³C NMR (75 MHz, MeOD) δ 173.9, 171.6, 157.2, 143.9, 141.2, 127.4, 126.8, 124.8, 119.5, 66.7, 60.8, 52.2, 41.2, 28.1, 26.2, 18.4, 18.1; HRMS (ESI⁺) calcd *m/z* for C₂₄H₂₇N₂O₅ [M+H]⁺, 423.1914 found 423.1917.

(*R*)-*N*-(Boc)-Methioninyl-(*R*)-valine *tert*-butyl ester [(*R*, *R*)-10]



N-Boc-(*R*)-Methionine [(*R*)-8, 1 eq., 1 g, 4 mmol] and (*R*)-valine *tert*-butyl ester hydrochloride [(*R*)-9 HCl, 1 eq., 840 mg, 4 mmol] were dissolved in dry DMF (6 mL). On treatment of the mixture with triethyl amine (1 eq., 400 mg, 0.56 mL, 4 mmol) a precipitate was formed, and HOBT (1 eq., 540 mg, 4 mmol) and DCC (1 eq., 830 mg, 4 mmol) were added to the mixture. The mixture was stirred at rt for 24 h, filtered and the filter cake was washed with DCM. The filtrate and washings were combined concentrated under vacuum. The residue was dissolved in EtOAc (6 mL), washed with 0.5 M citric acid (3 × 4 mL), 2 N aqueous NaHCO₃ (3 × 4 mL) and brine (4 mL), dried over Na₂SO₄, filtered and concentrated under vacuum to give (*R,R*)-dipeptide (*R,R*)-10 as a white foam (1.27 g, 3.13 mmol, 78% yield): *R*_f = 0.28 (20% EtOAc in hexane); [α]_D²⁵ −4.1° (c 1.95, CHCl₃); ¹H NMR (300 MHz, CDCl₃) δ 6.61 (d, *J* = 8.4, 1H), 5.20 (d, *J* = 8.0, 1H), 4.40 (dd, *J* = 8.8, 4.6, 1H), 4.35–4.22 (br, 1H), 2.59 (t, *J* = 7.2, 2H), 2.23–1.86 (m, 5H), 1.46 (s, 9H), 1.44 (s, 9H), 0.91 (dd, *J* = 7.6, 7.1, 6H); ¹³C NMR (75 MHz, CDCl₃) δ 171.4, 170.7, 155.6, 82.1, 80.2, 57.7, 53.4, 31.6, 31.4, 30.3, 28.4, 28.2, 19.1, 17.6, 15.3; HRMS (ESI⁺) calcd *m/z* for C₁₉H₃₆N₂O₅S [M+H]⁺, 405.2418 found 405.2433.

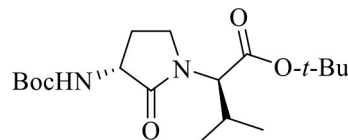
***N*-Boc-(*R*)-Methioninyl-(*R*)-valine *tert*-butyl ester methylsulfonium iodide [(*R*, *R*)-11]**



(*R,R*)-Dipeptide (*R,R*)-10 (1 eq., 500 mg, 1.24 mmol) was dissolved in CH₃I (39 eq., 3 mL, 48.2 mmol) and stirred at rt for 24 h, and concentrated under vacuum. The volatile contaminants were removed by repeated (3x) co-evaporation with DCM to give (*R,R*)-methylsulfonium iodide (*R,R*)-11 as yellow gummy foam (655 mg, 1.2 mmol, 97% yield): *R*_f = 0.2 (5% MeOH in DCM); [α]_D²⁵ 22° (c 1, MeOH); ¹H NMR (300 MHz, CDCl₃) δ 7.53 (d, *J* = 7.1, 1H), 5.98 (d, *J* = 7.2, 1H), 4.60 (dd, *J* = 12.5, 7.3, 1H), 4.24 (dd, *J* = 7.8, 5.2, 1H), 3.96–3.81 (m, 1H), 3.73–3.58 (m, 1H), 3.32 (s, 3H), 3.21 (s, 3H), 2.64–2.47 (m, 1H), 2.42–2.14 (m, 2H), 1.45 (s, 9H), 1.42 (s, 9H), 0.99 (t, *J* = 7.3, 6H); HRMS (ESI⁺) calcd *m/z* for C₂₀H₃₉N₂O₅S [M]⁺, 419.2574 found 419.2567.

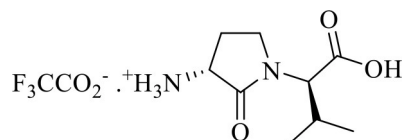
tert-Butyl (3*R*, 4*S*, 2'*R*)-2-[3-(Fmoc)amino-4-hydroxy-2-oxopyrrolidin-1-yl]-3-methylbutanoate [(3*R*, 4*S*, 2'*R*)-12] was prepared as previously described (Geranurimi and Lubell, 2018).

(3*R*, 2'*R*)-*tert*-Butyl 2-[3-(Boc)amino-2-oxopyrrolidin-1-yl]-3-methylbutanoate [(3*R*, 2'*R*)-13]



(*R,R*)-Methylsulfonium iodide (*R,R*)-11 (1 eq., 158 mg, 0.289 mmol) was dissolved in a 1:1 mixture of DMF (3.5 mL) and DCM (3.5 mL) under argon, cooled to 0°C, treated with NaH (60% dispersion in mineral oil, 1.2 eq., 14 mg, 0.347 mmol), and stirred at 0°C for 2.5 h. The reaction was diluted with methyl acetate (2.5 mL) and H₂O (0.5 mL) and allowed to warm to rt with stirring overnight. The reaction mixture was concentrated under vacuum, quenched with 1 M NaH₂PO₄, and extracted three times with EtOAc. The combined EtOAc layers were dried over MgSO₄, filtered and concentrated to a residue that was purified by column chromatography on silica gel using 20% of EtOAc in hexane as eluent. Evaporation of the collected fractions provided (3*R*,2'*R*)-lactam (3*R*,2'*R*)-13 (60 mg, 0.17 mmol, 58% yield): *R*_f = 0.31 (30% EtOAc in hexane); [α]_D²⁵ 35.8° (c 1.6, CHCl₃); ¹H NMR (300 MHz, CDCl₃) δ 5.09 (s, 1H), 4.39 (d, *J* = 9.3, 1H), 4.31–4.16 (br s, 1H), 3.72 (t, *J* = 9.1, 1H), 3.27 (m, 1H), 2.72–2.58 (m, 1H), 2.26–2.11 (m, 1H), 1.90–1.71 (m, 1H), 1.45 (s, 9H), 1.44 (s, 9H), 0.98 (d, *J* = 6.7, 3H), 0.89 (d, *J* = 6.8, 3H); ¹³C NMR (75 MHz, CDCl₃) δ 173.0, 169.7, 156.1, 82.1, 80.0, 61.0, 52.4, 41.7, 29.4, 28.8, 28.5, 28.2, 19.4, 19.3; HRMS (ESI⁺) calcd *m/z* for C₁₈H₃₃N₂O₅ [M+H]⁺, 357.2384 found 357.2399.

(3*R*, 2'*R*)-2-[3-Amino-2-oxopyrrolidin-1-yl]-3-methylbutanoate trifluoroacetate [(3*R*, 2'*R*)-14]



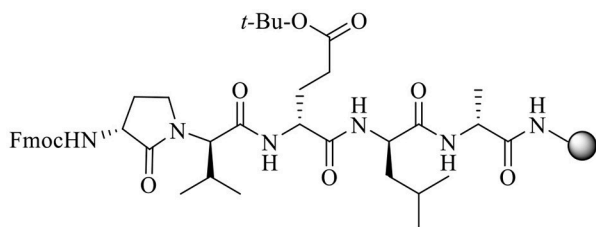
A solution of (3*R*,2'*R*)-lactam (3*S*,2'*S*)-13 (1 eq., 100 mg, 0.281 mmol) in TFA (1 mL) and DCM (1 mL) was stirred at rt. After TLC analysis revealed complete consumption of the carbamate, the volatiles were evaporated on a rotary evaporator, and the residue was precipitated from ice-cooled diethyl ether and collected using a centrifuge to yield (3*R*,2'*R*)-trifluoroacetate (3*R*,2'*R*)-14 (77.6 mg, 0.247 mmol, 88% yield) as white precipitate: *R*_f = 0.1 (1:9:90 Et₃N:MeOH:DCM); [α]_D²⁵ 45.6° (c 0.5, MeOH); ¹H NMR (400 MHz, MeOD) δ 4.40 (d, *J* = 9.3, 1H), 4.17 (dd, *J* = 11.0, 8.5, 1H), 3.92–3.81 (m, 1H), 3.60–3.45 (m, 1H), 2.66–2.54 (m, 1H), 2.35–2.19 (m, 1H), 2.14–1.97 (m, 1H), 1.05 (d, *J* = 6.7, 3H), 0.98 (d, *J* = 6.8, 3H); ¹³C NMR (75 MHz, MeOD) δ 171.3, 170.0, 60.8, 50.3, 41.6, 28.2, 24.5, 18.3, 18.2; HRMS (ESI⁺) calcd *m/z* for C₉H₁₇N₂O₃ [M+H]⁺, 201.1234 found 201.1226.

N-Fmoc-(R)-Methionine methyl ester [(R)-15] and N-Fmoc-(R)-Methionine sulfoxide methyl ester [(R)-16] were prepared by a modified version (vide infra) of the previously described method (Sicherl et al., 2010).

N-Fmoc-(2R)-Vinylglycine methyl ester [(R)-17] and (2R, 2'R)- and (2R, 2'S)-Methyl 2-(oxiranyl)-N-(Fmoc)glycinate [(2R, 2'R)-18 and (2R, 2'S)-18] were prepared as previously described (St-Cyr et al., 2010).

N-Fmoc-(3R, 4S, 2'R)-Hgl-Val-*t*Bu [(3R, 4S, 2'R)-19] and (3R, 4R, 2'R)-tert-Butyl 2-[3-(Fmoc)Amino-4-*p*-nitrobenzoyloxy-2-oxopyrrolidin-1-yl]-3-methylbutanoate [(3R, 4R, 2'R)-20] were prepared as previously described (Geranurimi and Lubell, 2018).

N-Fmoc-[(3R)-Agl³]-D-Val-D-Glu(*t*-Bu)-D-Leu-D-Ala-Rink amide resin (22)



A solution of acid (3R,2'R)-7 (1 eq., 87 mg, 0.2 mmol) and 2-(1H-benzotriazol-1-yl)-1,1,3,3-tetramethyluronium hexafluorophosphate (HBTU, 1 eq., 78 mg, 0.2 mmol) in dimethylformamide (DMF, 2 mL) was stirred for 1 min, treated with *N,N*-diisopropylethylamine (DIEA, 2 eq., 53.2 mg, 68 μ L, 0.4 mmol), stirred for 5 min and added to H-D-Glu(*t*-Bu)-D-Leu-D-Ala-Rink amide resin **21** (400 mg, 0.5 mmol/g, 0.2 mmol), which was placed earlier into a 3-mL plastic filtration tube equipped with a polyethylene filter and swollen in DMF (2 mL). The resin mixture was shaken at rt for 5 h, and the liquid phase was removed by filtration. The resin was repeatedly (3x per solvent) washed (15 s per wash) with DMF and DCM, and dried under vacuum to afford resin **22**. To assess resin-bound peptide purity, a resin aliquot (5 mg) was placed into a 1-mL plastic filtration tube equipped with a polyethylene filter and treated with 20% piperidine in DMF. After 0.5 h, the liquid phase was removed by filtration and the resin was treated with 0.5 mL of a 95:2.5:2.5 cocktail of TFA:H₂O:triethylsilane (TES) at rt for 1 h, and filtered. The filtrate was collected in a 1.5 mL tube and concentrated by purging with an air stream. The residue was treated with Et₂O (1 mL), and centrifuged for 2 min. After decantation, the precipitate was dissolved in H₂O (1 mL) and analyzed by LCMS [10–90% MeOH (0.1% FA)/ water (0.1% FA), 14 min, RT 9.2 min] and [10–90% MeCN (0.1% FA)/ water (0.1% FA), 14 min, RT 7.6 min].

Circular Dichroism Spectroscopy

CD spectra were recorded on a Chirascan CD Spectrometer (Applied Photophysics, Leatherhead, United Kingdom) using a 1.0 cm path-length quartz cell containing 20 μ M of peptide dissolved in Milli-Q water. The experimental settings were as follows: 1 nm, bandwidth; 0.5 nm, step size; 3 s, sampling time.

Animals

Timed-pregnant CD-1 mice were obtained from Charles River (Saint-Constant, QC, Canada) at gestational day 12 and were acclimatized for 4 days prior to experiments. Animals were used according to a protocol approved by the Animal Care Committee of Hôpital Sainte-Justine in accordance with the principles of the Guide for the Care and Use of Experimental Animals of the Canadian Council on Animal Care. The animals were maintained on standard laboratory chow under a 12 h:12 h light/dark cycle and allowed free access to chow and water.

Two-day-old (P2) Sprague Dawley rat pups and their mothers were ordered from Charles River (Saint-Constant, QC, Canada) and acclimatized for 3 days. The rats were housed in standard cages with *ad libitum* access to food and water and kept in a 12 h:12 h light/dark cycle. To control for the effects of litter size on retinal development, the sizes of litters were reduced to 12 by sacrificing excess pups by decapitation while under 2% isoflurane anesthesia. All procedures and protocols involving the use of these rats were approved by the Animal Care Committee of the research center of Hôpital Maisonneuve-Rosemont and are in accordance with the Statement for the Use of Animals in Ophthalmic and Vision Research approved by the Association for Research in Vision and Ophthalmology (ARVO), and guidelines established by the Canadian Council on Animal Care.

Reagents

Chemicals were purchased from the following manufacturers: human rIL-1 β (200-01B; PeproTech), LPS (L2630; Sigma-Aldrich), rytvela (peptide **1**) (Elim Biopharmaceuticals, Hayward, CA) and Kineret (Anakinra, Sobi, Biovitrum Stockholm, Sweden).

qPCR Experiments

HEK-Blue IL-33/IL-1 β cells were purchased from InvivoGen (San Diego, CA) and used at passages under 15. HEK-Blue cells were cultured in DMEM growth medium supplemented with 10% serum, 50 U/mL penicillin, 50 mg/mL streptomycin, 200 mg/mL zeocin, and 100 mg/mL hygromycin. Cells were grown in regular conditions (37°C, 5% CO₂). Cells were serum starved overnight and treated with 100 ng/mL IL-1 β for 4 h. Cells were pre-incubated for 30 min with peptides **1**, **5**, or **6** (10⁻⁶M) or Kineret (1.0 mg/mL) prior to the experiments to reach equilibrium ($n = 4$ each treatment). Cells were harvested and incubated for 5 min in RIBOzol (AMRESCO). RNA was extracted according to manufacturer's protocol and RNA concentration and integrity were measured with a NanoDrop 1,000 spectrophotometer. A total of 500 ng RNA was used to synthesize cDNA using iScript Reverse Transcription SuperMix (Bio-Rad, Hercules, CA). Primers were designed using National Center for Biotechnology Information Primer Blast and are shown in **Table 1**. Quantitative gene expression analysis was performed on Stratagene MXPro3000 (Stratagene) with SYBR Green Master Mix (Bio-Rad). Gene expression levels were normalized to 18S universal primer (Ambion Life Technology, Burlington ON, Canada). Genes analyzed include *IL1 β* , *IL6*, and *PTGHS2*.

TABLE 1 | List of primers for the human genes assessed by qPCR.

Gene	Forward primer (5' → 3')	Reverse primer (5' → 3')
<i>IL1β</i>	AGCTGGAGAGTGATAGCCCAA	ACGGGCATGTTTCTGCTTG
<i>IL6</i>	TTCAATGAGGAGACTTGCTGG	CTGGCATTGTGGTTGGGTC
<i>PTGHS2</i>	ATATTGGTGACCGTGGAGC	GTTCTCCGTACCTTCACCCC

[Prostaglandin H synthetase 2 or cyclooxygenase-2 (COX-2)]. Data are representative of 3 experiments (each with $n = 4$ per treatment group).

NF-κB QUANTI-Blue Assay

HEK-Blue IL-33/IL-1 β cells (InvivoGen) were pretreated with peptides **1**, **5**, or **6** (10^{-6} M) or Kineret (1.0 mg/mL) for 30 min, followed by treatment with a constant concentration of IL-1 β (100 ng/mL), and then incubated at 37°C for 4 h. Levels of secreted alkaline phosphatase in cell culture supernatant were determined using the QUANTI-Blue assay, according to the manufacturer's instructions (InvivoGen). Alkaline phosphatase activity was assessed by measuring the optical density (OD) at 620–655 nm with a micro plate reader (EnVision Multilabel reader; PerkinElmer, Waltham, MA). Data are representative of 3 experiments (each with $n = 4$ per treatment group).

p38 MAPK, ROCK2, and JNK Phosphorylation Assay

RAW Blue cells (InvivoGen) were grown under standard conditions (37°C, 5% CO₂) and maintained under passage number 15. Cells were equilibrated with **1**, **5**, or **6** (10^{-6} M) or Kineret (1.0 mg/mL) for 30 min, after which time they were exposed to IL-1 β (100 ng/mL) for 15 min. Cells were harvested and lysed on ice for 30 min using a radioimmunoprecipitation assay buffer (Cell Signaling) supplemented with 1 mM phenylmethylsulfonyl fluoride (PMSF) and cComplete™ EDTA-free protease inhibitor cocktail (Roche, Mannheim, Germany, prepared according to the manufacturer's instructions). Protein concentrations were determined using a Bradford protein assay (Bio-Rad) on 96-well plates with a microplate reader (EnVision Multilabel reader) measuring OD at 595 nm. Bovine serum albumin serial dilutions were used to generate a standard curve. Lysates were then mixed with 4X reducing sample buffer (Bio-Rad).

Lysates were loaded (30 μ g protein per well) in a 5% acrylamide stacking gel, and samples were electrophoresed in a 12% acrylamide resolving gel for 1.5 h at 120 V, followed by a 1 h transfer onto polyvinylidene difluoride (PDVF) membranes at 100 V. Membranes were blocked and incubated with 1:1,000 dilution of primary antibody and 1:20,000 dilution of secondary antibodies according to the manufacturer's instructions. Antibodies used were for phospho-p38 MAPK (Cell Signaling, #9211), p38 MAPK (Cell Signaling, #9212), SAPK/JNK (Cell Signaling, #9252), phospho-SAPK/JNK (Cell Signaling, #9251), ROCK2 (Thermo Fisher Scientific PA5-21131), phospho-ROCK2 (Thermo Fisher Scientific PA5-34895), and goat anti-rabbit conjugated to horseradish peroxidase (Abcam, ab6721).

Membranes were imaged using an Amersham Imager 600 (GE Healthcare) using Clarity Western ECL Substrate (Bio-Rad). The intensity of protein bands was quantified using ImageJ and standardized using total (phosphorylated + non-phosphorylated) protein content. Data are representative of three independent experiments.

Radioligand Displacement Assay

Displacement of radiolabeled peptide **1** was performed as described previously (Quiniou et al., 2008). Briefly, RAW-Blue macrophage cells (InvivoGen; San Diego, CA) were pre-incubated for 20 min with 100 μ M of non-radiolabeled ("cold") peptide **1**, **5**, or **6** followed by incubation for 2 h at 37°C with [¹²⁵I]-peptide **1** at 600 nM concentration to ensure maximal specific binding (Quiniou et al., 2008). Cells were washed four times with PBS buffer and lysed with 0.1 N NaOH/0.1% Triton X-100. Bound radioactivity was measured on cell lysates with a Hidex AMG gamma counter (Hidex; Turku Finland). Data are representative of three independent experiments.

LPS-Induced Preterm Model in Mice

Timed-pregnant CD-1 mice at 16.5 days of gestation (G16.5) were anesthetized with 2% isoflurane and received an intraperitoneal injection of LPS ($n = 4$ per group, a single dose of 10 μ g) (Nadeau-Vallée et al., 2015, and Kakinuma et al., 1997). A dosage of 2 mg/kg/day of peptide **1**, **5**, or **6** or vehicle was injected subcutaneously in the neck, every 12 h until delivery. On G16.5, a dose of 1 mg/kg was injected 30 min before stimulation with LPS (to allow distribution of drugs to target tissues) and 1 mg/kg was injected 12 h after stimulation ($n = 4$ each treatment). Mice delivery was assessed every hour until term (G19–G19.5). A mouse is considered as delivering prematurely if the first pup is delivered earlier than G18.5.

Oxygen-Induced Retinopathy in Sprague Dawley Rats

On P5, litters were transferred to a controlled hyperoxic environment (Biospherix OxyCycler A84XOV) and maintained at $80 \pm 1\%$ O₂, which is used to induce vaso-obliteration of the retinal vasculature. At this timepoint, the vasculature is immature and particularly susceptible to hypoxic insults resulting in vaso-obliteration, a defining characteristic of the early stage of retinopathies in premature infants (Garner and Ashton, 1971). Control litters were not exposed to hyperoxia and were kept in standard conditions with room air (21% O₂). To control for the effects of hyperoxia on the lactation of the dams, dams of hyperoxic litters were switched with dams of control litters on P8.

In litters exposed to hyperoxia, pups were randomized to receive phosphate-buffered saline (PBS) vehicle, 2 mg/kg/day of peptides **1**, **5**, or **6** or 3 mg/kg/day of Kineret from P5 to P10. These doses were determined from our previous study (Rivera et al., 2013) and administered in twice-daily intra-peritoneal injections titrated to 20 μ L per injection with 28-gauge insulin syringes. A total of 6–8 pups were used for each treatment group.

On P10, pups were euthanized by decapitation under 2% isoflurane anesthesia. Eyes were enucleated and fixed in 4%

paraformaldehyde for 1 h at room temperature before washing twice with PBS and storage at 4°C in PBS until further processing.

Retinal Flatmount and Immunohistochemistry

Under a dissecting microscope, the cornea and lens were gently removed from the eyes and remnants of the hyaloid vasculature were removed from the retinas using surgical scissors and tweezers. The retinas were gently removed from the underlying sclera/choroid complex.

Retinas were treated at room temperature for 1 h with a blocking solution consisting of 1% bovine serum albumin (BSA), 1% normal goat serum, 0.1% Triton X-100 and 0.05% Tween-20 in PBS. The retinas were then double-labeled overnight at 4°C with gentle shaking in an antibody solution consisting of 1 mM CaCl₂, 1% Triton X-100, 1% TRITC-conjugated lectin cell endothelial marker from *Bandeiraea simplicifolia* (Sigma-Aldrich, St Louis, MO) and a 1:500 dilution of rabbit anti-ionized calcium-binding adapter molecule (Iba)-1 antibody (Wako Chemicals USA) in PBS. The retinas were then washed thrice with PBS and incubated with a secondary antibody solution consisting of 1% BSA, 0.1% Triton X-100, 0.05% Tween-20 and 1:500 Alexa-594-conjugated donkey anti-rabbit IgG (ThermoFisher Scientific, Rockford, IL) in PBS for 2 h at room temperature. Retinas were washed thrice with PBS and then flat-mounted onto glass slides with coverslips and Fluoro-Gel mounting medium (Electron Microscopy Sciences, Hatfield, PA).

Microscopy

For assessment of vaso-obliteration, retinas were imaged using an epifluorescence microscope at 10X magnification (Zeiss AxioImager Z2) and version 4.8 of the AxioVision software. Images were captured and stitched together using the software's MosaiX feature. Iba-1 staining was assessed with the same microscope at 20X magnification, and a total of 4 fields per retina were imaged halfway between the optic nerve and the edge of the retina.

Representative images of Iba-1 staining were taken using a laser scanning confocal microscope (Olympus IX81 with Fluoview FV1000 Scanhead) with the Fluoview Software at 30X magnification.

Quantification and Data Analysis

The FIJI software was used to quantify the area of vaso-obliteration in each retina, expressed as a percentage of the area of the whole retina. The number of Iba-1-positive cells was counted using the cell counter plug-in in FIJI, and the average of cell counts in 4 fields per retina was calculated.

Data was analyzed using GraphPad Prism 7 with one-way ANOVA and Dunnett's test for multiple comparisons. Outliers were detected using Grubb's test. Results were treated as significant when *p* was <0.05 and expressed as mean ± SEM.

RESULTS

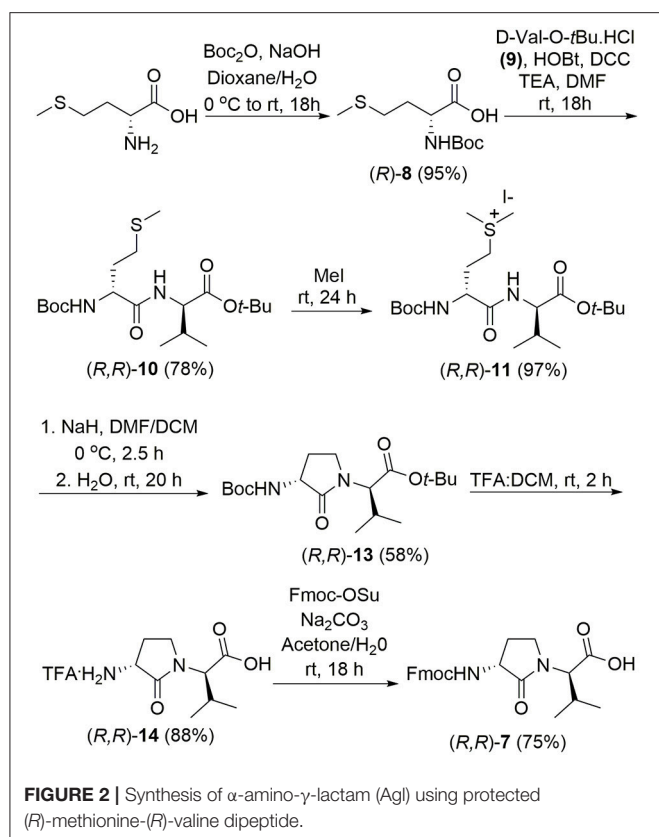
Chemical Synthesis

The application of lactam-bridged dipeptides by Freidinger et al. at Merck Sharp and Dohme Research Laboratories in the early

1980s marked an important milestone in the use of heterocycle synthesis to design constrained peptide mimics (Freidinger et al., 1980, 1982; Freidinger, 2003). Such so-called Freidinger-Weber lactams (e.g., Agl and Hgl) restrict backbone conformation by limiting rotation about the ϕ -, ψ -, and ω -dihedral angles such that Agl and Hgl residues prefer to situate at the *i*+1 residue in β -turn sequences contingent on sequence stereochemistry (Freidinger, 2003; St-Cyr et al., 2017). Moreover, in the case of Hgl, the hydroxyl group side chain orientation is locked due to restriction of the χ -dihedral angle (Sicherl et al., 2010). Although Freidinger-Weber lactams have been used to study a wide range of biologically active peptides (Freidinger, 2003), to the best of our knowledge, the application of all stereoisomers of the heterocyclic dipeptide in a sequence has yet to be explored.

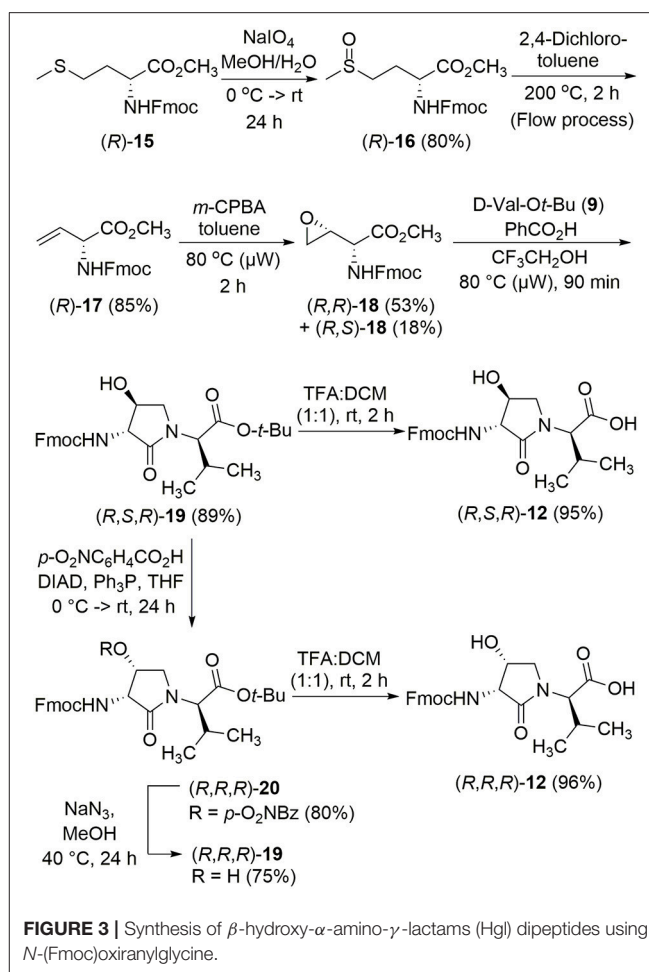
The syntheses of all four Agl-Val and eight Hgl-Val diastereomers of peptide **1** (e.g., **5** and **6**) were performed by approaches featuring preparation of the *N*-Fmoc-dipeptides in solution, followed by their incorporation into the final peptides using solid-phase peptide synthesis. Although effective means for introducing Agl and Hgl residues directly on solid phase have been developed (Jamieson et al., 2009, 2013; Ronga et al., 2010; Sicherl et al., 2010; St-Cyr et al., 2010; Boutard et al., 2011), the construction of dipeptide building blocks in solution prior to coupling on resin was selected to ensure significant amounts of each isomer for biological studies, as well as to minimize concerns of epimerization during peptide assembly. The *N*-Fmoc-Agl-Val-OH dipeptide building blocks **7** were synthesized by extension of the original method for Agl residue assembly featuring alkylation of the thioether of *N*-Boc-methionyl dipeptide ester, followed by intramolecular displacement of the resulting sulfonium ion under basic conditions (Freidinger et al., 1980, 1982). As illustrated for the synthesis of *N*-Fmoc-(*R*)-Agl-(*R*)-Val-OH [(*RR*)-**7**, **Figure 2**], *N*-Boc-D-methionine **8** was coupled to *tert*-butyl (*R*)-valinate **9** using DCC, HOBT and triethylamine to provide protected dipeptide **10** in 78% yield. The lactam was installed by *S*-alkylation using methyl iodide followed by intramolecular *N*-alkylation using sodium hydride to furnish *N*-Fmoc-(*R*)-Agl-(*R*)-Val-O*t*-Bu **11** in 58% yield (Freidinger et al., 1980, 1982). Subsequently, the acid labile carbamate and ester groups were removed using a 50% solution of TFA in DCM, and amine acylation was performed using Fmoc-OSu and sodium carbonate to provide dipeptide **7** for solid-phase synthesis. The other three diastereomers of **7** were, respectively, synthesized using different enantiomers of **8** and **9**, such that all four dipeptide building blocks were obtained in 26–32% overall yields from L- and D-methionine (**Figure 2**).

The synthesis of Hgl peptides in solution and on solid phase has been accomplished using oxiranyl glycine (Sicherl et al., 2010; St-Cyr et al., 2010, 2017). For preparation of *N*-Fmoc-Hgl-Val-OH diastereomers **12** possessing the *trans*-lactam residue, oxiranyl glycines (2*R*,3*R*)- and (2*S*,3*S*)-**18** were prepared from *N*-Fmoc-D- and L-methionine methyl esters (*R*- and *S*-**15**) using a modification of the reported three-step protocol in which *N*-Fmoc-vinylglycine methyl ester **17** was synthesized by a flow process featuring elimination of *N*-Fmoc-methionine sulfoxide methyl ester **16** using 2,4-dichlorotoluene at 200°C, and epoxidation of olefin **17** was performed by microwave irradiation using *m*-CPBA in toluene at 80°C (**Figure 3**). Epoxide



(2R,3R)-**18** was reacted with *tert*-butyl (R)-valinate **9** using a catalytic amount of benzoic acid and trifluoroethanol under microwave irradiation at 80°C for 90 min to provide *N*-Fmoc-(2R,3S,2'R)-Hgl-D-Val-Ot-Bu [(2R,3S,2'R)-**19**] in 89% yield. A Mitsunobu approach was employed for the synthesis of the *cis*-Hgl isomers by inversion of the alcohol stereochemistry of their *trans*-counterparts (Geranurimi and Lubell, 2018). *tert*-Butyl esters **19** were converted to the corresponding acids **12** using 1:1 TFA/DCM. Employing the respective (2R,3R)- and (2S,3S)-diastereomers of epoxide **18** and enantiomers of valine **9**, the *trans*- and *cis*-Hgl dipeptide diastereomers **12** were, respectively, synthesized in 84 and 83% yields.

With Agl and Hgl dipeptide diastereomers **7** and **12** in hand, the syntheses of the respective [Agl³]- and [Hgl³]-**1** peptides (**5** and **6**) were performed using standard Fmoc-based solid-phase synthesis on Rink amide resin (Lubell et al., 2005; **Figure 4**). To *O*-*tert*-butyl D-glutamyl-D-leucyl-D-alanine Rink amide resin **21**, the respective Agl and Hgl dipeptides **7** and **12** were coupled using HBTU, DIEA, and DMF to give the corresponding resin-bound pentapeptides **22** and **23**. Subsequent removals of the Fmoc protection were performed using 20% piperidine in DMF, and peptide elongation was completed by sequential couplings of *N*-Fmoc-*O*-*tert*-butyl-tyrosine and *N*-Boc-*N*-Pmc-arginine using HBTU and DIEA in DMF to give, respectively, the protected heptapeptide resins **24** and **25**. Resin cleavage was performed using a cocktail of 95:2.5:2.5 TFA/H₂O/TES to furnish



peptides **5** and **6** in 35–69% purities. Purification by HPLC provided peptides **5** and **6** in 8–16% overall yields (**Table 2**).

Circular Dichroism Spectra

Understanding the relationships between the preferred conformations of peptides **1**, **5**, and **6** and their modulator activity is critical toward the design of improved prototypes with therapeutic potential. In the absence of crystallographic data of their complex with IL-1R, circular dichroism (CD) spectroscopy of peptides **1**, **5**, and **6** in water were first measured to begin examining the influences of Agl-Val and Hgl-Val dipeptide configuration on conformation. The conformers in water likely represent the geometry that initially binds the receptor. Restraint that pre-organizes a favorable binding conformer may facilitate molecular recognition by diminishing the entropy costs for folding.

The CD spectrum of the parent peptide **1** exhibited a curve shape characteristic of a disordered random coil structure (**Figure 5**). Contingent on stereochemistry, certain Agl and Hgl analogs exhibited CD spectroscopic curve shapes characteristic of ideal β -turn peptides. For example, analogs with *R,R*-backbone conformation including [(3R)-Agl³]-, [(3R,4R)-Hgl³]- and [(3R,4S)-Hgl³]-**1**, all exhibited negative and positive

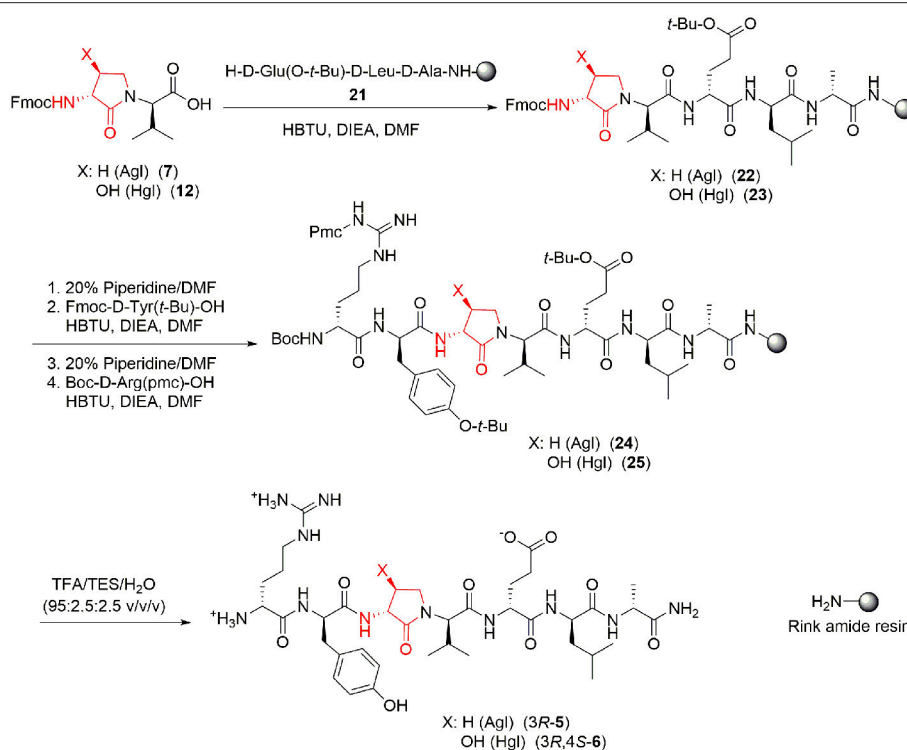


FIGURE 4 | Representative protocols for solid-phase synthesis of Agl and Hgl peptides 5 and 6.

TABLE 2 | Retention times, crude purity, final purity, yields, and mass spectrometric data for Agl and Hgl peptides 5 and 6.

Compound	RT (min)		Crude purity%	Final purity at 280 nm%	Yield% (>95%)	HRMS [M+1] in MeOH	
	CH ₃ OH	CH ₃ CN				m/z (calcd)	m/z (obsd)
[(3R)-Agl ³]-1, [(3R)-5]	8	5.6	44	>99	12	832.4676	832.4682
[(3R, 4R)-Hgl ³]-1, [(3R, 4R)-6]	7.8	5.4	42	>99	8	848.4625	848.4525
[(3R, 4S)-Hgl ³]-1, [(3R, 4S)-6]	7.5	5.2	69	>99	14	848.4625	848.4573
[(3R)-Agl ³ -(S)-Val]-1, [(3R, 2'S)-5]	7.6	5.3	63	>97	16	832.4676	832.4687
[(3R, 4R)-Hgl ³ -(S)-Val]-1, [(3R, 4R, 2'S)-6]	6.8	4.9	55	>99	13	848.4625	848.4629
[(3R, 4S)-Hgl ³ -(S)-Val]-1, [(3R, 4S, 2'S)-6]	6.9	4.9	52	>99	13	848.4625	848.4529
[(3S)-Agl ³]-1, [(3S)-5]	8	5.4	42	>99	15	832.4676	832.4680
[(3S, 4R)-Hgl ³]-1, [(3S, 4R)-6]	7.8	5.4	42	>99	11	848.4625	848.4625
[(3S, 4S)-Hgl ³]-1, [(3S, 4S)-6]	7.3	5.2	35	>99	9	848.4625	848.4627
[(3S)-Agl ³ -(S)-Val]-1, [(3S, 2'S)-5]	7.9	5.5	56	>99	13	832.4676	832.4676
[(3S, 4R)-Hgl ³ -(S)-Val]-1, [(3S, 4R, 2'S)-6]	7	4.9	39	>99	12	848.4625	848.4618
[(3S, 4S)-Hgl ³ -(S)-Val]-1, [(3S, 4S, 2'S)-6]	6.6	5.2	45	>99	12	848.4625	848.4635

Isolated purity ascertained by LC-MS using gradients of 10–90% A [H₂O (0.1% FA)/MeOH (0.1% FA)] or B [H₂O (0.1% FA)/MeCN (0.1% FA)] over 14 min.

maximum that were, respectively, observed at 198–207 and 221–227 nm, indicative of a β -turn conformation (Figure 5; Bush et al., 1978; Kelly et al., 2005). Inversion of the stereochemistry of both backbone centers in [(3S)-Agl³-(S)-Val⁴]-, [(3S,4S)-Hgl³-(S)-Val⁴]- and [(3S,4R)-Hgl³-(S)-Val⁴]-1 gave similar but inverted curve shapes typical of β -turn conformers with notably greater ellipticity (Kelly et al., 2005). On the other hand, among the

Agl and Hgl analogs with mixed backbone stereochemistry, only [(3R,4S)-Hgl³-(S)-Val⁴]-1 exhibited a curve shape indicative of a β -turn conformer (Kelly et al., 2005). A similar β -turn conformer curve shape was observed in CD spectra of [(3R,4S)-Hgl³]-1 examined in trifluoroethanol (TFE), MeOH and hexafluoroisopropanol (HFIP), and the greatest ellipticity was seen in 5% TFE in water.

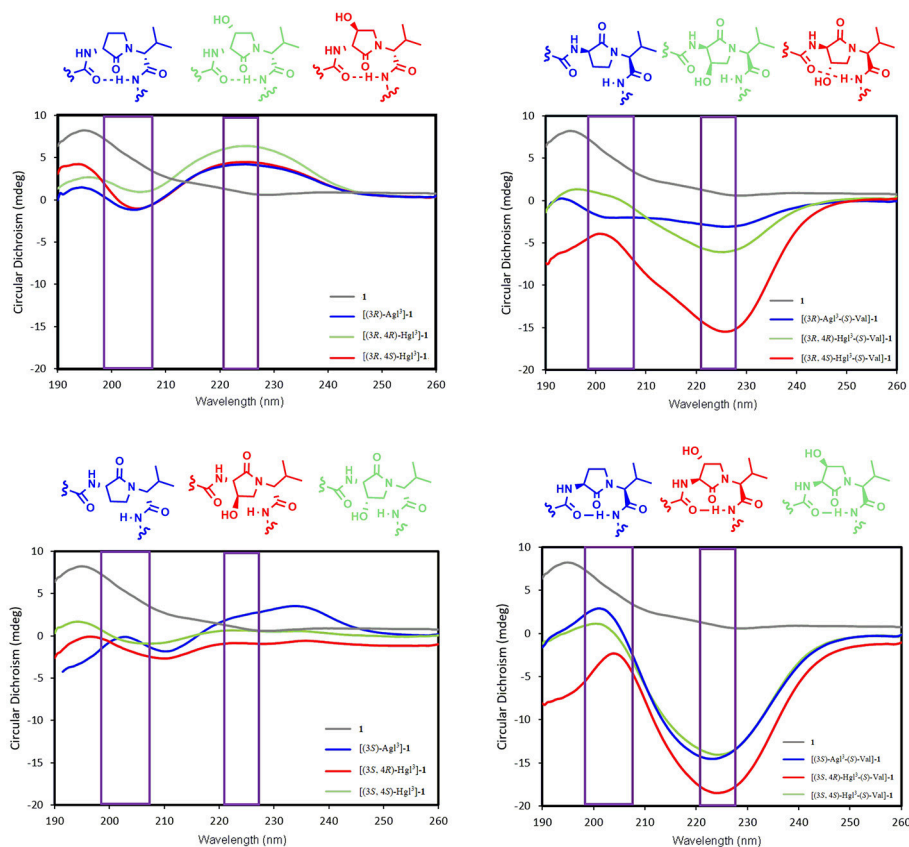


FIGURE 5 | The molar ellipticity circular dichroism spectra of peptides **1**, **5**, and **6**.

In vitro Inhibition of Signaling Pathways

The biological effects of peptide **1** and derivatives were ascertained *in vitro* in RAW-blue and HEK-blue cells which were stimulated with IL-1 β . The QUANTI-blue assay was employed to measure concentrations of secreted alkaline phosphatase, a reporter product from the transcription of the NF- κ B gene. No peptides that were tested exhibited any noticeable inhibition of NF- κ B signaling (**Figure 6**). On the other hand, Kineret, which is an FDA-approved recombinant IL-1 receptor antagonist, inhibited NF- κ B as previously reported (Nadeau-Vallée et al., 2015).

Western Blots were performed to measure phosphorylation of downstream c-Jun N-terminal kinases (JNK), p38 mitogen-activated protein kinases (p-38) and Rho-associated, coiled-coil-containing protein kinase 2 (ROCK2) in RAW-blue cells, after pre-incubation with peptides **1**, **5**, or **6** and stimulation with IL-1 β (**Figure 7**, **Data Sheet 1**). In contrast to peptide **1** which inhibited the effects of all three kinases, the Agl and Hgl analogs exhibited biased signaling contingent on stereochemistry and structure. For example, JNK phosphorylation was inhibited more profoundly by (R)- than (S)-Val⁴ derivatives **5** and **6**. In the (R)-Val series, the Agl and *trans*-Hgl isomers were more effective than the *cis*-Hgl counterparts. Phosphorylation of p-38 was inhibited most effectively by [(3R,4S)-Hgl³]- and [(3R)-Agl³-(S)-Val⁴]-**1**;

[(3S)-Agl³]-, [(3R)-Agl³]-, [(3R,4R)-Hgl³]- and [(3S,4S)-Hgl³-(S)-Val⁴]-**1** were inactive. Finally, ROCK2 phosphorylation was inhibited significantly ($p < 0.05$) by most derivatives, except for [(3S)-Agl³-(R)-Val⁴]- and [(3R)-Agl³-(R)-Val⁴]-**1**. In contrast to peptide **1** which inhibited effectively all three kinases, the inhibitory activity of the Agl and Hgl derivatives was contingent on configuration and the presence of the hydroxyl group. Conversely, these factors did not play a role in NF- κ B signaling, which was universally unaffected by all derivatives **5** and **6**.

The effects of peptides **1**, **5**, and **6** on the transcription of downstream pro-inflammatory genes that are mediated by IL-1 β were measured with focus on IL-6, cyclooxygenase-2 (COX2) and IL-1 β , which positively increases expression of itself (Weber et al., 2010). Quantitative polymerase chain reaction (qPCR) experiments were performed on HEK blue cells to ascertain the expression levels of the mRNA transcripts after pre-treatment with peptides **1**, **5**, and **6** and stimulation with IL-1 β . Parent peptide **1** exhibited strong suppression of transcription of all three genes. Moreover, Agl and Hgl analogs of **1** maintained similar inhibitory potency as the parent peptide (**Figure 8**). On the other hand, the ability to suppress the transcription of all three genes was lost in [(3R)-Agl³-(S)-Val⁴]- and [(3S)-Agl³-(S)-Val⁴]-**1** and recovered in part in certain Hgl³-(S)-Val⁴ analogs

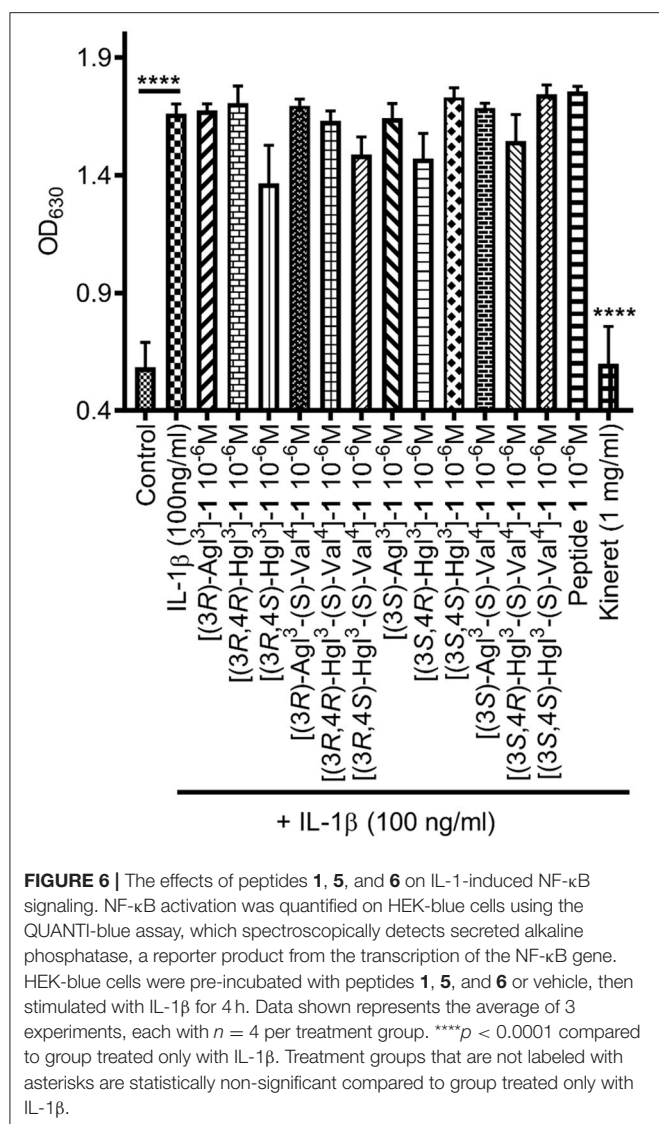


FIGURE 6 | The effects of peptides **1**, **5**, and **6** on IL-1-induced NF- κ B signaling. NF- κ B activation was quantified on HEK-blue cells using the QUANTI-blue assay, which spectroscopically detects secreted alkaline phosphatase, a reporter product from the transcription of the NF- κ B gene. HEK-blue cells were pre-incubated with peptides **1**, **5**, and **6** or vehicle, then stimulated with IL-1 β for 4 h. Data shown represents the average of 3 experiments, each with $n = 4$ per treatment group. **** $p < 0.0001$ compared to group treated only with IL-1 β . Treatment groups that are not labeled with asterisks are statistically non-significant compared to group treated only with IL-1 β .

with [(3S, 4S)-Hgl³-(S)-Val⁴]-**1** exhibiting ability to inhibit the expression of all three genes.

Displacement of Radiolabeled Peptide 1

Peptide **1** is known to bind to IL-1R (Quiniou et al., 2008). To determine if the AgI and Hgl derivatives occupied the same binding site as peptide **1**, a radio-ligand displacement assay was used to determine the extent to which peptides **5** and **6** displaced radiolabeled **1**. Compared to cold unlabeled peptide **1**, which was used to set the baseline for specific binding, a similar capacity to displace [¹²⁵I]-**1** was demonstrated by peptides **5** and **6**, except for [(3R,4S)-Hgl³]-**1**, which exhibited a significantly lower ($p = 0.0011$) ability to compete with radiolabeled peptide **1** (Table 3).

***In vivo* Inhibition of Preterm Labor**

The spectrum of *in vitro* profiles exhibited by peptides **5** and **6** offers a unique means for probing the specific signaling pathways

that contribute to the therapeutic potential of IL-1R modulators. Peptides **1**, **5**, and **6** were first examined in an established CD-1 mouse model of preterm birth (PTB, **Figure 9A**), featuring induction on administration of lipopolysaccharide (LPS) by intraperitoneal injection into pregnant dams on day 16.5 of gestation. The Agl and *trans*-Hgl analogs of peptide **1** exhibited equal potency as the parent peptide in delaying labor (**Figure 9B**). On the other hand, *cis*-Hgl derivatives of peptide **1** and (S)-Val peptides **5** and **6** exhibited little efficacy.

***In vivo* Inhibition of Vaso-Obliteration in Oxygen-Induced Retinopathy**

A model of OIR was next used to examine peptide **1** and a subset of analogs **5** and **6** that were previously tested in the PTB model: e.g., [(3*S*)-Agl³]-, [(3*R*)-Agl³]-, [(3*S*,4*R*)-Hgl³]-, and [(3*R*,4*S*)-Hgl³]-**1** which exhibited the best activity, [(3*S*,4*S*)-Hgl³]-**1** which had partial efficacy and [(3*S*,4*R*)-Hgl³-(*S*)-Val⁴]-**1**, which was inactive in delaying labor.

Exposure of rat pups to 80% oxygen from days 5 to 10 of life resulted usually in vaso-obliteration of ~35% of the retinal capillaries, extending radially from the optic nerve (**Figures 10A,B**). Peptide **1** and Kineret both diminished the extent of vaso-obliteration to 15–20% (**Figure 10B**; Rivera et al., 2013). Among the four peptides that were strongly effective in the PTB model, only two, [3R,4S-Hgl³]- and [3S,4R-Hgl³]-**1** exhibited efficacy in the OIR model and reduced vaso-obliteration to 15–25%. Furthermore, [3S,4S-Hgl³]- **1**, which was moderately effective (~50% efficacy) in the PTB model, demonstrated efficacy in reducing vaso-obliteration to a somewhat lesser extent than peptide **1**. On the other hand, [(3S,4R)-Hgl³-(S)-Val⁴]-**1**, which had no effect in the PTB model, was also ineffective in curbing vaso-obliteration.

Immuno-histochemical staining for Iba-1 was used to assess microglial activation and density, because microglia have been shown to be mediators of vaso-obliviation in the context of OIR (Rivera et al., 2013). Microglia morphology has been observed to change at different states of activation: microglia that are inactive and ramified possess numerous branches, which were observed in retina under normoxia and after treatment with peptide **1** (**Figure 11A**); on the other extreme, activated microglia retract their limbs and become amoeboid (Donat et al., 2017), as observed in vehicle-treated retina under hypoxia. Peptides [(3S,4R)-Hgl³]-, [(3R,4S)-Hgl³]- and [(3S,4S)-Hgl³]-**1** prevented partially the activation of microglia; [(3S)-Agl³]-, [(3R)-Agl³]- and [(3S,4R)-Hgl³-(S)-Val⁴]-**1** had no appreciable effect on microglial morphology (**Figure 11A**). Quantification of microglial density revealed similar trends (**Figure 11B**), except for [(3S)-Agl³]-**1**, which modestly (<20%) reduced microglial density despite not influencing microglial morphology. Peptides **1**, **5**, and **6**, which prevented microglia activation, caused a statistically significant reduction in vaso-obliviation area. In summary, certain [Hgl³]-**1** analogs behaved like the parent peptide and exhibited protection against vaso-obliviation in the hyperoxic phase of OIR, due in part to mitigation of microglial activation.

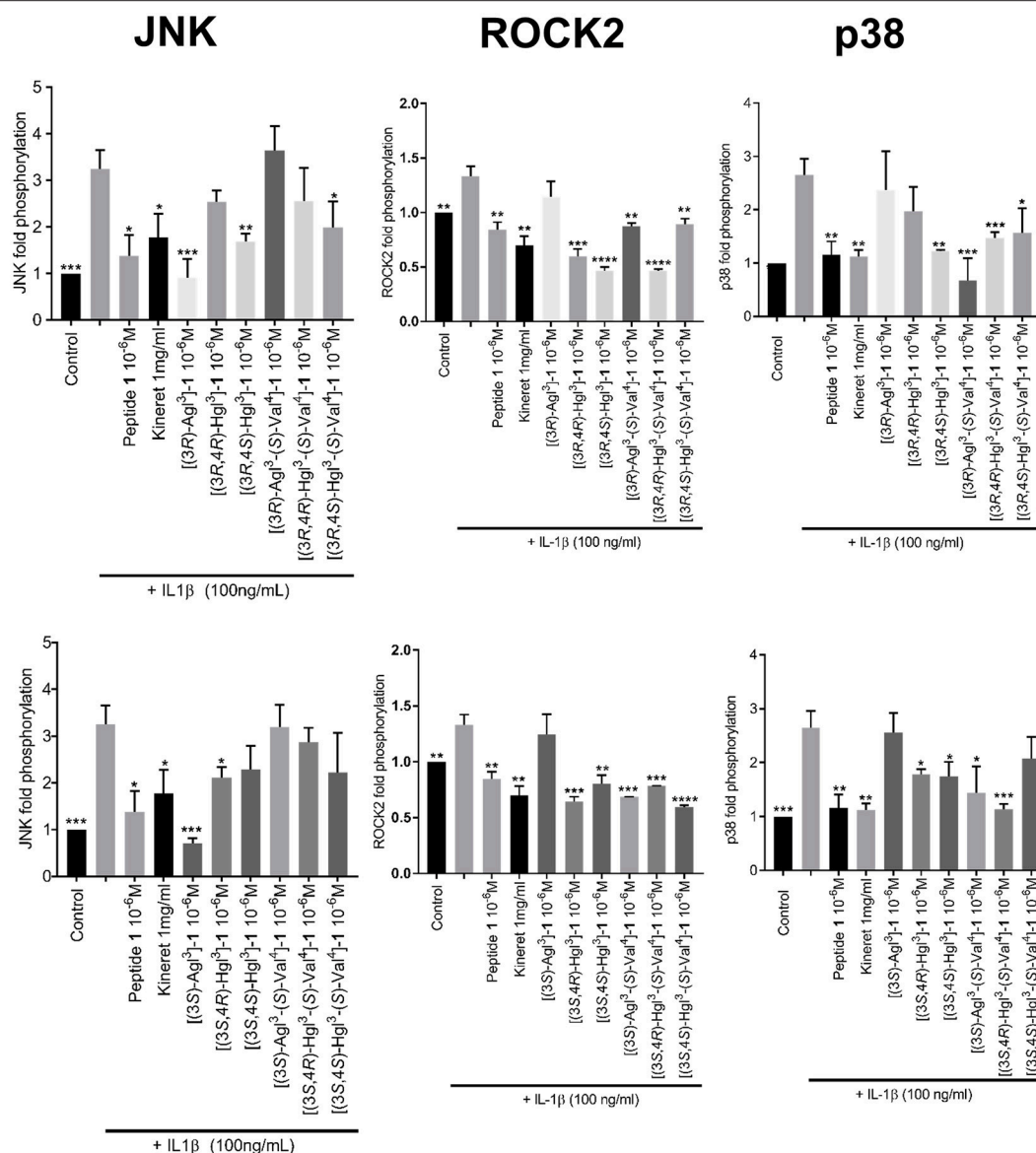


FIGURE 7 | The effects of peptides **1**, **5**, and **6** on IL-1 β -induced phosphorylation of JNK, ROCK2, and p38. Graphical representations of band density analysis of Western Blots, sorted into columns based on protein of interest (JNK, ROCK2, or p38) and rows by peptide configuration [(3R)- or (3S)]. RAW-blue cells were pretreated with peptides **1**, **5**, **6**, Kineret, or vehicle for 30 min and then stimulated with IL-1 β for 15 min. Images of representative Western Blots can be found in the **Supplementary Figure 1**. Results shown are the average of 3 independent experiments: * $p < 0.05$, ** $p < 0.01$, *** $p < 0.001$, **** $p < 0.0001$ compared to group treated only with IL-1 β . Treatment groups that are not labeled with asterisks are statistically non-significant compared to group treated only with IL-1 β .

DISCUSSION

PTB and ROP are medical conditions strongly associated with dysregulated inflammation. Current treatments for PTB, such as oxytocin antagonists and indomethacin, are targeted at reducing the contractility of the myometrium (tocolysis) but fail to address the underlying inflammatory processes responsible for labor (Olson et al., 2008). Current ROP treatments employ anti-vascular endothelial growth factor (VEGF) antibodies and laser photocoagulation

(Hellström et al., 2013) which treat the proliferative phase of the disease but fail to address earlier stage vaso-obliteration and associated inflammation. Modulation of IL-1R signaling offers the potential to mitigate both PTB and ROP as indicated by the *in vivo* results herein and previously reported (Rivera et al., 2013; Nadeau-Vallée et al., 2015, 2017; Beaudry-Richard et al., 2018).

Peptide **1** was shown to adopt a random coil CD spectrum. In the *in vitro* assays, peptide **1** exhibited inhibitory activity on the phosphorylation of the three kinases (JNK, p-38, and ROCK2)

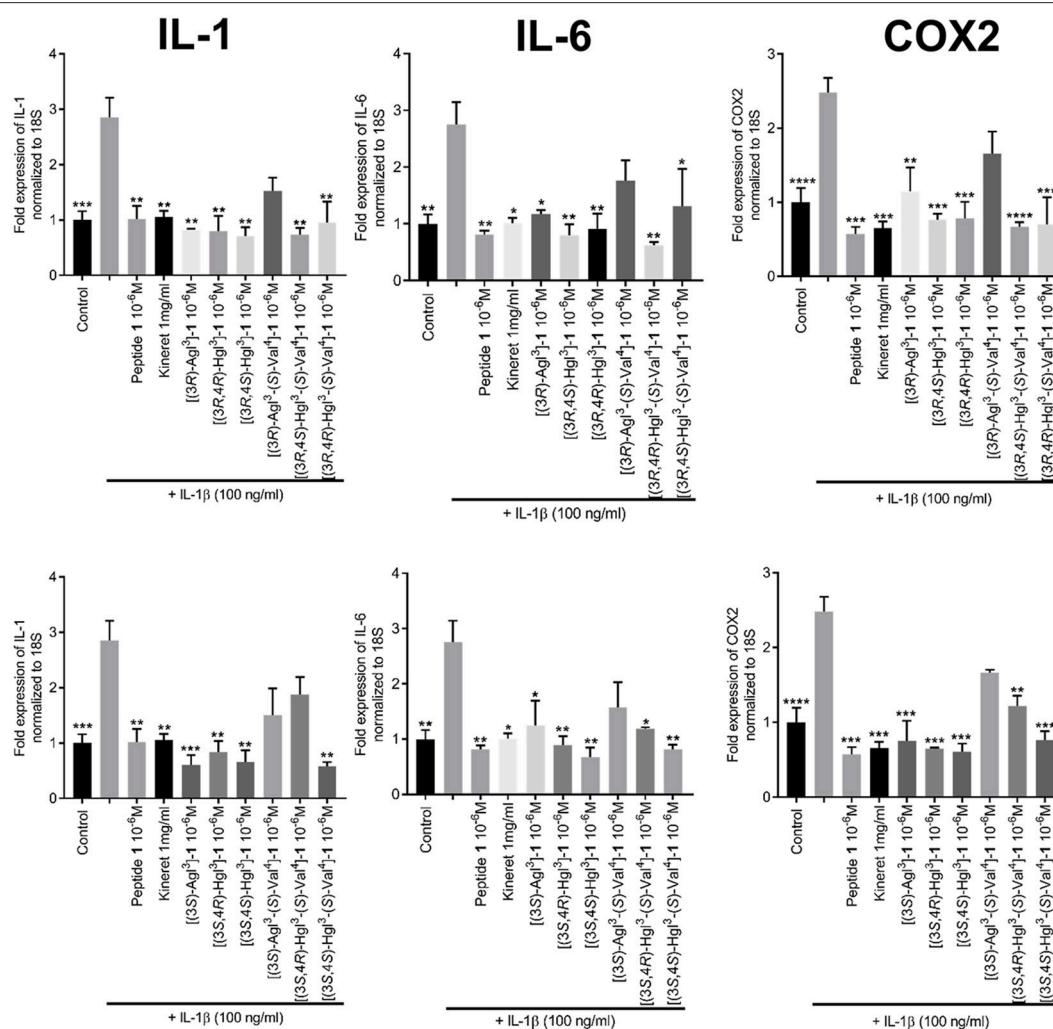


FIGURE 8 | The effects of peptides **1**, **5**, and **6** on the expression of pro-inflammatory genes. HEK-Blue cells were pre-treated with peptides **1**, **5**, and **6** as above and stimulated with IL-1 β overnight. qPCR was performed on cell lysates using 18S rRNA as internal control. Graphs are sorted in columns by gene of interest (COX-2, IL-1 β , or IL-6) and rows by peptide configuration [(3R)] or [(3S)]. Results are representative of an average of 3 independent experiments (each with $n = 4$ per treatment group) and are expressed as a fold-change of the non-stimulated control: * $p < 0.05$, ** $p < 0.01$, *** $p < 0.001$, **** $p < 0.0001$ compared to group treated only with IL-1 β . Treatment groups that are not labeled with asterisks are statistically non-significant compared to group treated only with IL-1 β .

and on the transcription of downstream pro-inflammatory genes that are mediated by IL-1 β (IL-6, COX2, and IL-1 β), but did not affect NF- κ B signaling. Moreover, peptide **1** delayed significantly PTB in mice induced with LPS and reduced vaso-obliteration in the OIR murine model.

Conformational constraint of peptide **1** was performed by replacing (2R,3S)-Thr³-(R)-Val⁴ with all four possible Agl³-Val⁴ (e.g., **5**) and eight possible Hgl³-Val⁴ (e.g., **6**) diastereomers. Among the twelve analogs of peptide **1**, those possessing common backbone stereochemistry (e.g., *R,R*- and *S,S*-) exhibited circular dichroism spectra indicative of β -turn conformers in water: [(3R)-Agl³]-, [(3R,4R)-Hgl³]- and [(3R,4S)-Hgl³]-, [(3S)-Agl³-(S)-Val⁴]-, [(3S,4S)-Hgl³-(S)-Val]-, [(3S,4R)-Hgl³-(S)-Val]- **1**. Moreover, [(3R,4S)-Hgl³-(S)-Val]- **1** also exhibited a CD curve indicative of a turn conformer.

Among the constrained analogs, [(3R,4S)-Hgl³]-**1** exhibited the most similar activity as the parent peptide in the *in vitro* and *in vivo* assays with slightly reduced potency in inhibiting JNK. Moreover, [(3S,4R)-Hgl³]-**1** was also typically as potent as **1** but had slightly reduced abilities in inhibiting p38 and ROCK2. Although their CD spectra and conformers differed in water, both isomers possess *trans*-Hgl residues and (*R*)-Val stereochemistry, indicating the importance of the β -hydroxyl group and gauche(-) χ -dihedral angle side chain geometry for maximum activity.

The contrast of high potency and inactivity exhibited in the PTB and OIR models, respectively, by both [(3R)-Agl³]- and [(3S)-Agl³]-**1** correlates with their ability to block JNK without inhibitory potency on p-38 and ROCK2. The importance of the hydroxyl group for activity on the latter kinases and

for ability to reduce vaso-obliteration in the OIR model is illustrated by the potency of the corresponding Hgl analogs. Notably, [(3*S*,4*S*)-Hgl³]-**1**, which positions the hydroxyl group in

a gauche-(+) χ -dihedral angle side chain orientation, maintains some potency on all three kinases—with best activity on ROCK2—and exhibits moderate and strong activities in the PTB and OIR models, respectively.

Some inhibitory activity on JNK appears necessary for potency in delaying labor in the PTB model. For example, [(3*R*,4*R*)-Hgl³]-**1**, which inhibited strongly ROCK2 but had no effects on JNK and p-38, was inactive in the PTB model. The weaker potency in the PTB assay of the (*S*)-Val analogs correlated with their lack of inhibitory activity on JNK. Although (*R*)- instead of (*S*)-Val may be a prerequisite for binding IL-1R, the latter may also be more susceptible to enzymatic cleavage by proteases (Carmona et al., 2013 and Najjar et al., 2017).

Correlations between peptide structure, *in vitro* activity and *in vivo* potency highlight the relative importance of blocking specific IL-1 signaling pathways to treat certain pathologies (Table 4). For example, inhibition of JNK phosphorylation was most strongly correlated with effectiveness in PTB inhibition. In agreement with an earlier study in which the use of a specific JNK inhibitor had delayed PTB which was induced by a type of LPS that activated both NF- κ B and JNK pathways (Pirianov et al., 2015), blocking JNK phosphorylation alone was sufficient for PTB prevention. On the other hand, efficacy in the OIR model necessitated inhibition of both JNK and

TABLE 3 | The ability of peptides **1**, **5**, and **6** to displace radio-labeled [¹²⁵I]-**1** in RAW-blue cells.

Compound	Percentage of displacement of [¹²⁵ I]- 1 , relative to unlabeled peptide 1 , \pm SEM	p-Value
[(3 <i>R</i>)-Agl ³]- 1	83.55 \pm 9.02	0.9908
[(3 <i>R</i> ,4 <i>S</i>)-Hgl ³]- 1 *	32.13 \pm 16.94	0.0011
[(3 <i>R</i> ,4 <i>R</i>)-Hgl ³]- 1	104.6 \pm 6.826	0.9997
[(3 <i>R</i>)-Agl ³ -(<i>S</i>)-Val ⁴]- 1	120.7 \pm 15.69	0.954
[(3 <i>R</i> ,4 <i>S</i>)-Hgl ³ -(<i>S</i>)-Val ⁴]- 1	58.63 \pm 13.45	0.0724
[(3 <i>R</i> ,4 <i>R</i>)-Hgl ³ -(<i>S</i>)-Val ⁴]- 1	82.12 \pm 14.12	0.9308
[(3 <i>S</i>)-Agl ³]- 1	106.6 \pm 12.39	0.9996
[(3 <i>S</i> ,4 <i>R</i>)-Hgl ³]- 1	78.64 \pm 21.22	0.9428
[(3 <i>S</i> ,4 <i>S</i>)-Hgl ³]- 1	69.73 \pm 8.897	0.2864
[(3 <i>S</i>)-Agl ³ -(<i>S</i>)-Val ⁴]- 1	102.7 \pm 8.637	0.9999
[(3 <i>S</i> ,4 <i>R</i>)-Hgl ³ -(<i>S</i>)-Val ⁴]- 1	48.32 \pm 21.13	0.0649
[(3 <i>S</i> ,4 <i>S</i>)-Hgl ³ -(<i>S</i>)-Val ⁴]- 1	86.06 \pm 6.46	0.9806

*p < 0.05 relative to cold peptide **1**-treated group.

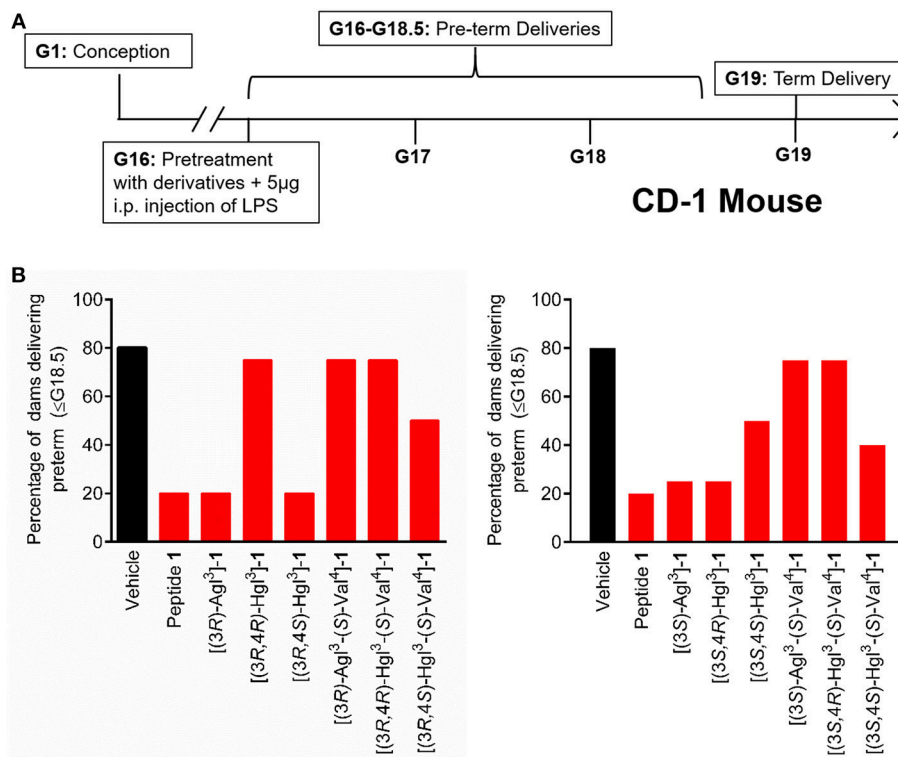


FIGURE 9 | The effects of peptides **1**, **5**, and **6** on prevention of PTB. **(A)** Schematic of the CD-1 mouse PTB model. In brief, pregnant dams on day 16.5 of gestation (G16.5) were subcutaneously pretreated with peptides **1**, **5**, and **6** or vehicle, followed by LPS, and observed for delivery of pups. A dam was considered as delivering preterm if at least one pup was delivered before G18.5. **(B)** The rates of PTB in dams treated with peptides **1**, **5**, and **6** are grouped into (3*R*)- (left) and (3*S*)- (right) derivatives; *n* = 4–5 dams per treatment group.

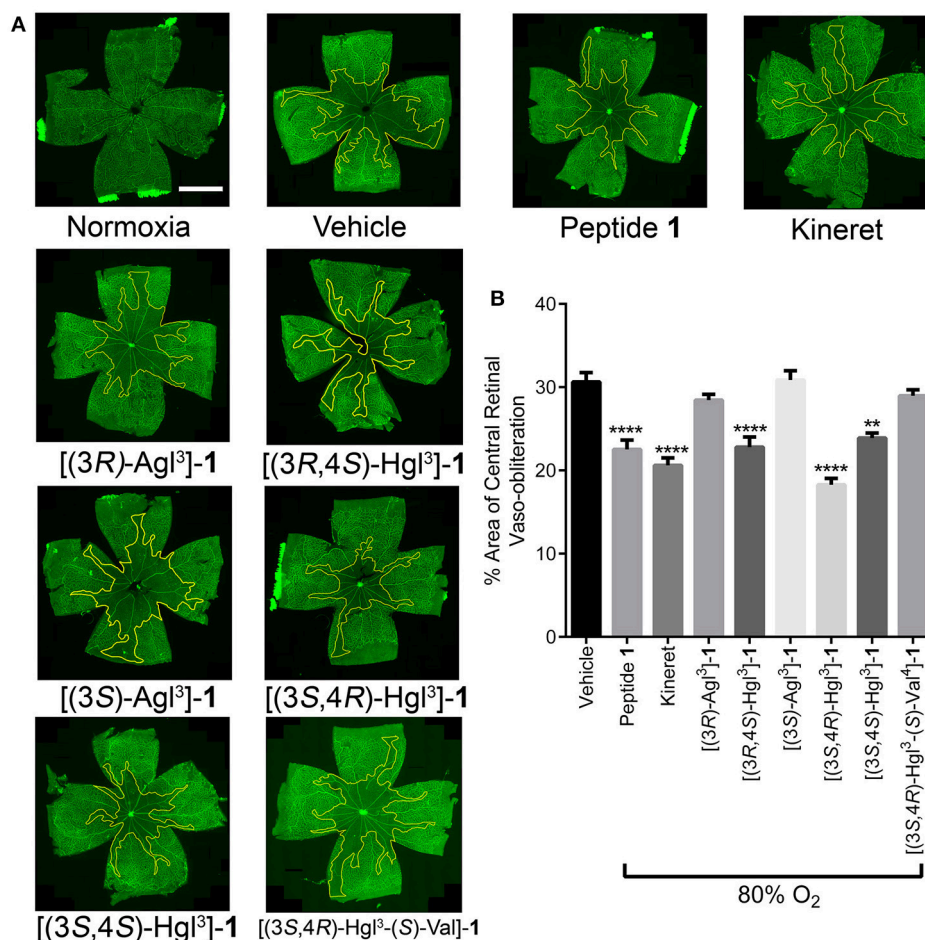


FIGURE 10 | The preventive effects of peptides **1**, **5**, and **6** against vaso-oblitration in an OIR model. Five-days old Sprague Dawley pups and their mothers were kept in 80% oxygen until the 10 day of life, receiving twice-daily intraperitoneal injections of peptides **1**, **5**, and **6** (2 mg/kg/day), Kineret (15 mg/kg/day) or PBS vehicle (each injection was titrated to a volume of 20 μ L). **(A)** Representative retinal flatmounts stained with FITC-conjugated *Bandeiraea simplicifolia* lectin, taken at 10X magnification and stitched with MosaiX in Axiovision 4.8. Yellow lines indicate the central area of vaso-oblitration extending from the optic nerve (center of each retina), scale bar 2 mm. **(B)** Quantification of area of vaso-oblitration performed using ImageJ, expressed as a percentage of the total retinal area: $n = 5-7$ of peptides **5** and **6** and Kineret, $n = 10-12$ for vehicle and peptide **1**; ** $p < 0.01$, **** $p < 0.0001$ relative to the vehicle group. Treatment groups that are not labeled with asterisks are statistically non-significant compared to the vehicle group.

ROCK2 phosphorylation. The latter was in accordance with a study demonstrating the utility of specific ROCK inhibitors in an *in vivo* model of OIR (Yamaguchi et al., 2016). Inactivity of specific compounds may be due to their pharmacokinetics and would require further study to address such issues. For example, delivery may play a role in efficacy because entrance into the retina is more challenging than the myometrium, due to the presence of a blood-retina-barrier that limits entrance from systemic circulation (del Amo et al., 2017) and may account for the enhanced activity of the Hgl relative to the Agl analogs in the OIR model.

Peptide **1** was previously shown to bind to IL-1R (Quiniou et al., 2008). Most of peptides **5** and **6** displaced radio-labeled **1** to the same extent as cold peptide **1**, suggesting they all compete for the same binding site on IL-1R, though not necessarily with the same binding affinity. The sole exception was [(3R,4S)-Hgl³]-1,

which displaced radio-labeled **1** to a lesser extent despite being the most efficacious molecule *in vitro* and *in vivo* (Table 4). This contradiction may be due to a different IL-1R binding pattern that retains desirable biased signaling and may require crystallographic analyses to confirm this hypothesis.

Compared to the larger proteins and non-selective competitive inhibitors currently used in anti-IL-1 therapies, peptides **1**, **5**, and **6** may offer benefits such as ease of administration, as well as the potential to reduce immunosuppression, immunogenicity and related side effects. The small peptides may be further optimized for oral administration, in contrast to antibodies, which must be administered by injection, predisposing patients to potentially unpleasant injection-site reactions leading to reduced patient compliance. Notably, anti-VEGF antibodies, a mainstay of ROP treatment, must be injected directly into the vitreous of the eye

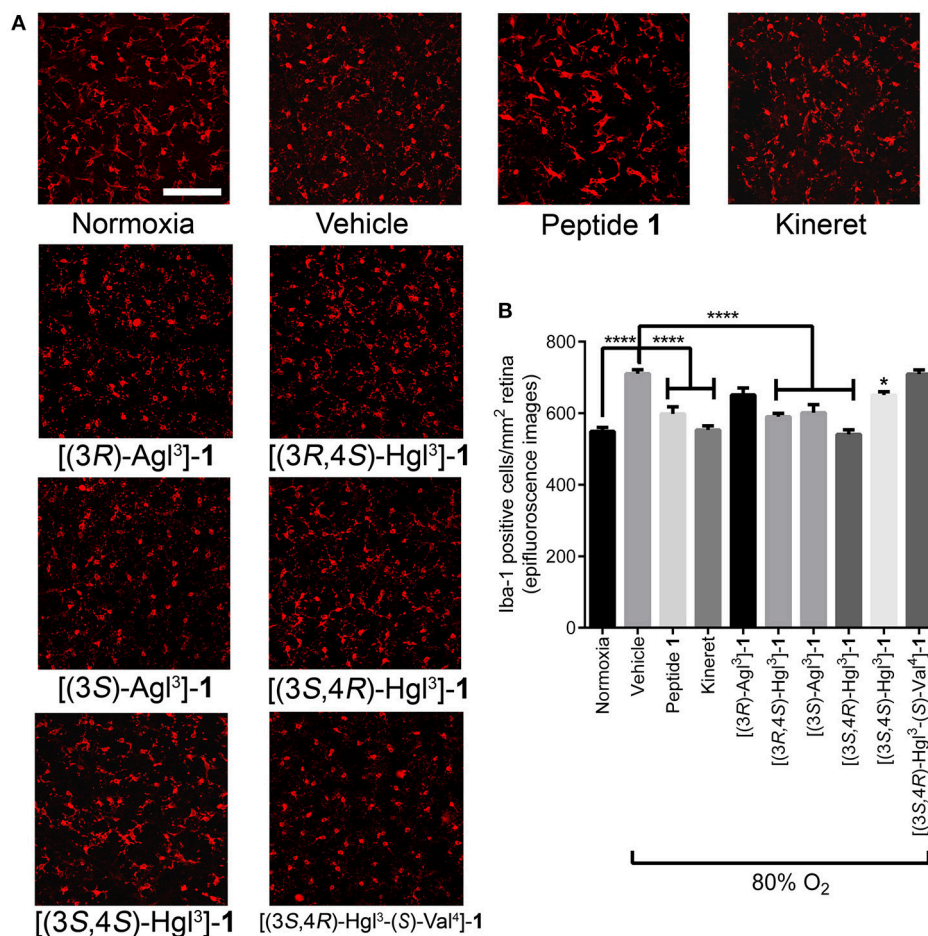


FIGURE 11 | The effects of peptides **1**, **5**, and **6** on retinal microglial activation and density. Retinas were obtained for immunohistochemistry from rat pups treated with the OIR protocol, and incubated with rabbit anti-iba-1 antibody, followed by donkey anti-rabbit antibody conjugated to Alexa 594. **(A)** Representative confocal images of retinal microglia at 30X magnification: scale bar 100 μ m. **(B)** Epifluorescence microscopy images at 20 \times magnification of retinal microglial density quantified using ImageJ: 4 images per retina were taken at a distance halfway between the optic nerve and the peripheral edge of the retina; $n = 5-7$ for peptide **1**, **5**, and **6**, and Kineret; $n = 8-10$ for normoxia and vehicle; * $p < 0.05$, **** $p < 0.0001$ relative to the vehicle group. Treatment groups that are not labeled with asterisks are statistically non-significant compared to the vehicle group.

(i.e., intravitreally), a technique that is invasive and technically demanding (del Amo et al., 2017).

To date, there are no clinically-approved allosteric inhibitors of IL-1 or its receptor. The anti-IL-1 β antibody Gevokizumab, which is currently under investigation, has been reported to bind to an allosteric site on IL-1 β (Blech et al., 2013; Issafras et al., 2014); however, like other antibodies it may be associated with similar drawbacks including large molecule size and high production costs.

CONCLUSION

The utility of conformational constraint to create folded synthetic peptides has for the first time been studied in the context of cytokine signaling and inflammation. Toward the development of immunomodulatory therapy, lactam constraint has been used to study the central D-Thr-D-Val dipeptide sequence of the allosteric IL-1R modulator peptide **1**, which has previously

exhibited efficacy in curbing inflammation in various models of disease, due in part to ability to maintain the beneficial effects of NF- κ B signaling (Castro-Alcaraz et al., 2002; Gerondakis and Siebenlist, 2010; Nadeau-Vallée et al., 2015). Although, the lactam analogs behaved like parent peptide **1** and did not inhibit NF- κ B, they exhibited different degrees of inhibitory potency on the kinases and cytokines activated by IL-1 β *in vitro*. Lactam analogs **5** and **6** are thus valuable probes for identifying specific inflammation-induced signaling pathways for intervention to treat specific medical conditions. Specifically, inhibition of JNK alone and in combination with ROCK2 were, respectively, identified for delaying preterm labor and mitigating retinopathy of prematurity. Peptides **1**, **5**, and **6** comprise a valuable set of selective probes for studying IL-1 signaling pathways in various inflammatory diseases. As promising leads for immune modulator therapy, they offer benefits over traditional protein-based counterparts due to biased signaling, which may avoid immunosuppression. The demonstrated methods for utilizing a

TABLE 4 | Heatmap summary of the *in vivo* and *in vitro* effects of peptides **1**, **5**, and **6**.

Structure		Western Blot			qPCR		Nf-κB	In vivo		
		JNK	p38	ROCK2	COX2	IL-1β		IL-6	PTB	OIR
Peptide 1	[(3 <i>R</i>)-Agi ³]-1	4	0	0	3	4	3	0	4	0
	[(3 <i>R</i> ,4 <i>R</i>)-Hgi ³]-1	0	0	4	4	4	4	0	0	
	[(3 <i>R</i> ,4 <i>S</i>)-Hgi ³]-1	4	4	4	4	4	4	0	4	4
	[(3 <i>R</i>)-Agi ³ -(<i>S</i>)-Val ⁴]-1	0	4	2	1	1	1	0	0	
	[(3 <i>R</i> ,4 <i>R</i>)-Hgi ³ -(<i>S</i>)-Val ⁴]-1	1	3	4	4	3	4	0	0	
	[(3 <i>R</i> ,4 <i>S</i>)-Hgi ³ -(<i>S</i>)-Val ⁴]-1	2	2	2	4	4	2	0	2	
	[(3 <i>S</i>)-Agi ³]-1	4	0	0	4	4	2	0	4	1
	[(3 <i>S</i> ,4 <i>R</i>)-Hgi ³]-1	3	3	3	4	4	4	0	4	4
	[(3 <i>S</i> ,4 <i>S</i>)-Hgi ³]-1	1	1	3	4	4	4	0	2	3
	[(3 <i>S</i>)-Agi ³ -(<i>S</i>)-Val ⁴]-1	0	2	3	1	1	1	0	0	
	[(3 <i>S</i> ,4 <i>R</i>)-Hgi ³ -(<i>S</i>)-Val ⁴]-1	0	3	3	3	1	3	0	0	0
	[(3 <i>S</i> ,4 <i>S</i>)-Hgi ³ -(<i>S</i>)-Val ⁴]-1	2	0	4	4	4	4	0	2	
	Kineret	4	4	4	4	4	4	4	0	3

Black = not tested.

No effect Maximum inhibition/efficacy.

combination of Agl and Hgl residues to make folded peptides may thus have broad utility for biomedical research.

AUTHOR CONTRIBUTIONS

AG wrote the manuscript, synthesized and purified compounds, and conducted circular dichroism analyses. CC wrote the manuscript and conducted *in vivo* and *in vitro* experiments. CQ and TZ edited the manuscript and conducted *in vitro* experiments. XH and JCR edited the manuscript and conducted *in vivo* experiments. CQ, DJS-C, KB, and VB-G conceptualized rytvela (peptide **1**) and assisted in synthesis of derivatives. SC and WL supervised the progress of the project, edited, and proofread the manuscript. All authors have read the final manuscript and agree to be accountable for the content of this work.

FUNDING

This work was supported by the Canadian Institutes of Health Research and the Natural Science and Engineering Research

Council of Canada (NSERC) under the Collaborative Health Research Project #355866, Targeting the interleukin-1 receptor for treating ischemic eye diseases; the NSERC Discovery Grant Program Project #06647 (WL); the Canada Foundation for Innovation; the FRQNT Centre in Green Chemistry and Catalysis, Project #171310 (WL), and the Université de Montréal.

ACKNOWLEDGMENTS

We would like to thank I. Lahaie for assistance in ethics approval of *in vivo* experiments, K. Gilbert and S. Comtois-Marotte for assistance in mass spectrometry, and S. Bilodeau and C. Malveau for performing NMR experiments in the respective regional centers at the Université de Montréal.

SUPPLEMENTARY MATERIAL

The Supplementary Material for this article can be found online at: <https://www.frontiersin.org/articles/10.3389/fchem.2019.00023/full#supplementary-material>

REFERENCES

- Aube, J. (1999). ChemInform abstract: synthetic routes to lactam peptidomimetics. *Cheminform* 30. doi: 10.1002/chin.199908314
- Beaudry-Richard, A., Nadeau-Vallée, M., Prairie, É., Maurice, N., Heckel, É., Nezhady, M., et al. (2018). Antenatal IL-1-dependent inflammation persists postnatally and causes retinal and sub-retinal vasculopathy in progeny. *Sci. Rep.* 8:11875. doi: 10.1038/s41598-018-30087-4
- Blech, M., Peter, D., Fischer, P., Bauer, M. M., Hafner, M., Zeeb, M., et al. (2013). One target-two different binding modes: structural insights into gevokizumab and canakinumab interactions to interleukin-1β. *J. Mol. Biol.* 425, 94–111. doi: 10.1016/j.jmb.2012.09.021
- Bourguet, C. B., Claing, A., Laporte, S. A., Hébert, T. E., Chemtob, S., and Lubell, W. D. (2014). Synthesis of azabicycloalkane amino acid and azapeptide mimics and their application as modulators of the prostaglandin F2α receptor for delaying preterm birth. *Can. J. Chem.* 92, 1031–1040. doi: 10.1139/cjc-2014-0289
- Boutard, N., Turcotte, S., Beauregard, K., Quiniou, C., Chemtob, S., and Lubell, W. D. (2011). Examination of the active secondary structure of the peptide 101.10, an allosteric modulator of the interleukin-1 receptor, by positional scanning using β-amino γ-lactams. *J. Pept. Sci.* 17, 288–296. doi: 10.1002/psc.1337
- Braddock, M., and Quinn, A. (2004). Targeting IL-1 in inflammatory disease: new opportunities for therapeutic intervention. *Nat. Rev. Drug Discov.* 3, 330–339. doi: 10.1038/nrd1342

- Bush, C. A., Sarkar, S. K., and Kopple, K. D. (1978). Circular dichroism of β turns in peptides and proteins. *Biochemistry* 17, 4951–4954. doi: 10.1021/bi00616a015
- Carmona, G., Rodríguez, A., Juárez, D., Corzo, G., and Villegas, E. (2013). Improved protease stability of the antimicrobial peptide Pin2 substituted with D-amino acids. *Protein J.* 32, 456–466. doi: 10.1007/s10930-013-9505-2
- Carney, D. W., Schmitz, K. R., Truong, J. V., Sauer, R. T., and Sello, J. K. (2014). Restriction of the conformational dynamics of the cyclic acyldepsipeptide antibiotics improves their antibacterial activity. *J. Am. Chem. Soc.* 136, 1922–1929. doi: 10.1021/ja410385c
- Castro-Alcaraz, S., Miskolci, V., Kalasapudi, B., Davidson, D., and Vancurova, I. (2002). NF-kappa B regulation in human neutrophils by nuclear I kappa B alpha: correlation to apoptosis. *J. Immunol.* 169, 3947–3953. doi: 10.4049/jimmunol.169.7.3947
- del Amo, E. M., Rimpelä, A. K., Heikkinen, E., Kari, O. K., Ramsay, E., and Lajunen, T., et al. (2017). Pharmacokinetic aspects of retinal drug delivery. *Prog. Retin. Eye Res.* 57, 134–185. doi: 10.1016/j.preteyeres.2016.12.001
- Dinarello, C. A. (2002). The IL-1 family and inflammatory diseases. *Clin. Exp. Rheumatol.* 20 (Suppl. 27), S1–13.
- Dinarello, C. A., Gatti, S., and Bartfai, T. (1999). Fever: links with an ancient receptor. *Curr. Biol.* 9, R147–R150. doi: 10.1016/S0960-9822(99)80085-2
- Dinarello, C. A., Simon, A., and van der Meer, J. W. (2012). Treating inflammation by blocking interleukin-1 in a broad spectrum of diseases. *Nat. Rev. Drug Discov.* 11, 633–652. doi: 10.1038/nrd3800
- Donat, C. K., Scott, G., Gentleman, S. M., and Sastre, M. (2017). Microglial Activation in Traumatic Brain Injury. *Front. Aging Neurosci.* 9:208. doi: 10.3389/fnagi.2017.00208
- Freidinger, R. M. (2003). Design and synthesis of novel bioactive peptides and peptidomimetics. *J. Med. Chem.* 46, 5553–5566. doi: 10.1021/jm030484k
- Freidinger, R. M., Perlow, D. S., and Veber, F. (1982). Protected lactam-bridged dipeptides for use as conformational constraints in peptides. *J. Org. Chem.* 47, 104–109. doi: 10.1021/jo00340a023
- Freidinger, R. M., Veber, D. F., Perlow, D. S., Brooks, J. R., and Saperstein, R. (1980). Bioactive conformation of luteinizing hormone-releasing hormone: evidence from a conformationally constrained analog. *Science* 210, 656–658. doi: 10.1126/science.7001627
- Garner, A., and Ashton, N. (1971). Vaso-obliteration and retrolental fibroplasia. *Proc. R. Soc. Med.* 64, 774–777.
- Geranurimi, A., and Lubell, W. D. (2018). Diversity-oriented syntheses of β -substituted α -amino γ -lactam peptide mimics with constrained backbone and side chain residues. *Org. Lett.* 20, 6126–6129. doi: 10.1021/acs.orglett.8b02575
- Gerondakis, S., and Siebenlist, U. (2010). Roles of the NF-kappaB pathway in lymphocyte development and function. *Cold Spring Harb. Perspect. Biol.* 2:a000182. doi: 10.1101/cshperspect.a000182
- Hallegua, D. S., and Weisman, M. H. (2002). Potential therapeutic uses of interleukin 1 receptor antagonists in human diseases. *Ann. Rheum. Dis.* 61, 960–967. doi: 10.1136/ard.61.11.960
- Hebert, T. E., Moffett, S., Morello, J. P., Loisel, T. P., Bichet, D. G., Barret, C., et al. (1996). A peptide derived from a β 2-adrenergic receptor transmembrane domain inhibits both receptor dimerization and activation. *J. Biol. Chem.* 271, 16384–16392. doi: 10.1074/jbc.271.27.16384
- Hellström, A., Smith, L. E., and Dammann, O. (2013). Retinopathy of prematurity. *Lancet* 382, 1445–1457. doi: 10.1016/S0140-6736(13)60178-6
- Issafras, H., Corbin, J. A., Goldfine, I. D., and Roell, M. K. (2014). Detailed mechanistic analysis of gevokizumab, an allosteric anti-IL-1 β antibody with differential receptor-modulating properties. *J. Pharmacol. Exp. Ther.* 348, 202–215. doi: 10.1124/jpet.113.205443
- Jamieson, A. G., Boutard, N., Beauregard, K., Bodas, M. S., Ong, H., Quiniou, C., et al. (2009). Positional scanning for peptide secondary structure by systematic solid-phase synthesis of amino lactam peptides. *J. Am. Chem. Soc.* 131, 7917–7927. doi: 10.1021/ja9010628
- Jamieson, A. G., Boutard, N., Sabatino, D., and Lubell, W. D. (2013). Peptide scanning for studying structure-activity relationships in drug discovery. *Chem. Biol. Drug Design* 81, 148–165. doi: 10.1111/cbdd.12042
- Kakinuma, C., Kuwayama, C., Kaga, N., Futamura, Y., Katsuki, Y., and Shibutani, Y. (1997). Trophoblastic apoptosis in mice with preterm delivery and its suppression by urinary trypsin inhibitor. *Obstet. Gynecol.* 90, 117–124. doi: 10.1016/S0029-7844(97)00176-2
- Kelly, S. M., Jess, T. J., and Price, N. C. (2005). How to study proteins by circular dichroism. *Biochim. Biophys. Acta Protein Proteom.* 1751, 119–139. doi: 10.1016/j.bbapap.2005.06.005
- Lubell, W. D., (ed.). (2017). “Preface,” in *Peptidomimetics I* (Cham: Springer), v–xiv.
- Lubell, W. D., Blankenship, J. W., Fridkin, G., and Kaul, R. (2005). “Peptides,” in *Science of Synthesis*, ed S. M. Weinreb (Stuttgart: Thieme), 713–809.
- Mantero, J. C., Kishore, N., Ziemek, J., Stifano, G., Zammitti, C., Khanna, D., et al. (2018). Randomised, double-blind, placebo-controlled trial of IL-1-trap, rilonacept, in systemic sclerosis. A phase I/II biomarker trial. *Clin. Exp. Rheumatol.* 36 (Suppl. 1), 146–149.
- Nadeau-Vallée, M., Chin, P. Y., Belarbi, L., Brien, M. È., Pundir, S., Berryer, M. H., et al. (2017). Antenatal suppression of IL-1 protects against inflammation-induced fetal injury and improves neonatal and developmental outcomes in mice. *J. Immunol.* 198, 2047–2062. doi: 10.4049/jimmunol.1601600
- Nadeau-Vallée, M., Quiniou, C., Palacios, J., Hou, X., Erfani, A., Madaan, A., et al. (2015). Novel noncompetitive IL-1 receptor-biased ligand prevents infection- and inflammation-induced preterm birth. *J. Immunol.* 195, 3402–3415. doi: 10.4049/jimmunol.1500758
- Najjar, K., Erazo-Oliveras, A., Brock, D. J., Wang, T. Y., and Pellois, J. P. (2017). An L- to D-amino acid conversion in an endosomolytic analog of the cell-penetrating peptide TAT influences proteolytic stability, endocytic uptake, and endosomal escape. *J. Biol. Chem.* 292, 847–861. doi: 10.1074/jbc.M116.759837
- Olson, D. M., Christiaens, I., Gracie, S., Yamamoto, Y., and Mitchell, B. F. (2008). Emerging tocolytics: challenges in designing and testing drugs to delay preterm delivery and prolong pregnancy. *Expert Opin. Emerg. Drugs* 13, 695–707. doi: 10.1517/14728210802568764
- Opal, S. M., Fisher, C. J., Dhainaut, J. F., Vincent, J. L., Brase, R., Lowry, S. F., et al. (1997). Confirmatory interleukin-1 receptor antagonist trial in severe sepsis: a phase III, randomized, double-blind, placebo-controlled, multicenter trial. the interleukin-1 receptor antagonist sepsis investigator group. *Crit. Care Med.* 25, 1115–1124. doi: 10.1097/00003246-199707000-00010
- Perdih, A., and Kikelj, D. (2006). The application of Freidinger lactams and their analogs in the design of conformationally constrained peptidomimetics. *Curr. Med. Chem.* 13, 1525–1556. doi: 10.2174/09298670677442066
- Pirianov, G., MacIntyre, D. A., Lee, Y., Waddington, S. N., Terzidou, V., and Mehmet, H., et al. (2015). Specific inhibition of C-Jun N-terminal kinase delays preterm labour and reduces mortality. *Reproduction* 150, 269–277. doi: 10.1530/REP-15-0258
- Puchner, K., Iavazzo, C., Gourgoutis, D., Boutsikou, M., Baka, S., Hassiakos, D., et al. (2011). Mid-trimester amniotic fluid interleukins (IL-1 β , IL-10 and IL-18) as possible predictors of preterm delivery. *In Vivo* 25, 141–148.
- Quiniou, C., Sapieha, P., Lahaie, I., Hou, X., Brault, S., Beauchamp, M., et al. (2008). Development of a novel noncompetitive antagonist of IL-1 receptor. *J. Immunol.* 180, 6977–6987. doi: 10.4049/jimmunol.180.6.6977
- Rihakova, L., Quiniou, C., Hamdan, F. F., Kaul, R., Brault, S., Hou, X., et al. (2009). VRQ397 (CRAVKY): a novel noncompetitive V2 receptor antagonist. *Am. J. Physiol. Regul. Integr. Comp. Physiol.* 297, R1009–R1018. doi: 10.1152/ajpregu.90766.2008
- Rivera, J. C., Sitaras, N., Noueihed, B., Hamel, D., Madaan, A., Zhou, T., et al. (2013). Microglia and interleukin-1 β in ischemic retinopathy elicit microvascular degeneration through neuronal semaphorin-3A. *Arterioscler. Thromb. Vasc. Biol.* 33, 1881–1891. doi: 10.1161/ATVBAHA.113.301331
- Roerink, M. E., Bredie, S. J. H., Heijnen, M., Dinarello, C. A., Knoop, H., and Van der Meer, J. W. M. (2017). Cytokine inhibition in patients with chronic fatigue syndrome: a randomized trial. *Ann. Intern. Med.* 166, 557–564. doi: 10.7326/M16-2391
- Romero, R., Brody, D. T., Oyarzun, E., Mazor, M., Wu, Y. K., Hobbins, J. C., et al. (1989). Infection and labor. III. Interleukin-1: a signal for the onset of parturition. *Am. J. Obstet. Gynecol.* 160 (Pt 1), 1117–1123. doi: 10.1016/0002-9378(89)90172-5
- Ronga, L., Jamieson, A. G., Beauregard, K., Quiniou, C., Chemtob, S., and Lubell, W. D. (2010). Insertion of multiple alpha-amino gamma-lactam (Agl) residues into a peptide sequence by solid-phase synthesis on synphase lanterns. *Biopolymers* 94, 183–191. doi: 10.1002/bip.21288

- Rubin, S., and Qvit, N. (2016). Cyclic peptides for protein-protein interaction targets: applications to human disease. *Crit. Rev. Eukaryot. Gene Expr.* 26, 199–221. doi: 10.1615/CritRevEukaryotGeneExpr.2016016525
- Sicherl, F., Cupido, T., and Albericio, F. (2010). A novel dipeptidomimetic containing a cyclic threonine. *Chem. Commun.* 46:1266–1268. doi: 10.1039/b915220b
- St-Cyr, D. J., García-Ramos, Y., Doan, N. D., and Lubell, W. D. (2017). “Aminolactam, N-aminoimidazolone, and N-aminoimidazolidinone peptide mimics,” in *Peptidomimetics I*, ed W. D. Lubell (Cham: Springer), 125–175.
- St-Cyr, D. J., Jamieson, A. G., and Lubell, W. D. (2010). Alpha-amino-beta-hydroxy-gamma-lactam for constraining peptide Ser and Thr residue conformation. *Org. Lett.* 12, 1652–1655. doi: 10.1021/ol1000582
- Tan, D. C., Kini, R. M., Jois, S. D., Lim, D. K., Xin, L., and Ge, R. (2001). A small peptide derived from Flt-1 (VEGFR-1) functions as an angiogenic inhibitor. *FEBS Lett.* 494, 150–156. doi: 10.1016/S0014-5793(01)02314-6
- Valle, G., Crisma, M., Toniolo, C., Yu, K. L., and Johnson, R. L. (2009). Crystal-state structural analysis of two γ -lactam-restricted analogs of Pro-Leu-Gly-NH₂. *Int. J. Pept. Protein Res.* 33, 181–190. doi: 10.1111/j.1399-3011.1989.tb00207.x
- Weber, A., Wasiliew, P., and Kracht, M. (2010). Interleukin-1 (IL-1) pathway. *Sci. Signal.* 3:cm1. doi: 10.1126/scisignal.3105cm1
- Yamaguchi, M., Nakao, S., Arita, R., Kaizu, Y., Arima, M., Zhou, Y., et al. (2016). Vascular normalization by ROCK inhibitor: therapeutic potential of Ripasudil (K-115) eye drop in retinal angiogenesis and hypoxia. *Invest. Ophthalmol. Vis. Sci.* 57, 2264–2276. doi: 10.1167/iops.15-17411
- Yoshimura, K., and Hirsch, E. (2005). Effect of stimulation and antagonism of interleukin-1 signaling on preterm delivery in mice. *J. Soc. Gynecol. Investig.* 12, 533–538. doi: 10.1016/j.jsig.2005.06.006
- Yu, K. L., Rajakumar, G., Srivastava, L. K., Mishra, R. K., and Johnson, R. L. (1988). Dopamine receptor modulation by conformationally constrained analogs of Pro-Leu-Gly-NH₂. *J. Med. Chem.* 31, 1430–1436. doi: 10.1021/jm00402a031
- Zhang, Y. L., Dawe, A. L., Jiang, Y., Becker, J. M., and Naider, F. (1996). A superactive peptidomimetic analog of a farnesylated dodecapeptide yeast pheromone. *Biochem. Biophys. Res. Commun.* 224, 327–331. doi: 10.1006/bbrc.1996.1028

Conflict of Interest Statement: The authors declare that the research was conducted in the absence of any commercial or financial relationships that could be construed as a potential conflict of interest.

Copyright © 2019 Geranurimi, Cheng, Quiniou, Zhu, Hou, Rivera, St-Cyr, Beauregard, Bernard-Gauthier, Chemtob and Lubell. This is an open-access article distributed under the terms of the Creative Commons Attribution License (CC BY). The use, distribution or reproduction in other forums is permitted, provided the original author(s) and the copyright owner(s) are credited and that the original publication in this journal is cited, in accordance with accepted academic practice. No use, distribution or reproduction is permitted which does not comply with these terms.



Self-Assembling Peptides as Extracellular Matrix Mimics to Influence Stem Cell's Fate

Katharina S. Hellmund and Beate Kokschr*

Department of Biology, Chemistry, and Pharmacy, Institute of Chemistry and Biochemistry, Freie Universität Berlin, Berlin, Germany

OPEN ACCESS

Edited by:

Jutta Eichler,
University of Erlangen Nuremberg,
Germany

Reviewed by:

Mare Cudic,
Florida Atlantic University,
United States
James Gardiner,
Commonwealth Scientific and
Industrial Research Organisation
(CSIRO), Australia

*Correspondence:

Beate Kokschr
Beate.Kokschr@fu-berlin.de

Specialty section:

This article was submitted to
Chemical Biology,
a section of the journal
Frontiers in Chemistry

Received: 17 January 2019

Accepted: 05 March 2019

Published: 27 March 2019

Citation:

Hellmund KS and Kokschr B (2019)
Self-Assembling Peptides as
Extracellular Matrix Mimics to Influence
Stem Cell's Fate. *Front. Chem.* 7:172.
doi: 10.3389/fchem.2019.00172

Interest in biologically active materials that can be used as cell culture substrates for medicinal applications has increased dramatically over the last decade. The design and development of biomaterials mimicking the natural environment of different cell types, the so-called extracellular matrix (ECM), is the focus of research in this field. The ECM exists as an ensemble of several adhesion proteins with different functionalities that can be presented to the embedded cells. These functionalities regulate numerous cellular processes. Therefore, different approaches and strategies using peptide- and protein-based biopolymers have been investigated to support the proliferation, differentiation, and self-renewal of stem cells, in the context of regenerative medicine. This minireview summarizes recent developments in this area, with a focus on peptide-based biomaterials used as stem cell culture substrates.

Keywords: extracellular matrix, stem cells, peptide-based biomaterials, self-assembling peptides, peptide hydrogels, stem cell differentiation, stem cell fate

INTRODUCTION

Developing cell culture materials is a challenging task for the chemistry community, but its successful realization would allow cellular behavior to be directly influenced in order to optimize their applications in regenerative medicine. By tuning the properties of such materials, i.e., stiffness or the presence of chemical inducers like recognition motifs, it is possible to tailor the stem cell's microenvironment to give information regarding proliferation and differentiation. In nature, stem cells are arranged in a defined microenvironment, referred to as stem cell niche, which regulates the stem cell's behavior based on input from all of the components that comprise it (Jones and Wagers, 2008; Köhl and Köhl, 2012). The stem cell niche theory was developed by Schofield (1978) and describes how stem cells are supported or influenced by the defined microenvironment, by means of physical interactions between the stem cells and other cells, the secretion of signal molecules, or the presence of molecules on the surface of other cells, like integrins (Fuchs et al., 2004; Li and Xie, 2005; Jones and Wagers, 2008; Köhl and Köhl, 2012).

The extracellular matrix (ECM) is the major and most important part of the stem cell niche. Numerous studies have shown that ECMs influence stem cell's fate (Guilak et al., 2009). The composition of natural ECM can differ and depends on its tissue of origin. It consists of different adhesion proteins like collagen, fibronectin, and laminin, to which the stem cells are exposed (Hynes, 2009; Köhl and Köhl, 2012; Watt and Huck, 2013). These adhesion proteins bind to integrins on the cell surface via cell-binding epitopes. Cell-binding epitopes are small peptide sequences derived from adhesion proteins, namely, RGD from collagen, RGDs from fibronectin and IKVAV and YIGSR from laminin (Lampe and Heilshorn, 2012). The stem cell senses the environment in which it is embedded and is able to modify its form and function accordingly;

this is its main mechanism of proliferation and differentiation. Understanding this mechanism in detail is of paramount importance to the development of new biomaterials for stem cell biology (Lutolf et al., 2009).

Stem cells have specific characteristics that differ from those of other cells in the body. In particular, they are able to differentiate into individual cell-types (Ding and Schultz, 2004; Griffin et al., 2015) and contribute to the regeneration of tissues (Kühl and Kühl, 2012; Griffin et al., 2015). Additionally, the unlimited self-regeneration by asymmetric cell division into a specialized and an unspecialized daughter cell constitutes one of the main characteristics of stem cells (Watt and Hogan, 2000; Knoblich, 2008). Two different types are known: embryonic stem cells (ESCs) and adult stem cells (ASCs) (Kühl and Kühl, 2012; Griffin et al., 2015). ESCs are derived from the inner cell mass of the blastocyst (Ding and Schultz, 2004; Kühl and Kühl, 2012) and have a pluripotent differentiation potential (Odorico et al., 2001; Kühl and Kühl, 2012). Induced pluripotent stem cells (iPSCs) are a nearly inexhaustible source of pluripotent stem cells. They are directly reprogrammed from fibroblasts by introduction of four growth factors Oct3/4, Sox2, c-Myc, and Klf4. iPSCs possess the properties similar to ESCs (Takahashi and Yamanaka, 2006) and are therefore an auspicious cell species to study the differentiation potential of artificial cell culture substrates for differentiation of pluripotent stem cell lines. ASCs are unspecialized, multipotent cells derived from adult tissues and can differentiate into restricted types of specialized cells (Ding and Schultz, 2004; Griffin et al., 2015). The most common type of ASCs are mesenchymal stem cells (MSCs). ASCs require a defined microenvironment in an adult organism to maintain their stem cell properties.

Over the last decade, the importance of identifying and exploring ECMs and their niches has been increasingly recognized (Morrison and Spradling, 2008; Walker et al., 2009). Peptides and peptide derivatives are excellent candidates for the development of 2D and 3D cell-culture materials, thanks to their biodegradability and biocompatibility, and make it possible to tailor biomaterials for different applications in tissue engineering and regenerative medicine (Lampe and Heilshorn, 2012; Wu et al., 2012). Specific types of peptide-based materials possess specific advantages: whereas 2D scaffolds present highly sensitive ligands bound to an inert substrate, elasticity and stiffness are key in obtaining differentiation signals for stem cells embedded in 3D scaffolds. The properties of each peptide-based material can be adjusted by the primary structure, and they are generally easy to procure by means of standard peptide synthesis protocols (Jung et al., 2010). Peptide structures, folding processes and stability are also for the most part well-established in the literature (Lakshmanan et al., 2012; Wu et al., 2012).

PARAMETERS OF A SYNTHETIC EXTRACELLULAR MATRIX

Stem cells are sensitive toward the physical parameters of the surrounding microenvironment and are able to adapt their differentiation lineage according to the topology, polarity

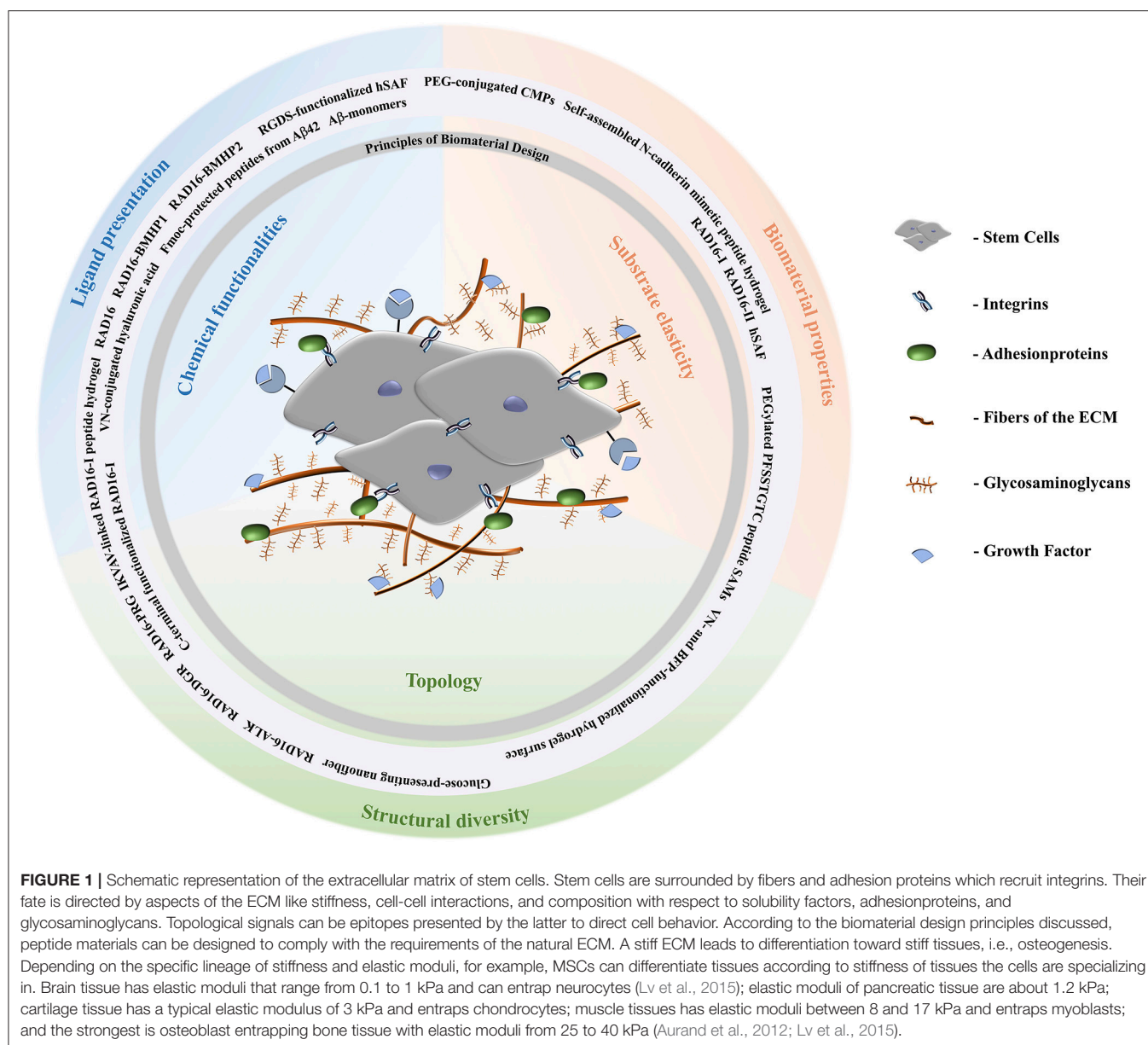
or the elasticity of the surface (Trappmann et al., 2012; Murphy et al., 2014).

Non-peptidic topological cues influencing stem cells include surfaces presenting different chemical functionalities; for example, glass silane modified substrates with diverse functional groups (methyl-, amino, silane-, hydroxy-, and carboxy-groups) on their surfaces were established to culture hMSCs (Curran et al., 2006). Methyl-substituted surfaces lead to maintenance of the hMSC phenotype, amino-surfaces promote and maintain osteogenesis, and hydroxyl- and carboxyl-groups promote and maintain chondrogenesis (Curran et al., 2005, 2006). Stiffness is one of the main parameters for directing the fate of a stem cell, and it is expressed by an elastic modulus. Stem cells are mechanically sensitive, thus their fate is directed by the stiffness of the environment into which it is embedded (see **Figure 1**). Examples of stiffness cues include the development of biomaterials for directed stem cell differentiation in 2D and 3D cell cultures. For example, polyethylene glycol silica nanocomposite gels containing RGD-peptides and exhibiting different degrees of stiffness were investigated regarding hMSC differentiation. Stiffer gels showed higher expression levels of Runx2, an early bone differentiation transcription factor, compared to gels having low or intermediate stiffness (Pek et al., 2010).

CELL ATTACHMENT AND PROLIFERATION ON PEPTIDE-BASED BIOMATERIALS

A prominent example of conjugation of adhesion proteins with different biologically relevant polymers was shown by Zhang et al. (2016), who functionalized hyaluronic acid (HA) with methacrylate to achieve photo-crosslinking on glass-slides and conjugation of a synthetic peptide derived from vitronectin (VN) to the glycosaminoglycan (Zhang et al., 2016). The growth rate of hiPSCs on these VN-MeHA surfaces was compared to that on Madrigal, a mixture of ECM proteins, and similar results were obtained (Zhang et al., 2016).

Another example of a 3D nanofibrous scaffold supporting cell differentiation is the RAD16 peptide family (Zhang et al., 2005; Wu et al., 2012). These two ionic peptides, named RAD16-I and RAD16-II, are able to form stable β -sheets in water and self-assemble spontaneously into nanofiber scaffolds, which could mimic the ECM of tissue cells (Yanlian et al., 2009; Wu et al., 2012). Furthermore, three different self-assembling peptide hydrogels were developed to mimic a 3D cell environment for human adipose stem cells by functionalization of RAD16-I with three biologically active peptide motifs (see **Table 1**) at its C-terminus (Liu et al., 2013). The functionalized RAD16-I peptide-based hydrogels were used for cell culture and showed that the peptide motifs increased the viability of human adipose stem cells compared to RAD16-I. The largest number of human adipose stem cells showing highest biological activities including migration, proliferation and growth factor-secretion were detected in case of RAD/PRGD. These kinds of biomaterials follow simple design principles and are easy



to connect with biologically relevant peptide epitopes to tune bioavailability.

Beside nanofibrous scaffolds, amyloids represent promising peptide species as substrates to control stem cell behavior. Amyloids are highly ordered peptide aggregates. Their formation from soluble proteins during the life-time of an organism is commonly associated with degenerative diseases including Alzheimer's and Parkinson's disease. It may seem unexpected to use motifs that are responsible for degenerative diseases as substrates for applications in regenerative medicine, but recent studies have shown that this is possible (Masliah et al., 2001; Hardy, 2002; Lashuel et al., 2002; Chiti and Dobson, 2006; Winner et al., 2011; Jacob et al., 2015). Amyloid folding can be tuned based on the amino acid composition (Mankar

et al., 2011). Amyloid structures exist predominantly as β -sheets, which are characteristically arranged in a highly repetitive cross- β structure, which forms stable, long, straight, and unbranched amyloid-fibrils consisting of individual subunits, named protofilaments (Goldsbury et al., 1999; Serpell et al., 2000; Nelson and Eisenberg, 2006; Rambaran and Serpell, 2008). Jacob et al. developed a series of peptides to form amyloid nanofibril based hydrogels for 2D and 3D stem cell culture and differentiation (Jacob et al., 2015). These amyloid nanofibrils, consisting of self-assembling Fmoc-protected peptides derived from β -sheet prone C-terminal A β 42 are non-toxic, thermoreversible and thixotropic. By varying the peptide and salt concentration, the stiffness of the resulting amyloid gels can be modulated. Most of them are supporting cell attachment,

TABLE 1 | Differentiation potential of 2D and 3D peptide-based biomaterials, differentiation features: 1, chemical group; 2, substrate elasticity; 3, topology.

Cell behavior	Cell type	Substrate description	Feature	References
Cell attachment and proliferation	hiPSC	VN (Ac-KGGPQVTRGDVFTMP)-conjugated hyaluronic acid	1	Zhang et al., 2016
	hASC	C-terminal functionalized RAD16-I: Bone Marrow Homing Peptide 1 (BMHP1, SKPPGTSS, RAD/SKP), heparin binding motif (FHRRIKA, RAD/FHR) and a PRGD-peptide motif (PRGDSGYRGDS, RAD/PRGD)	1	Liu et al., 2013
Neurogenesis inducing materials	hMSC	Fmoc-protected peptides from A β 42	1, 3	Jacob et al., 2015
	hMSC	Fmoc-protected peptides from A β 42	1, 3	Jacob et al., 2015
	ratNSC	A β -monomers	1	Collins et al., 2015
	ratNSC	IKVAV-linked RAD16-I peptide hydrogel	1, 2, 3	Cheng et al., 2013
	murine NSC	RAD16, RAD16-BMHP1, RAD16-BMHP2 (PFSSTKT)	1, 3	Gelain et al., 2006
	rat PC12	RAD16-I, RAD16-II	3	Holmes et al., 2000; Wu et al., 2012
	rat PC12, murine NSC	hSAF, RGDS-functionalized hSAF	1, 2	Banwell et al., 2009; Mehrban et al., 2015
Chondrogenesis inducing materials	MSC, Chondrocytes	PEG-conjugated CMPs	3	Lee et al., 2008; Deans and Elisseeff, 2010
	hMSC	Self-assembled N-cadherin mimetic peptide hydrogel	1, 2	Li et al., 2017
	ratMSC	Glucose-presenting peptide nanofiber	1	Yasa et al., 2017
Osteogenesis inducing materials	ratMSC	Glucose-presenting peptide nanofiber	1	Yasa et al., 2017
	hiPSC	VN- and BFP- functionalized hydrogel surfaces	1	Deng et al., 2018
	MSC	PEGylated PFSSTGTC peptide SAMs	1, 3	Han et al., 2015
	hMSC	Covalently grafted KRGDSPC modified silica-nanoribbons	1, 3	Das et al., 2013
	ratMSC	N-terminal palmitic acid modified RGDEAAAGGG	1, 2, 3	Hosseinkhani et al., 2006a,b
	MC3T3	RAD16, RAD16-ALKRQGRPLYGF (ALK), RAD16-DGRGDSVAYG (DGR), RAD16-PRGDSGYRGDS (PRG)	1, 3	Horii et al., 2007
	Primary rat osteoblasts, putative rat liver progenitor cells	RAD16-I coated H-PHP	1, 3	Semino et al., 2003; Bokhari et al., 2005

proliferation and influence the stem cell fate. The softest gel supports neuronal differentiation pathways for hMSCs. In summary, stem cell proliferation and adhesion can be supported by fibrous structures that provide a 3D environment which approximates the natural ECM. Additional approaches also use short self-assembling Fmoc-peptides as scaffolds, e.g., for the delivery of growth factors (Rodriguez et al., 2013, 2018; Bruggeman et al., 2016) or enzymatic self-assembly control (Williams et al., 2010). Furthermore, conjugation with short biologically relevant peptides enhances biocompatibility and differentiation activity.

NEUROGENESIS INDUCING BIOMATERIALS

Besides the described physical hydrogel support, it is well-known that β -amyloid peptide (A β) and prion protein (PrP), the A β -oligomer receptor, both influence neurogenesis. Studies by Collins *et al.* showed that neural stem cells (NSCs) were influenced by this interplay via different A β -pathway activation in presence or absence of PrP. The proliferation signals of NSCs

were inhibited by A β -PrP signaling (Collins et al., 2015). Short regions of the amyloid precursor protein, especially A β 42, could be suitable for the development of amyloid-based materials for NSCs cell culture and differentiation.

In contrast to β -sheet based amyloids, certain coiled coil forming peptides can adopt higher ordered structures that are α -helical in nature. Coiled-coil motifs are common among natural proteins, in fact, sequence analysis has shown that nearly 2–3% of natural proteins contain coiled-coils (Wolf et al., 1997; Burkhard et al., 2001). The coiled-coil consists of two to seven α -helical strands that form a left-handed superhelical twist (Woolfson, 2005; Falenski et al., 2010). Its amino acid sequence is characterized by a seven residue periodicity, called a heptad repeat and enables the rational design by modification, for example with carbohydrate or peptide ligands (Zacco et al., 2015a,b).

Based on this design, several groups have developed peptide-based materials for cell culture applications. A self-assembling α -helical peptide-based hydrogel was shown to support the growth and differentiation of rat adrenal pheochromocytoma cells. The developed hydrogelating self-assembling fibers (hSAFs) are able to form networks of α -helical fibrils and build hydrogels, which

entrap more than 99% of water by weight. The design of a self-assembling fiber (SAF) based on an α -helical coiled-coil peptide was previously described (Ryadnov and Woolfson, 2003; Papapostolou et al., 2007; Banwell et al., 2009). The resulting hSAFs were applied as suitable and defined microenvironments for cell growth and differentiation. A RGDS-functionalized hSAF demonstrated improved cellular attachment and differentiation compared to undecorated gels for NSC culture (Mehrban et al., 2015). NSC attachment to the developed hSAFs increases upon addition of the cell-adhesion motif RGDS. It was also shown that the NSCs form large neurospheres inside the functionalized gels and then mature into neurons. Thus, it was demonstrated that these α -helical peptide-based hydrogels provide an appropriate extracellular environment for NSCs and represent a starting point for the development of materials that support neural tissue engineering.

Additionally, nanofibrous structures, like RAD16, were shown to support gene expressions of neural stem cell differentiation by conjugation with BMHP1 and Bone Marrow Homing Peptide 2 (BMHP2) (Gelain et al., 2006). The conjugation of RAD16-I with IKVAV was realized with the aim of creating a self-assembling IKVAV-linked peptide hydrogel as a 3D scaffold for enhanced differentiation of neural stem cells and is a potential application for the regeneration of injured brain tissue (Cheng et al., 2013). The IKVAV motif is known to promote neurite outgrowth and enhances neuronal differentiation and neurite proliferation (Yamada et al., 2002). Similarly to RAD16-I, RAD16-II showed to be a suitable substrate for neurite outgrowth (Holmes et al., 2000; Wu et al., 2012). The conjugation of different peptide motifs to these peptide hydrogel scaffolds lead to an enhancement of neuronal differentiation behavior of different stem cell lines.

CHONDROGENESIS INDUCING BIOMATERIALS

Mimicking the structure of adhesion proteins like collagen is one approach to creating chondrogenesis inducing materials (Zhang et al., 2012). Collagen has a triple-helix structure (Brodsky and Ramshaw, 1997; Brodsky and Persikov, 2005; Wess, 2005) that can be mimicked by synthetic peptide-amphiphiles (Cen et al., 2008; Zhang et al., 2012) and coiled-coil peptides (Hennessy et al., 2009). Important examples include collagen mimetic peptides (CMPs), which are able to adopt the tertiary structure of natural collagen (Lee et al., 2006, 2008; Deans and Elisseeff, 2010). Conjugated with PEG, the CMP substrates retain their structure to help encapsulate collagen, which maintains chondrocytes (Lee et al., 2006; Deans and Elisseeff, 2010) and thus, serves as suitable substrate to enable MSCs chondrogenesis (Lee et al., 2008; Deans and Elisseeff, 2010). Also, a self-assembled N-cadherin mimetic peptide hydrogel was found to promote chondrogenic differentiation of hMSC (Li et al., 2017).

Another approach investigates the effect of glucose, carboxylate, and sulfonate attached to a peptide nanofiber on the differentiation behavior of rat MSCs (Yasa et al., 2017). It was shown that the presence of a glucose moiety on the peptide nanofiber leads to osteo/chondrogenic

differentiation of the tested cells. Chondrogenesis inducing peptidic biomaterials have to combine the structural and morphological features of cartilage tissue. Glycosaminoglycans play an important role in achieving the stiffness of natural ECM, and conjugation of simple functional groups to these substrates is a promising proof-of-concept to represent the complexity of natural ECMs.

OSTEOGENESIS INDUCING BIOMATERIALS

Bone tissue has the greatest stiffness of all types, but stem cells exist in the bone marrow niche, which is variable stiff and it is not clear how their fate will be directed after leaving their niche (Ivanovska et al., 2015). In addition to stiffness, substrates that enhance osteogenesis have to provide topological cues to induce osteogenic signals.

Self-assembled monolayers (SAMs) are highly organized substrates, which are adsorbed onto gold surfaces and suitable for development of 2D-cell culture materials due to tunable surface properties to regulate cell-substrate interaction via surface modifications (Hudalla and Murphy, 2009; Griffin et al., 2015; Kehr et al., 2015). To this end self-assembling peptides are optimal substrates; for example, a SAM consisting of PEGylated PFSSTKTC peptide modified on quartz substrate was shown to direct osteogenic differentiation of MSCs (Han et al., 2015).

The modification of hydrogels with biologically relevant peptide epitopes, derived from adhesion proteins of the ECM was shown to support long-term maintenance and induce osteogenic differentiation of hiPSCs. The VN and BFP (Bone Forming Peptide) concentration on the hydrogel surface was varied and different degrees of differentiation of hiPSCs were achieved (Deng et al., 2018).

Modification and covalent grafting of silica-nanoribbons with KRGDSPC peptide onto activated glass substrates highlights the influence of shape and topology of a synthetic ECM on cell fate. It was shown, that the studied helical nanoribbons induced differentiation into osteoblast lineage (Das et al., 2013).

C-terminal extension of RAD16 with different biologically relevant epitopes are shown to promote osteogenic differentiation of osteoblast precursor cells (Horie et al., 2007). Further developments investigated the design of peptide-amphiphiles including the recognition motif RGD (see **Table 1**) and N-terminal palmitic acid. This conjugate builds a 3D-network by mixing an aqueous solution of peptide-amphiphile with MSCs and influences the stem cells' attachment, proliferation, and differentiation to osteogenic lineage (Hosseinkhani et al., 2006a,b). Combination of PolyHIPE polymer (PHP) with RAD16-I produced a nanoscale environment and spontaneously self-assembled into highly hydrated nanofibers able to trap volume contents of 99.5% water and to envelope cells in a 3D environment (Semino et al., 2003; Bokhari et al., 2005). A significant increase of cell-number in RAD16-I coated H-PHP constructs was observed compared to H-PHP alone and osteoblast differentiation was observed (Bokhari et al., 2005). Several approaches dealing with osteoinductive materials are

focusing on signals sent by molecules covalently grafted onto inert surfaces or presented in a 3D nanofiber network.

CONCLUSION

With the help of 20 canonical amino acids nature builds a repertoire of structural motifs to determine stem cell fate. This repertoire can be extended via the use of synthetic amino acids and in creating biologically relevant recognition and signal motifs. The resulting structural motifs can build stable, flexible and regenerative assemblies to form artificial ECMs. The peptide-based materials presented in this review comply with the requirements of an artificial matrix for mimicking the natural environment of stem cells. It is important that such peptides and their resulting assemblies be stable enough to remain in stem cell culture medium without precipitation due to undesired further aggregation or degradation. Peptides have been successfully used to develop scaffolds of variable stiffness for stem cell culture and differentiation and have proven their potential for use as ECM mimetics and as potential stem cell culture substrates. The advantageous properties of these biopolymers include their ease of design and synthesis and their ability to form chemically well-defined higher order assemblies, which makes them ideal

candidates for both 2D and 3D tissue engineering applications. In this context, coiled-coil peptides have proven as highly suitable scaffolds for cell culture applications due to their predictable self-assembly properties, which also allow multivalent ligand presentation (Zacco et al., 2015a). However, to date, very few examples of 2D and 3D coiled-coil based scaffolds that influence stem cell behavior exist. Another limitation is our current understanding of stem cell niches and their differentiation mechanisms, which is not sufficient yet for either the rational design of ECM-materials or the prediction of the fate of the cell; more research is needed in this area.

AUTHOR CONTRIBUTIONS

All authors listed have made a substantial, direct and intellectual contribution to the work, and approved it for publication.

ACKNOWLEDGMENTS

Open Access Funding provided by the Freie Universität Berlin. The project was funded by the DFG-CRC 765 Multivalency (SFB 765/2-2014). We are grateful to Dr. Allison Ann Berger for polishing the English language of the manuscript.

REFERENCES

- Aurand, E. R., Lampe, K. J., and Bjugstad, K. B. (2012). Defining and designing polymers and hydrogels for neural tissue engineering. *Neurosci. Res.* 72, 199–213. doi: 10.1016/j.neures.2011.12.005
- Banwell, E. F., Abelardo, E. S., Adams, D. J., Birchall, M. A., Corrigan, A., Donald, A. M., et al. (2009). Rational design and application of responsive α -helical peptide hydrogels. *Nat. Mater.* 8, 596–600. doi: 10.1038/nmat2479
- Bokhari, M. A., Akay, G., Zhang, S., and Birch, M. A. (2005). The enhancement of osteoblast growth and differentiation *in vitro* on a peptide hydrogel—polyHIPE polymer hybrid material. *Biomaterials* 26, 5198–5208. doi: 10.1016/j.biomaterials.2005.01.040
- Brodsky, B., and Persikov, A. V. (2005). Molecular structure of the collagen triple helix. *Adv. Protein Chem.* 70, 302–333. doi: 10.1016/S0065-3233(04)70009-1
- Brodsky, B., and Ramshaw, J. A. (1997). The collagen triple-helix structure. *Matrix Biol.* 15, 545–554. doi: 10.1016/S0945-053X(97)90030-5
- Bruggeman, K. F., Rodriguez, A. L., Parish, C. L., Williams, R. J., and Nisbet, D. R. (2016). Temporally controlled release of multiple growth factors from a self-assembling peptide hydrogel. *Nanotechnology* 27:385102. doi: 10.1088/0957-4484/27/38/385102
- Burkhard, P., Stetefeld, J., and Strelkov, S. V. (2001). Coiled coils: a highly versatile protein folding motif. *Trends Cell Biol.* 11, 82–88. doi: 10.1016/S0962-8924(00)01898-5
- Cen, L., Liu, W., Cui, L., Zhang, W., and Cao, Y. (2008). Collagen tissue engineering: development of novel biomaterials and applications. *Pediatr. Res.* 63, 492–496. doi: 10.1203/PDR.0b013e31816c5bc3
- Cheng, T. Y., Chen, M. H., Chang, W. H., Huang, M. Y., and Wang, T. W. (2013). Neural stem cells encapsulated in a functionalized self-assembling peptide hydrogel for brain tissue engineering. *Biomaterials* 34, 2005–2016. doi: 10.1016/j.biomaterials.2012.11.043
- Chiti, F., and Dobson, C. M. (2006). Protein misfolding, functional amyloid, and human disease. *Annu. Rev. Biochem.* 75, 333–366. doi: 10.1146/annurev.biochem.75.101304.123901
- Collins, S. J., Tumpach, C., Li, Q. X., Lewis, V., Ryan, T. M., Roberts, B., et al. (2015). The prion protein regulates beta-amyloid-mediated self-renewal of neural stem cells *in vitro*. *Stem Cell Res. Ther.* 6:60. doi: 10.1186/s13287-015-0067-4
- Curran, J. M., Chen, R., and Hunt, J. A. (2005). Controlling the phenotype and function of mesenchymal stem cells *in vitro* by adhesion to silane-modified clean glass surfaces. *Biomaterials* 26, 7057–7067. doi: 10.1016/j.biomaterials.2005.05.008
- Curran, J. M., Chen, R., and Hunt, J. A. (2006). The guidance of human mesenchymal stem cell differentiation *in vitro* by controlled modifications to the cell substrate. *Biomaterials* 27, 4783–4793. doi: 10.1016/j.biomaterials.2006.05.001
- Das, R. K., Zouani, O. F., Labrugère, C., Oda, R., and Durrieu, M.-C. (2013). Influence of nanohelical shape and periodicity on stem cell fate. *ACS Nano* 7, 3351–3361. doi: 10.1021/nn4001325
- Deans, T. L., and Elisseeff, J. (2010). Mimicking extracellular matrix to direct stem cell differentiation. *World Stem Cell Rep.* 2009, 97–100.
- Deng, Y., Wei, S., Yang, L., Yang, W., Dargusch, S., Chen, Z., et al. (2018). A novel hydrogel surface grafted with dual functional peptides for sustaining long-term self-renewal of human induced pluripotent stem cells and manipulating their osteoblastic maturation. *Adv. Funct. Mater.* 28:1705546. doi: 10.1002/adfm.201705546
- Ding, S., and Schultz, P. G. (2004). A role for chemistry in stem cell biology. *Nat. Biotechnol.* 22, 833–840. doi: 10.1038/nbt987
- Falenski, J. A., Gerling, U. I. M., and Koksich, B. (2010). Multiple glycosylation of *de novo* designed α -helical coiled coil peptides. *Bioorg. Med. Chem.* 18, 3703–3706. doi: 10.1016/j.bmc.2010.03.061
- Fuchs, E., Tumber, T. and Gausch, G. (2004). Socializing with the neighbors: stem cells and their niche. *Cell* 116, 769–778. doi: 10.1016/S0092-8674(04)00255-7
- Gelain, F., Bottai, D., Vescovi, A., and Zhang, S. (2006). Designer self-assembling peptide nanofiber scaffolds for adult mouse neural stem cell 3-dimensional cultures. *PLoS ONE* 1:e119. doi: 10.1371/journal.pone.0000119
- Goldsbury, C., Kistler, J., Aebi, U., Arvinte, T., and Cooper, G. J. (1999). Watching amyloid fibrils grow by time-lapse atomic force microscopy. *J. Mol. Biol.* 285, 33–39. doi: 10.1006/jmbi.1998.2299
- Griffin, M. F., Butler, P. E., Seifalian, A. M., and Kalaskar, D. M. (2015). Control of stem cell fate by engineering their micro and nanoenvironment. *World J. Stem Cells* 7:37. doi: 10.4252/wjsc.v7.i1.37
- Guilak, F., Cohen, D. M., Estes, B. T., Gimble, J. M., Liedtke, W., and Chen, C. S. (2009). Control of stem cell fate by physical interactions with the extracellular matrix. *Cell Stem Cell* 5, 17–26. doi: 10.1016/j.stem.2009.06.016

- Han, K., Yin, W. N., Fan, J. X., Cao, F. Y., and Zhang, X. Z. (2015). Photo-activatable substrates for site-specific differentiation of stem cells. *ACS Appl. Mater. Interfaces* 7, 23679–23684. doi: 10.1021/acsaami.5b07455
- Hardy, J. (2002). The amyloid hypothesis of Alzheimer's disease: progress and problems on the road to therapeutics. *Science* 297, 353–356. doi: 10.1126/science.1072994
- Hennessy, K. M., Pollot, B. E., Clem, W. C., Phipps, M. C., Sawyer, A. A., Culpepper, B. K., et al. (2009). The effect of collagen I mimetic peptides on mesenchymal stem cell adhesion and differentiation, and on bone formation at hydroxyapatite surfaces. *Biomaterials* 30, 1898–1909. doi: 10.1016/j.biomaterials.2008.12.053
- Holmes, T. C., de Lacalle, S., Su, X., Liu, G., Rich, A., and Zhang, S. (2000). Extensive neurite outgrowth and active synapse formation on self-assembling peptide scaffolds. *Proc. Natl. Acad. Sci. U.S.A.* 97, 6728–6733. doi: 10.1073/pnas.97.12.6728
- Horii, A., Wang, X., Gelain, F., and Zhang, S. (2007). Biological designer self-assembling peptide nanofiber scaffolds significantly enhance osteoblast proliferation, differentiation and 3-D migration. *PLoS ONE* 2:e190. doi: 10.1371/journal.pone.0000190
- Hosseinkhani, H., Hosseinkhani, M., and Kobayashi, H. (2006a). Proliferation and differentiation of mesenchymal stem cells using self-assembled peptide amphiphile nanofibers. *Biomed. Mater.* 1, 8–15. doi: 10.1088/1748-6041/1/1/002
- Hosseinkhani, H., Hosseinkhani, M., Tian, F., Kobayashi, H., and Tabata, Y. (2006b). Osteogenic differentiation of mesenchymal stem cells in self-assembled peptide-amphiphile nanofibers. *Biomaterials* 27, 4079–4086. doi: 10.1016/j.biomaterials.2006.03.030
- Hudalla, G. A., and Murphy, W. L. (2009). Using “click” chemistry to prepare SAM substrates to study stem cell adhesion. *Langmuir* 25, 5737–5746. doi: 10.1021/la804077t
- Hynes, R. (2009). Extracellular matrix: not just pretty fibrils. *Science* 326, 1216–1219.
- Ivanovska, I. L., Shin, J. W., Swift, J., and Discher, D. E. (2015). Stem cell mechanobiology: diverse lessons from bone marrow. *Trends Cell Biol.* 25, 523–532. doi: 10.1016/j.tcb.2015.04.003
- Jacob, R. S., Ghosh, D., Singh, P. K., Basu, S. K., Jha, N. N., Das, S., et al. (2015). Self healing hydrogels composed of amyloid nano fibrils for cell culture and stem cell differentiation. *Biomaterials* 54, 97–105. doi: 10.1016/j.biomaterials.2015.03.002
- Jones, D. L., and Wagers, A. J. (2008). No place like home: anatomy and function of the stem cell niche. *Nat. Rev. Mol. Cell Biol.* 9, 11–21. doi: 10.1038/nrm2319
- Jung, J. P., Gasiorowski, J. Z., and Collier, J. H. (2010). Fibrillar peptide gels in biotechnology and biomedicine. *Biopolymers* 94, 49–59. doi: 10.1002/bip.21326
- Kehr, N. S., Atay, S., and Ergün, B. (2015). Self-assembled monolayers and nanocomposite hydrogels of functional nanomaterials for tissue engineering applications. *Macromol. Biosci.* 15, 445–463. doi: 10.1002/mabi.201400363
- Knoblich, J. A. (2008). Mechanisms of asymmetric stem cell division. *Cell* 132, 583–597. doi: 10.1016/j.cell.2008.02.007
- Kühl, S., and Kühl, M. (2012). *Stammzellbiologie*. Stuttgart: Verlag Eugen Ulmer.
- Lakshmanan, A., Zhang, S., and Hauser, C. A. (2012). Short self-assembling peptides as building blocks for modern nanodevices. *Trends Biotechnol.* 30, 155–165. doi: 10.1016/j.tibtech.2011.11.001
- Lampe, K. J., and Heilshorn, S. C. (2012). Building stem cell niches from the molecule up through engineered peptide materials. *Neurosci. Lett.* 519, 138–146. doi: 10.1016/j.neulet.2012.01.042
- Lashuel, H. A., Hartley, D., Petre, B. M., Walz, T., and Lansbury, P. T. (2002). Neurodegenerative disease: amyloid pores from pathogenic mutations. *Nature* 418, 291–291. doi: 10.1038/418291a
- Lee, H. J., Lee, J.-S., Chansakul, T., Yu, C., Elisseeff, J. H., and Yu, S. M. (2006). Collagen mimetic peptide-conjugated photopolymerizable PEG hydrogel. *Biomaterials* 27, 5268–5276. doi: 10.1016/j.biomaterials.2006.06.001
- Lee, H. J., Yu, C., Chansakul, T., Hwang, N. S., Varghese, S., Yu, S. M., et al. (2008). Enhanced chondrogenesis of mesenchymal stem cells in collagen mimetic peptide-mediated microenvironment. *Tissue Eng. Part A* 14, 1843–1851. doi: 10.1089/ten.tea.2007.0204
- Li, L., and Xie, T. (2005). Stem cell niche: structure and function. *Annu. Rev. Cell Dev. Biol.* 21, 605–631. doi: 10.1146/annurev.cellbio.21.012704.131525
- Li, R., Xu, J., Wong, D. S. H., Li, J., Zhao, P., and Bian, L. (2017). Self-assembled N-cadherin mimetic peptide hydrogels promote the chondrogenesis of mesenchymal stem cells through inhibition of canonical Wnt/ β -catenin signaling. *Biomaterials* 145, 33–43. doi: 10.1016/j.biomaterials.2017.08.031
- Liu, X., Wang, X., Wang, X., Ren, H., He, J., Qiao, L., et al. (2013). Functionalized self-assembling peptide nanofiber hydrogels mimic stem cell niche to control human adipose stem cell behavior *in vitro*. *Acta Biomater.* 9, 6798–6805. doi: 10.1016/j.actbio.2013.01.027
- Lutolf, M. P., Gilbert, P. M., and Blau, H. M. (2009). Designing materials to direct stem-cell fate. *Nature* 462, 433–441. doi: 10.1038/nature08602
- Lv, H., Li, L., Sun, M., Zhang, Y., Chen, L., Rong, Y., et al. (2015). Mechanism of regulation of stem cell differentiation by matrix stiffness. *Stem Cell Res. Ther.* 6:103. doi: 10.1186/s13287-015-0083-4
- Mankar, S., Anoop, A., Sen, S., and Maji, S. K. (2011). Nanomaterials: amyloids reflect their brighter side. *Nano Rev.* 2:6032. doi: 10.3402/nano.v2i0.6032
- Maslah, E., Rockenstein, E., Veinbergs, I., Sagara, Y., Mallory, M., Hashimoto, M., et al. (2001). -Amyloid peptides enhance -synuclein accumulation and neuronal deficits in a transgenic mouse model linking Alzheimer's disease and Parkinson's disease. *Proc. Natl. Acad. Sci. U.S.A.* 98, 12245–12250. doi: 10.1073/pnas.211412398
- Mehrban, N., Zhu, B., Tamagnini, F., Young, F. I., Wasmuth, A., Hudson, K. L., et al. (2015). Functionalized α -helical peptide hydrogels for neural tissue engineering. *ACS Biomater. Sci. Eng.* 1, 431–439. doi: 10.1021/acsbomaterials.5b00051
- Morrison, S. J., and Spradling, A. C. (2008). Stem cells and niches: mechanisms that promote stem cell maintenance throughout life. *Cell* 132, 598–611. doi: 10.1016/j.cell.2008.01.038
- Murphy, W. L., McDevitt, T. C., and Engler, A. J. (2014). Materials as stem cell regulators. *Nat. Mater.* 13, 547–557. doi: 10.1038/nmat3937
- Nelson, R., and Eisenberg, D. (2006). Recent atomic models of amyloid fibril structure. *Curr. Opin. Struct. Biol.* 16, 260–265. doi: 10.1016/j.sbi.2006.03.007
- Odorico, J. S., Kaufman, D. S., and Thomson, J. (2001). Multilineage differentiation from human embryonic stem cell lines. *Stem Cells* 19, 193–204. doi: 10.1634/stemcells.19-3-193
- Papapostolou, D., Smith, A. M., Atkins, E. D., Oliver, S. J., Ryadnov, M. G., Serpell, L. C., et al. (2007). Engineering nanoscale order into a designed protein fiber. *Proc. Natl. Acad. Sci. U.S.A.* 104, 10853–10858. doi: 10.1073/pnas.070801104
- Pek, Y. S., Wan, A. C., and Ying, J. Y. (2010). The effect of matrix stiffness on mesenchymal stem cell differentiation in a 3D thixotropic gel. *Biomaterials* 31, 385–391. doi: 10.1016/j.biomaterials.2009.09.057
- Rambaran, R. N., and Serpell, L. C. (2008). Amyloid fibrils. *Prion* 2, 112–117. doi: 10.4161/pri.2.3.7488
- Rodriguez, A. L., Bruggeman, K. F., Wang, Y., Wang, T. Y., Williams, R. J., Parish, C. L., et al. (2018). Using minimalist self-assembling peptides as hierarchical scaffolds to stabilise growth factors and promote stem cell integration in the injured brain. *J. Tissue Eng. Regen. Med.* 12, e1571–e1579. doi: 10.1002/term.2582
- Rodriguez, A. L., Parish, C. L., Nisbet, D. R., and Williams, R. J. (2013). Tuning the amino acid sequence of minimalist peptides to present biological signals via charge neutralised self assembly. *Soft Matter* 9, 3915–3919. doi: 10.1039/c3sm27758e
- Ryadnov, M. G., and Woolfson, D. N. (2003). Engineering the morphology of a self-assembling protein fibre. *Nat. Mater.* 2, 329–332. doi: 10.1038/nmat885
- Schofield, R. (1978). The relationship between the spleen colony-forming cell and the haemopoietic stem cell. *Blood Cells* 4, 7–25
- Semino, C. E., Merok, J. R., Crane, G. G., Panagiotakos, G., and Zhang, S. (2003). Functional differentiation of hepatocyte-like spheroid structures from putative liver progenitor cells in three-dimensional peptide scaffolds. *Differentiation* 71, 262–270. doi: 10.1046/j.1432-0436.2003.7104503.x
- Serpell, L. C., Sunde, M., Benson, M. D., Tennent, G. A., Pepys, M. B., and Fraser, P. E. (2000). The protofibril substructure of amyloid fibrils. *J. Mol. Biol.* 300, 1033–1039. doi: 10.1006/jmbi.2000.3908
- Takahashi and Yamanaka (2006). Induction of pluripotent stem cells from mouse embryonic and adult fibroblast cultures by defined factors. *Cell* 126, 663–676. doi: 10.1016/j.cell.2006.07.024

- Trappmann, B., Gautrot, J. E., Connelly, J. T., Strange, D. G., Li, Y., Oyen, M. L., et al. (2012). Extracellular-matrix tethering regulates stem-cell fate. *Nat. Mater.* 11, 642–649. doi: 10.1038/nmat3339
- Walker, M., Patel, K., and Stappenbeck, T. (2009). The stem cell niche. *J. Pathol.* 217, 169–180. doi: 10.1002/path.2474
- Watt, F. M., and Hogan, B. L. (2000). Out of Eden: stem cells and their niches. *Science* 287, 1427–1430. doi: 10.1126/science.287.5457.1427
- Watt, F. M., and Huck, W. T. (2013). Role of the extracellular matrix in regulating stem cell fate. *Nat. Rev. Mol. Cell Biol.* 14, 467–473. doi: 10.1038/nrm3620
- Wess, T. (2005). Collagen fibril form and function. *Adv. Protein Chem.* 70, 341–374. doi: 10.1016/S0065-3233(04)70010-8
- Williams, R. J., Mart, R. J., and Ulijn, R. V. (2010). Exploiting biocatalysis in peptide self-assembly. *Biopolymers* 94, 107–117. doi: 10.1002/bip.21346
- Winner, B., Jappelli, R., Maji, S. K., Desplats, P. A., Boyer, L., Aigner, S., et al. (2011). *In vivo* demonstration that α -synuclein oligomers are toxic. *Proc. Natl. Acad. Sci. U.S.A.* 108, 4194–4199. doi: 10.1073/pnas.1100976108
- Wolf, E., Kim, P. S., and Berger, B. (1997). MultiCoil: a program for predicting two- and three-stranded coiled coils. *Protein Sci.* 6, 1179–1189. doi: 10.1002/pro.5560060606
- Woolfson, D. N. (2005). The design of coiled-coil structures and assemblies. *Adv. Protein Chem.* 70, 79–112. doi: 10.1016/S0065-3233(05)70004-8
- Wu, E. C., Zhang, S., and Hauser, C. A. E. (2012). Self-assembling peptides as cell-interactive scaffolds. *Adv. Funct. Mater.* 22, 456–468. doi: 10.1002/adfm.201101905
- Yamada, M., Kadoya, Y., Kasai, S., Kato, K., Mochizuki, M., Nishi, N., et al. (2002). Ile-Lys-Val-Ala-Val (IKVAV)-containing laminin α 1 chain peptides form amyloid-like fibrils. *FEBS Lett.* 530, 48–52. doi: 10.1016/S0014-5793(02)03393-8
- Yanlian, Y., Ulung, K., Xiumei, W., Horii, A., Yokoi, H., and Shuguang, Z. (2009). Designer self-assembling peptide nanomaterials. *Nano Today* 4, 193–210. doi: 10.1016/j.nantod.2009.02.009
- Yasa, O., Uysal, O., Ekiz, M. S., Guler, M. O., and Tekinay, A. B. (2017). Presentation of functional groups on self-assembled supramolecular peptide nanofibers mimicking glycosaminoglycans for directed mesenchymal stem cell differentiation. *J. Mater. Chem. B* 5, 4890–4900. doi: 10.1039/C7TB00708F
- Zacco, E., Anish, C., Martin, C. E. V., Berlepsch, H., Brandenburg, E., Seeberger, P. H., et al. (2015a). A self-assembling peptide scaffold for the multivalent presentation of antigens. *Biomacromolecules* 16, 2188–2197. doi: 10.1021/acs.biomac.5b00572
- Zacco, E., Hütter, J., Heier, J. L., Mortier, J., Seeberger, P. H., Lepenies, B., et al. (2015b). Tailored presentation of carbohydrates on a coiled coil-based scaffold for asialoglycoprotein receptor targeting. *ACS Chem. Biol.* 10, 2065–2072. doi: 10.1021/acschembio.5b00435
- Zhang, S., Gelain, F., and Zhao, X. (2005). Designer self-assembling peptide nanofiber scaffolds for 3D tissue cell cultures. *Semin. Cancer Biol.* 15, 413–420. doi: 10.1016/j.semcancer.2005.05.007
- Zhang, X., Zhou, P., Zhao, Y., Wang, M., and Wei, S. (2016). Peptide-conjugated hyaluronic acid surface for the culture of human induced pluripotent stem cells under defined conditions. *Carbohydr. Polym.* 136, 1061–1064. doi: 10.1016/j.carbpol.2015.09.081
- Zhang, Z., Hu, J., and Ma, P. X. (2012). Nanofiber-based delivery of bioactive agents and stem cells to bone sites. *Adv. Drug Deliv. Rev.* 64, 1129–1141. doi: 10.1016/j.addr.2012.04.008

Conflict of Interest Statement: The authors declare that the research was conducted in the absence of any commercial or financial relationships that could be construed as a potential conflict of interest.

Copyright © 2019 Hellmund and Kokschi. This is an open-access article distributed under the terms of the Creative Commons Attribution License (CC BY). The use, distribution or reproduction in other forums is permitted, provided the original author(s) and the copyright owner(s) are credited and that the original publication in this journal is cited, in accordance with accepted academic practice. No use, distribution or reproduction is permitted which does not comply with these terms.



Novel Materials From the Supramolecular Self-Assembly of Short Helical β^3 -Peptide Foldamers

Ketav Kulkarni[†], Nathan Habila[†], Mark P. Del Borgo^{*} and Marie-Isabel Aguilar^{*}

Department of Biochemistry and Molecular Biology and Biomedicine Discovery Institute, Monash University, Melbourne, VIC, Australia

OPEN ACCESS

Edited by:

Alessandro Contini,
University of Milan, Italy

Reviewed by:

Xiao-Yu Hu,
Nanjing University of Aeronautics and
Astronautics, China
Sara Pellegrino,
University of Milan, Italy

*Correspondence:

Marie-Isabel Aguilar
mibel.aguilar@monash.edu
Mark P. Del Borgo
mark.delborgo@monash.edu

[†]These authors have contributed
equally to this work

Specialty section:

This article was submitted to
Supramolecular Chemistry,
a section of the journal
Frontiers in Chemistry

Received: 30 November 2018

Accepted: 25 January 2019

Published: 15 February 2019

Citation:

Kulkarni K, Habila N, Del Borgo MP
and Aguilar M-I (2019) Novel Materials
From the Supramolecular
Self-Assembly of Short Helical
 β^3 -Peptide Foldamers.
Front. Chem. 7:70.
doi: 10.3389/fchem.2019.00070

Self-assembly is the spontaneous organization of small components into higher-order structures facilitated by the collective balance of non-covalent interactions. Peptide-based self-assembly systems exploit the ability of peptides to adopt distinct secondary structures and have been used to produce a range of well-defined nanostructures, such as nanotubes, nanofibres, nanoribbons, nanospheres, nanotapes, and nanorods. While most of these systems involve self-assembly of α -peptides, more recently β -peptides have also been reported to undergo supramolecular self-assembly, and have been used to produce materials—such as hydrogels—that are tailored for applications in tissue engineering, cell culture and drug delivery. This review provides an overview of self-assembled peptide nanostructures obtained via the supramolecular self-assembly of short β -peptide foldamers with a specific focus on N-acetyl- β^3 -peptides and their applications as bio- and nanomaterials.

Keywords: β -peptide, supramolecular selfassembly, peptide materials, biomaterials, β -amino acid containing peptides

INTRODUCTION

Peptide-based self-assembly is the spontaneous formation of a stable hierarchical structure via a combination of molecular interactions that include hydrogen bonding, hydrophobic interactions, electrostatic interactions, π - π stacking and van der Waals forces (without an external trigger). In general, peptide-based self-assembly is mediated by a variety of secondary structural conformations. Peptides comprised of α -amino acids have the propensity to adopt secondary structures including α -helices, β -sheets and coiled-coils that influence the peptide-based self-assembly processes (Cui et al., 2010; Woolfson and Mahmoud, 2010; Matson and Stupp, 2012; Raymond and Nilsson, 2018). The challenge in the design of novel, functional peptide-based materials is to engineer the constituent peptide monomers that take advantage of these unique secondary structural conformations to establish complementary surfaces that interact non-covalently in a repeating fashion to create the desired nanostructure with favorable mechanical properties.

β -Peptides are polyamides composed of β -amino acids which differ from α -amino acids due to the presence of an extra methylene in the backbone (Cheng et al., 2001; Seebach et al., 2004; Gopalan et al., 2015). The extra CH_2 group (**Figure 1**) is inserted between the carboxy terminus and the α -carbon atom. The side chains can be positioned at either the α - or β -carbon, resulting in either β^2 or β^3 -amino acids.

The incorporation of an extra methylene results in both constitutional and configurational isomers (Steer et al., 2002; Seebach et al., 2004; Aguilar et al., 2007; Clerici et al., 2016) which are either R or S configuration at the α -(C²) carbon or the β -(C³) carbon, resulting in a total of 4 possible isomers for any given side chain. The advantages of β^3 -peptides over α -peptides depend on the application and whether single substitutions or entire β -peptides are considered. As a peptidomimetic, single substitution of α -amino acids by β^3 - or β^2 -amino acids in α -peptides confers resistance to enzymatic degradation as the extra methylene shifts the scissile bond away from the active site nucleophile, thereby stabilizing an otherwise metabolically sensitive bioactive peptide. β^3 - or β^2 -amino acids may also induce small changes in peptide conformation again leading to different biological activity (Sagan et al., 2003; Cabrele et al., 2014). The majority of studies have utilized β^3 -amino acids in favor of β^2 -amino acids, as the preparation of β^2 -amino acids requires more complex synthetic methods while β^3 amino acids can be obtained in a 2-step reaction from their α -amino acids counterparts. β^3 -peptides have been used in the design of a wide range of bioactive compounds and peptide and protein mimetics (Fülöp et al., 2006; Aguilar et al., 2007; Checcho and Gellman, 2016; Del Borgo et al., 2017; Kiss et al., 2017). These applications range from enzyme inhibitors, receptor agonists and antagonists and inhibitors of protein-protein interactions to antimicrobial agents.

The next major feature of β -peptides is their ability to adopt well-defined helical structures stabilized by hydrogen bonding (Appella et al., 1997, 1999; Seebach et al., 1997, 1998). While there are at least five different helices, including 8-, 10-, 12-, 14-, and 10/12-helix, (Cheng et al., 2001) that have been identified for β -peptides based on the number of atoms in the hydrogen-bonded rings, oligomers of β^3 -peptides are predominantly defined by either a 14- or 12-helical conformation. The 14-helix is stabilized by hydrogen bonding between the main chain amide proton (HN) at position *i* and the carbonyl (CO) at position *i*+2, forming a 14-membered pattern (Cheng et al., 2001). Similarly, the 12-helix is stabilized by hydrogen bonds between the backbone amides (HN) at positions *i* and *i*+3 (CO). The overall structure of the 14-helix differs from that of the α -helix with a slightly wider radius (14-helix = 2.7 Å and α -helix = 2.2 Å), a lower number of residues per turn (14-helix = 3.0 residues and α -helix = 3.6 residues) and a shorter rise per residue for a given chain length than the α -helix (14-helix = 1.56 Å and α -helix = 1.5 Å). The 12-helix has a radius of 2.3 Å and consists of 2.5 residues per turn with a rise per residue of 2.1 Å (Cheng et al., 2001).

The 14-helix is characterized by ~3 residues per turn, which results in the alignment of the side chains of every fourth residue directly along one face of the helix (Figure 2) (Cheng et al., 2001). These foldamers have been used as a template for a wide range of biomimetic studies as reviewed previously (Martinek and Fulop, 2012; Gopalan et al., 2015; Mándity and Fulop, 2015; Del Borgo et al., 2017). Moreover, the ability of β -peptides and α/β -peptide hybrids to adopt stable secondary structures has also underpinned the design of novel structure-based receptor inhibitors and

peptide bundles as protein mimics (Checcho et al., 2015a,b; Liu et al., 2018). In this review, we describe how the unique secondary structure of β -peptide fibers has been determined and how this structural template has been exploited to modulate the fiber morphology through lateral interactions, thereby providing new opportunities for the design of novel, stable materials.

β^3 -PEPTIDE BUNDLES

Prior to the recent reports of supramolecular self-assembly of β^3 -peptides, a number of groups have demonstrated the assembly of β^3 -peptides into bundles containing 4–10 individual β^3 -peptides (Raguse et al., 2001; Daniels et al., 2007; Goodman et al., 2007, 2008; Giuliano et al., 2009; Wang et al., 2012, 2014; Wang and Schepartz, 2016). A β^3 -peptide bundle arises from the cooperative folding of β^3 -peptides into higher-order quaternary assemblies in solution and exhibit protein-like properties in which the hydrophobic surfaces are buried in the interior core. The initial steps toward creating a specific helical-bundle with β^3 -amino acid oligomers used two oligomers of optically active trans-2-aminocyclohexanecarboxylic acid (ACHC) that assembled into a tetramer and a hexamer. Similarly, a 10-residue β^3 -peptide designed to adopt amphiphilic helical conformation was also observed to self-assemble in aqueous solution to form tetrameric and hexameric bundles (Raguse et al., 2001). This group has also shown the self-assembly of helical quaternary bundles that are arranged in a parallel orientation of oligomers comprising a mixture of α/β -peptides (Raguse et al., 2001; Horne et al., 2007; Giuliano et al., 2009).

The first stoichiometrically defined octameric β^3 -peptide bundle was designed and characterized with several high-resolution structures (Daniels et al., 2007; Goodman et al., 2007, 2008; Craig et al., 2011). The octameric bundles were made up of β^3 -decapeptides with three distinct faces: a hydrophobic β^3 -Leu face, a salt bridge face of alternating β^3 -Orn and β^3 -Asp residues, and an aromatic surface that contained two β^3 -Tyr or β^3 -Phe residues. The β -peptide oligomer assembled as antiparallel helices with the β^3 -Leu side chains forming the core of the bundle. The same group also described a series of β^3 -peptides which assembled into octameric β -peptide bundles with the aromatic face defined as Acid-1F, Base-1F, Zwit-1F, Acid-1Y, Zwit-EYYO, and Zwit-EYYK (Figure 3). The thermodynamic and kinetic stability of the bundle then allowed this structure to be used as a template for the design and functionalization of new protein-like β^3 -peptide bundles.

As a follow up to this model, the first functional β^3 -peptide helical bundle was recently reported (Wang et al., 2014). The β^3 -peptide bundles were capable of both substrate binding and catalysis of 8-acetoxypyrene-1,3,6-trisulfonate to release the fluorescent product pyranine upon ester hydrolysis. This is useful for optical sensor applications and a fluorescent pH indicator for the physiological range. A combination of kinetic and high-resolution structural analysis suggested the presence of an esterase active site comprising three functional groups, positioned on different strands of the octameric bundle structure.

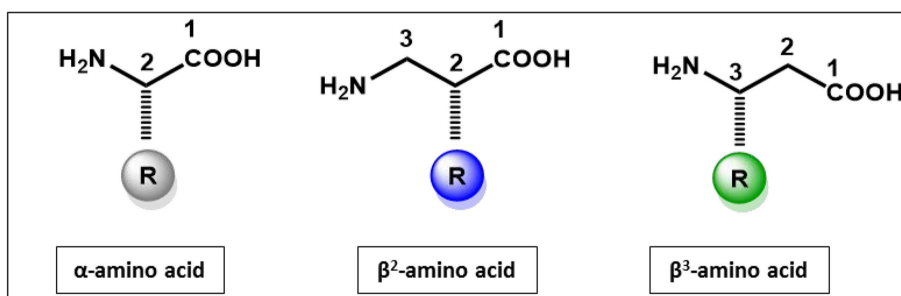


FIGURE 1 | Structural features of α -amino acid, β^2 and β^3 -amino acids.

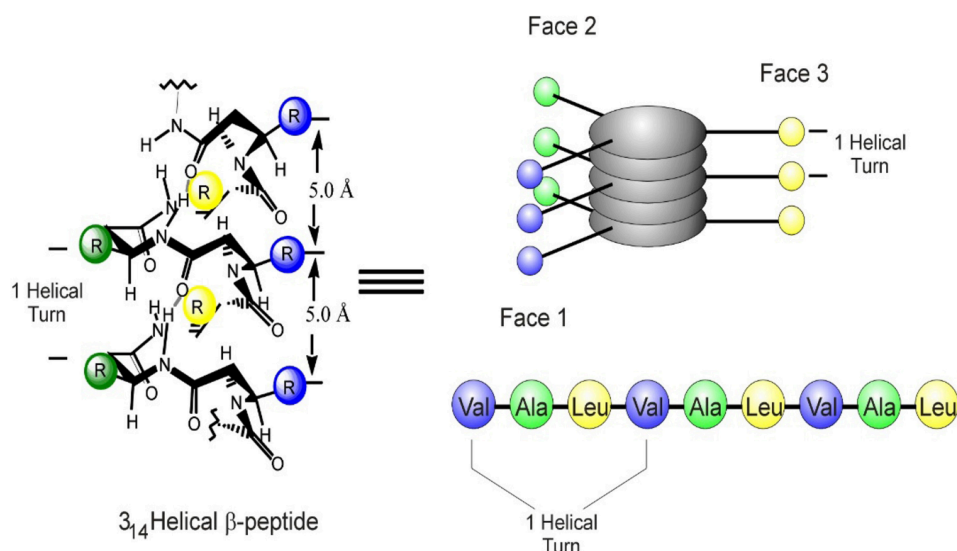


FIGURE 2 | Structure and geometry of a β^3 -peptide 14-helix with the longitudinal alignment of amino acid side chains on the helical surface resulting in a topology that mediates the formation of peptide bundles or for binding to specific targets.

SUPRAMOLECULAR SELF-ASSEMBLY OF β^3 -PEPTIDES

β -Peptides Containing Cyclic β -Amino Acids

Supramolecular self-assembly of β^3 -peptides is the formation of a well-defined large structure from the organization of β^3 -peptide monomers. Supramolecular self-assembly of β^3 -peptides can lead to materials ranging from nano- to macroscopic in dimension (Gopalan et al., 2015; Yoo and Lee, 2017). One of the earliest examples of a supramolecular self-assembling β -peptides was composed of either *cis*-(1R,2S)-ACPC_n (1–4; ACPC = *cis*-2-aminocyclopentanecarboxylic acid) or *trans*-(1S,2S)-ACHC_m (5–7; ACHC = *trans*-2-aminocyclohexanecarboxylic acid, which adopt a strand or a helix conformation, respectively, in solution (Figure 4) (Martinek et al., 2006). These β -peptide monomers were shown to undergo supramolecular self-assembly to yield fibrils of pleated-sheet sandwiches and helix-bundle membranes. Another group reported the production of nanostructures from

the self-assembly of a cyclobutane β -tetrapeptide (Rúa et al., 2007; Torres et al., 2010). These β -peptides comprising residues derived from (1R,2S)-2-aminocyclobutane-1-carboxylic acid adopted a β -strand-type conformation in solution and modeling indicated that self-assembly was mediated by intramolecular H-bonding to give the sheet structure.

The self-assembly of β -peptides containing ACHC was also reported by Gellman et al., with the hierarchical organization exhibiting lyotropic liquid crystalline behavior (Pomerantz et al., 2008, 2011). The designed peptide contained a minimum of three repeats of the ACHC-ACHC- β^3 -Lys triad (Figure 5). This peptide folded into a 14 helical conformation, leading to the segregation of the hydrophobic cyclohexyl ring and hydrophilic β^3 -Lys residue. The cyclohexyl units of the neighboring β^3 -peptide interdigitated to form a zipper-like motif—referred to as a “cyclohexyl zipper”—that was achieved by intermolecular association mediated by the amphiphilic nature of the molecule. Structural analysis revealed the existence of two different types of species, globular aggregates, and nanofibers, which were the

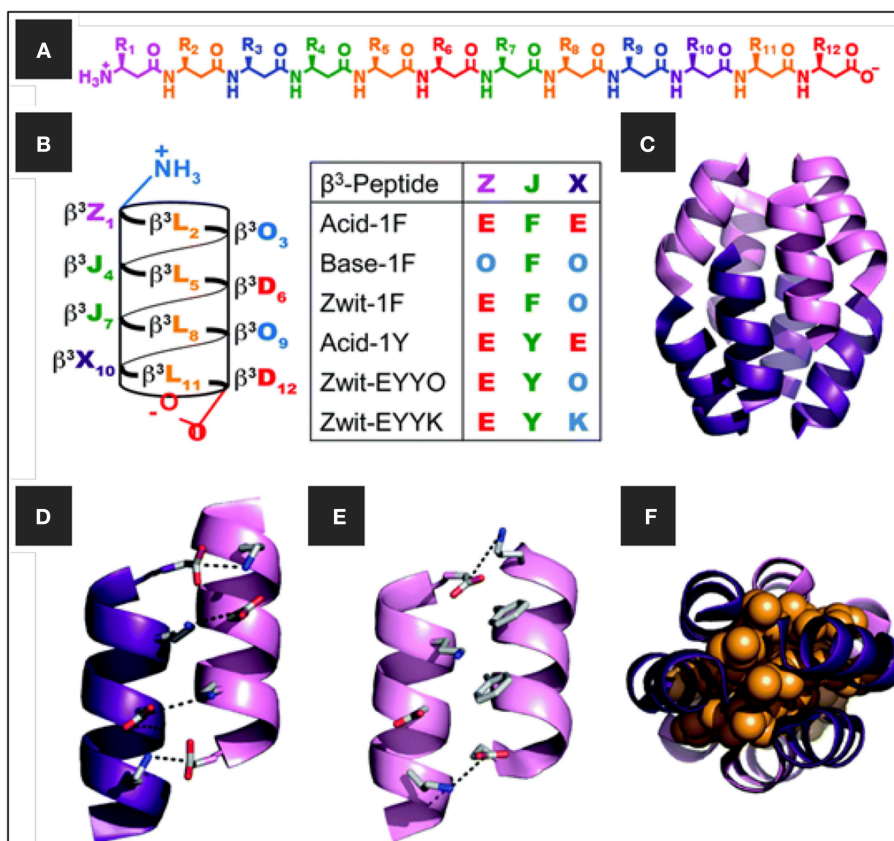


FIGURE 3 | (A) Chemical structure of β -dodecapeptide, (B) helical net representation of a β -dodecapeptide folded into a 14-helix with the different β^3 -peptide sequences (C) β -peptide bundle, the homo-octamer of Zwit-1F, (D,E) close-up view of salt-bridging interactions at the (D) anti-parallel and (E) parallel helical interfaces of Zwit-1F, and (F) space-filling model (orange) showing tight packing of β^3 -homoleucine side-chains in the Zwit-1F core. Adapted with permission from Daniels et al. (2007). Copyright 2007 American Chemical Society.

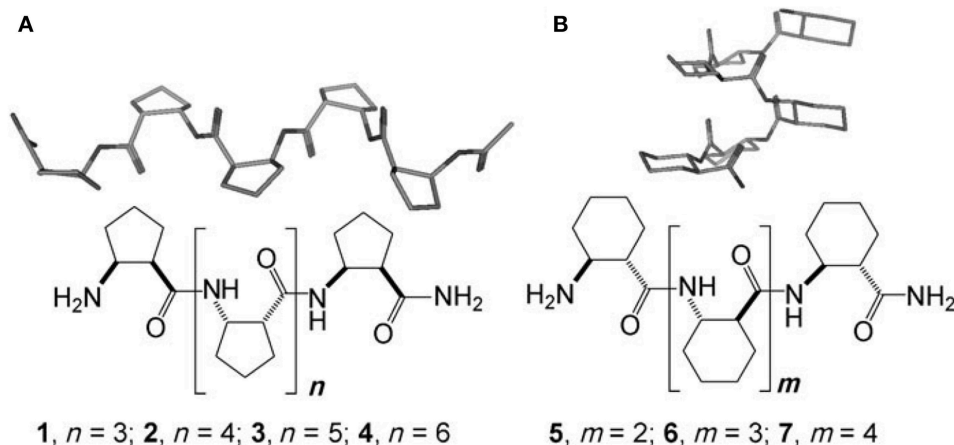


FIGURE 4 | Chemical structures and the secondary structures of (A) cis -ACPC_n (1–4) and (B) $trans$ -ACHC_m (5–7) homooligomers. Reproduced with permission from Martinek et al. (2006). Copyright 2006 John Wiley & Sons.

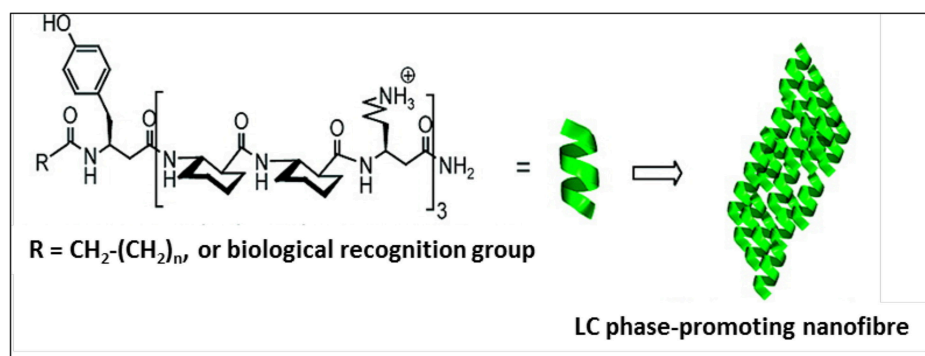


FIGURE 5 | Self-assembled lyotropic liquid crystals with a minimum of three repeats of the ACHC-ACHC- β^3 -Lys triad. Biological recognition group (biotin or the tripeptide RGD) was incorporated at R. Adapted with permission from Pomerantz et al. (2011) Copyright 2011 American Chemical Society.

predominant self-assembled structure that lead to lyotropic LC phase formation.

Spontaneous self-assembly of β -peptide monomers comprising of trans-2-aminocyclopentanecarboxylic acid (ACPC) homo-oligomers as a building block have resulted in a number of 3D microstructures (Kwon et al., 2010, 2011, 2015; Kim et al., 2012). These β -peptide monomers—ACPC₆, ACPC₇, and ACPC₄—have been shown to self-assemble into novel 3D tooth-shaped, windmill-shaped and tapered square rod structures and rectangular microtubes (**Figure 6**) (Kwon et al., 2010, 2011, 2015; Kim et al., 2012; Yoo and Lee, 2017). The monomers adopted a stable right-handed 12-helical conformation in solution. The self-assembly motif is based on the fact that the helix self-assembled in aqueous solution via lateral hydrophobic interactions between the helical faces as well as by head-to-tail intermolecular hydrogen bonding (Kwon et al., 2010). It was concluded that highly ordered anisotropic molecular packing motifs, contained within the foldamer building blocks, are responsible for their unique shapes. The ability of these structures to align and move under a magnetic field at the microscopic as well as macroscopic scales was recently demonstrated by integrating magneto-responsive foldamers within hydrogels (Kwon et al., 2015). These reports highlight the design of biocompatible 3D molecular architectures with different functions and morphologies that could potentially be used for the next generation of biocompatible peptide-based structures.

The approach of substituting β -amino acids to stabilize α -peptides against proteolytic stability has also been applied to the stabilization of α -peptide-based hybrid hydrogels (Yang et al., 2006, 2007). The gelation of these β -amino acid-containing peptide-based hydrogels was triggered by changes in pH and temperature. Another approach utilized mixed α/β -peptides that self-assemble to form hydrogels were shown to be stable to proteolysis and exhibited strong gelation properties (Mangelschots et al., 2016). The self-assembly of N-terminally protected β -alanine-containing dipeptides has also been reported to give a hydrogel which exhibited the controlled release of encapsulated vitamin B derivatives (Nanda and Banerjee, 2012).

N-Acetyl Acyclic β^3 -Peptide Assemblies Head-to-Tail 3-Point H-Bonding Motif

The geometry of the 14-helix means that there are ~ 3 residues per turn, which results in the alignment of the side chains of every fourth residue directly along one face of the helix (**Figure 2**) (Cheng et al., 2001; Martinek and Fulop, 2012). This molecular symmetry forms the core of the supramolecular self-assembly of β^3 -peptides and N-acetylation of β^3 -peptides containing at least three β^3 -amino acids and triggers self-assembly via a head-to-tail motif (Del Borgo et al., 2013; Christofferson et al., 2018). X-ray crystallography confirmed that the capping of the N-terminus provides the necessary H-bond donors and acceptors to facilitate a 3-point H-bond motif that drives the axial self-assembly of β -peptides (Del Borgo et al., 2013). The N-acetyl group plays a critical role by providing the third donor-acceptor interaction pair and thus promotes axial self-assembly and fiber growth into higher ordered structures (**Figure 7**). TEM and atomic force microscopy (AFM) revealed that the peptides with a free N-terminal amine showed no signs of self-assembly, whereas the N-acetylated peptides self-assembled into fibrous morphologies of varying sizes and shapes in different solvents. Interestingly, the structures of two β^3 -tripeptide monomers could be superimposed with a β^3 -hexapeptide to resemble a typical left-handed 14-helical structure with two turns, and internally supported by *i, i+2* intramolecular hydrogen bonds.

The β^3 -peptides self-assembled in water and methanol, forming fibers from several micrometers up to 3 cm in length and ~ 0.25 mm in diameter within 1 h of incubation (**Figure 7**). The large fibrillary structures self-assembled from β^3 -peptide monomers comprised of β^3 -amino acids in multiples of three residues. The head-to-tail model of β^3 -peptide self-assembly was shown to be persistent under a variety of conditions with fibers growing into large structures (Del Borgo et al., 2013). The variation in the thickness and morphology of the structures formed indicated that side chain interactions may influence the extent of inter-fibril interactions. The effect of different solvents on the superstructure morphology of a self-assembled β^3 -peptide, Ac- β^3 -[LIA], was thus investigated (Seoudi et al., 2015a). The fibrils interact through a combination of solvophobic,

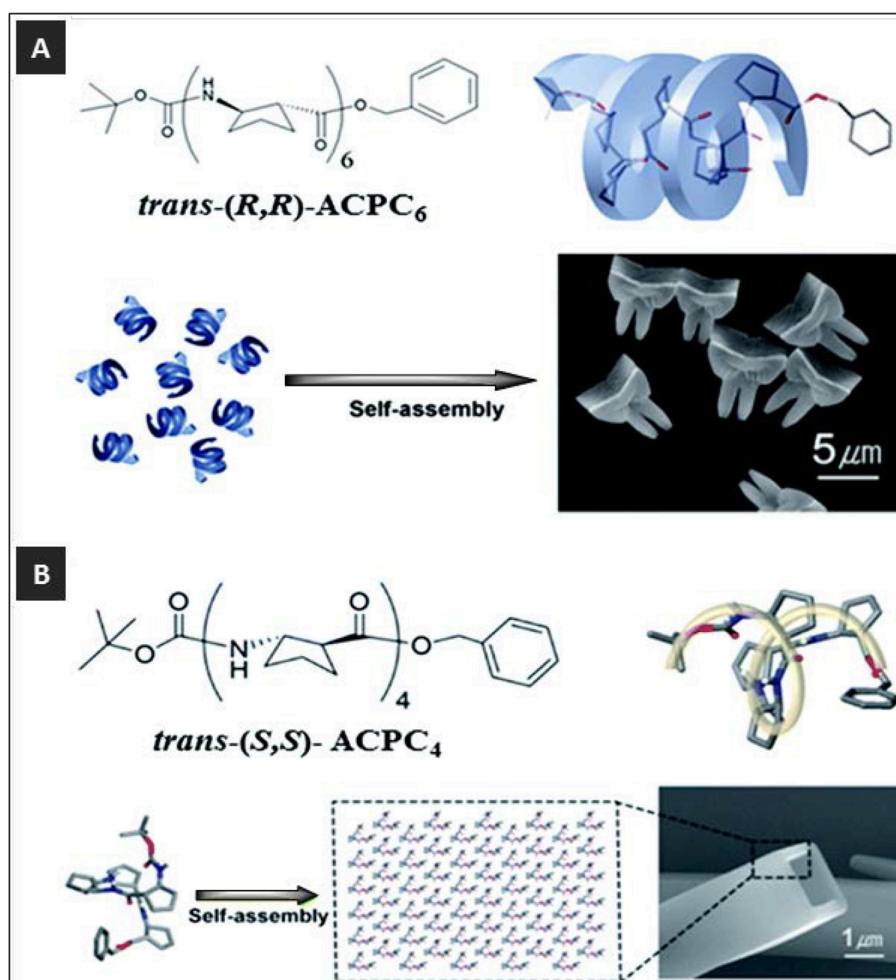


FIGURE 6 | (A) Self-assembly of tooth-shaped architectures from *trans*-(R,R)-ACPC₆ and **(B)** self-assembly of rectangular microtubes from *trans*-(S,S)-ACPC₄. Adapted with permission from Kwon et al. (2011), Copyright 2011 American Chemical Society.

van der Waals and H-bonding interactions, and a change in overall fibril structure was therefore achieved through tuning the relative strengths of the inter-fibril H-bonding, van der Waals and solvophobic interactions. In apolar solvents where the carboxyl-terminal residues do not interact with the solvent, inter-fibril H-bonding drives the formation of assemblies of straight fibers. In contrast, in protic solvents such as alcohols, carboxylic acid residues are solvated, resulting in less prominent inter-fibril H-bonding and a balance between solvophobic and van der Waals effects leads to the formation of dendritic structures. In water, hydrophobic effects dominate over van der Waals interactions, leading to the formation of rope-like twisted structures.

Given the sensitivity of inter-fibril interactions to the solvent environment, the effect of the hydrophobic and steric topography of the 14-helical nanorod on lateral self-assembly was also investigated (Seoudi et al., 2015b). In particular, the fiber structure of three isomeric peptides was studied, comprising the

same three β^3 -amino acid residues: β^3 -homoleucine (β^3 -L), β^3 -homoisoleucine (β^3 -I) β^3 -homoalanine (β^3 -A) to give peptides Ac- β^3 - [LIA], Ac- β^3 - [IAL], and Ac- β^3 - [ALI]. AFM imaging revealed different superstructures for each peptide, confirming that the surface topography of different non-polar side chains can drive an effective approach for the generation of different self-assembled nanomaterials. These studies also demonstrated that the combined effect of the relative spatial distribution of different non-polar side chains and the solvent polarity have an important role in the self-assembly of these compounds and the resulting self-assembled nanomaterials.

The majority of N-acetylated β^3 -peptides which have been reported contained either three or six β^3 -amino acids, i.e., multiples of three residues, resulting in one or two complete turns of the 14-helix, respectively. Therefore, to investigate the effect of perturbing the helical turn on the β^3 peptide self-assembly, β^3 -tetrapeptides (Ac- β^3 -[ALIA], Ac- β^3 -[SLIA], and Ac- β^3 -[KLIE]) with 1 1/3 turns of the helix were also studied (Seoudi et al., 2016).

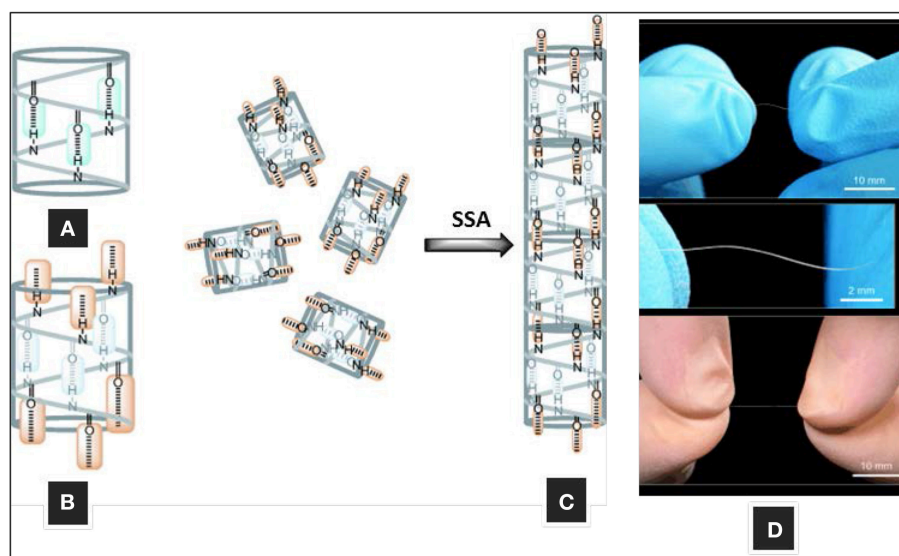


FIGURE 7 | Self-assembly of 14-helical β^3 -peptides. **(A)** Intramolecular hydrogen bonding motif for helix stabilization, **(B)** intermolecular hydrogen-bonding motif **(C)** fiber formation by head-to-tail hydrogen bonding, and **(D)** macroscopic fibers formed by β^3 -hexapeptide Ac-WKVWEV-OH. Adapted with permission from Del Borgo et al. (2013). Copyright 2013 John Wiley & Sons.

All peptides underwent self-assembly confirming that the head-to-tail H-bonding motif was unaffected by the sequence length and composition. Moreover, side chain polarity did not affect the ability of β^3 -tetrapeptides to self-assemble into helical nanorods.

A structural model for a three-stranded helical coiled coil derived from a self-assembled N-acetyl- β^3 -peptide was recently reported using X-ray fiber diffraction of Ac- β^3 -[LIA] and molecular dynamics simulations (Christofferson et al., 2018). The triple 14-helical coiled coil motif was characterized by a hydrophobic core with the twist along the fiber axis arising from interactions between the β^3 -homoleucines and β^3 -homoalanines of adjacent tripeptides on the solvent-exposed surface of the fiber. The computational methods established in this study can now be used to determine the fibril structure for other materials derived from N-acetylated- β^3 -peptides and allow rational engineering of nano- and biomaterials. The modular platform for the design of novel biomaterials has now been established, as shown schematically in **Figure 8A** and discussed in the sections below.

β^3 -Tripeptides Act as Sticky Ends

While the 14-helical structure of β^3 -peptides has been shown to be essential for the H-bonding required for self-assembly, the strength of the 3-point H-bonded self-assembly motif was investigated by integrating a rigid or flexible linker between two β^3 -tripeptide monomers to create a hybrid β^3 -peptide scaffold (Del Borgo et al., 2018). The flanking β^3 -peptides were comprised of three β^3 -amino acids and the results showed that incorporation of either a flexible hexyl linker or a rigid phenyl linker did not perturb self-assembly, demonstrating the dominance of the 3-point H-bonded motif in β^3 -peptide self-assembly (**Figure 8A–b**). This ability of the β^3 -tripeptides to act as sticky ends during self-assembly was further tested

by incorporation of the tripeptide cell-adhesion epitope, α -arginylglycylaspartic acid (RGD) resulting in an α/β hybrid peptide. This peptide also self-assembled to give fibers which acted as bioscaffolds for 2D culture of primary hippocampal neurons, further expanding the design template for new materials based on β^3 -peptides.

Control of Morphology Through Lateral Interactions

As a consequence of the 14-helical self-assembly of β^3 -peptide monomers, the side chains are aligned laterally, resulting in a high degree of symmetry along the periphery of the β^3 -peptide nanorods. This provides an opportunity to functionalize the structure at the side chain position without affecting the self-assembly. Most significantly, in contrast to other peptide-based self-assembling materials, N-acetylated β^3 -tripeptides form fibrous scaffolds in solution or on surfaces, irrespective of the amino acid sequence or solution conditions (Del Borgo et al., 2013; Gopalan et al., 2015). In order to characterize the impact of larger side chains on the self-assembly and to generate a biological scaffold, β^3 -tripeptides were functionalized with anchoring cell-adhesion signals IKVAV or RGD (**Figure 8A–c**) (Luder et al., 2016). Both epitopes were incorporated into a β^3 -peptide monomer as a functionalized side chain by reducing the γ -azido- β^3 -homoalanine (β^3 -Az) side chain using triphenylphosphine, followed by solid phase peptide synthesis (SPPS). The integration of α -peptide epitopes into the β^3 -peptide sequence did not disrupt their ability to self-assemble.

High-resolution analysis by AFM and EM of the fibrous structures generated by the IKVAV-containing peptide showed a helical periodicity of ~ 5 nm in height. If the diameter of a β^3 -tripeptide 14 helix is 0.5 nm and the length of IKVAV side chain in an extended structure is ~ 2 nm, the overall diameter

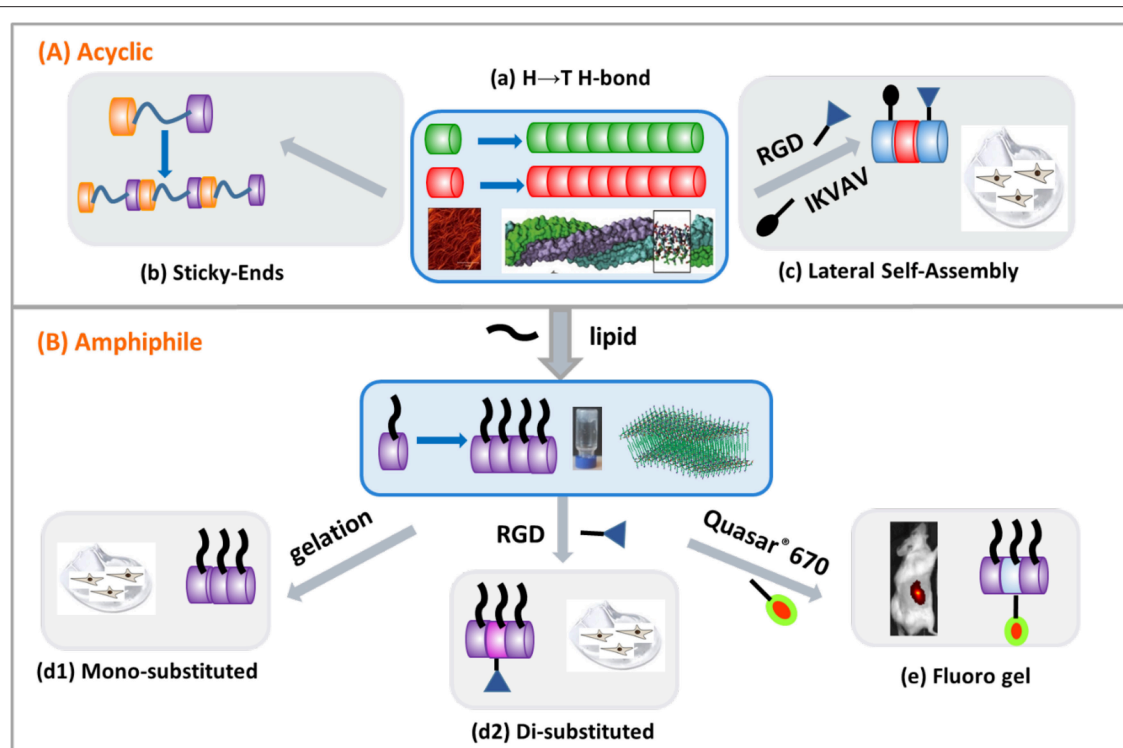


FIGURE 8 | Modular design of β^3 -peptide biomaterials by exploiting the head-to-tail (H \rightarrow T H-bond) 3-point H-bonding motif. Monomers comprised of (A) acyclic β^3 -amino acids or (B) lipo- β^3 -amino acids. (A) (a) Template self-assembly motif, (b) sticky ends, and (c) controlled morphology through lateral interactions. (B) (d1) mono-substituted hydrogel, (d2) disubstituted hydrogel and (e) fluoro hydrogel.

of the peptide monomer is estimated to be 2.5 nm, indicating that the observed fibrils are commensurate with the two peptide nanorods. Most significantly however, the size of the IKVAV side chain did not hinder peptide self-assembly via the head-to-tail motif. Moreover, the fibrils exhibited uniform width, further indicating that the incorporation of a large hydrophobic side chain inhibited lateral assembly. The central role of the head-to-tail H-bond motif in the self-assembly process was further demonstrated whereby mixtures of IKVAV and RGD functionalized β^3 -peptides were shown to self-assemble to give heterogeneous fiber scaffolding.

To determine whether the IKVAV and RGD motifs were accessible and able to support cell adhesion, the ability of mouse primary cardiac fibroblasts and bone marrow-derived macrophages (BMDM) to adhere to the β^3 -tripeptide scaffolds composed of either homogeneous or mixtures of both cell-adhesion motifs was investigated. While there was no additive effect on the growth of cardiac fibroblasts with any of the scaffolds, fibroblasts grown on scaffolds comprised solely of peptide with an RGD side chain showed a significant decrease in cell viability, reflecting the over-stimulation of cells by excess RGD, an effect that was reversed by reducing the amount of RGD peptide in the mixture. In comparison, a different effect of the scaffolds was observed for the BMDMs. While the RGD-peptide did not affect cell viability, mixtures of RGD and IKVAV peptides significantly were shown to be biocompatible and resulted in

greater cell adherence compared to controls. This demonstrated the ability to tailor the scaffolds for particular cell types with an ability to present a variety of cell-specific ligands attached to β^3 -peptide monomers to support and modulate bioactivity of cells (Luder et al., 2016).

β^3 -Peptide Amphiphiles

Peptide amphiphile is a term used to describe a molecule that comprises a hydrophobic lipid chain coupled to a hydrophilic oligopeptide sequence (Cui et al., 2010; Matson and Stupp, 2012; Dehsorkhi et al., 2014; Webber et al., 2016). Peptide amphiphiles self-assemble into a range of nanostructures including nanofibers (Hartgerink et al., 2002; Niece et al., 2003), nanotubes (Cui et al., 2010), twisted and helical ribbons (Pashuck and Stupp, 2010), micelles (Trent et al., 2011) and nanotapes (Miravet et al., 2013). The most widely studied class of peptide amphiphiles consists of one alkyl tail that is attached to the N-terminus which can self-assemble in water and through the influence of pH (Dehsorkhi et al., 2013), light (Muraoka et al., 2009), temperature (Hamley et al., 2013), proteolysis (Webber et al., 2011) and ionic strength (Dehsorkhi et al., 2014), with chemical diversity that is well tolerated within the new nanostructure (Paramonov et al., 2006; Cui et al., 2010; Stupp, 2010; Stupp et al., 2013; Korevaar et al., 2014).

Given that self-assembly of β^3 -peptides is unperturbed by the steric bulk of the side chain while the presence of a

hydrophobic sequence further inhibits the lateral assembly resulting in uniform fiber morphology, β^3 -peptide amphiphiles in which a lipid chain moiety is incorporated into a β^3 -peptide template have been synthesized and shown to undergo self-assembly. The first study reporting a β^3 -peptide-based amphiphile described the synthesis of a β^3 -amino acid containing two acyl chains which, when mixed with 1-palmitoyl-2-oleoyl-sn-glycero-3-phosphocholine, self-assembled to give lipid-like vesicles (Capone et al., 2008). More recently, an N-acetylated β^3 -peptide containing a lipid chain was synthesized, which self-assembled to form a hydrogel which was both a mechanically stable and biocompatible hydrogel (Motamed et al., 2016), illustrated in **Figure 8B–d1**. The tri- β^3 -peptide Ac- β^3 -[AzKA] was synthesized containing a β^3 -homolysine (β^3 -K) residue to enhance peptide solubility in aqueous buffer. The C14 alkyl chain was then introduced on solid support by reducing the azide moiety on β^3 -Az using triphenylphosphine followed by acylation with myristic acid to form the final peptide structure. This C14 acylated tri- β^3 -peptide resulted in the formation of fibers with uniform diameter and self-assembled into a fibrous mesh retaining water (**Figure 8B–d2**). The resulting hydrogel was shown to be non-toxic, exhibited a stiffness compatible with brain tissue, and supported the adherence and proliferation of dopaminergic neurons. Given that the alkyl chain was important for facile hydrogel formation, the design of the β^3 -peptide amphiphile was further extended by synthesizing a functional β^3 -peptide amphiphile by incorporating a C14 acyl chain and the cell adhesion motif RGD (Kulkarni et al., 2016). This was achieved by first synthesizing a new β^3 -amino acid with an allyloxycarbamate (alloc-) protected aminoethyl amide side chain to allow for the orthogonal attachment of functionalities to the β^3 -tripeptide amphiphile using solid-phase peptide synthesis (Kulkarni et al., 2016). The peptide acylated tri- β^3 -peptide when co-dissolved with C14 and formed a stable hydrogel at a concentration of 10 mg mL⁻¹. The dual-functionalized β^3 -tripeptide showed enhanced L929 cell (mouse fibroblastic cell line) adhesion by increasing the RGD concentration from 2 to 8% (Kulkarni et al., 2016) (**Figure 8B–d2**). These materials were proteolytically stable, were shear thinning and supported the growth of fibroblasts, thereby further demonstrating the potential of β^3 -peptide-based materials in tissue regeneration.

Fluoro- β^3 -Peptides for *in vivo* Imaging

The spontaneous self-assembly of N-acetylated β^3 -peptides irrespective of sequence and side chain structure, combined with the ability to introduce desirable properties by appending the β^3 -peptide monomers with functional payloads, opens the possibility to produce materials with different chemical and optical properties. As a result, the ability to introduce a fluorescent moiety in β^3 -peptide-based hydrogels for *in vivo* imaging applications has been recently demonstrated (Kulkarni et al., 2018). The incorporation of fluorescent peptide monomers within the fiber gel is necessary to maintain hydrogel fluorescence and to monitor the fate of the material *in vivo*. To generate a fluorescent β^3 -tripeptide amphiphile, Quasar[®] 670, a far-red emitting dye with excitation at

644 nm and emission at 670 nm, was attached to a lipidated β^3 -tripeptide. Super-resolution imaging through stimulated emission depletion (STED) microscopy confirmed that the fluorescent monomer successfully co-assembled with a C14 lipidated β^3 -tripeptide, with the fiber matrix showing even distribution of the fluorophore. Interestingly, the fluorescent β^3 -peptide did not co-assemble successfully within a matrix containing β^3 -peptide, confirming the important role of the lipid side chain in directing hydrogel formation. Rheological measurements showed the incorporation of the fluorescent peptide had no effect on hydrogel stiffness and was comparable to that of ECM found subcutaneously (**Figure 8B–e**). Following administration of the fluorescent hydrogels to mice via subcutaneous injection, visualization of the gel implants using real-time *in vivo* animal imaging showed no degradation 14 days post-implantation. Overall, these results demonstrate that β^3 -tripeptide fluorescent hydrogels which can be easily detected *in vivo* and functionalized with different bioactive epitopes may provide a template for the design of stable implantable materials for *in vivo* biomedical applications.

CONCLUSIONS AND OUTLOOK

The supramolecular self-assembly of β^3 -peptide foldamers is now generating a new class of nanomaterials by exploiting the persistent formation of the β^3 -peptide 14-helical template to achieve a new level of molecular engineering. Depending on the application, peptide-based self-assembled systems exhibit several advantages over other organic and inorganic self-assembled systems in terms of biocompatibility, low toxicity and potential for functionalization. More recently, the self-assembly of β^3 -peptides has led to novel nanomaterials that have significantly expanded the potential applications of β^3 -peptide foldamers (Gopalan et al., 2015; Del Borgo et al., 2017). We recently reported a novel mode of self-assembly of N-acetylated β^3 -peptides which leads to the formation of a wide range of nanomaterials (**Figure 8**). In particular, these β^3 -peptides comprised of different acyclic amino acid sequences, self-assemble into fibers of different dimensions in aqueous or organic solvents. Moreover, X-ray crystal and fiber diffraction studies have further confirmed the formation of a 14-helical structure which allows the formation of a unique 3-point H-bonding motif where the N-acetyl group contributes to the 3-point H-bonding interactions.

Significantly, the head-to-tail H-bonding motif dominates the self-assembly irrespective of the order and number of residues within the β^3 -peptide sequence, to the extent that the sequence can be disrupted through the introduction of rigid or flexible linkers or new functionalities that can be introduced on different sections of the tri- β^3 peptide while not impeding the self-assembly. This sequence independent “head-to-tail” self-assembly model, in combination with the unique 14-helical structure of the β^3 -peptides monomer, readily permits the decoration of the monomer with specific biorecognition motifs without impacting on their ability to form fibers. A consequence of this shape-persistent self-assembly motif is the ability to exploit this template to modulate morphology through

lateral side-chain interactions. This offers the opportunity for the introduction of a wide variety of functions by modifying the side chains of the β^3 -amino acids, without perturbation of the self-assembly motif. Our understanding of the intricacies observed in the different β^3 -peptide self-assembled morphologies, in terms of molecular interactions, highlights the crucial interplay between various non-covalent interactions, the sensitivity of inter-fibril interactions to the solvent environment and the effect of the hydrophobic and steric topography of the β^3 -peptide 14-helix on lateral self-assembly. This has led to the control over the morphology through lateral interactions, allowing for the first time the creation of 2D and 3D functional β^3 -peptide

materials. The inherent flexibility in this unique design, as well as the ability to functionalize and tailor it for different applications, provides a new strategy for the development of novel bio- and nanomaterials via N-acetyl β^3 -peptide supramolecular self-assembly.

AUTHOR CONTRIBUTIONS

KK, NH, MD, and M-IA contributed conception and design of the study. KK and NH wrote the first draft of the manuscript. All authors contributed to manuscript revision, read, and approved the submitted version.

REFERENCES

- Aguilar, M. I., Purcell, A. W., Devi, R., Lew, R., Rossjohn, J., Smith, A. I., et al. (2007). Beta-amino acid-containing hybrid peptides—new opportunities in peptidomimetics. *Org. Biomol. Chem.* 5, 2884–2890. doi: 10.1039/b708507a
- Appella, D. H., Christianson, L. A., Klein, D. A., Powell, D. R., Huang, X., Barchi Jr, J. J., et al. (1997). Residue-based control of helix shape in β -peptide oligomers. *Nature* 387, 381–384. doi: 10.1038/387381a0
- Appella, D. H., Christianson, L. A., Klein, D. A., Richards, M. R., Powell, D. R., and Gellman, S. H. (1999). Synthesis and structural characterization of helix-forming β -peptides: Trans-2-aminocyclopentanecarboxylic acid oligomers. *J. Am. Chem. Soc.* 121, 7574–7581. doi: 10.1021/ja991185g
- Cabrele, C., Martinek, T. A., Reiser, O., and Berlicki, L. (2014). Peptides containing beta-amino acid patterns: challenges and successes in medicinal chemistry. *J. Med. Chem.* 57, 9718–9739. doi: 10.1021/jm5010896
- Capone, S., Walde, P., Seebach, D., Ishikawa, T., and Caputo, R. (2008). pH-sensitive vesicles containing a lipidic beta-amino acid with two hydrophobic chains. *Chem. Biodivers.* 5, 16–30. doi: 10.1002/cbdv.200890006
- Checchio, J. W., and Gellman, S. H. (2016). Targeting recognition surfaces on natural proteins with peptidic foldamers. *Curr. Opin. Struct. Biol.* 39, 96–105. doi: 10.1016/j.sbi.2016.06.014
- Checchio, J. W., Kreitler, D. F., Thomas, N. C., Belair, D. G., Rettko, N. J., Murphy, W. L., et al. (2015a). Targeting diverse protein-protein interaction interfaces with alpha/beta-peptides derived from the Z-domain scaffold. *Proc. Natl. Acad. Sci. U.S.A.* 112, 4552–4557. doi: 10.1073/pnas.1420380112
- Checchio, J. W., Lee, E. F., Evangelista, M., Sleebs, N. J., Rogers, K., Pettikiriachchi, A., et al. (2015b). alpha/beta-Peptide Foldamers targeting intracellular protein-protein interactions with activity in living cells. *J. Am. Chem. Soc.* 137, 11365–11375. doi: 10.1021/jacs.5b05896
- Cheng, R. P., Gellman, S. H., and Degrad, W. F. (2001). β -peptides: from structure to function. *Chem. Rev.* 101, 3219–3232. doi: 10.1021/cr000045i
- Christofferson, A. J., Al-Garawi, Z. S., Todorova, N., Turner, J., Del Borgo, M. P., Serpell, L. C., et al. (2018). Identifying the coiled-coil triple helix structure of beta-peptide nanofibers at atomic resolution. *ACS Nano* 12, 9101–9109. doi: 10.1021/acsnano.8b03131
- Clerici, F., Erba, E., Gelmi, M. L., and Pellegrino, S. (2016). Non-standard amino acids and peptides: from self-assembly to nanomaterials. *Tetrahedron Lett.* 57, 5540–5550. doi: 10.1016/j.tetlet.2016.11.022
- Craig, C. J., Goodman, J. L., and Schepartz, A. (2011). Enhancing beta3-peptide bundle stability by design. *ChemBiochem* 12, 1035–1038. doi: 10.1002/cbic.201000753
- Cui, H., Webber, M. J., and Stupp, S. I. (2010). Self-assembly of peptide amphiphiles: from molecules to nanostructures to biomaterials. *Biopolymers* 94, 1–18. doi: 10.1002/bip.21328
- Daniels, D. S., Petersson, E. J., Qiu, J. X., and Schepartz, A. (2007). High-resolution structure of a beta-peptide bundle. *J. Am. Chem. Soc.* 129, 1532–1533. doi: 10.1021/ja068678n
- Dehsorkhi, A., Castelletto, V., and Hamley, I. W. (2014). Self-assembling amphiphilic peptides. *J. Pept. Sci.* 20, 453–467. doi: 10.1002/psc.2633
- Dehsorkhi, A., Castelletto, V., Hamley, I. W., Adamcik, J., and Mezzenga, R. (2013). The effect of pH on the self-assembly of a collagen derived peptide amphiphile. *Soft Matter* 9, 6033–6036. doi: 10.1039/c3sm51029h
- Del Borgo, M. P., Kulkarni, K., and Aguilar, M. I. (2017). Using andbeta-Amino Acids and andbeta-Peptide templates to create bioactive ligands and biomaterials. *Curr. Pharm. Des.* 23, 3772–3785. doi: 10.2174/1381612823666170616083031
- Del Borgo, M. P., Kulkarni, K., Tonta, M. A., Ratcliffe, J. L., Seoudi, R., Mechler, A. I., et al. (2018). β^3 -tripeptides act as sticky ends to self-assemble into a bioscaffold. *APL Bioeng.* 2:026104. doi: 10.1063/1.5020105
- Del Borgo, M. P., Mechler, A. I., Traore, D., Forsyth, C., Wilce, J. A., Wilce, M. C., et al. (2013). Supramolecular self-assembly of N-acetyl-capped beta-peptides leads to nano- to macroscale fiber formation. *Angew. Chem. Int. Ed Engl.* 52, 8266–8270. doi: 10.1002/anie.201303175
- Fülöp, F., Martinek, T. A., and Toth, G. K. (2006). Application of alicyclic beta-amino acids in peptide chemistry. *Chem. Soc. Rev.* 35, 323–334. doi: 10.1039/b501173f
- Giuliano, M. W., Horne, W. S., and Gellman, S. H. (2009). An alpha/beta-peptide helix bundle with a pure beta3-amino acid core and a distinctive quaternary structure. *J. Am. Chem. Soc.* 131, 9860–9861. doi: 10.1021/ja8099294
- Goodman, J. L., Molski, M. A., Qiu, J., and Schepartz, A. (2008). Tetrameric beta(3)-peptide bundles. *ChemBiochem* 9, 1576–1578. doi: 10.1002/cbic.200800039
- Goodman, J. L., Petersson, E. J., Daniels, D. S., Qiu, J. X., and Schepartz, A. (2007). Biophysical and structural characterization of a robust octameric beta-peptide bundle. *J. Am. Chem. Soc.* 129, 14746–14751. doi: 10.1021/ja0754002
- Gopalan, R. D., Del Borgo, M. P., Mechler, A. I., Perlmutter, P., and Aguilar, M. I. (2015). Geometrically precise building blocks: the self-assembly of beta-peptides. *Chem. Biol.* 22, 1417–1423. doi: 10.1016/j.chembiol.2015.10.005
- Hamley, I. W., Dehsorkhi, A., Castelletto, V., Furzeland, S., Atkins, D., Seitsonen, J., et al. (2013). Reversible helical unwinding transition of a self-assembling peptide amphiphile. *Soft Matter* 9, 9290–9293. doi: 10.1039/c3sm51725j
- Hartergerink, J. D., Benias, E., and Stupp, S. I. (2002). Peptide-amphiphile nanofibers: a versatile scaffold for the preparation of self-assembling materials. *Proc. Natl. Acad. Sci. U.S.A.* 99, 5133–5138. doi: 10.1073/pnas.072699999
- Horne, W. S., Price, J. L., Keck, J. L., and Gellman, S. H. (2007). Helix bundle quaternary structure from α/β -peptide foldamers. *J. Am. Chem. Soc.* 129, 4178–4180. doi: 10.1021/ja070396f
- Kim, J., Kwon, S., Kim, S. H., Lee, C. K., Lee, J. H., Cho, S. J., et al. (2012). Microtubes with rectangular cross-section by self-assembly of a short beta-peptide foldamer. *J. Am. Chem. Soc.* 134, 20573–20576. doi: 10.1021/ja3088482
- Kiss, L., Mandity, I. M., and Fulop, F. (2017). Highly functionalized cyclic beta-amino acid moieties as promising scaffolds in peptide research and drug design. *Amino Acids* 49, 1441–1455. doi: 10.1007/s00726-017-2439-9
- Korevaar, P. A., Newcomb, C. J., Meijer, E. W., and Stupp, S. I. (2014). Pathway selection in peptide amphiphile assembly. *J. Am. Chem. Soc.* 136, 8540–8543. doi: 10.1021/ja503882s
- Kulkarni, K., Hung, J., Fulcher, A. J., Chan, A. H. P., Hong, A., Forsythe, J. S., et al. (2018). β^3 -Tripeptides coassemble into fluorescent hydrogels

- for serial monitoring *in vivo*. *ACS Biomater. Sci. Eng.* 11, 3843–3847. doi: 10.1021/acsbiomaterials.8b01065
- Kulkarni, K., Motamed, S., Habila, N., Perlmutter, P., Forsythe, J. S., Aguilar, M. I., et al. (2016). Orthogonal strategy for the synthesis of dual-functionalised beta(3)-peptide based hydrogels. *Chem. Commun.* 52, 5844–5847. doi: 10.1039/C6CC00624H
- Kwon, S., Jeon, A., Yoo, S. H., Chung, I. S., and Lee, H. S. (2010). Unprecedented molecular architectures by the controlled self-assembly of a beta-peptide foldamer. *Angew. Chem. Int. Ed. Engl.* 49, 8232–8236. doi: 10.1002/anie.201003302
- Kwon, S., Kim, B. J., Lim, H. K., Kang, K., Yoo, S. H., Gong, J., et al. (2015). Magnetotactic molecular architectures from self-assembly of β -peptide foldamers. *Nat. Commun.* 6:8747. doi: 10.1038/ncomms9747
- Kwon, S., Shin, H. S., Gong, J., Eom, J. H., Jeon, A., Yoo, S. H., et al. (2011). Self-assembled peptide architecture with a tooth shape: folding into shape. *J. Am. Chem. Soc.* 133, 17618–17621. doi: 10.1021/ja2082476
- Liu, S., Cheloha, R. W., Watanabe, T., Gardella, T. J., and Gellman, S. H. (2018). Receptor selectivity from minimal backbone modification of a polypeptide agonist. *Proc. Natl. Acad. Sci. U.S.A.* 115, 12383–12388. doi: 10.1073/pnas.1815294115
- Luder, K., Kulkarni, K., Lee, H. W., Widdop, R. E., Del Borgo, M. P., and Aguilar, M. I. (2016). Decorated self-assembling beta(3)-tripeptide foldamers form cell adhesive scaffolds. *Chem. Commun.* 52, 4549–4552. doi: 10.1039/C6CC00247A
- Mándity, I. M., and Fulop, F. (2015). An overview of peptide and peptoid foldamers in medicinal chemistry. *Expert Opin. Drug Discov.* 10, 1163–1177. doi: 10.1517/17460441.2015.1076790
- Mangelschots, J., Bibian, M., Gardiner, J., Waddington, L., Van Wansele, Y., Van Eeckhaut, A., et al. (2016). Mixed alpha/beta-Peptides as a class of short amphipathic peptide hydrogelators with enhanced proteolytic stability. *Biomacromolecules* 17, 437–445. doi: 10.1021/acs.biomac.5b01319
- Martinek, T. A., and Fulop, F. (2012). Peptidic foldamers: ramping up diversity. *Chem. Soc. Rev.* 41, 687–702. doi: 10.1039/C1CS15097A
- Martinek, T. A., Hetenyi, A., Fulop, L., Mandity, I. M., Toth, G. K., Dekany, I., et al. (2006). Secondary structure dependent self-assembly of beta-peptides into nanosized fibrils and membranes. *Angew. Chem. Int. Ed Engl.* 45, 2396–2400. doi: 10.1002/anie.200504158
- Matson, J. B., and Stupp, S. I. (2012). Self-assembling peptide scaffolds for regenerative medicine. *Chem. Commun.* 48, 26–33. doi: 10.1039/C1CC15551B
- Miravet, J. F., Escuder, B., Segarra-Maset, M. D., Tena-Solsona, M., Hamley, I. W., Dehsorkhi, A., et al. (2013). Self-assembly of a peptide amphiphile: transition from nanotape fibrils to micelles. *Soft Matter* 9, 3558–3564. doi: 10.1039/c3sm27899a
- Motamed, S., Del Borgo, M. P., Kulkarni, K., Habila, N., Zhou, K., Perlmutter, P., et al. (2016). A self-assembling beta-peptide hydrogel for neural tissue engineering. *Soft Matter* 12, 2243–2246. doi: 10.1039/C5SM02902C
- Muraoka, T., Koh, C. Y., Cui, H., and Stupp, S. I. (2009). Light-triggered bioactivity in three dimensions. *Angew. Chem.* 48, 5946–5949. doi: 10.1002/anie.200901524
- Nanda, J., and Banerjee, A. (2012). A gel-based trihybrid system containing nanofibers, nanosheets, and nanoparticles: modulation of the rheological property and catalysis. *Soft Matter* 8, 3380–3386. doi: 10.1039/c2sm07168a
- Niece, K. L., Hartgerink, J. D., Donners, J. J. J. M., and Stupp, S. I. (2003). Self-assembly combining two bioactive peptide-amphiphile molecules into nanofibers by electrostatic attraction. *J. Am. Chem. Soc.* 125, 7146–7147. doi: 10.1021/ja028215r
- Paramonov, S. E., Jun, H. W., and Hartgerink, J. D. (2006). Self-assembly of peptide-amphiphile nanofibers: the roles of hydrogen bonding and amphiphilic packing. *J. Am. Chem. Soc.* 128, 7291–7298. doi: 10.1021/ja060573x
- Pashuck, E. T., and Stupp, S. I. (2010). Direct observation of morphological transformation from twisted ribbons into helical ribbons. *J. Am. Chem. Soc.* 132, 8819–8821. doi: 10.1021/ja100613w
- Pomerantz, W. C., Yuwono, V. M., Drake, R., Hartgerink, J. D., Abbott, N. L., and Gellman, S. H. (2011). Lyotropic liquid crystals formed from ACHC-rich beta-peptides. *J. Am. Chem. Soc.* 133, 13604–13613. doi: 10.1021/ja204874h
- Pomerantz, W. C., Yuwono, V. M., Pizzey, C. L., Hartgerink, J. D., Abbott, N. L., and Gellman, S. H. (2008). Nanofibers and lyotropic liquid crystals from a class of self-assembling beta-peptides. *Angew. Chem. Int. Ed Engl.* 47, 1241–1244. doi: 10.1002/anie.200704372
- Raguse, T. L., Lai, J. R., Leplae, P. R., and Gellman, S. H. (2001). Toward β -peptide tertiary structure: self-association of an amphiphilic 14-helix in aqueous solution. *Org. Lett.* 3, 3963–3966. doi: 10.1021/ol016868r
- Raymond, D. M., and Nilsson, B. L. (2018). Multicomponent peptide assemblies. *Chem. Soc. Rev.* 47, 3659–3720. doi: 10.1039/C8CS00115D
- Rúa, F., Bousset, S., Parella, T., Diez-Perez, I., Branchadell, V., Giral, E., et al. (2007). Self-assembly of a cyclobutane beta-tetrapeptide to form nanosized structures. *Org. Lett.* 9, 3643–3645. doi: 10.1021/ol701521k
- Sagan, S., Milcent, T., Ponsinet, R., Convert, O., Tasseau, O., Chassaing, G., et al. (2003). Structural and biological effects of a beta2- or beta3-amino acid insertion in a peptide. *Eur. J. Biochem.* 270, 939–949. doi: 10.1046/j.1432-1033.2003.03456.x
- Seebach, D., Abele, S., Gademann, K., Guichard, G., Hintermann, T., Jaun, B., et al. (1998). β 2- And β 3-Peptides with proteinaceous side chains: synthesis and solution structures of constitutional isomers, a novel helical secondary structure and the influence of solvation and hydrophobic interactions on folding. *Helv. Chim. Acta* 81, 932–982. doi: 10.1002/hlca.19980810513
- Seebach, D., Beck, A. K., and Bierbaum, D. J. (2004). The world of β - And γ -Peptides comprised of homologated proteinogenic amino acids and other components. *Chem. Biodivers.* 1, 1111–1239. doi: 10.1002/cbdv.200490087
- Seebach, D., Gademann, K., Schreiber, J. V., Matthews, J. L., Hintermann, T., Jaun, B., et al. (1997). 'Mixed' β -Peptides: a unique helical secondary structure in solution. *Helv. Chim. Acta* 80, 2033–2038. doi: 10.1002/hlca.19970800703
- Seoudi, R. S., Del Borgo, M. P., Kulkarni, K., Perlmutter, P., Aguilar, M. I., and And Mechler, A. (2015a). Supramolecular self-assembly of 14-helical nanorods with tunable linear and dendritic hierarchical morphologies. *N. J. Chem.* 39, 3280–3289. doi: 10.1039/C4NJ01926A
- Seoudi, R. S., Dowd, A., Del Borgo, M. P., Kulkarni, K., Perlmutter, P., Aguilar, M. I., et al. (2015b). Amino acid sequence controls the self-assembled superstructure morphology of N-acetylated tri- β -peptides. *Pure Appl. Chem.* 87, 1021–1028. doi: 10.1515/pac-2015-0108
- Seoudi, R. S., Hinds, M. G., Wilson, D. J., Adda, C. G., Del Borgo, M., Aguilar, M. I., et al. (2016). Self-assembled nanomaterials based on beta (beta(3)) tetrapeptides. *Nanotechnology* 27:135606. doi: 10.1088/0957-4484/27/13/135606
- Steer, D. L., Lew, R. A., Perlmutter, P., Smith, A. I., and Aguilar, M. I. (2002). Beta-amino acids: versatile peptidomimetics. *Curr. Med. Chem.* 9, 811–822. doi: 10.2174/0929867024606759
- Stupp, S. I. (2010). Self-assembly and biomaterials. *Nano Lett.* 10, 4783–4786. doi: 10.1021/nl103567y
- Stupp, S. I., Zha, R. H., Palmer, L. C., Cui, H., and Bitton, R. (2013). Self-assembly of biomolecular soft matter. *Faraday Discuss.* 166, 9–30. doi: 10.1039/c3fd00120b
- Torres, E., Gorrea, E., Burusco, K. K., Da Silva, E., Nolis, P., Rua, F., et al. (2010). Folding and self-assembling with beta-oligomers based on (1R,2S)-2-aminocyclobutane-1-carboxylic acid. *Org. Biomol. Chem.* 8, 564–575. doi: 10.1039/B918755C
- Trent, A., Marullo, R., Lin, B., Black, M., and Tirrell, M. (2011). Structural properties of soluble peptide amphiphile micelles. *Soft Matter* 7, 9572–9582. doi: 10.1039/c1sm05862b
- Wang, P. S., Craig, C. J., and Schepartz, A. (2012). Relationship between side-chain branching and stoichiometry in beta(3)-peptide bundles. *Tetrahedron* 68, 4342–4345. doi: 10.1016/j.tet.2012.03.079
- Wang, P. S., Nguyen, J. B., and Schepartz, A. (2014). Design and high-resolution structure of a beta(3)-peptide bundle catalyst. *J. Am. Chem. Soc.* 136, 6810–6813. doi: 10.1021/ja5013849
- Wang, P. S., and Schepartz, A. (2016). beta-Peptide bundles: design. Build. Analyze. Biosynthesize. *Chem. Commun.* 52, 7420–7432. doi: 10.1039/C6CC01546H
- Webber, M. J., Appel, E. A., Meijer, E. W., and Langer, R. (2016). Supramolecular biomaterials. *Nat. Mater.* 15, 13–26. doi: 10.1038/nmat4474
- Webber, M. J., Newcomb, C. J., Bitton, R., and Stupp, S. I. (2011). Switching of self-assembly in a peptide nanostructure with a specific enzyme. *Soft Matter* 7, 9665–9672. doi: 10.1039/c1sm05610g
- Woolfson, D. N., and Mahmoud, Z. N. (2010). More than just bare scaffolds: towards multi-component and decorated fibrous

- biomaterials. *Chem. Soc. Rev.* 39, 3464–3479. doi: 10.1039/c0cs00032a
- Yang, Z., Liang, G., Ma, M., Gao, Y., and Xu, B. (2007). *In vitro* and *in vivo* enzymatic formation of supramolecular hydrogels based on self-assembled nanofibers of a beta-amino acid derivative. *Small* 3, 558–562. doi: 10.1002/smll.200700015
- Yang, Z., Liang, G., and Xu, B. (2006). Supramolecular hydrogels based on beta-amino acid derivatives. *Chem. Commun.* 738–740. doi: 10.1039/b516133a
- Yoo, S. H., and Lee, H. S. (2017). Foldectures: 3D molecular architectures from self-assembly of peptide foldamers. *Acc. Chem. Res.* 50, 832–841. doi: 10.1021/acs.accounts.6b00545

Conflict of Interest Statement: The authors declare that the research was conducted in the absence of any commercial or financial relationships that could be construed as a potential conflict of interest.

Copyright © 2019 Kulkarni, Habila, Del Borgo and Aguilar. This is an open-access article distributed under the terms of the Creative Commons Attribution License (CC BY). The use, distribution or reproduction in other forums is permitted, provided the original author(s) and the copyright owner(s) are credited and that the original publication in this journal is cited, in accordance with accepted academic practice. No use, distribution or reproduction is permitted which does not comply with these terms.



Enhancement of the Stability and Anti-DPPIV Activity of Hempseed Hydrolysates Through Self-Assembling Peptide-Based Hydrogels

OPEN ACCESS

Edited by:

Jutta Eichler,
Friedrich-Alexander-Universität
Erlangen-Nürnberg, Germany

Reviewed by:

Paripok Phitsuwon,
King Mongkut's University of
Technology Thonburi, Thailand
Giovanni Signore,
Scuola Normale Superiore di Pisa, Italy

*Correspondence:

Carmen Lammi
carmen.lammi@unimi.it
orcid.org/0000-0002-7428-4486

[†]Fabrizio Gelain
orcid.org/0000-0002-2624-5853
Anna Arnoldi
orcid.org/0000-0002-0987-3014
Raffaele Pugliese
orcid.org/0000-0001-7669-4457

[‡]These authors have contributed
equally to this work

Specialty section:

This article was submitted to
Chemical Biology,
a section of the journal
Frontiers in Chemistry

Received: 02 November 2018

Accepted: 24 December 2018

Published: 24 January 2019

Citation:

Lammi C, Bollati C, Gelain F, Arnoldi A
and Pugliese R (2019) Enhancement
of the Stability and Anti-DPPIV Activity
of Hempseed Hydrolysates Through
Self-Assembling Peptide-Based
Hydrogels. *Front. Chem.* 6:670.
doi: 10.3389/fchem.2018.00670

Carmen Lammi^{1*}, Carlotta Bollati¹, Fabrizio Gelain^{2,3†}, Anna Arnoldi^{1†} and
Raffaele Pugliese^{2,3‡}

¹ Department of Pharmaceutical Sciences, University of Milan, Milan, Italy, ² Tissue Engineering Unit, Institute for Stem Cell
Biology, Regenerative Medicine and Innovative Therapies-ISRMIT, Fondazione IRCSS Casa Sollievo della Sofferenza, San
Giovanni Rotondo, Italy, ³ Center for Nanomedicine and Tissue Engineering, ASST Grande Ospedale Metropolitano Niguarda,
Milan, Italy

Although there is an increasing interest for bioactive food protein hydrolysates as valuable ingredients for functional food and dietary supplement formulations, their potential applications are hampered by their insufficient stability in physiological conditions. In this study, an innovative strategy based on nanomaterials was developed in order to increase the hempseed hydrolysate stability and the anti-diabetic properties, through their encapsulation into ionic self-complementary RADA16 peptide based-hydrogels. Atomic force microscope (AFM) morphological analysis indicated that the new nanomaterials were composed of a nanofibril network, whose increased diameter in respect to native RADA16 suggests the presence of transient non-covalent interactions among the RADA16 supramolecular assemblies and the embedded hempseed peptides. Structural analysis by FT-IR spectroscopy indicated typical β -sheet signatures. The RADA16-hempseed protein hydrolysate hydrogel was shown to act as a novel dipeptidyl peptidase IV (DPPIV) inhibitor in different biological assays. Finally, this nanoformulation was used as a drug delivery system of the anti-diabetic drug sitagliptin, helping to reduce its dosage and eventually associated side-effects.

Keywords: bioactive peptides, DPPIV, nano-nutraceutical, rheology, self-assembling peptide

INTRODUCTION

Bioactive peptides are increasingly recognized as valuable ingredients for the formulation of functional foods and dietary supplements providing useful health benefits (Arnoldi et al., 2015). They are rarely present in foods as such, whereas in most cases they are encrypted in protein sequences and may be delivered by digestion, enzymatic hydrolysis, or fermentation (Nongonierma et al., 2017). Different biological activities are currently under investigation, in particular, the hypotensive (Girgih et al., 2014a), hypocholesterolemic (Arnoldi et al., 2015), and hypoglycemic ones (Lammi et al., 2016b).

Protein hydrolysates may be obtained either from animal or plant proteins: in this context, hempseed proteins may represent an innovative source of bioactive peptides, since this seed contains more than 25% protein that can be hydrolyzed in different conditions using either digestive or food grade enzymes (Aiello et al., 2016). Enzyme/substrate ratios, pH, time, and temperature influence in a significant way the peptides release with a direct effect on bioactivity (Aiello et al., 2017; Zanoni et al., 2017). Only a few research groups are actively pursuing the biological activity of hydrolyzed hempseed proteins with specific interests for the antioxidant (Girgih et al., 2011, 2013, 2014b), hypocholesterolemic (Zanoni et al., 2017), and hypotensive activities (Girgih et al., 2014a; Malomo et al., 2015), whereas other biological properties, such as the anti-diabetic one, have been rarely considered (Nongonierma and Fitzgerald, 2015a).

In this context, dipeptidyl peptidase IV (DPPIV)/CD26 is considered an interesting anti-diabetic target. This ectoenzyme (EC 3.4.14.5), ubiquitously expressed on the surface of various cell types, such as intestinal epithelial cells (Abbott et al., 1994), cleaves dipeptides from the N-terminus of polypeptides in which proline is at the penultimate position. A truncated soluble form of this enzyme, which possesses a similar activity, is also found in serum. Enhanced serum DPPIV levels and/or activity have been suggested to be correlated with many metabolic diseases, such as type 2 diabetes (T2DM), obesity, cardiovascular disease, and non-alcoholic fatty liver disease (NAFLD) (Röhrborn et al., 2015; Nargis and Chakrabarti, 2018). This is considered a promising therapeutic target for glycemic control, because it plays a key role in glucose metabolism by N-terminal truncation and inactivation of the incretins glucagon-like peptide (GLP)-1 and gastrointestinal insulinotropic peptide (GIP) that together are responsible for up to 70% of post-prandial insulin secretion (Nauck et al., 2004). Since these hormones are rapidly inactivated by DPPIV (Doupis and Veves, 2008), the inhibition of this enzyme promotes insulin secretion and reduces glucagon release.

Even though synthetic DPPIV inhibitors are currently available on the market, several food-derived peptides and hydrolysates have been identified and found to act as promising DPPIV inhibitors (Lammi et al., 2016b; Nongonierma et al., 2018). Having verified that this kind of information was not available for hempseed peptides, this study's first aim was to evaluate the DPPIV inhibitory activities exerted by hempseed protein hydrolysates obtained by treating hempseed proteins with trypsin (HT) or pepsin (HP). The activity was assessed by different complementary methods, in particular an *in vitro* commercial test based on the purified enzyme, an *in situ* assay on Caco-2 cells, and an *ex vivo* test on human serum samples.

Although there are experimental evidences that some food-derived peptides may be absorbed at least in part at intestinal level (Lammi et al., 2016a), their low stability and bioavailability still remain major concerns for practical applications. These issues, however, may be overcome by the use of well-designed and controlled delivery systems (Park, 2014; Lopalco and Denora, 2018). The development of an efficient, biocompatible, and bio-absorbable release system requires the use of materials capable of delivering the bioactive compounds in a controlled manner, such as self-assembling peptide-based hydrogels (SAPs).

SAPs are recognized as useful tools in a broad range of biomedical and biotechnological applications, ranging from carriers for drug (Koutsopoulos et al., 2009; Gelain et al., 2010) or pesticides delivery (Bolat et al., 2018), scaffolds for regenerative medicine (Pugliese and Gelain, 2017), to actuators for optics and fluidics (Tao et al., 2017). Usually, SAPs are short peptides (8–16 residues) containing alternate charged hydrophilic and hydrophobic amino acids that, upon exposure to physiological conditions of pH, temperature, or electrolytes, spontaneously self-organize into interwoven nanofibers with diameters of 10–20 nm (Pugliese and Gelain, 2017). Peptide hydrogels are easy to use, biodegradable, non-toxic, non-immunogenic, and non-thrombogenic. They are generally more biocompatible (Zhang, 2003) than polymeric materials, such as PLLA, PLGA, PCL, and their degradation products are easily metabolized into natural amino acids. Moreover, molecular design permits to tailor SAPs sequences for specific application needs.

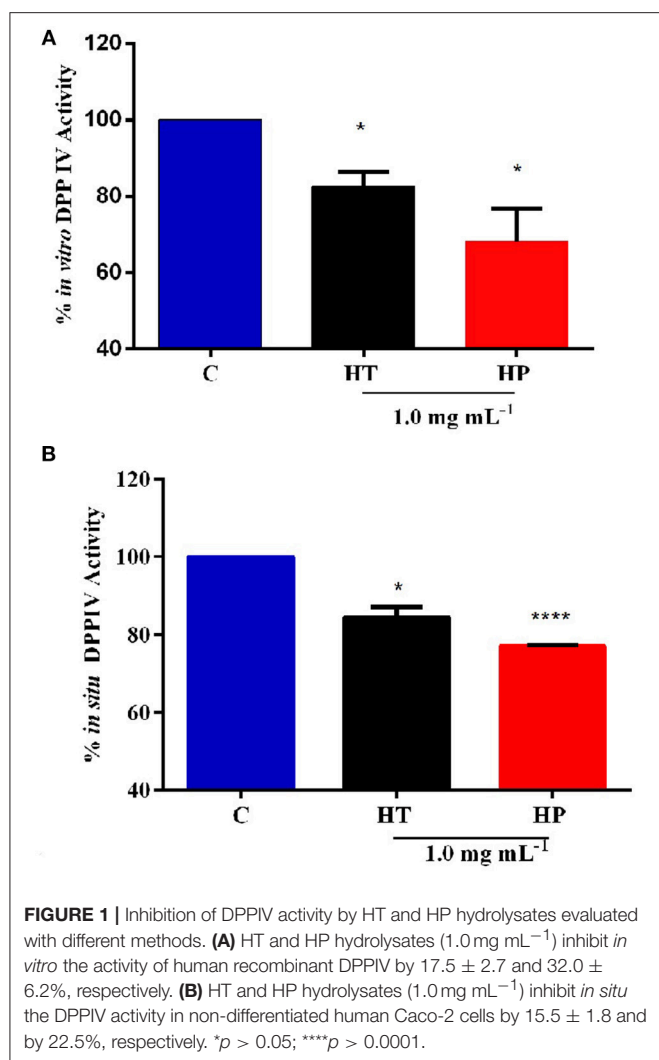
Taking all this information into account, the second objective of the study was to verify whether it was possible to enhance the stability of hempseed protein hydrolysates by combining them with the ionic self-complementary peptide RADA16 (i.e., Ac-RADARADARADARADA-CONH₂), a well-known and characterized SAP based-hydrogel (Zhang et al., 1993). This objective was achieved by performing different experiments in order to demonstrate the feasibility of this encapsulation procedure without disturbing the overall stability of the RADA16 cross- β secondary structures, to assess the morphology and biomechanics of the obtained nanofibers, and to evaluate the biological activity of these materials on DPPIV.

Finally, since previous literature has shown that interesting synergistic effects may be observed when milk peptides are combined with sitagliptin (Nongonierma and Fitzgerald, 2015b), one of the main DPPIV inhibitors successfully commercialized as oral drug for the treatment of T2DM, the third objective of the study was aimed at evaluating the possible synergistic activity of the RADA16-hemp hydrogels and sitagliptin.

RESULTS AND DISCUSSION

Evaluation of the Inhibitory Activity of HT and HP Hydrolysates on DPPIV

In order to assess the anti-diabetic properties of HT and HP hempseed protein hydrolysates, their ability to decrease *in vitro* the DPPIV activity was evaluated as a first biochemical approach. Preliminarily, HT and HP hydrolysates were tested *in vitro* at 0.5 and 1.0 mg mL⁻¹, respectively. Results suggest that HP is more active at 1.0 mg mL⁻¹, whereas HT shows comparable inhibitory activities at both concentrations (**Figure S1**). For this reason, it was decided to carry out all further experiments at 1.0 mg mL⁻¹ as the best concentration for both hydrolysates. **Figure 1A** clearly indicates that the HT and HP hydrolysates at 1.0 mg mL⁻¹ inhibit *in vitro* DPPIV activity by $17.5 \pm 2.7\%$ and $32.0 \pm 6.2\%$, respectively. The fact that the HP hydrolysate is 2-fold more active than the HT one highlights the importance of the specificity of the enzyme used to release the peptides from the parent proteins. The bioactivity of a single peptide is typically related to its size and amino acid sequence, whereas that of a



protein hydrolysate depends strictly on its total composition, including inactive and active species and possible synergistic or antagonistic effects (Aiello et al., 2017; Zanoni et al., 2017).

The inhibitory activity of these hydrolysates on DPP-IV is in agreement with those of other food protein hydrolysates (Lacroix and Li-Chan, 2012). For instance, simulated gastrointestinal digestion of the intact rice and hemp proteins yielded DPP-IV IC_{50} values between 1.85 ± 0.34 and $4.50 \pm 0.55 \text{ mg mL}^{-1}$, respectively (Nongonierma and Fitzgerald, 2015a). Moreover, a hydrolysate of Atlantic salmon skin gelatin generated using Flavorzyme® inhibits the DPP-IV activity by 45.0% at 5.0 mg mL^{-1} (Li-Chan et al., 2012), whereas a hydrolysate prepared by hydrolyzing Japanese rice bran using Umanizyme G® inhibits the DPP-IV activity with an IC_{50} value equal to 2.3 mg mL^{-1} (Hatanaka et al., 2012). It is important to underline that all these studies have been performed only using an *in vitro* tool in which porcine DPP-IV is involved. Although the sequence is highly conserved among mammalian species, human, and porcine DPP-IV enzymes have only an 88% sequence identity and there are evidences that porcine and human DPP-IV differ in their

susceptibility to inhibition by food-derived peptides (Lacroix and Li-Chan, 2015). Since the inhibition is stronger on the porcine DPP-IV enzyme than on the human one, the usage of the former to assess the inhibitory effect may lead to an overestimation of the potency or effectiveness on human DPP-IV (Lacroix and Li-Chan, 2015). This aspect clearly underlines the need to deeply investigate the DPP-IV inhibitory effects of food-derived peptides not only from a biochemical point of view but also at human cellular level (Lammi et al., 2018).

Further experiments were therefore performed using a cellular assay based on non-differentiated human intestinal Caco-2 cells, which has been recently developed and optimized by us as a useful tool for the screening and identification of new DPP-IV inhibitors (Lammi et al., 2018). These cells express several morphological and functional characteristics of enterocytes, possess a wide range of membrane peptidases naturally expressed by the apical side of enterocytes, DPP-IV included, and are useful to investigate the potential metabolism of tested compounds. Caco-2 cells were treated with 1.0 mg mL^{-1} of HT and HP hydrolysates for 24 h, then the AMC-Gly-Pro substrate ($50.0 \mu\text{M}$) was added, and the fluorescence signals were detected by a plate reader. **Figure 1B** shows that the HT hydrolysate inhibited the DPP-IV activity by $15.5 \pm 1.8\%$ and HP hydrolysate by $22.5 \pm 0.19\%$. These results confirm the *in vitro* tests although they also indicate that the incubation with the Caco-2 cells slightly impairs the inhibitory potencies of the hydrolysates, with a greater effect on the HP one. This may be possibly explained by metabolic effects.

A very critical issue in the practical application of food peptides regards the low stability especially in respect to the proteases present in the biological samples, in particular in serum. Therefore, *ex vivo* experiments were also performed spiking human serum samples with HT and HP hydrolysates at the concentration of 1.0 mg mL^{-1} and incubating at 37°C for 24 h. The next day, the AMC-Gly-Pro substrate ($50.0 \mu\text{M}$) was added and the fluorescence signals were measured. Small inhibitory activities were observed in both cases that were not significant (data not shown), whereas sitagliptin, used as a positive control, reduced the circulating enzyme activity by $68.5 \pm 5.3\%$ vs. the control sample. These results are indicative of an extensive degradation of the hydrolysates in this complex environment.

This whole body of information prompted us to develop a new strategy that might overcome the observed limitations and improve the DPP-IV inhibitory activity by incorporating them within the nanofibrous structures of RADA16 SAP-hydrogel.

Self-Assembly of RADA16-HT and RADA16-HP Hydrolysates Into Fibrillar Nanostructures

The ionic self-complementary RADA16 peptide is known to have a strong propensity to spontaneously self-assemble into ordered nanofibrous structures upon exposure to external stimuli (e.g., pH, temperature, monovalent, or divalent electrolyte ions). Typically, RADA16 fibrils are linear with a 10–20 nm diameter and a 2.5–5 nm length (Zhang et al., 1993). At the macroscale,

these nanofibers further organize to form highly hydrated hydrogels containing up to 99.5% (w/v) water, which can be easily and harmlessly used as drug delivery systems (Koutsopoulos et al., 2009; Gelain et al., 2010). To assess whether the hempseed hydrolysates modify the self-assembly propensity of RADA16, this material was dissolved in distilled water at the concentration of 10 mg mL^{-1} and mixed with the HT and HP hydrolysates (1.0 mg mL^{-1}) at a 3:1 (v/v) ratio. In order to further promote self-assembly, an isotonic saline solution (ionic strength 0.09%) was slowly added to the mixed peptide solutions, and the hydrogels were formed at room temperature. The 3:1 ratio between RADA16 and hempseed peptides was employed, since the increase of RADA16 concentration resulted in a higher density network of nanofibers that may possibly hinder the release of the hempseed peptides, and probably increase the interactions of RADA16 nanofiber-hemp diffusant yielding a decrease in apparent diffusivity (**Figure 2A**).

The freshly prepared RADA16-hemp hydrolysate solutions were viscous-liquid, clear, and homogeneous (**Figure 2B**); after the hydrogelation, the solutions took on a gel-like consistency and no noticeable aggregates were visualized (**Figure 2C**). Atomic force microscope (AFM) morphological analysis, carried out to monitor the effects of HT and HP peptides on the self-aggregated nanostructures of RADA16, showed a network of nanofibrils with $\sim 24 \text{ nm}$ diameter and up to 2 nm length (**Figure 2D**), similar to those previously reported (Yokoi et al., 2005). The slight increase of RADA16-hempseed peptides diameters from AFM imaging, compared to native RADA16, suggests the presence of transient non-covalent interactions (i.e., electrostatic forces, VDW, hydrogen bonds) among the RADA16 supramolecular assemblies and the embedded hempseed peptides (see **Table S1** in the ESM).

Overall, these AFM results confirmed the assembly propensity of RADA16-hempseed peptides into nanofibers, highlighting that HP and HT hydrolysates minimally perturb the RADA16 structures, and therefore they can be easily trapped inside the entangled nanofibrous domains of the RADA16 hydrogel, which allows less free motion of the hemp diffusants and facilitate their slow and sustained release.

Influence of HT and HP Hydrolysates on Assembled Secondary Structures

Structural analysis of assembled RADA16-hempseed hydrolysates was pursued by attenuated total reflection (ATR) Fourier transform infrared (FT-IR) spectroscopy. As expected, by analyzing the Amide I region ($1,600\text{--}1,700 \text{ cm}^{-1}$), which is mainly associated with C=O stretching vibration and related to the SAP-backbone conformation, native RADA16 showed β -sheet features characterized by the presence of the two components at $1,630$ and $1,695 \text{ cm}^{-1}$ (**Figure 3A**). FT-IR spectra of the RADA16-HP hydrolysate and RADA16-HT hydrolysate closely resembled that of the RADA16 in the native state, displaying typical β -sheet signatures. Moreover, in the Amide II region ($1,480\text{--}1,575 \text{ cm}^{-1}$), β -sheet aggregation for all tested RADA16-hempseed hydrolysates was confirmed by the presence of peaks at $1,530 \text{ cm}^{-1}$ (directly related to CN stretching and NH bending). Altogether, FT-IR analysis confirmed self-aggregation of tested RADA16-hempseed hydrolysates into β -sheets,

suggesting that the introduction of hempseed hydrolysates did not affect the macromolecular organization of the RADA16 hydrogel.

Furthermore, to get more information on the RADA16-hempseed hydrolysates capacity of forming cross- β fibril structure, thioflavin T (ThT) spectroscopy assay was carried out. It is widely accepted that β -rich structures feature ThT-binding sites, and that these interactions may give insights on cross- β structures and fibril formation (Biancalana and Koide, 2010). ThT has a weak fluorescence in aqueous environment, with excitation and emission bands centered at ~ 350 and 440 nm , respectively. Upon binding to β -rich fibrils, bathochromic shifts of both excitation and emission at 440 and 490 nm , respectively, are observed. The emission intensity at $\sim 490 \text{ nm}$ is assumed to be directly proportional to the quantity of cross- β fibrils present in the sample. When the probe ThT was applied to RADA16, a characteristic fluorescence emission at $\sim 490 \text{ nm}$ confirmed that the peptide had adopted a cross- β -sheet conformation (**Figure 3B**). Instead, an increase of ThT fluorescence intensity was found when RADA16 was mixed with either HT or HP peptides (**Figure 3B**). This suggested that hempseed peptides might increase the overall presence of cross- β structures in self-assembled RADA16 hydrogels, probably due to transient electrostatic repulsions that can be formed between hempseed peptides and RADA16 molecules during self-assembly and nanofiber formation. This shows that electrostatic interactions could play a pivotal role in the stability of fibrillar systems as carriers for drug delivery. A reasonable explanation concerning this behavior has been proposed by Zhang et al. (1993) using RADA16 hydrogel as a platform to release lysozyme, trypsin inhibitor, BSA, and IgG (Koutsopoulos et al., 2009). They speculated that SAPs charge may be an important factor affecting not only the fibers stability, but also the interactions and release kinetics when the release occurs through peptide hydrogels consisting of nanofibers that carry a net (positive or negative) charge.

Biomechanical Properties of RADA16-HT and RADA16-HP Hydrogels

In addition to morphological and structural properties, the biomechanics of the nanostructures play a significant role in translation for applications (e.g., nano-carriers, nano-devices, actuators for optics, and fluidics etc.) (Pugliese et al., 2018a,b). In the case of hydrogels, the most relevant biomechanical features to be characterized are the storage (G') and loss (G'') moduli. The former reflects the stiffness trend of the biomaterial, while the latter represents the energy dissipated during the test and correlates with the liquid-like response of the hydrogel. The ratio between G' and G'' provides insights of the viscoelastic profile of tested material, i.e., whether it behaves as a viscous liquid ($G' < G''$) or as an elastic solid ($G' > G''$). Accordingly, it was crucial to assess the elastic and viscous response of materials, by varying frequencies of applied oscillatory stress (see section Methods for further details), in order to investigate how the HT and HP hydrolysates could influence the mechanical strength of the RADA16 hydrogel. Upon comparing the rheological properties of native RADA16, and RADA16-HT or RADA16-HP hydrolysates

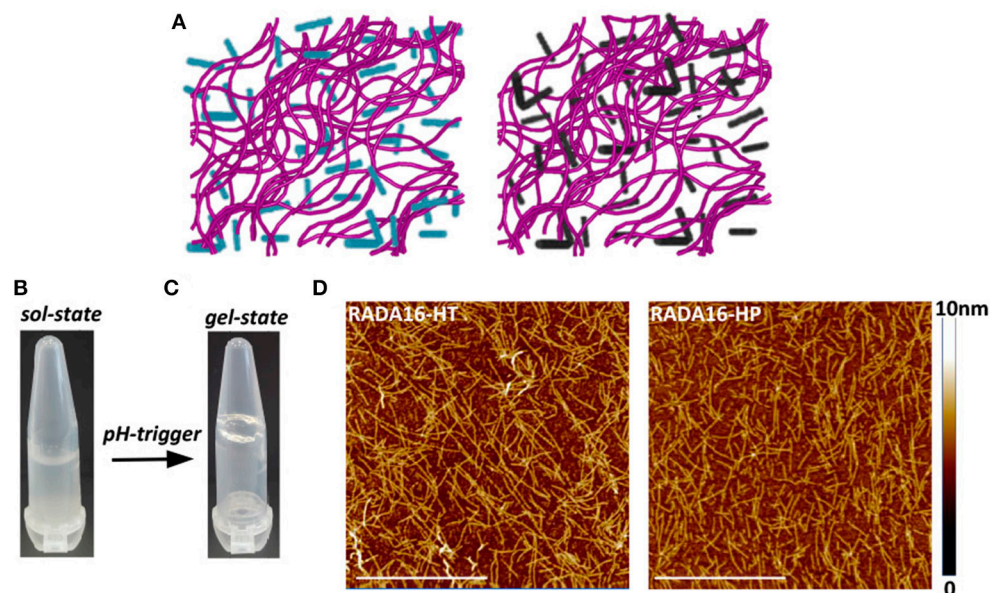


FIGURE 2 | Self-assembly of RADA16-hempseed hydrolysates. **(A)** Cartoon models of RADA16-HT (left) and RADA16-HP (right) peptide based-hydrogels. RADA16 network of nanofibers is shown in purple, while HT and HP are in cyan and dark gray, respectively. **(B)** Photographs of freshly prepared RADA16-hempseed solution and **(C)** after hydrogelation (in 0.09% saline). **(D)** AFM morphological analysis of RADA16-HT and RADA16-HP hydrogels. Images show a network of nanofibrils with ~24 nm diameter and up to 2 nm length (Scale bar, 1 μ m).

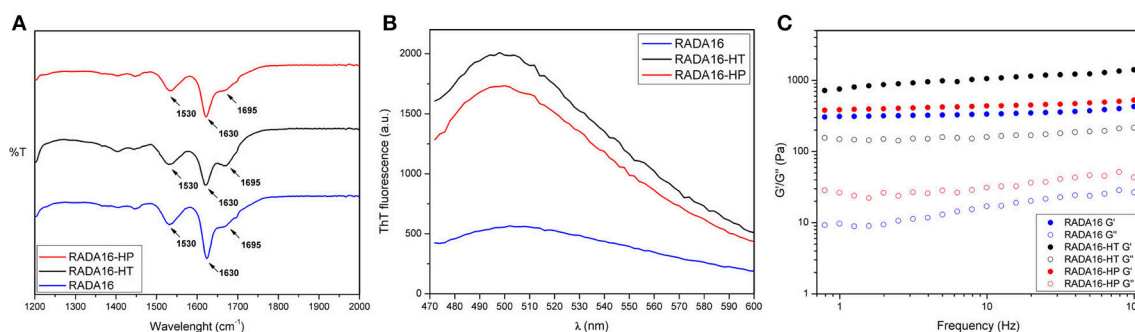


FIGURE 3 | Structural and biomechanical properties of RADA16-HT and RADA16-HP hydrogels. **(A)** ATR-FTIR spectra of RADA16-HT (dark) and RADA16-HP (red) hydrogels closely resemble that of pure RADA16 (blue), displaying typical β -sheet signature in Amide I (1,600–1,700 cm^{-1}) and Amide II (1,480–1,575 cm^{-1}) regions. **(B)** ThT emission spectra. Pure RADA16 (blue) showed an affinity for ThT ascribable to the presence of cross- β fibril structures, while RADA16-HT (dark) and RADA16-HP (red) produced an increase of ThT fluorescence intensity due to transient electrostatic interactions between the peptides and RADA16 molecules during self-assembly and nanofiber formation. **(C)** Rheological characterization. Assembled hydrogels were monitored by frequency sweep tests (0.1–100 Hz). All tested materials showed typical hydrogel-like profiles featuring a predominant elastic solid-like behavior (G'), as compared with the viscous component (G''). RADA16-HT and RADA16-HP showed a slight increase in the G' values (~750 and ~450 Pa, respectively) along the tested frequency range compared to pure RADA16 (~353 Pa), but they still showed strength profiles typical of soft peptide scaffolds.

(Figure 3C), trends of G' and G'' for all species showed typical hydrogel-like profiles, featuring a predominant elastic solid-like behavior (G'), as compared with the viscous component (G''). The G' and G'' values remained relatively constant throughout the test; hence all scaffolds were very resistant to deformation. Nevertheless, RADA16-HP hydrolysates and RADA16-HT hydrolysates showed a slight increase in the elastic shear modulus G' values (~450 and ~750 Pa, respectively) along the tested frequency range (0.1–100 Hz) at low strains

(1%) compared to the native RADA16 (~353 Pa), although they still were showing strength profiles typical of soft peptide scaffolds. This slight increase in the mechanical properties may be attributed to electrostatic interactions taking place between hempseed peptides and RADA16 molecules during self-assembly phenomena that increase the overall presence of β -structures (as investigated in the previous section). Indeed, it is widely accepted that in β -sheet-rich SAPs after self-assembly, interactions among self-assembled fibers lead to increase of G' values.

Overall, rheological assays showed that the RADA16 hydrogel mixed with the hempseed hydrolysates had stable mechanical features. Also, encapsulation of the hempseed hydrolysates did not alter the RADA16 self-assembling propensity, displaying instead a slight improvement in elastic shear modulus G' . Therefore, on the whole, these results provided insight on the feasibility of hempseed peptides encapsulation that may turn in their smart delivery and sustained release from the nanoformulation, which is an open challenging issue of nanotechnology in the food and agriculture sectors.

Enhanced DPPIV Inhibitory Activity and Stability of RADA16-HT and RADA16-HP Hydrogels

In order to verify the stability and activity of HT hydrolysates and HP hydrolysates embedded in the RADA16 hydrogel, their DPPIV inhibitory activities were performed by *in situ* and *ex vivo* experiments. Before performing the *in situ* experiments, MTT experiments were performed in order to exclude any potential cytotoxic effect mediated by the new hydrogels on non-differentiated Caco-2 cells. These experiments demonstrated that they are safe at 1.0 mg mL^{-1} , i.e., the concentration used for all biological experiments (Figure S2). After having assessed this important information, Caco-2 cells were seeded on the RADA16-HT and HP hydrogels (1.0 mg mL^{-1}) and after 24 h their effects on the DPPIV activity were measured using AMC-Gly-Pro as a substrate ($50 \mu\text{M}$). Figure 4A shows that RADA16-HT and RADA16-HP hydrogels reduced the DPPIV activity by 38.3 ± 5.6 and $42.2 \pm 3.0\%$ vs. the RADA16 hydrogel, respectively. These findings indicate that the activities of the HT and HP hydrolysates are enhanced by 2.5- and 2.0-folds, respectively, when they are embedded in the hydrogel in respect to their plain solutions. This seems to indicate that the structuring of the HT and HP hydrolysates within the RADA16 hydrogel provides higher resistance toward the proteases that are expressed by Caco-2 cells. The RADA16-HT and RADA16-HP hydrogels represent dynamic systems in which some peptides actively contribute to the biomechanical, morphological, and structural properties of the nanoformulations, since transient electrostatic repulsions, between the hempseed peptides and the RADA16 molecules during self-assembly and nanofiber formation, can occur. These electrostatic interactions contribute to the stabilization of the fibrillar systems making them good carriers for bioactive compounds delivery. The experimental findings suggest that hempseed peptides, trapped inside the entangled nanofibrous domains of the hydrogels, are slowly released allowing their interaction with the DPPIV catalytic site. In fact, results pointed out that both HT and HP are released from the hydrogels as a function of time with a linear trend. In particular, using an experimental method proposed by Goa (1953) and already used by us (Lammi et al., 2014, 2016a), the released peptide concentrations were measured after 1, 3, and 6 h of incubation. Figure 4B shows that released HT peptide concentrations were 0.36 ± 0.06 , 0.52 ± 0.15 , and $0.92 \pm 0.06 \mu\text{g mL}^{-1}$, whereas released HP concentrations were 0.23 ± 0.03 , 0.41 ± 0.09 , $0.79 \pm 0.08 \mu\text{g mL}^{-1}$ after 1, 3, and 6 h, respectively. Overall, HT peptides were more delivered

than HP peptides; this difference may be due to the different physical-chemical properties of each hempseed hydrolysate. As reported in Table S1 (see Supplementary Material), the HT hydrolysate shows a hydrophilicity of 63%, whereas HP peptides one of 57%. Being more hydrophobic, HP peptides are more retained within the shell of the hydrogel, whereas the more hydrophilic HT peptides are more released. Moreover, the HP hydrolysate contains longer peptides (>15 a.a. residues) than the HT hydrolysate. This explains why the HT peptides may more easily escape from the entangled nanofibrous domains of the hydrogels than HP peptides (Table S1). This slow release enhanced either the activity or the stability of both HT and HP hydrolysates.

This hypothesis was also confirmed by *ex vivo* experiments performed on human serum samples. More in detail, serum samples were incubated with either RADA16-HT or RADA16-HP hydrogels for 24 h at 37°C . Afterwards, the AMC-Gly-Pro substrate ($50.0 \mu\text{M}$) was added, and the fluorescence signals detected using a plate reader. Figure 4C indicates that both hydrogels are able to decrease the circulating DPPIV activity by 37.2 ± 2.3 and $36.2 \pm 2.6\%$, respectively, vs. native RADA16. These results underline the enhanced stability that hempseed peptides acquire when they are embedded in the nanoformulations: in fact, both native hydrolysates were unable to inhibit the activity of circulating DPPIV in the *ex vivo* system probably due to their scarce capacity of resisting to the serum proteases activity.

Synergistic Effect of RADA16-Hempseed Hydrolysates With Sitagliptin as DPPIV Inhibitors

The last part of the experimentation was dedicated to investigating the possible synergist effects of combining sitagliptin with the RADA16-hempseed hydrogels (Figures 5A–F) for DPPIV inhibition. RADA16 hydrogels containing sitagliptin (at the final concentration of $0.1 \mu\text{M}$) and RADA16 hempseed hydrogels containing sitagliptin (at the final concentration of $0.1 \mu\text{M}$) were prepared and Caco-2 cells were seeded on the hydrogel. After 24 h, the spent medium was removed, cells were washed, the Gly-Pro-AMC substrate was added, and the fluorescence signals were monitored for 10 min. The results (Figures 5A,B) clearly indicate that at all reaction times, the DPPIV activity was the highest in the control samples treated with RADA16-hydrogel, slightly lower in cells incubated with RADA16 hydrogel containing $0.1 \mu\text{M}$ sitagliptin, and further reduced in cells incubated with RADA16-HT and RADA16-HP hydrogels with or without sitagliptin $0.1 \mu\text{M}$. However, findings clearly suggest that only RADA16-HT containing $0.1 \mu\text{M}$ sitagliptin shows a synergistic inhibitory effect of DPPIV, which started 3 min after the addition of the Gly-Pro-AMC substrate and remained constant for up to 10 min of incubation (Figure 5B). The reaction rate followed a linear trend and 5 min of incubation with Gly-Pro-AMC corresponded to one half of the linear tract. Figure 5B shows the results at 5 min. RADA16 hydrogel containing $0.1 \mu\text{M}$ sitagliptin reduced the DPPIV activity by $13.2 \pm 8.3\%$ vs. RADA16 alone, whereas the inhibition of the enzyme activity reached 38.3 ± 5.6 and

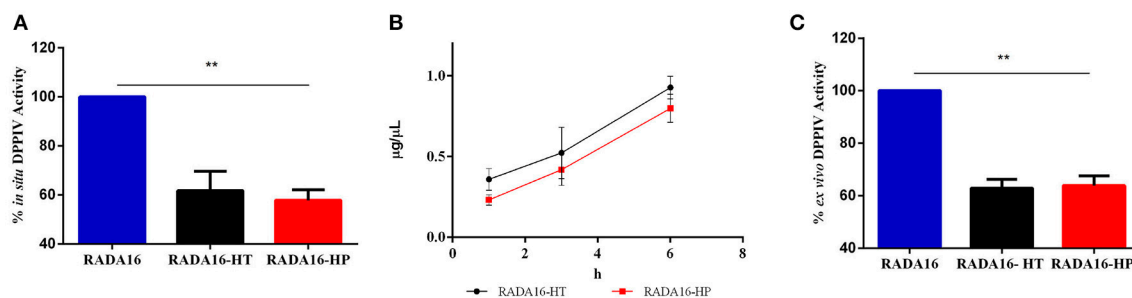


FIGURE 4 | DPPIV inhibitory activity, stability, and release of RADA16-HT and RADA16-HP hydrogels. **(A)** RADA16-HT and RADA16-HP hydrogels (1.0 mg mL^{-1}) reduce *in situ* the DPPIV activity in non-differentiated human Caco-2 cells by 38.3 ± 5.6 and $42.2 \pm 3.0\%$, respectively, vs. the RADA16 hydrogel. **(B)** Release of HT and HP peptides from the RADA16 hydrogel as a function of the time. **(C)** RADA16-HT and RADA16-HP hydrogels decrease the circulating DPPIV activity *ex vivo* on human serum samples by 37.2 ± 2.3 and $36.2 \pm 2.6\%$, respectively, vs. plain RADA16. $**p > 0.01$.

$42.2 \pm 3.0\%$, respectively, incubating with control RADA16-HT and RADA16-HP hydrogels, and 56.4 ± 0.8 and $40.0 \pm 9.1\%$, respectively, incubating with RADA16-HT and RADA16-HP hydrogels containing $0.1 \mu\text{M}$ sitagliptin.

From a nanostructural point of view, the addition of sitagliptin did not affect the physicochemical properties of the RADA16-HT and RADA16-HP hydrogels. The ATR-FTIR structural analysis highlighted typical β -sheet signatures in the Amide I and Amide II regions (**Figure 5C**) and the ThT spectroscopy assay confirmed the cross- β -sheet conformation of both hydrogels in the presence of sitagliptin (**Figure 5D**). In the same way, frequency sweep tests of the resulting RADA16-HP-sitagliptin and RADA16-HT-sitagliptin hydrogels revealed elastic moduli of 486 and 1,028 Pa, respectively (**Figure 5E**), indicating that they still maintain viscoelastic profiles similar to those of RADA16-HT and RADA16-HP samples. Lastly, an insight of the RADA16 nanofibers bundles formation trapped with hempseed peptides and sitagliptin is provided through a cartoon model as depicted on **Figure 5F**.

In summary, these results underline one important aspect, namely that RADA16-hempseed hydrolysates hydrogels are not only good sitagliptin delivery carriers, but are also active as DPPIV inhibitors suggesting that the combination of sitagliptin with food protein based hydrogels may help reducing drug dosage and their potential side-effects.

CONCLUSION

This work offers a new route for the formulation of nano-nutraceuticals entirely made of biocompatible/bioabsorbable SAP based-hydrogels and bioactive hydrolysates to be exploited in diabetes and metabolic diseases prevention.

METHODS

Materials

Fmoc-Arg(Pbf)-OH, Fmoc-Ala-OH, and Fmoc-Asp(OtBu)-OH were purchased from the Aapptec (Louisville, USA)

and used as received. N,N-dimethylformamide (DMF), N,N-diisopropylethylamine (DIPEA), N-methyl-2-pyrrolidone (NMP), trifluoroacetic acid (TFA) and triisopropylsilane were purchased from VWR (Radnor, USA). N,N,N',N'-tetramethyl-O-(1H-benzotriazol-1-yl)uronium hexafluorophosphate (HBTU), 1-hydroxybenzotriazole hydrate (HOBt), 4-methylpiperidin and Thioflavin T were purchased from Sigma-Aldrich. HPLC grade water (resistivity $18 \text{ M}\Omega \text{ cm}$) and DPBS (pH 7.4) were purchased from Thermo Fisher scientific (Waltham, USA).

Production of HT and HP Hydrolysates

HT and HP hydrolysates were obtained extracting the proteins from the seeds of *Cannabis sativa* cultivar Futura, by hydrolyzing them with pepsin or trypsin and by analyzing them as described elsewhere (Aiello et al., 2017; Zanoni et al., 2017).

In vitro DPPIV Activity Assay

The experiments were carried out using a procedure previously reported (Lammi et al., 2018). Briefly, 0.5 and 1.0 mg mL^{-1} of HT and HP hydrolysates were tested *in vitro* using the purified recombinant DPP-IV enzyme and fluorescent substrate (AMC-Gly-Pro, ex/em 360/465 nm). Fluorescence signals were measured using the Synergy H1 from Biotek (Bad Friedrichshall, Germany). More details are reported in the **Supplementary Materials**.

Cell Culture

Caco-2 cells, obtained from INSERM (Paris), were cultured at 50% density following the procedure previously reported (Lammi et al., 2018). More details are reported in the **Supplementary Materials**.

In situ DPPIV Activity Assay

HT and HP hydrolysates were tested on Caco-2 cells (5×10^4 /well in black 96-well plates) at 1.0 mg mL^{-1} or vehicle in growth medium for 24 h at 37°C , following the method previously optimized and reported (Lammi et al., 2018). For 2D cell culture on RADA16-HT and RADA-HP hydrogels, Caco-2 cells were seeded on the surface of the above mentioned

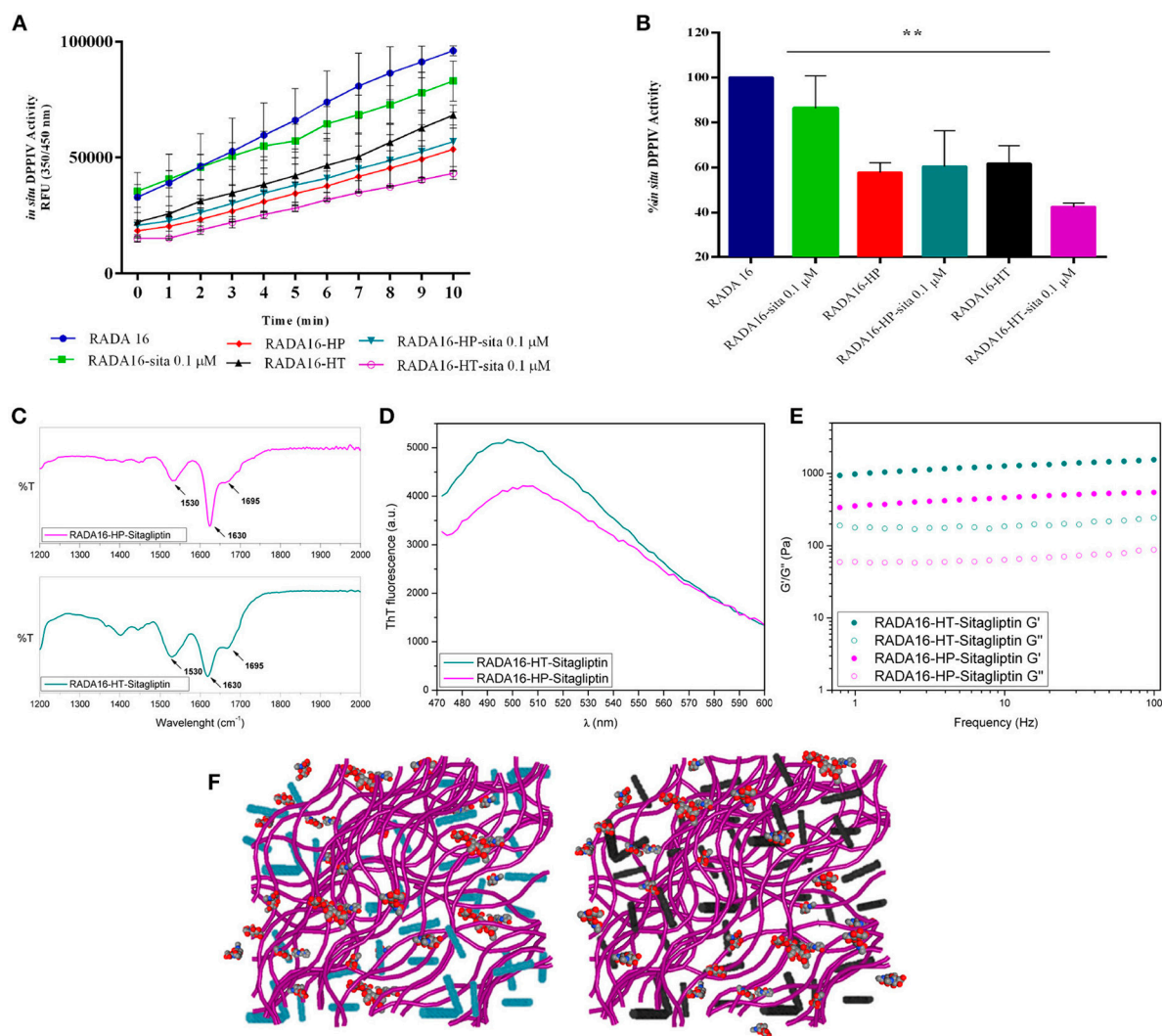


FIGURE 5 | Synergistic effect of RADA16-hempseed hydrolysates with sitagliptin as DPPIV inhibitor in the Caco-2 cells. **(A)** Kinetics of the degradation of substrate Gly-Pro-AMC catalyzed by DPPIV. In respect to the control sample (RADA16-hydrogel), the DPPIV activity is slightly decreased when Caco-2 cells are incubated with RADA16 hydrogel containing 0.1 μ M sitagliptin and it is much more reduced when cells are treated with either RADA16-HT or RADA16-HP hydrogels with or without 0.1 μ M sitagliptin. **(B)** DPPIV activity after incubating Caco-2 cells with different hydrogels (at 5 min). The RADA16 hydrogel containing 0.1 μ M sitagliptin reduced the DPPIV activity by $13.2 \pm 8.3\%$ vs. pure RADA16, whereas RADA16-HT and RADA16-HP alone drop the enzyme activity by 38.3 ± 5.6 and $42.2 \pm 3.0\%$, respectively. RADA16-HT and RADA16-HP containing 0.1 μ M sitagliptin reduced the enzyme activity by 56.4 ± 0.8 and $40.0 \pm 9.1\%$, respectively. **(C,D)** Structural properties of RADA16-HT-sitagliptin (cyan) and RADA16-HP-sitagliptin (magenta) hydrogels. The ATR-FTIR structural analysis highlighted typical β -sheet signature in the Amide I and Amide II regions. ThT spectroscopy assay confirmed the cross- β -sheet conformation of both hydrogels in presence of sitagliptin. **(E)** Rheological characterization of RADA16-HT-sitagliptin and RADA16-HP-sitagliptin hydrogels monitored by frequency sweep tests (0.1–100 Hz) revealed elastic moduli of 1,028 Pa and 486 Pa, respectively. Both samples maintained viscoelastic profiles similar to those of RADA16-HT and RADA16-HP hydrogels along the tested frequency range at low strains (1%). **(F)** Cartoon models of RADA16-HT-Sitagliptin (left) and RADA16-HP-Sitagliptin (right) peptide based hydrogels. RADA16 network of nanofibers is shown in purple, HT peptides in cyan, HP peptides in dark gray and sitagliptin is shown as spheres representation. ** $p > 0.01$.

hydrogels at the density of 5×10^4 /well; on the day after the spent media were removed and cells were washed with 100 μ L of PBS without Ca^{++} and Mg^{++} , and 100 μ L of DPPIV substrate at the concentration of 50.0 μ M in PBS without Ca^{++} and Mg^{++} were added in each well. Fluorescence signals (ex./em. 350/450 nm) were measured using the Synergy H1 from Biotek every 1 min for 10 min.

Ex vivo DPP-IV Activity Assay

A volume of 40 μ L of serum samples was loaded in each well of the black 96-well plates and 10 μ L of the $5 \times$ HT and HP hydrolysates were spiked in order to have the final concentration of 1.0 mg mL^{-1} in the total volume of 50 μ L. For hydrogel experiments, 40 μ L of human serum samples were incubated with RADA16-HT and RADA-HP. Samples were then

incubated for 24 h at 37°C. Subsequently, 50 μL of the AMC-Gly-Pro at the initial concentration of 100 μM were added in each well in order to obtain the final 50 μM substrate concentration in the final volume of 100 μL . Fluorescence signals (ex/em. 350/450 nm) were measured using the Synergy H1 every 1 min for 10 min.

Determination of HT and HP Peptides Release From the Hydrogels

The peptide leaking from the hydrogels as a function of time was measured according to a method previously described (Goa, 1953; Lammi et al., 2016a). Briefly, a sterile solution of peptone from casein at 10 mg mL^{-1} in water was prepared and used as standard for the calibration curves. Thus, a solution of X μL of HT and HP peptides contained in the hydrogels after 1, 3, and 6 h of incubation and/or peptone mixture, (100 – X) μL water, 95 μL 6% (w/w) NaOH in water, and 9.5 μL of active reagent (containing 0.6 M sodium citrate, 0.9 M sodium carbonate, and 0.07 M copper sulfate, 2.4 M NaOH, pH 10.6) was prepared. The reaction mixture was incubated for 15 min at RT and the absorbance was measured at 330 nm using the Synergy H1 plate reader.

Peptide Synthesis and Purification

RADA16 was synthesized by solid-phase Fmoc-based chemistry on Rink amide 4-methyl-benzhydrylamine resin (0.5 mmol g^{-1} substitution) using the Liberty-Discovery (CEM) microwave automated synthesizer (Matthews, USA), as previously described (Gelain et al., 2010).

Assembly of RADA16 Embedded With Hemp-Protein Hydrolysates

The purified RADA16 was dissolved at 10 mg mL^{-1} in distilled water, sonicated for 30 min, and incubated at 4°C for 24 h. HT and HP hydrolysates were dissolved at 1.0 mg mL^{-1} in distilled water. Sitagliptin was used at a final concentration of 0.1 μM . The RADA16 solution was then mixed with HT and HP solutions at a ratio of 3:1 (v/v), whereas RADA16 was mixed with the solution containing both hempseed hydrolysates and sitagliptin at a final ratio of 3:0.5:0.5 (v/v).

Spectroscopic Analysis

FT-IR analysis of assembled nanostructures was performed on peptides dissolved at a concentration of 1% (w/v) in distilled water, after 24 h incubation at 4°C. All spectra were collected in attenuated total reflection (ATR) using Perkin Elmer Spectrum 100 spectrometer. All the collected spectra were reported after ATR correction, smoothing, and automatic baseline correction using OriginTM8 software. Each sample was analyzed in triplicate. In order to assess the presence of cross- β fibril structures, ThT binding assay was monitored by exciting the sample at 440 nm (5 nm band-pass) and recording the emission fluorescence spectrum from 460 to 600 nm.

Rheological Tests

Rheological properties of assembled nanostructures were carried out using a controlled stress AR-2000ex Rheometer (TA instruments). A truncated cone-plate geometry (acrylic truncated diameter, 20 mm; angle, 1°; truncation gap, 34 μm) was used. All measurements were obtained at 25°C using a Peltier cell as a lower plate of the instrument to keep the temperature controlled during each test. All samples were tested 1 day after dissolution at the concentration of 1% (w/v). Frequency sweep experiments were recorded as a function angular frequency (0.1–100 Hz) at a fixed strain of 1%. Strain sweeps were performed on samples from 0.01% to a maximum strain of 1,000% for determining the limit of the linear viscoelastic region and the maximum strain to which the sample can be subjected. Each experiment was performed in triplicate.

Atomic Force Microscopy

AFM tests were performed in tapping mode by a Multimode Nanoscope V (Digital Instrument, Veeco), using a single-beam silicon cantilever probes (Veeco RFESP MPP-21100-10, cantilever f0, resonance frequency 59–69 KHz, constant force 3 N m^{-1}), as previously described (Pugliese et al., 2018a).

Statistical Analysis

Statistical analyses were carried out by t-student and One-way ANOVA using Graphpad Prism 6 (Graphpad, La Jolla, CA, USA) followed by Dunnett's test. Values were expressed as means \pm SD; $P < 0.05$ were considered to be significant.

AUTHOR CONTRIBUTIONS

CL and RP conceived the project and designed the experiments. CL performed all *in vitro*, *in situ*, and *ex vivo* tests and the preparation of hempseed hydrolysates. CB performed technical work in the bioactivity characterization. RP synthesized the RADA16 peptide and carried out all structural, morphological, and biomechanical experiments. FG co-supervised the SAP characterizations. CL, AA, and RP wrote the manuscript.

FUNDING

Supported by the Fondazione Cariplo, project SUPER-HEMP: Sustainable Process for Enhanced Recovery of Hempseed Oil.

ACKNOWLEDGMENTS

We are indebted to Carlo Sirtori Foundation (Milan, Italy) for having provided part of equipment used in this experimentation.

SUPPLEMENTARY MATERIAL

The Supplementary Material for this article can be found online at: <https://www.frontiersin.org/articles/10.3389/fchem.2018.00670/full#supplementary-material>

REFERENCES

- Abbott, C. A., Baker, E., Sutherland, G. R., and McCaughan, G. W. (1994). Genomic organization, exact localization, and tissue expression of the human CD26 (dipeptidyl peptidase IV) gene. *Immunogenetics* 40, 331–338. doi: 10.1007/BF01246674
- Aiello, G., Fasoli, E., Boschin, G., Lammi, C., Zanoni, C., Citterio, A., et al. (2016). Proteomic characterization of the protein-rich seed of *Cannabis sativa*. *J. Proteomics* 147, 187–119. doi: 10.1016/j.jprot.2016.05.033
- Aiello, G., Lammi, C., Boschin, G., Zanoni, C., and Arnoldi, A. (2017). Exploration of potentially bioactive peptides generated from the enzymatic hydrolysis of hempseed proteins. *J. Agric. Food Chem.* 65, 10174–10184. doi: 10.1021/acs.jafc.7b03590
- Arnoldi, A., Zanoni, C., Lammi, C., and Boschin, G. (2015). The role of grain legumes in the prevention of hypercholesterolemia and hypertension. *Crit. Rev. Plant Sci.* 34, 144–168. doi: 10.1080/07352689.2014.897908
- Biancalana, M., and Koide, S. (2010). Molecular mechanism of Thioflavin-T binding to amyloid fibrils. *Biochim. Biophys. Acta* 1804, 1405–1412. doi: 10.1016/j.bbapap.2010.04.001
- Bolat, G., Abaci, S., Vural, T., Bozdogan, B., and Denkbaz, E. B. (2018). Sensitive electrochemical detection of fenitrothion pesticide based on self-assembled peptide-nanotubes modified disposable pencil graphite electrode. *J. Electroanal. Chem.* 809, 88–95. doi: 10.1016/j.jelechem.2017.12.060
- Doupis, J., and Veves, A. (2008). DPP4 inhibitors: a new approach in diabetes treatment. *Adv. Ther.* 25, 627–643. doi: 10.1007/s12325-008-0076-1
- Gelain, F., Unsworth, L. D., and Zhang, S. (2010). Slow and sustained release of active cytokines from self-assembling peptide scaffolds. *J. Control Release* 145, 231–239. doi: 10.1016/j.jconrel.2010.04.026
- Girgih, A. T., Alashi, A., He, R., Malomo, S., and Aluko, R. E. (2014a). Preventive and treatment effects of a hemp seed (*Cannabis sativa* L.) meal protein hydrolysate against high blood pressure in spontaneously hypertensive rats. *Eur. J. Nutr.* 53, 1237–1246. doi: 10.1007/s00394-013-0625-4
- Girgih, A. T., Alashi, A. M., He, R., Malomo, S. A., Raj, P., Netticadan, T., et al. (2014b). A novel hemp seed meal protein hydrolysate reduces oxidative stress factors in spontaneously hypertensive rats. *Nutrients* 6, 5652–5666. doi: 10.3390/nu6125652
- Girgih, A. T., Udenigwe, C. C., and Aluko, R. E. (2011). *In vitro* antioxidant properties of hemp seed (*Cannabis sativa* L.) protein hydrolysate fractions. *J. Am. Oil Chem. Soc.* 88, 381–389. doi: 10.1007/s11746-010-1686-7
- Girgih, A. T., Udenigwe, C. C., and Aluko, R. E. (2013). Reverse-phase HPLC separation of hemp seed (*Cannabis sativa* L.) protein hydrolysate produced peptide fractions with enhanced antioxidant capacity. *Plant Foods Hum. Nutr.* 68, 39–46. doi: 10.1007/s11130-013-0340-6
- Goa, J. (1953). A micro biuret method for protein determination; determination of total protein in cerebrospinal fluid. *Scand. J. Clin. Lab. Invest.* 5, 218–222. doi: 10.3109/00365515309094189
- Hatanaka, T., Inoue, Y., Arima, J., Kumagai, Y., Usuki, H., Kawakami, K., et al. (2012). Production of dipeptidyl peptidase IV inhibitory peptides from defatted rice bran. *Food Chem.* 134, 797–802. doi: 10.1016/j.foodchem.2012.02.183
- Koutsopoulos, S., Unsworth, L. D., Nagai, Y., and Zhang, S. (2009). Controlled release of functional proteins through designer self-assembling peptide nanofiber hydrogel scaffold. *Proc. Natl. Acad. Sci. U.S.A.* 106, 4623–4628. doi: 10.1073/pnas.0807506106
- Lacroix, I. M., and Li-Chan, E. C. (2015). Comparison of the susceptibility of porcine and human dipeptidyl-peptidase IV to inhibition by protein-derived peptides. *Peptides* 69, 19–25. doi: 10.1016/j.peptides.2015.03.016
- Lacroix, I. M. E., and Li-Chan, E. C. Y. (2012). Dipeptidyl peptidase-IV inhibitory activity of dairy protein hydrolysates. *Int. Dairy J.* 25, 97–102. doi: 10.1016/j.idairyj.2012.01.003
- Lammi, C., Aiello, G., Vistoli, G., Zanoni, C., Arnoldi, A., Sambuy, Y., et al. (2016a). A multidisciplinary investigation on the bioavailability and activity of peptides from lupin protein. *J. Funct. Foods* 24, 297–306. doi: 10.1016/j.jff.2016.04.017
- Lammi, C., Bollati, C., Ferruzza, S., Ranaldi, G., Sambuy, Y., and Arnoldi, A. (2018). Soybean- and lupin-derived peptides inhibit DPP-IV activity on *in situ* human intestinal caco-2 cells and *ex vivo* human serum. *Nutrients* 10:E1082. doi: 10.3390/nu10081082
- Lammi, C., Zanoni, C., Arnoldi, A., and Vistoli, G. (2016b). Peptides derived from soy and lupin protein as Dipeptidyl-Peptidase IV inhibitors: *in vitro* biochemical screening and *in silico* molecular modeling study. *J. Agric. Food Chem.* 64, 9601–9606. doi: 10.1021/acs.jafc.6b04041
- Lammi, C., Zanoni, C., Scigliuolo, G. M., D'Amato, A., and Arnoldi, A. (2014). Lupin peptides lower low-density lipoprotein (LDL) cholesterol through an up-regulation of the LDL receptor/sterol regulatory element binding protein 2 (SREBP2) pathway at HepG2 cell line. *J. Agric. Food Chem.* 62, 7151–7159. doi: 10.1021/jf500795b
- Li-Chan, E. C., Hunag, S. L., Jao, C. L., Ho, K. P., and Hsu, K. C. (2012). Peptides derived from atlantic salmon skin gelatin as dipeptidyl-peptidase IV inhibitors. *J. Agric. Food Chem.* 60, 973–978. doi: 10.1021/jf204720q
- Lopalco, A., and Denora, N. (2018). Nanoformulations for Drug delivery: safety, toxicity, and efficacy. *Methods Mol. Biol.* 1800, 347–365. doi: 10.1007/978-1-4939-7899-1_17
- Malomo, S. A., Onuh, J. O., Girgih, A. T., and Aluko, R. E. (2015). Structural and antihypertensive properties of enzymatic hemp seed protein hydrolysates. *Nutrients* 7, 7616–7632. doi: 10.3390/nu7095358
- Nargis, T., and Chakrabarti, P. (2018). Significance of circulatory DPP4 activity in metabolic diseases. *IUBMB Life* 70, 112–119. doi: 10.1002/iub.1709
- Nauck, M. A., Baller, B., and Meier, J. J. (2004). Gastric inhibitory polypeptide and glucagon-like peptide-1 in the pathogenesis of type 2 diabetes. *Diabetes* 53(Suppl. 3), S190–S196. doi: 10.2337/diabetes.53.suppl_3.S190
- Nongonierma, A. B., and Fitzgerald, R. J. (2015a). Investigation of the potential of hemp, pea, rice and soy protein hydrolysates as a source of Dipeptidyl Peptidase IV (DPP-IV) inhibitory peptides. *Food Dig. Res. Curr. Opin.* 6, 19–29. doi: 10.1007/s13228-015-0039-2
- Nongonierma, A. B., and Fitzgerald, R. J. (2015b). Utilisation of the isobole methodology to study dietary peptide-drug and peptide-peptide interactive effects on dipeptidyl peptidase IV (DPP-IV) inhibition. *Food Funct.* 6, 313–320. doi: 10.1039/C4FO00883A
- Nongonierma, A. B., Mazzocchi, C., Paoletta, S., and Fitzgerald, R. J. (2017). Release of dipeptidyl peptidase IV (DPP-IV) inhibitory peptides from milk protein isolate (MPI) during enzymatic hydrolysis. *Food Res. Int.* 94, 79–89. doi: 10.1016/j.foodres.2017.02.004
- Nongonierma, A. B., Paoletta, S., Mudgil, P., Maqsood, S., and Fitzgerald, R. J. (2018). Identification of novel dipeptidyl peptidase IV (DPP-IV) inhibitory peptides in camel milk protein hydrolysates. *Food Chem.* 244, 340–348. doi: 10.1016/j.foodchem.2017.10.033
- Park, K. (2014). Controlled drug delivery systems: past forward and future back. *J. Control Release* 190, 3–8. doi: 10.1016/j.jconrel.2014.03.054
- Pugliese, R., Fontana, F., Marchini, A., and Gelain, F. (2018a). Branched peptides integrate into self-assembled nanostructures and enhance biomechanics of peptidic hydrogels. *Acta Biomater.* 66, 258–271. doi: 10.1016/j.actbio.2017.11.026
- Pugliese, R., and Gelain, F. (2017). Peptidic biomaterials: from self-assembling to regenerative medicine. *Trends Biotechnol.* 35, 145–158. doi: 10.1016/j.tibtech.2016.09.004
- Pugliese, R., Marchini, A., Saracino, G. A., and Gelain, F. (2018b). “Functionalization of self-assembling peptides for neural tissue engineering,” in *Molecular Design, Characterization and Application in Biology and Medicine*, eds H. S. Azevedo and R. M. P. da Silva (Woodhead Publishing Series in Biomaterials), 475–493. doi: 10.1016/B978-0-08-102015-9.00023-X
- Röhrborn, D., Wronkowitz, N., and Eckel, J. (2015). DPP4 in diabetes. *Front. Immunol.* 6:386. doi: 10.3389/fimmu.2015.00386
- Tao, K., Makam, P., Aizen, R., and Gazit, E. (2017). Self-assembling peptide semiconductors. *Science* 358:eaam9756. doi: 10.1126/science.aam9756

- Yokoi, H., Kinoshita, T., and Zhang, S. (2005). Dynamic reassembly of peptide RADA16 nanofiber scaffold. *Proc. Natl. Acad. Sci. U.S.A.* 102, 8414–8419. doi: 10.1073/pnas.0407843102
- Zanoni, C., Aiello, G., Arnoldi, A., and Lammi, C. (2017). Hempseed peptides exert hypocholesterolemic effects with a statin-like mechanism. *J. Agric. Food Chem.* 65, 8829–8838. doi: 10.1021/acs.jafc.7b02742
- Zhang, S. (2003). Fabrication of novel biomaterials through molecular self-assembly. *Nat. Biotechnol.* 21, 1171–1178. doi: 10.1038/nbt874
- Zhang, S., Holmes, T., Lockshin, C., and Rich, A. (1993). Spontaneous assembly of a self-complementary oligopeptide to form a stable macroscopic membrane. *Proc. Natl. Acad. Sci. U.S.A.* 90, 3334–3338 doi: 10.1073/pnas.90.8.3334

Conflict of Interest Statement: The authors declare that the research was conducted in the absence of any commercial or financial relationships that could be construed as a potential conflict of interest.

Copyright © 2019 Lammi, Bollati, Gelain, Arnoldi and Pugliese. This is an open-access article distributed under the terms of the Creative Commons Attribution License (CC BY). The use, distribution or reproduction in other forums is permitted, provided the original author(s) and the copyright owner(s) are credited and that the original publication in this journal is cited, in accordance with accepted academic practice. No use, distribution or reproduction is permitted which does not comply with these terms.

Advantages of publishing in Frontiers



OPEN ACCESS

Articles are free to read
for greatest visibility
and readership



FAST PUBLICATION

Around 90 days
from submission
to decision



HIGH QUALITY PEER-REVIEW

Rigorous, collaborative,
and constructive
peer-review



TRANSPARENT PEER-REVIEW

Editors and reviewers
acknowledged by name
on published articles

Frontiers

Avenue du Tribunal-Fédéral 34
1005 Lausanne | Switzerland

Visit us: www.frontiersin.org

Contact us: info@frontiersin.org | +41 21 510 17 00



REPRODUCIBILITY OF RESEARCH

Support open data
and methods to enhance
research reproducibility



DIGITAL PUBLISHING

Articles designed
for optimal readership
across devices



FOLLOW US

@frontiersin



IMPACT METRICS

Advanced article metrics
track visibility across
digital media



EXTENSIVE PROMOTION

Marketing
and promotion
of impactful research



LOOP RESEARCH NETWORK

Our network
increases your
article's readership